ADVANCES IN ANALYTICAL TECHNIQUES AND METHODOLOGY FOR CHEMICAL SPECIATION STUDY

EDITED BY: Ottavia Giuffrè, Carlos Rey-Castro and Anna Napoli
PUBLISHED IN: Frontiers in Chemistry

frontiers Research Topics

frontiers

ISSN 1664-8714
ISBN 978-2-88966-978-3
DOI 10.3389/978-2-88966-978-3

About Frontiers

Frontiers is more than just an open-access publisher of scholarly articles: it is a pioneering approach to the world of academia, radically improving the way scholarly research is managed. The grand vision of Frontiers is a world where all people have an equal opportunity to seek, share and generate knowledge. Frontiers provides immediate and permanent online open access to all its publications, but this alone is not enough to realize our grand goals.

Frontiers Journal Series

The Frontiers Journal Series is a multi-tier and interdisciplinary set of open-access, online journals, promising a paradigm shift from the current review, selection and dissemination processes in academic publishing. All Frontiers journals are driven by researchers for researchers; therefore, they constitute a service to the scholarly community. At the same time, the Frontiers Journal Series operates on a revolutionary invention, the tiered publishing system, initially addressing specific communities of scholars, and gradually climbing up to broader public understanding, thus serving the interests of the lay society, too.

Dedication to Quality

Each Frontiers article is a landmark of the highest quality, thanks to genuinely collaborative interactions between authors and review editors, who include some of the world's best academicians. Research must be certified by peers before entering a stream of knowledge that may eventually reach the public - and shape society; therefore, Frontiers only applies the most rigorous and unbiased reviews.
Frontiers revolutionizes research publishing by freely delivering the most outstanding research, evaluated with no bias from both the academic and social point of view. By applying the most advanced information technologies, Frontiers is catapulting scholarly publishing into a new generation.

What are Frontiers Research Topics?

Frontiers Research Topics are very popular trademarks of the Frontiers Journals Series: they are collections of at least ten articles, all centered on a particular subject. With their unique mix of varied contributions from Original Research to Review Articles, Frontiers Research Topics unify the most influential researchers, the latest key findings and historical advances in a hot research area! Find out more on how to host your own Frontiers Research Topic or contribute to one as an author by contacting the Frontiers Editorial Office: frontiersin.org/about/contact

ADVANCES IN ANALYTICAL TECHNIQUES AND METHODOLOGY FOR CHEMICAL SPECIATION STUDY

Topic Editors:
Ottavia Giuffrè, University of Messina, Italy
Carlos Rey-Castro, Universitat de Lleida, Spain
Anna Napoli, University of Calabria, Italy

Citation: Giuffrè, O., Rey-Castro, C., Napoli, A., eds. (2021). Advances in Analytical Techniques and Methodology for Chemical Speciation Study.
Lausanne: Frontiers Media SA. doi: 10.3389/978-2-88966-978-3

Table of Contents

frontiers in Chemistry

EDITORIAL
published: 10 May 2021
doi: 10.3389/fchem.2021.692144

Editorial: Advances in Analytical Techniques and Methodology for Chemical Speciation Study

Ottavia Giuffrè [1], Anna Napoli [2]* and Carlos Rey-Castro [3]**

[1] *Dipartimento di Scienze Chimiche, Biologiche, Farmaceutiche ed Ambientali, Università di Messina, Messina, Italy,* [2] *Dipartimento di Chimica e Tecnologie Chimiche, Università della Calabria, Arcavacata di Rende, Italy,* [3] *Departament de Química, Universitat de Lleida and AGROTECNIO-CERCA, Lleida, Spain*

Keywords: speciation and sequestering ability, remediation techniques, chelation therapy, modeling and computational approach, sensors

Editorial on the Research Topic

Advances in Analytical Techniques and Methodology for Chemical Speciation Study

On the basis of the International Union for Pure and Applied Chemistry (IUPAC) definition "speciation analysis" involves those "analytical activities of identifying and/or measuring the quantities of one or more individual chemical species in a sample". "Speciation of an element" is also defined as "distribution of an element amongst defined chemical species in a system" (Templeton et al., 2000; Templeton and Fujishiro, 2017). It is now established that speciation studies in aqueous media are crucial for assessing species toxicity and bioavailability, biogeochemical cycling, and many biological phenomena. Novel studies in this field include a multidisciplinary approach *via* the use of different experimental analytical techniques as well as their combination with simulation methods.

Several examples of speciation of metal cations in aquatic environment are reported in this Research Topic. The speciation of trace metals aquatic systems includes the determination of free ions, metal complexes, colloidal species, etc., as well as the total dissolved concentration. The integrated assessment of free ions and labile metal complexes can be obtained by Diffusive Gradients in Thin-films (DGT), a dynamic speciation technique. The determination of the organic pools of trace metals in freshwaters and the characterization of organic and inorganic complexes in sea waters were obtained by this procedure (Galceran et al.). For organic Cu speciation, an improved anodic stripping voltammetry (ASV) method, employed to eliminate the surface-active substances (SAS) interference on the voltammetric signal, was used in samples containing high organic matter concentration. Fulvic acid was used as a model of natural organic matter and the method was applied for Cu speciation in samples collected in the Arno River estuary (Italy) (Padan et al.). The binding of Cd(II), Pb(II), and Zn(II) by silica nanoparticles was studied using a combination of the electroanalytical techniques Scanned Stripping ChronoPotentiometry (SSCP) and Absence of Gradients and Nernstian Equilibrium Stripping (AGNES). The experimental system was chosen as a representative model for the role of natural and anthropogenic nanoparticles in the fate and behavior of trace metals in aqueous environmental systems (Rotureau et al.).

Speciation studies on the interaction of metal cations with ligands having multiple binding sites, such as tannic acid, a natural polyphenolic compound, and phytate ligand, are very important for the fate of those metals. In the study regarding tannic acid, the approach used combines UV-vis and fluorescence spectroscopy with chemometrics, namely Multivariate Curve Resolution-Alternating Least Squares (MCR-ALS) and Parallel Factor Analysis

OPEN ACCESS

Edited and reviewed by:
Paolo Oliveri,
University of Genoa, Italy

****Correspondence:***
Ottavia Giuffrè
ogiuffre@unime.it
Anna Napoli
amc.napoli@unical.it
Carlos Rey-Castro
carlos.rey@udl.cat

Specialty section:
This article was submitted to Analytical Chemistry, a section of the journal Frontiers in Chemistry

Received: *07 April 2021*
Accepted: *12 April 2021*
Published: *10 May 2021*

Citation:
Giuffrè O, Napoli A and Rey-Castro C (2021) Editorial: Advances in Analytical Techniques and Methodology for Chemical Speciation Study. Front. Chem. 9:692144. doi: 10.3389/fchem.2021.692144

(PARAFAC) (Berto and Alladio). The investigation of the interaction of phytate ligand with biologically relevant cations, namely Mg^{2+}, Zn^{2+}, Fe^{2+}, Cu^{+}, and Cu^{2+} revealed that alkaline earth metals interact with different binding sites than the transition metals. Experiments with Cu^{+}, and Cu^{2+} confirmed similar complexing behaviors, depending mainly on the ionic radius (Marolt et al.).

Metal speciation can be also performed by Electrospray Ionization Mass Spectrometry (ESI-MS). In this field, MS-MS approach guarantees exceptional sensitivity, as well as the use of high-resolution sectors, capable of well-resolving isotopic clusters. A further development is the merging of ESI-MS information with data obtained *via* synergistic techniques, as ICP-MS, NMR, X-RAY, CLE-ACSV, Ab-Initio, or DFT quantum mechanical calculations (Indelicato et al.). The necessary degree of specificity in discriminating all the species of a given element in a sample can be attained by ultrahigh-resolution mass spectrometry based on the Fourier transformation, Orbitrap and Ion Cyclotron Resonance (ICR) cell. The case of the speciation analysis of the products of selenium metabolism by FT ICR MS was described (Bierla et al.). Metal speciation can be also performed by MALDI-MS and tandem mass spectrometry (MS-MS). The results obtained for Ca^{2+} interaction with biologically relevant ligands, as cysteine, D-penicillamine, reduced glutathione, and oxidized glutathione obtained by potentiometry and ^{1}H-NMR spectroscopy were confirmed by MALDI-MS and MS-MS, elucidating also the mechanism of interaction (Aiello et al.).

Speciation studies also include the search for novel drug delivery systems able to improve the performance of old-generation antibiotics. For example, the capability of two micellar polycationic calix[4]arene derivatives to recognize and host ofloxacin, chloramphenicol, or tetracycline in aqueous solution was investigated by nano-isothermal titration calorimetry, dynamic light scattering, and mono- and bi-dimensional NMR. Results evidenced that the formation of the chloramphenicol–micelle adduct is enthalpy driven, whereas entropy drives the formation of the adducts with both ofloxacin and tetracycline. NMR spectra confirmed ITC data about the positioning of the antibiotics in the calixarene nanoaggregates (Migliore et al.).

Speciation studies are also very useful for the development of techniques for the decontamination of natural waters and soils containing toxic metals. In recent years, many efforts have been made to discover new technologies that are effective, robust, cost-effective and easy to handle for the decontamination of downstream water without endangering human health. Among nanomaterials and nanostructures proposed in the remediation field, graphene-based materials (G), are particularly suitable for the development of reliable water decontamination treatments, in particular for arsenic remediation (Foti et al.). Different methodologies are employed for soil remediation. Among them, the use of chelating agents is one of the most promising method for removal of metal ions preserving the most meaningful properties of the original soils. One of these methodologies, the Nurchi's method, an extension of the Reilley procedure for EDTA titrations, is based on speciation studies, namely on the knowledge of the related protonation and complex formation constants. Its employment in biomedical and industrial applications is also discussed, namely in the evaluation of the role of different biomolecules such as bacterial metallophores, in metal uptake and homeostasis in living organism (Nurchi et al.).

Determination of organic analytes such as urea or biotoxins in environmental and food samples using novel, advanced and combined analytical techniques was also performed. More in detail, the determination of saxitoxin in seawater samples was made by a novel flow injection microfluidic immunoassay system which allows *in situ* monitoring (Celio et al.). Ultra-trace urea in synthetic and real milk samples was determined by sensitive and selective methods using Fe/N-codoped carbon dots (CDFeN) and a probe with surface-enhanced Raman scattering (SERS), resonance Rayleigh scattering (RRS), and fluorescence (FL) signals (Li C. et al.). Novel methods for the monitoring of microcystins (MCs), one of the most common and harmful cyanotoxins, involve the use of aptasensors (aptamer-based biosensors) and immunosensors (antibody-based biosensors) for rapid, portable, easy-to-use, and on-site determinations (Wang et al.). Early diagnosis of diabetes on entire blood samples was performed *via* near-infrared spectra (NIRS) combined with a support vector machine (SVM) and aquaphotomics (Li Y. et al.).

Quality of milk was assessed by an innovative MicroNIR and chemometric platform for the on-site and contactless monitoring of the samples (Risoluti et al.).

This Research Topic emphasizes the recent methodological improvements made in quantifying and identifying (either explicitly or *via* indirect proxies) those specific chemical species in waters, soil solutions, biological fluids and food products, that provide the most relevant information in human health and environmental safety research. Altogether, these studies point to the wide possibilities underlying the combined use of active/passive sampling strategies, fractionation methods, orthogonal or hyphenated techniques and advanced multivariate analysis for the improvement of the accuracy and specificity of speciation data obtained in complex matrices.

AUTHOR CONTRIBUTIONS

All authors wrote the Editorial and reviewed it.

ACKNOWLEDGMENTS

We sincerely thank all the authors in this Research Topic for their contributions, as well as the reviewers for their selfless, rigorous, and impartial feedback. Finally, we hope readers will enjoy these articles as much as we have.

REFERENCES

Templeton, D. M., Ariese, F., Cornelis, R., Danielsson, L. G., Muntau, H., Van Leeuwen, H. P., et al. (2000). IUPAC guidelines for terms related to speciation of trace elements. *Pure Appl. Chem*. 72, 1453–1470. doi: 10.1351/pac200072081453

Templeton, D. M., and Fujishiro, H. (2017). Terminology of elemental speciation – an IUPAC perspective. *Coord. Chem. Rev*. 352, 424-431. doi: 10.1016/j.ccr.2017.02.002

Conflict of Interest: The authors declare that the research was conducted in the absence of any commercial or financial relationships that could be construed as a potential conflict of interest.

frontiers in Chemistry

ORIGINAL RESEARCH
published: 23 September 2020
doi: 10.3389/fchem.2020.582746

Complex Formation of Phytic Acid With Selected Monovalent and Divalent Metals

*Gregor Marolt, Ema Gričar, Boris Pihlar and Mitja Kolar**

Department of Analytical Chemistry, Faculty of Chemistry and Chemical Technology, Universitly of Ljubljana, Ljubljana, Slovenia

The formation of metal complexes with phytic acid is a complex process that depends strongly on the metal-to-ligand molar ratio, pH value and consequent protonation level of the phytate ligand as well as accompanying side reactions, in particular metal hydrolysis and precipitation of the formed coordination compounds. In the present work, the potentiometric titration technique was used in combination with a detailed analysis of the equivalent point dependencies for selected biologically relevant monovalent and divalent cations from the groups of alkaline earths and transition metals, namely: Mg(II), Zn(II), Fe(II), Cu(I), and Cu(II) ions. The investigation of complex formation mechanism, the evaluation of the species formed, and the identification of other side reactions was based on the examination of three distinct equivalent points, which were detectable by alkalimetric titrations of phytic acid in the presence of selected metal ions. It has been demonstrated that alkaline earth metals interact with different binding site(s) than the transition metals, and experiments with both oxidation states of copper revealed similar complexing characteristics, which depend mainly on the ionic radius (and not on the ionic charge as initially expected). Quantitative data on phytate complexation, hydroxide formation and complex precipitation are presented herein for all metals studied, including Cu(I), which was investigated for the first time by means of alkalimetric titration.

Keywords: phytic acid, inositol hexaphosphate, metal complexes, magnesium, zinc, iron, copper, phytate

OPEN ACCESS

Edited by:
Anna Napoli,
University of Calabria, Italy

Reviewed by:
Emilia Furia,
University of Calabria, Italy
Silvia Berto,
University of Turin, Italy

****Correspondence:***
Mitja Kolar
mitja.kolar@fkkt.uni-lj.si

Specialty section:
This article was submitted to Analytical Chemistry, a section of the journal Frontiers in Chemistry

Received: *13 July 2020*
Accepted: *17 August 2020*
Published: *23 September 2020*

Citation:
Marolt G, Gričar E, Pihlar B and Kolar M (2020) Complex Formation of Phytic Acid With Selected Monovalent and Divalent Metals. Front. Chem. 8:582746. doi: 10.3389/fchem.2020.582746

INTRODUCTION

Phytic acid ($H_{12}Phy$), a naturally occurring compound found in many biological systems (Sasakawa et al., 1995; Zi et al., 2000), is also known as *myo*-inositol 1,2,3,4,5,6-heksakis(dihydrogen phosphate) and consists of six phosphate esters with two protons per group (see structure in **Figure 1**), making it a unique molecule with 12 reversibly exchangeable protons that can be released depending on the experimental conditions, i.e., the pH and the presence of metal ions (De Stefano et al., 2004; Crea et al., 2007, 2008; Bretti et al., 2013). Because of its ability to form strong complexes with many metal ions (Evans and Pierce, 1982; Crea et al., 2008), phytic acid, as phytate in its various deprotonated states, is generally considered as an anti-nutrient when present in food (Oatway et al., 2001; Kumar et al., 2010), as it can interfere and thus reduce the bioavailability and consequent absorption of nutrients, including proteins (Cheryan and Rackis, 1980), carbohydrates (Yoon et al., 1984), lipids (Kumar et al., 2010), and minerals (Lopez et al., 2002), such as zinc(II), iron(II/III), calcium(II), magnesium(II), manganese(II), and copper(II) (Nissar et al., 2017). Many papers have also been dealing with antioxidant (Graf and Eaton, 1990) and anti-corrosive (Gao et al., 2014)

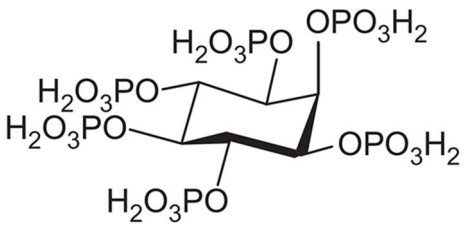

FIGURE 1 | Structure of phytic acid.

properties of phytic acid, as well as its environmental (Oatway et al., 2001) and biological (Sasakawa et al., 1995; Vucenik and Shamsuddin, 2003) roles.

These important (biological) properties and effects arise mostly from electrostatic interactions between negatively charged phytate species and metal cations and ability for their chelation (Crea et al., 2008). They have been studied by many researchers using various analytical techniques, including potentiometry (Torres et al., 2005; Šala et al., 2011; Marolt and Pihlar, 2015), spectrophotometry (Heighton et al., 2008), and NMR (Bebot-Brigaud et al., 1999) in combination with computational data analysis (Torres et al., 2008), which has led to numerous series of papers reporting the thermodynamic protonation and formation stability constants of phytic acid and its corresponding metal complexes (De Stefano et al., 2006; Crea et al., 2008). However, many useful information can be derived from these data, but it has been recently shown that a particular attention should be given to the precise standardization of phytic acid prior to measurements, since even a relatively small uncertainty in determination of concentration can cause significant deviations of the derived stability constants using computational methods (Marolt and Pihlar, 2015). As a supplement to the thermodynamic data, it has been shown that the detailed analysis of the titration curves provides additional information on the formation of metal complexes, particularly when other processes, such as precipitation and metal hydroxide formation, accompany the investigated complexation reactions (Šala et al., 2011; Marolt and Pihlar, 2015).

In the case of multiple oxidation states of metal ions, voltammetric methods have proven to be useful as they can provide complementary data on chelation mechanism, molar ratios, complex stability, and other accompanying processes (Torres et al., 2005). In this regard, cyclic voltammetry with the use of Au and HMDE as working electrodes has recently been applied for the detailed characterization of Fe(II) and Fe(III) phytate complexes (Marolt et al., 2015). The investigation of their reaction mechanism at different pH conditions showed a significantly higher stability as well as the predominance of phytate species with a lower protonation level for coordination compounds with trivalent iron ions compared to the divalent ions.

In this context, the aim of this study was to investigate the interactions between phytic acid and selected monovalent and divalent metal ions from the groups of alkaline earth and transition metals by alkalimetric potentiometric titrations. With the analysis of equivalent point(s) (EPs) dependence on the metal-to-ligand molar ratio, new complex formation data regarding complex stability, binding sites, and precipitation reactions are presented herein for selected biologically relevant metals, namely Mg(II), Zn(II), Fe(II), Cu(I), and Cu(II), in the form of coordination compounds with the phytate ligand. Fundamental titrimetric data represent an important contribution to the complete understanding of phytic acid complex formation mechanism, as well as complementary information to the existing literature, including for Cu(I) phytate coordination compounds, which to our knowledge, have not been investigated before.

MATERIALS AND METHODS

Aqueous solution of phytic acid was prepared by weighing the dipotassium salt (K_2H_{10}Phy, Sigma-Aldrich, min. 95%) and dissolving in ultrapure water with resistivity of > 18.2 MΩ/cm (Millipore/MilliQ system). The protonated form of phytate (i.e., H_{12}Phy) was obtained by passing the solution over a strong cation exchange resin (Dowex 50WX8) using a 100 mL preparative glass column and ∼40 g of resin which was wetted in ultrapure water overnight prior to the experiment. The amount of phytate added for each procedure was calculated considering its initial protonation level as well as the volume (∼75 mL) and capacity (1.7 meq/mL) of the wetted cation exchange resin. During the ion exchange procedure the column flow was set to 0.25 mL/min and the total contact time between phytate and resin was 5 h. An additional extension of the contact time (using a reduced flow) did not increase the protonation level of phytate, which was typically 11.5 ± 0.2. A differential alkalimetric standardization approach introduced by Marolt and Pihlar (2015) was used to accurately determine the phytic acid concentration (amount). The potassium, sodium, calcium and magnesium concentrations in the eluate were analyzed with an atomic absorption spectrometer (Varian AA240), and were all below 2.0×10^{-6} M after single ion exchange procedure. $MgCl_2 \cdot 6H_2O$ (Carlo Erba, p. a. grade), $ZnCl_2$ (Merck, p. a. grade), $FeSO_4$ (Sigma, p. a. grade), CuCl, and $CuCl_2$ (both Merck, p. a. grade) salts were used without further purification. Cu(I) and Fe(II) solutions were prepared in 0.20 M HCl which was previously deaerated with argon (purity 5.0) in order to prevent the formation of metal hydroxides and the oxidation of the metal ions with oxygen. Both solutions were kept in a dark room with continuous argon flow and used max. 24 h after the preparation. All titration curves were corrected for the contribution of the added HCl amount, subsequently.

The potentiometric titrations were carried out at 25 ± 1°C by automatic titrator Metrohm 799 GPT Titrino, equipped with a 20 mL burette (accuracy of the increment ± 0.5 μL), a carbon dioxide trap, a magnetic stirrer (Metrohm) and a combined glass electrode (Metrohm 6.0234.100, pH 0–14), calibrated with five buffer solutions (pH 2.00, 4.00, 7.00, 10.00, and 12.00, Merck). Titrations and calculations of titration curve derivatives were performed by TiNet 2.4 software (Metrohm). The titrant

was carbonate-free 0.10 M NaOH, which was prepared from concentrated NaOH (Carlo Erba, p. a. grade), dissolved in ultrapure water, deaerated with argon, and standardized weekly with potassium hydrogen phthalate primary standard (Merck). The initial volume of the solution in titration cell was set to 50.0 mL for all experiments.

In the case of Cu(I) and Fe(II), all solutions used, including phytic acid and titrant, were deaerated hitherto and the experiments were carried out in a tightly sealed titration (originally electrochemical) cell (Metrohm) with a constant argon flow. After performing the titration, a sample (1.0 mL) of the final solution was taken using 1 mL micropipette and transferred to a separate electrochemical cell with previously deaerated electrolyte (0.1 M KNO_3). Metrohm Autolab PGSTAT302N potentiostat was used in combination with 663 VA Stand, equipped with hanging mercury drop electrode (HMDE) as working, Ag/AgCl as reference, and Pt as counter electrode. Cyclic voltammogram (CV) was recorded starting from the open current potential (OCP) toward more negative potential in order to check for the absence/presence of oxidized metals, i.e., Cu(II) and Fe(III) ions, which could be possibly formed during the titration in case oxygen would have entered the cell. However, in all the studied cases, no such oxidized products were detected, confirming the stability of the reduced forms of selected metals, i.e., Cu(I) and Fe(II), which were thus kept in the cell throughout the titration procedure.

RESULTS AND DISCUSSION

Phytic Acid Titration and General Acid-Base Properties

As stated above, phytic acid in its fully protonated form ($H_{12}Phy$) consists of 12 exchangeable protons, and the protonation equilibrium of phytate (Phy^{12-}) is usually considered in the literature (De Stefano et al., 2004; Torres et al., 2005; Crea et al., 2008) by the following reaction:

$$H^+ + H_{i-1}Phy^{(12-i+1)-} \overset{K_i^H}{\longleftrightarrow} H_iPhy^{(12-i)-}, \quad (1)$$

where Phy^{12-}represents the completely deprotonated form of phytic acid and the index i is the number of protonation step, $0 \leq i \leq 12$. At constant ionic strength and temperature one can define the apparent protonation constant K_i^H, which is given according to the equilibrium (1):

$$K_i^H = \frac{[H_iPhy^{(12-i)-}]}{[H^+]\,[H_{i-1}Phy^{(12-i+1)-}]} \quad (2)$$

Large sets of thermodynamic speciation data, given as protonation constants of phytate at different experimental conditions, namely ionic strengths and temperatures, can be found in numerous publications (De Stefano et al., 2003a; Bretti et al., 2013) and collected in the review (Crea et al., 2008). However, in order to demonstrate the actual process of alkalimetric titration it is also suitable to write the general form of deprotonation of phytic acid:

$$H_{12}Phy + jOH^- \longleftrightarrow H_{12-j}Phy^{\,j-} + jH_2O, \quad (3)$$

where j represents the molar ratio between the added titrant and the phytate: $j = n(NaOH)/n(Phy)$, and can also be expressed as deprotonation step number. As reported before (Marini et al., 1981; Evans et al., 1982; Veiga et al., 2014; Marolt and Pihlar, 2015), the titration curve of phytic acid exhibits relatively complicated characteristics due to the high number of (de)protonation steps, and usually only some of them (2–4 deprotonation steps, depending on experimental conditions) are expressed as distinct EPs because of small differences between their corresponding K_i^H values and consequently smaller pH steps for given EPs. Therefore, the use of titration curve derivatives $\partial pH/\partial n(NaOH)$ is necessary for the determination of EPs. A similar behavior can be observed in **Figure 2** (at molar ratio $m = 0$), where three EPs have been distinguished for the titration of phytic acid in the absence of multivalent metal ions. EP1, EP2, and EP3 appear around pH 4, pH 8, and pH 10.5 and correspond to the 6th, 8th, and 12th deprotonation step (i.e., $j =$ 6, 8, and 12), respectively (Marolt and Pihlar, 2015):

$$H_{12}Phy + 6OH^- \longleftrightarrow H_6Phy^{6-} + 6H_2O \quad (4)$$

$$H_6Phy^{6-} + 2OH^- \longleftrightarrow H_4Phy^{8-} + 2H_2O \quad (5)$$

$$H_4Phy^{8-} + 4OH^- \longleftrightarrow Phy^{12-} + 4H_2O \quad (6)$$

On this basis, the exchangeable phytic acid protons can be divided into three groups according to their acidity (Marolt and Pihlar, 2015) and used for further analysis of the titration curves in the presence of metal ions:

- First group of the 6 most acidic protons with $log\ K_{7-12}^H < 2.7 \pm 0.1$, released before EP1
- Second group of 2 intermediate protons with an average $log\ K_{5-6}^H$ of 5.6 ± 0.6, released between EP1 and EP2
- Third group of the 4 most strongly bound protons with $log\ K_{1-4}^H > 8.0 \pm 0.1$, released between EP2 and EP3.

Another process, that can also accompany deprotonation and make the titration curve of the phytic acid even more complicated, is the pH-dependent inversion of the molecule from the equatorial (1a5e) to the axial (5a1e) orientation of 6 phosphate groups of phytate (Torres et al., 2008). This molecular switch is reported to appear between pH 9.0 and pH 9.5 and has been well-studied by Brigando et al. (1995) and by Veiga et al. (2014) using ^{31}P NMR titrations and molecular modeling in combination with NMR spectroscopy, respectively. When dealing with the analysis of phytic acid titration curves and EPs dependencies in combination with the addition of metal ions, all this knowledge is a prerequisite for the correct investigation of the formation of corresponding complexes.

Phytic Acid Interactions With Mg(II) Ions

Due to the high affinity of negatively charged phytate to various cations, the presence of mono- and multivalent metal ions affects the shape of the phytic acid titration curves and can therefore be used to identify the undergoing processes and the complex formation. As shown in **Figure 2A**, the addition of Mg(II) affects the shape of the whole titration curve of phytic acid, particularly in the range between EP1 and EP3, similar to the observations for Ca(II) interactions described in our previous work (Marolt

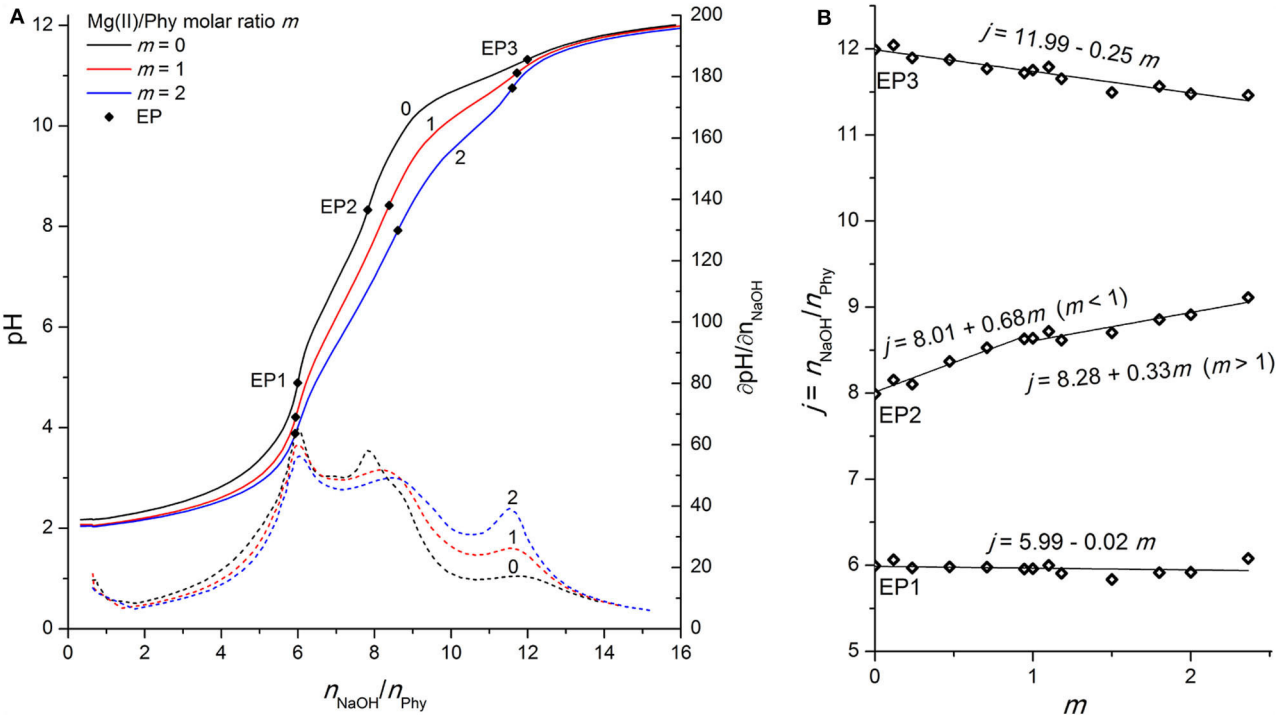

FIGURE 2 | (A) Titration of 0.1421 mmol H_{12}Phy with 0.1038 M NaOH at various molar ratios *m:* Mg(II)/Phy = 0:1, 1:1, and 2:1, accompanied by corresponding derivatives $\partial pH/\partial n$(NaOH); **(B)** Equivalents of NaOH per amount of phytic acid *j* consumed for individual equivalent point at different molar ratios *m* from part **(A)**.

and Pihlar, 2015). The decrease of pH before EP1 in the presence of Mg(II) compared to the pH values recorded for phytic acid alone is the result of interactions between added metal ions and phytic acid already before EP1 is reached and consequently an increased acidity of the first (i.e., most acidic) group of protons of phytic acid. A similar behavior can also be observed for the recorded pH values at EP1, while the consumption of NaOH at EP1 remains unchanged for all investigated molar ratios, showing that the amount of released protons before EP1 does not change with the addition of Mg(II) ions. In the following region, between equivalent points EP1 and EP3, one can observe more pronounced effect, since the EP2 is moved toward greater titrant consumption upon gradual addition of the Mg(II) concentration and consequently increased metal-to-ligand molar ratio: $m = n(M^{z+})/n$(Phy). This means that Mg(II) ions compete with protons for binding sites of the phytate ligand between pH 4 and pH 10 and therefore increase the acidity of the second group of protons (*vide infra*), which causes the pH drop for a given amount of added NaOH. Another consequence is also the gradual shift of EP2 and EP3 while the position of EP1 remains constant, as stated before. This can be clearly seen on the **Figure 2B** which shows the dependence of titrant equivalent consumption *j* on the molar ratio *m* for each EP observed. A linear slope value of +0.68 is observed at EP2 for $m \leq 1$, and the slope is halved to +0.33 for $m > 1$. This shows that when phytate is in excess, around 2 mol of protons are released per 3 mol of added Mg(II), and "only" 1 mol of protons per 3 mol of Mg(II) when the amount of Mg(II) in the solution is higher than the amount of phytate, indicating a change in the reaction mechanism after the first equivalent of Mg(II) is bound to the ligand. The position of EP1 remains constant while EP3 is shifted toward a slightly lower consumption of NaOH, which means that a complete deprotonation of phytic acid at EP3 is reached earlier, presumably due to the precipitation of phytate at pH > 10 in the form of the Mg(II) complex, according to the literature data (Evans and Pierce, 1982; Veiga et al., 2006). The EP3 derivative values increase as the final deprotonation step becomes more pronounced at higher metal-to-ligand molar ratios. This is due to the well-known decrease in K_i^H values and the increased acidity of the last (third) proton group with the highest affinity for phytate, which has also been reported for phytic acid titrations in the presence of other alkaline earths (Martin and Evans, 1986; Marolt and Pihlar, 2015) and alkali metals (Li et al., 1989a,b; De Stefano et al., 2003b).

Phytic Acid Interactions With Zn(II) Ions

As shown in **Figure 3A**, the complexation of Zn(II) ions with phytic acid exhibits similar behavior to that of Mg(II), as the pH of the titration curve in the region before EP1 as well as between EP1 and EP3 is shifted toward lower values and the EP2 is shifted toward a higher NaOH consumption with increasing molar ratio *m*. This can again be explained by the complexation of metal ions competing for binding sites of the phytate ligand and consequently increasing the acidity of the first, second, and third group of protons which are therefore released earlier. However, compared to Mg(II) the slope of the

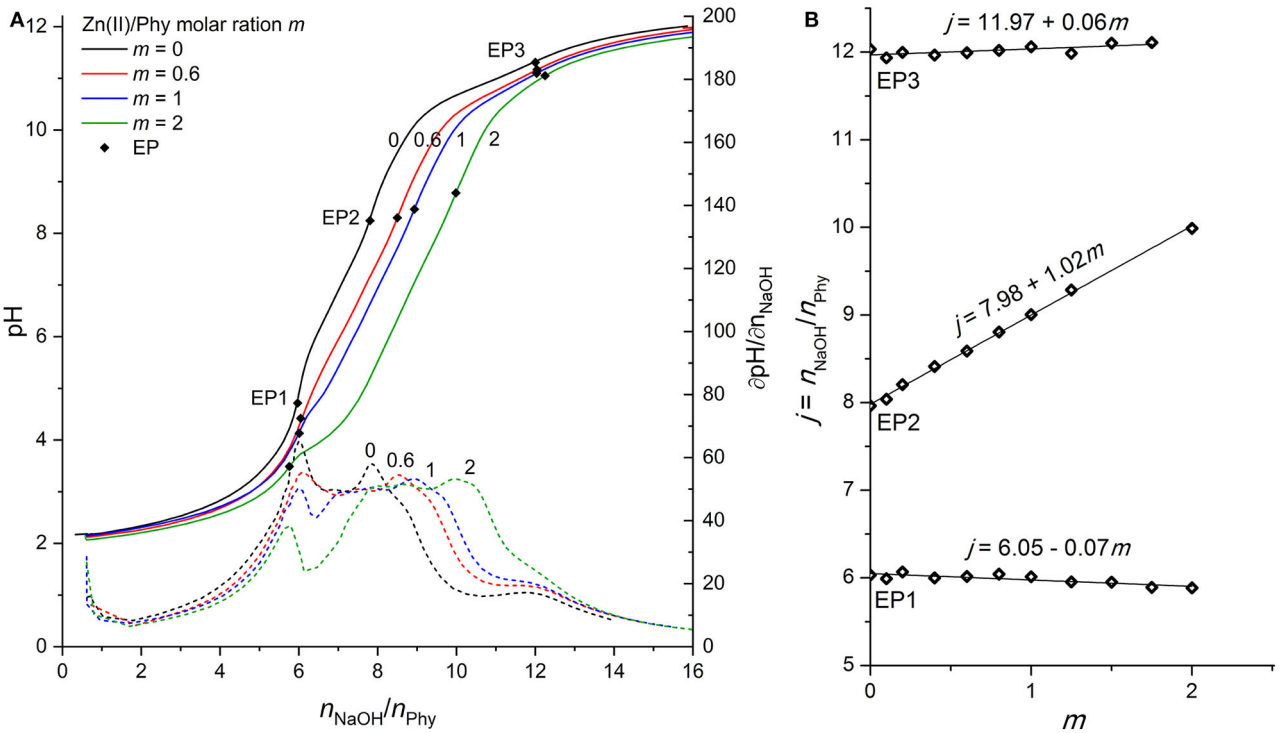

FIGURE 3 | (A) Titration of 0.1389 mmol H_{12}Phy with 0.1032 M NaOH at various molar ratios *m:* Zn(II)/Phy = 0:1, 0.6:1, 1:1, and 2:1, accompanied by corresponding derivatives ∂pH/∂*n*(NaOH); **(B)** Equivalents of NaOH per amount of phytic acid *j* consumed for individual equivalent point at different molar ratios *m* from part **(A)**.

titrant equivalent consumption *j* at EP2 to the molar ratio *m* is higher (+1.02) and constant for all molar ratios studied (see **Figure 3B**), which means that 1 mol of protons is released per 1 mol of added Zn(II). This is an indication that Zn(II) ions are attached to a different binding site than Mg(II) and other alkaline earth metals, since a similarly lower slope (+0.59) of EP2 has also been reported for Ca(II) (Marolt and Pihlar, 2015). While EP2 is shifted, EP3 remains constant for all molar ratios studied, which means that the final deprotonation step appears at the same position, indicating the absence of precipitation of Zn(II) phytate complexes in this pH range, in contrast to the case of Mg(II). Although the NaOH consumption remained constant at EP1, a detailed analysis of the titration curves in **Figure 3A** shows that the pH of titration curve before and at EP1 decreases with increasing *m*, which is an evidence of metal complex formation already at low pH where phytate species with a higher level of protonation are present in solution and in accordance with reports of complex formation below pH 6 for Zn(II) ions (Torres et al., 2005). Furthermore, at higher excess of Zn(II) ions, e.g., at $m = 2$, a significantly lower pH slope in the region closely after the EP1 can be observed, as well as the decreased values of corresponding derivatives, shown in **Figure 3A**. This could again be explained by the occurrence of metal complexes with a higher level of protonation, i.e., $[ZnH_6Phy]^{4-}$ (Torres et al., 2005), and by higher stability constants of Zn(II) complexes with phytic acid (Crea et al., 2008). Hereby, it is worth mentioning that due to the relatively low values of the derivative curves around EP2 and consequently less distinct maxima, 3 to 5 replicates were derived for each molar ratio studied in order to provide an accurate determination of EP2, which was placed at the same position within the experimental error < 2% using the software equipment.

Phytic Acid Interactions With Fe(II) Ions

Phytic acid complexes with iron are known for their high stability and important biological role, including antioxidant properties, as reported in many publications (Lee et al., 1998; Vucenik and Shamsuddin, 2003; Oomah et al., 2008; Quirrenbach et al., 2009). The complexes are strongly dependent on the pH, the metal-to-ligand molar ratio, and the corresponding stability constants of trivalent iron complexes are significantly higher than those of divalent iron (Torres et al., 2005). Coordination compounds of iron phytates and their antioxidant role in preservation chemistry (Kolar et al., 1998, 2005; Strlič et al., 2001; Wagner and Bulska, 2003) have also been extensively studied by our research group, especially Fe(III) ions using various analytical techniques, including potentiometric (Šala et al., 2011; Marolt and Pihlar, 2015) and NMR titrations (Bebot-Brigaud et al., 1999; Mali et al., 2006), while "only" voltammetric methods have recently been used (Marolt et al., 2015) to study the Fe(II)/Fe(III) redox couple in the presence of phytic acid, providing important information about the electrochemical mechanism that is strongly dependent on the pH and the consequent protonation level of the ligand. Therefore, the aim of this work was to evaluate the Fe(II) phytate acid-base properties using alkalimetric titration and to

obtain a deeper understanding of the iron phytate complex formation mechanism.

As stated above, the interactions of phytic acid with trivalent iron are several orders of magnitude greater (Torres et al., 2005) than those with divalent iron, which can also be confirmed in **Figure 4A**, where only a minor differentiation of the phytic acid titration curve is observed upon the addition of Fe(II) ions. While the position of EP1 remains almost constant (the corresponding slope is −0.11), EP2 and EP3 shift at an increased molar ratio m with an average slope of +0.29 mol and −0.43 mol of titrant per 1 mol of added Fe(II), respectively (see **Figure 4B**). These values differ significantly from the values reported for the Fe(III) ions with slopes of +1.67, +2.26, and +1.94 for EP1, EP2, and EP3, respectively (Marolt and Pihlar, 2015). This is a clear identification of different phytic acid complex formation mechanisms between divalent and trivalent iron and is in good agreement with the reports of voltammetric investigation of Fe(II)/Fe(III) phytates (Marolt et al., 2015). Fe(II) ions do not form coordination compounds with highly protonated phytate species before EP1 (below pH 5), and also have much less influence on the acidity of the second and third group of phytic acid protons, based on the observed EP2 dependence. Due to the smaller positive charge and the larger ionic radius of Fe(II) compared to Fe(III), divalent ions sustain significantly weaker binding interactions with phytate and therefore have less effect on the acidity of phytic acid protons. From the analysis and comparison with the titration curves of other divalent ions discussed above, it can be deduced that Fe(II) ions form less stable complexes under given conditions than Mg(II) and Zn(II), as also reported by Torres et al. (2005). A negative slope of EP3 implies that Fe(II) phytate complexes precipitate above pH 9, which was also observed during the titrations already at low metal-to-ligand molar ratios. Hence, only experiments up to $m = 1$ were conducted for Fe(II) due to the large amounts of white-colored precipitate. However, contrary to the titrations with trivalent iron (Marolt and Pihlar, 2015), divalent did not undergo the metal hydrolysis under the experimental conditions applied in this work.

Phytic Acid Interactions With Cu(II) Ions

In contrast to the Fe(II) experiments, the titration curve of phytic acid in the presence of Cu(II) ions exhibits more pronounced alternations over the entire titration range, as shown in **Figure 5A**. As in the case of Zn(II), the pH value before and at the EP1 decreases with increasing metal-to-ligand molar ratio, which can be explained by the onset of complex formation already before EP1. Cu(II) ions therefore compete with the first group of protons for binding sites of phosphate groups and increase their acidic properties, which is also confirmed by the increased titrant consumption at EP1 for $m \leq 1$ with the slope value of +0.32, meaning around 1 mol of protons is released per 3 mol of added Cu(II) in the region before EP1 (**Figure 5B**). Similarly, the positive shift of EP2 with an average slope of +1.00 is due to the complexation of Cu(II) with the phytate ligand, which indicates that 1 mol of protons is exchanged by 1 mol of added Cu(II) in the pH range of the second proton

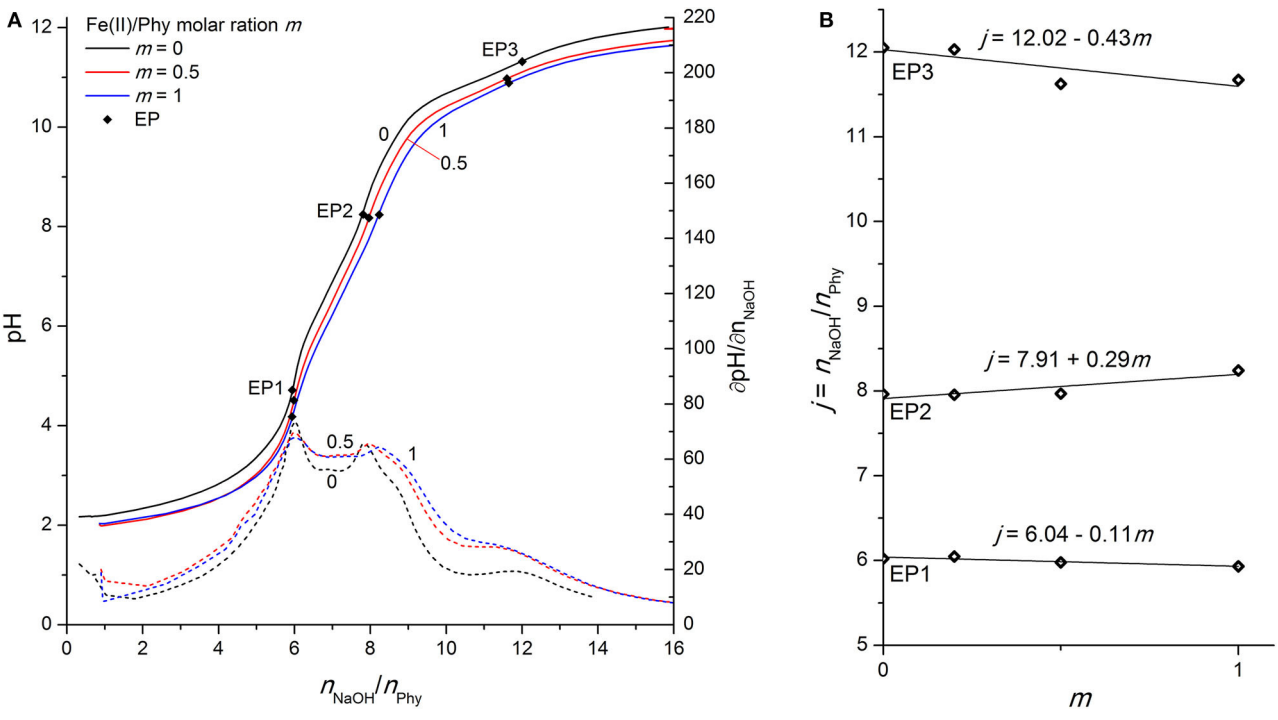

FIGURE 4 | (A) Titration of 0.1528 mmol H_{12}Phy with 0.1002 M NaOH at various molar ratios *m:* Fe(II)/Phy = 0:1, 0.5:1, and 1:1, accompanied by corresponding derivatives ∂pH/∂*n*(NaOH); **(B)** Equivalents of NaOH per amount of phytic acid *j* consumed for individual equivalent point at different molar ratios *m* from part **(A)**.

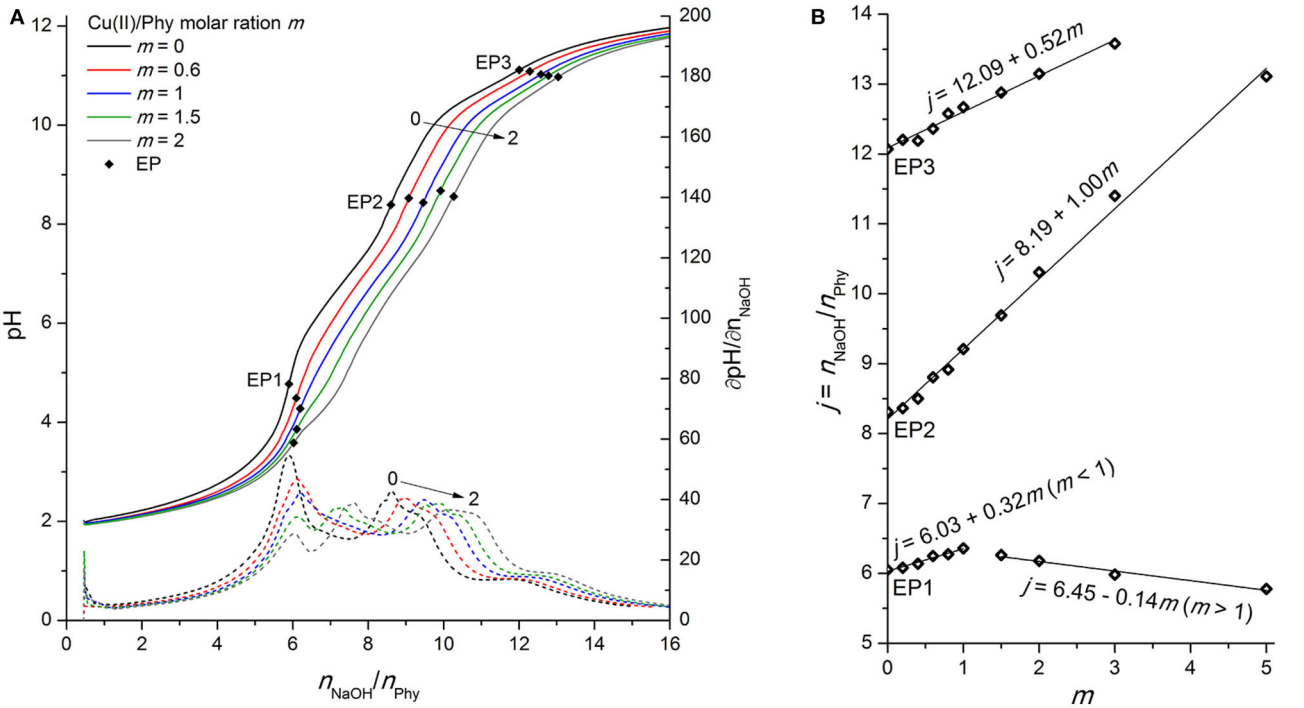

FIGURE 5 | (A) Titration of 0.0951 mmol H_{12}Phy with 0.1178 M NaOH at various molar ratios *m:* Cu(II)/Phy = 0:1, 0.6:1, 1:1, 1.5:1, and 2:1, accompanied by corresponding derivatives ∂pH/∂*n*(NaOH); **(B)** Equivalents of NaOH per amount of phytic acid *j* consumed for individual equivalent point at different molar ratios *m* from part **(A)**.

group with intermediate acidity. On the other hand, the increased consumption of NaOH with the slope of + 0.51 at the final equivalent point (EP3), corresponding to the neutralization of the last (12th) phytate proton, is an identification of the formation of stable Cu(II) hydroxide species, which are also observed as a light blue precipitate that was formed in the titration cell at pH 9 and above, according to the reactions from the literature (Martell and Smith, 1977):

$$Cu^{2+} + 2OH^- \overset{K_{2,1}}{\longleftrightarrow} [Cu(OH)_2]_{(s)} \quad (7)$$

$$Cu^{2+} + 3OH^- \overset{K_{3,1}}{\longleftrightarrow} [Cu(OH)_3]^- \quad (8)$$

$$2Cu^{2+} + 2OH^- \overset{K_{2,2}}{\longleftrightarrow} [Cu_2(OH)_2]^{2+} \quad (9)$$

with considerably high values of the corresponding stability constants: $log\ K_{2,1} = 12.8$, $log\ K_{3,1} = 14.5$, and $log\ K_{2,2} = 17.8$ (Martell and Smith, 1977), confirming that the soluble Cu(II)-hydroxo species and $Cu(OH)_2$ precipitate are predominant forms of copper(II) under alkaline conditions, as discussed by Cuppett et al. (2006). The titration of Cu(II) with NaOH in the absence of phytic acid (not shown), revealed the non-stoichiometric molar ratio between Cu(II) and OH^- ions, indicating the formation of mixed Cu(II) hydroxide species. The equivalent point for this reaction was found at pH 8.4, which is close to the range of the second EP of phytic acid titration curve, indicating that the shift of EP2 could also be partly due to the occurrence of Cu(II) hydroxo species.

A detailed analysis of the dependence of NaOH consumption on the metal-to-molar ratio on **Figure 5B** shows a positive shift of EP1 with a slope of +0.32 until the equimolar ratio between Cu(II) and phytate is reached ($m \leq 1$) and a negative slope of −0.14 hereinafter ($m > 1$). This is most likely due to the altered reaction mechanism for $m > 1$, e.g., the formation of polynuclear Cu(II) phytate species, such as $[Cu_2H_5Phy]^{3-}$, which were also observed by Crea et al. (2007) and Vasca et al. (2002). However, another reason could be the precipitation of the complex before reaching EP1 (and the resulting dissolution due to the positive slope of EP2 and EP3 in the whole range of molar ratios studied), but is very unlikely at such a low pH, and there was also no visible evidence of any precipitate formation during titration under acidic pH conditions, which supports the first explanation.

Phytic Acid Interactions With Cu(I) Ions

In the literature there are not many studies that address the Cu(I) complexes with phytic acid (Li et al., 2013), probably also due to the unstable nature of monovalent copper, which can be rapidly oxidized to divalent state in the presence of dissolved oxygen. Therefore, likewise in the case of Fe(II), all titrations were carried out in a tightly-sealed cell with an inert atmosphere under constant Ar flow and special care was taken to prevent the entry of oxygen at any stage of the experiment. **Figure 6A** shows the behavior of phytic acid titration curve upon addition of Cu(I) ions, which is similar to that of Cu(II) (see **Figure 5A**), since

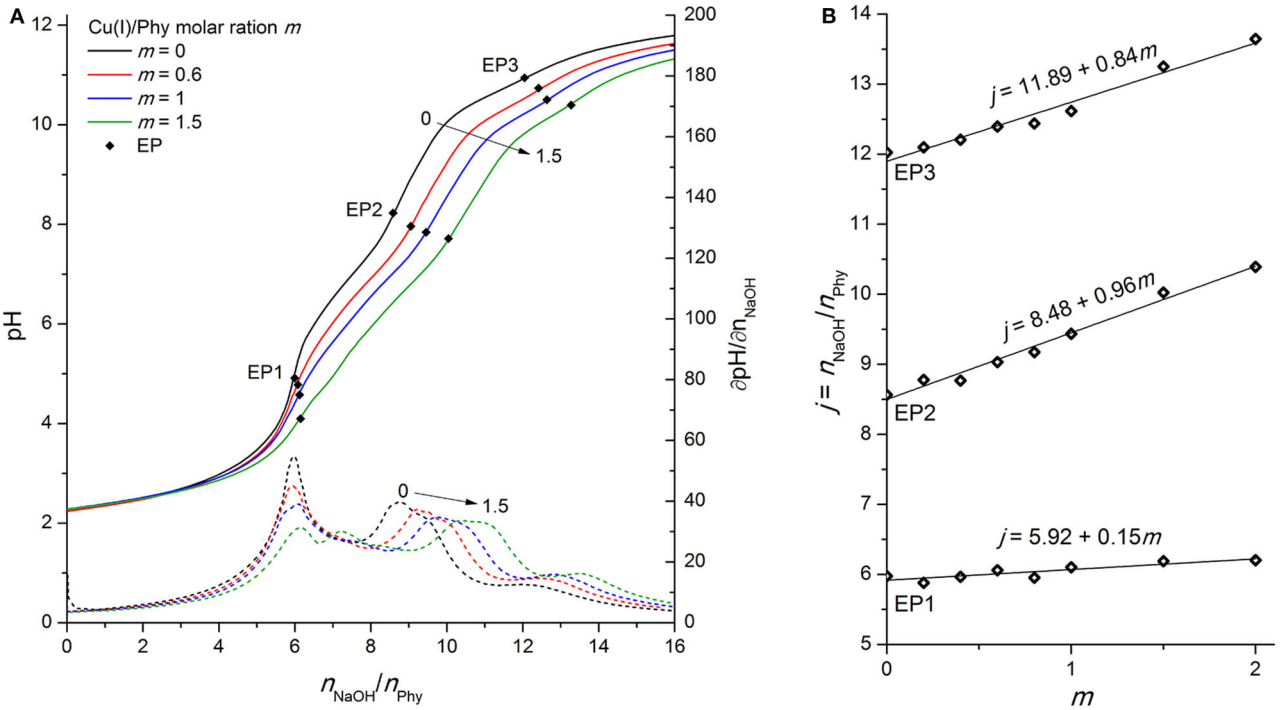

FIGURE 6 | (A) Titration of 0.1096 mmol H_{12}Phy with 0.1105 M NaOH at various molar ratios *m:* Cu(I)/Phy = 0:1, 0.6:1, 1:1, and 1.5:1, accompanied by corresponding derivatives ∂pH/∂*n*(NaOH); **(B)** Equivalents of NaOH per amount of phytic acid *j* consumed for individual equivalent point at different molar ratios *m* from part **(A)**.

the curve and consequent EP shifts can be observed practically throughout the whole titration range.

However, some differences between the two oxidation states can be observed, starting with the constant slope of the consumed NaOH dependence on the added Cu(I) for all studied molar ratios ($m \leq 2$). This is an indication of "only" one complex formation mechanism in the pH range around EP1, in contrast to the Cu(II) complexes where two types of behavior depending on *m* were found. The lower value of the slope of EP1 [+0.15 vs. +0.32 for Cu(I) vs. Cu(II)] is presumably due to the weaker interactions of the less-positively charged monovalent ion with the most acidic group of phytic acid protons. However, perhaps contrary to one's initial expectations, the slope of titrant consumption at EP2 (+0.96) is very close to that of divalent copper (+1.00), which shows that a similar complex formation mechanism is taking place in the region of the second proton group with intermediate acidity for both oxidation states, regardless the difference of their charge. Considering the similarity of the ionic radius of Cu(I) and Cu(II) with values of 0.77 and 0.73 Å, respectively, it can be assumed that, rather than the total ion charge (or charge density), the ionic radius of transition metal ion is of greater importance for phytic acid complex formation and resulting deprotonation of the ligand, particularly in the intermediate pH range between EP1 and EP3. In support of this, a similar EP2 dependence (with a slope of +1.02) was also observed for Zn(II) ions (see **Figure 3B**) with similar ionic radius as copper (0.74 Å), while significantly less pronounced shift of EP2 (with slope of +0.29, **Figure 4B**) was found for much smaller Fe(II) ions (0.61 Å). Furthermore, if we take into consideration the reports of Fe(III) ions (0.55 Å) (Šala et al., 2011; Marolt and Pihlar, 2015), the distinction between titration curves of divalent and trivalent iron can be explained by the difference of ionic radii, which is in contrast to the previously mentioned case of the two oxidation states of copper. Fe(III) revealed a remarkably greater EP2 dependence on *m* with a slope of +2.26 (Marolt and Pihlar, 2015), which is much higher not only in comparison to that of Fe(II) but also to other metals investigated and thus shows the strongest binding interactions with phytate. This is in good agreement with stability constants with several orders of magnitude higher values, which were reported by Torres et al. (2005), as well as with recent findings of the electrochemical study of the Fe(II)/Fe(III) phytate complex mechanism by Marolt et al. (2015). However, in the case of Fe(III), strong binding affinity to the phytate ligand is also due to the electrostatic effects, caused by the higher cation charge of trivalent iron (Crea et al., 2008), which is also the reason for the interaction with the most acidic proton group and the resulting shift of EP1 with a slope of +1.67.

On the other hand, the results of Mg(II) and Ca(II), the latter of which was published previously (Marolt and Pihlar, 2015), do not follow the same trend, since an evidently lower slope of the EP2 position was found in the case of both alkaline earth metal ions. This could be explained by differences in the binding sites of phytate, as an individual group of metals (i.e., alkaline

earth metals vs. transition metals) interact with their preferred phosphate position(s) of the ligand (Marolt and Pihlar, 2015) and cause deprotonation of proton(s) with different acidic properties (i.e., K_i^H values), resulting as a shift of different EPs on the titration curve of phytic acid. For clarification, all discussed EP slopes and ionic radii of the studied metal complexes with phytic acid from previous and this work are summarized in **Table 1**.

As clarly seen from **Figure 6A**, the final deprotonation step is also shifted to a higher consumption of the titrant at increased concentration of Cu(I) ions with an average slope of +0.84 mol per 1 mol of added copper (see **Figure 6B**). The higher slope of monovalent compared to divalent copper (+0.52) demonstrates that the Cu(I) undergoes a metal hydrolysis reaction to a greater extent, which was also confirmed by the visual detection of yellow-colored precipitate that was formed in the titration cell during the titration. As a result, a lower concentration of Cu(I) ions is present in chelated form of the phytate complex around EP3, which is detected at pH > 10.5. Titration of Cu(I) ions in the absence of phytic acid (and with the addition of HCl prior to titration to increase the solubility of CuCl salt) revealed the molar ratio of the reaction between hydroxide and monovalent copper; $n(OH^-) : n(Cu(I)) = 3 : 2$ (not shown). This indicates the presence of two Cu(I) hydroxo species; $[Cu(OH)_2]^-$ and [Cu(OH)] in the molar ratio 1:1 (Illas et al., 1984). The formation of the latter can also be better described by the following reaction (Martell and Smith, 1977):

$$2Cu^+ + 3H_2O \longleftrightarrow Cu_2O_{(s)} + 2H_3O^+, \quad (10)$$

but the logarithmic value of the corresponding reaction constant is considerably low (−14.7) (Martell and Smith, 1977), which means that the Cu_2O precipitate is stable only under alkaline conditions with sufficiently high concentration of hydroxide ions (and consequently low concentration of H_3O^+).

CONCLUSIONS

In summary, the formation of metal complexes with phytic acid is a complex process that depends strongly on the molar ratios, the pH conditions, and the associated protonation level of phytate ligand as well as on the accompanying side reactions, in particular metal ion hydrolysis and precipitation of the formed coordination compounds. In this work, the potentiometric titration technique was applied in combination with a detailed analysis of the detected equivalent point dependencies on the metal-to-ligand molar ratios for the selected divalent and monovalent cations. The differences in the slope values of NaOH consumption observed at individual EPs suggest that the alkaline earth metals, i.e., Mg(II), discussed here, and previously studied Ca(II) (Marolt and Pihlar, 2015), presumably bind to different phosphate groups than the transition metals, i.e., Zn(II), Cu(I), Cu(II), and Fe(II). It is important to note that this could be also due to the formation of metal-phytate species with different stoichiometry. Although several NMR titration studies have been conducted on (metal-)phytate systems (Brigando et al., 1995; Bebot-Brigaud et al., 1999; Mali et al., 2006; Šala et al., 2011), to the best of our knowledge, only Champagne et al. (1990) reports the same preferential phytate binding site for Ca(II) and Cu(II) ions, which appears to be the P5 phosphate group or position between P5 and P4 or P6 phosphate groups. However, no specifications about the proton release has been provided. In general, the metal-phytate interactions are of high complexity, as the multivalent metals typically interact with two or three phosphate groups simultaneously and can therefore cause the release of proton(s) and/or favorize the inversion of phytate from equatorial to axial conformation (Torres et al., 2008; Veiga et al., 2014).

In the present work, it was shown that Fe(II) has a significantly distinct complex formation mechanism than the rest of the transition metal group, which is due to the well-known specific binding interactions between phytic acid and iron ions in general, as well as the accompanying precipitation process which is more pronounced compared to other metal complexes investigated in this work. Experiments with different oxidation states of copper revealed similar complexation characteristics for both monovalent and divalent metal ions, which supports the explanation that the reaction mechanism depends primarily on the ionic radius and is independent of the total charge and/or charge density of the complexed metal ions. A similar reaction mechanism has been also found for Zn(II) with an ionic radius comparable to that of the two copper oxidation states, while a considerably smaller Fe(II) and Fe(III) ions exhibit contrasting behavior (Marolt and Pihlar, 2015). The latter one exhibits significantly higher EP2 dependence and thus the strongest

TABLE 1 | Ionic radii and slope values of the dependence of the molar ratio j[a] between titrant (NaOH) and phytic acid on the metal-to-ligand molar ratio m[b] at individual equivalent point (EP).

Metal ion	Ionic radius [Å]	EP1	EP2	EP3	References
Mg(II)	0.72	−0.02	+0.68; +0.33[c]	−0.25[d]	This work
Ca(II)	1.00	+0.01	+0.59	−0.03	Marolt and Pihlar, 2015
Cu(I)	0.77	+0.15	+0.96	+0.84	This work
Cu(II)	0.73	+0.32; −0.14[c]	+1.00	+0.52	This work
Zn(II)	0.74	−0.07	+1.02	+0.06	This work
Fe(II)	0.61	−0.11	+0.29	−0.43[d]	This work
Fe(III)	0.55	+1.67	+2.26	+1.94	Marolt and Pihlar, 2015

[a] $j = n_{OH}/n_{Phy}$; [b] $m = n_M/n_{Phy}$; [c] *Values given for m ≤ 1 and m > 1, respectively;* [d] *Observed precipitation.*

binding interaction with phytate among the metals investigated, which could be confirmed by the reported stability constants with several orders of magnitude higher values (Torres et al., 2005) as well as by the findings of our previous electrochemical study of the Fe(II)/Fe(III) phytate complex mechanism (Marolt et al., 2015).

Based on the present work, other phytic acid coordination compounds with alkaline earth metals, e.g., Sr(II) and Ba(II) ions, and/or transition metals of different oxidation states and ionic radii are to be investigated in the future, possibly by potentiometric and/or NMR titrations in combination with voltammetric techniques in order to confirm and/or obtain a deeper insight into the phytate complex formation mechanism(s) and understanding of the interactions between phytic acid and metal ions.

DATA AVAILABILITY STATEMENT

The raw data supporting the conclusions of this article will be made available by the authors, without undue reservation.

AUTHOR CONTRIBUTIONS

GM and MK: conceptualization. GM, EG, BP, and MK: methodology. GM and EG: validation, formal analysis, and investigation. GM: writing—original draft preparation. GM, BP, and MK: writing—review and editing. BP and MK: supervision. All authors contributed to the article and approved the submitted version.

FUNDING

This research was funded by SLOVENIAN RESEARCH AGENCY, grant number P1-0153.

ACKNOWLEDGMENTS

This work is dedicated to the memory of Dr. Tatjana Zupančič. The authors gratefully acknowledge to Ms. Josselyn Arroyo Stucchi and Mr. Dejan Slapšak for their contribution in laboratory work.

REFERENCES

Bebot-Brigaud, A., Dange, C., Fauconnier, N., and Gérard, C. (1999). ^{31}P NMR, potentiometric and spectrophotometric studies of phytic acid ionization and complexation properties toward Co^{2+}, Ni^{2+}, Cu^{2+}, Zn^{2+} and Cd^{2+}. *J. Inorg. Biochem*. 75, 71–78. doi: 10.1016/S0162-0134(99)00041-0

Bretti, C., De Stefano, C., Lando, G., and Sammartano, S. (2013). Thermodynamics for proton binding of phytate in $KNO_{3(aq)}$ at different temperatures and ionic strengths. *Thermochim. Acta*. 566, 193–202. doi: 10.1016/j.tca.2013.05.044

Brigando, C., Mossoyan, J. C., Favier, F., and Benlian, D. (1995). Conformational preferences and protonation sequence of *myo*-inositol hexaphosphate in aqueous-solution; potentiometric and multinuclear magnetic-resonance studies. *J. Chem. Soc. Dalton Trans*. 1995, 575–578. doi: 10.1039/dt9950000575

Champagne, E. T., Fisher, M. S., and Hinojosa, O. (1990). NMR and ESR studies of interactions among divalent-cations, phytic acid, N-acetyl-amino acids. *J. Inorg. Biochem*. 38, 199–215. doi: 10.1016/0162-0134(90)84013-F

Cheryan, M., and Rackis, J. J. (1980). Phytic acid interactions in food systems. *C R C Crit. Rev. Food Sci. Nutr*. 13, 297–335. doi: 10.1080/10408398009527293

Crea, F., De Stefano, C., Milea, D., and Sammartano, S. (2008). Formation and stability of phytate complexes in solution. *Coord. Chem. Rev*. 252, 1108–1120. doi: 10.1016/j.ccr.2007.09.008

Crea, P., De Stefano, C., Milea, D., Porcino, N., and Sammartano, S. (2007). Speciation of phytate ion in aqueous solution. Protonation constants and copper(II) interactions in $NaNO_{3aq}$ at different ionic strengths. *Biophys. Chem*. 128, 176–184. doi: 10.1016/j.bpc.2007.04.003

Cuppett, J. D., Duncan, S. E., and Dietrich, A. M. (2006). Evaluation of copper speciation and water quality factors that affect aqueous copper tasting response. *Chem. Senses* 31, 689–697. doi: 10.1093/chemse/bjl010

De Stefano, C., Milea, D., Pettignano, A., and Sammartano, S. (2003b). Speciation of phytate ion in aqueous solution. Alkali metal complex formation in different ionic media. *Anal. Bioanal. Chem*. 376, 1030–1040. doi: 10.1007/s00216-003-2056-1

De Stefano, C., Milea, D., Porcino, N., and Sammartano, S. (2006). Speciation of phytate ion in aqueous solution. Cadmium(II) interactions in aqueous NaCl at different ionic strengths. *Anal. Bioanal. Chem*. 386, 346–356. doi: 10.1007/s00216-006-0620-1

De Stefano, C., Milea, D., and Sammartano, S. (2003a). Speciation of phytate ion in aqueous solution. Protonation constants in tetraethylammonium iodide and sodium chloride. *J. Chem. Eng. Data* 48, 114–119. doi: 10.1021/je020124m

De Stefano, C., Milea, D., and Sammartano, S. (2004). Speciation of phytate ion in aqueous solution - thermodynamic parameters for protonation in NaCl. *Thermochim. Acta* 423, 63–69. doi: 10.1016/j.tca.2004.04.017

Evans, W. J., McCourtney, E. J., and Shrager, R. I. (1982). Titration studies of phytic acid. *J. Am. Oil Chem. Soc*. 59, 189–191. doi: 10.1007/BF02680274

Evans, W. J., and Pierce, A. G. (1982). Interaction of phytic acid with the metal ions, copper(II), cobalt(II), iron(III), magnesium(II), and manganese(II). *J. Food Sci*. 47, 1014–1015. doi: 10.1111/j.1365-2621.1982.tb12769.x

Gao, X., Zhao, C., Lu, H., Gao, F., and Ma, H. (2014). Influence of phytic acid on the corrosion behavior of iron under acidic and neutral conditions. *Electrochim. Acta* 150, 188–196. doi: 10.1016/j.electacta.2014.09.160

Graf, E., and Eaton, J. W. (1990). Antioxidant functions of phytic acid. *Free Radical Biol. Med*. 8, 61–69. doi: 10.1016/0891-5849(90)90146-A

Heighton, L., Schmidt, W. F., Rice, C. P., and Siefert, R. L. (2008). Electrospray ionization mass spectroscopy shows speciation of phytate to be pH dependent. *J. Food Agric. Environ*. 6, 402–407.

Illas, F., Rubio, J., Centellas, F., and Virgili, J. (1984). Molecular structure of copper (I) hydroxide and copper hydroxide (1-)(Cu (OH) 2-). An *ab initio* study. *J. Phys. Chem*. 88, 5225–5228. doi: 10.1021/j150666a022

Kolar, J., Šala, M., Strlič, M., and Šelih, V. S. (2005). Stabilisation of paper containing iron-gall ink with current aqueous processes. *Restaurator* 26, 181–189. doi: 10.1515/rest.2005.26.3.181

Kolar, J., Strlič, M., Novak, G., and Pihlar, B. (1998). Aging and stabilization of alkaline paper. *J. Pulp Pap. Sci*. 24, 89–94.

Kumar, V., Sinha, A. K., Makkar, H. P. S., and Becker, K. (2010). Dietary roles of phytate and phytase in human nutrition: a review. *Food Chem*. 120, 945–959. doi: 10.1016/j.foodchem.2009.11.052

Lee, B. J., Hendricks, D. G., and Cornforth, D. P. (1998). Antioxidant effects of carnosine and phytic acid in a model beef system antioxidant. *J. Food Sci*. 63, 394–398. doi: 10.1111/j.1365-2621.1998.tb15750.x

Li, N., Wahlberg, O., and Puigdomenech, I. (1989b). Equilibrium studies of phytate ions - metal-ion phytate complexes formed in aqueous-solution - methods and characterization of the phytate ligand. *Chem. Scripta* 29, 91–95.

Li, N., Wahlberg, O., Puigdomenech, I., and Öhman LO. (1989a). Equilibrium studies of phytate ions. 1. Equilibria between phytate ions and protons in 3 M $(Na)ClO_4$ medium. *Acta Chem. Scand*. 43, 331–339. doi: 10.3891/acta.chem.scand.43-0331

Li, Y., He, J.-B., Zhang, M., and He, X.-L. (2013). Corrosion inhibition effect of sodium phytate on brass in NaOH media. Potential-resolved formation of soluble corrosion products. *Corros. Sci*. 74, 116–122. doi: 10.1016/j.corsci.2013.04.031

Lopez, H. W., Leenhardt, F., Coudray, C., and Remesy, C. (2002). Minerals and phytic acid interactions: is it a real problem for human nutrition? *Int. J. Food Sci. Technol*. 37, 727–739. doi: 10.1046/j.1365-2621.2002.00618.x

Mali, G., Šala, M., Arčon, I., Kaučič, V., and Kolar, J. (2006). Insight into the short-range structure of amorphous iron inositol hexaphosphate as provided by ^{31}P NMR and Fe X-ray absorption spectroscopy. *J. Phys. Chem. B* 110, 23060–23067. doi: 10.1021/jp0633805

Marini, M. A., Evans, W. J., and Martin, C. J. (1981). Thermal and potentiometric titrations of phytic acid. *Anal. Lett*. 14, 707–717. doi: 10.1080/00032718108081432

Marolt, G., and Pihlar, B. (2015). Potentiometric determination of phytic acid and investigations of phytate interactions with some metal ions. *Acta Chim. Slovenica* 62, 319–327. doi: 10.17344/acsi.2014.1127

Marolt, G., Šala, M., and Pihlar, B. (2015). Voltammetric investigation of iron (III) interactions with phytate. *Electrochim. Acta* 176, 1116–1125. doi: 10.1016/j.electacta.2015.06.120

Martell, A. E., and Smith, R. M. (1977). *Critical Stability Constants, Other Organic Ligands*. New York, NY: Plenum Press.

Martin, C. J., and Evans, W. J. (1986). Phytic acid-metal ion interactions. II. The effect of pH on Ca(II) binding. *J. Inorg. Biochem*. 27, 17–30. doi: 10.1016/0162-0134(86)80105-2

Nissar, J., Ahad, T., Naik, H., and Hussain, S. (2017). A review phytic acid: as antinutrient or nutraceutical. *J. Pharmacogn. Phytochem*. 6, 1554–1560.

Oatway, L., Vasanthan, T., and Helm, J. H. (2001). Phytic acid. *Food Rev. Int*. 17, 419–431. doi: 10.1081/FRI-100108531

Oomah, B. D., Blanchard, C., and Balasubramanian, P. (2008). Phytic acid, phytase, minerals, and antioxidant activity in Canadian dry bean (Phaseolus vulgaris L.) cultivars. *J. Agric. Food. Chem*. 56, 11312–11319. doi: 10.1021/jf801661j

Quirrenbach, H. R., Kanumfre, F., Rosso, N. D., and Carvalho, M. A. (2009). Behaviour of phytic acid in the presence of iron(II) and iron(III). *Cienc. Tecnol. Aliment*. 29, 24–32. doi: 10.1590/S0101-20612009000100005

Šala, M., Makuc, D., Kolar, J., Plavec, J., and Pihlar, B. (2011). Potentiometric and ^{31}P NMR studies on inositol phosphates and their interaction with iron(III) ions. *Carbohydr. Res*. 346, 488–494. doi: 10.1016/j.carres.2010.12.021

Sasakawa, N., Sharif, M., and Hanley, M. R. (1995). Metabolism and biological activities of inositol pentakisphosphate and inositol hexakisphosphate. *Biochem. Pharmacol*. 50, 137–146. doi: 10.1016/0006-2952(95)00059-9

Strlič, M., Kolar, J., and Pihlar, B. (2001). Some preventive cellulose antioxidants studied by an aromatic hydroxylation assay. *Polym. Degrad. Stab*. 73, 535–539. doi: 10.1016/S0141-3910(01)00120-3

Torres, J., Domínguez, S., Cerdá, M. F., Obal, G., Mederos, A., Irvine, R. F., et al. (2005). Solution behaviour of *myo*-inositol hexakisphosphate in the presence of multivalent cations. Prediction of a neutral pentainagnesium species under cytosolic/nuclear conditions. *J. Inorg. Biochem*. 99, 828–840. doi: 10.1016/j.jinorgbio.2004.12.011

Torres, J., Veiga, N., Gancheff, J. S., Domínguez, S., Mederos, A., Sundberg, M., et al. (2008). Interaction of myo-inositol hexakisphosphate with alkali and alkaline earth metal ions: spectroscopic, potentiometric and theoretical studies. *J. Mol. Struct*. 874, 77–88. doi: 10.1016/j.molstruc.2007.03.035

Vasca, E., Materazzi, S., Caruso, T., Milano, O., Fontanella, C., and Manfredi, C. (2002). Complex formation between phytic acid and divalent metal ions: a solution equilibria and solid state investigation. *Anal. Bioanal. Chem*. 374, 173–178. doi: 10.1007/s00216-002-1469-6

Veiga, N., Torres, J., Domínguez, S., Mederos, A., Irvine, R. F., Díaz, A., et al. (2006). The behaviour of myo-inositol hexakisphosphate in the presence of magnesium(II) and calcium(II): protein-free soluble InsP(6) is limited to 49 mu M under cytosolic/nuclear conditions. *J. Inorg. Biochem*. 100, 1800–1810. doi: 10.1016/j.jinorgbio.2006.06.016

Veiga, N., Torres, J., Macho, I., Gomez, K., Gonzalez, G., and Kremer, C. (2014). Coordination, microprotonation equilibria and conformational changes of myo-inositol hexakisphosphate with pertinence to its biological function. *Dalton Trans*. 43, 16238–16251. doi: 10.1039/C4DT01350F

Vucenik, I., and Shamsuddin, A. M. (2003). Cancer inhibition by inositol hexaphosphate (IP_6) and inositol: from laboratory to clinic. *J. Nutr*. 133, 3778–3784. doi: 10.1093/jn/133.11.3778S

Wagner, B., and Bulska, E. (2003). Towards a new conservation method for ancient manuscripts by inactivation of iron via complexation and extraction. *Anal. Bioanal. Chem*. 375, 1148–1153. doi: 10.1007/s00216-003-1819-z

Yoon, J. H., Thompson, L., and Jenkins, D. J. A. (1984). The effect of phytic acid on *in vitro* rate of starch digestibility and blood glucose response. *Am. J. Clin. Nutr*. 38, 835–842. doi: 10.1093/ajcn/38.6.835

Zi, X., Singh, R. P., and Agarwal, R. (2000). Impairment of erbB1 receptor and fluid-phase endocytosis and associated mitogenic signaling by inositol hexaphosphate in human prostate carcinoma DU145 cells. *Carcinogenesis* 21, 2225–2235. doi: 10.1093/carcin/21.12.2225

Conflict of Interest: The authors declare that the research was conducted in the absence of any commercial or financial relationships that could be construed as a potential conflict of interest.

frontiers in Chemistry

MINI REVIEW
published: 02 November 2020
doi: 10.3389/fchem.2020.597400

Chelating Agents in Soil Remediation: A New Method for a Pragmatic Choice of the Right Chelator

Valeria Marina Nurchi[1], Rosita Cappai[1], Guido Crisponi[1], Gavino Sanna[2], Giancarla Alberti[3], Raffaela Biesuz[3] and Sofia Gama[4]*

[1] Dipartimento di Scienza della Vita e dell'Ambiente, University of Cagliari, Cittadella Universitaria, Monserrato, Italy, [2] Dipartimento di Chimica e Farmacia, University of Sassari, Sassari, Italy, [3] Dipartimento di Chimica, University of Pavia, Pavia, Italy, [4] Department of Analytical Chemistry, Faculty of Chemistry, University of Białystok, Białystok, Poland

Soil pollution by metal ions constitutes one of the most significant environmental problems in the world, being the ecosystems of extended areas wholly compromised. The remediation of soils is an impelling necessity, and different methodologies are used and studied for reaching this goal. Among them, the application of chelating agents is one of the most promising since it could allow the removal of metal ions while preserving the most meaningful properties of the original soils. The research in this field requires the joined contribute of different expertise spanning from biology to chemistry. In this work, we propose a parsimonious and pragmatic approach for screening among a range of potential chelating agents. This methodology, the *Nurchi's method*, is based on an extension of the Reilley procedure for EDTA titrations. This allows forecasting the binding ability of chelating agents toward the target polluting metal ions and those typically found in soils, based on the knowledge of the related protonation and complex formation constants. The method is thoroughly developed, and then tested by application to some representative cases. Its use and relevance in biomedical and industrial applications is also discussed.

Keywords: chelating agents, speciation, soil remediation, metal pollution, stability constants

OPEN ACCESS

Edited by:
Anna Napoli,
University of Calabria, Italy

Reviewed by:
Daniela Piazzese,
University of Palermo, Italy
Stefano Materazzi,
Sapienza University of Rome, Italy

****Correspondence:***
Valeria Marina Nurchi
nurchi@unica.it

Specialty section:
This article was submitted to Analytical Chemistry, a section of the journal Frontiers in Chemistry

Received: *21 August 2020*
Accepted: *28 September 2020*
Published: *02 November 2020*

Citation:
Nurchi VM, Cappai R, Crisponi G, Sanna G, Alberti G, Biesuz R and Gama S (2020) Chelating Agents in Soil Remediation: A New Method for a Pragmatic Choice of the Right Chelator. Front. Chem. 8:597400. doi: 10.3389/fchem.2020.597400

INTRODUCTION

Several metal ions, throughout the evolution of living organisms, resulted in essential for plants, animals, and man. Nevertheless, the introduction of exogenous metal ions that compete with essential ones can perturb the homeostasis of ecosystems until their disruption. For thousands of years, man used metals for necessities and progress, without forecasting about drawbacks of such custom. As result, the environment, as well as the human body, get intoxicated by polluting metal ions affecting water systems, plant, and animal life, mostly the whole ecosystem. The leading causes of metal environmental pollution are industrial drains, mining drains, urban wastes, residues of coal combustion, acid rains, fertilizers, and pesticides (Teng et al., 2020). Contamination by radionuclides is also a rising problem due to the increasing nuclear activities worldwide.

The metal pollution of water and soil compartments involves a definite and continuous exchange between them. Contrarily to soil pollution by organic substances, which can be transformed in the time into non-polluting ones by the degrading action of microbes, metal ions cannot be significantly

transformed and persist indefinitely in the soil, or they pass to aquatic systems by the action of weathering. US Agency for Toxic Substances and Disease Registry periodically publishes a list of organic and inorganic toxic substances, ordered according to their inherent toxicity and to their dissemination, i.e., to their potential environmental impact. In 2019, arsenic, lead and mercury occupied the first three positions, being cadmium the seventh (ATSDR, 2020). These elements, commonly reported as heavy metals (Duffus, 2002), share the properties of being not biodegradable and of accumulating in living organisms and soils, entering the food chain, being its limits of concentration on soils well-defined (see details on following section), due to their toxicity.

Noxious elements exert their action through different mechanisms, such as absorption by plants entering the food chain directly or animal mediated, and hindrance of the microbial action in the soil. Consequently, heavily contaminated metal-polluted areas have led to definite health problems in the surrounding populations, whose intensity depends both on the kind of pollutant and on its concentration. In this way, the soils contaminated with toxic metal ions and radionuclides, constitute a significant problem both in advanced and in developing countries.

Due to the serious environmental and health consequences, with related social costs, the release of these metal ions has to be avoided—in the last 30 years different countries and supranational organizations adopted drastic resolutions to limit most of their uses–and efficient methods for their scavenging and removal from wastewaters and soils must be adopted. As such, prevention and remediation of polluted soils thus constitute important environmental, health and economic objectives that must be urgently faced by early aware local administrators. Several methods are being exploited, being *absorption* and (*bio) remediation* preferred due to their effectiveness and low cost.

The *remediation* methods can be roughly classified in two categories: (a) those that leave the toxic elements on the soil, immobilizing them to avoid their migration, and (b) those that remove contaminants from the soil, potentially saving it for future uses. In the present work, we are interested in the second class, and in particular in the *soil washing technology*. Among the different approaches on soil remediation processes, the *soil washing method* has attracted considerable attention, mainly for its ability to permanently remove heavy metals form the contaminated soil, combined with short duration procedure and remarkable cost effectiveness, when compared with other methods. Another advantage is the possibility of recovery of recyclable material or even energy production (Wuana et al., 2010; Cheng et al., 2020). The details of soil washing were primarily explored in the thorough review by Peters (Peters, 1999), being the *soil washing* described as a process in which excavated soil is first treated by physical separation, and it is then washed to remove contaminants using a chemical extracting solution. After the chemical treatments, the cleaned soil is returned to the original place. Due to this, the selection of effective and harmless washing reagents should be carefully pondered. Considering the methodology and the principle of the washing soil method, it is only applicable if there is an efficient transfer of the metal contaminants from the soil to the extracting solution. To achieve that, and due to the fact that heavy metals in the soils occur predominantly in an absorbed state, strongly bound to soil particles, is fundamental the use of extractant agents optimized for the solubilization of the target metals. For this purpose, several chemicals have been used, namely surfactants, cyclodextrins, organic acids and chelating agents. Among them, the selection and applicability is being studied on a case-by-case basis, as it depends on several parameters as the metal to remove and the characteristics of the soil as, for example, the pH. Furthermore, being one of the main goals of soil remediation the preservation as much as possible of the natural properties of the soil, it limits the number of possible extracting agents as, for example; strong acids can attack and degrade the soil structure, reason why the use of weak organic acids or chelating agents is often preferred (Wuana et al., 2010).

Chelating agents are applied in a considerable number of activities, spanning from medicine (Aaseth et al., 2016) to industry, from agriculture to domestic activities, from analytical chemistry to alimentary industry, and also in soil *remediation*, all due to their ability to complex metal ions. They act in different ways, such as (i) removing target metal ions from environment, (ii) avoiding metal precipitation, (iii) favoring ion crossing through biological membranes. Despite the fact that the complexing ability and the acid-base properties of chelating agents have been the object of extensive research, a detailed design of proper chelators according to the target metal ions and to their process requirements (solubility, lipo/hydrophilic properties, etc.) has not yet been fully exploited.

This work aims to give a methodological contribution in the choice of chelating agents for *soil washing remediation* based on our knowledge and expertise on the use of metal chelators in clinical and environmental applications (Crisponi et al., 1999, 2012; Villaescusa et al., 2002; Nurchi and Villaescusa, 2008, 2012; Nurchi et al., 2010, 2016; Crespo-Alonso et al., 2013; Aaseth et al., 2016).

In particular, a method that allow a preliminary screening among various potential ligands toward target metal ions will be proposed, based on simplifying assumptions, saving time and money need for a thorough experimental study on the behavior of these ligands in the field.

SOIL CONCENTRATION RANGES AND REGULATORY GUIDELINES FOR RELEVANT METAL IONS

A first step of the restoration of metal-polluted ecosystems requires a correct characterization of the state of pollution and preliminary knowledge of the characteristics of the soil. To access the concentration of metals contaminants in soil, total elemental analysis is usually the preferred method, as it is not affected by the chemical or physical form on which the metal is present. In this sense, the level of metal contamination is expressed by mg metal per kg of soil (mg Kg^{-1}). This quantification is then the basis of the establishment of adequate remediation processes, and several guidelines can be recommended. This is done

TABLE 1 | Soil concentration ranges, regulatory guidelines, intervention and target values for various metal ions of ascertained and potential toxicity.

Metal ion		Intervention value		Target value	
Symbol	**Atomic weight**	**mg.Kg^{-1}**	**mM***	**mg.Kg^{-1}**	**mM***
Hg	200.59	530	2.6	85	0.4
Cd	112.41	380	3.4	100	0.89
Pb	207.20	210	1.0	35	0.17
Cu	63.55	10	0.2	0.3	0.01
Ni	58.69	720	12.3	140	2.4

Data from ref. Wuana and Okieimen (2011).
**mM concentration corresponds to the concentration of a solution obtained suspending 1 Kg of soil in 1 L.*

following two well-established parameters: intervention values and target values. Intervention values specify the concentration limits (in mg Kg^{-1} or mmol Kg^{-1}) after which the quality of soil for human, animal and plant life starts to be severely compromised and concentrations in excess of the intervention values correspond to serious contamination. On the other hand, target values indicate the soil quality levels required for the full restoration of the functionality of soil. In **Table 1** we report the intervention and target values for various metal ions of ascertained and potential toxicity, as previously reported by Wuana and Okieimen (2011).

METHOD FOR ASSESSING THE CHELATING ABILITY

The right selection of the chelating agent is the fundamental step for a successful chelating agent-based soil washing process. With this in mind, we developed a simple method to assess the ability of different ligands in chelating metal ions, which provides at a glance information on this ability and allows a preliminary classification of the ligands on the base of their chelating properties toward the target metal ions. The procedure is based on an extension of Reilley's method used mainly in analytical applications of titrations with ethylene-diamine-tetraacetic acid (EDTA) (Reilley and Schmid, 1958; Crisponi et al., 2000).

Our method, from now on designated as *Nurchi's method*, is a simplistic method that focuses on the complex formation reaction between the metal ion M (assumed as a free ion in solution) and the chelating agent L, neglecting all the influences of non-thermodynamic contributions, including the binding with soil components. In a first stage, we assume (a) that the ligand does not interact with protons, and (b) the formation of a simple 1:1 complex ML through the equilibrium depicted on Equation (1). The latest assumption is generally valid for the polyamino carboxylic acids used in soil remediation.

$$M + L \leftrightarrows ML \tag{1}$$

The related complex formation constant is thus defined as:

$$K = \frac{[ML]}{(L_0 - [ML])\,(M_0 - [ML])} \tag{2}$$

TABLE 2 | Values of log *K* to obtain the values of *f* (ratio between complexed and total metal ion) reported in the first column, for given values of total metal ion M_0 and ratio $R = L_0/M_0$.

		log *K*			
M_0	***f***	***R* = 2**	***R* = 10**	***R* = 50**	***R* = 100**
2×10^{-5} M	0.25	3.98	3.23	2.53	2.22
	0.50	4.52	3.72	3.00	2.70
	0.75	5.08	4.21	3.48	3.18
	0.99	6.69	5.74	5.00	4.70
2×10^{-4} M	0.25	2.98	2.23	1.53	1.22
	0.50	3.52	2.72	2.00	1.70
	0.75	4.08	3.21	2.48	2.18
	0.99	5.69	4.74	4.00	3.70
2×10^{-3} M	0.25	1.98	1.23	0.53	0.22
	0.50	2.52	1.72	1.00	0.70
	0.75	3.08	2.21	1.48	1.18
	0.99	4.69	3.74	3.00	2.70

where M_0 and L_0 are the total concentration of metal and ligand, respectively. Equation (2) can then be rearranged in a suitable form in order to calculate the value of the constant *K* necessary to reach a desired amount of M_0 in the complexed form (ML), expressed as the ratio of the complex concentration to the total concentration of metal, i.e., as $f = [ML]/[M_0]$, for given values of the total metal concentration M_0 and of total ligand concentration L_0 expressed by the ratio $R = L_0/M_0$. Equation (2) is thus transformed in Equation (3):

$$K = \frac{f}{M_0\,(R - f)\,(1 - f)} \tag{3}$$

If we have an estimate of the content of the metal ion in the soil, roughly assuming that it is totally transferred to solution when treating a given weight of soil with a defined volume of a solution of the chelating agent with a L_0 concentration, we can establish the values M_0 and R. For clarification, in **Table 2** we report the values of log *K* to obtain 25, 50, 75, and 99% of the total metal transformed in the complex form (i.e., $f = 0.25$, 0.50, 0.75, and 0.99 respectively) for different M_0 concentration ranging from 2 $\times 10^{-5}$ M to 2 $\times 10^{-3}$ M, and for *R*-values from 2 to 100.

For a better understanding of *Nurchi's method* and its way of application we will use, as examples several amino carboxylic ligands (see **Table 3**), largely used in soil remediation mainly due to their biodegradability properties. EDTA will be also considered for comparison purposes. The present ligands are characterized by a definite number *n* of protonation equilibria and, consequently, protons compete with metal ions for the same basic sites where protonation and metal coordination occur. In this case, the *effective* or *conditional stability constant* β_{eff} (Ringbom, 1963) is an actual measure of the real capacity of a ligand to bind a metal ion at any given pH value.

The *effective stability constant,* expressed as a function of the total concentrations of chelating agent and metal ion, takes into account all the different protonated species according to

TABLE 3 | Structure, IUPAC name, acronym and molecular formula of the ligands considered in this study.

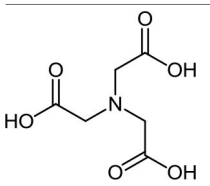	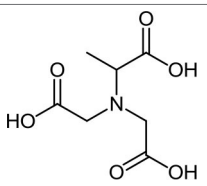	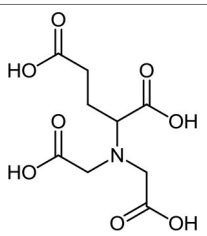
2, 2', 2" -Nitrilotriacetic acid **NTA**, $C_6H_9NO_6$	*N*, *N*-Bis(carboxymethyl)alanine **MNTA**, $C_7H_{11}NO_6$	*N*, *N*-Bis(carboxymethyl)-glutamic acid **GLDA**, $C_9H_{13}NO_8$
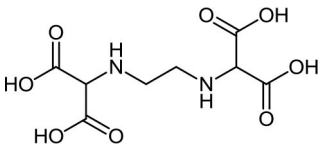	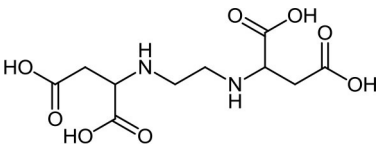	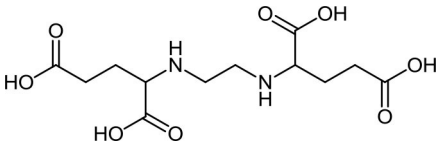
2, 2' -(1, 2-Ethanediyldiimino) dimalonic acid **EDDM**, $C_8H_{12}N_2O_8$	2, 2' -(1, 2-Ethanediyldiimino) disuccinic acid **EDDS**, $C_{10}H_{16}N_2O_8$	2, 2' -(1,2-Ethanediyldiimino) diglutamic acid **EDDG**, $C_{12}H_{20}N_2O_8$
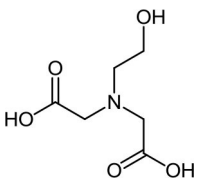	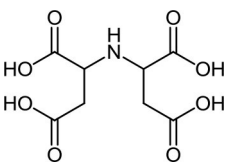	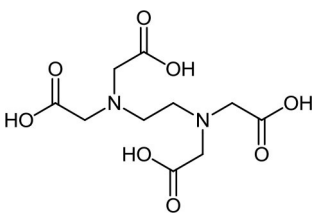
2, 2' -[(2-Hydroxyethyl) imino]diacetic acid **HIMDA**, $C_6H_{11}NO_5$	2, 2' -Iminodisuccinic acid **IDS**, $C_8H_{11}NO_8$	2, 2', 2", 2"' -(1, 2-Ethanediyldinitrilo) tetraacetic acid **EDTA**, $C_{10}H_{16}N_2O_8$

the protonation equilibria summarized on Equation (4), and the complex formation equilibrium (Equation 5):

$$\begin{aligned} L^{n-} + H^{+} &\leftrightarrows LH^{(n-1)-} \\ LH^{(n-1)-} + H^{+} &\leftrightarrows LH_2^{(n-2)-} \\ &\cdots\cdots \\ LH_{(n-1)}^{-} + H^{+} &\leftrightarrows LH_n \end{aligned} \quad (4)$$

$$L^{n-} + M^{p+} \leftrightarrows LM^{(n-p)-} \quad (5)$$

Being the complex formation constant described as:

$$\beta_{LM} = \frac{[LM^{(n-p)-}]}{[L^{n-}][M^{p+}]} \quad (6)$$

The mass balance equation for total ligand can then be expressed by Equation (7):

$$[L_{tot}] = [L^{n-}] + [LH^{(n-1)-}] + [LH_2^{(n-2)-}] + ... + [LH_n] + [LM^{(n-p)-}] \quad (7)$$

that, using the protonation constants of equilibria (4), is converted in:

$$[L_{tot}] = [L^{n-}](1 + \beta_1[H] + \beta_2[H]^2 + \beta_3[H]^3 + + \beta_n[H]^n) + [LM^{(n-p)-}] \quad (8)$$

At this point, the complex formation constant [Equation (6)] can be written as:

$$\beta_{LM} = \frac{[LM^{(n-p)-}]}{\frac{\left([L_{tot}] - \left[LM^{(n-p)-}\right]\right)}{D(H)}([M_{tot}] - [LM^{(n-p)-}])} \quad (9)$$

and the effective stability constant β_{eff} can be determined as:

$$\beta_{eff} = \frac{\beta_{LM}}{D(H)} = \frac{[LM^{(n-p)-}]}{\left([L_{tot}] - \left[LM^{(n-p)-}\right]\right)([M_{tot}] - [LM^{(n-p)-}])} \quad (10)$$

Interestingly, Equation (10) is formally identical to Equation (2). As such, all the considerations made above, regarding the values

TABLE 4 | Protonation and complex formation constants of the amino carboxylic ligands considered in this study.

	log β								
Species	**NTA**	**MNTA[9]**	**GLDA[10]**	**HIMDA**	**EDDM**	**EDDS**	**EDDG**	**IDS**	**EDTA**
LH	9.84[1]	10.39	9.36	8.59[11]	9.4[16]	10.1[20]	9.46[25]	10.28[29]	10.21[34]
LH_2	12.40[1]	12.83	14.39	10.83[11]	16.16[16]	17.01[20]	16.27[25]	14.77[29]	16.41[34]
LH_3	14.23[1]	14.27	17.88	12.29[11]	19.06[16]	20.85[20]	20.52[25]	18.23[29]	19.18[34]
LH_4			20.44		21.27[16]	23.90[20]	23.80[25]	20.81[29]	21.20[34]
LH_5						25.3[20]		22.83[29]	
LH_6						27.4[20]			
CdL	9.8[2]	10.61		7.21[12]		10.3[21]	8.76[25]		16.41[35]
PbL	11.34[3]	12.07		9.45[3]	11.12[17]	11.3[21]	8.62[25]		17.93[35]
HgL	13.48[4]		14.33	5.48[7]	18.64[16]	14.40[22]	16.66[25]		22.02[36]
FeL	15.87[5]			11.60[11]		20.6[20]	15.7[26]	14.70[30]	25.10[37]
MnL	7.44[6]			5.55[7]	8.50[18]	8.63[22]	6.74[27]		13.8[35]
CuL	12.94[3]	13.88	13.09	11.72[3]	13.0[19]	18.7[20]	12.65[28]	12.69[31]	18.7[35]
ZnL	10.67[7]	11.06		8.02[13]		13.58[20]	10.25[25]	10.30[32]	16.39[35]
CaL	6.57[8]	6.97	5.18	4.58[14]	4.80[16]	4.58[23]	2.59[25]	4.63[33]	10.69[35]
MgL		5.83	5.93	3.5[15]	4.51[16]	5.82[24]	3.0[25]	5.52[33]	8.9[35]

[1]*Ref. Daniele et al. (1985), I = 0.1 M (R4N.X) and T = 25°C.*
[2]*Ref. Schwarzenbach and Gut (1956), I = 0.1 M (KNO_3) and T = 20°C.*
[3]*Ref. Felcman and Da Silva (1983), I = 0.1 M (KNO_3) and T = 25°C.*
[4]*Ref. Gritmon et al. (1977), I = 0.5 M ($NaClO_4$) and T = 25°C.*
[5]*Ref. Motekaitis and Martell (1994), I = 0.1 M (KCl) and T = 25°C.*
[6]*Ref. Schwarzenbach and Freitag (1951), I = 0.1 M (KCl) and T = 20°C.*
[7]*Ref. Schwarzenbach et al. (1955), I = 0.1 M (KCl) and T = 20°C.*
[8]*Ref. Moeller and Ferrus (1962), I = 0.1 M (KNO_3) and T = 25°C.*
[9]*Ref. Riečanská et al. (1974), I = 0.1 M (KNO_3) and T = 20°C.*
[10]*Ref. Gorelov and Nikolskii (1977), I = 0.1 M (KNO_3) and T = 25°C.*
[11]*Ref. Anderegg, 1986, I = 1.0 M ($NaClO_4$) and T = 25°C.*
[12]*Ref. Kodama et al. (1974), I = 0.3 M ($NaNO_3$) and T = 25°C.*
[13]*Ref. Kodama (1974), I = 0.3 M ($NaClO_4$) and T = 25°C.*
[14]*Ref. Mighri and Rumpf (1975), I = 0.1 M (?) and T = 25°C.*
[15]*Ref. Verdier and Piro (1969), I = 0.1 M ($NaClO_4$) and T = 25°C.*
[16]*Ref. Gorelov and Babich (1972b), I = 0.1 M (KNO_3) and T = 25°C.*
[17]*Ref. Gorelov et al. (1973), I = 0.1 M (KNO_3) and T = 25°C.*
[18]*Ref. Samsonov and Gorelov (1974), I = 0.1 M (KNO_3) and T = 25°C.*
[19]*Ref. Mashihara et al. (1973), I = 0.1 M (KNO_3) and T = 25°C.*
[20]*Ref. Orama et al. (2002), I = 0.1 M (NaCl) and T = 25°C.*
[21]*Ref. Vasilev et al. (1990), I = 0.1 M (KNO_3) and T = 25°C.*
[22]*Ref. Vasilev and Zaitseva (1993), I = 0.1 M (KNO_3) and T = 25°C.*
[23]*Ref. Vasilev et al. (1989), I = 0.1 M (KNO_3) and T = 25°C.*
[24]*Ref. Gorelov and Babich (1971), I = 0.1 M (KNO_3) and T = 25°C.*
[25]*Ref. Gorelov and Babich (1972a), I = 0.1 M (KNO_3) and T = 25°C.*
[26]*Ref. Sunar and Trivedi (1971), I = 0.1 M (KNO_3) and T = 30°C.*
[27]*Ref. Samsonov and Gorelov (1974), I = 0.1 M (KNO_3) and T = 25°C.*
[28]*Ref. Trivedi et al. (1971), I = 0.1 M (KNO_3) and T = ?.*
[29]*Ref. Knyazeva et al. (2002), I = 0.1 M (KCl) and T = 25°C.*
[30]*Ref. Nikol'skii and Knyazeva (2002), I = 0.1 M (KCl) and T = 25°C.*
[31]*Ref. Vasilev and Al (1998), I = 0.1 M (KNO_3) and T = 25°C.*
[32]*Ref. Vasilev and Al (1994), I = 0.1 M (?) and T = 25°C.*
[33]*Ref. Vasilev et al. (1999), I = 0.1 M (KNO_3) and T = 25°C.*
[34]*Ref. Gridchin et al. (2004), I = 0.1 M (KNO_3) and T = 25°C.*
[35]*Ref. Sarma and Ray (1956), I = 0.1 M ($NaClO_4$) and T = 25°C.*
[36]*Ref. Brunetti et al. (1969), I = 0.1 M (KNO_3) and T = 25°C.*
[37]*Ref. Delgado et al. (1997), I = 0.1 M (KNO_3) and T = 25°C.*

of log K necessary to reach a given percent of the total metal transformed in the complex form (f = 0.25, 0.50, 0.75, and 0.99 respectively) for different M_0 values, are valid, as well as the values reported in **Table 2**.

With base on the literature protonation constants reported in **Table 4**, we could calculate the representative curves of log $D(H)$ values as a function of pH for all the eight ligands in study. The corresponding trend lines are presented in **Figure 1**.

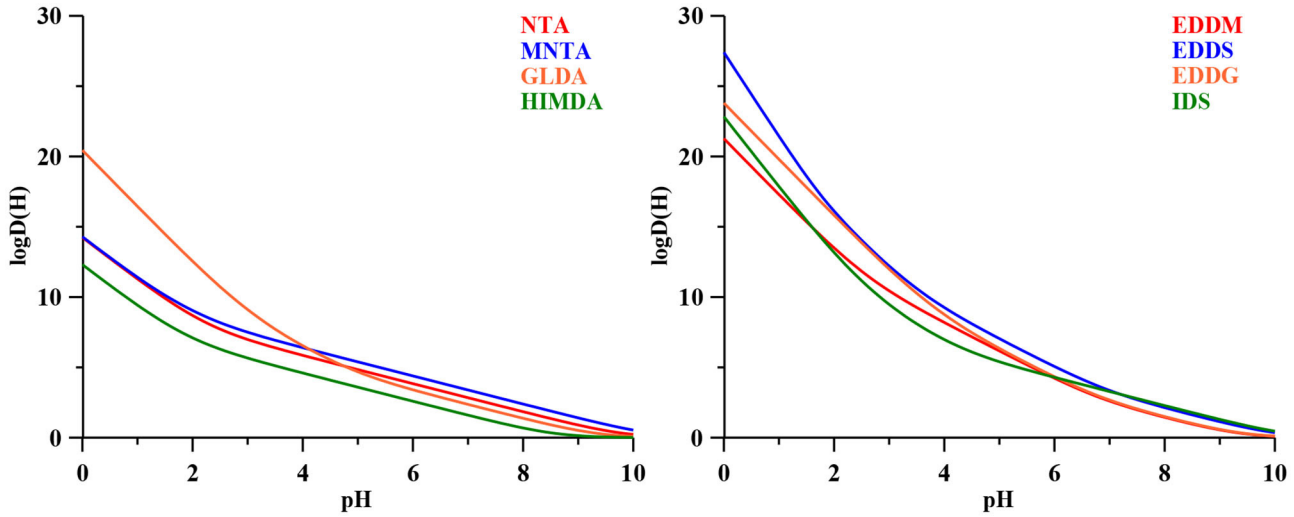

FIGURE 1 | The log *D(H)* functions for the amino carboxylic ligands considered in this study (**Table 3**), calculated with the literature protonation constants presented in **Table 4**.

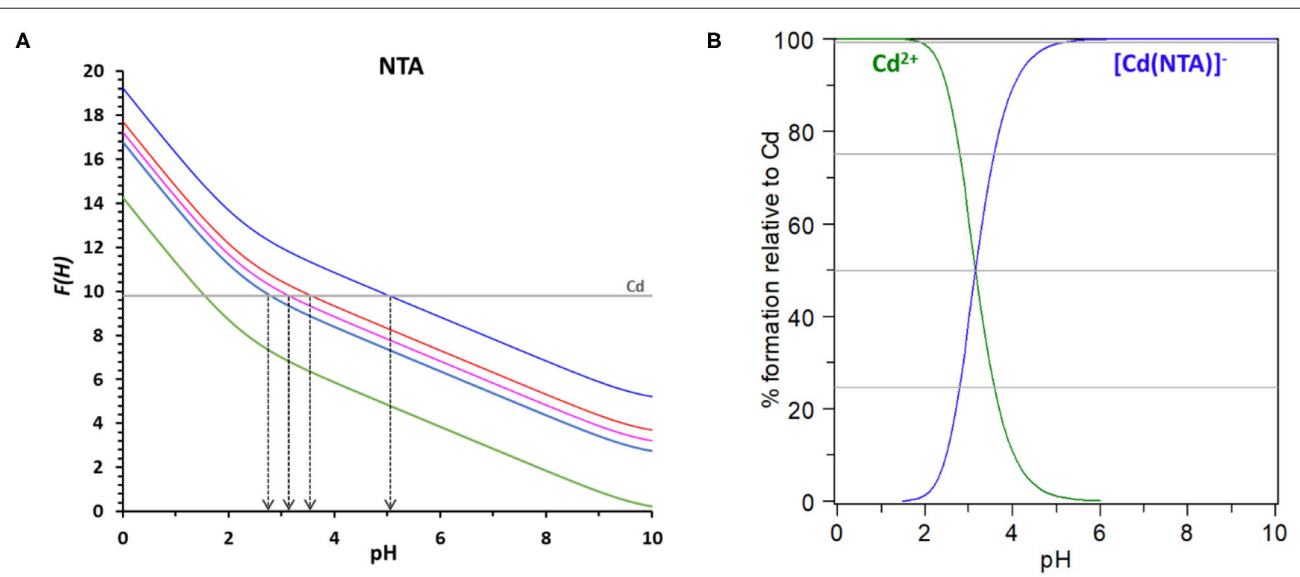

FIGURE 2 | (A) The *D(H)* function for NTA is reported in red, the *F(H)* functions for the system Cd-NTA with total cadmium 2×10^{-5} M and $R = 50$ are reported for the 0% of complex formation (green), 25% (light blue), 50% (pink), 75% (red) and 99% (blue). **(B)** Speciation plot for the system Cd-NTA with $[Cd_{tot}] = 2 \times 10^{-5}$ M and $[NTA_{tot}] = 1 \times 10^{-3}$ M ($R = 50$).

In **Table 4** are also depicted the complex formation constants for the mentioned ligand toward several metal ions of interest.

These functions constitute the basis for determining the behavior of each ligand. In fact, if we present Equation (10) in its logarithmic form (Equation 11) we can see that function *F(H)* is obtained by adding to log *D(H)* the log βeff required for the transformation of the given % of total metal ion in the complexed form.

$$F(H) = \log \beta_{\text{eff}} + \log D(H) = \log \beta_{\text{LM}} \qquad (11)$$

F(H) representation will then be the basis for the evaluation of the chelating ability of the ligands of interest on *Nurchi's method*. For a clear elucidation of the method, we will now describe, in detail, the procedure applied to the system NTA/Cd^{2+}, with $M_0 = 2 \times 10^{-5}$ *M* and $R = 50$. In such a case, the value of log β_{eff} to reach 25% of complexed Cd^{2+} is 2.53, for 50% is 3.00, for 75% is 3.48 and is 5.00 for 99% (**Table 1**). These values, added to the function *D(H)* for NTA reported in green in **Figure 2A**, allow the calculation of the *F(H)* functions for NTA corresponding to 25, 50, 75, and 99 % of complex formation reported in different colors in the same **Figure 2A**. The value log $\beta_{\text{CdNTA}} = 9.8$ is

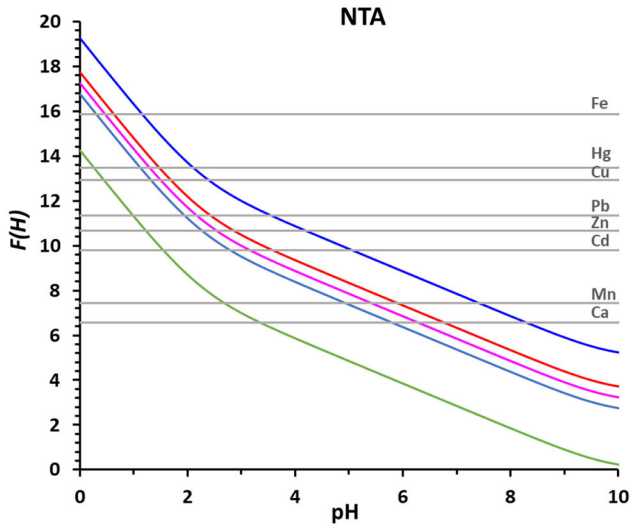

FIGURE 3 | The *F(H)* functions of NTA (total metal ion concentration 2×10^{-5} M and $R = 50$) for 0% of complex formation (green), 25% (light blue), 50% (pink), 75% (red), and 99% (blue). The straight gray lines correspond to the log β_{LM} of the indicated metal ions with NTA.

reported as a straight line parallel to the pH axis. This line intersects the 25% *F(H)* function at pH = 2.79, the 50% *F(H)* function at pH = 3.15, the 75% *F(H)* function at pH = 3.58 and the 99% *F(H)* function at pH = 5.05. It means that the log β_{CdNTA} = 9.8 determines a conditional constant at pH = 2.79 that allows the 25% complexation of total cadmium, and so on till the 99% of complexation at pH = 5.05.

The same information can be obtained from the speciation plot, calculated with Hyss program (Alderighi et al., 1999) for the referred system (**Figure 2B**), where can be easily seen that the formation curve of the cadmium complex reaches 25% at pH = 2.79, 50% at pH = 3.15, 75% at pH = 3.87 and 99% at pH = 5.05.

The advantage of the proposed method based on the *F(H)* function is most evident in **Figure 3** were the log β_{MNTA}'s of NTA with all the metal ions reported in **Table 3** are represented as straight gray lines. **Figure 3** gives at a glance the pH ranges at which the complexation of each metal ion takes place, that could be deducted in a very laborious way from the corresponding speciation plots created for all the metal ions with NTA, HIMDA, EDDG, EDDS, and EDTA, from the stability constants reported in **Table 4** (summary in **Supplementary Figure 1**).

It is clearly inferred, from **Figure 3**, that Fe^{3+}, the metal ion with the strongest stability constant (log β_{LM} = 15.87), is already complexed at low pH values (25% at pH 0.3 and 99% at pH 1.2) and the complex formation happens in a narrow range (0.9 pH units from 25 to 99%). On the contrary, Ca^{2+}, the metal ion with the lowest stability constant (log β_{LM} = 6.57), is complexed at higher pH values (25% at pH 5.8 and 99% at pH 8.3) and the complex formation happens in a broader pH range (2.5 pH units from 25 to 99%).

The range of complexation increases as the complexation occurs in a flatter part of curve *D(H)*, and so of curve *F(H)*. As

TABLE 5 | pH range of complex formation (from 25 to 99%) for different metal ions with the indicated chelating agents.

	pH range				
Metal ion	**NTA**	**HIMDA**	**EDDG**	**EDDS**	**EDTA**
Fe^{3+}	0.30–1.15	1.02–2.46	2.69–3.40	1.56–2.13	< 0–0.3
Hg^{2+}	1.12–2.06	5.81–8.51	2.41–3.12	3.12–3.93	0.4–1.1
Cu^{2+}	1.28–2.32	0.99–2.41	3.55–4.45	1.99–2.59	1.2–1.9
Pb^{2+}	1.84–3.55	2.27–4.40	5.05–6.38	4.18–5.34	1.5–2.2
Zn^{2+}	2.27–4.20	3.35–5.82	4.40–5.60	3.41–4.26	1.9–2.7
Cd^{2+}	2.70–5.00	4.16–6.67	5.05–6.38	4.68–5.86	1.9–2.7
Mn^{2+}	4.85–7.45	5.81–8.51	6.05–7.80	5.46–6.81	2.7–3.8
Ca^{2+}	5.80–8.27	6.75–> 10.0	9.93–> 10.0	8.08–> 10.0	4.1–5.4

mentioned above, once calculated the *D(H)* curve for a given ligand, the *F(H)* curves at different M_0 and R values can be easily derived by adding to the *D(H)* values the proper values of log β_{eff}.

Using the proposed method and with base on the complex formation constants reported in **Table 4**, we could compare the binding ability of the four ligands for which literature data are available for all the chosen metal ions (NTA, HIMDA, EDDS, EDDG), and the corresponding *F(H)* plots are presented in **Figure 4**. For simplifying the discussion, we collected from these plots the pH range of complex formation for the eight metal ions and the four ligands, i.e., the pH of the intersection points of log β_{LM} with the $F(H)_{25\%}$ and the $F(H)_{99\%}$ (**Table 5**). Lower intervals correspond to a stronger complex. As a first step, a comparison can be made between the structurally similar NTA and HIMDA: the lack of the third carboxylic group in HIMDA drastically reduces its binding ability, in a marked extent with Hg^{2+} and in a minor extent in Mn^{2+}, Cd^{2+}, Zn^{2+} and Fe^{3+}, being Cu^{2+} practically unaffected. In case of Cu^{2+} we hypothesize that this is due to the fact that this metal ion may form a stable square planar complex with HIMDA, structurally similar to that with Pd^{2+} (BIACDD structure, **Supplementary Figure 3**). The comparison between EDDS and EDDG shows a slightly higher coordination capability of EDDS for all metal ions, except for Hg^{2+}. Presumably, the longer arms connecting two of the carboxylic groups favor the coordination of the larger mercuric ion.

EDTA is also reported, as being one of the most used chelating agents. From the plots presented in **Figure 4**, and data on **Table 5**, we can see that EDTA is, among all the evaluated ligands, the most efficient chelator for all the metals considered. Although, in case of Cu^{2+} and Hg^{2+}, NTA can be used with the same expected rate of success in terms of metal remediation.

This preliminary screening gives evidence of the superiority of EDTA, immediately followed by NTA among the examined ligands, and of the inability of HIMDA to act as a ligand for environmental remediation. EDDS, and in a lower extent, EDDG can instead be used, even if with a lower capability.

We must remember that the results here reported assumed the presence of a free metal ion in the soil in contact with the washing solution. In reality, the metal ion is usually complexed

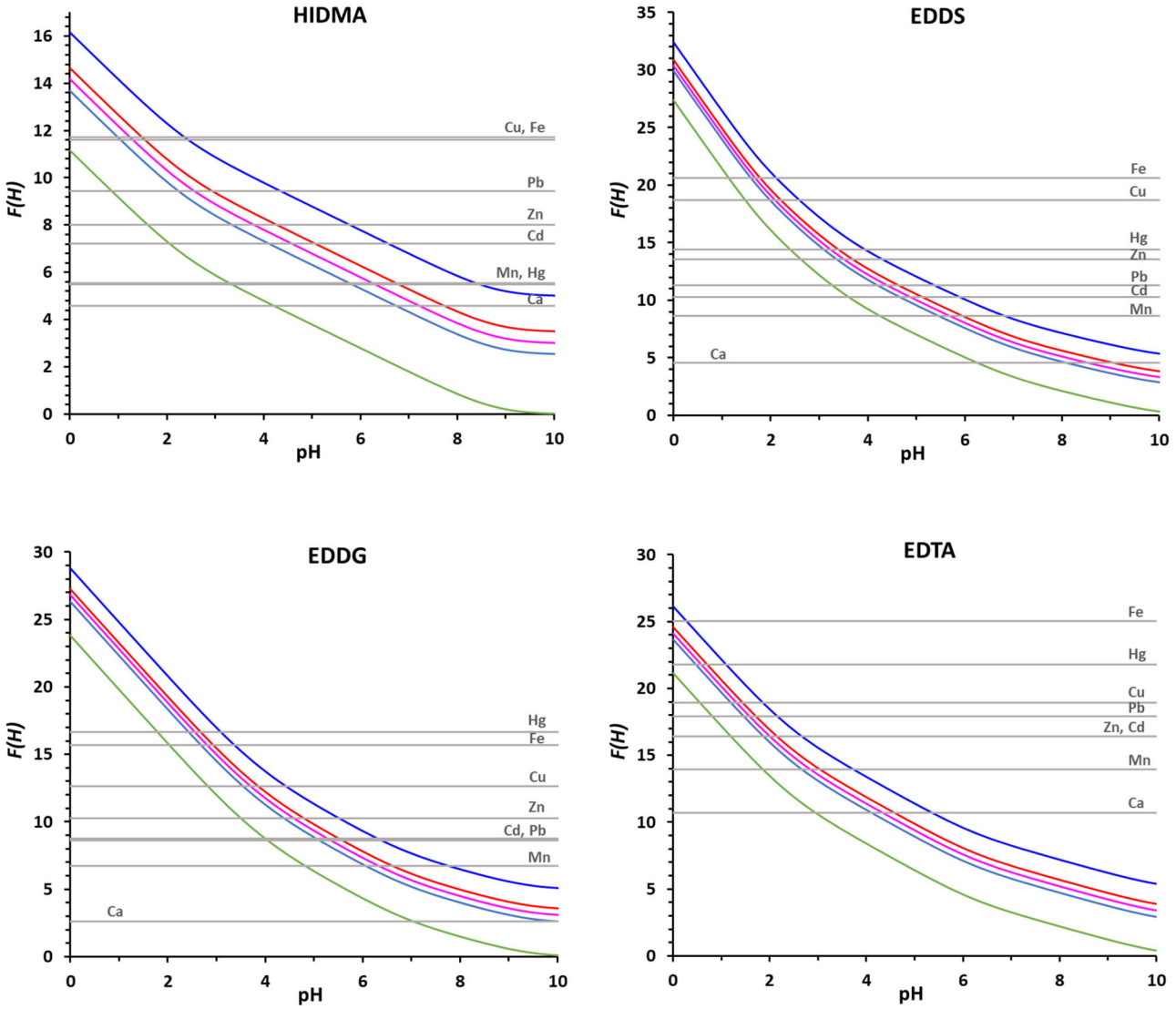

FIGURE 4 | The *F(H)* functions for the ligands HIMDA, EDDS, EDDG and EDTA with the metal ions in **Table 3**, at [M_{tot}] 2×10^{-5} M and $R = 50$, are reported for the 0% of complex formation (green), 25% (light blue), 50% (pink), 75% (red) and 99% (blue).

by the inorganic and organic components of the soil, and the complex formation reaction is, in reality, a competition between the chelating agent and the soil ligands for the target metal ion. Since the hydroxide formation constitutes probably the most competitive reaction, we checked the validity, or the limits, of our assumptions recalculating the speciation plots (**Supplementary Figure 2**) this time using a model that included the hydroxide formation constants [**Supplementary Table 1**, from Baes and Mesmer (Baes and Mesmer, 1976)]. As can be observed, in the generality of the cases, the inclusion of hydrolysis equilibria does not change the speciation plots. Only in the case of Hg^{2+} and Fe^{3+} the formation of hydroxides is apparent at high pH values. In particular, the formation of the weak complex between HIMDA and Hg^{2+} is completely hindered, and partially the formation of the complex with EDDS. In this way we can conclude that the action of neglecting the competitive reactions of hydrolysis can be considered valid in the majority of situations. Furthermore, HIMDA can form with Fe^{3+} complexes with different protonation degrees, instead of the unique assumed complex, but this ligand presents peculiar features that differentiate it from amino poly-carboxylic ligands.

To sum up, we can say that *Nurchi's method* provides a primary fundamental picture of the main features of the complexing ability of a given chelator as the minimum pH values at which it can operate and the competition among the present metal ions, but most importantly permits a preliminary screening between a set of potential ligands. This treatment can act as a guide in the design of metal chelators specific for target metal ions by showing the behavior of existing ligands characterized

by selected binding groups, as, for example, mercapto ligands for mercury.

CONCLUSION

The method here proposed allows determining both the suitability of the ligand for scavenging the target metal ions, and the minimal concentration of ligand to be used, minimizing the adverse effects on essential metal ions. This is particularly relevant when studying the real application of a washing ligand to a specific soil, knowing the total concentrations of metals to be removed before the experimental determination of its behavior. For that purpose, the use of databases of stability constants is highly recommended, together with speciation programs.

We would remember here that different approaches have been proposed in the literature to assess the sequestering ability of ligands toward metal cations, which can be complementary to the here proposed method. The reviews by Bazzicalupi et al. (2012) and by Crea et al. (2014) examine these treatments and thoroughly discusses their *pros* and *cons*. The necessity to use suitable data, obtained in the possible similar conditions to those of soils under treatment and the necessity of reliable stability constants must be stressed. In essence, inefficient treatments and severe procedural errors can sometimes derive from the use of bad/unreliable data. Besides allowing a preliminary screening of the binding ability of chelating agents toward the target polluting metal ions, and those typical of the soils, the proposed method can be applied in the multiple uses of chelating agents, spanning from biomedical to industrial applications. As an example, we can envisage its use on the evaluation of the role of different biomolecules, as for example bacterial metallophores, on metal uptake and homeostasis in living organisms. This information is paramount for different actions, namely, for the development of new strategies for the fight of antibiotic resistant pathogenic bacteria.

AUTHOR CONTRIBUTIONS

VN, GC, and RB: conceptualization. RC, GS, and SG: data elaboration. VN, GC, SG, and RB: data curation. All authors have read and agreed to the published version of the manuscript.

FUNDING

VN thanks Regione Autonoma della Sardegna for the financial support of the project RASSR79857 Metallo-farmaci innovativi: biotrasformazione e target biologici. Un approccio integrato, RC acknowledges the financial support to the international Ph.D. program in Innovation Sciences and Technologies (PON RI 2014-2020) at the University of Cagliari.

ACKNOWLEDGMENTS

This publication is based upon work from COST Action CA18202 NECTAR–Network for Equilibria and Chemical Thermodynamics Advanced Research, supported by COST (European Cooperation in Science and Technology).

SUPPLEMENTARY MATERIAL

The Supplementary Material for this article can be found online at: https://www.frontiersin.org/articles/10.3389/fchem.2020.597400/full#supplementary-material

REFERENCES

Aaseth, J., Crisponi, G., and Andersen, O. (2016). *Chelation Therapy in the Treatment of Metal Intoxication*. London: Elsevier–Academic Press.

Alderighi, L., Gans, P., Ienco, A., Peters, D., Sabatini, A., and Vacca, A. (1999). Hyperquad simulation and speciation (HySS): a utility program for the investigation of equilibria involving soluble and partially soluble species. *Coord. Chem. Rev.* 184, 311–318. doi: 10.1016/S0010-8545(98)00260-4

Anderegg, G. (1986). The stability of iron(III) complexes formed below pH=3 with glycinate, iminodiacetate, β-hydroxyethyliminodiacetate, N,N-Di-(hydroxyethyl)-glycinate, nitrilotriacetate and triethanolamine. *Inorg. Chim. Acta* 121, 229–231. doi: 10.1016/S0020-1693(00)84525-9

ATSDR (2020). *Agency for Toxic Substances and Disease Registry (ATSDR)*. Available online at: https://www.atsdr.cdc.gov/ (accessed July 15, 2020).

Baes, C. F., and Mesmer, R. E. (1976). *The Hydrolysis of Cations*. New York, NY: John Wiley and Sons.

Bazzicalupi, C., Bianchi, A., Giorgi, C., Clares, M. P., and García-España, E. (2012). Addressing selectivity criteria in binding equilibria. *Coord. Chem. Rev.* 256, 13–27. doi: 10.1016/j.ccr.2011.05.013

Brunetti, A. P., Nancollas, G. H., and Smith, P. N. (1969). Thermodynamics of ion association. XIX. Complexes of divalent metal ions with monoprotonated ethylenediaminetetraacetate. *J. Am. Chem. Soc.* 91, 4680–4683. doi: 10.1021/ja01045a014

Cheng, S., Lin, Q., Wang, Y., Luo, H., Huang, Z., Fu, H., et al. (2020). The removal of Cu, Ni, and Zn in industrial soil by washing with EDTA-organic acids. *Arabian J Chem.* 13, 5160–5170. doi: 10.1016/j.arabjc.2020.02.015

Crea, F., Stefano, C. D., Foti, C., Milea, D., and Sammartano, S. (2014). Chelating agents for the sequestration of mercury(II) and monomethyl mercury(II). *Curr. Med. Chem.* 21, 3819–3836. doi: 10.2174/0929867321666140601160740

Crespo-Alonso, M., Nurchi, V. M., Biesuz, R., Alberti, G., Spano, N., Pilo, M. I., et al. (2013). Biomass against emerging pollution in wastewater: ability of cork for the removal of ofloxacin from aqueous solutions at different pH. *J. Environ. Chem. Eng.* 1, 1199–1204. doi: 10.1016/j.jece.2013.09.010

Crisponi, G., Nurchi, V. M., Crespo-Alonso, M., and Toso, L. (2012). Chelating agents for metal intoxication. *Curr. Med. Chem.* 19, 2794–2815. doi: 10.2174/092986712800609742

Crisponi, G., Nurchi, V. M., Pinna, R., and Pivotta, T. (2000). Titolazioni chelometriche con EDTA: considerazioni sul grafico di Reilley. *Rend. Sem. Fac. Sci. Univ. Cagliari* 70, 83–89.

Crisponi, G., Nurchi, V. M., Silvagni, R., and Faa, G. (1999). Oral iron chelators for clinical use. *Polyhedron* 18, 3219–3226. doi: 10.1016/S0277-5387(99)00277-6

Daniele, P. G., Rigano, C., and Sammartano, S. (1985). Ionic strength dependence of formation constants. Alkali metal complexes of ethylenediaminetetraacetate nitrilotriacetate, diphosphate, and tripolyphosphate in aqueous solution. *Anal. Chem.* 57, 2956–2960. doi: 10.1021/ac00291a046

Delgado, R., Do Carmo Figueira, M., and Quintino, S. (1997). Redox method for the determination of stability constants of some trivalent metal complexes. *Talanta* 45, 451–462. doi: 10.1016/S0039-9140(97)00157-4

Duffus, J. H. (2002). "Heavy metals" a meaningless term?. *Pure Appl. Chem.* 74, 793–807. doi: 10.1351/pac200274050793

Felcman, J., and Da Silva, J. J. R. F. (1983). Complexes of oxovanadium (IV) with polyaminocarboxylic acids. *Talanta* 30, 565–570. doi: 10.1016/0039-9140(83)80134-9

Gorelov, I., and Babich, V. (1971). Complex formation by alkaline earth elements with ethylenediaminedisuccinic acid. *Zh. Neorg. Khim.* 16, 481–482.

Gorelov, I., and Babich, V. (1972a). *Zh. Obshch. Khim.* 42:434.

Gorelov, I., and Babich, V. (1972b). *Zh. Neorg. Khim.* 17:641.

Gorelov, I., and Nikolskii, V. (1977). *Zh. Obshch. Khim.* 47:1696.

Gorelov, I., Samsonov, A., and Kolosova, M. (1973). *Zh. Neorg. Khim.* 18, 1767.

Gridchin, S. N., Kochergina, L. A., Pyreu, D. F., and Shmatko, Y. M. (2004). Stability constants of manganese(II) alkylenediaminetetraacetates. *Russ. J. Coord. Chem.* 30, 781–785. doi: 10.1023/B:RUCO.0000047464.55087.cb

Gritmon, T. F., Goedken, M. P., and Choppin, G. R. (1977). The complexation of lanthanides by aminocarboxylate ligands—I: stability constants. *J. Inorg. Nucl. Chem.* 39, 2021–2023. doi: 10.1016/0022-1902(77)80538-1

Knyazeva, N. E., Nikol'skii, V. M., Alekseev, V. G., Ryasenskii, S. S., and Gorelov, I. P. (2002). *Zh. Neorg. Khim.* 47, 262–266.

Kodama, M. (1974). Kinetics of multidentate ligand substitution reactions. XVI. Substitution reactions of l, 2-cyclohexanediamine-N,N,N′,N′-tetraacetic Acid (CyDTA) with the zinc(II)–ethylenediaminemonoacetate (EDMA) and -ethylenediamine-N,N′-diacetate (EDDA) complexes and that of ethylenediamine-N,N,N′,N′-tetraacetic acid (EDTA) with the nickel(II)–EDDA complex. *Bull. Chem. Soc. Jpn.* 47, 1430–1433. doi: 10.1246/bcsj.47.1430

Kodama, M., Namekawa, K., and Horiuchi, T. (1974). A polarographic study of the rates of the dissociation reactions of aminopolycarboxylato–zinc(II), –lead(II), and –cadmium(II) complexes. *Bull. Chem. Soc. Jpn.* 47, 2011–2016. doi: 10.1246/bcsj.47.2011

Mashihara, M., Ando, T., and Murase, I. (1973). Synthesis and metal chelate stability of N,N′-ethylenebis(aminomalonic) acid. *Bull. Chem. Soc. Jpn.* 46, 844–847. doi: 10.1246/bcsj.46.844

Mighri, Z., and Rumpf, P. (1975). *Bull. Soc. Chim. Fr.* 1155–1160.

Moeller, T., and Ferrus, R. (1962). Observations on the rare Earths. LXXIV. The enthalpy and entropy of formation of the 1:1 and 1:2 chelates of nitrilotriacetic acid with tripositive cations. *Inorg. Chem.* 1, 49–55. doi: 10.1021/ic50001a010

Motekaitis, R. J., and Martell, A. E. (1994). The iron(III) and iron(II) complexes of nitrilotriacetic acid. *J. Coord. Chem.* 31, 67–78. doi: 10.1080/00958979408022546

Nikol'skii, V., and Knyazeva, N. (2002). *Zh. Neorg. Khim.* 47:1184.

Nurchi, V. M., Crisponi, G., Lachowicz, J. I., Medici, S., Peana, M., and Zoroddu, M. A. (2016). Chemical features of in use and in progress chelators for iron overload. *J. Trace Elem. Med. Biol.* 38, 10–18. doi: 10.1016/j.jtemb.2016.05.010

Nurchi, V. M., Crisponi, G., and Villaescusa, I. (2010). Chemical equilibria in wastewaters during toxic metal ion removal by agricultural biomass. *Coord. Chem. Rev.* 254, 2181–2192. doi: 10.1016/j.ccr.2010.05.022

Nurchi, V. M., and Villaescusa, I. (2008). Agricultural biomasses as sorbents of some trace metals. *Coord. Chem. Rev.* 252, 1178–1188. doi: 10.1016/j.ccr.2007.09.023

Nurchi, V. M., and Villaescusa, I. (2012). Sorption of toxic metal ions by solid sorbents: a predictive speciation approach based on complex formation constants in aqueous solution. *Coord. Chem. Rev.* 256, 212–221. doi: 10.1016/j.ccr.2011.09.002

Orama, M., Hyvönen, H., Saarinen, H., and Aksela, R. (2002). Complexation of [*S, S*] and mixed stereoisomers of *N, N′*-ethylenediaminedisuccinic acid (EDDS) with Fe(iii), Cu(ii), Zn(ii) and Mn(ii) ions in aqueous solution. *J. Chem. Soc., Dalton Trans.* 4644–4648. doi: 10.1039/B207777A

Peters, R. W. (1999). Chelant extraction of heavy metals from contaminated soils. *J. Hazard Mater.* 66, 151–210. doi: 10.1016/S0304-3894(99)00010-2

Reilley, C. N., and Schmid, R. W. (1958). Chelometric titrations with potentiometric end point detection. *Anal. Chem.* 30, 947–953. doi: 10.1021/ac60137a021

Riečanská, E., Bumbálová, J. M. A., and Kalina, M. (1974). *Chem. Pap.* 28, 332–335.

Ringbom, A. (1963). *Complexation in Analytical Chemistry.* New York, NY: Interscience.

Samsonov, A., and Gorelov, I. (1974). *Zh. Neorg. Khim.* 19:2115.

Sarma, B., and Ray, P. (1956). *J.Indian Chem.Soc.* 33:841.

Schwarzenbach, G., Anderegg, G., Schneider, W., and Senn, H. (1955). Komplexone XXVI. Über die Koordinationstendenz von N-substituierten Iminodiessigsäuren. *Helv. Chim. Acta* 38, 1147–1170. doi: 10.1002/hlca.19550380509

Schwarzenbach, G., and Freitag, E. (1951). Komplexone XX. Stabilitätskonstanten von Schwermetallkomplexen der Äthylendiamin-tetraessigsäure. *Helv. Chim. Acta* 34, 1503–1508. doi: 10.1002/hlca.19510340534

Schwarzenbach, G., and Gut, R. (1956). Die komplexe der seltenen erdkationen und die gadoliniumecke. *Helv. Chim. Acta* 39, 1589–1599. doi: 10.1002/hlca.19560390618

Sunar, O. P., and Trivedi, C. P. (1971). Complexes of palladium(II) with multidentate ligands. *J. Inorg. Nucl. Chem.* 33, 3990–3993. doi: 10.1016/0022-1902(71)80318-4

Teng, D., Mao, K., Ali, W., Xu,G., Huang, G., Niazi, N. K., et al. (2020). Describing the toxicity and sources and the remediation technologies for mercurycontaminated soil. *RSC Adv.* 10, 23221–23232. doi: 10.1039/D0RA01507E

Trivedi, C., Sunar, O., and Tak, F. (1971). *Indian J. Chem.* 9:1155.

Vasilev, V., and Al, A. K. E. (1994). *Zh. Neorg Khim.* 39:470.

Vasilev, V., and Al., A. K. E. (1998). *Zh. Neorg Khim.* 43:808.

Vasilev, V., and Zaitseva, G. (1993). *Zh. Neorg. Chim.* 38:1341.

Vasilev, V., Zaitseva, G., and Logacheva, N. (1990). *Zh. Neorg. Khim.* 35:2858.

Vasilev, V., Zaitseva, G., and Matrenina, S. (1989). *Zh. Neorg. Khim.* 3:92.

Vasilev, V., Zaitseva, G., Tukumova, N., and Bukushina, G. (1999). *Russian J. Inorg. Chem.* 44, 1557–1560.

Verdier, E., and Piro, J. (1969). *Ann. Chim.* 4:213.

Villaescusa, I., Fiol, N., Cristiani, F., Floris, C., Lai, S., and Nurchi, V. M. (2002). Equilibrium study on Cd(II) and Zn(II) chelates of mercapto carboxylic acids. *Polyhedron* 21, 1363–1367. doi: 10.1016/S0277-5387(02)00957-9

Wuana, R. A., and Okieimen, F. E. (2011). Heavy metals in contaminated soils: a review of sources, chemistry, risks and best available strategies for remediation. *ISRN Ecol.* 2011:402647. doi: 10.5402/2011/402647

Wuana, R. A., Okieimen, F. E., and Imborvungu, J. A. (2010). Removal of heavy metals from a contaminated soil using organic chelating acids. *Int. J. Environ. Sci. Technol.* 7, 485–496. doi: 10.1007/BF03326158

Conflict of Interest: The authors declare that the research was conducted in the absence of any commercial or financial relationships that could be construed as a potential conflict of interest.

frontiers in Chemistry

ORIGINAL RESEARCH
published: 01 December 2020
doi: 10.3389/fchem.2020.614718

Assessing the Quality of Milk Using a Multicomponent Analytical Platform MicroNIR/Chemometric

*Roberta Risoluti, Giuseppina Gullifa and Stefano Materazi**

Department of Chemistry, Sapienza University of Rome, Rome, Italy

In this work, an innovative screening platform based on MicroNIR and chemometrics is proposed for the on-site and contactless monitoring of the quality of milk using simultaneous multicomponent analysis. The novelty of this completely automated tool consists of a miniaturized NIR spectrometer operating in a wireless mode that allows samples to be processed in a rapid and accurate way and to obtain in a single click a comprehensive characterization of the chemical composition of milk. To optimize the platform, milk specimens with different origins and compositions were considered and prediction models were developed by chemometric analysis of the NIR spectra using Partial Least Square regression algorithms. Once calibrated, the platform was used to predict samples acquired in the market and validation was performed by comparing results of the novel platform with those obtained from the chromatographic analysis. Results demonstrated the ability of the platform to differentiate milk as a function of the distribution of fatty acids, providing a rapid and non-destructive method to assess the quality of milk and to avoid food adulteration.

Keywords: milk, microNIR, chemometrics, quality control, new methods, multiparametric analysis

OPEN ACCESS

Edited by:
Ottavia Giuffrè,
University of Messina, Italy

Reviewed by:
Carlo Siciliano,
University of Calabria, Italy
Rita Giovannetti,
University of Camerino, Italy

****Correspondence:***
Stefano Materazi
stefano.materazzi@uniroma1.it

Specialty section:
This article was submitted to Analytical Chemistry, a section of the journal Frontiers in Chemistry

Received: *06 October 2020*
Accepted: *27 October 2020*
Published: *01 December 2020*

Citation:
Risoluti R, Gullifa G and Materazi S (2020) Assessing the Quality of Milk Using a Multicomponent Analytical Platform MicroNIR/Chemometric. Front. Chem. 8:614718. doi: 10.3389/fchem.2020.614718

INTRODUCTION

Milk is one of the most investigated food matrices worldwide and the analyses usually aim at estimating its chemical composition, in order to evaluate its quality (Hambraeus, 1984; Cunsolo et al., 2017). In particular, the quality of milk is mainly related to the fatty acid content (Napoli et al., 2007; Zhou et al., 2014), as well as the amount of lactose, proteins, and vitamin D. The increasing demand from consumers for innovative dietary products has globally led to an increasing request of procedures and methods to detect adulteration of food matrices (Cossignani et al., 2011; Materazzi et al., 2012). In particular, adulteration of milk mainly consists of the addition or the illegal use of additives or molecules, including melamine (Balabin and Smirnov, 2011), sugars (Kamboj et al., 2020), urea (Mabood et al., 2019), and formalin (Saha and Thangavel, 2018).

Therefore, a method which could assess the quality of a food product and perform a multicomponent characterization at the first level test represents an important issue when dealing

with the monitoring of food quality or human health. For this reason, innovative screening systems, able to rapidly process samples without requiring any pretreatment or clean up, in a non-destructive way, are becoming more and more recommended (Dunn et al., 2011; Risoluti et al., 2016, 2019a,b,c; D'Elia et al., 2018). Reference analytical procedures for milk analyses usually require chromatographic techniques, such as High Performance Liquid Chromatography associated to Mass Spectrometry (HPLC-MS) (Chotyakul et al., 2014; Aiello et al., 2015; Rocchetti et al., 2020), Gas Chromatography coupled to Mass Spectrometry (GC-MS) (Marchetti et al., 2002; Materazzi and Risoluti, 2014; Teng et al., 2017), and Nuclear Magnetic Resonance (NMR) (Garcia et al., 2012; Crea et al., 2014; Santos et al., 2016; Aiello et al., 2018).

Spectroscopic techniques are widely recognized as solvent-free, fast, and easy-to-use tools to perform the chemical investigation of different matrices without destroying samples (Oliveri et al., 2011; Materazzi et al., 2017a,b; Véstia et al., 2019). In particular, NIR spectroscopy associated with chemometric analysis proved its high potential in multicomponent analyses, at low costs and without requiring the supervision of specialized personnel (Kurdziel et al., 2003; Migliorati et al., 2013; Kordi et al., 2017; Materazzi et al., 2017c; Mees et al., 2018). NIR spectroscopy has been largely proposed for the investigation of milk with the aim of providing innovative and rapid methods for the detection of lactose, proteins, carotenoids, and fatty acid contents (Jankovskà and Šustovà, 2003; Numthuam et al., 2017; Risoluti et al., 2017; Wang et al., 2019; Soulat et al., 2020). In addition, NIR spectroscopy allows users moving out of the laboratory and performing prediction of analytes in complex matrices (Navarra et al., 2003; Bretti et al., 2013; Paiva et al., 2015; Basri et al., 2017; da Silva et al., 2017; Modrono et al., 2017; Risoluti and Materazzi, 2018; Risoluti et al., 2018a,b) by means of portable instruments that directly analyze milk and provide the results (De Angelis Curtis et al., 2008; Bian et al., 2017; Ferreira de Lima et al., 2018). Despite these instruments permitting the transfer of validated methods directly on site, they do not provide a tool enabling consumers to rapidly check the product by itself for application to real situations.

Based on these considerations, this work proposes a novel method based on a miniaturized spectrometer, the MicroNIR OnSite, for the multicomponent analysis of milk for food quality control. This platform uses chemometric tools to develop models of prediction that, once validated, provide the fast and accurate characterization of milk specimens in a "click," using a contactless and wireless miniaturized instrument that can be installed on a consumer's smartphone.

MATERIALS AND METHODS

Experimental

Analytical Workflow

Milk specimens were provided by different producers in Italy and included cow, goat, and donkey milk, as well as rice milk. In addition, samples were selected considering their different amounts of fats and treatments and considering whole, skimmed, and low-fat milk and UHT milk. For each sample, about 1 ml of milk was directly analyzed by the MicroNIR equipped with a special accessory for liquids; no sample pre-treatment was necessary. A detailed list of the investigated samples is reported in **Table 1**.

TABLE 1 | List of the investigated milk specimens.

Samples	Number of spectra	Fats (g/100 mL)
Whole Milk		
Goat Milk—Fresh Whole Milk—Amalattea	100	3.9
Goat Milk—Latte UHT Intero—Amalattea	150	3.9
Cow Milk—Fresh Whole Milk—Centrale del Latte	100	3.6
Cow Milk—Fresh Organic Whole Milk—Centrale del Latte	100	3.6
Semi Skimmed Milk		
Goat Milk—Semi Skimmed UHT Milk—Amalattea	150	1.6
Cow Milk—Fresh Semi Skimmed Milk—Centrale del Latte	150	1.6
Cow Milk—Semi Skimmed Organic UHT Milk—Granarolo	150	1.6
Cow Milk—Semi Skimmed UHT Milk—Zymil Parmalat	150	1
Cow Milk—Semi Skimmed Organic UHT Milk—Zymil Parmalat	150	1
Cow Milk—Microfiltered Semi Skimmed UHT Milk—Selex	150	1
Cow Milk—Semi Skimmed UHT Milk—Accadì	50	1
Skimmed Milk		
Cow Milk—Fresh Skimmed Milk—Centrale del Latte	50	<0.5
Cow Milk—Skimmed UHT Milk—Parmalat	150	<0.5
Cow Milk—Skimmed UHT Milk—Centrale del Latte	100	0.1
Cow Milk—Skimmed UHT Milk—Zymil Parmalat	150	0.1
Cow Milk—Skimmed UHT Milk—Accadì	100	0.1
Rice Milk		
UHT Rice Milk—Vital Nature	100	1
Donkey Milk		
UHT Donkey Milk	50	

Chemometric analysis was performed by Principal Component Analysis in order to evaluate correlations among measurements and to provide a rapid tool able to identify the adulteration of milk as a function of the fats contents.

Calibration and validation of the platform was obtained by dividing the data set of measurements in the training set and evaluation set, while the prediction of real samples was achieved by processing 17 additional samples not previously included in the dataset and thus processed as an independent batch. This step is strictly required, in order to guarantee the results are not bath-dependent and to ensure reproducibility and effectiveness of the platform.

MicroNIR On-Site Spectrometer

The MicroNIR On-Site is a portable spectrometer device operating in the NIR region of the spectrum (900–1,700 nm)

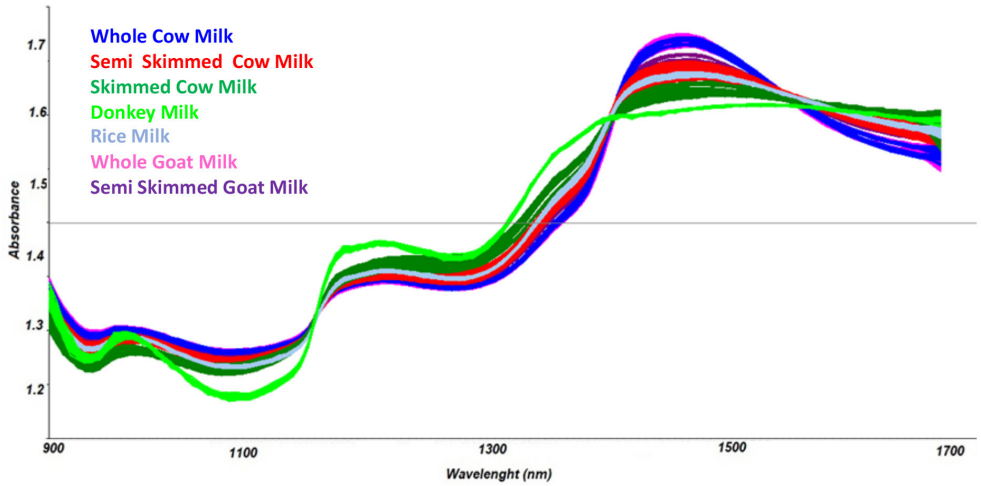

FIGURE 1 | Collected spectra of milk specimens.

and distributed by Viavi Solutions (JDSU Corporation, Milpitas, USA). It is specifically the latest version of the ultracompact MicroNIR from Viavi and represents the real update in the field of the miniaturized device, moving out of the laboratory. In fact, it is provided by two different pieces of software (JDSU Corporation, Milpitas, USA): the first is the MicroNIR Pro software that allows trained users to collect samples and develop a model of prediction; the second is the MicroNIR OnSite-W system for real-time prediction of samples and it is suitable even for untrained users.

Calibration of the instrument was obtained prior to the acquisition of the sample, by means of a special accessory that permitted the registration of a dark reference (total absorbance) and a white reference (total reflectance) using Spectralon. The instrumental settings included a nominal spectral resolution of the acquisitions at 6.25 nm and an integration time of 10 ms, for a total measurement time of 2.5 s per sample. Chemometric analysis was performed by V-JDSU Unscrambler Lite (Camo software AS, Oslo, Norway). Ten spectra for each sample were collected in order to ensure heterogeneity of the measurement and the mean was considered for the chemometric analysis. The investigation of samples' correlation was first performed by Principal Component Analysis and the models of prediction were developed by the mean of Partial Least Square regression algorithms.

RESULTS AND DISCUSSION

The feasibility of innovative techniques to address specific issues strictly relies on the standardization of the method on reference samples as representative as possible of those to be processed. To this aim, a reference dataset of samples was considered by processing a number of different kinds of milk, such as cow, goat, and donkey, with different fatty acid contents. In addition, milk specimens after UHT treatments were also included, in order to provide a comprehensive method able to be used for a variety of products. With the aim of avoiding a batch dependent response of the analytical platform, different batches of the same milk and different providers were considered.

Spectra in the NIR region were recorded by the MicroNIR OnSite device, as reported in **Figure 1**, and chemometric pre-treatments were investigated in order to separate samples according to the different types of milk.

Mathematical transformations usually recommended for spectroscopic data (Barnes et al., 1989) were evaluated; in particular, scatter-correction methods were applied, such as Standard Normal Variate transform (SNV) (Geladi et al., 1985), Multiplicative Scatter Correction (MSC), Mean Centering (MC) (Wold and Sjöström, 1977), and normalization (Savitzky and Golay, 1964). In addition, spectral derivation techniques, including Savitzky-Golay (SG) polynomial derivative filters (Rinnan et al., 2009) were considered. Among the investigated spectra pre-treatments, combination of the baseline correction, first derivative transform, and Multiplicative Scatter Correction (MSC) were used to highlight differences among spectra and thus to separate samples according to the different chemical compositions.

Results of the NIR spectra interpretation from Sÿasic and Ozaki (2001) were confirmed, as shown in **Figure 2**, where the graph of the loadings vs. components PC1 and PC4 is reported.

Therefore, the preliminary Principal Component Analysis performed on the entire dataset of measurements shows a good accordance among samples belonging to the same class (**Figure 3**) and shows a distribution of the samples as a function of the increasing fatty acid content (**Figure 4**).

This behavior led us to develop a quantitation model by considering a Partial Least Square Regression algorithm in order to develop a model of predicting milk that permits the rapidly evaluation of its origin and its quality. As required for the validation of analytical methods, all the collected spectra were divided into a training set (about 75% of samples) and evaluation

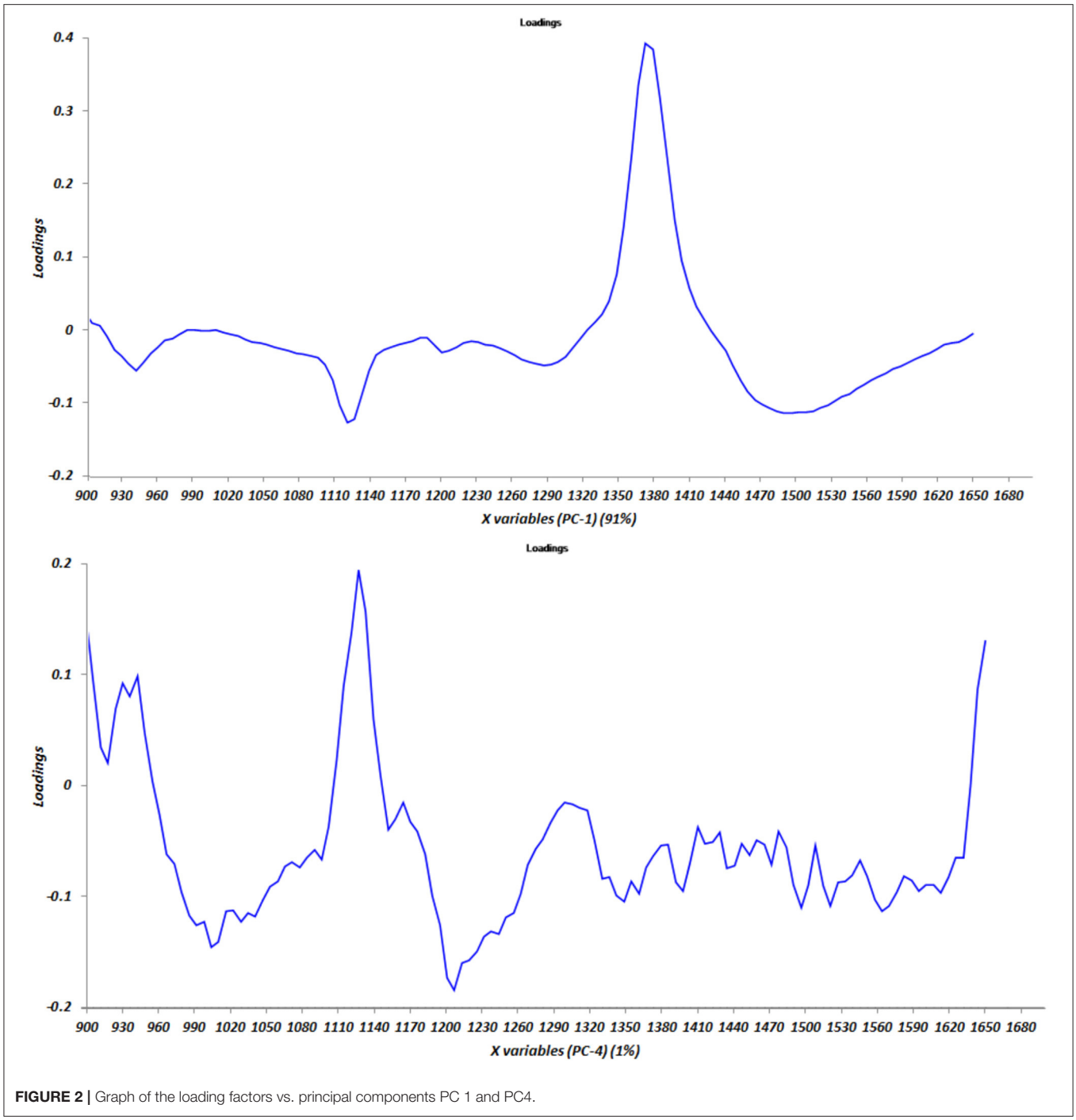

FIGURE 2 | Graph of the loading factors vs. principal components PC 1 and PC4.

set (about 25% of samples), and a number of parameters were assessed in order to calculate the model's performances.

Among these, the Root Mean Squared Errors (RMSEs) and the correlation coefficient (R^2) were estimated in calibration and cross-validation by using seven latent variables, while precision and sensitivity were calculated to provide fast and accurate outcomes when dealing with real samples analysis.

As reported in **Figure 5**, the model allows users to simultaneously differentiate whole, semi-skimmed, and skimmed milk and to identify the different origins.

As a consequence, the model may recognize the milk quality as a function of the belonging cluster of the spectra and preliminarily addresses the subsequent analyses.

The prediction ability of the model was evaluated by estimating the figures of merit and satisfactory

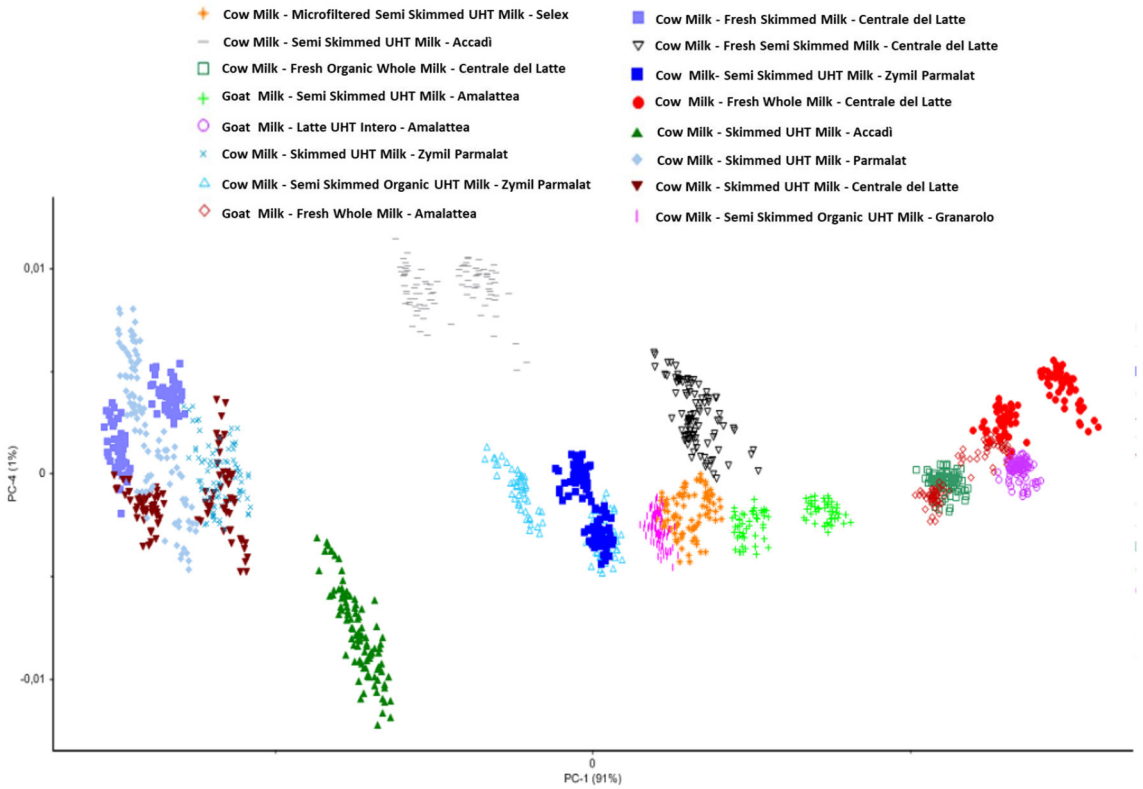

FIGURE 3 | Principal component analysis performed on all the collected samples.

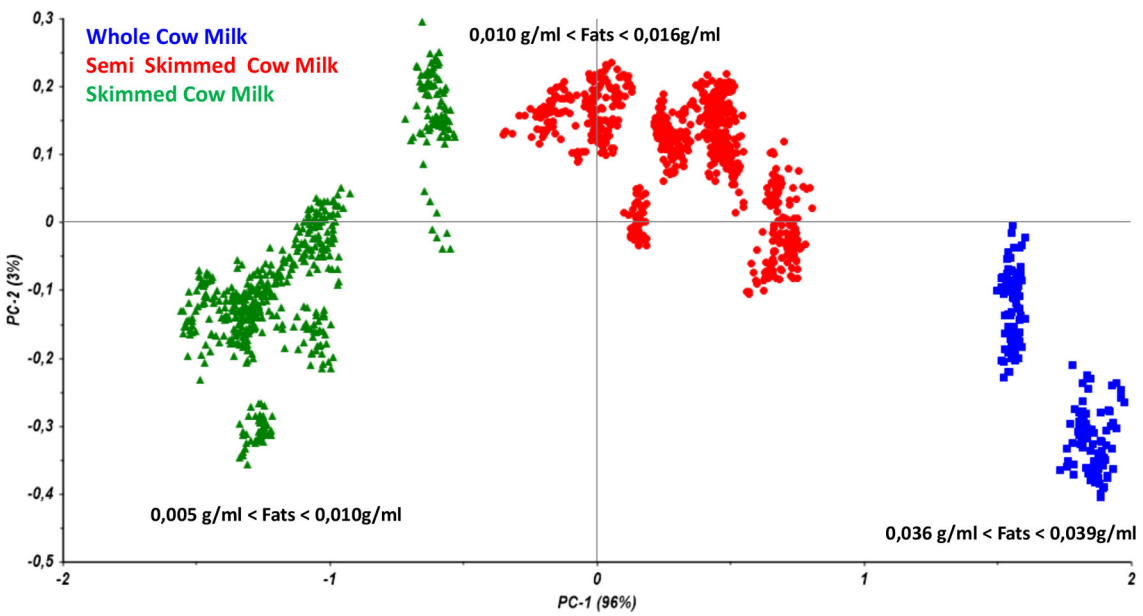

FIGURE 4 | Principal component analysis performed on all the collected samples from cow milk with different fats content.

outcomes may be observed; in fact, the correlation values were never lower than 0.99 in calibration or in cross-validation.

In addition, accuracy, precision, the slope, and the Root Mean Square Error (RMSE) were calculated considering seven latent variables. Results are summarized in **Table 2**.

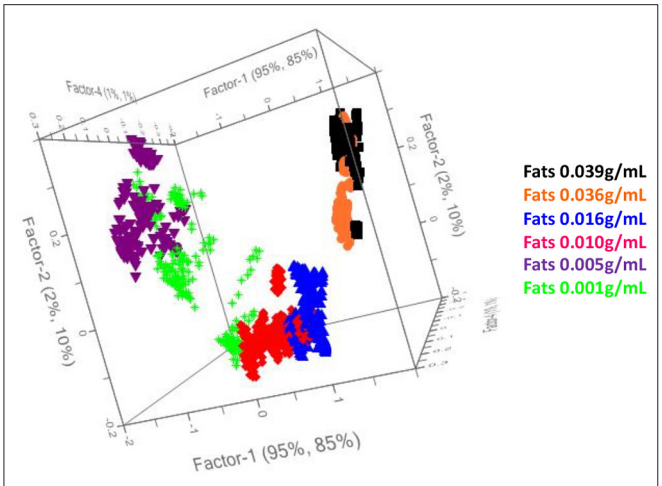

FIGURE 5 | PLS model for fat quantitation in milk specimens.

TABLE 2 | PLS model for milk: estimation of the figures of merit in calibration and cross-validation.

	Calibration	Cross-validation
Slope	0.97	0.97
R^2	0.099	0.98
RMSE (g/mL)	0.002	0.002
Accuracy (%)	98.4	97.1
Precision (%)	75.3	74.6
LVs	7	7

Satisfactory performances of the model may be observed, leading to errors in cross-validation no higher than 0.002 g/mL and accuracy values no lower than 97.1%. Precision of the method was also calculated and suitable outcomes were obtained, resulting in precision values about 74.6%.

Feasibility of the Platform

Prediction of the real samples was performed by processing 17 milk specimens commercially available in the Italian markets, in order to evaluate the platform performances. Samples were analyzed by the MicroNIR On-Site and spectra were processed by the optimized chemometric model. Good accordance among measurements was observed from MicroNIR outcomes, as reported in **Table 3**. The graph of the measured vs. predicted samples provided for a correlation coefficient of about 0.996, as all the samples were correctly predicted by the model, confirming the promising application of the platform.

CONCLUSIONS

In this work, a novel analytical platform based on NIR spectroscopy and chemometrics is proposed for the monitoring of milk quality. The novelty of the platform is strictly related to the innovative MicroNIR On-Site device which can be used to collect samples and to perform the prediction in few seconds, even by untrained personnel with an automated platform available on a smartphone. Reliability of this novel test was assessed by processing independent real samples, confirming the feasibility of this novel platform. In addition, the model was validated by estimating the characteristic figures of merit, such as the accuracy, slope, precision, and the RMSE, demonstrating its suitability for application as a screening test for consumers for food monitoring.

TABLE 3 | Results obtained from the novel platform for independent real samples.

Prediction results	Fats (g/mL)	Predicted	DS
Goat milk–Fresh whole milk–Amalattea	0.039	0.0422	0.0002
Goat milk–Latte UHT intero–Amalattea	0.039	0.0372	0.0005
Cow milk–Fresh whole milk–Centrale del Latte	0.036	0.0337	0.0003
Cow milk–Fresh organic whole milk–Centrale del Latte	0.036	0.0331	0.0004
Goat milk–Semi skimmed UHT milk–Amalattea	0.016	0.0178	0.0004
Cow milk–Fresh semi skimmed milk–Centrale del Latte	0.016	0.0130	0.0005
Cow milk–Semi skimmed organic UHT milk–Granarolo	0.016	0.0139	0.0004
Cow milk–Semi skimmed UHT milk–Zymil Parmalat	0.01	0.0083	0.0003
Cow milk–Semi skimmed organic UHT milk–Zymil Parmalat	0.01	0.0089	0.0004
Cow milk–Microfiltered Semi skimmed UHT milk–Selex	0.01	0.0140	0.0005
Cow milk–Semi skimmed UHT milk–Accadì	0.01	0.0084	0.0004
UHT Rice milk–Vital Nature	0.01	0.0108	0.0004
Cow milk–Fresh Skimmed milk–Centrale del Latte	0.005	0.0067	0.0003
Cow milk–Skimmed UHT milk–Parmalat	0.005	0.0042	0.0006
Cow milk–Skimmed UHT milk–Centrale del Latte	0.001	0.0030	0.0003
Cow milk–Skimmed UHT milk–Zymil Parmalat	0.001	0.0011	0.0004
Cow milk–Skimmed UHT milk–Accadì	0.001	0.0032	0.0004

DATA AVAILABILITY STATEMENT

The raw data supporting the conclusions of this article will be made available by the authors, without undue reservation.

AUTHOR CONTRIBUTIONS

SM and RR conceived the study and interpreted the data by chemometrics and GG performed the analyses. The manuscript was written through contributions of all authors. All authors have given approval to the final version of the manuscript.

REFERENCES

Aiello, D., Furia, E., Siciliano, C. Bongiorno, D., and Napoli, A. (2018). Study of the coordination of ortho-tyrosine and trans-4-hydroxyproline with aluminum(III) and iron(III). *J. Mol. Liq.* 269, 387–397. doi: 10.1016/j.molliq.2018.08.074

Aiello, D., Materazzi, S., Risoluti, R., Thangavel, H., Di Donna, L., and Mazzotti, (2015). A major allergen in rainbow trout (*Oncorhynchus mykiss*): complete sequences of parvalbumin by MALDI tandem mass spectrometry. *Mol. Biosyst.* 11, 2373–2382. doi: 10.1039/C5MB00148J

Balabin, R. M., and Smirnov, S. V. (2011). Melamine detection by mid- and near-infrared (MIR/NIR) spectroscopy: a quick and sensitive method for dairy products analysis including liquid milk, infant formula, and milk powder. *Talanta* 85, 562–568. doi: 10.1016/j.talanta.2011.04.026

Barnes, R. J., Dhanoa, M. S., and Lister, S. J. (1989). Standard normal variate transformation and detrending of near-infrared diffuse reflectance spectra. *Appl. Spectrosc.* 43, 772–777. doi: 10.1366/0003702894202201

Basri, K. N., Hussain, M. N., Bakar, J., Khir, M. F. A., and Zoolfakar, A. S. (2017). Classification and quantification of palm oil adulteration via portable NIR spectroscopy. *Spectrochim. Acta Mol. Biomol. Spectrosc.* 173, 335–342. doi: 10.1016/j.saa.2016.09.028

Bian, X., Zhang, C., Liu, P., Wei, J., Tan, X., Lin, L., et al. (2017). Rapid identification of milk samples by high and low frequency unfolded partial least squares discriminant analysis combined with near-infrared spectroscopy. *Chemom. Intell. Lab. Syst.* 170, 96–101. doi: 10.1016/j.chemolab.2017.09.004

Bretti, C., Crea, F., De Stefano, C., Foti, C., Materazzi, S., and Vianelli, G. (2013). Thermodynamic properties of dopamine in aqueous solution. acid-base properties, distribution, and activity coefficients in NaCl aqueous solutions at different ionic strengths and temperatures. *J. Chem. Eng. Data* 58, 2835–2847. doi: 10.1021/je400568u

Chotyakul, N., Pateiro-Moure, M., Saraiva, J. A., Torres, J. A., and Pérez-Lamela, C. (2014). Simultaneous HPLC–DAD quantification of vitamins A and E content in raw, pasteurized, and UHT cow's milk and their changes during storage. *Eur. Food Res. Technol.* 238, 535–547. doi: 10.1007/s00217-013-2130-7

Cossignani, L., Blasi, F., Bosi, A., D'Arco, G., Maurelli, S., Simonetti, M., et al. (2011). Detection of cow milk in donkey milk by chemometric procedures on triacylglycerol stereospecific analysis result. *J. Dairy Res.* 78, 335–342. doi: 10.1017/S0022029911000495

Crea, F., Falcone, G., Foti, C., Giuffrè, O., and Materazzi, S. (2014). Thermodynamic data for Pb^{2+} and Zn^{2+} sequestration by biologically important S-donor ligands, at different temperatures and ionic strengths. *New J. Chem.* 38, 3973–3983. doi: 10.1039/C4NJ00830H

Cunsolo, V., Saletti, R., Muccilli, V., Gallina, S., Di Francesco, A., and Foti, S. (2017). Proteins and bioactive peptides from donkey milk: the molecular basis for its reduced allergenic properties. *Food Res. Int.* 99, 41–57. doi: 10.1016/j.foodres.2017.07.002

da Silva, N. C., Cavalcanti, C. J., Honorato, F. A., Amigo, J. M., and Pimentel, M. F. (2017). Standardization from a benchtop to a handheld NIR spectrometer using mathematically mixed NIR spectra to determine fuel quality parameters. *Anal. Chim. Acta* 954, 32–42. doi: 10.1016/j.aca.2016.12.018

De Angelis Curtis, S., Kurdziel, K., Materazzi, S., and Vecchio, S. (2008). Crystal structure and thermoanalytical study of a manganese(II) complex with 1-allylimidazole. *J. Therm. Anal. Calorim.*. 92, 109–114. doi: 10.1007/s10973-007-8747-7

D'Elia, V., Montalvo, G., Garca Ruiz, C., Ermolenkov, V. V., Ahmed, Y., and Lednev, I. K. (2018). Ultraviolet resonance Raman spectroscopy for the detection of cocaine in oral fluid. *Spectrochim. Acta Mol. Biomol. Spectrosc.* 188, 338–340. doi: 10.1016/j.saa.2017.07.010

Dunn, J. D., Gryniewicz-Ruzicka, C. M., Kauffman, J. F., Westenberger, B. J., and Buhse, L. F. (2011). Using a portable ion mobility spectrometer to screen dietary supplements for sibutramine. *J. Pharm. Biomed. Anal.* 54, 469–474. doi: 10.1016/j.jpba.2010.09.017

Ferreira de Lima, G., Cardoso Andrade, S. A., da Silva, V. H., and Araújo Honorato, F. (2018). Multivariate classification of UHT milk as to the presence of lactose using benchtop and portable NIR spectrometers. *Food Anal. Methods* 11, 2699–2706. doi: 10.1007/s12161-018-1253-7

Garcia, C., Luts, N. W. Confort-Gouny, S., Cozzone, P. J., Armand, M., and Bernard, M. (2012). Phospholipid fingerprints of milk from different mammalians determined by 31P NMR: towards specific interest in human health. *Food Chem.* 135, 1777–1783. doi: 10.1016/j.foodchem.2012.05.111

Geladi, P., MacDougall, D., and Martens, H. (1985). Linearization and scatter-correction for near-infrared reflectance spectra of meat. *Appl. Spectrosc.* 39, 491–500. doi: 10.1366/0003702854248656

Hambraeus, L. (1984). Human milk composition. *Nutr. Abstr. Rev.* 54, 219–236.

Jankovskà, R., and Šustovà, K. (2003). Analysis of cow milk by near-infrared spectroscopy. *Czech J. Food Sci.* 21, 123–128. doi: 10.17221/3488-CJFS

Kamboj, U., Kaushal, N., and Jabeen. S. (2020). Near infrared spectroscopy as an efficient tool for the qualitative and quantitative determination of sugar adulteration in milk. *J. Phys. Conf. Ser.* 1531:012024. doi: 10.1088/1742-6596/1531/1/012024

Kordi, B., Kovacevi, M., Slobod, T., Vidovi, A., and Jovi, B. (2017). FT-IR and NIR spectroscopic investigation of hydrogen bonding in indole-ether systems. *J. Mol. Struct.* 1144, 159–165. doi: 10.1016/j.molstruc.2017.05.035

Kurdziel, K., Głowiak, T., Materazzi, S., and Jezierska, J. (2003). Crystal structure and physico-chemical properties of cobalt(II) and manganese(II) complexes with imidazole-4-acetate anion. *Polyhedron* 22, 3123–3128. doi: 10.1016/j.poly.2003.07.004

Mabood, F., Ali, L., Boque, R., Abbas, G., Jabeen, F., Haq, Q. M. I., et al. (2019). Robust Fourier transformed infrared spectroscopy coupled with multivariate methods for detection and quantification of urea adulteration in fresh milk samples. *Food Sci. Nutr.* 8, 5249–5458. doi: 10.1002/fsn3.987

Marchetti, L., Sabbieti, M. G., Menghi, M., Materazzi, S., Hurley, M. M., Menghi, G. (2002). Effects of phthalate esters on actin cytoskeleton of Py1a rat osteoblasts. *Histol. Histopathol.* 17, 1061–1066. doi: 10.14670/HH-17.1061

Materazzi, S., Gregori, A., Ripani, L., Apriceno, A., and Risoluti, R. (2017b). Cocaine profiling: Implementation of a predictive model by ATR-FTIR coupled with chemometrics in forensic chemistry. *Talanta* 166, 328–335. doi: 10.1016/j.talanta.2017.01.045

Materazzi, S., Peluso, G., Ripani, L., and Risoluti, R. (2017c). High-throughput prediction of AKB48 in emerging illicit products by NIR spectroscopy and chemometrics. *Microchem. J.* 134, 277–283. doi: 10.1016/j.microc.2017.06.014

Materazzi, S., and Risoluti, R. (2014). Evolved gas analysis by mass spectrometry. *Appl. Spectrosc. Rev.* 49, 635–665. doi: 10.1080/05704928.2014.887021

Materazzi, S., Risoluti, R., Pinci, S., and Romolo, F. S. (2017a). New insights in forensic chemistry: NIR/Chemometrics analysis of toners for questioned documents examination. *Talanta* 174, 673–678. doi: 10.1016/j.talanta.2017.06.044

Materazzi, S., Vecchio, S., Wo, L. W., and De Angelis Curtis, S. (2012). TG-MS and TG-FTIR studies of imidazole-substituted coordination compounds: Co(II) and Ni(II)-complexes of bis(1-methylimidazol-2-yl)ketone. *Thermochim. Acta* 543, 183–187. doi: 10.1016/j.tca.2012.05.013

Mees, C., Souard, F., Delported, C., Deconinck, E., Stoffelen, P., Stévigny, C., et al. (2018). Identification of coffee leaves using FT-NIR spectroscopy and SIMCA. *Talanta* 177, 4–11. doi: 10.1016/j.talanta.2017.09.056

Migliorati, V., Ballirano, P., Gontrani, L., Materazzi, S., Ceccacci, F., and Caminiti, R. (2013). A combined theoretical and experimental study of solid octyl and decylammonium chlorides and of their aqueous solutions. *J. Phys. Chem. B* 117, 7806–7818. doi: 10.1021/jp403103w

Modrono, S., Soldado, A., Martínez-Fernández, A., and de la Roza Delgado, B. (2017). Handheld NIRS sensors for routine compound feed quality control: real time analysis and field monitoring. *Talanta* 162, 597–603. doi: 10.1016/j.talanta.2016.10.075

Napoli, A., Aiello, D., Di Donna, L., Prendushi, H., and Sindona, G. (2007). Exploitation of endogenous protease activity in raw mastitic milk by MALDI-TOF/TOF. *Anal. Chem.* 79, 5941–5948. doi: 10.1021/ac0704863

Navarra, M.A., Materazzi, S., Panero, S., and Scrosati, B. (2003). PVdF-based membranes for DMFC applications. *J. Electrochem. Soc.* 150, A1528–A1532. doi: 10.1149/1.1615607

Numthuam, S., Hongpathong, J., Charoensook, R., and Rungchang, S. (2017). Method development for the analysis of total bacterial count in raw milk using near-infrared spectroscopy. *J. Food Saf.* 37:e12335. doi: 10.1111/jfs.12335

Oliveri, P., Di Egidio, V., Woodcock, T., and Downey, G. (2011). Application of class-modelling techniques to near infrared data for food authentication purposes. *Food Chem.* 125, 1450–1456. doi: 10.1016/j.foodchem.2010.10.047

Paiva, E. M., Rohwedder, J. J. R., Pasquini, C., Pimentel, M. F., and Pereira, C. F. (2015). Quantification of biodiesel and adulteration with vegetable oils in

diesel/biodiesel blends using portable near-infrared spectrometer. *Fuel* 160, 57–63. doi: 10.1016/j.fuel.2015.07.067

Rinnan, A., van den Berg, F., and Engelsen, S. B. (2009). Review of the most common pre-processing techniques for near-infrared spectra. *Trends Anal. Chem.* 28:10. doi: 10.1016/j.trac.2009.07.007

Risoluti, R., Fabiano, M. A., Gullifa, G., Vecchio Ciprioti, S., and Materazzi, S. (2017). FTIR-evolved gas analysis in recent thermoanalytical investigations. *Appl. Spectrosc. Rev.* 52, 39–72. doi: 10.1080/05704928.2016.1207658

Risoluti, R., Gregori, A., Schiavone, S., and Materazzi, S. (2018a). "Click and Screen" technology for explosives detection on human hands by portable MicroNIR/Chemometrics platform. *Anal. Chem.* 90, 4288–4292. doi: 10.1021/acs.analchem.7b03661

Risoluti, R., Gullifa, G., Battistini, A., and Materazzi, S. (2019b). "Lab-on-click" detection of illicit drugs in oral fluids by microNIR–chemometrics. *Anal. Chem.* 91, 6435–6439. doi: 10.1021/acs.analchem.9b00197

Risoluti, R., Gullifa, G., Battistini, A., and Materazzi, S. (2019c). MicroNIR/Chemometrics: A new analytical platform for fast and accurate detection of Δ9-Tetrahydrocannabinol (THC) in oral fluids. *Drug Alcohol Depend.* 205:107578. doi: 10.1016/j.drugalcdep.2019.107578

Risoluti, R., and Materazzi, S. (2018). MicroNIR/Chemometrics assessement of occupational exposure to hydroxyurea. *Front. Chem.* 6:228. doi: 10.3389/fchem.2018.00228

Risoluti, R., Materazzi, S., Tau, F., Russo, A., and Romolo, F. S. (2018b). Towards innovation in paper dating: a MicroNIR analytical platform and chemometrics. *Analyst* 143, 4394–4399. doi: 10.1039/C8AN00871J

Risoluti, R., Piazzese, D., Napoli, A., and Materazzi, S. (2016). Study of [2-(2′-pyridyl)imidazole] complexes to confirm two main characteristic thermoanalytical behaviors of transition metal complexes based on imidazole derivatives. *J. Anal. Appl. Pyrol.* 117, 82–87. doi: 10.1016/j.jaap.2015.11.018

Risoluti, R., Pichini, S., Pacifici, R., and Materazzi, S. (2019a). Miniaturized analytical platform for cocaine detection in oral fluids by MicroNIR/Chemometrics. *Talanta* 202, 546–553. doi: 10.1016/j.talanta.2019.04.081

Rocchetti, G., Gallo, A., Nocetti, M., Lucini, L., and Masoero, F. (2020). Milk metabolomics based on ultra-high-performance liquid chromatography coupled with quadrupole time-of-flight mass spectrometry to discriminate different cows feeding regimens. *Food Res. Int.* 134:109279. doi: 10.1016/j.foodres.2020.109279

Saha, D., and Thangavel, K. (2018). Rapid detection of formalin in milk by Fourier-transform Near-infrared spectroscopy. *J. Agric. Res.* 55, 772–774. doi: 10.5958/2395-146X.2018.00143.6

Santos, M. P., Pereira-Filhos, E. R., and Colnago, L. A. (2016). Detection and quantification of milk adulteration using time domain nuclear magnetic resonance (TD-NMR). *Microchem. J.* 124, 15–19. doi: 10.1016/j.microc.2015.07.013

Savitzky, M. J., and Golay, E. (1964). Smoothing and differentiation of data by simplified least squares procedures. *Anal. Chem.* 36, 1627–1639. doi: 10.1021/ac60214a047

Soulat, J., Andueza, D., Graulet, B., Girard, C. L., Labonne, C., Aït-Kaddour, A., et al. (2020). Comparison of the potential abilities of three spectroscopy methods: near-infrared, mid-infrared, and molecular fluorescence, to predict carotenoid, vitamin and fatty acid contents in cow milk. *Foods* 9:592. doi: 10.3390/foods9050592

Sÿasic, S., and Ozaki, Y. (2001). Short-wave near-infrared spectroscopy of biological fluids. Quantitative analysis of fat, protein, and lactose in raw milk by partial least-squares regression and band assignment. Anal. Chem. 73, 64–71. doi: 10.1021/ac000469c

Teng, F., Wang, P., Yang, L., Ma, Y., and Day, L. (2017). Quantification of fatty acids in human, cow, buffalo, goat, yak, and camel milk using an improved one-step GC-FID method. *Food Anal. Methods* 10, 2881–2891. doi: 10.1007/s12161-017-0852-z

Véstia, J., Barros, J. M., Ferreira, H., Gaspar, L., and Rato, A.E. (2019). Predicting calcium in grape must and base wine by FT-NIR spectroscopy. *Food Chem.* 276, 71–76. doi: 10.1016/j.foodchem.2018.09.116

Wang, Y., Guo, W., Zhu, X., and Liu, Q. (2019). Effect of homogenisation on detection of milk protein content based on NIR diffuse reflectance spectroscopy. *Int. J. Food Sci. Technol.* 54, 387–395. doi: 10.1111/ijfs.13948

Wold, S., and Sjöström, M. (1977). Chemometrics: theory and applications. *Am. Chem. Soc. Symp. Series* 52, 243–282. doi: 10.1021/bk-1977-0052.ch012

Zhou, Q., Gao, B., Zhang, X., Xu, Y., Shi, H., and Yu, L. (2014). Chemical profiling of triacylglycerols and diacylglycerols in cow milk fat by ultra-performance convergence chromatography combined with a quadrupole time-of-flight mass spectrometry. *Food Chem.* 143, 199–204. doi: 10.1016/j.foodchem.2013.07.114

Conflict of Interest: The authors declare that the research was conducted in the absence of any commercial or financial relationships that could be construed as a potential conflict of interest.

frontiers in Chemistry

ORIGINAL RESEARCH
published: 07 December 2020
doi: 10.3389/fchem.2020.580489

Early Diagnosis of Type 2 Diabetes Based on Near-Infrared Spectroscopy Combined With Machine Learning and Aquaphotomics

Yuanpeng Li[1,2†], Liu Guo[3†], Li Li[4], Chuanmei Yang[1], Peiwen Guang[5], Furong Huang[5], Zhenqiang Chen[5*], Lihu Wang[1] and Junhui Hu[1]*

[1] College of Physical Science and Technology, Guangxi Normal University, Guilin, China, [2] Guangxi Key Laboratory Nuclear Physics and Technology, Guangxi Normal University, Guilin, China, [3] Guangdong Hongke Agricultural Machinery Research & Development Co., Ltd., Guangzhou, China, [4] First Affiliated Hospital of Jinan University, Guangzhou, China, [5] Guangdong Provincial Key Laboratory of Optical Sensing and Communications, Department of Optoelectronic Engineering, Jinan University, Guangzhou, China

OPEN ACCESS

Edited by:
Anna Napoli,
University of Calabria, Italy

Reviewed by:
Roberta Risoluti,
Sapienza University of Rome, Italy
Jelena Muncan,
Kobe University, Japan

****Correspondence:***
Furong Huang
furong_huang@163.com
Zhenqiang Chen
tzqchen@jnu.edu.cn

† These authors have contributed equally to this work

Specialty section:
This article was submitted to Analytical Chemistry, a section of the journal Frontiers in Chemistry

Received: *06 July 2020*
Accepted: *03 November 2020*
Published: *07 December 2020*

Citation:
Li Y, Guo L, Li L, Yang C, Guang P, Huang F, Chen Z, Wang L and Hu J (2020) Early Diagnosis of Type 2 Diabetes Based on Near-Infrared Spectroscopy Combined With Machine Learning and Aquaphotomics. Front. Chem. 8:580489. doi: 10.3389/fchem.2020.580489

Early diagnosis is important to reduce the incidence and mortality rate of diabetes. The feasibility of early diagnosis of diabetes was studied via near-infrared spectra (NIRS) combined with a support vector machine (SVM) and aquaphotomics. Firstly, the NIRS of entire blood samples from the population of healthy, pre-diabetic, and diabetic patients were obtained. The spectral data of the entire spectra in the visible and near-infrared region (400–2,500 nm) were used as the research object of the qualitative analysis. Secondly, several preprocessing steps including multiple scattering correction, variable standardization, and first derivative and second derivative steps were performed and the best pretreatment method was selected. Finally, for the early diagnosis of diabetes, models were established using SVM. The first overtone of water (1,300–1,600 nm) was used as the research object for an aquaphotomics model, and the aquagram of the healthy group, pre-diabetes, and diabetes groups were drawn using 12 water absorption patterns for the early diagnosis of diabetes. The results of SVM showed that the highest accuracy was 97.22% and the specificity and sensitivity were 95.65 and 100%, respectively when the pretreatment method of the first derivative was used, and the best model parameters were $c = 18.76$ and $g = 0.008583$.The results of the aquaphotomics model showed clear differences in the 1,400–1,500 nm region, and the number of hydrogen bonds in water species (1,408, 1,416, 1,462, and 1,522 nm) was evidently correlated with the occurrence and development of diabetes. The number of hydrogen bonds was the smallest in the healthy group and the largest in the diabetes group. The suggested reason is that the water matrix of blood changes with the worsening of blood glucose metabolic dysfunction. The number of hydrogen bonds could be used as biomarkers for the early diagnosis of diabetes. The result show that it is effective and feasible to establish an accurate and rapid early diagnosis model of diabetes via NIRS combined with SVM and aquaphotomics.

Keywords: type 2 diabetes, early diagnosis, near-infrared spectroscopy(NIR), support vector machine (SVM), aquaphotomics

INTRODUCTION

Pre-diabetes refers to abnormal fasting glucose or impaired glucose tolerance that has not yet reached the diagnostic criteria for diabetes. It is the only reversible stage in the course of type 2 diabetes (Yu et al., 2013). One study has indicated that there will be 472 million people in the world with diabetes by the year 2025 (Xiaomin et al., 2016). Patients have no specific symptoms in the early stages of type 2 diabetes. Once diagnosed, the majority of cases have serious complications associated with them that will affect the patients' physical and mental health (Fukuda and Mizobe, 2017). Therefore, it is important to develop methods for the early diagnosis of type 2 diabetes so that appropriate diet and lifestyle interventions can be provided at an early stage to reduce the incidence of diabetes and control the condition of pre-diabetes.

At present, the screening test for pre-diabetes involves fasting plasma glucose (FPG), urine glucose, hemoglobin A1C (HbA1C), and gene testing. The detection of FPG and urine glucose is not easy to operate, is time-consuming, and has a low cost, but the missed diagnosis rate is high. The HbA1c detection method has little variability, and the result is not affected by eating time and short-term lifestyle factors. However, there is no unified diagnostic standard associated with the HbA1c detection method, which does not represent the current blood glucose level and easily results in misdiagnosis (Vajravelu and Lee, 2018). Genetic testing methods are varied and are selected according to particular requirements, but there are still legal and social ethics issues (Etchegary et al., 2010; Prior et al., 2012). Glucose tolerance test (OGTT) methods have the advantages of objectivity and accuracy, which is the "gold standard" for the diagnosis of pre-diabetes. However, the testing is complicated and time-consuming, causes great discomfort and increases the unnecessary psychological burden on patients, and is not suitable for large-scale population screening. Therefore, the development of fast, simple, and accurate methods is urgently required.

Patients with symptoms can undergo diagnostic methods, such as FPG, glucose tolerance tests, and glycated hemoglobin tests. However, these cannot be applied to large-scale screening (American Diabetes Association, 2012; Rosella et al., 2015; Mainous et al., 2016; Nakagami et al., 2017). Additionally, biomarkers have been investigated and applied to the early diagnosis of diabetes in a study by Lina et al. in 2013 that focused on the examination of whether there is a potential biomarker of T2DM in urine. The research showed that the expression of three types of polypeptides decreased in diabetes patients. It was further determined that these three polypeptides were fragments of histidine trimer nucleotide-binding protein 1 (HINT1), bifunctional aminoacyl tRNA synthetase (EPRS), and agrin precursor protein (CLU) and that they could be used as potential biomarkers for type 2 diabetes (Lina et al., 2013). In 2017, Hsiao-Feng et al. used laser doppler blood flow measurements and spectroscopic analysis to study different microcirculation effects and applied them to the early diagnosis of diabetes. Relative energy contribution and Doppler frequency shifts were found to decrease sequentially from the healthy group to the pre-diabetes group to the diabetes group. This shows that the relative energy contribution and Doppler frequency shift have a certain correlation with the progression of diabetes (Hsiao-Feng et al., 2017). In 2020, Yuanjie et al. used a wearable active acetone biosensor for the non-invasive diagnosis of pre-diabetes. Breath acetone on the order of ppm was measured, which showed that the sensor had a good response (Yuanjie et al., 2020). In new biomarker detection, laser doppler and acetone biosensors have been used in the early diagnosis of diabetes, and have made some progress, but these research results are very preliminary (Yuanjie et al., 2020).

Near-infrared spectroscopy (NIRS), as a non-destructive, rapid, and green analytical technique, has been widely used in the biomedical field (Workman, 1993; Beć et al., 2020). Metabolic or compositional changes occur during disease progression in most cases, beginning with abnormal changes in the molecular structure of tissue cells or humoral metabolism, and no obvious clinical symptoms are observed until the middle or late stages of disease onset. Consequently, analyzing the concentration and structural changes of proteins, fats, and water in human tissues, cells, and body fluids using NIRS, which is a more objective, reliable, and accurate tool has been proposed for the early diagnosis of diseases (Sakudo, 2016). The main component of blood is water, and other components include protein, lipid, sugar, and additional organic compounds. These substances have strong infrared activity, but the information of other components can be easily obscured owing to the strong absorption of water. Due to the influence of water absorption, NIRS has strong overlapping characteristics, and it is difficult to find the fingerprint features related to disease development. Besides, due to individual differences and instrument noise, it is difficult to detect subtle differences in the peak position of NIRS. To reduce the influence of these factors and extract useful information, it is necessary to combine spectral information with a machine learning method to establish a diagnostic model for the accurate diagnosis of pre-diabetes, which can reduce the influence of these factors and extract effective information (Huazhou et al., 2020).

In recent years, a novel approach called aquaphotomics has been proposed by Tsenkova (2005, 2009). This approach provides a new view of NIRS analysis. It allows analysis of NIR absorption changes of water and other substances as interference factors, and the changes in water absorption patterns associated with the occurrence and development of diseases can be determined by an extended water mirror approach (EWMA). Tsenkova et al. analyzed the number of body cells in the milk produced by cows with mastitis and healthy cows, and collected a large amount of milk component data and observed the changes in water absorption patterns in NIRS for the fast and accurate diagnosis of mastitis (Atanassova et al., 2009). Kinoshita et al. predicted whether a panda was in estrus by observing the changes in 12 water matrix coordinates—WAMACS in the urine of female pandas using the aquaphotomics method (Tsenkova, 2009; Kinoshita et al., 2012). For exploring the potential diagnostic information from serum samples, temperature-dependent near-infrared (NIR) spectroscopy was developed to obtain the spectral change of water reflecting the interactions in serum solution, and chemometric methods were employed to discriminate the patients of diabetes and heart disease. However, there

TABLE 1 | Blood glucose information includes 2 h post-load blood glucose (2 hPG) and fasting plasma glucose (FPG).

Blood sugar target	Max	Min	Average	Standard deviation
2 hPG(mmol/L)	11.8	5.40	9.10	1.14
FPG(mmol/L)	7.60	3.7	5.09	0.674

TABLE 2 | Division of blood samples into the training set and prediction set.

Sample	Total samples	Healthy group	Pre-diabetes group	Diabetes group
Total samples	147	53	46	48
Training set	111	40	35	36
Validation set	36	13	11	12

have been no reports concerning the diagnosis of pre-diabetes using aquaphotomics.

The present work aims to develop a rapid and accurate diagnosis of pre-diabetes. A model for the diagnosis of pre-diabetes was established, which combined NIRS and a support vector machine (SVM). The changes in water absorption patterns in the blood of normal, pre-diabetic, and diabetic patients were extracted using the aquaphotomics method, which not only provides immediate insight for the occurrence and development of diabetes but also provides a novel method for the diagnosis of pre-diabetes that can hopefully be used for early diagnosis.

MATERIALS AND METHODS

Materials and Sample Preparation

A total of 147 blood samples comprehensively diagnosed as healthy, pre-diabetic, or type 2 diabetic by 2-h post-load blood glucose (2hPG) of OGTT and FPG were collected from the Department of Endocrinology, First Affiliated Hospital of Jinan University. Peripheral blood samples were preserved (about 1 mL), kept in an anticoagulant tube (test tube treated with an anticoagulant to prevent blood from clotting), and stored in a −20°C refrigerator. All the peripheral blood samples are collected on the same day and spectral acquisition was performed immediately. Blood samples were collected from 53 healthy (24 males and 29 females, with an average age of 44 ± 12 years), 46 pre-diabetic (18 males and 28 females, with an average age of 47 ± 10 years), and 48 type 2 diabetic (25 males and 23 females, with an average age of 49 ± 12 years) patients. All specimens were from the same ethnic group with the same socioeconomic background, and all specimens were collected in accordance with relevant laws and regulations.

In the early morning of the second day, venous blood was collected from the patients and the FPG test was performed. Also, the OGTT test was performed on all subjects, and venous blood was collected after 2 h of glucose loading, and the venous blood glucose level was measured. During the OGTT test, subjects would sit and rest, and drinking coffee, tea, and other substances was prohibited. The detailed results of the blood glucose analyses are provided in **Table 1**.

In this study, the diagnostic criteria for type 2 diabetes and pre-diabetes used the standards formulated in the "Guidelines for Prevention and Treatment of Type 2 Diabetes (2013 Edition)" as the reference basis (Diabetes Branch of Chinese Medical Association, 2014): (1) normal blood glucose: FPG < 7.0 mmo1/L and (or) 2hPG < 7.8 mmol/L; (2) diabetes: FPG > 7.0 mmol/L and (or) 2hPG > 11.1 mmol/L (patients with a diagnosis of diabetes); (3) pre-diabetes mellitus (PDM): FPG range: 6.1 ≤ FPG < 7.0 mmo1/L and (or) 7.8 mmol/L < 2hPG ≤ 11.1 mmol/L.

In this study, the sample set was divided into a training set and a prediction set at a ratio of 3:1 by using a random selection method and repeating sampling 10 times. The random division ensures that the sample sets generated every time by setting random seeds were different and can be compared with the results of multiple runs because the method remarkably influences the model robustness, and an optimal sample set was obtained. The division of the blood samples into the training set and the prediction set is presented in **Table 2**.

Collection of Near-Infrared Spectra

NIRS were acquired using a grating NIR spectrometer (XDS Rapid Content Analyzer, Foss, Denmark) with transmission accessories. The spectra acquisition range was 400–2,500 nm, and the detectors were Si (400–1,100 nm) and PbS (1,100–2,500 nm). When acquiring NIRS of the blood samples from a group of healthy, pre-diabetic, and diabetic patients, 1-mL sample portions were placed in a quartz cuvette (optical path of 1 mm), and spectra were recorded at a wavelength increment of 2 nm in the range of 400–2,500 nm. The spectral data of each sample were measured in triplicate and averaged. The laboratory temperature was 24 ± 1°C and the relative humidity was 41%.

Data preprocessing is an important factor to improve prediction accuracy (Byrne et al., 2016). Random noise is often a component of the original data, resulting in differences between the true and the measured value. To eliminate errors as much as possible, it is necessary to weaken and even eliminate various disturbance factors through various data processing methods, which lay the foundation for next data processing. Therefore, it is very necessary to preprocess the original spectra. In this study, spectral data were preprocessed by a first derivative, a second derivative, a multiple scattering correction (MSC), and a standard normal variable transform (SNV) which can be used to reduce or even remove the influence of various interference factors.

Support Vector Machine (SVM)

SVM is a machine learning method that was developed based on dimensional theory and the statistical learning theory of Vapnik (1995). SVM is used to investigate pattern recognition and regression prediction problems with small sample sizes and can solve many practical problems, such as small sample size, nonlinearity, and high-dimensional problems. The problems of poor generalization ability and the difficult convergence of neural networks were solved by SVM. In recent years, good progress

TABLE 3 | Water absorption pattern in NIR range.

WAMSCs	Range (nm)	Characteristic wavelengths (nm)	Assignment	References
C1	1,336–1,348	1,344	υ_3	Kondepati et al., 2008
C2	1,360–1,366		Water shell	Robertson et al., 2003
C3	1,370–1,376	1,374	$\upsilon_1 + \upsilon_3$	Roggo et al., 2007
C4	1,380–1,390	1,382	Water shell	Ludwig, 2001
C5	1,398–1,418	1,408, 1,416	S_0	Donis-Gonzalez et al., 2016
C6	1,420–1,428		Water hydration	Cao et al., 2006
C7	1,434–1,444		S_1	Cattaneo et al., 2009
C8	1,448–1,454	1,448	$\upsilon_1 + \upsilon_3$	Kalinin et al., 2013
C9	1,460–1,468	1,462	S_2	Jaenicke and Lilie, 2000
C10	1,472–1,482	1,470	S_3	Diller, 1992
C11	1,482–1,495		S_4	Gowen et al., 2009
C12	1,506–1,516		Strongly bonded water or υ_2	Xantheas, 1995a,b

WAMACS, water matrix coordinates.
ν_1, *symmetric stretching of first overtone of water.*
ν_2, *bending of first overtone of water.*
ν_3, *asymmetric stretching of first overtone of water.*
S_{0-4}, $(H_2O)_{1-5}$.

has been made in studies on disease diagnosis by using NIRS combined with SVM (Sylvain and Cecile, 2018; Afara et al., 2020).

In the SVM method, different kernel functions can generate different SVM algorithms. A radial basis function (RBF) kernel function is used to realize the modeling classification of SVM because it can process nonlinear problems. RBF is a scalar function that is symmetric along the radial direction. It is usually defined as a monotonic function of the Euclidean distance between any point x in the space and a certain center x_c, which can be recorded as $k(||x\text{-}x_c||)$, and its effect is often local, that is, when x is far away from x_c, the value of the function is very small (Sánchez, 2003). Moreover, several optimization algorithms have been adopted to optimize the internal parameters of the model, obtain better results, and increase model robustness. Kernel function optimization is mainly solved by using penalty parameter C and kernel function parameter g. Parameter optimization is implemented based on the principle of minimum mean square error. The two parameters, namely, the selected kernel function type and support vector type, determine the optimization performance of the model. No universally agreed method has been reported for the optimization of SVM parameters worldwide. At present, the common methods include test method, grid search (GS), genetic algorithm (GA), and particle swarm optimization (PSO) (Sánchez, 2003; Peng-Wei et al., 2004).

Principal component analysis was used for dimension reduction to decrease model complexity (Abdi and Williams, 2010). The data after dimension reduction determined the data of principal components with a cumulative contribution rate higher than 99%, which are used as the input of the SVM model. Moreover, the kernel function was used for SVM modeling because RBF can accurately process nonlinear problems. The penalty parameter c and kernel function parameter g were used as two important parameters of RBF. These two parameters have important control impacts on model complexity, approximation error, and measurement accuracy of the model (Schlkopf and Smola, 2001; Aljarah et al., 2018; Li et al., 2019; Yalsavar et al., 2019). The penalty parameter c in the SVM model represents the degree of the penalty of an incorrect classification under linearly inseparable situations. This parameter adjusts the preferred weights of two indexes (interval and classification accuracies) in the optimization direction. This problem is equal to the prohibition of incorrectly classified samples (overfitting) when c tends to be infinitely large. The accurate classification of samples is ignored, and the maximum interval is pursued when c tends to be 0. Relevant solutions are then not obtained, and the algorithm does not converge (underfitting). The kernel function parameter g is the first r (γ) in Equation (2), and the default value is 1/k where k is the number of categories. The value of γ is used to set the "spread" of the function when RBF is utilized as the kernel. This condition applies the data mapping distribution to the new characteristic space. The value of γ is negatively correlated with the number of support vectors which influences the training and prediction speeds.

$$K(x, y) = \exp\{-\gamma \left\| x - y \right\|^2\} \quad (1)$$

Aquaphotomics

Water, as a natural biological matrix, is composed of small molecules with a great capacity for hydrogen bonding. Water alters the absorption pattern according to the physical and chemical properties of biological systems (Tsenkova, 2008). The basis component of blood is water, and the water absorption pattern will change due to the changes in material metabolism in the human body with disease. Consequently, changes in water absorption patterns of the blood can be used to diagnose the disease. The 12 water absorption bands - WAMACS in the NIR range are presented in **Table 3** (Tsenkova, 2009; Tsenkova et al., 2015, 2018; Bázár et al., 2016).

As water is susceptible to disturbance factors, analyzing the spectral changes of water and living systems subjected to these factors can be used to study the water matrix and other molecules in the water. The spectral ranges of water absorbance bands called water matrix coordinates ($WAMAC_S$), where specific water absorbance bands related to specific water molecular conformations (water species, water molecular structures) are found with the highest probability (Tsenkova, 2009). For the first overtone of water (1,300–1,600 nm), 12 WAMACs (labeled Ci, i = 1, 12) have been experimentally discovered (each of 6–20 nm in width) and they have been confirmed by overtone calculations of already reported water bands in the infrared range (Tsenkova, 2009). The combination of the activated water bands, at which the light absorbance gets influenced by the perturbations, depicts a characteristic spectral pattern called a water spectral pattern (WASP), which reflects the condition of the whole water molecular system. It contains a huge amount of physical and chemical information for the solution because the water hydrogen bonding network is easily influenced by any kind of even subtle perturbations (Kinoshita et al., 2012) including the solutes. At the moment, even without the assignment and understanding of water absorbance bands, WASPs can be used as holistic (bio)markers for system functionality.

The trajectory of the water absorption pattern obtained under a specific disturbance can be used as a spectral pattern in the multidimensional space of the water matrix coordinates, that is, as a spectral biological indicator to distinguish substances and explain the difference in function and the structural characteristics of the two. The application of water absorption patterns in disease diagnosis can be used as a biological indicator to help us better understand the role of water in life systems, and for disease diagnosis (Mengli et al., 2015; Xiaoyu et al., 2019).

Graphically, WASP is presented as an aquagram, which is a radial graphic of the normalized absorbance of characteristic water bands. The values for the aquagram on the coordinate axis can be obtained according to Equation (1) (Tsenkova et al., 2015).Here, A_λ is the absorbance after multiplicative scatter correction (MSC) applied on the first derivative overtone region, μ_λ is the mean value of all spectra, and σ_λ is the standard deviation of all spectra at wavelength λ.

$$Aq_\lambda = \frac{A_\lambda - \mu_\lambda}{\sigma_\lambda} \tag{2}$$

Evaluation of Model Parameters

Accuracy, specificity, and sensitivity are used as important evaluation indexes for the SVM models. The calculation equations of different parameters are expressed as follows:

$$Accuracy = \frac{n_{correct}}{n_{total}} \tag{3}$$

$$TPR = \frac{TP}{TP + FN} \tag{4}$$

$$FPR = \frac{FP}{FP + TN}$$

In Equation (4), TPR is the sensitivity, and FPR is the specificity. *TP* represents the number of positive samples in the verification set that are accurately classified by the model, and *FN* represents the number of positive samples in the verification set that are incorrectly classified by the model. *FP* is the number of negative samples in the verification set that are incorrectly classified by the model. *TN* is the number of negative samples in the verification set that are accurately classified by the model.

RESULT AND DISCUSSION

Spectral Analysis

NIRS of the blood and water samples are shown in **Figure 1** and the raw spectra of the blood samples are shown in **Figure 1A**. In the figure, there are two main absorption peaks at 1,452 and 1,951 nm in the NIR region, which are in accordance with the fingerprint region of water as reported in the literature. The absorption peak at 1,452 nm is the first overtone of the O-H stretching vibration in water, and that at 1,951 nm is the combination of O-H stretching and bending vibrations in water (Sakudo, 2016; Bishop and Neary, 2018; Pasquini, 2018).

In addition to water as the main component of blood, cholesterol, triglycerides, glucose, proteins, and other organic compounds are found in blood, but the absorption region of these substances are masked by the absorption of water molecules. The shape and trend of the NIRS of the healthy group, pre-diabetes group, and diabetes group are very similar, but the absorption intensity is dissimilar (shown in **Figure 1B**). It can be observed that the absorption intensity is healthy group > diabetes group > pre-diabetes group in the 400–1,200 nm region, and at 1,452 nm it changes to healthy group > pre-diabetes group > diabetes group, which is probably due to the changes in water and other organic compounds caused by changed blood glucose concentration.

Result of SVM Model

The results of the SVM model based on different preprocessing methods are shown in **Table 4**. It was concluded that the first derivative had the best preprocessing effect, so the first derivative was chosen as the preprocessing method for this data. GS, GA, and PSO were used to optimize c and g in this study. The optimum c and g values were selected based on the principle of highest accuracy, which is gained by cross-verification of the leave-one-out method. It follows from **Table 5** that the model has the best effect under the condition of GA (c = 11.62, g = 0.009346) optimization. The accuracy, specificity, and sensitivity are: 97.22%, 95.65% (22/23), 100% (13/13), respectively with the prediction set.

The optimal results of the healthy, pre-diabetic, and type 2 diabetic patient samples are shown in **Figure 2**. The 3D diagram of the optimization results for c and g using the GS methods is shown in **Figure 2A**. The contour map in **Figure 2A** projected onto a 2D plane is shown in **Figure 2B**. The contour map shows that c and accuracy rate gradually increase, and the gradient gradually converges from left to right. The highest accuracy rate of interactive verification is 90.99% when the penalty parameter c = 16 and the kernel function parameter

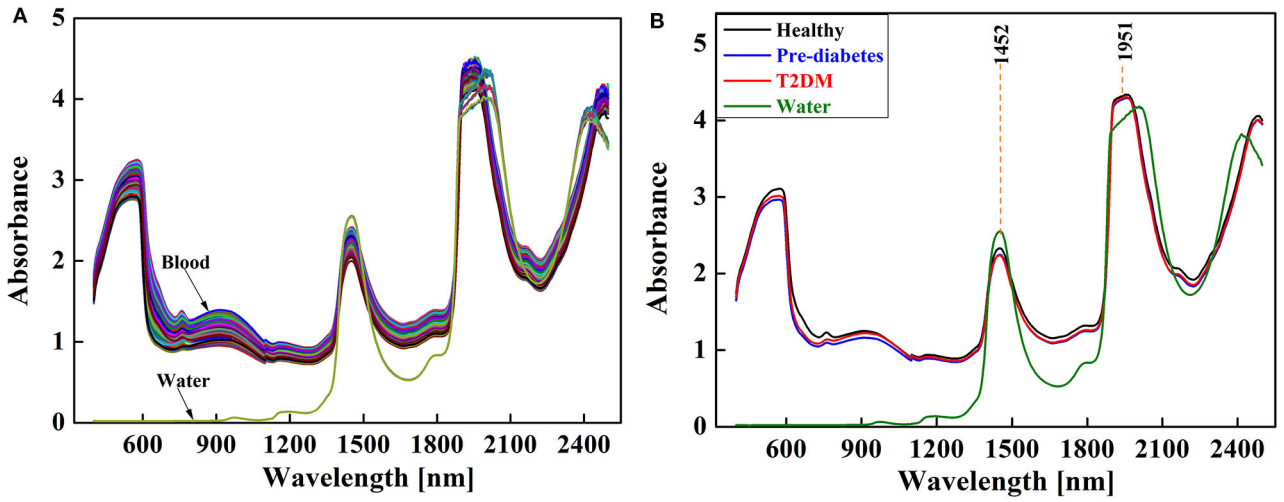

FIGURE 1 | NIR spectra of the blood samples: **(A)** raw and **(B)** average spectra.

TABLE 4 | Results of SVM model based on different preprocessing methods.

Pre-treatment	C	g	CV accuracy (%)	Accuracy (%)	Sensitivity	Specificity
Untreated	147.0	0.0068	77.04	91.66	95.65 (22/23)	84.62 (11/13)
First derivative	**16.00**	**0.006801**	**90.99**	**97.22**	**95.65 (22/23)**	**100.0 (13/13)**
Second derivative	48.50	0.003963	90.99	94.44	95.65 (22/23)	92.00 (12/13)
Msc	48.50	0.003906	80.18	94.44	95.65 (22/23)	92.00 (12/13)
Snv	27.85	0.006801	79.27	94.44	95.65 (22/23)	92.00(12/13)

The bold font represents the best results.

g = 0.006801. The optimization results using GA are shown in **Figure 2C**. The accuracy rate continuously increases when the population evolution algebra increases from 0 to 30, and the population reaches its saturation point at 30. Therefore, c = 11.62 and g = 0.009346 are the optimal results with the highest accuracy rate of the interactive verification of 92.80% when the population evolution algebra is 30. The optimization results for PSO are shown in **Figure 2D**. Results show that the accuracy rate is saturated at all times when the population evolution algebra is between 0 and 100. Therefore, c = 1.5 and g = 1.7 are the optimal results with the highest accuracy rate of the interactive verification of 89.58% when the population evolution algebra is between 0 and 100.

Graphs for the estimated class values (y axis) vs. the number of samples (x axis) are shown in **Figure 3**. The best fit between the true and predicted values of the training set is shown in **Figure 3A**. The fitting effect of the true value and predicted value of the prediction set is shown in **Figure 3B**, and only one outlier sample is found.

Result of Aquaphotomics

The average and corresponding different spectra of healthy, pre-diabetic, type 2 diabetic, and pure water in 1,300–1,600 nm are shown in **Figure 4**. It shows that the spectra of healthy, pre-diabetic, and type 2 diabetic almost overlapped, except at 1,450 nm where large differences were observed. The resulting spectra obtained by subtracting the healthy spectra from the pre-diabetic and type 2 diabetic spectra showed a maximum negative peak at 1,412 and 1,476 nm, which are attributable to the stretching vibration peak of water molecules without hydrogen bonds (1,412 nm) and water molecules with three hydrogen bonds (1,476 nm) (Tsenkova, 2009; Tsenkova et al., 2018; Xueguang et al., 2018). Error bars represent the fluctuation range of absorbance of different individuals. Due to the influence of noise and individual variation, it was difficult to diagnose diabetes in the early stages when the differences from the raw spectra were barely visible, but in the range of individual differences, the difference between pre-diabetes and type 2 diabetes can be observed from the differential spectra.

Figure 6A shows the results of the second derivative of the raw spectra and the corresponding different spectra of the healthy, pre-diabetic, and type 2 diabetic samples. The second derivative spectra can effectively expand the resolution of the spectra and find the differences among the spectra of healthy, pre-diabetic, and type 2 diabetic. More distinctive peaks appeared after the second derivative transformation, including a maximum positive peak centered at 1,382 nm and a maximum negative peak centered at 1,416 nm. The peak at 1,382 nm was ascribed to the solvent layer of water and

TABLE 5 | Results of SVM model based on different optimization algorithms.

Optimization algorithms	C	g	CV accuracy (%)	Accuracy (%)	Sensitivity	Specificity
GS	16.00	0.006801	90.99	97.22	95.56 (22/23)	100.0 (13/13)
GA	**11.62**	**0.009346**	**92.80**	**97.22**	**95.65 (22/23)**	**100.0 (13/13)**
PSO	1.500	1.700	9.580	91.66	91.31 (21/23)	92.00(12/13)

The bold font represents the best results.

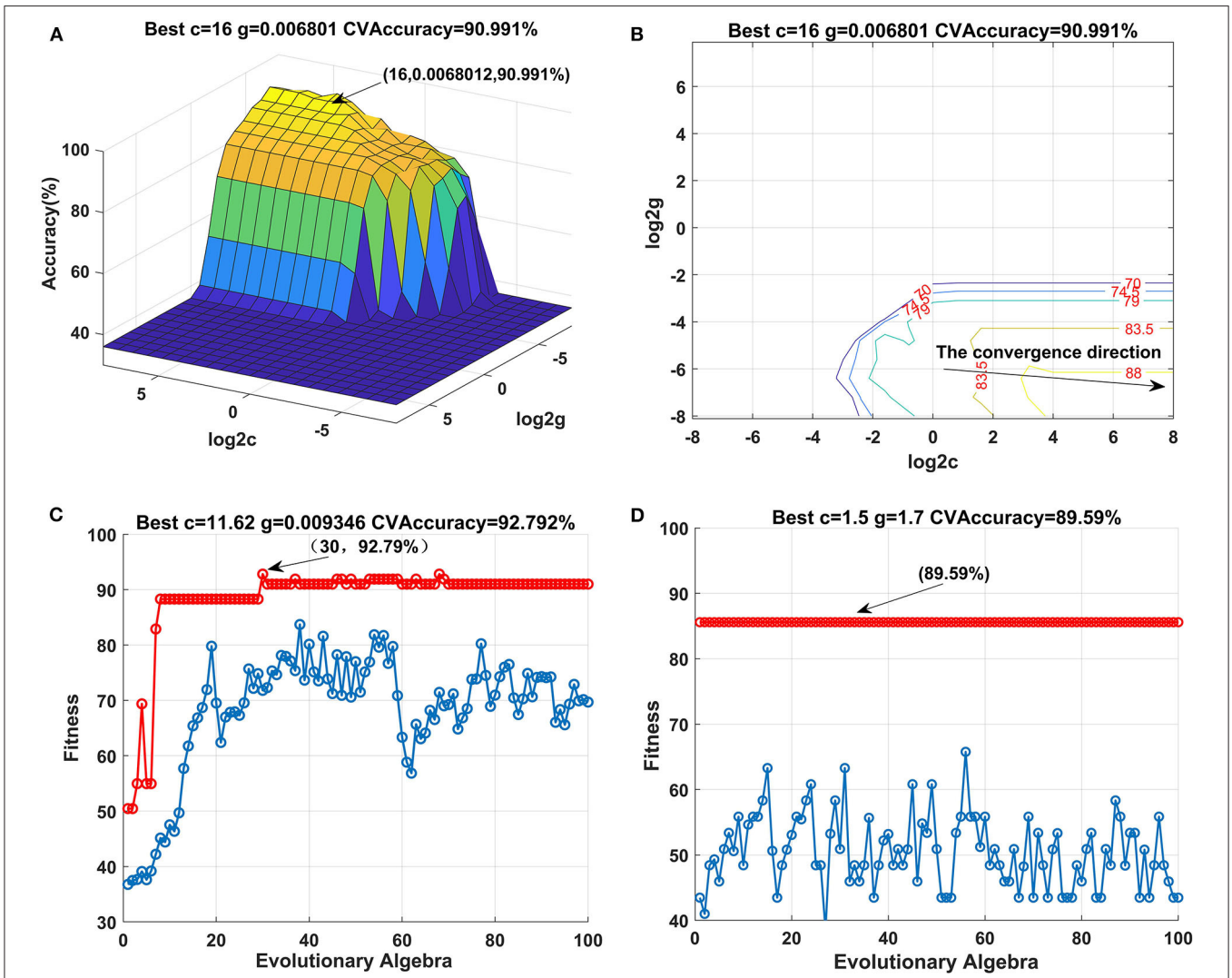

FIGURE 2 | Optimization result map for healthy, pre-diabetic, and type 2 diabetic samples: **(A,B)** optimization result map for GS; **(C)** optimization result map for GA; and **(D)** optimization result map for PSO.

1,416 nm was ascribed to water molecules without hydrogen bonds (Tsenkova, 2009; Tsenkova et al., 2018; Xueguang et al., 2018). The resulting spectra obtained by subtracting the healthy spectra from the pre-diabetic and type 2 diabetic spectra showed the differences at 1,408 nm (water molecules that do not contain hydrogen bonds), 1,416 nm (water molecules without hydrogen bonds), 1,448 nm (the solvated layer of water), 1,462 nm (water species containing two hydrogen bonds), 1,470 nm (unknown) (Tsenkova, 2009; Tsenkova et al., 2018; Xueguang et al., 2018). Error bars represent the fluctuation range of absorbance of different individuals. In the range of individual differences, the difference between pre-diabetes and type 2 diabetes can be observed from the corresponding different spectra of the second derivatives.

In general, NIRS are highly correlated and cause data redundancy to a certain extent. Principal component analysis

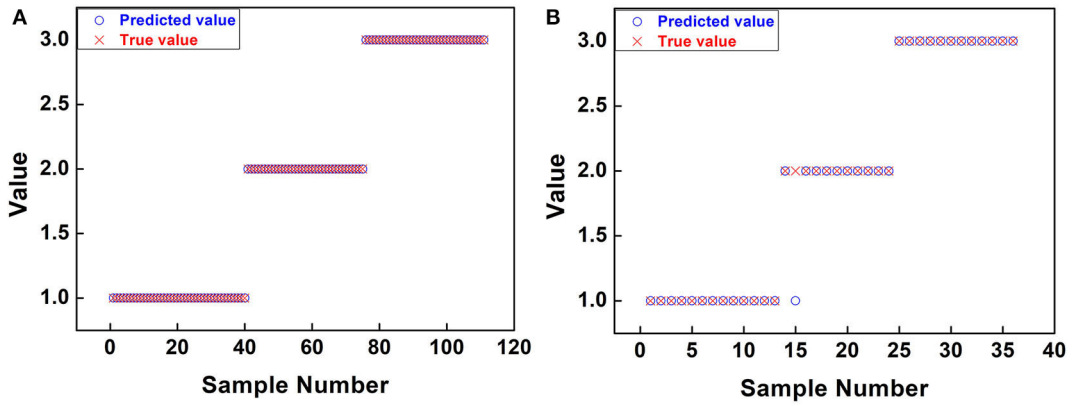

FIGURE 3 | Graphs for the estimated class values (y axis) vs. the number of samples (x axis). **(A)** Training set. **(B)** Prediction set.

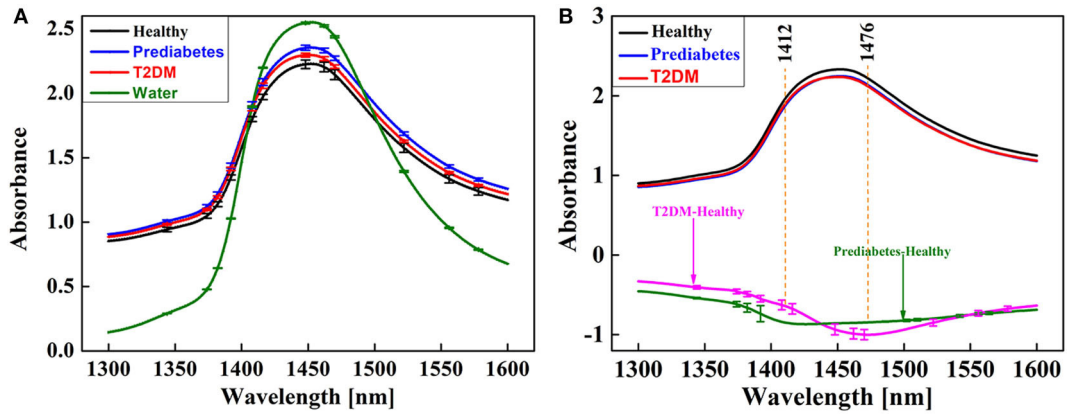

FIGURE 4 | Average spectra of the blood samples in the 1,300–1,600 nm region: **(A)** raw spectra; **(B)** difference spectra of pre-diabetes and type 2 diabetes.

(PCA) was applied to the NIRS of all samples from 1,300 to 1,600 nm because of its ability for data reduction. **Figure 5A** presents the three-dimensional score plots, which show the projection of raw data onto the 3D plane of the first three principal components of PCA. The cumulative explained variance of the first three principal components was 99.98%, indicating that the first three principal components were able to reflect most of the essential characteristics of the raw data. As shown in **Figure 5A**, from healthy, pre-diabetes, and type 2 diabetes, there was a trend along the PC2-coordinate from negative to positive values, suggesting that as diabetes progresses the original water structures of the whole blood were gradually disrupted. The water structures of the pre-diabetes gradually approached the water structures of the type 2 diabetes as diabetes progressed. **Figure 5B** is the loading plot of the first three principal components of PCA. PC3 showed higher loading values at 1,416 nm, whereas the loading values of PC1 and PC2 mainly were highest at 1,374, 1,382, 1,392, 1,448, 1,470, and 1,522 nm. In addition to the aforementioned distinctive peaks, the peak at 1,416 nm represented water molecules without hydrogen bonds and 1,522 nm was strongly bound water, water species with four hydrogen bonds absorbed in 1,482–1,495 nm (Esquerre et al., 2009; Gowen et al., 2009; Tsenkova, 2009).

Several studies have shown that there are 12 characteristic bands in the first overtone region of water (1,300–1,600 nm). As shown in **Table 3**, there were eight peaks, including 1,344, 1,374, 1,382, 1,408, 1,406, 1,448, 1,462, and 1,470 nm, in the NIRS of healthy, pre-diabetes, and type 2 diabetes samples found within these 12 characteristic bands. Each band corresponded to a peak, except for the two peaks in the C5 region. The 12 characteristic wavelengths were selected (1,344, 1,374, 1,382, 1,392, 1,408, 1,416, 1,448, 1,462, 1,470, 1,522, 1,556, 1,578 nm) according to the results of spectral variance analysis. PCA analysis to construct aquagrams for the evaluation of water structural changes in whole blood shows how diabetes progresses. The selected 12 characteristic wavelengths were the WAMACs of the entire complex system of the whole blood in healthy, pre-diabetes, and type 2 diabetes patients, and the changes in absorbance of these 12 characteristic wavelengths corresponded to the WASP of the samples.

The radar chart called an "aquagram" was drawn according to Equation (2) above as shown in **Figure 6B**. Error bars

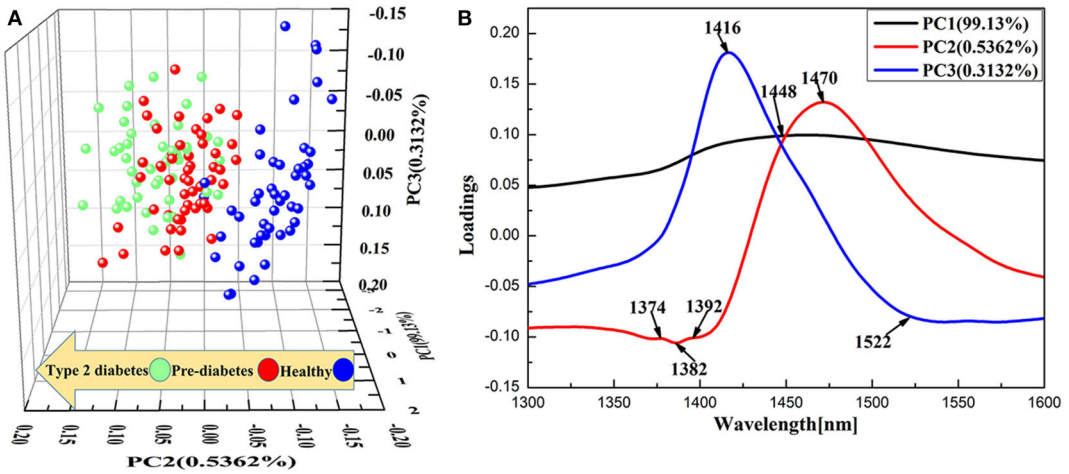

FIGURE 5 | PCA results of NIR spectra (1,300–1,600 nm) collected from all samples. **(A)** PCA 3D score plot. **(B)** PCA loading plot.

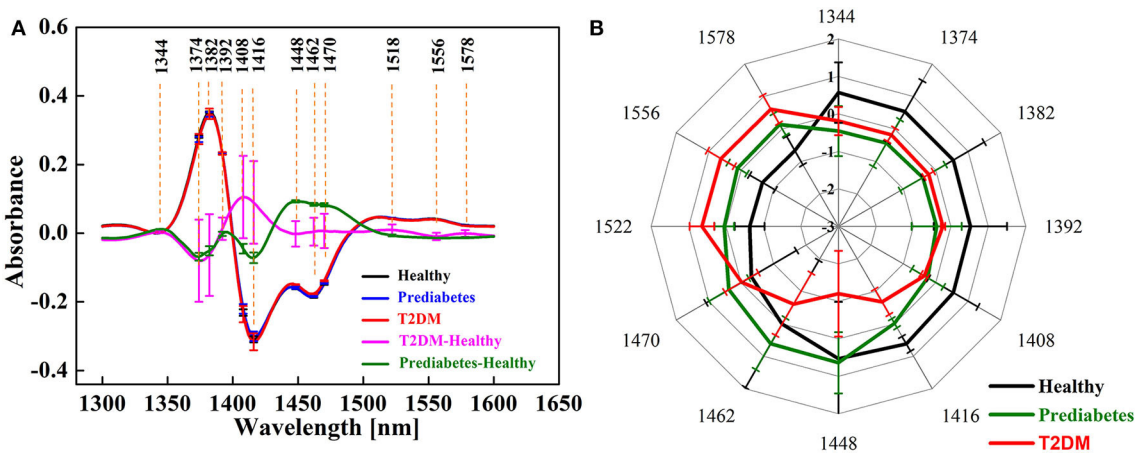

FIGURE 6 | Second derivative spectra and aquagram: **(A)** average and difference spectra in the 1,300–1,600 nm region; **(B)** aquagram of healthy, pre-diabetes, and type 2 diabetes samples in 12 fingerprint regions of water.

represent the fluctuation range of absorbance of different individuals. Within the error fluctuation range as shown in **Figure 6B**, water absorption patterns for the early diagnosis of diabetes are feasible and the differences were observed in aquagrams. The aquagrams of the healthy, pre-diabetes, and diabetes groups are clearly biased differently. The healthy group has the strongest absorbance at six WAMACS of 1,344 nm (anti-symmetric stretching fundamental frequency vibration), 1,374 nm (symmetrical and anti-symmetrically stretching fundamental frequency vibration), 1,382 nm (solvent layer of water), 1,392 nm (trapped water), 1,408 nm (water molecules that do not contain hydrogen bonds), and 1,416 nm (water molecules without hydrogen bonds).The absorbance of blood in the diabetes group was evidently closer to the center of the aquagram, and that in the pre-diabetes group was far away from the center of the aquagram in the 1,448 nm region (the solvated layer of water). In addition, the average intensity of absorbance of the pre-diabetic group at 1,462 nm (water species containing two hydrogen bonds) and 1,470 nm (unknown) was stronger than the diabetes group, while the absorbance of blood in the diabetes group at 1,522 nm (water species containing four hydrogen bonds), 1,556 nm (unknown) and 1,578 nm region (unknown) was stronger than that in the pre-diabetes group.

The 1,462 and 1,470 nm bands are found in sugar-water systems, and are also similar to the bands we found in the region above 1,500 nm (Esquerre et al., 2009; Gowen et al., 2009; Tsenkova, 2009). Also, the result shows that there is a trend in the increased concentration in the aquagrams of water-sugar solutions which is consistent with the findings of Bázár et al. (2015). The error bars on the aquagram show a large overlap between different classes, but there is no overlap in the 1,416 nm band. Therefore, judging the progress of diabetes by the number of hydrogen bonds is affected by individual

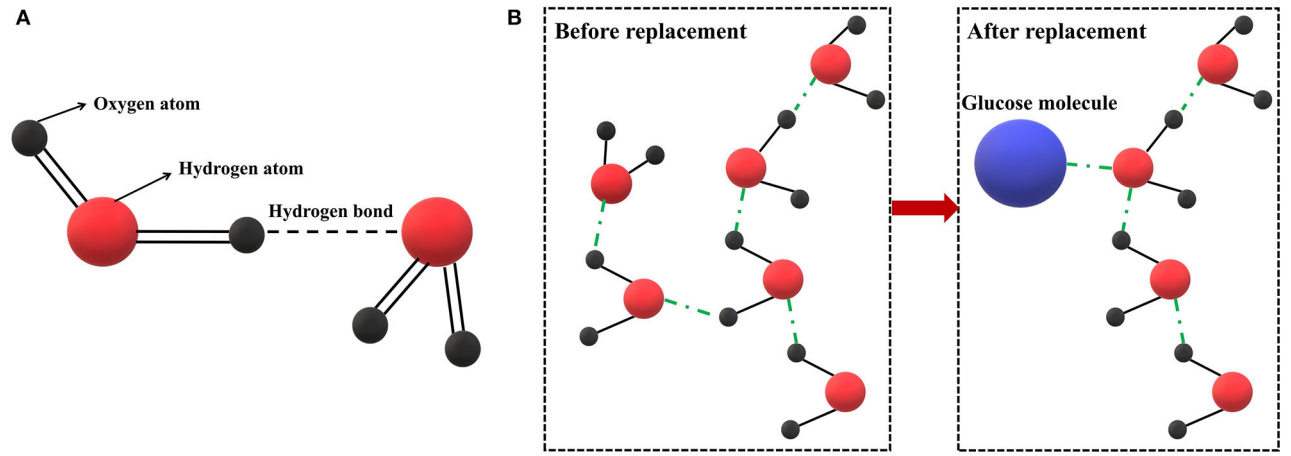

FIGURE 7 | Hydrogen bond interaction: **(A)** schematic diagram of hydrogen bonding between water molecules; **(B)** replacement effect of glucose on water in blood glucose.

differences to a certain extent, except at 1,416 nm (water molecules without hydrogen bonds) where large differences were observed without overlap.

It can be observed that the symmetric and antisymmetric stretching fundamental frequency vibrations of the water molecules are much stronger in the healthy group. Water molecules without hydrogen bonds indicated that the Van der Waals force played a significant role in the water molecules of blood, which showed that healthy people had normal blood glucose metabolism. In this case, the H in the hydrogen bonds of glucose that participates in the formation of hydrogen bonds is almost negligible, and only a small amount of H in hydrogen bonds of water molecule participates in hydrogen bonding. Therefore, the absorbance of blood in the healthy group at 1,408 nm (water molecules without hydrogen bonds) and 1,416 nm (water molecules without hydrogen bonds) was higher than that in the pre-diabetes group and diabetes group.

The number of hydrogen bonds contained in the water species are in the order of diabetes group > pre-diabetes group > healthy group, indicating that as the blood glucose metabolic dysfunction becomes more serious, the H in blood glucose replaces the H in water to participate in the formation of hydrogen bonds (shown in **Figure 7**). This indicates that the hydrogen of -OH in glucose competes with the hydrogen of -OH in water. The water environment in human blood has been changed by the aggravation of abnormal blood glucose metabolism. The H of -OH in glucose replaces the H of -OH in water to participate in hydrogen bonding and forms many glycosylation products such as glycated hemoglobin and glycated albumin (Yun, 2009). The interaction between high concentrations of blood sugar and other blood components in the long-term leads to serious effects on the health of the human body owing to the further aggravation of the disorder of glucose metabolism. Therefore, the number of non-bonded water molecules can be used as a biomarker for the early diagnosis of diabetes.

DISCUSSION

According to the results of the SVM model, the accuracy of the early diagnosis of diabetes can reach 97%. However, the model is not interpretable and cannot explain the process of diabetes occurrence and development, nor can confirm whether blood composition has changed, resulting in the corresponding changes of spectral characteristics. However, the difference in water absorption patterns of blood among the healthy group, pre-diabetes group, and diabetes group can be visually observed using the aquaphotomics method. With the intensification of blood glucose metabolism disorders, the water environment in the blood changes significantly. The H of -OH in glucose slowly replaces the H of -OH in water to participate in hydrogen bonding. The progress of diabetes can be observed in water absorption patterns at 1,408, 1,416, 1,462, and 1,522 nm which are assigned to water molecules with a different number of hydrogen bonds. The displacement effect of glucose on water has been discovered and experimentally verified in aqueous glucose solution (Brady and Schmidt, 1993; Yun, 2009; Cong et al., 2012; Xiaoyu et al., 2017; Sae et al., 2018; Arai and Shikata, 2019; Beganović et al., 2020). Therefore, it is speculated that this phenomenon is also applicable to complex solution systems such as blood, and this experiment has observed the displacement effect of glucose on the water in blood, and is applied to the early diagnosis of diabetes.

Pre-diabetes is a condition defined as having blood glucose levels above normal but below the defined threshold of diabetes. It is considered to be an at-risk state, with a high chance of developing diabetes (Tabák et al., 2012). While pre-diabetes is commonly an asymptomatic condition, it is always present before the onset of diabetes. The elevation of blood sugar is a continuum and hence pre-diabetes cannot be considered an entirely benign condition. Therefore, pre-diabetes is a necessary stage for diabetic patients. The early diagnosis of diabetes is an important way to reduce morbidity, complications, and mortality, and has

important significance for the clinical evaluation and prevention of diabetes (Cefalu et al., 2014; Yi et al., 2014; Huang et al., 2016; Khokhar et al., 2017).

This study, different to those conducted previously, has used near-infrared spectroscopy combined with machine learning and aquaphotomics for the early diagnosis of diabetes. The diagnosis accuracy has reached 97%. Differences in water absorption patterns were analyzed, and the specific features of the water spectra that can be used as a biomarker for the early diagnosis of diabetes were found. Besides, the occurrence and development of diabetes were explained at the molecular level. Specifically, as the disorder of blood glucose metabolism intensifies, the water environment of blood changes significantly. The H of -OH in glucose replaces the H of -OH in water to participate in hydrogen bonding, and the severity of diabetes can be reflected via the number of hydrogen bonds contained in the water species.

CONCLUSION

In this study, the near-infrared spectra of blood samples from healthy, pre-diabetes, and diabetes groups were collected and it was found that the raw near-infrared spectra were not significantly different. However, after the second-order derivative was used to improve the spectral resolution, significant differences were found in the 1,400–1,500 nm region, which shows that water absorption patterns could be used for the early diagnosis of diabetes. Therefore, NIRS combined with machine learning and aquaphotomics were used for the early diagnosis of diabetes in this paper. The results show that the optimization of different preprocessing methods and optimization algorithms (GS, GA, PSO) can greatly improve the accuracy rate of the SVM model, and a high accuracy rate of 97% was obtained by the SVM model for recognizing the healthy, pre-diabetes, and diabetes groups. Difference of water absorption patterns in blood was analyzed by aquaphotomics method, and results show that the number of hydrogen bonds contained in the water species decreased in the order of diabetes group > pre-diabetes group > healthy group, which indicated a significant change in the water environment between the groups. Owing to the dysfunction of the blood glucose metabolism, the H of -OH in glucose replaces the H of -OH in water to participate in hydrogen bonding, and the severity of the diabetes can be reflected via the number of hydrogen bonds.

DATA AVAILABILITY STATEMENT

The raw data supporting the conclusions of this article will be made available by the authors, without undue reservation.

ETHICS STATEMENT

The studies involving human participants were reviewed and approved by Ethics Committee of the First Affiliated Hospital of Jinan University. The patients/participants provided their written informed consent to participate in this study.

AUTHOR CONTRIBUTIONS

FH and YL: conceptualization of the project. YL and LG: data curation, data analysis and validation, and writing the original draft. YL, LG, and LL: laboratory investigation. FH and ZC: project administration and funding resources. YL, LG, CY, PG, and FH: writing—review and editing. All authors contributed to the article and approved the submitted version.

FUNDING

The authors are grateful for all the subjects who participated in the study. This research was supported by the National Natural Science Foundation of China (61975069), the National Natural Science Foundation of China (62005056), the Natural Science Foundation of Guangdong Province, China (2018A0303131000), the Key-Area Research and Development Program of Guangdong Province (2020B090922006), and the Guangzhou Science and Technology Project (201903010042).

REFERENCES

Abdi, H., and Williams, L. J. (2010). Principal component analysis. *Wiley Interdiscip. Rev. Comput. Stat.* 2, 433–459. doi: 10.1002/wics.101

Afara, I. O., Sarin, J. K., Ojanen, S., Finnilä, M. A., Herzog, W., Saarakkala, S., et al. (2020). Machine learning classification of articular cartilage integrity using near infrared spectroscopy. *Cell. Mol. Bioeng.* 13, 219–228. doi: 10.1007/s12195-020-00612-5

Aljarah, I., Ala, M. A. Z., Faris, H., Hassonah, M. A., Mirjalili, S., et al. (2018). Simultaneous feature selection and support vector machine optimization using the grasshopper optimization algorithm. *Cogn. Comput.* 10, 478–495. doi: 10.1007/s12559-017-9542-9

American Diabetes Association (2012). Diagnosis and classification of diabetes mellitus. *Diabetes Care* 33, S64–S71. doi: 10.2337/dc12-s064

Arai, K., and Shikata, T. (2019). Molecular motions, structure and hydration behaviour of glucose oligomers in aqueous solution. *Phys. Chem. Chem. Phys.* 21:25379. doi: 10.1039/C9CP05214C

Atanassova, S., Tsenkova, R., Vasu, R. M., Koleva, M., and Dimitrov, M. (2009). Identification of mastitis pathogens in raw milk by near infrared spectroscopy and SIMCA classification method. *Works Univ. Food Tech. Plovdiv.* 56, 567–572.

Bázár, G., Romvári, R., Szabó, A., Somogyi, T., Éles, V., and Tsenkova, R. (2016). NIR detection of honey adulteration reveals differences in water spectral pattern. *Food Chem.* 194, 873–880. doi: 10.1016/j.foodchem.2015.08.092

Beć, K. B., Grabska, J., and Huck, C. W. (2020). Near-infrared spectroscopy in bio-applications. *Molecules* 25:2948. doi: 10.3390/molecules25122948

Beganović, A., Beć, K. B., Grabska, J., Stanzl, M. T., Brunner, M. E., and Huck, C. W. (2020).Vibrational coupling to hydration shell-Mechanism to performance enhancement of qualitative analysis in NIR spectroscopy of carbohydrates in aqueous environment. *Spectrochim. Acta Part A Mol. Biomol. Spectrosc.* 237:118359. doi: 10.1016/j.saa.2020.118359

Bishop, S. A., and Neary, J. P. (2018). Assessing prefrontal cortex oxygenation after sport concussion with near-infrared spectroscopy. *Clin Physiol Funct Imaging.* 38, 573–585. doi: 10.1111/cpf.12447

Brady, J. W., and Schmidt, R. K. (1993). The role of hydrogen bonding in carbohydrates: molecular dynamics simulations of maltose in aqueous solution. *J. Phys. Chem*. 97, 958–966. doi: 10.1021/j100106a024

Byrne, H. J., Knief, P., Keating, M. E., and Bonnier, F. (2016). Spectral pre and post processing for infrared and Raman spectroscopy of biological tissues and cells. *Chem. Soc. Rev*. 45, 1865–1878. doi: 10.1039/C5CS00440C

Cao, W. J., Mao, C., Chen, W., Lin, H., Krishnan, S., and Cauchon, N. (2006). Differentiation and quantitative determination of surface and hydrate water in lyophilized mannitol using NIR spectroscopy. *J. Pharm. Sci.* 95, 2077–2086. doi: 10.1002/jps.20706

Cattaneo, T. M. P., Cabassi, G., Profaizer, M., and Giangiacomo, R. (2009). Contribution of light scattering to near infrared absorption in milk. *J. Near Infrared Spectrosc.* 17, 337–343. doi: 10.1255/jnirs.867

Cefalu, W. T., Petersen, M. P., and Ratner, R. E. (2014). The alarming and rising costs of diabetes and pre-diabetes: a call for action. *Diabetes Care* 37, 3137–3138. doi: 10.2337/dc14-2329

Cong, C., Wei, Z. L., Yong, C. S., Lin, D. W., and Ning, Z. (2012). Formation of water and glucose clusters by hydrogen bonds in glucose aqueous solutions. *Comput. Theoret. Chem*. 984, 85–92. doi: 10.1016/j.comptc.2012.01.013

Diabetes Branch of Chinese Medical Association (2014). Guidelines for the prevention and treatment of type 2 diabetes in china (2013 edition). *Chin. J. Diabetes* 88, 26–29. doi: 10.3760/cma.j.issn.1000-6699.2014.10.020

Diller, K. R. (1992). Modeling of bioheat transfer processes at high and low temperatures. *Adv. Heat Transf.* 22, 157–357. doi: 10.1016/S0065-2717(08)70345-9

Donis-Gonzalez, I. R., Guyer, D. E., and Pease, A. (2016). Postharvest noninvasive assessment of undesirable fibrous tissue in fresh processing carrots using computer tomography images. *J. Food Eng.* 190, 154–166. doi: 10.1016/j.jfoodeng.2016.06.024

Esquerre, C., Gowen, A. A., O'Donnell, C. P., and Downey, G. (2009). Water absorbance pattern of physically-damaged mushrooms stored at ambient conditions. *J. Near Infrared Spectrosc*. 17, 353–361. doi: 10.1255/jnirs.859

Etchegary, H., Cappelli, M., Potter, B., Vloet, M., Graham, I., Walker, M., et al. (2010). Attitude and knowledge about genetics and genetic testing. *Public Health Genom.* 13, 80–88. doi: 10.1159/000220034

Fukuda, H., and Mizobe, M. (2017). Impact of nonadherence on complication risks and healthcare costs in patients newly-diagnosed with diabetes. *Diabetes Res. Clin. Pract.* 123, 55–62. doi: 10.1016/j.diabres.2016.11.007

Gowen, A. A., Tsenkova, R., Esquerre, C., Downey, G., and O'Donnell, C. P. (2009). Use of near infrared hyperspectral imaging to identify water matrix Co-ordinates in mushrooms *(Agaricus Bisporus)* subjected to mechanical vibration. *J. Near Infrared Spectrosc.* 17, 363–371. doi: 10.1255/jnirs.860

Hsiao-Feng, H., Hsin, H., Ciao-Jyuan, S., and Chien-Hsing, L. (2017). Combining laser-doppler flowmetry measurements with spectral analysis to study different microcirculatory effects in human pre-diabetic and diabetic subjects. *Lasers Med. Sci*. 32, 327–334. doi: 10.1007/s10103-016-2117-2

Huang, Y., Cai, X., Mai, W., Li, M., Hu, Y. (2016). Association between pre-diabetes and risk of cardiovascular disease and all cause mortality: systematic review and meta-analysis. *Br. Med. J*. 355:i5953. doi: 10.1136/bmj.i5953

Huazhou, C., Lili, X., Wu, A., Bin, L., Quanxi, F., and Ken, C. (2020). Kernel functions embedded in support vector machine learning models for rapid water pollution assessment via near-infrared spectroscopy. *Sci. Total Environ.* 714:136765. doi: 10.1016/j.scitotenv.2020.136765

Jaenicke, R., and Lilie, H. (2000). Folding and association of oligomeric and multimeric proteins. *Adv. Protein Chem.* 53, 329–362. doi: 10.1016/S0065-3233(00)53007-1

Kalinin, A., Krasheninnikov, V., Sadovskiy, S., and Yurova, E. (2013). Determining the composition of proteins in milk using a portable near infrared spectrometer. *J. Near Infrared Spectrosc.* 21, 409–415. doi: 10.1255/jnirs.1054

Khokhar, A., Naraparaju, G., Friedman, M., Perez-Colon, S., Umpaichitra, V., and Chin, V. L. (2017). Comparison of a1c to oral glucose tolerance test for the diagnosis of pre-diabetes in overweight and obese youth. *Clin. Diabetes* 35, 133–140. doi: 10.2337/cd16-0037

Kinoshita, K., Miyazaki, M., Morita, H., Vassileva, M., Tang, C., and Li, D. (2012). Spectral pattern of urinary water as a biomarker of estrus in the giant panda. *Sci. Rep*. 2, 1–9. doi: 10.1038/srep00856

Kondepati, V. R., Heise, H. M., and Backhaus, J. (2008). Recent applications of near-infrared spectroscopy in cancer diagnosis and therapy. *Anal. Bioanal. Chem.* 390, 125–139. doi: 10.1007/s00216-007-1651-y

Li, Y., Xie, X., Yang, X., Guo, L., Liu, Z., Zhao, X., et al. (2019). Diagnosis of early gastric cancer based on fluorescence hyperspectral imaging technology combined with partial-least-square discriminant analysis and support vector machine. *J. Biophot*. 12:e201800324. doi: 10.1002/jbio.201800324

Lina, C., Guangzhen, F., Qian, M., Hui, Z., and Man, Z. (2013). Identification of urinary biomarkers for type 2 diabetes using bead-based proteomic approach. *Diabetes Res. Clin. Pract*. 101, 187–193. doi: 10.1016/j.diabres.2013.05.004

Ludwig, R. (2001). Water: From clusters to the bulk. *Angew. Chem. Int. Ed.* 40, 1808–1827. doi: 10.1002/1521-3773(20010518)40:10<1808::AID-ANIE1808>3.0.CO;2-1

Mainous, A. G., Tanner, R. J., and Baker, R. (2016).Pre-diabetes diagnosis and treatment in primary care. *J. Am. Board Fam. Med. March* 29, 283–285. doi: 10.3122/jabfm.2016.02.150252

Mengli, F., Yue, Z., Yan, L., Wensheng, C., and Xueguang, S. (2015). Aquaphotomics of near infrared spectroscopy. *Progr. Chem*. 27, 242–250. doi: 10.7536/PC140803

Nakagami, T., Takahashi, K., Suto, C., Oya, J., Tanaka, Y., Kurita, M., et al. (2017). Diabetes diagnostic thresholds of the glycated hemoglobin A1c and fasting plasma glucose levels considering the 5-year incidence of retinopathy. *Diabetes Res. Clin. Pract.* 124, 20–29. doi: 10.1016/j.diabres.2016.12.013

Pasquini, C. (2018). Near infrared spectroscopy: a mature analytical technique with new perspectives-A review. *Anal. Chim. Acta* 1026, 8–36. doi: 10.1016/j.aca.2018.04.004

Peng-Wei, C., Jung-Ying, W., and Hahn-Ming, L. (2004). "Model selection of SVMs using GA approach," in *Proc of 2004 IEEE Int Joint Conf on Neural Networks. 2035-2040* (Budapest).

Prior, S. L., Clark, A. R., Jones, D. A., Bain, S. C., Hurel, S. J., Humphries, S. E., et al. (2012). Association of the PCG-1αrs8192678 variant with microalbuminuria in subjects with type 2 diabetes mellitus. *Dis. Mark*. 32:363. doi: 10.1155/2012/416138

Robertson, W. H., Diken, E. G., Price, E. A., Shin, J. W., and Johnson, M. A. (2003).Spectroscopic determination of the OH^- solvation shell in the OH^- (H_2O) n clusters. *Science* 299, 1367–1372. doi: 10.1126/science.1080695

Roggo, Y., Chalus, P., Maurer, L., Martinez, C. L., Edmond, A., and Jent, N. (2007). A review of near infrared spectroscopy and chemometrics in pharmaceutical technologies. *J. Pharm. Biomed. Anal.* 44, 683–700. doi: 10.1016/j.jpba.2007.03.023

Rosella, L. C., Lebenbaum, M., Fitzpatrick, T., Zuk, A., and Booth, G. L. (2015). Prevalence of pre-diabetes and undiagnosed diabetes in Canada (2007–2011) according to fasting plasma glucose and HbA1c screening criteria. *Diabetes Care* 38, 1299–1305. doi: 10.2337/dc14-2474

Sae, T., Kojić, D., Tsenkova, R., and Yasui, M. (2018). Quantification of anomeric structural changes of glucose solutions using near-infrared spectra. *Carbohydr. Res*. 463, 40–46. doi: 10.1016/j.carres.2018.04.012

Sakudo, A. (2016). Near-infrared spectroscopy for medical applications: current status and future perspectives. *Clin. Chim. Acta* 455, 181–188. doi: 10.1016/j.cca.2016.02.009

Sánchez, A. V. D. (2003). Advanced support vector machines and kernel methods. *Neurocomputing* 55:5. doi: 10.1016/S0925-2312(03)00373-4

Schlkopf, B., Smola, A. J. (2001). *Learning with Kernels: Support Vector Machines, Regularization, Optimization, and Beyond*. The MIT Press. 2018:648.

Sylvain, T., and Cecile, L. G. (2018). Disease identification: a review of vibrational spectroscopy applications. *Compr. Anal. Chem*. 80, 195–225. doi: 10.1016/bs.coac.2018.03.005

Tabák, A. G., Herder, C., Rathmann, W., Brunner, E. J., and Kivimäki, M. (2012). Pre-diabetes: a high-risk state for diabetes development. *Lancet*. 379, 2279–2290. doi: 10.1016/S0140-6736(12)60283-9

Tsenkova, R. (2005). "Visible-near infrared perturbation spectroscopy: water in action seen as a source of information," in *12th International Conference on Near-infrared Spectroscopy* (Auckland), 607–612.

Tsenkova, R. (2008). "Aquaphotomics: VIS-near infrared spectrum of water as biological marker," in *Conference on the Physics, Chemistry and Biology of Water* (Sofia).

Tsenkova, R. (2009). Aquaphotomics: Dynamic spectroscopy of aqueous and biological systems describes peculiarities of water. *J. Near Infrared Spectrosc.* 17, 303–313. doi: 10.1255/jnirs.869

Tsenkova, R., Kovacs, Z., and Kubota, Y. (2015). Aquaphotomics: near infrared spectroscopy and water states in biological systems. *Subcell. Biochem.* 71, 189–210. doi: 10.1007/978-3-319-19060-0_8

Tsenkova, R., Munćan, J., Pollner, B., and Kovacs, Z. (2018). Essentials of aquaphotomics and its chemometrics approaches. *Front. Chem.* 6:363. doi: 10.3389/fchem.2018.00363

Vajravelu, M. E., and Lee, J. M. (2018). Identifying pre-diabetes and type 2 diabetes in asymptomatic youth: should hba1c be used as a diagnostic approach? *Curr. Diabetes Rep*. 18:43. doi: 10.1007/s11892-018-1012-6

Vapnik, V. (1995). *The Nature of Statistical Learning Theory*. New York, NY: Springer-Verlag.

Workman, J. A. (1993). A review of process near infrared spectroscopy: 1980-1994. *J. Near Infrared Spectrosc.* 1, 221–245. doi: 10.1255/jnirs.25

Xantheas, S. S. (1995a). *Ab initio* studies of cyclic water clusters $(H_2O)n$, n=1-6. III. Comparison of density functional with MP2 result. *J. Chem. Phys.* 102, 4505–4517. doi: 10.1063/1.469499

Xantheas, S. S. (1995b). Heoretical study of hydroxide ion-water clusters. *J Am. Chem. Soc.* 117, 10373–10380.

Xiaomin, S., Miaoyan, Q., Xuan'e, Z., Haiyan, W., Wenxin, T., Liping, J., et al. (2016). Gender-related affecting factors of pre-diabetes on its 10 year outcome. *MJ Open Diabetes Res. Care* 4:e0001699. doi: 10.1136/bmjdrc-2015-000169

Xiaoyu, C., Xiaoming, Y., Cai, W., and Shao, X. (2019). Water as a probe for serum–based diagnosis by temperature–dependent near–infrared spectroscopy. *Talanta* 204, 359–366. doi: 10.1016/j.talanta.2019.06.026

Xiaoyu, C., Xiuwei, L., Xiaoming, Y., Wensheng, C., and Xueguang, S. (2017). Water can be a probe for sensing glucose in aqueous solutions by temperature dependent near infrared spectra. *Anal. Chim. Acta* 957, 47–54. doi: 10.1016/j.aca.2017.01.004

Xueguang, S., Xiaoyu, C., Xiaoming, Y., and Wensheng, C., (2018). Mutual factor analysis for quantitative analysis by temperature dependent near infrared spectra. *Talanta* 183, 142–148. doi: 10.1016/j.talanta.2018.02.043

Yalsavar, M., Karimaghaee, P., Sheikh-Akbari, A., Dehmeshki, J., Khooban, M. H., and Al-Majeed, S. (2019). "Sliding mode control based support vector machine rbf kernel parameter optimization," in *IEEE International Conference on Imaging Systems and Techniques* (Abu Dhabi), 1-6.

Yi, H., Xiaoyan, C., Miaozhen, Q., Peisong, C., Hongfeng, T., Yunzhao, H., et al. (2014). Pre-diabetes and the risk of cancer: a meta-analysis. *Diabetologia*. 57:2261–2269. doi: 10.1007/s00125-014-3361-2

Yu, X., Limin, W., Jiang, H., Yufang, B., and Mian, L.,Tiange, W. (2013). Prevalence and control of diabetes in Chinese adults. *JAMA* 310, 948–959. doi: 10.1001/jama.2013.168118

Yuanjie, S., Tiannan, Y., Xun, Z., Zhixiang, C., Guorui, C., Mingliang, Y., et al. (2020). A wireless energy transmission enabled wearable active acetone biosensor for noninvasive pre-diabetes diagnosis. *Nano Energy*74:104941. doi: 10.1016/j.nanoen.2020.104941

Yun, C. (2009). *Study on Reference Wavelength Method for Non-invasive Blood Glucose Sensing With Near Infrared Spectroscopy* (Doctoral dissertation). Tianjin University, Tianjin.

Conflict of Interest: LG was employed by the company Guangdong Hongke Agricultural Machinery Research & Development Co., Ltd.

The remaining authors declare that the research was conducted in the absence of any commercial or financial relationships that could be construed as a potential conflict of interest.

frontiers in Chemistry

PERSPECTIVE
published: 09 December 2020
doi: 10.3389/fchem.2020.612387

Potential of Fourier Transform Mass Spectrometry (Orbitrap and Ion Cyclotron Resonance) for Speciation of the Selenium Metabolome in Selenium-Rich Yeast

*Katarzyna Bierla[1], Giovanni Chiappetta[2], Joëlle Vinh[2], Ryszard Lobinski[1,3,4] and Joanna Szpunar[1]**

[1] Universite de Pau et des Pays de l'Adour, E2S UPPA, CNRS, IPREM UMR5254, Institut des Sciences Analytiques et de Physico-chimie pour l'Environnement et les Matériaux, Hélioparc, Pau, France, [2] SMBP, ESPCI Paris, Université PSL, CNRS, Paris, France, [3] Laboratory of Molecular Dietetics, IM Sechenov First Moscow State Medical University (Sechenov University), Moscow, Russia, [4] Faculty of Chemistry, Warsaw University of Technology, Warsaw, Poland

The evolution of the field of element speciation, from the targeted analysis for specific element species toward a global exploratory analysis for the entirety of metal- or metalloid-related compounds present in a biological system (metallomics), requires instrumental techniques with increasing selectivity and sensitivity. The selectivity of hyphenated techniques, combining chromatography, and capillary electrophoresis with element-specific detection (usually inductively coupled plasma mass spectrometry, ICP MS), is often insufficient to discriminate all the species of a given element in a sample. The necessary degree of specificity can be attained by ultrahigh-resolution (R >100,000 in the m/z < 1,000 range for a 1 s scan) mass spectrometry based on the Fourier transformation of an image current of the ions moving in an Orbitrap or an ion cyclotron resonance (ICR) cell. The latest developments, allowing the separate detection of two ions differing by a mass of one electron (0.5 mDa) and the measurement of their masses with a sub-ppm accuracy, make it possible to produce comprehensive lists of the element species present in a biological sample. Moreover, the increasing capacities of multistage fragmentation often allow their *de novo* identification. This perspective paper critically discusses the potential state-of-the-art of implementation, and challenges in front of FT (Orbitrap and ICR) MS for a large-scale speciation analysis using, as example, the case of the metabolism of selenium by yeast.

Keywords: orbitrap, selnometabolomics, FT ICR MS, fourier transfom, selenium speciation

OPEN ACCESS

Edited by:
Anna Napoli,
University of Calabria, Italy

Reviewed by:
Serena Indelicato,
University of Palermo, Italy
Cosima Damiana Calvano,
University of Bari Aldo Moro, Italy

***Correspondence:**
Joanna Szpunar
joanna.szpunar@univ-pau.fr

Specialty section:
This article was submitted to Analytical Chemistry, a section of the journal Frontiers in Chemistry

Received: *30 September 2020*
Accepted: *10 November 2020*
Published: *09 December 2020*

Citation:
Bierla K, Chiappetta G, Vinh J, Lobinski R and Szpunar J (2020) Potential of Fourier Transform Mass Spectrometry (Orbitrap and Ion Cyclotron Resonance) for Speciation of the Selenium Metabolome in Selenium-Rich Yeast. Front. Chem. 8:612387. doi: 10.3389/fchem.2020.612387

INTRODUCTION

For decades, hyphenated techniques combining the selectivity of chromatography or capillary electrophoresis with an atomic absorption (AAS), fluorescence (AFS), microwave plasma source emission (MIP AES), or inductively coupled plasma mass spectrometry (ICP MS) detectors remained a standard tool for speciation analysis (Lobinski, 1997; Szpunar et al., 2003). Their success was based on the detector's selectivity for the target element and on the baseline separation of the target species from other species of the same element.

The increasing detection sensitivity has put in evidence the fact that, in many cases, chromatography, even multidimensional, was unable to ensure the molecular specificity of the analytical signal measured. When all the complexes of an element with proteins and low-molecular-weight biological ligands have to be determined within one run, the chromatographic peak capacity becomes insufficient to offer the baseline separation of all its compounds of interest; in addition, risks, inherent to chromatography, of incomplete recoveries, and species transformation occur (Lobinski et al., 2010). This has been leading to the shift of paradigm in speciation analysis. Rather than by chromatography, the specificity is more and more often ensured by the separation of ions, characteristic of the individual metal complexes, in a mass spectrometer. Electrospray MS, which has been considered for a long time as a technique complementary to ICP MS and used to confirm or enable the species identification, is becoming a standalone tool for speciation analysis. It can be used in direct (infusion) mode or coupled to HPLC sample introduction and is able to produce data on tens or hundreds of element species in a single mass spectrum.

The use of electrospray MS as a standalone technique for speciation analysis imposes conditions on its performance, especially in terms of resolution and mass accuracy. Not only should the target species ion be separated from the ions of other species of the same element, but also it should be separated from any other ion produced by the ionization of other concomitant molecules. Complex natural mixtures may contain several hundreds of thousands of molecules with close mass differences spread over a wide mass range (Palacio Lozano et al., 2020). The resolution of at least 0.1 mDa is necessary to allow the separation of all the generated ions (Kim et al., 2006). Moreover, the baseline separation of the ions is a *sine qua non*-condition for the sub-ppm mass accuracy, which is important for the confident assignment of individual molecular compositions (empiric formulae) within a mass spectrum.

The demanded figures of merit can only be obtained by MS techniques based on the Fourier transformation of an image current of the ions moving in an Orbitrap or an ion cyclotron resonance (ICR) cell (Marshall and Hendrickson, 2008). The image current is detected as a function of time and is recorded as a composite sum of sinusoidal waves with different frequencies, referred to as a transient. A Fourier transform is applied to this signal to convert it to the *m/z* domain and produce a mass spectrum. Consequently, detailed compositional profiles, with many thousands of unique molecular (empiric formula) assignments, can be obtained from a single mass spectrum. Dedicated data mining procedures have to be used to extract metal speciation-related data from global datasets. Furthermore, multistage fragmentation and the analysis of the dissociation patterns offer data enabling the structural characterization of element species and their unequivocal identification (Dernovics and Lobinski, 2008a).

The emerging paradigm in speciation analysis is therefore based on the assumptions that (i) large numbers of species of metal/metalloids can be ionized in parallel with all the other organic matrix constituents; (ii) all the ions can be ultimately separated in a mass spectrometer; (iii) the molecular masses can be measured with accuracy allowing the unambiguous determination of the empiric formula; (iv) information on element-species of interest can be extracted from large data sets, and (v) these metal species can be structurally characterized by multistage fragmentation and unambiguously identified.

When implemented to a real case study, however, this hypothetical workflow raises a number of practical questions that are discussed below using an example of speciation of selenium following its metabolism by yeast. Such a process leads to hundreds of selenium species of which the identity still remains limited.

INTEREST IN THE IDENTIFICATION OF THE PRODUCTS OF THE SELENIUM METABOLISM BY YEAST

Selenium is an essential element for human and animal nutrition (Rayman, 2012). The addition of Se to the diet through supplements or fortified food/feed is increasingly common owing to the often suboptimal content of Se in staple foods in many countries (Fairweather-Tait et al., 2011; Rayman, 2012). The popular basis of such supplements is Se-rich yeast (Fagan et al., 2015) produced by growing different yeast varieties, usually *Saccharomyces cerevisiae* and *Candida utilis*, in the presence of selenite or selenate. Protein-incorporated selenomethionine is the primary selenium species produced in *S. cerevisiae* (Fagan et al., 2015), whereas selenohomolanthione is the most abundant species (ca. 80%) produced by *C. utilis* (Bierla et al., 2017). In either case, in a good-quality yeast, selenium is metabolized completely to organic forms and plethora of LMW (<1,000 Da) species, referred to as selenometabolome, are produced. Its detailed characterization is essential for the control of the reproducibility of the fermentation process, variance of different strains, and traceability of the product's origin (Ward et al., 2019). Furthermore, as some of the metabolites may have superior beneficial activity (and, on the other hand, others can be toxic), the motivation of the producers to offer a well-characterized unique product is evident. Also, it is important for the consumer to understand differences between formulations available on the market.

CHARACTERIZATION OF THE Se-RICH YEAST METABOLOME: STATE-OF-THE-ART

The selenium non-proteic metabolome constitutes between 10% and more than 90% of the total selenium present. It is isolated with quantitative recovery by extraction with water or water-ethanol mixture. The extraction is reproducible within a few percent in terms of retention time of selenium species and their peak intensity is demonstrated by HPLC-ICP MS. The extract is sometimes pre-concentrated by freeze-drying and often fractionated by size exclusion (SEC) and/or anion-exchange chromatography (AEC). The analysis can be carried out either directly (by infusion) or by coupling of HILIC/reversed-phase

TABLE 1 | Summary of the mass spectrometry reports of the characterization of the Se-rich yeast metabolome.

Year	Instrument	Sample (aqueous extract) prior fractionation	Resolution	Sample introduction (transient)	Nr of species	Ref.
2002	QTOF MS (QSTAR2 Pulsar, AB/MDS SCIEX)	SEC/AEC		Infusion: 1 min (60 cycles of 1 s)	5 out of 8 identified (out of 8 detected)	McSheehy et al., 2002
2006	Q-TOF MS (QSTAR XL, Applied Biosystems)	SEC		RP nanoHPLC (0.8 s)	7 identified (5 novel)	García-Reyes et al., 2006
2008	LTQ-Orbitrap MS (Thermo Fisher Scientific)	SEC/AEC	60,000 at *m/z* 400		8 identified (6 novel)	Dernovics and Lobinski, 2008b
2008	LTQ-Orbitrap MS (Thermo Fisher Scientific)	SEC	60,000 at *m/z* 400	HILIC (1 s)	9 identified	Dernovics and Lobinski, 2008a
2009	LTQ-Orbitrap MS (Thermo Fisher Scientificany)	AEC	60,000 at *m/z* 400	HILIC or RP HPLC (1s)	9 detected 8 identified 5 novel	Dernovics et al., 2009
2010	LTQ-Orbitrap MS (Thermo Fisher Scientific)	None*	30,000	RP HPLC	10 identified	Rao et al., 2010
2012	LTQ-Orbitrap Velos (Thermo-Fisher Scientific)	None		2D (SEC-RP) HPLC	49 identified 30 novel	Preud'homme et al., 2012
2012	LTQ-Orbitrap Velos (Thermo-Fisher Scientific)	SEC		HILIC or RP HPLC	64 detected 52 identified 9 novel	Arnaudguilhem et al., 2012
2017	TOF MS (Agilent TOF 6210)	SEC		HPLC	103 detected	Gilbert-López et al., 2017
2019	Q-TOF MS (Agilent 6545)	Ultrafiltration		HPLC (1 s)	188 detected 14 identified out of 129 novel	Ward et al., 2019

**75% ethanol.*

HPLC to ESI MS. The water-soluble high molecular weight (proteic) species can be eliminated by 3-kDa cutoff filtration before the analysis. **Table 1** summarizes the mass spectrometry-based procedures which have contributed to the characterization of the metabolome of the Se-rich yeast. The analyses have been carried out by TOF MS or Orbitrap MS.

The literature reports show a steady increase in the number of detected and confirmed species with a clear lack of the definitive confirmation of the identity, and thus speciation. Indeed, the progress in terms of the identification of the detected compounds has been largely unsatisfactory. Recent studies (Gilbert-López et al., 2017; Ward et al., 2019) show that only a small fraction of the detected, previously unreported compounds could be identified. This clearly demonstrates the need for analytical methods allowing the large-scale speciation analysis of the Se-rich yeast metabolome. A further tangible progress is unlikely to be possible without the implementation of FT ICR MS into the speciation protocols, the improvement of the multistage fragment analysis, and a re-design of the upstream chromatographic fractionation approaches.

ULTRAHIGH-RESOLUTION HIGH MASS ACCURACY MS: RESOLVING POWER AND ACCURATE MASS MEASUREMENT

The unique species identity assignment can only be attained if the ions of interest can be separated from all those produced by any other molecule present. In a landmark thought experiment, Marshall et al. considered all the possible elemental compositions $C_cH_hN_nO_oS_s$, where c, h, n, o, and s are the numbers of the respective elements in the molecule structure. They concluded that for even-electron ions $(M+H)^+$ and $(M-H)^-$, mass resolution and accuracy of 0.1 mDa are generally sufficient to yield a unique elemental composition for molecules of up to 500 Da, even in the most complex natural mixtures (Kim et al., 2006). Consequently, for a broadband accurate (sub-ppm) mass measurement, the discrimination of the difference of one electron (0.5 mDa) is sufficient for the assignment of a unique empiric formula to an *m/z* 300 molecule (Kim et al., 2006). For the metal speciation analysis, this conclusion is likely to be valid even for higher *m/z* and/or for lower resolution values because (i) not all theoretically possible elemental compositions are chemically possible and (ii) the presence of a heteroelement, often with a characteristic isotopic pattern, is a potent discriminatory factor.

Figure 1A demonstrates that in order to distinguish the species with one electron mass difference, a resolution of 1,400,000 is necessary at *m/z* 400; it increases with the *m/z* of the target molecules. Standard 7T FT ICR MS instruments offer resolution of ca. 750,000 for *m/z* 400 although it can be doubled to reach 1,500,000 (*m/z* 400, 4 s transient signal) (Cho et al., 2017). The highest resolutions reported for *m/z* 400 in real sample measurement conditions, 1,200,000 (3-s transient, magnitude mode) and 2,700,000 (for a 6.3-s transient, absorption mode), were reported using a 21-T FT ICR instrument (Palacio Lozano et al., 2020). The resolutions of the new Orbitrap MS models are comparable with the 7-T FT ICR; the highest reported resolution at *m/z* 400 was 841,000 (absorption mode, 3-s transient) (Schmidt et al., 2018). It is worth noting that

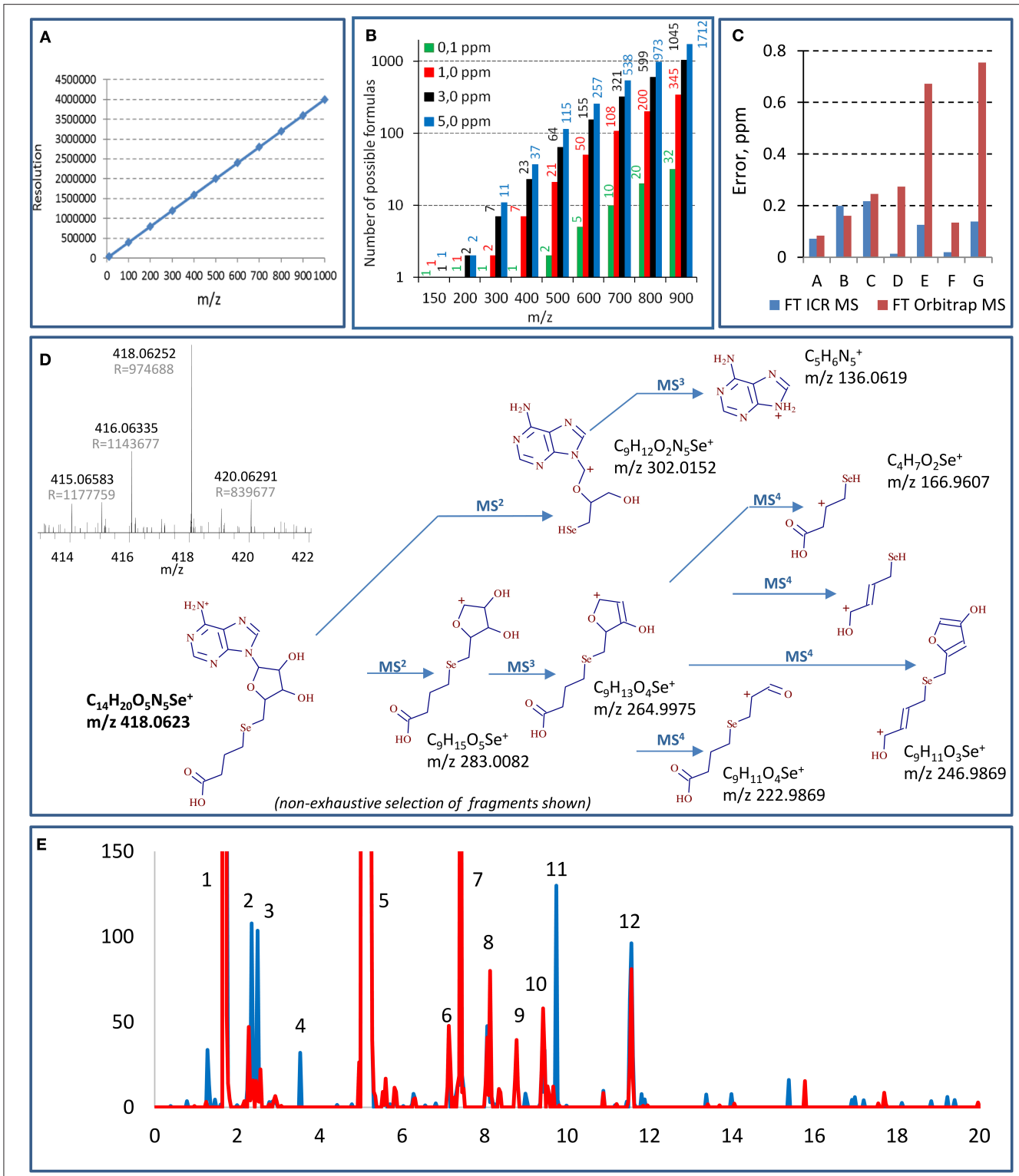

FIGURE 1 | Principal aspects of selenium speciation by ultrahigh-resolution mass spectrometry: **(A)** theoretical resolution necessary for the baseline resolve of equimolar mixtures of species of different *m/z*; **(B)** number of possible molecular formulas for different *m/z* at different levels of mass accuracy (according to Kind and Fiehn, 2006); **(C)** comparison of mass errors observed for different Se-adenosyl derivatives (*m/z* 300–700 Da) in FT Orbitrap MS (Lumos, transient 2.4 s, resolution 1 M) and FT ICR MS (7 T, transient 12.6 s for resolution of 1 M); **(D)** multistage (MS^4) fragmentation of a previously unreported Se species using QqOrbitrap MS. A high-resolution mass spectrum (FT ICR MS) having allowed the detection of the species an shown in inset; **(E)** example chromatograms generated from the same

(Continued)

FIGURE 1 | data set targeting different sets of selenium isotopes (red line—77, 78, and 80, black line—78, 80, and 82). Masses of the selenium species identified in the peaks: 1—348.0199, 431.0569, 449.0674, 453.0387, 487.0144, 471.0492; 2—364.0147; 3—344.0250, 362.0364; 4—416.0459; 5—332.0246, 387.0671, 433.072, 455.0544, 471.0194; 6—404.04677; 7—442.0365; 8—521.0886, 637.0819; 9—475.0830; 10—713.0985, 388.0510, 446.0567, 346.0406; 11—418.0615; 12—681.0100. The compounds are not retention time but mass resolved.

these resolutions can be improved by instrumental and/or data processing techniques; the acquisition of full transients for custom-designed signal processing allowed a resolution of 3.5 M at *m/z* 600 (6-s transient) in a model experiment using Orbitrap Lumos (Tsybin et al., 2019). The resolving power decreases when *m/z* increases (linearly for FT ICR and as square root for Orbitrap). It is proportional to the scan duration, which may favor the chromatographic fraction collection and infusion over HPLC sample introduction. The molecular mass determination provides hypotheses on the identity of the detected selenium compound. Indeed, the higher the accuracy, the shorter the list of candidate molecular formulas (**Figure 1B**) varying from 1 to 2 candidates for low *m/z* (150) and from 32 to 3,447 candidates for higher *m/z* (900) with the respective mass accuracy at 0.1 and 10 ppm (Kind and Fiehn, 2006). The compound's identity has, however, to be verified by the targeted fragmentation of the ion in question, which also provides the structural information on the molecule.

IDENTIFICATION OF SELENIUM SPECIES BY ULTRAHIGH-RESOLUTION HIGH MASS ACCURACY MS IN Se-RICH YEAST

Ionization of Selenospecies: Infusion vs. HPLC MS

Selenium compounds are typically analyzed as protonated $[M+H]^+$ species. As discussed above, ultrahigh resolutions can be readily obtained only for several second transients which require sample introduction by infusion. However, in contrast to the examples of complex matrix analysis, such as petroleomics, reports of selenium speciation in the infusion mode are rare, and none of them concerned a raw unprocessed extract (Casiot et al., 1999; McSheehy et al., 2002). The main reason is a big excess of the concomitant matrix species with regard to the selenium analyte concentration and the consequent suppression of the Se-species ionization efficiency which requires the isolation and purification of the analytes. An additional difficulty is the separation of polar selenium species from the matrix salts. Consequently, various chromatographic methods have been coupled to UHR MS, utilizing separation steps to reduce matrix effects for low-ion-yield species. In particular, the high efficiency of HILIC for the studies of polar selenium compounds should be noted (Aureli et al., 2012; Ouerdane et al., 2013).

FT ICR MS Detection of Se Species

Figure 1C shows that the mass accuracies reached by a 7-T FT ICR obtained for 7 Se-adenosyl derivatives (*m/z* 300–700 Da) are 0.1 ± 0.1 ppm. The mass accuracy errors obtained by Orbitrap MS may be an order of magnitude higher. The inset in **Figure 1D** shows a mass spectrum obtained for a previously unreported compound at m/z 418.0630 obtained at 1 M resolution and 0.2 ppm mass accuracy (7 T, 2 s transient). This molecular mass corresponds to a unique combination of C, H, S, N, and Se atoms giving the molecular formula of $C_{14}H_{19}O_5N_5Se$.

Orbitrap MS^n Species Identification

Data-dependent acquisition MS^n mode usually fails for selenium speciation unless HPLC is carried out for a sample having undergone multistage purification and enrichment. Concentrations should be high enough to allow the fragmentation even if performed in targeted mode (Ward et al., 2019). Hence, as a rule, MS^2 (and especially MS^3 and MS^4) runs in selenium speciation studies are targeted. In this context, an ion trap instrument with high-accuracy fragment measurement is essential for the structure confirmation and elucidation (Dernovics and Lobinski, 2008a). **Figure 1D** shows an MS^4 insight into the structure of a novel selenium compound detected by FT ICR MS. The numerous MS^4 fragments of various sizes allow one to put forward hypotheses regarding the composition of ions at the M^3 and M^2 levels and to validate or reject them as a function of fitting the exact molecular mass. The big number of fragments at the different MS stages, their empiric formula measured with reasonable high accuracy (<3 ppm), and the unique empiric formula of the parent ion obtained owing to the ultrahigh mass accuracy of the FT ICR MS measurement make feasible the unique structure assignment in most cases.

AUXILIARY TOOLS FOR SELENIUM LARGE-SCALE SPECIATION ANALYSIS

Even if, technically speaking, high-resolution high-accuracy MS detection is sufficient to carry out large-scale metabolomics, some particular features of the system facilitate data analysis and allow the validation of the obtained results.

Selenium Isotopic Pattern Recognition

As demonstrated above, selenium compounds can be assigned the empiric formula on the basis of a single isotope molecular mass. However, the distinct natural isotopic distribution of selenium is a precious and widely used tool to assist the detection and unambiguous confirmation of the presence of selenium-containing compounds in complex data sets. Selenium has six stable isotopes with detectable distribution: ^{74}Se (0.86%), ^{76}Se (9.23%), ^{77}Se (7.60%), ^{78}Se (23.69%), ^{80}Se (49.80%), and ^{82}Se (8.82%) which can be detected in mass spectra by a unique isotope envelope pattern. The selenium metabolome is also known to contain (about 5 times fewer in number) compounds with two selenium atoms per molecule which requires the search for another characteristic pattern. The pattern to be recognized is distorted by the contribution of minor isotopes of other

elements in the molecule (e.g., ^{13}C, ^{15}N, ^{34}S) and suffers from the spectral interferences in the case of insufficient resolution in a complex matrix. A development trend in large-scale selenium speciation is an automatic generation of isotope-pattern selective chromatograms on the basis of a set of parameters such as the number and choice of isotopes, intra-isotope mass defect, and isotope ratio intensity. The definition of the data mining parameters greatly influences the result obtained (Bierla et al., 2018; Gao et al., 2018) as shown for the example chromatograms generated from the same data set using 2, 3, or 5 most abundant selenium isotopes (**Figure 1E**). Any choice of the parameters carries a certain risk of false negatives or false positives, and a critical evaluation of the generated results is necessary. Also, the detection of the isotopic pattern includes adducts such as $[M+Na^+]$, $[M+K^+]$, and $[M+NH_4^+]$ that have to be identified (e.g., by their co-occurrence after the chromatographic separation) and eliminated by data treatment (Ward et al., 2019).

Selenium/Sulfur Homology

A particularity of selenium speciation studies is the fact that selenium shares similar chemical properties with those of sulfur and competes with sulfur in biological processes. As a rule, a selenium species is likely to be accompanied by its sulfur analog which offers multiple opportunities for the analysis of high-resolution high-accuracy MS data sets. As the sulfur metabolic pathways in yeast are known (Mapelli et al., 2012), lists of putative selenium metabolites for targeted analysis can be made. The accurate mass difference measurement allows the identification of the S–Se homologs in data sets. Also, as demonstrated elsewhere (Casiot et al., 1999) the easier availability of sulfur standards allows the validation of the identification of their selenium analogs.

Lessons From the Chemistry

The observed multitude of detected selenium species is likely to come from the unspecific oxidation and the formation of Se–Se and/or Se–S bonds. The moment in which the oxidation occurs (production process, storage, extraction) is unknown. The acquisition of a chromatogram in the reducing conditions offers direct access to the identity of the–SeH containing original species and facilitates the interpretation of data.

OUTLOOK

Ultrahigh resolution mass spectrometry is likely to be the ultimate tool for speciation analysis as it inherently offers the required species specificity in complex matrices as demonstrated by recent studies of metal porphyrins in crude oils (Palacio Lozano et al., 2020) or metallophores in the environment (Boiteau et al., 2019). The instrumental power of state-of-the-art FT instruments (ICR and Orbitrap) seems to be sufficient for large-scale selenium speciation in a biological matrix, especially that the Se isotopic pattern can be exploited to improve data mining. However, the potential of FT ICR MS, and especially HPLC-FT ICR MS for the detection of Se species, is still largely unexplored. MS coupled to prior separation is required to differentiate structural isomers of species with the same elemental composition whereas ion mobility MS is expected to provide meaningful complementary data regarding the presence of conformers. Whereas, the large-scale mapping of the entire yeast metabolome is within the reach of high-resolution high-mass-accuracy MS, the quantification of all the individual species by this approach seems to be a remote goal. Its achievement requires the availability of individual standards of the Se species to be quantified.

DATA AVAILABILITY STATEMENT

The datasets presented in this study can be found in online repositories. The names of the repository/repositories and accession number(s) can be found at: EBI, MTBLS2132.

AUTHOR CONTRIBUTIONS

KB, GC, and JV carried out the expeiments. KB, JS, and RL planned the work. JS and RL prepared the draft. All authors completed and appoved the manuscript.

FUNDING

The FT ICR experiments in this work were financed by the French Federation FR 3624 TGE FT-ICR (CNRS, France).

REFERENCES

Arnaudguilhem, C., Bierla, K., Ouerdane, L., Preud'homme, H., Yiannikouris, A., and Lobinski, R. (2012). Selenium metabolomics in yeast using complementary reversed-phase/hydrophilic ion interaction (HILIC) liquid chromatography-electrospray hybrid quadrupole trap/orbitrap mass spectrometry. *Anal. Chim. Acta* 757, 26–38. doi: 10.1016/j.aca.2012.10.029

Aureli, F., Ouerdane, L., Bierla, K., Szpunar, J., Prakash, N. T., and Cubadda, F. (2012). Identification of selenosugars and other low-molecular weight selenium metabolites in high-selenium cereal crops. *Metallomics* 4, 968–978. doi: 10.1039/c2mt20085f

Bierla, K., Godin, S., Lobinski, R., and Szpunar, J. (2018). Advances in electrospray mass spectrometry for the selenium speciation: focus on Se-rich yeast. *TrAC Trends Anal. Chem.* 104, 87–94. doi: 10.1016/j.trac.2017.10.008

Bierla, K., Suzuki, N., Ogra, Y., Szpunar, J., and Lobinski, R. (2017). Identification and determination of selenohomolanthionine – the major selenium compound in Torula yeast. *Food Chem.* 237, 1196–1201. doi: 10.1016/j.foodchem.2017.06.042

Boiteau, R. M., Fansler, S. J., Farris, Y., Shaw, J. B., Koppenaal, D. W., Pasa-Tolic, L., et al. (2019). Siderophore profiling of co-habitating soil bacteria by ultra-high resolution mass spectrometry. *Metallomics* 11, 166–175. doi: 10.1039/C8MT00252E

Casiot, C., Vacchina, V., Chassaigne, H., Szpunar, J., Potin-Gautier, M., and Łobiński, R. (1999). An approach to the identification of selenium species in yeast extracts using pneumatically-assisted electrospray tandem mass spectrometry. *Anal. Commun.* 36, 77–80. doi: 10.1039/a900319c

Cho, E., Witt, M., Hur, M., Jung, M. J., and Kim, S. (2017). Application of FT-ICR MS equipped with quadrupole detection for analysis of crude oil. *Anal. Chem.* 89, 12101–12107. doi: 10.1021/acs.analchem.7b02644

Dernovics, M., Far, J., and Lobinski, R. (2009). Identification of anionic selenium species in Se-rich yeast by electrospray QTOF MS/MS and hybrid linear ion trap/orbitrap MSn. *Metallomics* 1, 371–329. doi: 10.1039/b901184f

Dernovics, M., and Lobinski, R. (2008a). Speciation analysis of selenium metabolites in yeast-based food supplements by ICPMS-assisted hydrophilic interaction HPLC-hybrid linear ion trap/orbitrap MSn. *Analy. Chem*. 80, 3975–3984. doi: 10.1021/ac8002038

Dernovics, M., and Lobinski, R. (2008b). Characterization of the selenocysteine-containing metabolome in selenium-rich yeast: part 1. Identification of new species by multi-dimensional liquid chromatography with parallel ICP-MS and electrospray Q-TOFMS/MS detection. *J. Analy. Atomic Spestrom.* 23, 744–751. doi: 10.1039/B708294K

Fagan, S., Owens, R., Ward, P., Connolly, C., Doyle, S., and Murphy, R. (2015). Biochemical comparison of commercial selenium yeast preparations. *Biol. Trace Elem. Res*. 166, 245–259. doi: 10.1007/s12011-015-0242-6

Fairweather-Tait, S. J., Bao, Y., Broadley, M. R., Collings, R., Ford, D., Hesketh, J. E., et al. (2011). Selenium in human health and disease. *Antioxid. Redox Signal.* 14, 1337–1383. doi: 10.1089/ars.2010.3275

Gao, J., Yang, F., Che, J., Han, Y., Wang, Y., Chen, N., et al. (2018). Selenium-encoded isotopic signature targeted profiling. *ACS Central Sci*. 4, 960–970. doi: 10.1021/acscentsci.8b00112

García-Reyes, J. F., Dernovics, M., Giusti, P., Lobinski, R. (2006). Identification of new selenium non-peptide species in selenised yeast by nanoHPLC electrospray Q/time-of-flight-MS/MS. *J. Anal. At. Spectrom.* 21, 655–665. doi: 10.1039/B518297B

Gilbert-López, B., Dernovics, M., Moreno-González, D., Molina-Díaz, A., and García-Reyes, J. F. (2017). Detection of over 100 selenium metabolites in selenized yeast by liquid chromatography electrospray time-of-flight mass spectrometry. *J. Chromatogr. B* 1060, 84–90. doi: 10.1016/j.jchromb.2017.06.001

Kim, S., Rodgers, R. P., and Marshall, A. G. (2006). Truly "exact" mass: elemental composition can be determined uniquely from molecular mass measurement at ∼0.1 mDa accuracy for molecules up to ∼500 Da. *Int. J. Mass Spectrom*. 251, 260–265. doi: 10.1016/j.ijms.2006.02.001

Kind, T., and Fiehn, O. (2006). Metabolomic database annotations via query of elemental compositions: mass accuracy is insufficient even at less than 1 ppm. *BMC Bioinformatics* 7:234. doi: 10.1186/1471-2105-7-234

Lobinski, R. (1997). Elemental speciation and coupled techniques. *Appl. Spectroscopy* 51, 260A−278A. doi: 10.1366/000370297 1941340

Lobinski, R., Becker, J. S., Haraguchi, H., and Sarkar, B. (2010). Metallomics: guidelines for terminology and critical evaluation of analytical chemistry approaches (IUPAC technical report). *Pure Appl. Chem*. 82, 493–504. doi: 10.1351/PAC-REP-09-03-04

Mapelli, V., Hillestrøm, P. R., Patil, K., Larsen, E. H., and Olsson, L. (2012). The interplay between sulphur and selenium metabolism influences the intracellular redox balance in saccharomyces cerevisiae. *FEMS Yeast Res*. 12, 20–32. doi: 10.1111/j.1567-1364.2011.00757.x

Marshall, A. G., and Hendrickson, C. L. (2008). High-resolution mass spectrometers. *Ann. Rev. Analy. Chem.* 1, 579–599. doi: 10.1146/annurev.anchem.1.031207.112945

McSheehy, S., Szpunar, J., Haldys, V., and Tortajada, J. (2002). Identification of selenocompounds in yeast by electrospray quadrupole-time of flight mass spectrometry. *J. Anal. At. Spectrom.* 17, 507–514. doi: 10.1039/B201015C

Ouerdane, L., Aureli, F., Flis, P., Bierla, K., Preud'homme, H., Cubadda, F., et al. (2013). Comprehensive speciation of low-molecular weight selenium metabolites in mustard seeds using HPLC-electrospray linear trap/orbitrap tandem mass spectrometry. *Metallomics* 5, 1294–1304. doi: 10.1039/c3mt00113j

Palacio Lozano, D. C., Thomas, M. J., Jones, H. E., and Barrow, M. P. (2020). Petroleomics: tools, challenges, and developments. *Ann. Rev. Analy. Chem*. 13, 405–430. doi: 10.1146/annurev-anchem-091619-091824

Preud'homme, H., Far, J., Gil-Casal, S., and Lobinski, R. (2012). Large-scale identification of selenium metabolites by online size-exclusion-reversed phase liquid chromatography with combined inductively coupled plasma (ICP-MS) and electrospray ionization linear trap-orbitrap mass spectrometry (ESI-MSn). *Metallomics* 4:422. doi: 10.1039/c2mt00172a

Rao, Y., McCooeye, M., Windust, A., Bramanti, E., D'Ulivo, A., and Mester, Z. (2010). Mapping of selenium metabolic pathway in yeast by liquid chromatography–orbitrap mass spectrometry. *Anal. Chem*. 82, 8121–8130. doi: 10.1021/ac1011798

Rayman, M. P. (2012). Selenium and human health. *Lancet*. 379, 1256–1268. doi: 10.1016/S0140-6736(11)61452-9

Schmidt, E. M., Pudenzi, M. A., Santos, J. M., Angolini, C. F. F., Pereira, R. C. L., Rocha, Y. S., et al. (2018). Petroleomics: via orbitrap mass spectrometry with resolving power above 1=000=000 at m/z 200. *RSC Adv*. 8, 6183–6191. doi: 10.1039/C7RA12509G

Szpunar, J., Lobinski, R., and Prange, A. (2003). Hyphenated techniques for elemental speciation in biological systems. *Appl. Spectroscopy* 57, 102A−112A. doi: 10.1366/000370203321558128

Tsybin, Y. O., Nagornov, K. O., and Kozhinov, A. N. (2019). "Advanced fundamentals in Fourier transform mass spectrometry," in *Fundamentals and Applications of Fourier Transform Mass Spectrometry*, eds B. Kanawati and P. Schmitt-Kopplin (Amsterdam: Elsevier), 113–132.

Ward, P., Chadha, M., Connolly, C., Stalcup, A., and Murphy, R. (2019). A comparative assessment of water-soluble selenium metabolites in commercial selenised yeast supplements by liquid chromatography-electrospray ionisation QTOF-MS. *Int. J. Mass Spectrom*. 439, 42–52. doi: 10.1016/j.ijms.2018.10.040

Conflict of Interest: The authors declare that the research was conducted in the absence of any commercial or financial relationships that could be construed as a potential conflict of interest.

frontiers in Chemistry

ORIGINAL RESEARCH
published: 11 December 2020
doi: 10.3389/fchem.2020.614171

Application of Chemometrics Tools to the Study of the Fe(III)–Tannic Acid Interaction

Silvia Berto and Eugenio Alladio**

Department of Chemistry, University of Turin, Turin, Italy

Chemometric techniques were applied to the study of the interaction of iron(III) and tannic acid (TA). Modeling the interaction of Fe(III)–TA is a challenge, as can be the modeling of the metal complexation upon natural macromolecules without a well-defined molecular structure. The chemical formula for commercial TA is often given as $C_{76}H_{52}O_{46}$, but in fact, it is a mixture of polygalloyl glucoses or polygalloyl quinic acid esters with the number of galloyl moieties per molecule ranging from 2 up to 12. Therefore, the data treatment cannot be based on just the stoichiometric approach. In this work, the redox behavior and the coordination capability of the TA toward Fe(III) were studied by UV-vis spectrophotometry and fluorescence spectroscopy. Multivariate Curve Resolution-Alternating Least Squares (MCR-ALS) and Parallel Factor Analysis (PARAFAC) were used for the data treatment, respectively. The pH range in which there is the redox stability of the system Fe(III)–TA was evaluated. The binding capability of TA toward Fe(III), the spectral features of coordination compounds, and the concentration profiles of the species in solution as a function of pH were defined. Moreover, the stability of the interaction between TA and Fe(III) was interpreted through the chemical models usually employed to depict the interaction of metal cations with humic substances and quantified using the concentration profiles estimated by MCR-ALS.

Keywords: tannic acid, iron(III), chemometric techniques, spectrophotometry, fluorescence, coordination compounds

OPEN ACCESS

Edited by:
Ottavia Giuffrè, University of Messina, Italy

Reviewed by:
Sara García Ballestreros, Universitat Politècnica de València, Spain
Sofia Gama, University of Białystok, Poland

****Correspondence:***
Silvia Berto
silvia.berto@unito.it
Eugenio Alladio
eugenio.alladio@unito.it

Specialty section:
This article was submitted to Analytical Chemistry, a section of the journal Frontiers in Chemistry

Received: *05 October 2020*
Accepted: *16 November 2020*
Published: *11 December 2020*

Citation:
Berto S and Alladio E (2020) Application of Chemometrics Tools to the Study of the Fe(III)–Tannic Acid Interaction. Front. Chem. 8:614171. doi: 10.3389/fchem.2020.614171

INTRODUCTION

Tannic acid (TA) is a naturally derived polyphenolic compound. It belongs to the class of hydrolyzable tannins (Barbehenn and Peter Constabel, 2011; Rhodes, 2020) that are natural polymers derived from the vegetable kingdom. TA possesses diverse bonding abilities. It is able to complex or cross-link macromolecules through multiple interactions, such as hydrogen and ionic bonding and hydrophobic interactions (Heijmen et al., 1997; Shutava et al., 2005; Erel-Unal and Sukhishvili, 2008). It can also coordinate metal ions through the oxygenated functions and the coordination capability was exploited to form TA–metal networks (Ejima et al., 2013; Guo et al., 2014). The molecule of TA is based on a α/β-D-glucopyranose skeleton whose hydroxyl groups are partially esterified by gallic acid (GA, 3,4,5-trihydroxybenzoic acid). The GA molecules form chains composed of two or more units linked together by ester bonds. The chemical formula for commercial TA is often given as $C_{76}H_{52}O_{46}$, which corresponds to decagalloyl glucose, with a 1,701.20 g mol^{-1} molecular weight, but in fact, it is a mixture of polygalloyl glucoses or polygalloyl quinic acid esters with the number of galloyl moieties per molecule ranging from 2 up to 12

depending on the plant source used to extract the TA (Arapitsas et al., 2007). Despite this, TA is used successfully in many application fields without further purification or separation of the single components (Albu et al., 2009; Gülçin et al., 2010; Ejima et al., 2013), suggesting that the main chemical properties of the commercial products are quite similar.

The TA shows affinity toward iron cations since its numerous oxygenated functions. A work of J.D. Hem, published in the 1960, titled "Complexes of ferrous iron with tannic acid" (States and Printing, 1960) attests that this capability is known for a long time. Notwithstanding, the interpretation of the interaction between the Fe(III) and TA in aqueous solution still presents many deficiency. There are ambiguous information about the redox behavior of Fe(III) in the presence of TA as a function of pH. It is known that TA shows reduction capability toward the Fe(III) cation (States and Printing, 1960), as it is common for polyphenolic molecules (Kipton et al., 1982), and its reduction capability is higher in acidic conditions (States and Printing, 1960). Nevertheless, some recent works dealing about the complexation of iron cations by TA reported the formation of coordination compounds of Fe(III) and TA at very low pH (Sungur and Uzar, 2008; Fu and Chen, 2019).

Modeling the interaction of Fe(III)–TA is a challenge, as can be the modeling of the metal complexation upon natural macromolecules, such as Humic Substances (HS) (Filella and Hummel, 2011). Unlike HS, however, TA shows a restricted variety of binding sites. TA can interact with metal cations through the phenolic groups, which only differ each other for the position in the polymer structure. Moreover, it is possible to assign to TA a molecular weight mean value, which allows calculating a theoretical value of the molar concentration and, therefore, using experimental protocols usually suitable for low-molecular-mass ligands. A previous study was conducted on the protogenic properties of TA (Ghigo et al., 2018) revealing that its protogenic behavior can be explained by a model that supposes the presence of gallic acid and of three different types of phenolic functions. The protonation constants estimated correspond to the dissociation of different types of phenolic groups but cannot be attributed to a protogenic function with a univocal position in the ligand molecule (Ghigo et al., 2018) as well as for low-molecular-mass ligands. The work was carried out combining potentiometry, UV-vis and fluorescence spectroscopy, as well as *ab initio* calculations. The experimental data were treated by both thermodynamic and chemometric approaches, and the Multivariate Curve Resolution-Alternating Least Squares (MCR-ALS) technique turned out to be useful in the interpretation of the spectroscopic data and, in particular, in differentiating the contribution of GA on the fluorescence spectra of TA.

In this work the redox behavior and the coordination capability of the TA toward Fe(III) were studied by UV-vis spectrophotometry and fluorescence spectroscopy. Unfortunately, the use of potentiometry for the study of the Fe(III)–TA system is not allowed because of the low solubility of the coordination compounds formed. The concentration permitted are in the order of 10^{-5} mol L^{-1}, values not proper for the potentiometric technique sensitivity.

Since TA is actually a mixture of different polymeric structures, the most conventional hard-modeling methods, based on molar concentration and mass/charge balance equations, may not be the best way to define the type and the strength of the interaction between TA and Fe(III); therefore, chemometric ways (soft-modeling methods) were tested. Since MCR-ALS technique turned out useful for the interpretation of TA protonation (Ghigo et al., 2018), it was used also here for the spectroscopic data treatment, together with Parallel Factor Analysis (PARAFAC). MCR-ALS and PARAFAC are probably the most used multivariate analysis methods to study chemical solution equilibria (de Juan and Tauler, 2003; Jaumot et al., 2011; Ruckebusch and Blanchet, 2013). These methods obtain to recover information without any assumption about the stoichiometry of the species involved or law that governs the chemical reaction. The aim of the work was to evaluate (*i*) the pH range in which there is the redox stability of the system Fe(III)–TA, (*ii*) the binding capability of TA toward Fe(III), (*iii*) the spectral features on coordination compounds, and (*iv*) the concentration profiles of the species in solution as a function of pH. The stability of the interaction between phenolic moieties of the TA and Fe(III) was interpreted through the chemical models usually employed to depict the interaction of metal cations with humic substances.

MATERIALS AND METHODS

Chemicals

TA (puriss.), 1-10-phenanthroline (≥99%), iron(III) nitrate nonahydrate (ACS reagent, ≥98%), potassium nitrate (≥99.0%), nitric acid (65%), and sulfuric acid (95–97%) were from Sigma-Aldrich (St. Louis, Missouri, USA). A stock solution of $Fe(NO_3)_3$ 1×10^{-3} mol L^{-1} was prepared dissolving iron(III) nitrate nonahydrate in HNO_3 0.01 mol L^{-1} in order to avoid the precipitation of metal hydrolytic species. A stock solution of TA 1×10^{-3} mol L^{-1} was prepared daily in ultrapure water, to avoid the degradation of the organic compound. Potassium hydroxide and hydrochloric acid solutions used as titrant, or for adjusting pH, were prepared by diluting Merck (Darmstadt, Germany) concentrated products. The concentration of the potassium hydroxide solution was assessed by standardization against potassium hydrogen phthalate (Sigma-Aldrich). The purity and the title of the used acids were evaluated by pH-metric titrations. Ultrapure water (Milli-Q, Millipore) was used to prepare all the solutions.

Apparatuses

A Metrohm (Herisau, Switzerland) potentiometer (model 713, resolution of ± 0.1 mV) was used for pH measurements. It was coupled with Metrohm 765 Dosimat burettes (minimum deliverable volume of ± 0.001 cm^3) and equipped with Metrohm combined glass electrodes (mod. 6.0259.100). The temperature control (25.0 ± 0.1°C) was achieved by means of water circulation, in the outer chamber of the titration cell, from a thermocryostat (mod. D1-G Haake, Victoria, Australia).

The absorption spectra were recorded with a Jasco (Cremella, LC, Italy) double-beam spectrophotometer UV-vis, model V-550, equipped with Hellma (Jena, Germany) quartz cuvettes (1.000 cm optical path length). In order to record the spectra as a function of pH, the solutions under alkalimetric titration were transferred to and from the optical cell by a peristaltic pump (model SP311, VELP Scientifica, Usmate, MB, Italy).

A Varian (Segrate MI, Italy) Cary Eclipse fluorescence spectrofluorometer was used to record the fluorescence excitation–emission matrix (EEM) spectra with Hellma cuvettes (1.000 × 1.000 cm optical path lengths).

Procedures

The electrode couple was daily calibrated in terms of H^+ concentration by titrating a 5×10^{-3} mol L^{-1} HCl solution at the working ionic strength (0.001 mol L^{-1}, KNO_3) with standard KOH. In this way, we can assess the slope and the formal potential E^0 of the Nernst equation in conditions like those of the sample solutions under study. In order to avoid O_2 and CO_2 contamination during the titration, a stream of purified N_2 was bubbled in the titration cell.

The spectrophotometric titrations were carried out on 50 ml of solutions of Fe(III)–TA, with cation concentrations included between 2.0×10^{-5} and 8.0×10^{-5} mol L^{-1} and metal-to-ligand ratios comprised between 1:1 and 3:1. The titrant was 0.1 mol L^{-1} KOH standard solutions. The TA concentration was calculated based on the formal molecular weight. The ionic strength was 0.001 mol L^{-1}, and it was obtained considering the different ionic components of the solution and the eventual addition of potassium nitrate to reach the exact value. The addition of higher amount of salt would have been preferable in order to maintain the ionic strength at a fixed value during the titration process, but it was not possible because it leads to the formation of a solid purple compound, probably for salting out effect. The titrations were conducted from pH ∼3.5 to pH 8.5 because, as explained below, this is the pH range in which it is possible to exclude the presence of redox equilibria. The spectra were recorded in the wavelength range 400–900 nm and a baseline was taken in air before each absorbance measurement. Each absorbance spectrum was taken against the reference cuvette filled with Milli-Q water. UV-vis spectra were also recorded on solutions with different metal-to-ligand ratios, at fixed pH, in order to estimate the metal binding capacity of TA.

The fluorescence EEMs were taken with excitation wavelengths in the range of 200–500 nm, at 10 nm intervals, and emission wavelengths from 250 to 600 nm. A 10 nm bandpass was adopted on both excitation and emission. Solutions with Fe(III) 5.0×10^{-6} mol L^{-1} and TA 5.0×10^{-6} mol L^{-1}, at pH 4.0, 4.2, 4.4, 5.2, 5.7, 5.9, 6.2, 6.7, 7.1, and 8.1, or with only TA 5.0×10^{-6} mol L^{-1}, at pH 4.0, 5.0, 6.0, 7.0, and 8.0, were analyzed. The pH of the solutions was adjusted with KOH. The Raman signal of water was taken as a reference for signal stability within different measurements.

Data Handling

Calibration Data Analysis

The electrode calibration data were elaborated by the ESAB2M program (De Stefano et al., 1987) in order to refine the electrode parameters: formal potential E^0, Nernstian slope, and analytical concentration of reagents.

Multivariate Curve Resolution–Alternating Least Squares Regression (MCR-ALS)

The UV-vis spectra were evaluated by Multivariate Curve Resolution–Alternating Least Squares regression (MCR-ALS) chemometric approach, whose goal is to decompose the collected data into their pure chemical components, by providing their spectra and their concentration profiles (Tauler, 1995; de Juan et al., 2000; Jaumot et al., 2005, 2015; Ruckebusch and Blanchet, 2013). The MCR-ALS approach has been deeply used in several applications such as, for instance, voltammetry (Serrano et al., 2020), UV-vis (Veselinović et al., 2012; Ghigo et al., 2018), IR (Shariati-Rad and Hasani, 2009), Raman (Andrew and Hancewicz, 1998; Lyndgaard et al., 2013), hyperspectral imaging (Piqueras et al., 2011; Laborde et al., 2021), NMR (Huo et al., 2004), EPR (Abou Fadel et al., 2014; Berto et al., 2019), GC-MS (Lebanov et al., 2020), UHPLC (Wehrens, 2011), etc. It is particularly helpful in case of measurements following Lambert-Beer's law, i.e., in case the collected overall spectra consist in a linear combination of the spectra of their pure components. Briefly, MCR-ALS deconvolution is made as follows (Equation 1):

$$X = CS^T + E \tag{1}$$

where X represent the collected data matrix, C is the matrix of the pure concentration profiles, S^T is the transposed matrix of the pure spectra, and E is the residuals (error) matrix. Therefore, each x collected spectrum constituting the X matrix can be written, as follows (Equation 2):

$$x = c_1 s_1^T + \ldots + c_n s_n^T \tag{2}$$

where $c_1, \cdots, c_n$ represent the concentrations of the n pure components/chemical species for the evaluated x mixture, while $s_1, \cdots, s_n$ stand for the spectra of the n pure components. Consequently, this approach can be easily extended to all the collected spectra of the samples included into the X matrix. The first step of MCR-ALS decomposition is represented by the initial estimation of the set of pure concentrations C or the pure spectra S. This initial estimation can be performed by means of several algorithms such as, for instance, Evolving Factor Analysis (EFA) (Maeder, 1987), Evolving Windowed Factor Analysis (EWFA) (Keller and Massart, 1991), Orthogonal Projection Approach (OPA) (Sánchez et al., 1994), and SIMPLISMA (Windig et al., 2012). It has to be noted that it is useful to spend some time in obtaining satisfactory initial estimates since, if they show a good quality in terms of results, ALS algorithm (that consists in a repeated application of multiple least squares regression) will need a quite small number of iterations before reaching a convergence. In fact, once an initial estimate of, for instance, S has been obtained, the initial C matrix is calculated by

ALS by minimizing the residuals *E*. The described process is performed several times until an optimal convergence value is obtained. Furthermore, several constraints can be adopted in the MCR-ALS calculation in accordance with the chemical and physical properties of the samples and the data under investigation (Wehrens, 2011). They are functions that can be applied separately to the estimates of the spectra or the concentration profiles on every step of the algorithm, aiming to minimize the overall error. In the case of UV-vis spectra, for instance, a non-negativity constraint can be applied to both the pure concentration profiles (i.e., no negative concentrations) and the pure spectra (no negative signals). Further constraints can be implemented such as, for instance, (*i*) a closure constraint, which is usually adopted for the contribution profiles and aims at conserving the mass balance (i.e., the overall sum of the concentrations of the chemical compounds in the mixture is constant); (*ii*) a unimodality constraint, which is employed to let the reconstituted signals having only one maximum; (*iii*) a normalization constraint, whose goal is to normalize the pure spectra or the concentration profiles of the *n* components to a specific reference value; (*iv*) an angle constraint, which can be set in order to enhance the contrast among the obtained solutions (Windig et al., 2012).

Parallel Factor Analysis (PARAFAC)

The fluorescence EEMs were elaborated by Parallel Factor Analysis (PARAFAC, also known as canonical decomposition, CANDECOMP) chemometric approach (Carroll and Chang, 1970; Smilde, 1992; Bro, 1997). PARAFAC is undoubtedly one of the most frequently used approach for deconvolving EEM (Leurgans and Ross, 1992; Murphy et al., 2013). PARAFAC's main goal is the identification of the independent species (named components) that are present into the collected data (in this case, EEM). This is achieved by performing a decomposition of the trilinear multi-way data arrays, but the PARAFAC approach can be adopted also with higher-order arrays [since it belongs to the group of multivariate modeling known as multi-way methods (Murphy et al., 2013)]. The PARAFAC approach is particularly helpful when evaluating EEM data since the independent components that are obtained during the decomposition can be chemically interpreted. In fact, EEM data follow Lambert–Beer's law since the measured fluorescence shows a quite linear correlation with the concentrations of the *N* chemical compounds constituting the analyzed samples. Consequently, EEM data can be considered as trilinear since emission and excitation spectra are independent of one another, and the recorded fluorescence can be seen as a sum of the signals of the different *N* components.

The overall PARAFAC trilinear decomposition is, as follows (Equation 3):

$$x_{ijk} = \sum_{n=1}^{N} a_{in} b_{jn} c_{kn} + e_{ijk} \quad (3)$$

where *a*, *b*, and *c* represent the three terms that are provided by the decomposition, while e_{ijk} represents the residual array (i.e., the difference between the original three-way dataset and the one that has been obtained after the PARAFAC decomposition). *i*, *j*, and *k* stand for the three modes of a three-way dataset so that, for EEM data, the element x_{ijk} represents the i^{th} sample (mode 1) for the j^{th} emission variable (mode 2) and the k^{th} excitation variable (mode 3). Finally, *n* is the number of independent species/components that can extracted from the original data during the deconvolution process. Therefore, each *n* component has its own *i*, *j*, and *k* values for each sample, emission wavelength, and excitation wavelength. The analyst must define the proper number of *n* components composing the EEM data by evaluating when they significantly deviate from Lambert–Beer's law (Bro, 1997; Murphy et al., 2013).

RESULTS

Redox Behavior

The instability of TA in alkaline conditions was previously tested (Ghigo et al., 2018). The UV-vis spectra at alkaline pH showed the instability of TA for pH higher than 8.5.

The TA also shows reducing capability, particularly in acidic conditions, and this could lead to the reduction of Fe(III) to Fe(II) present in solution as reported by Kipton et al. (1982) for GA and its homologs. In order to assess this redox behavior and to identify the pH threshold below which the phenomenon can happen, some experiments were carried out. A series of solutions of Fe(III) 2.0×10^{-5} mol L^{-1}, 1,10-phenantroline 6.5×10^{-5} mol L^{-1}, and TA 4.0×10^{-5} mol L^{-1} were prepared. The pH was controlled adding H_2SO_4 1.0 mol L^{-1} or KOH 1.0 mol L^{-1}, in order to prepare solutions with pH comprised between 1.8 and 8.5. The UV-vis spectra of the solutions were recorded after 2 h from the preparation, the time needed for a stable color development. For the solutions in which the Fe(III) was reduced to Fe(II), the red color appeared because of the formation of the complex Fe(II)-1,10-phenantroline that shows an absorption maximum at about 510 nm. The spectra collected highlighted that the reduction of Fe(III) to Fe(II) induced by TA starts for pH lower than 3.5. It is possible to observe in **Figure 1** that for pH 3.57, the signal typical of the complex Fe(II)-1,10-phenantroline is absent, whereas for pH 3.15, it is clearly detectable, although the solutions are kept in the presence of oxygen. For this reason, the investigation of the coordination capability of TA toward Fe(III) was conducted in the pH range 3.5–8.5. This result agrees with the statements reported by Kipton et al. (1982).

UV-Vis Spectra

Absorption spectra of Fe(III)–TA systems were recorded on solutions with different metal-to-ligand ratios. The spectra recorded on a solution with metal-to-ligand ratios 1:1 as a function of pH are shown in **Figure 2**. It is possible to note that the intensity of the absorption band with the maximum at 570 nm increases as the pH of the solution rises, until ∼pH 5. After this value, there is a shift of the absorption band toward lower wavelengths and the color of the solution changes from dark purple to wine-red. This behavior is similar for all the Fe(III)–TA ratios studied.

The absorption maxima can be easily compared with those of catechol reported before. Sever and Wilker (Sever and

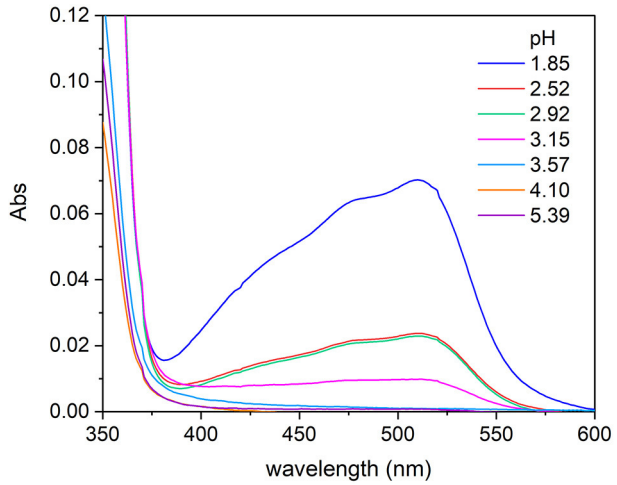

FIGURE 1 | Absorption spectra recorded on solutions of Fe(III)/1,10-phenantroline/TA with concentrations 2.0×10^{-5}, 6.5×10^{-5}, and 4.0×10^{-5} mol L^{-1}, respectively, at different pH, after 2 h from the preparation.

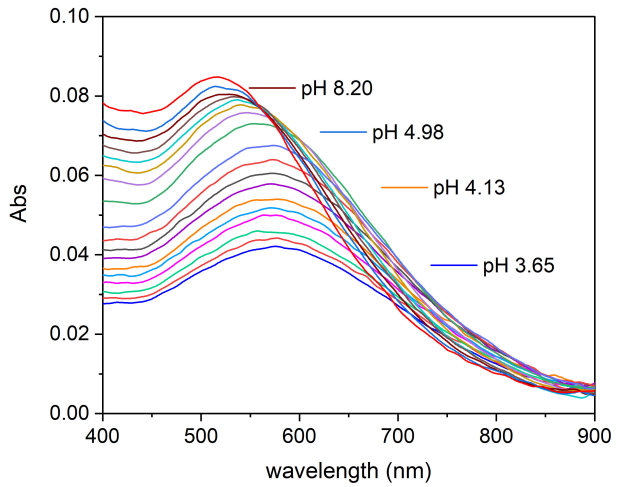

FIGURE 2 | Absorption spectra recorded on a solution of Fe(III)/TA with concentration 2.00×10^{-5} and 2.01×10^{-5} mol L^{-1}, respectively, at different pH values.

Wilker, 2004) reported the wavelength maxima (λ_{max}) for mono-, bis-, and tris-catecholate defined by themselves and by other authors. The Fe(III)–mono-catecholate complex shows two maxima at about 430 and 700 nm, but the bands are not well-defined, whereas the Fe(III)–bis-catecholate complex shows a better characterized absorption spectrum and, in particular, the scientists agree on the presence of a band at about 570 nm with an extinction coefficient ranged between 3,000 and 3,500 mol^{-1} L cm^{-1}. Sever and Wilker (Sever and Wilker, 2004) observed that the deep blue–violet bis-catecholate was followed by a transformation to a wine-red colored species (isosbestic point at 547 nm), increasing the pH, and they supposed the formation of a tris-catecholate species. The Fe(III)–tris-catecholate complex has a band comprised between 470 and 490 nm with an extinction coefficient ranging between 3,700 and 4,320 mol^{-1} L cm^{-1} (Avdeef et al., 1978; Kipton et al., 1982; Sever and Wilker, 2004). This description is in accordance with what happens in the Fe(III)–TA system under study (**Figure 2**). The spectra of the species formed between pH 3.5 and 5 is coherent with a bis-catecholate coordination type. While the shift of the absorption maximum toward lower wavelengths with the pH increase is coherent with the Fe(III)–tris-catecholate spectral features, but it is not possible to exclude the deprotonation of a coordinated water molecule.

Binding Capacity

Since the polymeric structure, TA can coordinate more than one Fe(III) cation. In order to evaluate the maximum number of iron cations that can be coordinated by a mole of TA, Job's plot method was used. Based on the spectral behavior, in the pH range comprised between 3.5 and 4.5, there is probably only a complex species; therefore, Job's method can be applied. Nine solutions of Fe(III) and TA with a total nominal concentration of 2.00×10^{-5} mol L^{-1}, but with different molar fraction of the two components, were prepared, and the pH was adjusted at 4.0 with KOH. The absorption spectra of the solutions were recorded and the absorbance at 570 nm was plotted toward the molar fraction of Fe(III). The plot is reported in **Figure 3A**. The maximum of Job's plot is positioned at a molar fraction of 0.8, suggesting that TA can coordinate at most four Fe(III) cations. This result agrees with the observation that the Fe(III)–TA solutions with increasing metal-to-ligand ratio, from 1:1 to 5:1, at similar pH (pH ~4.0), showed absorbances that rise linearly with the metal-to-ligand ratio until a ratio of 4:1 (see **Figure 3B**). Therefore, the number of chromophores increases linearly with the concentration of Fe(III) until there are available binding sites. For molar ratios higher than 5, the precipitation occurs.

The data collected for Job's plot can be represented as absorbances *vs* mol Fe(III) per gram of TA in solution. As it is possibly observed in **Figure 3C**, the maximum absorbance value was reached for a ratio of 2.35×10^{-3} mol of Fe(III) per gram of TA. This notation allows the avoidance of the calculation of a molar concentration of TA, which may be considered as a forcing if we are working with a natural polymer such as TA.

Fluorescence Spectra

Fluorescence EEMs were taken on solutions containing TA and TA with Fe(III) at different pH. **Figure 4** shows some fluorescence EEMs recorded on the two different systems. The fluorescence signals are quite different. The contour plots highlight that the emission peak of TA, located at excitation/emission wavelengths (Ex/Em) of 210/360 (i.e., peak A), is no longer visible in the presence of Fe(III). The solution containing the cation shows a defined emission peak at 260/358 nm (i.e., peak B), corresponding to the second emission peak of TA (Ghigo et al., 2018). The peak of TA at 325/395 nm (i.e., peak C), which is characteristic of pH higher than 8, is visible in both conditions, with and without the metal cation. A quenching effect of Fe(III) was previously detected on fluorescence signals of dissolved organic matter (DOM) (Poulin

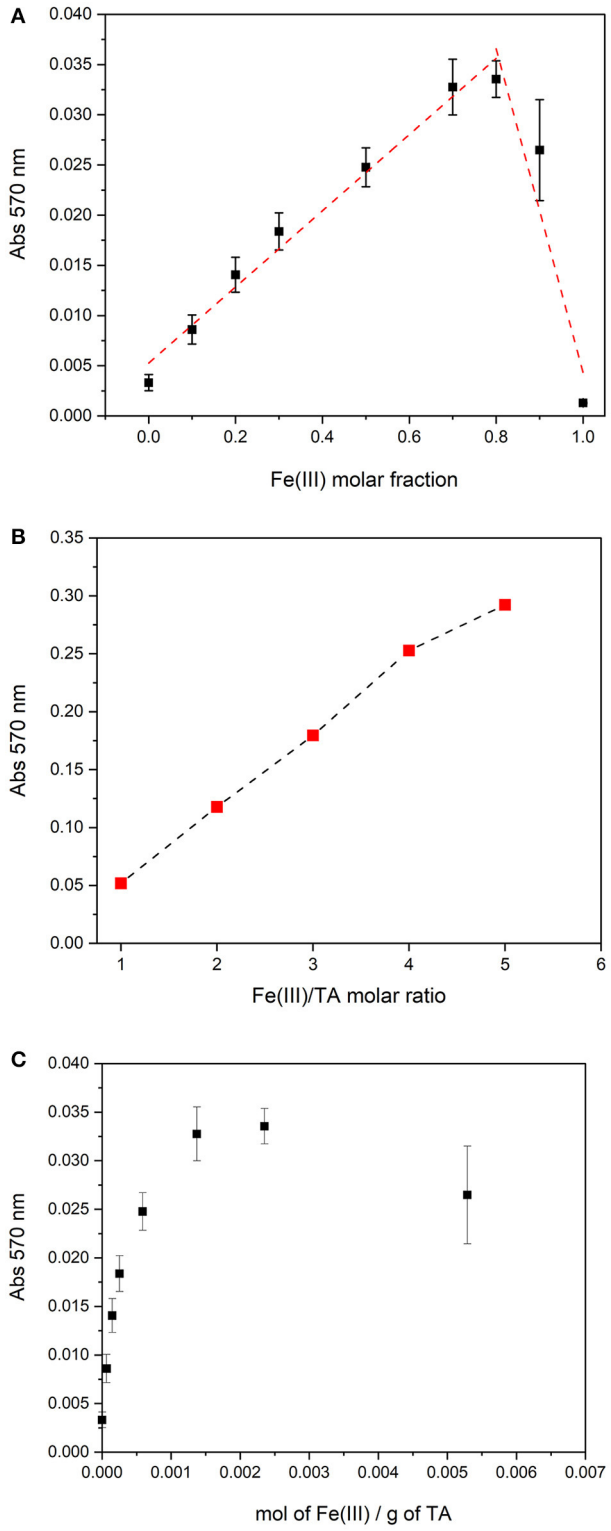

FIGURE 3 | (A) Job's plot for solutions with a total concentration of 2.00 × 10^{-5} mol L^{-1} and pH = 4.0. **(B)** Absorbance at 570 nm of Fe(III)/TA solutions at pH ~4 with different molar ratios (TA concentration 2.00 × 10^{-5} mol L^{-1}). **(C)** Absorbance at 570 nm of Fe(III)/TA solutions at pH = 4.0 as a function of the total mol of Fe(III) per total mass of TA.

et al., 2014) and of soluble bio-organic substances (SBO) isolated from the organic fraction of solid urban wastes (Ballesteros et al., 2017). These results are (quite) confirmed by PARAFAC modeling. PARAFAC was performed by means of in-house code involving R software (version 4.0.2) (R Core Team, 2020) and the R packages *staRdom* (Pucher et al., 2019) and *eemR* (Massicotte, 2019). Two distinct PARAFAC models have been built, firstly on the EEM data involving the solutions containing only TA and then on those containing TA with Fe(III) (experimental details are reported in *Procedures* paragraph). EEM data were pre-processed. Different data pre-processing approaches were tested, before and after calculating the PARAFAC models, such as the removal of Raman and Rayleigh scattering and the Inner-Filter Effects (IFE—traditionally occurring when the chromophores absorb the excitation light). Only the removal of Raman and Rayleigh scattering provided good and interpretable results; therefore, only these results were reported. The removed scatter areas have also been interpolated [by means of splines (Lee et al., 1997)] to fasten the calculation. Both the PARAFAC models were built by calculating 50 starting models in order to achieve the global minimum, 5,000 maximum number of iteration steps, and a convergence value (tolerance) of 10^{-6}. Non-negativity constraints were selected for all the modes, and both B and C modes were rescaled to a maximum fluorescence of 1 for all the evaluated components. Core consistency, R^2, and number of iterations and residuals were evaluated as diagnostic parameters to define the proper number of components. The noisiness of the modeled components was considered, too (Bro, 1997; Murphy et al., 2013). Split-half analysis could not be performed since the number of evaluated samples was relatively low. The first PARAFAC model evaluating the solutions containing only TA provided a 2-component model (reported in **Figure 5**) showing an overall R^2 of 0.921. The first component showed the excitation/emission peaks of TA, located at wavelengths of 210/360 nm. A shoulder peak is observed for the excitation spectrum around 260 nm, too. On the other hand, the second component showed the excitation/emission peaks that are characteristic of pH higher than 8, around 325/405 nm (actually, the original spectra of TA above pH = 8 showed an emission peak at 395 nm). Consequently, the PARAFAC model supported the results observed by evaluating the EEM data by indicating the existence of two different components with peculiar emission and excitation peaks.

The second PARAFAC model calculated on the solutions containing TA with Fe(III) provided a 1-component model (reported in **Figure 6**) showing an overall R^2 of 0.833. In the present case, the solution containing the cation provided a component with an emission/excitation peak at 260/370 nm, roughly corresponding to the emission peak B of TA. In the present case, the peak C of TA at 325/395 nm, which is characteristic of pH higher than 8, is not noticed.

MCR-ALS Results

MCR-ALS was performed once again by means of in-house code involving R software (version 4.0.2) (R Core Team, 2020) and the R package *mdatools* (Kucheryavskiy, 2020).

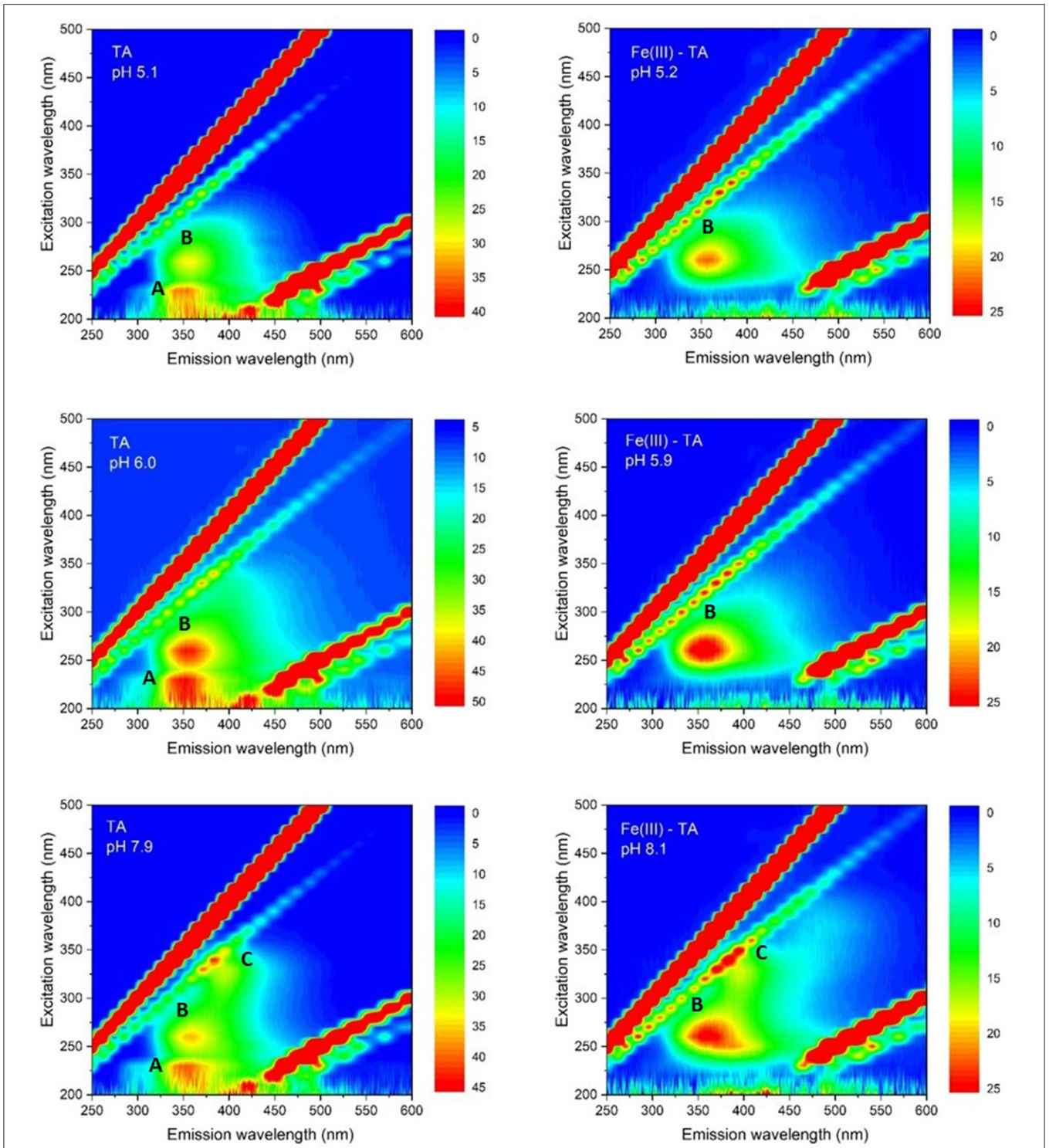

FIGURE 4 | Contour plots of fluorescence EEMs recorded as a function of pH on water solutions of TA 5.0 × 10^{-6} mol L^{-1}; Fe(III)/TA 5.0 × 10^{-6} /5.0 × 10^{-6} mol L^{-1}, respectively.

The UV-vis spectra obtained on solutions with metal/ligand molar ratio 1:1 were analyzed by MCR-ALS technique. SIMPLISMA algorithm was employed to calculate the initial estimates, non-negativity constraints were selected for both the concentration profiles and the spectra, while a closure constraint was adopted for the concentration profiles by setting

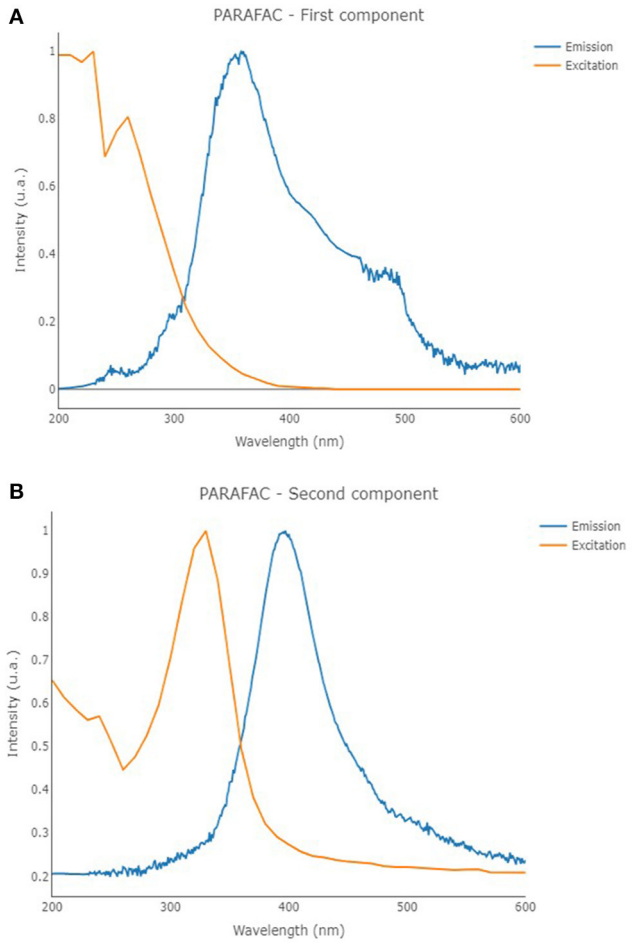

FIGURE 5 | Excitation (orange line) and emission (blue line) profiles of the first **(A)** and second **(B)** components of the PARAFAC model that was built on the solutions containing only TA.

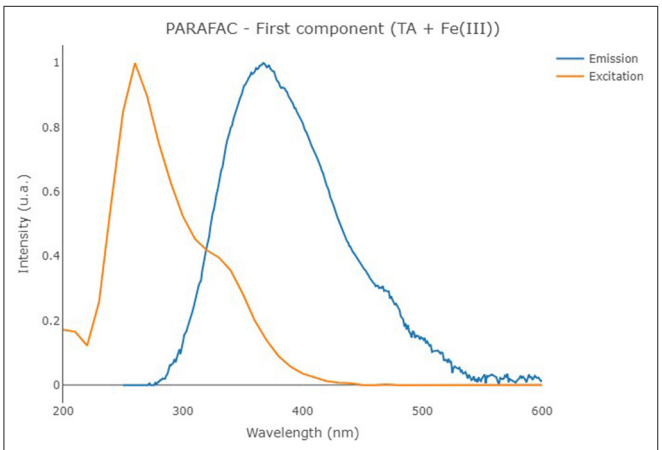

FIGURE 6 | Excitation (orange line) and emission (blue line) profiles of the first component of the PARAFAC model that was built on the solutions containing TA with Fe(III).

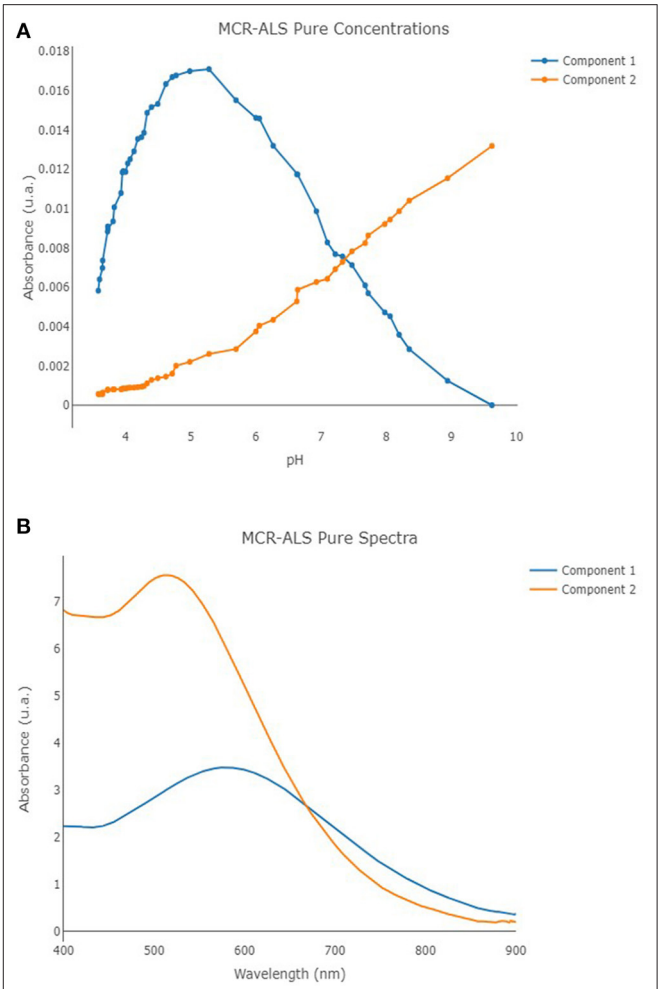

FIGURE 7 | Component 1 (blue line) and component 2 (orange line) pure concentrations **(A)** and pure spectra **(B)** profiles for the developed MCR-ALS model.

an overall concentration equal to 2.00×10^{-5} mol L^{-1}. A total of 150 maximum number of iteration steps and a convergence value (tolerance) of 10^{-6} were defined, too. Two independent components were observed as the optimal number of components for the MCR-ALS model, involving an overall cumulative explained variance of 93.02% (consisting of 65.28% of explained variance for the first component, and 27.74% of explained variance for the second component), showing an R^2 equal to 0.926. The profiles of the calculated pure spectra and pure concentrations are reported in **Figures 7A,B**. The molar extinction coefficients of the two species (hereinafter, component 1 = MTA1, component 2 = MTA2) were also estimated: $\epsilon_{max}^{MTA1} = 3487\ mol^{-1}\ L\ cm^{-1}$ ($\lambda_{max} = 580$ nm); $\epsilon_{max}^{MTA2} = 7576\ mol^{-1}\ L\ cm^{-1}$ ($\lambda_{max} = 513$ nm). The molar extinction coefficients of the species MTA1 is in good agreement with the values usually proposed for the bis-catecholate complexes (Sever and Wilker, 2004).

Chemical Model

The impossibility to define a real molar concentration of TA hinders defining thermodynamic parameters to quantitatively describe the chemical system because these parameters are based on the ratio of the molar concentration of the species in solution. Since this condition is an analogous with HS, the "single-site model" proposed by Hummel for HS (Hummel, 1997) was borrowed in this work to formalize the Fe(III)–TA interaction. Based on this model, a conditional formation constant that quantitatively expresses the strengthening of the interaction between the TA and the metal cation can be expressed as (Equation 4):

$$ {}^{c}K = \frac{[MTA]}{[M]\ (TA)_{total}} \tag{4} $$

where $[MTA]$ is the molar concentration of the metal bound to TA, $[M]$ is the molar concentration of the free metal cation, and $(TA)_{total}$ is the concentration of total TA in solution expressed as mass per unit of volume (g L^{-1}). The ${}^{c}K$ is a conditional value that depends on both pH and solution component concentration. The simplest model proposed by Hummel is based on six assumptions (Hummel, 1997): (1) The metal ion M forms only 1:1 complexes with ligand sites L of the macro-molecule. The macro-molecule has several functional groups S. The number of S is not specified in the model but is assumed to be fixed within the pH and metal concentration range where the model is applied. (2) For each metal ion M under study, only one kind of ligand site L predominates within the parameter range where the model is used. (3) The complexing strength of the ligand sites L is constant and does not vary with the location within the macro-molecule; i.e., the influence of different substituents and varying stereochemistry on L is ignored. (4) Chemical changes of the macro-molecules have no influence on the number of active ligand sites available for metal complexation. (5) The functional groups involved in metal binding do not undergo any proton exchange reactions in the pH range of interest. (6) There are no interactions between functional groups S of the macro-molecule, i.e., electrostatic effects that change the binding characteristics of S are ignored.

Based on the model, the concentration of the macro-molecules is in relation with the concentration of the ligand sites through the Site Complexation Capacity (SCC – mol g^{-1}),

$$ (TA)_{total} \cdot SCC = [L]_{total} \tag{5} $$

The SCC can be defined also as the maximum number of moles of metal cation bound per unit of mass of macro-molecule at metal saturation. For the case under study, the SCC can be defined considering the results obtained by Job's plot method. Each mole of TA can bind four moles of Fe(III); therefore, the SCC results in 2.35×10^{-3} mol of Fe(III) per gram of TA (**Figures 3A,C**) and, for a nominal molar TA concentration of 1.0×10^{-5} mol L^{-1}, the concentration of the ligand sites is $[L]_{total} = 4.0 \times 10^{-5}$ mol L^{-1}. Based on the spectral features and on the value estimated for $[L]_{total}$, it is reasonable interpret that the nature of L should correspond to a bis-catecholate group.

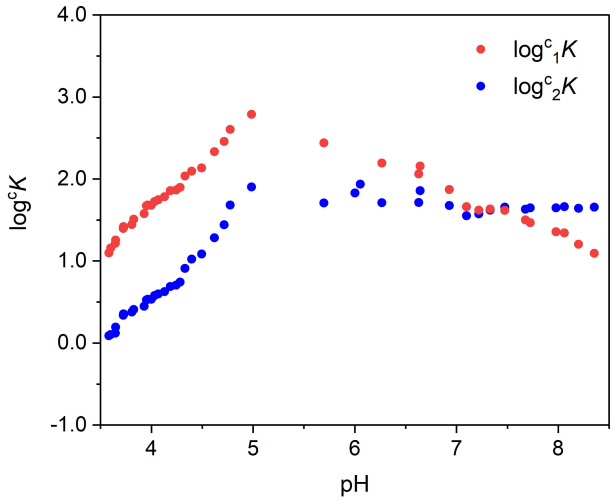

FIGURE 8 | Values of $\log_n^c K$ as a function of pH (some experimental points corresponding to the curve inflection were excluded).

The concentration of the species in solution estimated by MCR-ALS, for each pH value, was hence used to calculate ${}^{c}K$ applying Equation (4). Two conditional formation constants were defined, one for each of the two species detected, and Equations (6) and (7) were used:

$$ {}^{c}_{1}K = \frac{[MTA1]}{[M]\ (TA)_{total}} \tag{6} $$

$$ {}^{c}_{2}K = \frac{[MTA2]}{[M]\ (TA)_{total}} \tag{7} $$

where [MTA1] and [MTA2] are the concentrations of the two complex species, defined by MCR-ALS, and [M] is the concentration of the non-complexed metal cation. The values of $\log^c K$ obtained were then plotted as a function of pH (**Figure 8**). The $\log^c K$ linearly increases with pH until pH ~5. This behavior is expected because the assumption number 5 of the Hummel's model, which asserts that the functional groups L involved in metal binding do not undergo any proton exchange reactions in the pH range of interest, is not true for TA. In the pH range 3.5–5.0, the coordination of the binding sites involves the proton exchange reaction and at least a fraction of binding sites dissociates for competition of metal cation toward the proton. On the other hand, the pH 5 corresponds to the maximum formation of the first species and to the start point of formation of the second one, and between pH 4.5–6, it is possible to observe an inflection point of the alkalimetric titration.

Rearranging Equations (6) and (7) as reported below (Equation 8), and combining Equation (8) with the mass balance (Equation 9), it is possible to define the concentration of the complex species as a function of the total concentration of the cation ad of the total amount of TA:

$$ {}^{c}_{n}K \times (TA)_{total} = \frac{[MTAn]}{[M]} = {}^{c'}_{n}K \tag{8} $$

$$(M)_{total} = [M] + [MTA1] + [MTA2] \quad (9)$$

$$[MTAn] = \left(\frac{{}^{c'}_{n}K}{{}^{c'}_{1}K + {}^{c'}_{2}K + 1} \right) (M)_{total} \quad (10)$$

With the absorbance being proportional to the concentration of the chromophore and having additive property, it is possible to write Equation (10) as follows:

$$Abs^{\lambda} = \left(\varepsilon^{\lambda}_{MTA1} \left(\frac{{}^{c'}_{1}K}{{}^{c'}_{1}K + {}^{c'}_{2}K + 1} \right) + \varepsilon^{\lambda}_{MTA2} \left(\frac{{}^{c'}_{2}K}{{}^{c'}_{1}K + {}^{c'}_{2}K + 1} \right) \right) (M)_{total} \quad (11)$$

By the application of Equation (11), it was possible to foresee the absorbance values for solutions containing Fe(III) and TA having a metal-to-ligand ratio 1:1, at a defined pH. Equation (11) was employed to calculate the absorbance at pH 4.0 of the solutions containing increasing amount of metal cation to validate the chemical model proposed. The parameters used for the estimation of $Abs^{570}_{pH=4}$ were: $\varepsilon^{570}_{MTA1} = 3,472$ mol^{-1}L cm^{-1}, $\varepsilon^{570}_{MTA2} = 6,419$ mol^{-1} L cm^{-1}, ${}^{pH\ 4}_{1}K = 52.9\ L\ g^{-1}$, ${}^{pH\ 4}_{2}K = 3.78\ \ L\ g^{-1}$, $(TA)_{total}$, and $(M)_{total}$.The relative differences between experimental and calculated values ranged between 12 and 5.2%, revealing a quite good prediction capability.

DISCUSSION

The pH range in which the system Fe(III)–TA is not affected by redox reactions and the binding capability of TA toward Fe(III) were defined. The UV-vis spectrophotometry and the chemometric tools used to analyze the spectroscopic data recorded on the metal–ligand system turned out useful to interpret the chemistry of the system and allowed to evaluate the spectral features and the concentration profiles of the species in solution as a function of pH. In particular, the application of the MCR-ALS technique allowed obtaining quantitative information. The impossibility to define a molar concentration of the ligand prevents the use of hard-modeling methods for the analysis of the dataset; moreover, the necessity to work with a very restricted concentration scale limits the range and the techniques of investigation. These conditions strongly affect the possibility to define a speciation model and to achieve thermodynamic parameters that explain the chemistry of the system, but the approach here used enabled us to quantitatively interpret the behavior of Fe(III) in the presence of TA. The capacity of MCR-ALS to apply constraints contributed to define the chemical meaning of the mathematical solutions. Then, the MCR-ALS results were used to formalize the parameters that control the chemical system having the possibility to overcome the definition of an exact stoichiometry and a molar concentration of the ligand through the application of the chemical modeling proposed for HS.

The combination of the chemometric tools with the formalism used to interpret the metal cation interaction with HS could be a useful way to model those chemical systems in which the ligands are characterized by a not well-defined mass. This work reports a first exploratory application and the methodology needs to be tested further on different chemical systems, but the development of this approach could lead to formulate models with a good predictive capacity as it is already possible to do for the chemical systems that treat low-molecular-mass ligands.

DATA AVAILABILITY STATEMENT

The original contributions presented in the study are included in the article/supplementary material, further inquiries can be directed to the corresponding author/s.

AUTHOR CONTRIBUTIONS

SB devised and designed the study. EA dealt with the application of the chemometric techniques. SB and EA contributed to the data collection, interpretation, both participated in the writing, and editing of the manuscript.

FUNDING

This work was supported by the University of Turin and by the Italian Ministry of Education, Universities and Research.

ACKNOWLEDGMENTS

This contribution is based upon work from COST Action CA18202, NECTAR—Network for Equilibria and Chemical Thermodynamics Advanced Research, supported by COST (European Cooperation in Science and Technology).

REFERENCES

Abou Fadel, M., de Juan, A., Touati, N., Vezin, H., and Duponchel, L. (2014). New chemometric approach MCR-ALS to unmix EPR spectroscopic data from complex mixtures. *J. Magn. Reson.* 248, 27–35. doi: 10.1016/j.jmr.2014.09.013

Albu, M. G., Ghica, M. V., Giurginca, M., Trandafir, V., Popa, L., and Cotrut, C. (2009). Spectral characteristics and antioxidant properties of tannic acid immobilized on collagen drug-delivery systems. *Rev. Chim.* 60, 666–672.

Andrew, J. J., and Hancewicz, T. M. (1998). Rapid analysis of Raman image data using two-way multivariate curve resolution. *Appl. Spectrosc.* 52, 797–807. doi: 10.1366/0003702981944526

Arapitsas, P., Menichetti, S., Vincieri, F. F., and Romani, A. (2007). Hydrolyzable tannins with the hexahydroxydiphenoyl unit and the m-depsidic link: HPLC-DAD-MS identification and model synthesis. *J. Agric. Food Chem.* 55, 48–55. doi: 10.1021/jf0622329

Avdeef, A., Sofen, S. R., Bregante, T. L., and Raymond, K. N. (1978). Coordination chemistry of microbial iron transport compounds. 9.' Stability constants for catechol models of enterobactin. *J. Am. Chem. Soc.* 460, 5362–5370. doi: 10.1021/ja00485a018

Ballesteros, S. G., Costante, M., Vicente, R., Mora, M., Amat, A. M., Arques, A., et al. (2017). Humic-like substances from urban waste as auxiliaries for photo-Fenton treatment: a fluorescence EEM-PARAFAC study. *Photochem. Photobiol. Sci.* 16, 38–45. doi: 10.1039/C6PP00236F

Barbehenn, R. V., and Peter Constabel, C. (2011). Tannins in plant-herbivore interactions. *Phytochemistry* 72, 1551–1565. doi: 10.1016/j.phytochem.2011.01.040

Berto, S., Alladio, E., Daniele, P. G., Laurenti, E., Bono, A., Sgarlata, C., et al. (2019). Oxovanadium(IV) Coordination compounds with Kojic acid derivatives in aqueous solution. *Molecules* 24:3768. doi: 10.3390/molecules24203768

Bro, R. (1997). PARAFAC. tutorial and applications. *Chemometr. Intellig. Lab. Syst.* 38, 149–171. doi: 10.1016/S0169-7439(97)00032-4

Carroll, J. D., and Chang, J. J. (1970). Analysis of individual differences in multidimensional scaling via an n-way generalization of "Eckart-Young" decomposition. *Psychometrika* 35, 283–319. doi: 10.1007/BF02310791

de Juan, A., Maeder, M., Martínez, K., and Tauler, R. (2000). Combining hard- and soft-modelling to solve kinetic problems. *Chemom. Intell. Lab. Syst.* 54, 123–141. doi: 10.1016/S0169-7439(00)00112-X

de Juan, A., and Tauler, R. (2003). Chemometrics applied to unravel multicomponent processes and mixtures: revisiting latest trends in multivariate resolution. *Anal. Chim. Acta* 500, 195–210. doi: 10.1016/S0003-2670(03)00724-4

De Stefano, C., Princi, P., Rigano, C., and Sammartano, S. (1987). Computer analysis of equilibrium data in solution. ESAB2M: an improved version of the ESAB program. *Ann. di Chim.* 77, 643–675.

Ejima, H., Richardson, J. J., Liang, K., Best, J. P., van Koeverden, M. P., Such, G. K., et al. (2013). One-step assembly of coordination complexes for versatile film and particle engineering. *Science* 341, 154–157. doi: 10.1126/science.1237265

Erel-Unal, I., and Sukhishvili, S. A. (2008). Hydrogen-bonded multilayers of a neutral polymer and a polyphenol. *Macromolecules* 41, 3962–3970. doi: 10.1021/ma800186q

Filella, M., and Hummel, W. (2011). Trace element complexation by humic substances: Issues related to quality assurance. *Accredit. Qual. Assur.* 16, 215–223. doi: 10.1007/s00769-010-0716-3

Fu, Z., and Chen, R. (2019). Study of complexes of tannic acid with Fe(III) and Fe(II). *J. Anal. Methods Chem.* 2019:3894571. doi: 10.1155/2019/3894571

Ghigo, G., Berto, S., Minella, M., Vione, D., Alladio, E., Nurchi, V. M., et al. (2018). New insights into the protogenic and spectroscopic properties of commercial tannic acid: the role of gallic acid impurities. *New J. Chem.* 42, 7703–7712. doi: 10.1039/C7NJ04903J

Gülçin, I., Huyut, Z., Elmasta,ş, M., and Aboul-Enein, H. Y. (2010). Radical scavenging and antioxidant activity of tannic acid. *Arab. J. Chem.* 3, 43–53. doi: 10.1016/j.arabjc.2009.12.008

Guo, J., Ping, Y., Ejima, H., Alt, K., Meissner, M., Richardson, J. J., et al. (2014). Engineering multifunctional capsules through the assembly of metal-phenolic networks. *Angew. Chem. Int. Ed.* 53, 5546–5551. doi: 10.1002/anie.201311136

Heijmen, F. H., Du Pont, J. S., Middelkoop, E., Kreisn, R. W., and Hoekstra, M. J. (1997). Cross-linking of dermal sheep collagen with tannic acid. *Biomaterials* 18, 749–754. doi: 10.1016/S0142-9612(96)00202-5

Hummel, W. (1997). *Modelling in Aquatic Chemistry*. ed I. P. I. Grenthe (Paris: OECD Nuclear Energy Agency), 153–206.

Huo, R., Wehrens, R., and Buydens, L. M. C. (2004). Improved DOSY NMR data processing by data enhancement and combination of multivariate curve resolution with non-linear least square fitting. *J Magn Reson.* 169, 257–69. doi: 10.1016/j.jmr.2004.04.019

Jaumot, J., de Juan, A., and Tauler, R. (2015). MCR-ALS GUI 2.0: new features and applications. *Chemom. Intell. Lab. Syst.* 140, 1–12. doi: 10.1016/j.chemolab.2014.10.003

Jaumot, J., Eritja, R., and Gargallo, R. (2011). Chemical equilibria studies using multivariate analysis methods. *Anal. Bioanal. Chem.* 399, 1983–1997. doi: 10.1007/s00216-010-4310-7

Jaumot, J., Gargallo, R., de Juan, A., and Tauler, R. (2005). A graphical user-friendly interface for MCR-ALS: a new tool for multivariate curve resolution in MATLAB. *Chemom. Intell. Lab. Syst.* 76, 101–110. doi: 10.1016/j.chemolab.2004.12.007

Keller, H. R., and Massart, D. L. (1991). Peak purity control in liquid chromatography with photodiode-array detection by a fixed size moving window evolving factor analysis. *Anal. Chim. Acta* 246, 379–390. doi: 10.1016/S0003-2670(00)80976-9

Kipton, H., Powell, J., and Taylor, M. C. (1982). Interactions of iron(II) and iron(III) with gallic acid and its homologues: a potentiometric and spectrophotometric study. *Aust. J. Chem.* 35, 739–756. doi: 10.1071/CH9820739

Kucheryavskiy, S. (2020). mdatools — R package for chemometrics. *Chemometr. Intell. Lab. Syst.* 198:103937. doi: 10.1016/j.chemolab.2020.103937

Laborde, A., Puig-Castellví, F., Jouan-Rimbaud Bouveresse, D., Eveleigh, L., Cordella, C., and Jaillais, B. (2021). Detection of chocolate powder adulteration with peanut using near-infrared hyperspectral imaging and multivariate curve resolution. *Food Control* 119:107454. doi: 10.1016/j.foodcont.2020.107454

Lebanov, L., Tedone, L., Ghiasvand, A., and Paull, B. (2020). Characterisation of complex perfume and essential oil blends using multivariate curve resolution-alternating least squares algorithms on average mass spectrum from GC-MS. *Talanta* 219:121208. doi: 10.1016/j.talanta.2020.121208

Lee, S., Wolberg, G., and Shin, S. Y. (1997). Scattered data interpolation with multilevel B-splines. *IEEE Trans. Vis. Comput. Graph.* 3, 228–244. doi: 10.1109/2945.620490

Leurgans, S., and Ross, R. T. (1992). Multilinear models: applications in spectroscopy. *Stat. Sci.* 7, 289–310. doi: 10.1214/ss/1177011225

Lyndgaard, L. B., Van den Berg, F., and De Juan, A. (2013). Quantification of paracetamol through tablet blister packages by Raman spectroscopy and multivariate curve resolution-alternating least squares. *Chemom. Intell. Lab. Syst.* 125, 58–66. doi: 10.1016/j.chemolab.2013.03.014

Maeder, M. (1987). Evolving factor analysis for the resolution of overlapping chromatographic peaks. *Anal. Chem.* 59, 527–530. doi: 10.1021/ac00130a035

Massicotte, P. (2019). *eemR: Tools for Pre-Processing Emission-Excitation-Matrix (EEM) Fluorescence Data*. R package version 1.0.1. Available online at: https://CRAN.R-project.org/package=eemR

Murphy, K. R., Stedmon, C. A., Graeber, D., and Bro, R. (2013). Fluorescence spectroscopy and multi-way techniques. PARAFAC. *Anal. Methods* 5, 6557–6566. doi: 10.1039/c3ay41160e

Piqueras, S., Duponchel, L., Tauler, R., and De Juan, A. (2011). Resolution and segmentation of hyperspectral biomedical images by multivariate curve resolution-alternating least squares. *Anal. Chim. Acta* 705, 182–192. doi: 10.1016/j.aca.2011.05.020

Poulin, B. A., Ryan, J. N., and Aiken, G. R. (2014). Effects of iron on optical properties of dissolved organic matter. *Environ. Sci. Technol.* 48, 10098–10106. doi: 10.1021/es502670r

Pucher, M., Wünsch, U., Weigelhofer, G., Murphy, K., Hein, T., and Graeber, D. (2019). staRdom: versatile software for analyzing spectroscopic data of dissolved organic matter in R. *Water* 11:2366. doi: 10.3390/w11112366

R Core Team. (2020). *R: A Language and Environment for Statistical Computing.*

Rhodes, M. J. C. (2020). Physiologically-active compounds in plant foods: an overview. *Proc. Nutr. Soc.* 55, 371–384. doi: 10.1079/PNS19960036

Ruckebusch, C., and Blanchet, L. (2013). Multivariate curve resolution: a review of advanced and tailored applications and challenges. *Anal. Chim. Acta* 765, 28–36. doi: 10.1016/j.aca.2012.12.028

Sánchez, F. C., Khots, M. S., Massart, D. L., and De Beer, J. O. (1994). Algorithm for the assessment of peak purity in liquid chromatography with photodiode-array detection. *Anal. Chim. Acta* 285, 181–192. doi: 10.1016/0003-2670(94)85022-4

Serrano, N., Pérez-Ràfols, C., Ariño, C., Esteban, M., and Manuel Díaz-Cruz, J. (2020). MCR-ALS of voltammetric data for the study of environmentally relevant substances. *Microchem. J.* 158:105177. doi: 10.1016/j.microc.2020.105177

Sever, M. J., and Wilker, J. J. (2004). Visible absorption spectra of metal – catecholate and metal – tironate complexes. *Dalt. Trans.* 1061–1072. doi: 10.1039/B315811J

Shariati-Rad, M., and Hasani, M. (2009). Application of multivariate curve resolution-alternating least squares (MCR-ALS) for secondary structure resolving of proteins. *Biochimie* 91, 850–856. doi: 10.1016/j.biochi.2009.04.005

Shutava, T., Prouty, M., Kommireddy, D., and Lvov, Y. (2005). pH responsive decomposable layer-by-layer nanofilms and capsules on the basis of tannic acid. *Macromolecules* 38, 2850–2858. doi: 10.1021/ma047629x

Smilde, A. K. (1992). Three-way analyses problems and prospects. *Chemom. Intell. Lab. Syst.* 15, 143–157. doi: 10.1016/0169-7439(92)85005-N

States, I., and Printing, G. (1960). *Complexes of Ferrous Iron with Tannic Acid; Geological Survey Water-Supply Paper, 1459-D, Chemistry of iron in natural water*. ed D. I. Geological Survey (U.S.) Washington: US GPO.

Sungur, S., and Uzar, A. (2008). Investigation of complexes tannic acid and myricetin with Fe(III). *Spectrochim. Acta Part A Mol. Biomol. Spectrosc.* 69, 225–229. doi: 10.1016/j.saa.2007.03.038

Tauler, R. (1995). Multivariate curve resolution applied to second order data. *Chemom. Intell. Lab. Syst.* 30, 133–146. doi: 10.1016/0169-7439(95)00047-X

Veselinović, A., Nikolić, R., and Nikolić, G. (2012). Application of multivariate curve resolution-alternating least squares (MCR-ALS) for resolving pyrogallol autoxidation in weakly alkaline aqueous solutions. *Open Chem.* 10, 1942–1948. doi: 10.2478/s11532-012-0125-z

Wehrens, R. (2011). *Chemometrics with R*. Berlin: Springer Berlin Heidelberg.

Windig, W., Shaver, J. M., Keenan, M. R., and Wise, B. M. (2012). Simplification of alternating least squares solutions with contrast enhancement. *Chemom. Intell. Lab. Syst.* 117, 159–168. doi: 10.1016/j.chemolab.2012.01.013

Conflict of Interest: The authors declare that the research was conducted in the absence of any commercial or financial relationships that could be construed as a potential conflict of interest.

frontiers in Chemistry

MINI REVIEW
published: 14 December 2020
doi: 10.3389/fchem.2020.608236

Recent Advances of Graphene-Based Strategies for Arsenic Remediation

Claudia Foti[1]*, *Placido Giuseppe Mineo*[2]*, *Angelo Nicosia*[2], *Angela Scala*[1], *Giulia Neri*[1] *and Anna Piperno*[1]*

[1] Department of Chemical, Biological, Pharmaceutical and Environmental Sciences, University of Messina, Messina, Italy,
[2] Department of Chemical Sciences, University of Catania, Catania, Italy

The decontamination of water containing toxic metals is a challenging problem, and in the last years many efforts have been undertaken to discover efficient, cost-effective, robust, and handy technology for the decontamination of downstream water without endangering human health. According to the World Health Organization (WHO), 180 million people in the world have been exposed to toxic levels of arsenic from potable water. To date, a variety of techniques has been developed to maintain the arsenic concentration in potable water below the limit recommended by WHO (10 μg/L). Recently, a series of technological advancements in water remediation has been obtained from the rapid development of nanotechnology-based strategies that provide a remarkable control over nanoparticle design, allowing the tailoring of their properties toward specific applications. Among the plethora of nanomaterials and nanostructures proposed in the remediation field, graphene-based materials (G), due to their unique physico-chemical properties, surface area, size, shape, ionic mobility, and mechanical flexibility, are proposed for the development of reliable tools for water decontamination treatments. Moreover, an emerging class of 3D carbon materials characterized by the intrinsic properties of G together with new interesting physicochemical properties, such as high porosity, low density, unique electrochemical performance, has been recently proposed for water decontamination. The main design criteria used to develop remediation nanotechnology-based strategies have been reviewed, and special attention has been reserved for the advances of magnetic G and for nanostructures employed in the fabrication of membrane filtration.

Keywords: arsenic, graphene, potable water, magnetic nanomaterials, nanofiltration membrane, nanoadsorbent, remediation

OPEN ACCESS

Edited by:
Carlos Rey-Castro, Universitat de Lleida, Spain

Reviewed by:
Václav Ranc, Palacký University, Olomouc, Czechia
Valeria Marina Nurchi, University of Cagliari, Italy

***Correspondence:**
Placido Giuseppe Mineo
gmineo@unict.it
Claudia Foti
cfoti@unime.it
Anna Piperno
apiperno@unime.it

Specialty section:
This article was submitted to Green and Sustainable Chemistry, a section of the journal Frontiers in Chemistry

Received: *21 September 2020*
Accepted: *11 November 2020*
Published: *14 December 2020*

Citation:
Foti C, Mineo PG, Nicosia A, Scala A, Neri G and Piperno A (2020) Recent Advances of Graphene-Based Strategies for Arsenic Remediation. Front. Chem. 8:608236. doi: 10.3389/fchem.2020.608236

INTRODUCTION

Arsenic is a ubiquitous element, present in all environmental compartments as well as in living organisms (Merian et al., 2004). It is a component of the earth's crust, minerals, and soils, and it is used as a wood preservative, a component of fertilizers and pesticides, in the mining, metallurgical, glass-making and semiconductor industries. Arsenic toxicity has become a public health problem and an environmental question. The World Health Organization (WHO) estimated that about 180 million people in 50 countries have been exposed to toxic arsenic levels (at least 10 μg/L in drinking water) (International Agency for Research on Cancer IARC, 2012). Arsenic is included

among class I carcinogens (International Agency for Research on Cancer IARC, 2012); its toxicity and bioaccumulation greatly depend on its chemical state and on the metabolic pathways in which it is involved (Costa, 2019). Acute and chronic toxicity mechanisms are well-studied, whereas the mechanisms that underlie arsenic-mediated carcinogenesis, including epigenetic alterations, remain largely unknown (Costa, 2019; Nurchi et al., 2020). Arsenic is a metalloid, with four oxidation states (−3, 0, +3, +5), and it exists in a variety of inorganic and organic forms with different toxicity levels, depending on its speciation.

Speciation in aqueous solutions is mostly controlled by redox potential (Eh) and pH. Potential-pH diagrams (Brookins, 1988) show that arsenic in water exists mainly in trivalent or pentavalent form.

Under oxidizing conditions (high E_h values), the As (V) species prevail, and their distribution is related to their pH. In natural pH environments (i.e., $4 < pH < 8$), As(V) is present as $H_2AsO_4^-$ and $HAsO_4^{2-}$(Cassone et al., 2018), and the presence of other metal cations must be considered in the natural waters (Nordstrom et al., 2014; Cardiano et al., 2018; Chillè et al., 2018; Giuffrè et al., 2020). Speciation studies performed in presence of Ca^{2+} and Mg^{2+} highlighted the fact that the distribution of As(V) is strongly influenced by the high concentration of these cations and, in sea water, As (V) is mainly present as $CaAsO_4^-$ (46.8%) and $MgHAsO_4^0$ (31.8%), while in fresh water, the main species are $HAsO_4^{2-}$ and $H_2AsO_4^-$ (31% each), together with $CaHAsO_4^0$ (25.8%) (Chillè et al., 2018).

Under reducing conditions (low E_h values), arsenic mainly exists as As (III) and (Cassone et al., 2018) the oxoanions distribution is associated with the pH; up to $pH \approx 9$, As (III) is present as arsenous acid H_3AsO_3, whereas its anion $H_2AsO_3^-$ represents the stable species for $9 < pH \leq 11$. As (III) can also interact with different classes of chelators (Cassone et al., 2019, 2020; Chillè et al., 2020a,b).

Recently, the techniques developed for arsenic removal, such as membrane filtration, coagulation, adsorption, ion exchange, have been implemented by nanotechnology-based strategies (Ungureanu et al., 2015; Siddiqui et al., 2019). Here, we discuss and summarize (**Table 1**) the literature on technological advancements in arsenic remediation using graphene-based materials.

Graphene-Based Materials Employed for Arsenic Remediation

Graphene-based materials (G) include numerous carbon nanomaterials with different morphology, size, shape, chemical surface, and physical-chemical properties (Georgakilas et al., 2012; Yang et al., 2016; Siddiqui and Chaudhry, 2018; Neri et al., 2019; Cordaro et al., 2020; Kokkinos et al., 2020). The G family includes several members such as graphene oxide (GO), reduced graphene oxide (RGO), and their derivatives (e.g., functionalized G and G nanocomposites). Native G showed many remarkable properties, but its poor processability together with the production difficulty on a large scale limited its practical use (Neri et al., 2015b). The development of new derivatives hosting additional functional groups is the main strategy for developing G for practical applications (Neri et al., 2015a). The modification/functionalization processes tune the intrinsic features and allow the assembly of G in various structures (**Figure 1**).

GO and its composites, in the form of membranes, thin films, paper-like materials, have increasing use in water decontamination, due to their unique physicochemical features (Siddiqui and Chaudhry, 2018).

DFT calculations pointed out that pristine GO binds strongly to heavy metals, like As and Pb, with binding energy of −4.5 and −4.7 eV, respectively, and weakly to Hg (Panigrahi et al., 2018).

The capability of GO to adsorb As species is directly affected by GO oxidation, and its increase from 1.98 to 1.35 (C/O ratio) prompted the As (III) maximum adsorption capacity from 123 to 288 mg/g (Reynosa-Martínez et al., 2020).

The use of GO-based chromatographic stationary phases has allowed the simultaneous separation of different types of arsenic species, avoiding multiple analyses (Reid et al., 2020). Porous GO functionalized with hyperbranched polyethyleneimine (PEI-GO) was proposed for arsenic-selective solid phase extraction (SPE) column. PEI increased the sorption capacity by interacting with both As (III) and As (V) through complexation and electrostatic interactions, respectively (Ahmad et al., 2018).

GO-functionalized silica microspheres (GO@SiO_2) was investigated for metal speciation analysis of two inorganic arsenicals (arsenite and arsenate) and two organic arsenicals (monomethyl arsenic MMA and dimethylarsenic DMA). No retention by the native GO@SiO_2 column was observed for the tested arsenicals, that are anions around pH 6.0, as they may be electrostatically expelled. To improve their retaining behaviors, aromatic quaternary ammoniums were added to electrostatically attract arsenic anions. The separation performance of GO@SiO_2 was compared with that of G@SiO_2, showing a negligible difference in retention time and resolution, confirming no affinity of oxygenated groups on pristine GO to arsenic anions (Cheng et al., 2018; Zhao et al., 2018).

One of the main concerns related to the use of GO-based materials is the problem of recovery after adsorption, which was resolved using magneto-responsive GO (Hemmati et al., 2018). Iron compounds were reported to form cross-linking with the oxygen functionalities on the surface of carbon materials (Su et al., 2017a). The incorporation of magnetic nanoparticles in GO prevents the aggregation and eases the separation by using an external magnetic field. A comparative study highlighted the fact that As removal was more effective using Fe_3O_4-GO composite (M-GO) than Fe_3O_4-reduced GO composite (M-RGO), due to the difference in the amount of oxygenated functional groups (Yoon et al., 2016).

Magnetic nanoparticles decorated with β-cyclodextrins-functionalized GO (β-CDs-GO@Fe_3O_4 NPs) were proposed as scalable adsorbents of As (III)/As (V) for their excellent water dispersibility and magnetic properties due to the combination of the individual advantages of both materials (Kumar and Jiang, 2017). A nanocomposite based on chitosan and magnetic GO (CMGO) showed the best As (III) adsorption capacity (45 mg/g) at pH 7 (Sherlala et al., 2019).

TABLE 1 | Graphene-based Nanoadsorbents and Membranes.

Graphene-based system	Features	Adsorption capacity or rejection	References
GO	GO as adsorbent	As(III) 288 mg/g^{F}	Reynosa-Martínez et al., 2020
PEI-GO	GO modified with PEI Solid Phase Extraction	As(III) 125 mg/g^{E}	Ahmad et al., 2018
GO@SiO_2 and G@SiO_2	GO or G and SiO_2 as chromatographic stationary phases	Not specified	Cheng et al., 2018
M-GO	GO, Fe_3O_4 nanocomposite as adsorbent	As(III) 85 mg/g^{E} As(V) 38 mg/g^{E}	Yoon et al., 2016
M-RGO	RGO, Fe_3O_4 nanocomposite as adsorbent	As(III) 57 mg/g^{E} As(V) 12 mg/g^{E}	Yoon et al., 2016
β-CDs-GO@Fe_3O_4	GO modified with β-CDs, Fe_3O_4 nanocomposite as adsorbent	As(III) 100.23 mg/g^{E} As(V) 99.51 mg/g^{E}	Kumar and Jiang, 2017
CMGO	Chitosan-magnetic-graphene oxide, nanocomposite as adsorbent	As(III) 45 mg/g^{E}	Sherlala et al., 2019
mGO/bead	Alginate, GO, Fe_3O_4 nanocomposite as adsorbent	As(V) ∼99%^{E}	Vu et al., 2017
GFeN	GO and Fe/Fe_xO_y core-shell as adsorbent	As(III) 306 mg/g^{L} As(V) 431 mg/g^{L}	Das et al., 2020
Mag-PRGO	Partially reduced GO and Fe_3O_4 nanocomposite as adsorbent	As(V) 132 mg/g^{E}	Bobb et al., 2020
SMG	G, Fe (∼5 nm) nanocomposite as adsorbent	As(V) 3.26 mg/g^{L}	Gollavelli et al., 2013
GNP/Fe-Mg	G nanoplates, Fe-Mg nanocomposite as adsorbent	As(V) 103.9 mg/g^{L}	La et al., 2017b
GNP/$CuFe_2O_4$	G nanoplates, $CuFe_2O_4$ nanocomposite as adsorbent	As(III) 236.29 mg/g^{L} As(V) 172.27 mg/g^{L}	La et al., 2017a
Fe@CuO&GO	Fe/Cu/GO nanocomposite as adsorbent	As(III) 70.36 mg/g^{L} As(V) 62.60 mg/g^{L}	Wu et al., 2019
Fe-GO-Gd	Gd_2O_3, Fe_2O_3, GO nanocomposite as adsorbent	As(V) 35.84 mg/g^{E}	Lingamdinne et al., 2020
MG@PDA@PGMA-AET	G/Fe_3O_4, Polydopamine, 2-aminoethanethiol as adsorbent	As(III) 62.7 mg/g^{E} As(V) 19.3 mg/g ^{E}	Wang et al., 2019
M-RGO	Fe_2O_3 NPs, persulfate (PS) and RGO as catalyst/adsorbent	Total As 89.8%^{E}	Wu et al., 2020
MAF-RGO	Mn-Al-Fe and RGO as adsorbent	As(III) 402 mg/g^{F} As(V) 339 mg/g^{F}	Penke et al., 2020
G-CNT-Fe 3D	Engineered G, CNT Fe_3O_4	Not specified	Vadahanambi et al., 2013
3D G Fe_3O_4/aerogel	Fe_3O_4/graphene aerogel as adsorbent	As(V) 40.048 mg/g^{L}	Ye et al., 2015
MGOH	Graphene hydrogel as adsorbent	As (III) 25.1 mg/g^{L} As(V) 74.2 mg/g^{L}	Liang et al., 2019
FeO_x-CNs	Engineered carbon nanospheres-iron oxide	As (III) 416 mg/g^{F} As(V) 201 mg/g^{F}	Su et al., 2017b
PSU-GO	Membrane produced by phase inversion, used in direct flow filter	As(V) 82.3%^{E}	Rezaee et al., 2015
PSU-GO	Membrane produced by phase inversion, used in cross-flow filter	As(V) 99%^{E}	Shukla et al., 2018
GO-coated TFC-NF	PES-supported membrane produced by GO covalent coating on Polyamide, used in cross-flow filter	As(V) 98%^{E}	Pal et al., 2018a,b
PAN-GO-γ-Fe_2O_3	Membrane produced by electrospinning used as batch adsorption	As(V) 95.72%^{E}	Tripathy and Hota, 2019
PES-GMF	Produced by phase inversion, used in cross-flow filter	As(V) 28.70 mg/g^{E}	Shahrin et al., 2019
PGLa-Glu-GO-CNT	Membrane produced by spin-casting	As(V) 92%^{E} As(III) 96%^{E}	Viraka Nellore et al., 2015
PLGO	Membrane produced by filtration over cellulose, used as fix-bed adsorption column	As(III) 99.8%^{E}	Ahmad et al., 2020
DMSPE	Adsorbent deposited on membrane, used in direct flow filter	As(V) 43.9 mg/g^{L}	Baranik et al., 2018

^{F}*Freundlich model;* ^{L}*Langmuir model;* ^{E}*Experimental.*

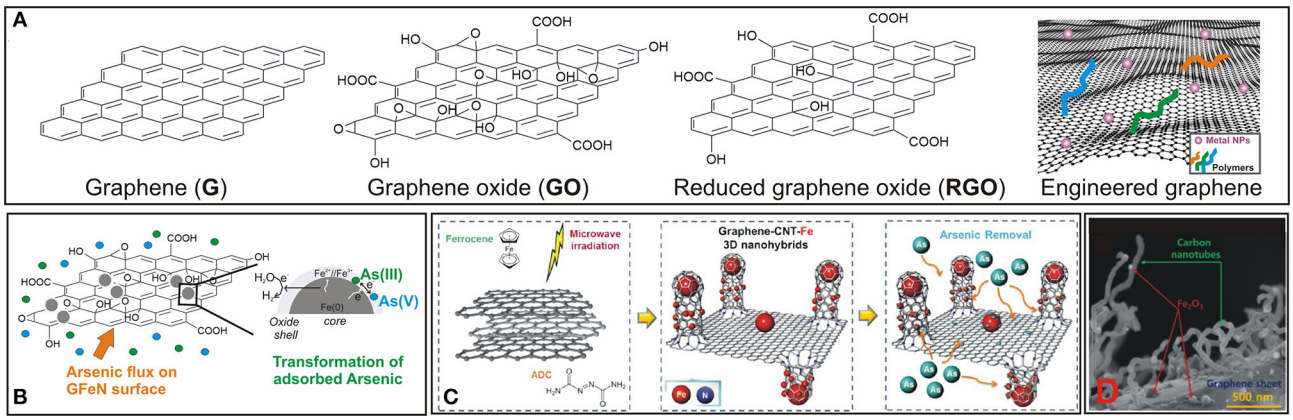

FIGURE 1 | (A) Graphene-based materials (graphene, graphene oxide, reduced graphene oxide and engineered graphene). **(B)** Schematic representation of GO-iron nanohybrid (GFeN) and the proposed mechanism involved for arsenic removal. **(C)** Representative example of hierarchically porus 3D assembly (G-CNT-Fe 3D) and the related SEM image **(D)** "Reproduced with permission of (Vadahanambi et al., 2013), (Copyright 2020), American Chemical Society".

To increase the water stability, magnetite and GO were encapsulated inside a non-toxic alginate bead (mGO/bead) and the adsorption of Cr (VI) and As (V) from multicomponent systems and contaminated wastewater was evaluated. mGO/bead showed excellent performance (80–100% removal) and recyclability in a complex mixture of heavy metals (Vu et al., 2017).

GO-iron nanohybrid (GFeN) systems were prepared by a sol-gel process for the concurrent removal of As(III)/As(V), without previous oxidation of As(III) to As(V) (Das et al., 2020). As(V) absorption involves electrostatic interactions as well as surface complexation with corrosion products, whereas only surface complexation leads the As(III) absorption. Adsorption capacity was high for both As (V) and As(III) species (**Table 1**) without iron leaching while it decreased in the presence of PO_4^{2-} and SiO_3^{2-} ions. GO acts as a reservoir for the electrons released during the oxidation of Fe^0, allowing the electrons to come back to Fe NPs (**Figure 1B**).

Magnetite partially reduced GO (Mag-PRGO) nanocomposite obtained *via* laser vaporization-controlled condensation method (Bobb et al., 2020) was exploited to remove As(V). Mag-PRGO showed the ability to remove 100% of As(V) up to 100 ppm final concentration (pH range 4–6), without the loss of iron ions in solution.

GO and ferrocene were used for the preparation of smart magnetic graphene (SMG) by a solvent-free microwave-induced process (Gollavelli et al., 2013). Upon irradiation, GO became graphene and ferrocene decomposed to metallic Fe core (∼5 nm in size). SMG showed a maximum As(V) absorption capacity of 3.26 mg/g (**Table 1**), starting from an arsenic concentration of 5.0 ppm.

Adsorbent systems containing two or more metals or metal oxides were designed to improve arsenic adsorption performance. Graphene nanoplates (GNPs) supported with Fe-Mg binary oxide (La et al., 2017b) or spinel $CuFe_2O_4$ (La et al., 2017a) showed a significant As(V) adsorption. The better adsorption capacity was reached at low pH values, due to the protonation of OH, which attract As(V) oxyanions, whereas the decrease of net positive charge, at higher pH values, leads to a decrease of As(V) adsorption ability. Both systems showed a relevant selectivity toward arsenic anions compared to other ion species.

Fe@Cu&GO systems fabricated by coprecipitation of CuO and Fe_3O_4 on GO surface showed good values of absorption for both As(III)/As(V) (**Table 1**) with a competitive adsorption of phosphate ions (Wu et al., 2019). As(III) adsorption was independent from pH variation, whereas As(V) adsorption decreases under alkali conditions.

Considering the ability of Gadolinium (Gd) oxonium to form binary compounds with arsenic species and its sizeable magnetic moment, a Fe-GO-Gd system (Lingamdinne et al., 2020) was tested for As(V) adsorption. Both ion exchange surface complexation and electrostatic interactions allowed As(V) removal. The adsorption ability decreased in the presence of competitive ions (SO_4^{2-}, PO_4^{3-}, and CO_3^{2-}) and after four adsorption/desorption cycles, probably due to the leak of Fe and Gd ions from the GO surface.

Multifunctional magnetic graphene (MG@PDA@PGMA-AET), prepared by surface-initiated ICAR ATRP, was investigated for simultaneous adsorption and sequential elution of As(III) and As(V) (Wang et al., 2019). As(V) oxyanions were absorbed by electrostatic interactions by protonated functional groups of MG@PDA@PGMA-AET, conversely neutral H_3AsO_3 species were absorbed by chelation mechanism with –OH, –SH and –NH_2 groups. The speciation analysis demonstrated a quantitative and simultaneous adsorption of both arsenic species (**Table 1**), using MG@PDA@PGMA-AET as column packing material.

The heterogeneous Fenton-like system (M-RGO) was proposed for the degradation of 4-aminophenylarsonic (*p*-ASA) and for the adsorption of arsenic species from wastewater (Wu et al., 2020). Removal rate of 89.8% for total As and 98.8% for *p*-ASA were estimated at neutral pH value.

Mn-Al-Fe RGO based hybrid system (MAF-RGO) was proposed to remove arsenic species by electro-sorption and

reduction process (Penke et al., 2020). Relevant maximum sorption values for both As(III)/As(V) (**Table 1**) were estimated by the Freundlich model. Interestingly, the irradiation of MAF-RGO with white light (> 420 nm) increased two-fold the arsenic loading.

Macro/micro/meso porous structures guarantee an excellent permeation of gas and solution, promoting active interior sites. Moreover, 3D G systems are characterized by major mechanical stability avoiding the aggregation phenomenon typical of graphene layers (He et al., 2020). G-CNT-Fe 3D nanohybrid (**Figure 1C**), composed of CNTs vertically standing on G surface and Fe_nO_m NPs dispersed on CNT and G surfaces, (Vadahanambi et al., 2013) showed a higher performance to capture As(III) species compared to 2D iron-decorated G system. The high surface-to-volume ratio and the mesoporous morphology facilitated the molecular diffusion and the accessibility of iron oxides, which acted as arsenic interactions sites.

Mesoporous 3D G aerogels (GA) homogenously decorated with Fe_3O_4 NPs (Ye et al., 2015) showed a higher maximum adsorptive capacity (**Table 1**) compared with 2D Fe-G systems and porous Fe_3O_4. To keep the chemical structure of GO sheets and avoid the damage of oxygen groups, porous 3D magnetic GO hydrogel (MGOH) was prepared by generation of chemical bubbles mixing GO, Fe_3O_4 NPs, and polyacrylamide hydrochloride (PA) at room temperature (Liang et al., 2019). MGOH showed good maximum adsorption capacity values (**Table 1**) with one of the fastest adsorption speeds, reaching equilibrium within only 2 min for both As(III)/As(V) species.

Arsenic capture ability of engineered carbon nanospheres (CNs) with a mesopore/macropore structure depends on the amount of loaded Fe_nO_m (Su et al., 2017b). Fe_nO_m content of 7 and 13 wt% resulted in a maximum adsorption capacity of 246 and 416 mg/g for As(III), and 93 and 201 mg/g for As(V), respectively; at higher Fe_nO_m content a significant decrease in absorption capacity was observed, probably due to the formation of Fe oxide agglomerates that block the pores.

Graphene-Based Membranes for Arsenic Remediation

Nanofiltration membranes technology is a promising environment-friendly alternative to the conventional adsorbent materials or ion exchange resins (Shukla et al., 2018), providing the rejection of arsenic pollutants by low-cost filtration operations at low transmembrane pressure, through systems suitable to avoid fouling (i.e., cross-flow module) (Sen et al., 2010; Pal et al., 2014). Nanofiltration membranes suitability is mainly affected by the Donnan exclusion principle (Dresner, 1972; Bowen and Mukhtar, 1996; Jye and Ismail, 2017).

The structure and the porosity of polysulfone (PSU)-based membranes including GO can be tuned by exploiting PSU hydrophobicity and GO hydrophilicity (Rezaee et al., 2015; Shukla et al., 2018).

Pure PSU membrane exhibited a sponge-like system with a dense skin layer and a few pores with drop-like ends; the addition of 0.5 (w)% GO resulted in the formation of finger-like pores with closed ends. Further GO loading resulted in a drastic drop of the sponge-like structure, while the pores appeared open-ended and even bigger in size. The negatively charged surface was active in Donnan repulsion of negatively charged pollutants. With an increase in pH, the negative charge of the membrane surface increases, and the predominant arsenate species becomes the divalent ion ($HAsO_4^{2-}$), enhancing the rejection performances (Rezaee et al., 2015). Although the rejection performance is negatively influenced by the contemporary presence of cations and anions, a higher efficiency of the PSU/carboxylated-GO membrane to reject mixed metal ions solutions than that of pure PPSU was evidenced (Shukla et al., 2018). PSU-based membranes containing GO were prepared also by interfacial polymerization (Pal et al., 2018b). The polyethersulfone (PES) membrane was covered with polyamide, and the residual acid groups belonging to the polyamide-matrix were used to bind a GO layer. This membrane was able to selectively remove ionic As(V) (**Table 1**), retaining useful metal ions of drinking water, without GO losses in the permeated stream. An economic industrial scale-up was also considered (Pal et al., 2018a).

A PAN-based electrospun composite containing GO and γ-Fe_2O_3 was developed by electrospinning of PAN in DMF with GO and γ-Fe_2O_3 (Tripathy and Hota, 2019). PAN-GO-γ-Fe_2O_3 membrane exhibited high affinity toward As(V) removal (36.1 mg/g) and the presence of anions such as chloride, nitrate, and sulfate do not affect the efficiency, whereas phosphate anions' copresence strongly decreases As(V) chemisorption. As(V) adsorption is proposed as an electrostatic attraction and surface complexation mechanism, operated by the -C-OH and Fe-O groups present on the membrane surface, able to form a complex with arsenate species $H_2AsO_4^-$.

GO-manganese ferrite membranes (PES-GMF, from 0.5 to 2 wt% content) were prepared by dispersing GO-manganese ferrite (GMF) in a polymer mixed matrix of polyvinylpyrrolidone (PVP) and polyethersulfone (PES) that acted as a pore former and support, respectively. GO induced a pore size increase, although high GMF content prompted the agglomerates' formation due to dipole-dipole interactions. GMF increased the membrane hydrophilicity, and the addition of 2 w% of GMF resulted in an increased membrane water flux of 46% in the pure PES membrane. A pH-dependent efficiency was detected: in acidic conditions the electrostatic attraction prevails—positively charged GMF and As(V) in the form of $H_2AsO_4^-$; in alkali conditions the electrostatic rejection occurs (due to the deprotonation of GMF and As(V) in form of $HAsO_4^{2-}$. The maximum As(V) adsorption capacity of 75.5 mg/g was found for the membrane loaded with 2% GMF (Shahrin et al., 2019).

The adsorptive processes based on electrostatic interactions are suitable only for As(V) species rejection whereas for As(III) removal the affinity of thiolated groups grafted onto engineered membranes was exploited.

A complex 3D porous membrane was synthesized by using GO, single-walled carbon nanotubes (SWCNT) and an antimicrobial PGLa peptide (Viraka Nellore et al., 2015) and tested for the removal of toxic As(III), As(V), Pb(II) and for the disinfection of pathogenic bacteria. Nanofiltration of multiple metal ions solution containing both As(III) and As(V)

(10 ppm) and bacteria revealed that 96% of As(III) and 92% of As(V) were rejected from the membrane (**Table 1**). Although As(III) ions are difficult to remove through nanofiltration, they exhibit high affinity for thiolated groups of glutathione. As a confirmation of the binding affinity of thiolated proteins and As(III), an efficient GO-based membrane suitable for As(III) preconcentration in column phase processes was reported (Ahmad et al., 2020). GO and Bovine Serum albumin (BSA) solution was vacuum-filtered through a cellulose nitrate paper (0.22 μm) to obtain a self-standing polymer-laminated GO membrane (PLGO). BSA was physisorbed onto the GO sheets through electrostatic interactions inducing the formation of interlayer nano capillaries on the membrane surface. PLGO exhibited a maximum adsorption capacity of 140 mg/g, which is about three times higher than that of GO. The presence of other metal ions in solution slightly influences the As(III) selectivity. The recovery and reuse of the membrane do not affect the adsorption efficiency, confirming their usefulness for pre-concentration and speciation of As(III).

A Dispersive Micro-Solid Phase Extraction (DMSPE) membrane was developed by deposition of Al_2O_3/GO onto a membrane filter through a vacuum filtration procedure (Baranik et al., 2018). The membrane quantitatively binds As(V) deprotonated species (i.e. $H_2AsO_4^-$ and $HAsO_4^{2-}$) thanks to the high concentrations of surface hydroxylic groups with a pH-dependent performance.

DISCUSSION

The selected case studies showed the high potentiality of G nanotechnology to remove As from contaminated water. It is worth noting the ability of engineered graphene to effectively remove complex mixtures of organic and inorganic pollutants from water and its remarkable antimicrobial activity (Karahan et al., 2018).

Although some nanotechnological tools for water purification are already marketed (Khan and Malik, 2019), the use of G in water purification, in particular for As remediation, must be implemented to advance G nanotechnology from lab to the market. Specifically, major concerns such as safety, economic feasibility, and aggregation phenomena, especially in scaled up water purification systems, need to be reasonably addressed. To minimize the health risk, safety issues require a careful evaluation (Caccamo et al., 2020) with the implementation of *in-vivo* studies. The lack of standardized ways for G univocal characterization and the different fabrication methods make the replication of G published results difficult (Piperno et al., 2018). Characterization of G should be carried out by standardized ways to support the new laws for their regulation. REACH (Registration, Evaluation, Authorization, and Restriction of Chemicals) in the European Union is being updated for nanomaterial regulation. Finally, for commercial applications, G would need to be manufactured in standardized way and reduced cost considering that water scarcity is a serious problem in underdeveloped countries.

AUTHOR CONTRIBUTIONS

CF, PM, AN, AS, GN, and AP contributed to the design and writing of the mini-review. CF, PM, and AP supervision the work. AP funding acquisition. All authors contributed to the article and approved the submitted version.

FUNDING

Publication fees will be partially covered by Department Fund and by Frontiers discount DSC-07001469422PRD.

REFERENCES

Ahmad, H., Huang, Z., Kanagaraj, P., and Liu, C. (2020). Separation and preconcentration of arsenite and other heavy metal ions using graphene oxide laminated with protein molecules. *J. Hazard. Mater.* 384:121479. doi: 10.1016/j.jhazmat.2019.121479

Ahmad, H., Umar, K., Ali, S. G., Singh, P., Islam, S. S., and Khan, H. M. (2018). Preconcentration and speciation of arsenic by using a graphene oxide nanoconstruct functionalized with a hyperbranched polyethyleneimine. *Microchim. Acta* 185:290. doi: 10.1007/s00604-018-2829-z

Baranik, A., Gagor, A., Queralt, I., Marguí, E., Sitko, R., and Zawisza, B. (2018). Determination and speciation of ultratrace arsenic and chromium species using aluminium oxide supported on graphene oxide. *Talanta* 185, 264–274. doi: 10.1016/j.talanta.2018.03.090

Bobb, J. A., Awad, F. S., Moussa, S., and El-Shall, M. S. (2020). Laser synthesis of magnetite-partially reduced graphene oxide nanocomposites for arsenate removal from water. *J. Mater. Sci.* 55, 5351–5363. doi: 10.1007/s10853-020-04363-6

Bowen, W. R., and Mukhtar, H. (1996). Characterisation and prediction of separation performance of nanofiltration membranes. *J. Memb. Sci.* 112, 263–274. doi: 10.1016/0376-7388(95)00302-9

Brookins, D. G. (1988). *Eh-pH Diagrams for Geochemistry*. Heidelberg: Springer-Verlag. doi: 10.1007/978-3-642-73093-1

Caccamo, D., Currò, M., Ientile, R., Verderio, E. A., Scala, A., Mazzaglia, A., et al. (2020). Intracellular fate and impact on gene expression of doxorubicin/cyclodextrin-graphene nanomaterials at sub-toxic concentration. *Int. J. Mol. Sci.* 21:4891. doi: 10.3390/ijms21144891

Cardiano, P., Chillè, D., Foti, C., and Giuffrè, O. (2018). Effect of the ionic strength and temperature on the arsenic(V) -Fe^{3+} and -Al^{3+} interactions in aqueous solution. *Fluid Phase Equilib* 458, 9–15. doi: 10.1016/j.fluid.2017.11.002

Cassone, G., Chillé, D., Foti, C., Giuffré, O., Ponterio, R. C., Sponer, J., et al. (2018). Stability of hydrolytic arsenic species in aqueous solutions: As^{3+}vs. As^{5+}. *Phys. Chem. Chem. Phys.* 20, 23272–23280.

Cassone, G., Chillè, D., Giacobello, F., Giuffrè, O., Mollica Nardo, V., Ponterio, R. C., et al. (2019). Interaction between As(III) and simple thioacids in water: an experimental and ab initio molecular dynamics investigation. *J. Phys. Chem. B* 123, 6090–6098. doi: 10.1021/acs.jpcb.9b04901

Cassone, G., Chillè, D., Mollica Nardo, V., Giuffrè, O., Ponterio, R. C., Sponer, J., et al. (2020). Arsenic–nucleotides interactions: an experimental and computational investigation. *Dalton Trans.* 49, 6302–6311. doi: 10.1039/D0DT00784F

Cheng, H., Zhang, W., Wang, Y., and Liu, J. (2018). Graphene oxide as a stationary phase for speciation of inorganic and organic species of mercury, arsenic and selenium using HPLC with ICP-MS detection. *Microchim. Acta* 185:425. doi: 10.1007/s00604-018-2960-x

Chillè, D., Aiello, D., Grasso, G. I., Giuffrè, O., Napoli, A., Sgarlata, C., et al. (2020a). Complexation of As(III) by phosphonate ligands in aqueous fluids: thermodynamic behavior, chemical binding forms and sequestering abilities. *J. Environ. Sci.* 94, 100–110. doi: 10.1016/j.jes.2020.03.056

Chillè, D., Cassone, G., Giacobello, F., Giuffrè, O., Nardo, V. M., Ponterio, R. C., et al. (2020b). Removal of As(III) from biological fluids: mono- versus dithiolic ligands. *Chem. Res. Toxicol.* 33, 967–974. doi: 10.1021/acs.chemrestox.9b00506

Chillè, D., Foti, C., and Giuffrè, O. (2018). Thermodynamic parameters for the protonation and the interaction of arsenate with Mg^{2+}, Ca^{2+} and Sr^{2+}: application to natural waters. *Chemosphere* 190, 72–79. doi: 10.1016/j.chemosphere.2017.09.115

Cordaro, A., Neri, G., Sciortino, M. T., Scala, A., and Piperno, A. (2020). Graphene-based strategies in liquid biopsy and in viral diseases diagnosis. *Nanomaterials* 10:1014. doi: 10.3390/nano10061014

Costa, M. (2019). Review of arsenic toxicity, speciation and polyadenylation of canonical histones. *Toxicol. Appl. Pharmacol.* 375, 1–4. doi: 10.1016/j.taap.2019.05.006

Das, T. K., Sakthivel, T. S., Jeyaranjan, A., Seal, S., and Bezbaruah, A. N. (2020). Ultra-high arsenic adsorption by graphene oxide iron nanohybrid: removal mechanisms and potential applications. *Chemosphere* 253:126702. doi: 10.1016/j.chemosphere.2020.126702

Dresner, L. (1972). Some remarks on the integration of the extended nernst-planck equations in the hyperfiltration of multicomponent solutions. *Desalination* 10, 27–46. doi: 10.1016/S0011-9164(00)80245-3

Georgakilas, V., Otyepka, M., Bourlinos, A. B., Chandra, V., Kim, N., Kemp, K. C., et al. (2012). Functionalization of graphene: covalent and non-covalent approaches, derivatives and applications. *Chem. Rev.* 112, 6156–6214. doi: 10.1021/cr3000412

Giuffrè, O., Aiello, D., Chillè, D., Napoli, A., and Foti, C. (2020). Binding ability of arsenate towards Cu^{2+} and Zn^{2+}: thermodynamic behavior and simulation under natural water conditions. *Environ. Sci. Process. Impacts* 22, 1731–1742. doi: 10.1039/D0EM00136H

Gollavelli, G., Chang, C.-C., and Ling, Y.-C. (2013). Facile synthesis of smart magnetic graphene for safe drinking water: heavy metal removal and disinfection control. *ACS Sustain. Chem. Eng.* 1, 462–472. doi: 10.1021/sc300112z

He, J., Ni, F., Cui, A., Chen, X., Deng, S., Shen, F., et al. (2020). New insight into adsorption and co-adsorption of arsenic and tetracycline using a Y-immobilized graphene oxide-alginate hydrogel: adsorption behaviours and mechanisms. *Sci. Tot. Environ.* 701:134363. doi: 10.1016/j.scitotenv.2019.134363

Hemmati, M., Rajabi, M., and Asghari, A. (2018). Magnetic nanoparticle based solid-phase extraction of heavy metal ions: a review on recent advances. *Microchim. Acta* 185:160. doi: 10.1007/s00604-018-2670-4

International Agency for Research on Cancer IARC (2012). "Arsenic, metals, fibres and dusts", in *Monographs on the Evaluation of Carcinogenic Risks to Humans*. (Lyon: International Agency for Research on Cancer IARC).

Jye, L. W., and Ismail, A. F. (2017). *Nanofiltration Membranes: Synthesis, Characterization, and Applications*. Boca Raton, FL: CRC Press, Taylor and Francis Group. doi: 10.1201/9781315181479

Karahan, H. E., Wiraja, C., Xu, C., Wei, J., Wang, Y., Wang, L., et al. (2018). Graphene materials in antimicrobial nanomedicine: current status and future perspectives. *Adv. Healthc. Mater.* 7:1701406. doi: 10.1002/adhm.201701406

Khan, S. T., and Malik, A. (2019). Engineered nanomaterials for water decontamination and purification: from lab to products. *J. Hazard. Mater.* 363, 295–308. doi: 10.1016/j.jhazmat.2018.09.091

Kokkinos, P., Mantzavinos, D., and Venieri, D. (2020). Current trends in the application of nanomaterials for the removal of emerging micropollutants and pathogens from water. *Molecules* 25:2016. doi: 10.3390/molecules25092016

Kumar, A. S. K., and Jiang, S.-J. (2017). Synthesis of magnetically separable and recyclable magnetic nanoparticles decorated with β-cyclodextrin functionalized graphene oxide an excellent adsorption of As(V)/(III). *J. Mol. Liq.* 237, 387–401. doi: 10.1016/j.molliq.2017.04.093

La, D. D., Nguyen, T. A., Jones, L. A., and Bhosale, S. V. (2017a). Graphene supported spinel $CuFe_2O_4$ composites: novel adsorbents for arsenic removal in aqueous media. *Sensors* 17:1292. doi: 10.3390/s17061292

La, D. D., Patwari, J. M., Jones, L. A., Antolasic, F., and Bhosale, S. V. (2017b). Fabrication of a GNP/Fe–Mg binary oxide composite for effective removal of arsenic from aqueous solution. *ACS Omega* 2, 218–226. doi: 10.1021/acsomega.6b00304

Liang, J., He, B., Li, P., Yu, J., Zhao, X., Wu, H., et al. (2019). Facile construction of 3D magnetic graphene oxide hydrogel via incorporating assembly and chemical bubble and its application in arsenic remediation. *Chem. Eng. J.* 358, 552–563. doi: 10.1016/j.cej.2018.09.213

Lingamdinne, L. P., Choi, J.-S., Choi, Y.-L., Chang, Y.-Y., Yang, J.-K., Karri, R. R., et al. (2020). Process modeling and optimization of an iron oxide immobilized graphene oxide gadolinium nanocomposite for arsenic adsorption. *J. Mol. Liq.* 299:112261. doi: 10.1016/j.molliq.2019.112261

Merian, E., Anke, M., Ihnat, M., and Stoeppler, M. (2004). *Elements and Their Compounds in the Environment: Occurrence, Analysis and Biological Relevance*. Weinheim: WILEY-VCH Verlag GMBH and Co. KGaA. doi: 10.1002/9783527619634

Neri, G., Fazio, E., Mineo, P. G., Scala, A., and Piperno, A. (2019). SERS sensing properties of new graphene/gold nanocomposite. *Nanomaterials* 9:1236. doi: 10.3390/nano9091236

Neri, G., Scala, A., Barreca, F., Fazio, E., Mineo, P. G., Mazzaglia, A., et al. (2015a). Engineering of carbon based nanomaterials by ring-opening reactions of a reactive azlactone graphene platform. *Chem. Commun.* 51, 4846–4849. doi: 10.1039/C5CC00518C

Neri, G., Scala, A., Fazio, E., Mineo, P. G., Rescifina, A., Piperno, A., et al. (2015b). Repurposing of oxazolone chemistry: gaining access to functionalized graphene nanosheets in a top-down approach from graphite. *Chem. Sci.* 6, 6961–6970. doi: 10.1039/C5SC02576A

Nordstrom, D. K., Majzlan, J., and Königsberger, E. (2014). Thermodynamic properties for arsenic minerals and aqueous species. *Rev. Mineral. Geochem.* 79, 217–255. doi: 10.2138/rmg.2014.79.4

Nurchi, V. M., Buha Djordjevic, A., Crisponi, G., Alexander, J., Bjørklund, G., and Aaseth, J. (2020). Arsenic toxicity: molecular targets and therapeutic agents. *Biomolecules* 10:235. doi: 10.3390/biom10020235

Pal, M., Chakrabortty, S., Nayak, J., and Pal, P. (2018a). Removing toxic contaminants from groundwater by graphene oxide nanocomposite in a membrane module under response surface optimization. *Int. J. Environ. Sci. Technol.* 16, 4583–4594. doi: 10.1007/s13762-018-1924-3

Pal, M., Mondal, M. K., Paine, T. K., and Pal, P. (2018b). Purifying arsenic and fluoride-contaminated water by a novel graphene-based nanocomposite membrane of enhanced selectivity and sustained flux. *Environ. Sci. Pollut. Res.* 25, 16579–16589. doi: 10.1007/s11356-018-1829-1

Pal, P., Chakrabortty, S., and Linnanen, L. (2014). A nanofiltration–coagulation integrated system for separation and stabilization of arsenic from groundwater. *Sci. Tot. Environ.* 476–477, 601–610. doi: 10.1016/j.scitotenv.2014.01.041

Panigrahi, P., Dhinakaran, A. K., Sekar, Y., Ahuja, R., and Hussain, T. (2018). Efficient adsorption characteristics of pristine and silver-doped graphene oxide towards contaminants: a potential membrane material for water purification? *Chemphyschem* 19, 2250–2257. doi: 10.1002/cphc.201800223

Penke, Y. K., Yadav, A. K., Sinha, P., Malik, I., Ramkumar, J., and Kar, K. K. (2020). Arsenic remediation onto redox and photo-catalytic/electrocatalytic Mn-Al-Fe impregnated rGO: sustainable aspects of sludge as supercapacitor. *Chem. Eng. J.* 390:124000. doi: 10.1016/j.cej.2019.124000

Piperno, A., Scala, A., Mazzaglia, A., Neri, G., Pennisi, R., Sciortino, M. T., et al. (2018). Cellular signaling pathways activated by functional graphene nanomaterials. *Int. J. Mol. Sci.* 19:3365. doi: 10.3390/ijms19113365

Reid, M. S., Hoy, K. S., Schofield, J. R. M., Uppal, J. S., Lin, Y., Lu, X., et al. (2020). Arsenic speciation analysis: a review with an emphasis on chromatographic separations. *TrAC Trends Anal. Chem.* 123:115770. doi: 10.1016/j.trac.2019.115770

Reynosa-Martínez, A. C., Tovar, G. N., Gallegos, W. R., Rodríguez-Meléndez, H., Torres-Cadena, R., Mondragón-Solórzano, G., et al. (2020). Effect of the degree of oxidation of graphene oxide on As(III) adsorption. *J. Hazard. Mater.* 384:121440. doi: 10.1016/j.jhazmat.2019.121440

Rezaee, R., Nasseri, S., Mahvi, A. H., Nabizadeh, R., Mousavi, S. A., Rashidi, A., et al. (2015). Fabrication and characterization of a polysulfone-graphene oxide nanocomposite membrane for arsenate rejection from water. *J. Environ. Health Sci. Eng.* 13:61. doi: 10.1186/s40201-015-0217-8

Sen, M., Manna, A., and Pal, P. (2010). Removal of arsenic from contaminated groundwater by membrane-integrated hybrid treatment system. *J. Memb. Sci.* 354, 108–113. doi: 10.1016/j.memsci.2010.02.063

Shahrin, S., Lau, W.-J., Goh, P.-S., Ismail, A. F., and Jaafar, J. (2019). Adsorptive mixed matrix membrane incorporating graphene oxide-manganese ferrite (GMF) hybrid nanomaterial for efficient As(V) ions removal. *Composites B Eng.* 175:107150. doi: 10.1016/j.compositesb.2019.107150

Sherlala, A. I. A., Raman, A. A. A., Bello, M. M., and Buthiyappan, A. (2019). Adsorption of arsenic using chitosan magnetic graphene oxide nanocomposite. *J. Environ. Manage.* 246, 547–556. doi: 10.1016/j.jenvman.2019.05.117

Shukla, A. K., Alam, J., Alhoshan, M., Arockiasamy Dass, L., Ali, F. A. A., Muthumareeswaran, M. R., et al. (2018). Removal of heavy metal ions using a carboxylated graphene oxide-incorporated polyphenylsulfone nanofiltration membrane. *Environ. Sci. Water Res. Technol.* 4, 438–448. doi: 10.1039/C7EW00506G

Siddiqui, S. I., and Chaudhry, S. A. (2018). A review on graphene oxide and its composites preparation and their use for the removal of $As^{3+}$and As^{5+} from water under the effect of various parameters: application of isotherm, kinetic and thermodynamics. *Process Saf. Environ. Protect.* 119, 138–163. doi: 10.1016/j.psep.2018.07.020

Siddiqui, S. I., Naushad, M., and Chaudhry, S. A. (2019). Promising prospects of nanomaterials for arsenic water remediation: a comprehensive review. *Process Saf. Environ. Protect.* 126, 60–97. doi: 10.1016/j.psep.2019.03.037

Su, H., Ye, Z., and Hmidi, N. (2017a). High-performance iron oxide–graphene oxide nanocomposite adsorbents for arsenic removal. *Colloids Surfaces A Physicochem. Eng. Aspects* 522, 161–172. doi: 10.1016/j.colsurfa.2017.02.065

Su, H., Ye, Z., Hmidi, N., and Subramanian, R. (2017b). Carbon nanosphere–iron oxide nanocomposites as high-capacity adsorbents for arsenic removal. *RSC Adv.* 7, 36138–36148. doi: 10.1039/C7RA06187K

Tripathy, M., and Hota, G. (2019). Maghemite and graphene oxide embedded polyacrylonitrile electrospun nanofiber matrix for remediation of arsenate ions. *ACS Appl. Polym. Mater.* 2, 604–617. doi: 10.1021/acsapm.9b00982

Ungureanu, G., Santos, S., Boaventura, R., and Botelho, C. (2015). Arsenic and antimony in water and wastewater: overview of removal techniques with special reference to latest advances in adsorption. *J. Environ. Manage.* 151, 326–342. doi: 10.1016/j.jenvman.2014.12.051

Vadahanambi, S., Lee, S.-H., Kim, W.-J., and Oh, I.-K. (2013). Arsenic removal from contaminated water using three-dimensional graphene-carbon nanotube-iron oxide nanostructures. *Environ. Sci. Technol.* 47, 10510–10517. doi: 10.1021/es401389g

Viraka Nellore, B. P., Kanchanapally, R., Pedraza, F., Sinha, S. S., Pramanik, A., Hamme, A. T., et al. (2015). Bio-conjugated CNT-bridged 3D porous graphene oxide membrane for highly efficient disinfection of pathogenic bacteria and removal of toxic metals from water. *ACS Appl. Mater. Interfaces* 7, 19210–19218. doi: 10.1021/acsami.5b05012

Vu, H. C., Dwivedi, A. D., Le, T. T., Seo, S.-H., Kim, E.-J., and Chang, Y.-S. (2017). Magnetite graphene oxide encapsulated in alginate beads for enhanced adsorption of Cr(VI) and As(V) from aqueous solutions: role of crosslinking metal cations in pH control. *Chem. Eng. J.* 307, 220–229. doi: 10.1016/j.cej.2016.08.058

Wang, J., Zhang, W., Zheng, Y., Zhang, N., and Zhang, C. (2019). Multi-functionalization of magnetic graphene by surface-initiated ICAR ATRP mediated by polydopamine chemistry for adsorption and speciation of arsenic. *Appl. Surf. Sci.* 478, 15–25. doi: 10.1016/j.apsusc.2019.01.188

Wu, K., Jing, C., Zhang, J., Liu, T., Yang, S., and Wang, W. (2019). Magnetic Fe_3O_4@CuO nanocomposite assembled on graphene oxide sheets for the enhanced removal of arsenic(III/V) from water. *Appl. Surf. Sci.* 466, 746–756. doi: 10.1016/j.apsusc.2018.10.091

Wu, S., Yang, D., Zhou, Y., Zhou, H., Ai, S., Yang, Y., et al. (2020). Simultaneous degradation of p-arsanilic acid and inorganic arsenic removal using M-rGO/PS fenton-like system under neutral conditions. *J. Hazard. Mater.* 399:123032. doi: 10.1016/j.jhazmat.2020.123032

Yang, X., Xia, L., and Song, S. (2016). Arsenic adsorption from water using graphene-based materials: a critical review. *Surface Rev. Lett.* 24:1730001. doi: 10.1142/S0218625X17300015

Ye, Y., Yin, D., Wang, B., and Zhang, Q. (2015). Synthesis of three-dimensional Fe_3O_4-graphene aerogels for the removal of arsenic ions from water. *J. Nanomater.* 2015:864864. doi: 10.1155/2015/864864

Yoon, Y., Park, W. K., Hwang, T.-M., Yoon, D. H., Yang, W. S., and Kang, J.-W. (2016). Comparative evaluation of magnetite–graphene oxide and magnetite-reduced graphene oxide composite for As(III) and As(V) removal. *J. Hazard. Mater.* 304, 196–204. doi: 10.1016/j.jhazmat.2015.10.053

Zhao, H., Wang, Y., Zhang, D., Cheng, H., and Wang, Y. (2018). Electrochromatographic performance of graphene and graphene oxide modified silica particles packed capillary columns. *Electrophoresis* 39, 933–940. doi: 10.1002/elps.201700435

Conflict of Interest: The authors declare that the research was conducted in the absence of any commercial or financial relationships that could be construed as a potential conflict of interest.

frontiers in Chemistry

ORIGINAL RESEARCH
published: 16 December 2020
doi: 10.3389/fchem.2020.614574

Investigating the Binding Heterogeneity of Trace Metal Cations With SiO_2 Nanoparticles Using Full Wave Analysis of Stripping Chronopotentiometry at Scanned Deposition Potential

Elise Rotureau[1], *Luciana S. Rocha*[2], *Danielle Goveia*[3], *Nuno G. Alves*[2] *and José Paulo Pinheiro*[1]*

[1] Université de Lorraine, CNRS, LIEC, Nancy, France, [2] Centro Interdisciplina de Quimica do Algarve (CIQA), Departamento de Quimica e Bioquimica (DQB)/Faculdade de Ciencia e Tecnologia (FCT), University of Algarve, Faro, Portugal, [3] Universidade Estadual Paulista (Unesp)-Campus de Itapeva, Itapeva, Brazil

OPEN ACCESS

Edited by:
Carlos Rey-Castro,
Universitat de Lleida, Spain

Reviewed by:
Dario Omanovic,
Rudjer Boskovic Institute, Croatia
José Manuel Díaz-Cruz,
University of Barcelona, Spain

***Correspondence:**
José Paulo Pinheiro
jose-paulo.pinheiro@univ-lorraine.fr

Specialty section:
This article was submitted to Analytical Chemistry, a section of the journal Frontiers in Chemistry

Received: 06 October 2020
Accepted: 11 November 2020
Published: 16 December 2020

Citation:
Rotureau E, Rocha LS, Goveia D, Alves NG and Pinheiro JP (2020) Investigating the Binding Heterogeneity of Trace Metal Cations With SiO_2 Nanoparticles Using Full Wave Analysis of Stripping Chronopotentiometry at Scanned Deposition Potential. Front. Chem. 8:614574. doi: 10.3389/fchem.2020.614574

Silica oxides nano- and microparticles, as well as silica-based materials, are very abundant in nature and industrial processes. Trace metal cation binding with these bulk materials is generally not considered significant in speciation studies in environmental systems. Nonetheless, this might change for nanoparticulate systems as observed in a previous study of Pb(II) with a very small SiO_2 particle (7.5 nm diameter). Besides, metal binding by those nanoparticles is surprisingly characterized by a heterogeneity that increases with the decrease of metal-to-particle ratio. Therefore, it is interesting to extend this study to investigate different trace metals and the influence of the nanoparticle size on the cation binding heterogeneity. Consequently, the Cd(II), Pb(II), and Zn(II) binding by two different sized SiO_2 nanoparticles (Ludox LS30 and TM40) in aqueous dispersion was studied for a range of pH and ionic strength conditions, using the combination of the electroanalytical techniques Scanned Stripping ChronoPotentiometry and Absence of Gradients and Nernstian Equilibrium Stripping. The coupling of these techniques provides the free metal concentration in the bulk (AGNES) and information of the free and complex concentration at the electrode surface for each Stripping Chronopotentiometry at Scanned deposition Potential (SSCP). A recent mathematical treatment allows the reconstruction of a portion of the metal to ligand binding isotherm with the included heterogeneity information using the full SSCP wave analysis. In this work, we observed that the Zn(II) binding is homogeneous, Cd(II) is slightly heterogeneous, and Pb(II) is moderately heterogeneous, whereas the results obtained with the 7.5 nm diameter nanoparticle are slightly more heterogeneous than those obtained with the one of 17 nm. These findings suggest that the Zn(II) binding is electrostatic in nature, and for both Cd(II) and Pb(II), there should be a significant chemical binding contribution.

Keywords: trace metal, binding heterogeneity, SiO_2 nanoparticles, SSCP, AGNES

INTRODUCTION

The mobility and the bioavailability of trace metal elements (TME) in aquatic systems are largely mediated by their interaction with organic ligands, such as humic matter, exopolymeric substances, and/or inorganic surfaces, such as clays, silicates, aluminum, iron, and manganese (hydro)oxides (Buffle, 1988; Lead and Wilkinson, 2006).

Physicochemical heterogeneity is an intrinsic characteristic of most of these natural particles (Riemsdijk and Koopal, 1992; Duval et al., 2005; Duval and Gaboriaud, 2010), which generally arises from the diverse structures and morphologies of the particles, their polyfunctional chemical binding sites, and the polyelectrolytic nature of the particle charge. Accordingly, the metal ions binding/adsorption toward these natural particles is chemically heterogeneous, with binding association or adsorption constants that increase with the decrease of the metal-to-ligand ratio. This heterogeneity was initially estimated using the empirical Γ parameter of a Freundlich-type isotherm, which averages all contributions, covalent and electrostatic into a single descriptor (Filella and Town, 2001).

Later, the modeling of metal ion adsorption in mineral surfaces was refined by the separation of electrostatic and chemical binding contributions within the framework of surface complexation models [Dzombak and Morel (1990), CD-Music (Hiemstra and Van Riemsdijk, 1996)]. Similarly, the modeling of metal ion binding by natural organic matter was improved by the introduction of complexation codes that consider both an electrostatic contribution and a chemically heterogeneous metal ion binding by either a sum of discrete sites WHAM (Tipping, 1994) or a continuous site distribution (NICA) (Kinniburgh et al., 1996; Milne et al., 2003).

The experimental study of chemical heterogeneity in natural systems is complicated due to the low levels of trace metals and the complex interplay between those and the different ligands in solution. Recently, we proposed a new methodology in Pinheiro et al. (2020a) to investigate trace metal binding heterogeneity based on the full wave analysis of the electroanalytic technique of Stripping Chronopotentiometry at Scanned deposition Potential (SSCP). From the conversion of the experimental data obtained at the electrode surface, it is possible to recover a portion of the binding isotherm at realistic environmental trace metal concentrations.

The objective of this work is to apply this novel methodology to study the surprising metal binding heterogeneity of silica nanoparticles, first reported for Pb(II) ions by Goveia et al. (2011). The origin of this phenomenon remains uncertain, since at first sight one did not expect a significant chemical heterogeneity from metal binding to amorphous SiO_2 nanoparticles considering their chemically homogeneous composition and monodisperse particle size distribution. Several electrokinetic (Allison, 2009) or aggregation (Škvarla and Škvarla, 2017) studies reported a gel-like layer at the silica/solution interphase, namely, a gradual distribution of the component material from the particle core to the particle/water interphase. For charged particles, the presence of a water- and ion-permeable surface layer implies a tridimensional distribution of functional sites. An electric field spans from the bulk electrolyte solution to the inner part of the particle, likely generating a spatially dependent metal complexation heterogeneity. Several types of chemical metal complexes may be formed at the particulate interfaces, such as the monodentate or bidentate complexes that may occur at the orthosilicic acid sites in the SiO_2 nanoparticle. Additionally, structural impurities occluding the silica surface may arise from the synthesis of silica, which are depicted, e.g., by the isomorphic substitution of one Si by one Al atom (Bergna and Roberts, 2005).

In this work, we applied a methodology consisting first in a qualitative diagnosis of the effects of heterogeneity on the SSCP wave (Town and van Leeuwen, 2004; Town, 2008; Rotureau, 2014; Rotureau et al., 2016) according to (i) the nature of the metal ions, where we used Pb(II), Cd(II), and Zn(II), (ii) the physicochemical conditions of the medium, namely, the pH and ionic strengths of the solution, and (iii) the variation of particles size, using nanoparticles of 8 and 17 nm radius. Second, the quantitative reconstruction of the low coverage fraction of the binding isotherm contained in the SSCP wave is achieved using the mathematical treatment developed by Pinheiro et al. (2020a).

MATERIALS AND METHODS

Reagents

The chemicals used in the present work were of analytical reagent grade and used as received, unless stated otherwise. All solutions were prepared with ultra-pure water (18.3 MΩ cm, Milli-Q systems, Millipore-waters). The nitric acid 65% (suprapur) and the standard stock solutions of mercury nitrate (1,001 $\pm$ 2 mg L^{-1}), cadmium nitrate (999 $\pm$ 2 mg L^{-1}), lead nitrate (999 $\pm$ 2 mg L^{-1}), and zinc nitrate (1,000 $\pm$ 2 mg L^{-1}) were purchased from Merck. Cd(II), Pb(II), and Zn(II) solutions were prepared from dilution of the certified standard. Ludox® TM40 [40% (w/w) suspension in water] and LS30 [30% (w/w) suspension in water] colloidal silica (SiO_2) were purchased from Aldrich. Sodium nitrate electrolyte solution (10, 30, and 100 mM), MES [2-(N-morpholino)ethanesulfonic acid] buffer (200 mM), and MOPS [3-(N-morpholino)propanesulfonic acid] buffer (200 mM) were prepared from solids (Merck, suprapur and Merck >99%, respectively). The pH adjustments were performed using nitric acid (Merck, suprapur) and sodium hydroxide (100 mM standard, Merck) solutions.

Potassium thiocyanate, hydrochloric acid, and potassium chloride, all p.a. from Merck, were used to prepare the solution for the re-dissolution of the mercury film. Solutions of ammonium acetate [NH_4CH_3COO (1,000 mM)/CH_3COOH (1,000 mM)] (Merck) were prepared monthly and used without further purification.

Electrochemical Apparatus

An Ecochemie Autolab PGSTAT10 and μAutolab potentiostats (controlled by GPES 4.9 software from EcoChemie, the Netherlands) were used in conjunction with a Metrohm 663 VA stand (Metrohm, Switzerland). A three electrode configuration was used comprising a Hg thin film plated onto a rotating glassy carbon (GC) disk (2 mm diameter, Metrohm) as the

working electrode, a GC rod counter electrode, and an Ag/AgCl reference electrode from World Precision Instruments DRIREF-5 (electrolyte leakage $<8 \times 10^{-4}$ µl h^{-1}). A Denver Instrument (model 15) and a Radiometer analytical combined pH electrode calibrated with Titrisol buffers (Merck) were used to measure pH.

Preparation of the GC Substrate

Prior to deposition of the Hg films, the GC electrode was conditioned following a previously reported polishing/cleaning procedure (Monterroso et al., 2004). In brief, the electrode was polished with alumina slurry (grain size 0.3 µm, Metrohm) and sonicated in pure water for 60 s to obtain a renewed surface. Then, an electrochemical pre-treatment was carried out using a 50× cyclic voltammetric scan between −0.8 and +0.8 V at 0.1 V s^{-1}, in NH_4CH_3COO (1,000 mM)/HCl (500 mM) solution. The surface area of the GC electrode was measured by chronoamperometry in 1.124 mM ferricyanide/1,000 mM KCl solution (purged for 300 s). Before the measurements, the solution was stirred for 30 s (2,000 rpm) and followed by a resting period of 120 s. The parameters used were: $E = 0.5$ V and $t = 3$ s, and the measured response was the current I as a function of time t. The electrochemically active area of the GC electrode was calculated from the slope of I vs. $t^{-1/2}$ Cottrell equation (diffusion coefficient of ferricyanide $D = 7.63 \times 10^{-10}$ m^2 s^{-1}). The electrochemically active area obtained was $(3.334 \pm 0.062) \times 10^{-6}$ m^2 (two polishing experiments, each with four replicate determinations). When not in use, the bare GC electrode was stored dry in a clean atmosphere.

Preparation of the Hg Electrode

The thin Hg film was prepared *ex-situ* in 0.12 mM Hg(II) nitrate in nitric acid 0.73 mM (pH 1.9) by electrodeposition at −1.3 V for 700 s at a rotation rate of 1,000 rpm. The charge associated with the deposited Hg (Q_{Hg}) was calculated by electronic integration of the linear sweep stripping peak of Hg, for $v = 0.005$ V s^{-1}. The electrolyte solution was ammonium thiocyanate 5 mM (pH 3.4). The stripping step began at −0.15 V and ended at +0.4 V (Rocha et al., 2007).

SSCP and AGNES-SCP Measurements

Stripping chronopotentiometric measurements were carried out in 20 ml 10, 30, and 100 mM $NaNO_3$ solutions containing a concentration of 5.0×10^{-4} mM of the following individual metals: Cd(II), Pb(II), and Zn(II). The experimental conditions used were: deposition time (t_d) 45 s, oxidizing current (I_s) 2×10^{-6} A, applied until the potential reached −0.30 V, and electrode rotation speed 1,000 rpm. All solutions were purged for 20 min at the beginning of every experiment and for 20 s (assisted by mechanical stirring of the rotating electrode) after each stripping chronopotentiometry (SCP) measurement. Measurements were made for a range of deposition potentials, from the foot to the plateau of the SSCP wave, i.e., from −1.25 to −1.00 for Zn(II), from 0.85 to −0.60 V for Cd(II), and from −0.70 to −0.40 V for Pb(II). The free metal ion concentration was determined by the AGNES-SCP according to the procedure developed by Parat et al. (2011). The measurements were performed by applying a deposition potential E_1 of −1.085, −0.655, and −0.465 V, for Zn(II), Cd(II), and Pb(II), respectively, and for a period of time t_1 ranging between 240 and 300 s. All measurements were carried out at room temperature (21–23°C).

THEORY

The theoretical basis for SCP and its use in SSCP are well-established in the literature. Therefore, the reader is referred to the supporting information and reference (van Leeuwen and Town, 2002) for more details on the theoretical aspects of the technique. The principles and key equations relevant for the present work in brief are evoked here. The SCP measurement comprises two steps. During the first stage, metal ions are accumulated at the electrode by application of a constant deposition potential (E_d) for a given time (t_d). Then, the metal is re-solubilized by imposing a constant oxidizing current (I_s), and the resulting analytical time (τ) is directly proportional to the quantity of total accumulated metal. SSCP waves are obtained from a series of SCP measurements achieved at different E_d and by plotting the data couple (τ, E_d).

Considering the formation of a labile 1:1 metal complex, ML, between the electroactive metal ion M and the ligand L:

$$\begin{array}{l} \mathrm{M} + \mathrm{L} \underset{k_a}{\overset{k_d}{\leftrightarrows}} \mathrm{ML} \\ \downarrow\uparrow \; ne^- \\ \mathrm{M}^0 \end{array} \quad (1)$$

where k_a and k_d are the association and dissociation rate constants, respectively. The system is dynamic at bulk level if the rates for the volume reactions are fast on the experimental time scale, t:

$$k_d t, \quad k'_a t >> 1 \quad (2)$$

where $k'_a = k_a c^*_{L,t}$. For labile complexes, the rates of dissociation/association are sufficiently high relative to the experimental timescale, to maintain full equilibrium between complexed and free metal (van Leeuwen and Town, 2002; Town and van Leeuwen, 2003). Under conditions of sufficiently excess of ligand (as typically used in stripping experiments), k'_a is approximately constant, and we can define $K' = \frac{k'_a}{k'_d} = \frac{c^*_{ML}}{c^*_M} = K c^*_{L,T}$, where K represents the stability constant of ML, and $c^*_{L,T}$ represents the total ligand concentration in the bulk solution (mM).

For Homogeneous and Labile Metal Binding Systems

For a given potential, the deposition current, $I^*_{d,M+L}$, originating from reduction of the metal ion of interest is given by:

$$I^*_{d,M+L} = \frac{nFA\bar{D}c^*_{M,T}}{\bar{\delta}} \quad (3)$$

where $c^*_{M,T}$ is the total metal concentration in the bulk solution (mM), A is the electrode surface area, $\overline{D}$ is the mean diffusion coefficient of the metal ion ($m^2\ s^{-1}$) given by:

$$\overline{D} = \frac{D_M c^*_M + D_{ML} c^*_{ML}}{c^*_{M,T}} \quad (4)$$

and $\overline{\delta}$(m) is the thickness of the diffusion layer, which is expressed by, for a RDE (Levich, 1962):

$$\overline{\delta} = 1.61\, \overline{D}^{1/3} \omega^{-1/2} \nu^{1/6} \quad (5)$$

The characteristic time constant for the deposition process τ_d (s) for a mercury drop or film electrode is defined by:

$$\tau_d = \frac{V_{Hg}\overline{\delta}}{A\overline{D}(1+K')\theta} \quad (6)$$

where θ is the free metal surface concentration ratio for a given deposition potential, and V_{Hg} (m^3) is the volume of the mercury electrode.

Then, the equation for the SSCP wave for a fully labile complex ML, τ, is given by:

$$\tau = \frac{I^*_{d,M+L}\tau_d}{I_S}\left[1 - \exp\left(\frac{t_d}{\tau_d}\right)\right] \quad (7)$$

Thermodynamic complex stability constants, K', can be retrieved from the shift in the half-wave deposition potential, $\Delta E_{d,1/2}$ between the SSCP curve with metal only and the one after addition of ligands (DeFord and Hume, 1951):

$$\ln\left(1+K'\right) = -\left(\frac{nF}{RT}\right)\Delta E_{d,1/2} - \ln\left(\frac{\tau^*_{M+L}}{\tau^*_M}\right) \quad (8)$$

where τ^*_M and τ^*_{M+L} are the limiting wave heights in the absence and in the presence of ligands, respectively. R is the gas constant, F is the Faraday constant, n is the number of electrons involved in the reduction/oxidation processes, and T is the temperature.

For Heterogeneous Metal Binding Systems

SSCP is also able to provide an evaluation of the chemical heterogeneity through the changing slope of the SSCP wave. For heterogeneous ligands systems, constructing SSCP curves involves also probing a range of metal complexes with various stability constants along the slope of the wave. At the foot of the wave, the weaker metal complexes dissociate to release the free metal toward the electrode, whereas by going closer to the top of the wave, the stronger ones start to contribute to the electrochemical signal. As a result, the SSCP wave is more elongated regarding the homogeneous case, and the extent of the spreading out of the wave reflects the degree of heterogeneity, as can be observed for the metal/humic acid curves in Pinheiro et al. (2020a).

Wave Analysis in Heterogeneous Metal Binding Systems and Computation of $c_M(0,t_d)$ and $c_{ML}(0,t_d)$ at the Electrode Surface

The concentrations $c_M(0,t_d)$ and $c_{ML}(0,t_d)$ are determined for every experimental point of the SSCP curves in the region of the slope portion (Pinheiro et al., 2020a).

As detailed in Serrano et al. (2007), the free metal ion concentration at the electrode surface can be evaluated by coupling the amount of reduced metal accumulated in the electrode together with the Nernst equation. Under the conditions where a RDE is used, the equation becomes (Pinheiro et al., 2020a):

$$c^0_M = c_M(0,t_d) = u_{1/2} c^*_{T,M} \frac{\tau}{\tau^*_M} \exp\left(\frac{nF}{RT}\left(E_d - E^M_{d,1/2}\right)\right) \quad (9)$$

where $u_{1/2}$ is 1.5936 (Rocha et al., 2015), and $E^M_{d,1/2}$ is the deposition half-wave potential in the system with only metal.

The determination of $c_{ML}(0,t_d)$ arises from the balance of the arriving flux of metal species at the electrode times the electrode area with the time variation of the accumulated number of moles, which gives the following differential equation:

$$c^0_{ML} = c_{ML}(0,t_d) = c^*_{ML} - \frac{dc_M(0,\zeta)}{d\zeta} + \frac{c^*_M - c^0_M}{\varepsilon^{2/3}} \quad (10)$$

In this expression, ε corresponds to the coefficient diffusion ratio $\frac{D_{ML}}{D_M}$, and ζ stands for a new variable:

$$\zeta = \frac{\varepsilon^{2/3} u_{1/2} t}{t_d} \exp\left(\frac{nF}{RT}\left(E_d - E_{d,1/2}\right)\right) \quad (11)$$

The total metal concentration at the electrode surface $c^0_{M,T}$ is thus given by the sum of c^0_{ML} and c^0_M. Along the SSCP wave, the $c^0_{M,T}$ varies from the bulk value ($c^*_{M,T}$) in the very beginning of the wave to very close to zero in the plateau. Since the total ligand concentration is in excess over the total metal, investigating the individual points along the wave is analogous to performing a bulk metal titration at fixed ligand concentration.

In Equation (10), the bulk free metal ion concentration c^*_M is experimentally determined using the AGNES technique for which the theoretical and experimental details are recalled in the supporting information.

RESULTS

To investigate qualitatively the binding heterogeneity from the SSCP waves, two normalization operations are needed. First, each point of the SSCP wave (τ) is divided by its limiting value (τ^*), thus obtaining a dimensionless y-axis (τ^{norm}) normalizing the differences in transport (diffusion coefficients of the different species) and total metal concentrations. Then, the so-obtained τ^{norm} in the presence of ligand is subtracted point by point from the metal only calibration yielding the potential difference ($\Delta E = E_{d,tit} - E_{d,cal}$). This procedure normalizes the

potential shift regarding the different metal standard potential reductions, thus allowing the comparison of the three metals in the x-axis.

Due to the experimental errors, it is necessary to ignore at least the points below 0.05 and above 0.95 in the y-axis after normalization (Pinheiro et al., 2020a). Nevertheless, it was observed that in some cases, it is required to neglect more points due to the influence of point scattering in the derivative computation (Equation 10).

Evaluation of the Heterogeneity for the Different Metal Ions

The results obtained are presented as raw SSCP waves (A; τ vs. E_d) and double normalized curves (B; τ^{norm} vs $E_{d,tit}$-$E_{d,cal}$). Each figure contains the information corresponding to a daily experiment comprising a pH titration (three different pH values) at a fixed ionic strength for a metal ion in the presence of nanoparticles. This originates 18 figures corresponding to three metals, three ionic strengths, and two particle sizes. **Figures 1–3** presented in this section show the results for Zn, Cd, and Pb in the presence of the TM40 nanoparticle at 10 mM $NaNO_3$, whereas the other 15 double normalized curves can be found in **Supplementary Figure 1**.

As described in the theoretical section, the heterogeneity of the metal binding system modifies the slope of the experimental SSCP waves (left side of **Figures 1–3**) as compared with the analytical simulation of the homogeneous case (lines) based on the equilibrium bulk situation measured by AGNES. In **Figure 3A**, a deviation can be observed between the experimental calibration points and the theoretically simulated line. In over 18 experiments performed, we have seen these phenomena only twice; thus, the theoretical simulations were used in our calculations. Similar deviations have been described for pseudopolarograms by Omanović and Branica (2003); hence, a correction reported therein is necessary if a majority of the calibrations present this shape.

The B panels of the three figures give a double normalized representation of the impact of metal binding heterogeneity on SSCP curves as explained above. A homogeneous case is represented by a perfectly vertical alignment, whereas a heterogeneous situation is materialized by a progressive shifting along the y-axis. An increase of the shift in the x-axis with pH indicates a greater binding strength (K') along the lines of the DeFord–Hume theory (DeFord and Hume, 1951).

In some situations, such as the pH 5.5 Pb case, and several other examples in **Supplementary Figure 1**, one observes two parts in the curve, initially showing a homogeneous tendency (vertical), followed by a marked inclination at higher $E_{d,tit}$–$E_{d,cal}$ values.

The three metal ions tested show a markedly different behavior. For Zn, the metal interaction with SiO_2 can be considered as quite homogeneous, with a minor deviation as compared with the fully homogeneous case. In contrast, the lead binding to silica nanoparticle shows a significant heterogeneity, whereas cadmium case corresponds to a slightly heterogeneous system with abundant examples of the two-part curves.

Impact of pH and Ionic Strengths on the Heterogeneity

The shifting operating at the x-axis upon increase of pH or decrease of ionic strength is due to the higher binding affinity of the metal for the silica particle owing to the increased number of binding sites by deprotonation or the lower screening effect of the electrolyte, respectively. The expected increase of binding strength with pH is observed for all metal cases. In the case of Pb, the heterogeneity degree also increases with pH (from 5.5 to 6.5) as depicted in **Figure 3B** for Ludox TM40 and **Supplementary Figure 1** for Ludox LS30 at 10 mM ionic strength. This pH dependency of the heterogeneity is still observed although less evident for the higher ionic strengths. For Cd (**Figure 2B** and **Supplementary Figure 1**) this increase in heterogeneity with pH cannot be observed clearly in the double normalized figures, probably due to experimental errors in the measurement coupled with the smaller heterogeneity evidenced by these cations. Since Zn shows an almost homogeneous behavior, it was not expected to observe significant variations of heterogeneity with pH for this metal. Increasing the ionic strength does not affect the concentration of deprotonated groups in the nanoparticles, but: (i) it does provide a greater screening effect of the particle charges, thus decreasing the electrostatic ion accumulation, and (ii) it impacts the activity coefficients of both ligand and metal ions, thus reducing the covalent binding.

Influence of the Particle Size on the Heterogeneity

The Ludox LS30 and TM40 nanoparticles are chemically identical, being only different in their physical characteristics as presented in **Table 1** (supplier information).

In this section, we analyze only the Pb results since this is the metal ion that presents the highest binding heterogeneity. **Figure 5** shows the double normalized curves at 10 mM ionic strength for both nanoparticles at pH 5.5, 6.0, and 6.5. We can observe that there is a difference in the x-axis at the low τ^{norm} where the TM40 values are more negative than the LS30 ones. This indicates a higher TM40 binding strength in the bulk, which is confirmed by the stability constant values presented in **Table 2**.

At pH 5.5, results suggest that the LS30 is more heterogeneous than the TM40; however, for the higher pH values, this representation does not show meaningful differences. The double normalized representation is not able to discriminate between the Pb/Ludox particle binding heterogeneities; hence, it is necessary to start using the more quantitative full wave analysis to achieve a better discrimination. **Figure 6** shows the result of this analysis for the same points presented in **Figure 5**. One of the best ways to investigate heterogeneity from the full wave analysis results is to draw the electrode surface stability constant $K^{0\prime}$ ($= c^0_{ML}/c^0_M$) computed from Equations (9, 10) as function of the total metal surface concentration, $c^0_{M,T}$, and compare this with the bulk equilibrium parameter (K'_{bulk}). A homogeneous

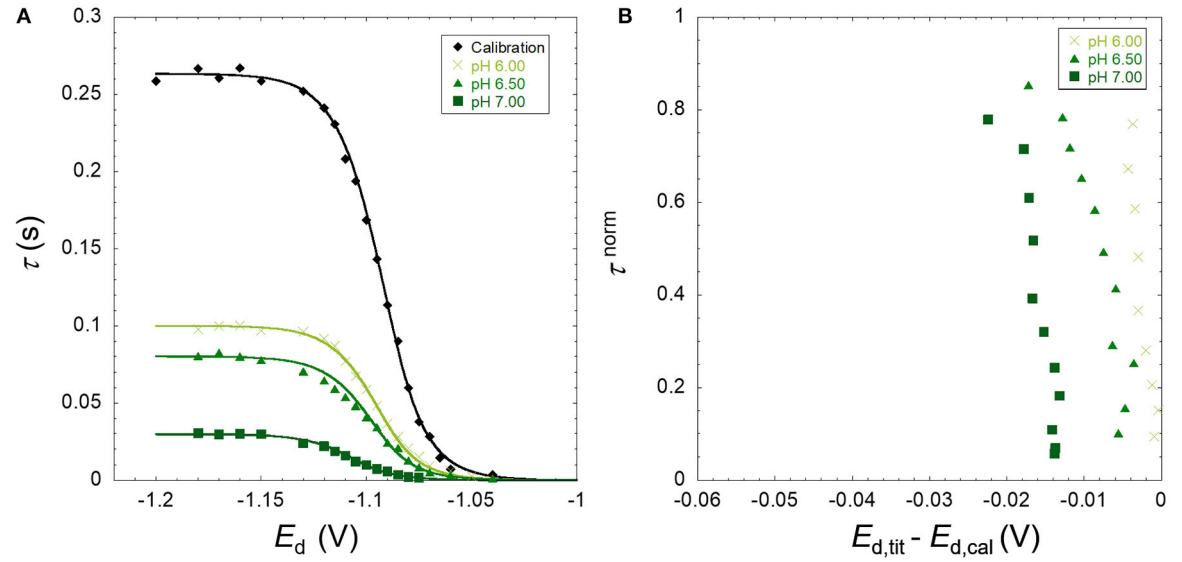

FIGURE 1 | (A) Experimental SSCP waves for the zinc only at pH 4 (calibration) and in the presence of SiO_2 nanoparticles (TM40) obtained at 10 mM $NaNO_3$, pH 6.00, 6.50, and 7.00 for a total Zn concentration of 5×10^{-4} mM and particle concentration of 0.3 wt%. The lines represent the analytical simulation of the experimental results as described in the theoretical section. **(B)** The normalized analytical times τ^{norm} derived from the SSCP waves plotted against $E_{d,tit} - E_{d,cal}$.

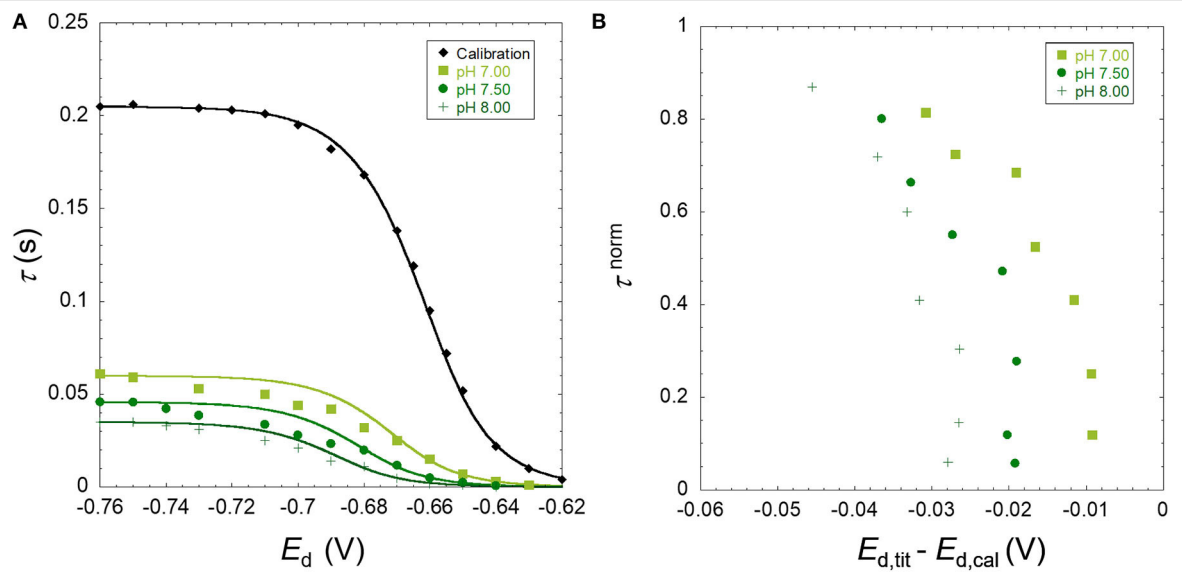

FIGURE 2 | (A) Experimental SSCP waves for the cadmium only at pH 4 (calibration) and in the presence of SiO_2 nanoparticles (TM40) obtained at 10 mM $NaNO_3$, pH 7.00, 7.50, and 8.00 for a total Cd concentration of 5×10^{-4} mM and particle concentration of 0.3 wt%. The lines represent the analytical simulation of the experimental results as described in the theoretical section. **(B)** The normalized analytical times τ^{norm} derived from the SSCP waves plotted against $E_{d,tit} - E_{d,cal}$.

system will have a constant K', whether in the surface or bulk, whereas a heterogeneous system will show a $K^{0\prime}$ decrease with increasing $c^0_{M,T}$.

Figure 6A (TM40 and LS30) depicts a situation where both systems have a pronounced heterogeneity. Since they also have quite different bulk stability constants, it is interesting to normalize these curves by their respective K'_{bulk} (**Figure 6B**). By doing so, we observe that the relative heterogeneity of the two systems is clearly different. Pb/TM40 presents a quasi-homogenous behavior between 5 and 3×10^{-4} mM, and below this value, it becomes strongly heterogeneous, whereas Pb/LS30 depicts a strong relative heterogeneity in all the concentration range, albeit with significantly more experimental point scattering.

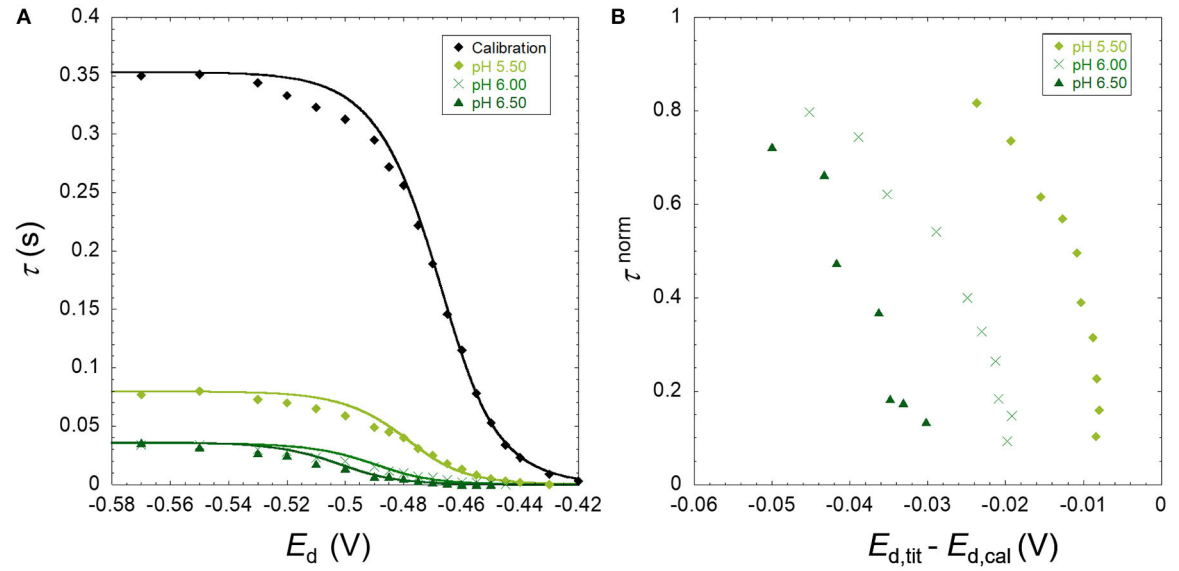

FIGURE 3 | (A) Experimental SSCP waves for the lead only at pH 4 (calibration) and in the presence of SiO_2 nanoparticles (TM40) obtained at 10 mM $NaNO_3$, pH 5.50, 6.00, and 6.50 for a total Pb concentration of 5×10^{-4} mM and particle concentration of 0.3 wt%. The lines represent the analytical simulation of the experimental results as described in the theoretical section. **(B)** The normalized analytical times τ^{norm} derived from the SSCP waves plotted against $E_{d,tit} - E_{d,cal}$.

TABLE 1 | Physical characteristics of the Ludox nanoparticles.

Particle	Radius (nm)	Surface area (BET; $m^2\ g^{-1}$)	Density ($g\ cm^3$)	Particle number (particle g^{-1})
LS30	8	215	1.2	3.86×10^{17}
TM40	17	140	1.3	3.74×10^{16}

TABLE 2 | Deprotonated ligand concentrations for the Ludox nanoparticles at 10 mM ionic strength and respective bulk Pb thermodynamic binding constants computed from AGNES results.

	Ludox LS30			Ludox TM40		
$[SiO_2]$ (w/w)	**0.10%**			**0.30%**		
pH	5.50	6.00	6.50	5.50	6.00	6.50
$c_{L,T}$ (mM)*	0.013	0.020	0.030	0.037	0.052	0.070
K'_{bulk}	2.25	5.78	15.92	8.78	52.81	146.8
log K^{**}_{bulk}	2.25	2.45	2.72	2.38	3.01	3.32

Values for Ludox LS30 are from Goveia et al. (2011), and values for TM40 are our own unpublished results.
$^{**}K_{bulk}$ in mM equivalent to mol m^{-3}.

DISCUSSION

Methodological Aspects of Heterogeneity Analysis

One of the main advantages of electroanalytical techniques, namely, SSCP, is the ability to scan the low surface coverages that are relevant in environmental systems, where the ligands are usually in excess over the metal ions. In this work, the highest degree of coverage is 4% of deprotonated sites for Pb in the presence of LS30 at pH 5.5- and 10-mM ionic strengths.

A fast and informative way of obtaining direct qualitative information at low surface coverage on the system heterogeneity is to apply the double normalization of the SSCP wave (**Figures 1–5**). However, like the Γ parameter of the Freundlich isotherm, this normalized description does not discriminate the electrostatic and chemical binding contributions.

This qualitative approach can be improved by applying a quantitative full SSCP wave analysis that allows a better interpretation of the experimental data as exemplified by the study of the effect of particle size on the heterogeneity in **Figure 6** than the qualitative equivalent in **Figure 5**.

To advance further into the differentiation of the electrostatic and covalent contributions, it is necessary to interpret the experimental data by fitting the results with pertinent physicochemical models. In a future work, our goal will be to obtain the electrostatic properties of the nanoparticle from protolytic titrations at different ionic strengths. Hence, to determine the electrostatic descriptors, an electrostatic model will be used, namely, the one recently proposed by our group (Pinheiro et al., 2020b). This model applies a Poisson–Boltzmann equation considering particles with an impermeable core and a permeable shell, thus taking into account the permeable gel-like layer present in the SiO_2/solution interphase (Allison, 2009). Then, the covalent part of the binding will be initially described using a surface complexation model comprising the contribution of mono and bidentate silanol groups and, if necessary, a contribution of stronger aluminum hydroxide groups originating from the aluminum impurity present in the SiO_2 nanoparticles (Bergna and Roberts, 2005).

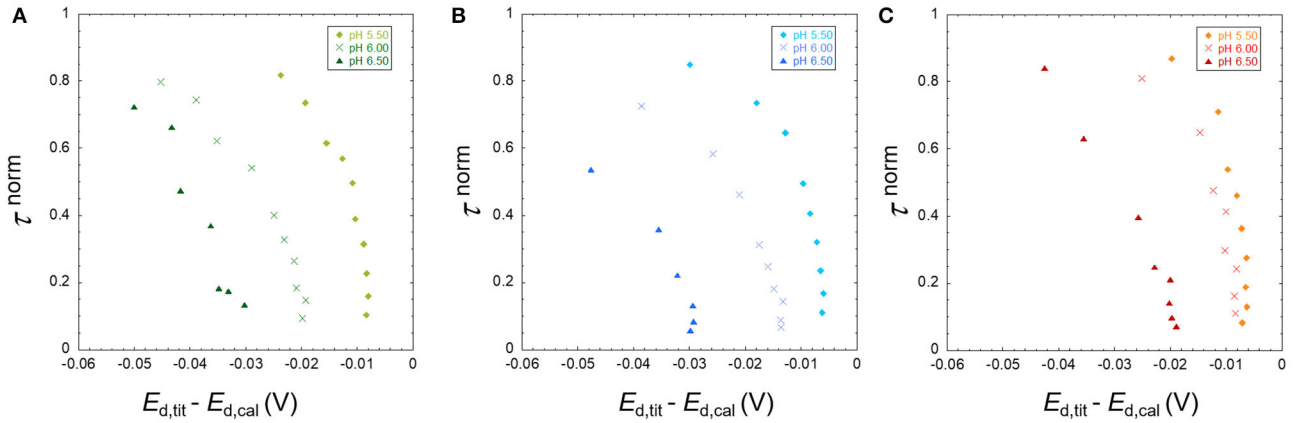

FIGURE 4 | The normalized analytical times τ^{norm} derived from the SSCP waves of Pb in the presence of TM40 silica nanoparticles plotted against $E_{d,tit}$ –$E_{d,cal}$ for the three pH 5.50, 6.00, and 6.50 for a total Pb concentration of 5×10^{-4} mM and particle concentration of 0.3 wt%, at ionic strengths of 10 **(A)**, 30 **(B)**, and 100 mM **(C)**.

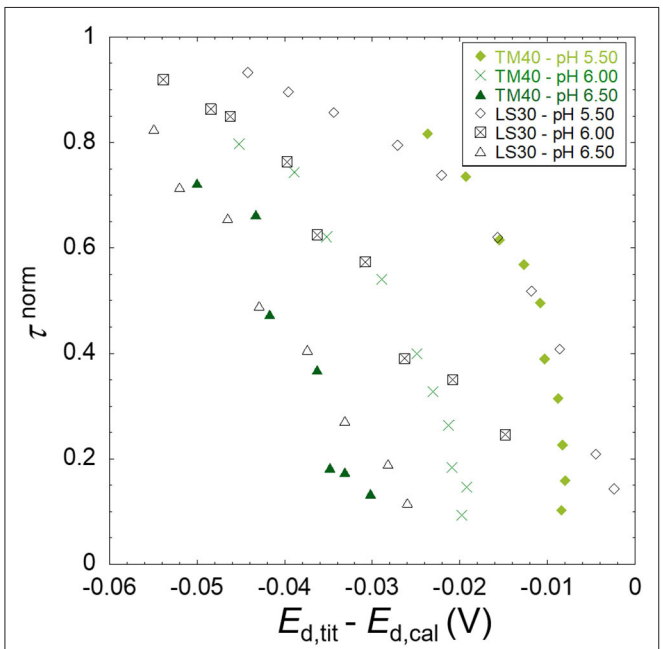

FIGURE 5 | Comparison between the normalized transition times τ^{norm} derived from the SSCP waves of 5×10^{-4} mM Pb in the presence of TM40 (0.3 wt%) and LS30 (0.1 wt%) SiO_2 nanoparticles plotted against $E_{d,tit}$ –$E_{d,cal}$ for the three pH 5.50, 6.00, and 6.50 at ionic strength of 10 mM.

Evaluation of the Heterogeneity for the Different Metal Ions

There is a striking difference between the Pb (**Figure 3**) and Zn (**Figure 1**) binding heterogeneities with the SiO_2 nanoparticles. Pb shows a significant heterogeneity in all conditions, whereas Zn is almost homogeneous at lower pH and higher ionic strengths, showing a small heterogeneity at higher pH and lower ionic strengths.

The Pb heterogeneity starts at lower pH, already evident at pH 5.5, where there are less deprotonated groups ($c_{L,T}$) available for covalent binding (**Table 2**) as well as a smaller electrostatic potential in the nanoparticle. No binding of Zn and Cd was observed in at this pH during the preliminary experiments.

One possible contribution to the Pb heterogeneity is given by the formation of bidentate complexes with the surface silanol groups. Schindler et al. (1976) reported values of log β_2 of −17.23 and log K_1 of −7.75 for the bidentate and monodentate complexes of Pb, whereas for Cd, only the monodentate complex is formed presenting a log K_1 of −10.4, all values being measured at $I = 1{,}000$ mM.

The binding heterogeneity of the SiO_2 nanoparticles is closer to the one observed in environmental mineral particles, such as clays or iron oxyhydroxides, than the strong chemical heterogeneity characteristic of the natural organic matter. In the case of metal association to clay minerals as reported by Rotureau (2014), cadmium displays homogeneous binding dominated by the formation of ion-pair complexes, whereas lead shows a relatively weak chemical heterogeneity, suggesting the formation of edge inner-sphere surface complexes.

Metal/humic matter systems are heterogeneous in nature due to the variety of chemical binding sites present in these colloids, resulting in values of Γ of 0.9–0.8 for Cd and 0.7–0.5 for Pb (Town et al., 2019) depending on the type of organic matter (fulvic, humic, NOM, etc.). In the double normalized curves, this would produce well-spread points with a linear dependency in the x-axis without vertical portions. The mixed curves observed for most of the Cd and some Pb samples are peculiar since it evidences a system that is heterogeneous for low metal-to-ligand ratios and becomes homogeneous for higher degrees of coverage.

Considering the chemically homogeneous nature of the particles, the experimental evidence presented suggests that Pb binding is predominantly covalent, the Zn binding is predominantly electrostatic (low heterogeneity), and the Cd binding is a combination of the two. To quantitatively clarify this aspect, we will carry out the modeling studies described

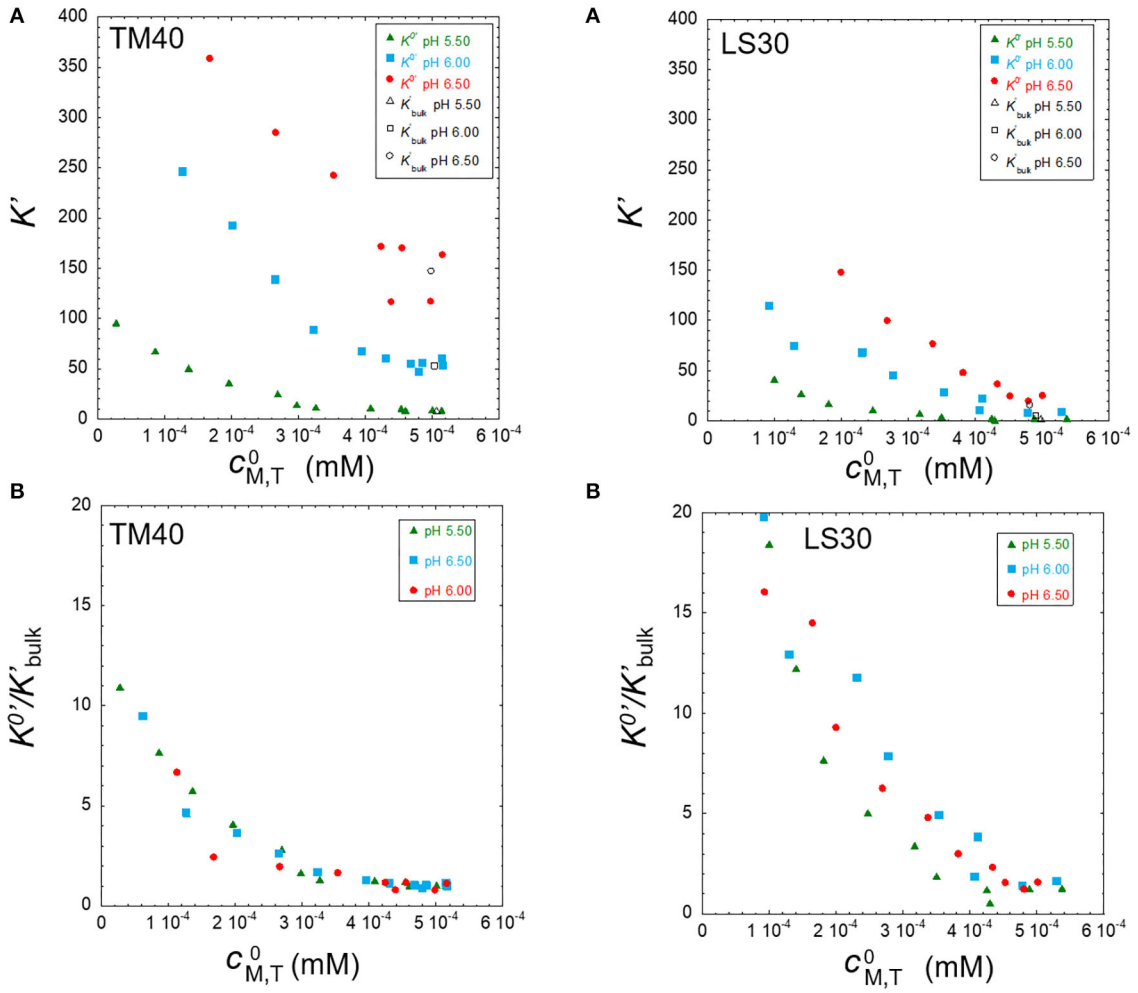

FIGURE 6 | Stability constants at the electrode surface ($K^{0\prime}$) and bulk solution (K'_{bulk}) **(A)** and $K^{0\prime}$ normalized by K'_{bulk} **(B)** as function of surface total metal concentration for 5×10^{-4} mM Pb in the presence of TM40 (0.3 wt%) and LS30 (0.1 wt%) silica particles for the three pH 5.50, 6.00, and 6.50 at ionic strength of 10 mM.

in the previous section on the data presented in this work as future work.

Evaluation of the Heterogeneity for the Different Nanoparticle Sizes

When comparing the metal binding properties of nanoparticles of different sizes, the key aspect is to consider all the factors that may influence the complexation. In this case, one must consider mass particle concentration, the number of particles, their specific surface area, the permeable shell volume, and the total concentration of deprotonated binding groups as function of pH, as well as the associated surface and shell volume charge densities and potential profile in the shell volume.

Table 3 shows the values for both silica nanoparticles in the measured solutions computed using the manufacturer data. For the LS30 shell volume, we used the values given by Allison (2009) of 9 nm effective particle radius and 1.7 nm shell thickness computed at 10 mM ionic strength. In the absence of measured data for the TM40, we assumed, as a first order approximation, the same increase in radius (+1 nm) and the same shell thickness, i.e., 18 nm radius and 1.7 nm shell thickness.

The physicochemical parameters presented in **Table 3** suggest that both the Pb binding and heterogeneity would be larger for the TM40 than for the LS30. As commented in the results, **Figure 6A** shows that the bulk stability constants are effectively larger for the TM40; nonetheless, the binding heterogeneity is surprisingly larger in the case of the LS30. The normalization by the bulk stability constant, K'_{bulk}, evidenced a homogeneous/heterogeneous behavior for the TM40 and a predominantly heterogeneous character for the LS30.

Therefore, the parameters given in **Table 3** do not explain the larger heterogeneity of the LS30. One possible origin of the heterogeneity difference is the likely presence of aluminum impurities (Bergna and Roberts, 2005). Since the ratio area/volume is larger for smaller particles, it is likely that more Al impurities are present in the surface/shell volume of the LS30 than of the TM40. Another hypothesis for the difference in heterogeneity between the particles arises from the

TABLE 3 | Comparison of nanoparticles properties in the measured solution.

	Ludox LS30			Ludox TM40		
$[SiO_2]$ (w/w)	0.10%			0.30%		
Particle concentration (particle m^{-3})	4.28×10^{20}			1.15×10^{20}		
Surface area (m^2 m^{-3})	2.38×10^{5}			4.32×10^{5}		
Shell volume (m^3 m^{-3})	6.09×10^{-4}			$7.26 \times 10^{-4(1)}$		
pH	5.50	6.00	6.50	5.50	6.00	6.50
$c_{L,T}$ (mM)*	0.013	0.020	0.030	0.037	0.052	0.070
Surface charge density (mol m^{-2})	5.34×10^{-8}	8.51×10^{-8}	12.7×10^{-8}	8.53×10^{-8}	12.0×10^{-8}	16.3×10^{-8}
Shell volume charge density (mM)	20.87	33.28	49.68	50.80	71.15	97.00

**Values for Ludox LS30 are from Goveia et al. (2011), and values for TM40 are our own unpublished results.*
(1) Value computed by analogy with the Ludox LS30.

non-homogeneous charge distribution. Allison (2009) suggested that 2/3 of the charge lies in the core surface and 1/3 in the shell volume for the LS30. In this work, we approximated the TM40 shell volume by analogy with the smaller particle, which needs to be experimentally verified. On that point, we previously demonstrated the strong influence of the shell structure and ensuing charge profiles on the metal binding heterogeneity with a different core/shell nanoparticle system (Rotureau et al., 2016).

To tackle this new problem, it is necessary to carry out electrokinetic experiments, in addition to the protolytic titrations, of the two nanoparticles to be able to reconstruct the charge distribution between core surface and shell volume as well as the potential profile in the shell/solution interface, as described by Duval et al. (2005) for the humic substances. This procedure will allow us to obtain a proper electrostatic description of these nanoparticles, prior to application of a surface complexation model, as referred in the Methodological Aspects of Heterogeneity Analysis section.

DATA AVAILABILITY STATEMENT

The original contributions presented in the study are included in the article/**Supplementary Material**, further inquiries can be directed to the corresponding author/s.

AUTHOR CONTRIBUTIONS

ER: conceptualization, methodology, writing—original draft, and review & editing. LR: investigation, data curation, formal analysis, writing—original draft, and writing-review & editing. DG: investigation and writing—review & editing. NA: investigation and writing—review & editing. JP: conceptualization, methodology, formal analysis, data curation, writing—original draft, and review & editing. All authors contributed to the article and approved the submitted version.

FUNDING

JP, LR, and NA acknowledge the support of the French national research agency (ANR; Blanc International II-SIMI 6-Système Terre, environnement, risques SPECIES projet Mesure *in situ* de la speciation des métaux trace-SPECIES) and of the Portuguese national funding agency for science, research, and technology (FCT-ANR/AAG-MAA/0065/2012, SPECIES). ER acknowledges the support of the French INSU/EC2CO program for the 2017–2019 period.

ACKNOWLEDGMENTS

DG acknowledges Conselho Nacional de Desenvolvimento Científico e Tecnologico (CNPq) for two visiting scholarships to the University of Algarve in 2011 and 2012.

SUPPLEMENTARY MATERIAL

The Supplementary Material for this article can be found online at: https://www.frontiersin.org/articles/10.3389/fchem.2020.614574/full#supplementary-material

REFERENCES

Allison, S. (2009). Electrokinetic modeling of metal oxides. *J. Colloid Interface Sci.* 332, 1–10. doi: 10.1016/j.jcis.2008.12.004

Bergna, H. E., and Roberts, W. O. (2005). *Colloidal Silica: Fundamentals and Applications*. New York, NY: CRC Press.

Buffle, J. (1988). *Complexation Reactions in Aquatic Systems: An Analytical Approach*. Chichester: E. Horwood.

DeFord, D. D., and Hume, D. N. (1951). The determination of consecutive formation constants of complex ions from polarographic data. *J. Am. Chem. Soc.* 73, 5321–5322. doi: 10.1021/ja01155a093

Duval, J. F. L., and Gaboriaud, F. (2010). Progress in electrohydrodynamics of soft microbial particle interphases. *Curr. Opin. Colloid Interface Sci.* 15, 184–195. doi: 10.1016/j.cocis.2009.12.002

Duval, J. F. L., Wilkinson, K., Van Leeuwen, H., and Buffle, J. (2005). Humic substances are soft and permeable: evidence from their electrophoretic mobilities RID H-6421-2011. *Environ. Sci. Technol.* 39, 6435–6445. doi: 10.1021/es050082x

Dzombak, D. A., and Morel, F. M. M. (1990). *Surface Complexation Modeling: Hydrous Ferric Oxide*. New York, NY: John Wiley & Sons.

Filella, M., and Town, R. M. (2001). Heterogeneity and lability of Pb(II) complexation by humic substances: practical interpretation

tools. *Fresenius J. Anal. Chem.* 370, 413–418. doi: 10.1007/s002160100812

Goveia, D., Pinheiro, J. P., Milkova, V., Rosa, A. H., and van Leeuwen, H. P. (2011). Dynamics and heterogeneity of Pb(II) binding by SiO_2 nanoparticles in an aqueous dispersion. *Langmuir* 27, 7877–7883. doi: 10.1021/la2008182

Hiemstra, T., and Van Riemsdijk, W. H. (1996). A surface structural approach to ion adsorption: the charge distribution (CD) model. *J. Colloid Interface Sci.* 179, 488–508. doi: 10.1006/jcis.1996.0242

Kinniburgh, D. G., Milne, C. J., Benedetti, M. F., Pinheiro, J. P., Filius, J., Koopal, L. K., et al. (1996). Metal ion binding by humic acid: application of the NICA-donnan model. *Environ. Sci. Technol.* 30, 1687–1698. doi: 10.1021/es950695h

Lead, J. R., and Wilkinson, K. J. (2006). Aquatic colloids and nanoparticles: current knowledge and future trends. *Environ. Chem.* 3, 159–171. doi: 10.1071/EN06025

Levich, V. G. (1962). *Physicochemical Hydrodynamics.* Englewood Cliffs, NJ: Prentice-Hall.

Milne, C. J., Kinniburgh, D. G., van Riemsdijk, W. H., and Tipping, E. (2003). Generic NICA–donnan model parameters for metal-ion binding by humic substances. *Environ. Sci. Technol.* 37, 958–971. doi: 10.1021/es0258879

Monterroso, S. C. C., Carapuca, H. M., Simao, J. E. J., and Duarte, A. C. (2004). Optimisation of mercury film deposition on glassy carbon electrodes: evaluation of the combined effects of pH, thiocyanate ion and deposition potential. *Anal. Chim. Acta* 503, 203–212. doi: 10.1016/j.aca.2003.10.034

Omanović, D., and Branica, M. (2003). Pseudopolarography of trace metals: Part I. The automatic ASV measurements of reversible electrode reactions. *J. Electroanal. Chem.* 543, 83–92. doi: 10.1016/S0022-0728(02)01484-5

Parat, C., Schneider, A., Castetbon, A., and Potin-Gautier, M. (2011). Determination of trace metal speciation parameters by using screen-printed electrodes in stripping chronopotentiometry without deaerating. *Anal. Chim. Acta* 688, 156–162. doi: 10.1016/j.aca.2010.12.034

Pinheiro, J. P., Galceran, J., Rotureau, E., Companys, E., and Puy, J. (2020a). Full wave analysis of stripping chronopotentiometry at scanned deposition potential (SSCP): obtaining binding curves in labile heterogeneous macromolecular systems for any metal-to-ligand ratio. *J. Electroanal. Chem.* 873:114436. doi: 10.1016/j.jelechem.2020.114436

Pinheiro, J. P., Rotureau, E., and Duval, J. F. L. (2020b). Addressing the electrostatic component of protons binding to aquatic nanoparticles beyond the non-ideal competitive adsorption (NICA)-donnan level: theory and application to analysis of proton titration data for humic matter. *J. Colloid Interface Sci.* 583, 642–651. doi: 10.1016/j.jcis.2020.09.059

Riemsdijk, W. H. V., and Koopal, L. K. (1992). Ion binding by natural heterogeneous colloids. *Environ. Part.* 1, 455–496. doi: 10.1201/9780429286223-12

Rocha, L. S., Botero, W. G., Alves, N. G., Moreira, J. A., da Costa, A. M. R., and Pinheiro, J. P. (2015). Ligand size polydispersity effect on SSCP signal interpretation. *Electrochim. Acta* 166, 395–402. doi: 10.1016/j.electacta.2015.03.035

Rocha, L. S., Pinheiro, J. P., and Carapuça, H. M. (2007). Evaluation of nanometer thick mercury film electrodes for stripping chronopotentiometry. *J. Electroanal. Chem.* 610, 37–45. doi: 10.1016/j.jelechem.2007.06.018

Rotureau, E. (2014). Analysis of metal speciation dynamics in clay minerals dispersion by stripping chronopotentiometry techniques. *Colloids Surf. A Physicochem. Eng. Asp.* 441, 291–297. doi: 10.1016/j.colsurfa.2013.09.006

Rotureau, E., Waldvogel, Y., Pinheiro, J. P., Farinha, J. P. S., Bihannic, I., Présent, R. M., et al. (2016). Structural effects of soft nanoparticulate ligands on trace metal complexation thermodynamics. *Phys. Chem. Chem. Phys.* 18, 31711–31724. doi: 10.1039/C6CP06880D

Schindler, P. W., Fürst, B., Dick, R., and Wolf, P. U. (1976). Ligand properties of surface silanol groups. I. surface complex formation with Fe3+, Cu2+, Cd2+, and Pb2+. *J. Colloid Interface Sci.* 55, 469–475. doi: 10.1016/0021-9797(76)90057-6

Serrano, N., Díaz-Cruz, J. M., Ariño, C., and Esteban, M. (2007). Stripping chronopotentiometry in environmental analysis. *Electroanalysis* 19, 2039–2049. doi: 10.1002/elan.200703956

Škvarla, J., and Škvarla, J. (2017). A swellable polyelectrolyte gel-like layer on the surface of hydrous metal oxides in simple electrolyte solutions: hematite vs. silica colloids. *Colloids Surf. A Physicochem. Eng. Asp.* 513, 463–467. doi: 10.1016/j.colsurfa.2016.11.018

Tipping, E. (1994). WHAMC—A chemical equilibrium model and computer code for waters, sediments, and soils incorporating a discrete site/electrostatic model of ion-binding by humic substances. *Comput. Geosci.* 20, 973–1023. doi: 10.1016/0098-3004(94)90038-8

Town, R. M. (2008). Metal binding by heterogeneous ligands: kinetic master curves from SSCP waves. *Environ. Sci. Technol.* 42, 4014–4021. doi: 10.1021/es703236b

Town, R. M., and van Leeuwen, H. P. (2003). Stripping chronopotentiometry at scanned deposition potential (SSCP): Part 2. Determination of metal ion speciation parameters. *J. Electroanal. Chem.* 541, 51–65. doi: 10.1016/S0022-0728(02)01314-1

Town, R. M., and van Leeuwen, H. P. (2004). Dynamic speciation analysis of heterogeneous metal complexes with natural ligands by stripping chronopotentiometry at scanned deposition potential(SSCP). *Aust. J. Chem.* 57, 983–992. doi: 10.1071/CH04088

Town, R. M., van Leeuwen, H. P., and Duval, J. F. L. (2019). Rigorous physicochemical framework for metal ion binding by aqueous nanoparticulate humic substances: implications for speciation modeling by the NICA-donnan and WHAM codes. *Environ. Sci. Technol.* 53, 8516–8532. doi: 10.1021/acs.est.9b00624

van Leeuwen, H., and Town, R. (2002). Stripping chronopotentiometry at scanned deposition potential (SSCP). Part 1. fundamental features. *J. Electroanal. Chem.* 536, 129–140. doi: 10.1016/S0022-0728(02)01212-3

Conflict of Interest: The authors declare that the research was conducted in the absence of any commercial or financial relationships that could be construed as a potential conflict of interest.

frontiers in Chemistry

ORIGINAL RESEARCH
published: 14 January 2021
doi: 10.3389/fchem.2020.626467

Binding Affinity and Driving Forces for the Interaction of Calixarene-Based Micellar Aggregates With Model Antibiotics in Neutral Aqueous Solution

Rossella Migliore[1], *Giuseppe Granata*[2], *Andrea Rivoli*[1], *Grazia Maria Letizia Consoli*[2]* and *Carmelo Sgarlata*[1]*

[1] Dipartimento di Scienze Chimiche, Università Degli Studi di Catania, Catania, Italy, [2] Istituto di Chimica Biomolecolare, Consiglio Nazionale delle Ricerche (CNR), Catania, Italy

The search for novel surfactants or drug delivery systems able to improve the performance of old-generation antibiotics is a topic of great interest. Self-assembling amphiphilic calix[4]arene derivatives provide well-defined nanostructured systems that exhibit promising features for antibiotics delivery. In this work, we investigated the capability of two micellar polycationic calix[4]arene derivatives to recognize and host ofloxacin, chloramphenicol, or tetracycline in neutral aqueous solution. The formation of the nanoaggregates and the host–guest equilibria were examined by nano-isothermal titration calorimetry, dynamic light scattering, and mono- and bi-dimensional NMR. The thermodynamic characterization revealed that the calix[4]arene-based micellar aggregates are able to effectively entrap the model antibiotics and enabled the determination of both the species and the driving forces for the molecular recognition process. Indeed, the formation of the chloramphenicol–micelle adduct was found to be enthalpy driven, whereas entropy drives the formation of the adducts with both ofloxacin and tetracycline. NMR spectra corroborated ITC data about the positioning of the antibiotics in the calixarene nanoaggregates.

Keywords: amphiphilic calixarenes, antibiotics, micelles, drug delivery systems, speciation, isothermal titration calorimetry, NMR, aqueous solution

OPEN ACCESS

Edited by:
Ottavia Giuffrè,
University of Messina, Italy

Reviewed by:
Carmine Gaeta,
University of Salerno, Italy
Andrea Melchior,
University of Udine, Italy

***Correspondence:**
Carmelo Sgarlata
sgarlata@unict.it
Grazia Maria Letizia Consoli
grazia.consoli@icb.cnr.it

Specialty section:
This article was submitted to Analytical Chemistry, a section of the journal Frontiers in Chemistry

Received: *05 November 2020*
Accepted: *04 December 2020*
Published: *14 January 2021*

Citation:
Migliore R, Granata G, Rivoli A, Consoli GML and Sgarlata C (2021) Binding Affinity and Driving Forces for the Interaction of Calixarene-Based Micellar Aggregates With Model Antibiotics in Neutral Aqueous Solution. Front. Chem. 8:626467. doi: 10.3389/fchem.2020.626467

INTRODUCTION

The entrapment of target molecules in drug delivery systems (DDSs) is an emerging approach employed to improve the therapeutic effectiveness of a drug (Patra et al., 2018). A DDS can enhance essential drug properties such as solubility and stability in water and may allow for repurposing existing drugs by identifying new applications (Pushpakom et al., 2019; Dinić et al., 2020). This could be the case of old-generation antibiotics, which could take advantage of suitable nanocarriers for overcoming problems associated with resistance phenomena (Kobayashi and Nakazato, 2020). Indeed, the transport of an antibiotic by a nanocarrier might improve the drug bioavailability and pharmacokinetics, change the mechanism of penetration in resistant bacteria with modified walls, and prevent the inactivation by bacterial enzymes and the clearance by efflux

pumps as well as further causes of antibiotic resistance (Gupta et al., 2019; Lima et al., 2019; Pham et al., 2019; Eleraky et al., 2020).

In the search for novel DDSs, calix[*n*]arene macrocycles, a family of oligomers in which a number *n* of phenolic units are bridged by methylene groups (**Figure 1**), are attracting great attention. The possibility to functionalize the calixarene upper and lower rim with polar and apolar groups has provided a variety of amphiphilic derivatives with appealing assembly and recognition properties, in which the macrocycle cavity can also act as an additional recognition site. A variety of papers has described the potentialities of cationic or anionic calixarene-based micelles, vesicles, solid lipid nanoparticles, nanocapsules, etc. as DDSs (Lee et al., 2004; Consoli et al., 2018a; Wang et al., 2019).

Polycationic calix[4]arene derivatives that self-assemble in nanoaggregates are promising nanocontainers for delivering antibiotics to bacteria due to their ability to establish electrostatic interactions with the negatively charged bacterial membrane (Formosa et al., 2012). Interestingly, it has been reported that the clustering of cationic groups by a calix[4]arene scaffold (Grare et al., 2007) and the assembly of quaternary ammonium salts in nanoaggregates (Lallemand et al., 2012) result in derivatives with higher antibacterial activity and reduced cytotoxicity to eukaryotic cells when compared with monomeric analogs (Mourer et al., 2009) and other known disinfectants (Grare et al., 2010).

Among the polycationic calix[4]arene amphiphiles, CholineC4dod (**Figure 1**), bearing choline groups and dodecyl aliphatic chains at the cavity upper and lower rim, respectively, turned out to be a promising nanocarrier for gene (Rodik et al., 2015) and drug delivery (Di Bari et al., 2016a,b). The micellar CholineC4dod system, in the form of colloidal solution (Granata et al., 2017) and hydrogel (Granata et al., 2020), was successfully used for ocular and skin drug delivery in *in vivo* animal models of uveitis and psoriasis (Filippone et al., 2020). Noteworthy, the presence of choline ligands makes CholineC4dod a promising candidate for the vehiculation of antibiotics into bacterial cells. In addition to generating a polycationic surface, the choline moieties could operate as further points of attack for bacterial cell penetration by binding the choline transporters (BCCT, Betaine-Choline-Carnitine Transporter family) present on the surface of bacteria such as *P. aeruginosa* (Lucchesi et al., 1998; Chen et al., 2010; Malek et al., 2011). With this in mind, we decided

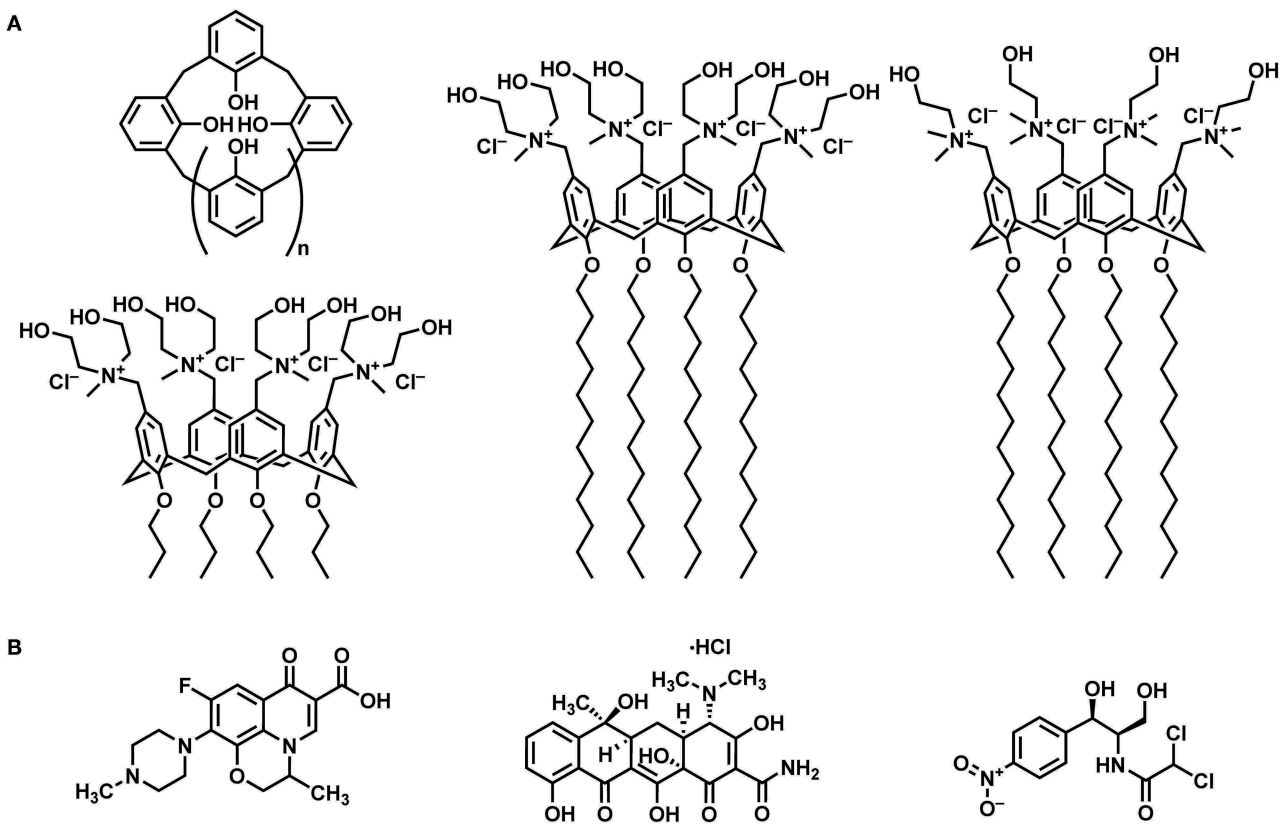

FIGURE 1 | Systems investigated: **(A)** From left to right: schematic representation of a calix[*n*]arene macrocycle, tetra-propoxy-*p*-tetra-(*N,N*-dihydroxyethyl-*N*-methylammonium)-methylene-calix[4]arene (MedeaC4prop), tetra-dodecoxy-*p*-tetra-(*N,N*-dihydroxyethyl-*N*-methylammonium)-methylene-calix[4]arene (MedeaC4dod), and tetra-dodecoxy-*p*-tetra-(*N,N*-dimethyl-*N*-hydroxyethylammonium)-methylene-calix[4]arene (CholineC4dod). **(B)** From left to right: ofloxacin, tetracycline hydrochloride, and chloramphenicol.

to investigate whether the amphiphilic CholineC4dod receptor is able to bind target molecules, such as known antibiotics, by non-covalent interactions in aqueous solution.

The determination of the strength and nature of the interactions of a drug with proper carriers, such as micellar assemblies, is essential for the design of novel medicines as well as for the modification or selection of shuttles for target-oriented drug delivery. However, a quantitative analysis of the species, binding affinity, as well as thermodynamic parameters for the recognition/inclusion of drugs in micelles has rarely been addressed (Bouchemal, 2008; Waters et al., 2012; Huang et al., 2020; Kaur et al., 2020).

The present work deals with the study of the binding features of the amphiphilic CholineC4dod receptor with three old-generation antibiotics (**Figure 1**) in neutral aqueous solution. The interactions of the polycationic derivatives MedeaC4dod and MedeaC4prop (**Figure 1**) with the same antibiotics were also investigated with the aim of developing new and efficient DDSs.

The examination of the solution equilibria and the determination of species, binding affinity as well as thermodynamic parameters in neutral aqueous solution were carried out using nano-isothermal titration calorimetry (nano-ITC). This is an invaluable technique for determining both stability constant and enthalpy change values for host–guest complex formation (Sgarlata et al., 2009a; Bonaccorso et al., 2012; Giglio et al., 2015) and/or self-organization of surfactants into micelles by a single experiment (Perger and Bešter-Rogač, 2007; De Lisi et al., 2009; Moulik and Mitra, 2009; Loh et al., 2016). Results from calorimetric experiments provided key information on the forces driving the molecular recognition processes involving calixarene-based micellar aggregates and model drugs in water at neutral pH. Dynamic light scattering measurements provided evidences of the nanoaggregate formation whereas mono- and bi-dimensional NMR experiments confirmed the drug–micelle interaction and supported the picture obtained from ITC results on the antibiotic positioning within the calix[4]arene-based micellar backbone. Ofloxacin, tetracycline, and chloramphenicol were selected as models of antibiotics affected by the onset of resistance phenomena with the aim of offering a contribution to the design and development of effective DDSs for the revaluation and use of old-fashioned antibiotics.

MATERIALS AND METHODS

Materials

All chemicals and solvents were purchased from Sigma-Aldrich (Milan, Italy) and used without purification. The hosts tetra-dodecoxy-*p*-tetra-(*N*,*N*-dimethyl-*N*-hydroxyethylammonium)-methylene-calix[4]arene (CholineC4dod) (Rodik et al., 2015, Granata et al., 2017) and tetra-propoxy-*p*-tetra-(*N*,*N*-dihydroxyethyl-*N*-methylammonium)-methylene-calix[4]arene (MedeaC4prop) (Consoli et al., 2018b) were synthesized as previously reported. The guests (chloramphenicol, ofloxacin, and tetracycline hydrochloride) were purchased from Sigma-Aldrich and used as received. MOPS salt was purchased from Sigma-Aldrich and was of the highest purity commercially available. High-purity water (Millipore, Milli-Q Element A 10 ultrapure water) and A grade glassware were employed throughout.

Synthesis and Characterization of MedeaC4dod

A solution of *N*-methyldiethanolamine (26 mg, 218 μmol) in THF (0.4 ml) was added to a stirring solution of tetra-dodecoxy-*p*-chloromethyl calix[4]arene (52 mg, 40 μmol) in THF (1.5 ml). The reaction mixture was refluxed for 24 h. After cooling, the suspension was diluted with THF (5 ml) and diethyl ether (15 ml) and centrifuged (4,000 rpm, 5 min). The precipitate was washed with a mixture of THF (2 ml) and diethyl ether (8 ml) and then with diethyl ether (3 × 5 ml) by repeated centrifugation (4,000 rpm, 5 min) and removal of the supernatant. The solid was dried under vacuum for 24 h to give a white powder (61 mg, 86% yield). NMR spectra were recorded on a Bruker 400-mHz spectrometer equipped with a 5-mm inverse detection gradient probe. Chemical shifts (δ, ppm) are relative to the residual proton solvent peak; coupling constant (J) values are given in Hz. ^{1}H-NMR (MeOD): δ 0.89 (t, 12H, $J = 7.2$ Hz, 4 × CH_3), 1.31 (br m, 64H, 32 × CH_2), 1.46 (br m, 8H, 4 × CH_2), 2.00 (br m, 8H, 4 × CH_2), 2.95 (s, 12H, 4 × NCH_3), 3.30–3.45 (overlapped, 12H, 2 × $ArCH_2Ar$ and 4 × CH_2N), 3.49 (br t, 8H, 4 × CH_2N), 3.88 (t, $J = 7.2$ Hz, 8H, 4 × OCH_2), 3.90–4.10 (overlapped, 16H, 8 × CH_2OH), 4.45–4.56 (overlapped, 12H, 2 × $ArCH_2Ar$ and 4 × $ArCH_2N$), 7.05 (s, 8H, 8 × ArH). ^{13}C-NMR (MeOD): δ 14.5 (q), 23.8, 27.8, 30.7, 31.0, 31.1, 31.2, 31.4, 31.8, 33.2 (t), 49.4 (q), 56.5, 56.8, 58.9, 64.2, 68.9, 77.0 (t), 122.9 (d), 135.1, 136.9, 159.7 (s). ESI-HRMS spectra were acquired on a Thermo Scientific Exactive Plus Orbitrap MS (source voltage 3.5 kV; capillary voltage 82.5 V; tube lens voltage 150 V). HR ESI-MS: (m/z) calcd for $C_{100}H_{176}Cl_3N_4O_{12}^+$ $[M\text{-}Cl^-]^+ = 1732.2316$, found $[M\text{-}Cl^-]^+ = 1732.2292$; calcd for $C_{100}H_{176}Cl_2N_4O_{12}^{2+}$ $[M\text{-}2Cl^-]^{2+} = 848.6311$, found $[M\text{-}2Cl^-]^{2+} = 848.6317$.

Dynamic Light Scattering (DLS)

The samples were prepared by dissolution of CholineC4dod, MedeaC4dod, and MedeaC4prop (0.2 mM) in 10 mM MOPS buffer (pH 7.2). Size measurements were performed on a ZetaSizer Nano ZS90 Malvern Instrument (UK), equipped with a 633-nm laser, at a scattering angle of 90° and at 25°C. Each measurement was performed three times.

ITC Titrations

ITC titrations were carried out at 25°C with a nano-isothermal titration calorimeter (nano-ITC, TA Instruments) having an active cell volume of 988 μl and equipped with a 250-μl injection syringe. The reaction mixture in the sample cell was stirred at 250 rpm during the titration. Measurements were run in the overfilled mode to prevent possible issues from liquid evaporation or the presence of the vapor phase (Bundle and Sigurskjold, 1994; Hansen et al., 2011).

The power curve was integrated by using the NanoAnalyze software (TA Instruments) to obtain the gross heat evolved/absorbed in the reaction. The calorimeter was calibrated chemically by a test reaction (HCl/TRIS) according to the procedure previously described (Sgarlata et al., 2013). An

electrical calibration of the instruments was also performed. All solutions were degassed with gentle stirring under vacuum for about 15 min before each titration experiment.

ITC measurements for the study of the interactions of the guests with the micellar aggregates were carried out titrating a solution of tetracycline (2 ÷ 2.5 mM), ofloxacin (2 ÷ 2.5 mM), or chloramphenicol (from 2 to 10 mM) into a CholineC4dod or MedeaC4dod solution (0.2 mM) in the micellar/aggregated form. The same conditions were used for the titrations of the antibiotics with MedeaC4prop host. Further experiments were carried out titrating a solution of tetracycline (2 ÷ 2.5 mM), ofloxacin (2 ÷ 2.5 mM), or chloramphenicol (from 2 to 10 mM) into a solution of CholineC4dod or MedeaC4dod in their monomeric form (2.5 μM).

Both host and guest solutions were prepared at pH 7.2, dissolving proper amounts of the compounds in 10 mM MOPS, in order to reproduce conditions for neutral pH aqueous solutions and minimize any heat contribution resulting from the interaction of the compounds with the proton.

Typically, at least three independent titrations were run for each host–guest system in order to collect a suitable number of points to obtain a satisfactory fit of the calorimetric curves. The heats of dilution were determined in separate blank experiments titrating solutions of each guest (prepared in MOPS buffer) into a solution containing MOPS buffer only.

The net heats of reaction, obtained by subtracting the gross heat by that evolved/absorbed in the blank experiments, were analyzed by HypCal (Arena et al., 2016). This software allows for the simultaneous determination of standard enthalpy and binding constant values and has been specifically designed for the treatment of data obtained from ITC instruments operating in overfilled mode. The thermodynamic parameters were obtained by optimizing the agreement between observed and calculated reaction heats. The optimization is performed by a non-linear least squares analysis, minimizing the objective function (U):

$$U = \sum (Q_{obs.} - Q_{calc.})^2 \quad (1)$$

where Q_{obs} is the observed heat for a given reaction step, corrected for the dilution (blank) effects, while Q_{calc} is calculated as:

$$Q_{calc.} = -\sum \delta n \Delta H^0 \quad (2)$$

where δn is the change in the number of moles of a reaction product and ΔH^0 is the molar formation enthalpy of the reaction product. The sum is carried out over all the reaction steps; the squared residuals $(Q_{obs} - Q_{calc.})^2$ are summed over all the titration points. Stability constant values and thermodynamic parameters were obtained analyzing simultaneously calorimetric data obtained from different titrations.

NMR Analysis

The samples were prepared by addition of chloramphenicol, ofloxacin, or tetracycline hydrochloride (2.1 mM) to a solution of CholineC4dod (1.4 mM) in MOPS/D_2O (10 mM). All 1D- and 2D-NMR spectra were acquired on a Bruker Avance 400 spectrometer (^{1}H NMR 400.13 MHz) at 297 K. Chemical shifts (δ) are expressed in parts per million (ppm), referenced to the residual proton water peak. The proton spectra were recorded with a water suppression program. In 2D-NOESY experiments, the mixing time was 360 ms with 2 s of recycle delay. Data were processed using the TopSpin 2.1 software (Bruker).

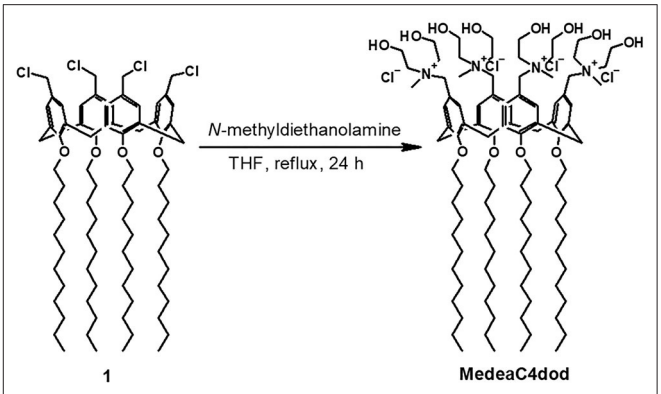

FIGURE 2 | Synthesis of MedeaC4dod from the precursor **1**.

RESULTS AND DISCUSSION

Calix[4]arene Derivatives Preparation and Characterization

CholineC4dod (Rodik et al., 2015; Granata et al., 2017) and MedeaC4prop (Consoli et al., 2018b) were prepared and characterized as previously reported while MedeaC4dod was prepared by adapting the same synthetic procedure. Tetra-dodecoxy-chloromethyl-calix[4]arene derivative **1** reacted with *N*-methyldiethanolamine in THF (**Figure 2**) to give MedeaC4dod in high yield (86%). MedeaC4dod was characterized by high-resolution ESI-MS and 1D- and 2D-NMR spectra (**Supplementary Figures 1–4**) that clearly indicated the exhaustive tetra-functionalization of the calix[4]arene upper rim. The mass spectrum showed two ion peaks at 1732.23 and 848.63 relative to $[M\text{-}Cl^-]^+$ and $[M\text{-}2Cl^-]^{2+}$, respectively. The presence of one AX system for the $ArCH_2Ar$ groups of the macrocycle in the proton NMR spectrum was consistent with a *cone* conformation (Gutsche, 1989) and a fully symmetric structure, corroborated by the resonances of the *N*-methyldiethanolammonium substituents.

Dynamic light scattering measurements showed that, in MOPS buffer (10 mM, pH 7.2), CholineC4dod and MedeaC4dod (0.2 mM) form nanoaggregates with mean hydrodynamic diameters of 7.0 and 7.5 nm, respectively (**Supplementary Figures 5**, **6**). The length and dimensions of a single calixarene lead to the conclusion that these size values are consistent with the formation of a micellar-like structure. No well-defined aggregates were instead observed at

the same concentration for MedeaC4prop, which bears shorter alkyl chains.

Solution Thermodynamics of the Drug–Micelle Systems

Depending on the type and site of interaction, a guest can arrange with a micellar system in different ways. It may be completely incorporated in the hydrophobic core by selective interaction with the aliphatic or bulkier chains, may penetrate up to a certain depth, or may be adsorbed on the micellar surface. Nano-calorimetric experiments were carried out to (1) evaluate whether selected model antibiotics are able to effectively interact with micellar aggregates formed by the polycationic amphiphilic calixarenes and (2) determine the binding parameters and driving forces for the molecular recognition equilibria involving drugs and micelles in aqueous solution at neutral pH.

The ITC study was carried out by titrating solutions of tetracycline, ofloxacin, and chloramphenicol into MedeaC4dod or CholineC4dod solutions at 0.2 mM concentration, in order to have the micellar aggregate into the calorimetric vessel at the tested conditions (Di Bari et al., 2016b).

A typical ITC titration for the tetracycline–CholineC4dod system in neutral aqueous solution (pH 7.2, MOPS) at 25°C is shown in **Figure 3**. ITC titration curves for the other drug-calixarene systems are shown in **Supplementary Figures 7–11** together with the corresponding blank experiments (**Supplementary Figures 12–14**).

The curves clearly show that the net heat released/adsorbed when the antibiotics are titrated into a micellar calixarene solutions is remarkable (i.e., the gross reaction heat is significantly larger than the heat from blank experiments) and the integrated heat data exhibit a pattern that may be analyzed for obtaining thermodynamic parameters. Interestingly, the interaction of chloramphenicol with both the calixarene micellar systems is exothermic (**Supplementary Figures 10**, **11**) while the reaction of the other two drugs with the same systems are endothermic, thus indicating that different driving forces are involved in the recognition process of these drugs in solution.

To assess whether the guest molecules are able to interact with the calixarene receptor regardless of its form (i.e., monomer vs. micellar aggregate) and hence to explore whether the formation of micelles is required for guest recognition, ITC measurements were also carried out titrating the drugs into MedeaC4dod or CholineC4dod solutions at a 500-fold lower concentration (2.5 μM) in order to deal only with the monomeric form. The overlap between blank experiments and titrations (**Supplementary Figures 15–20**) unambiguously revealed that, at this concentration, both the calixarenes are not capable of establishing any significant interaction with tetracycline, ofloxacin, and chloramphenicol as no detectable net heat is released/absorbed upon host–guest titration. This result highlights the key role played by the micellar assembly: the effective recognition/entrapment of the target guest cannot occur unless multiple host molecules are suitably aggregated to form a micellar-like arrangement.

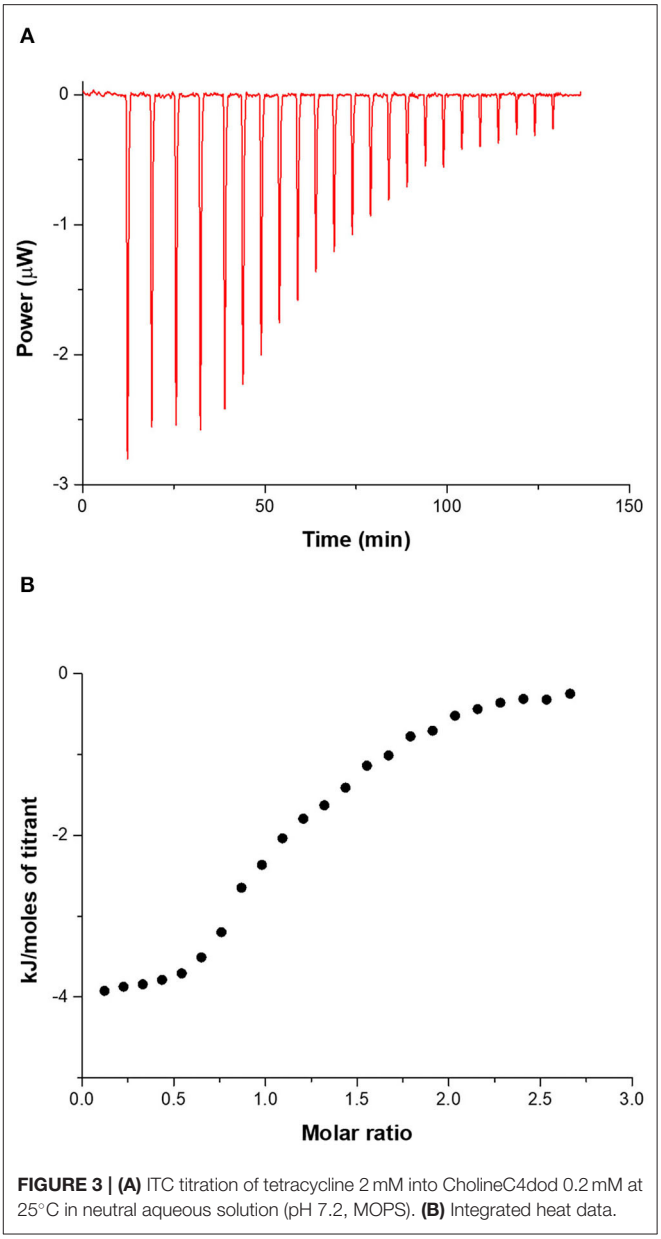

FIGURE 3 | (A) ITC titration of tetracycline 2 mM into CholineC4dod 0.2 mM at 25°C in neutral aqueous solution (pH 7.2, MOPS). **(B)** Integrated heat data.

ITC titrations were also carried out, at the same experimental conditions employed for the micellar aggregates, using MedeaC4prop, which has the same upper rim of MedeaC4dod but shorter alkyl substituents at the lower rim and, consequently, is not able to form micelles at the tested concentration (0.2 mM). The aim of these experiments is to (1) define the portion or rim of calixarene backbone actually involved in the interaction/recognition of the model drugs and (2) examine whether the guest is included into the calixarene cavity. The negligible heat values recorded in these ITC experiments (**Supplementary Figure 21**), the shape of the calorimetric curves (**Supplementary Figure 22**), and the basically full overlap between the heat rate from blank experiments and host–guest titrations (**Supplementary Figure 23**) indicated

that no detectable reaction occurred in the calorimetric vessel upon titration and thus no binding interactions are observed in the presence of the non-aggregating MedeaC4prop host. Overall, these evidences proved that the guests are not included into the host cavity and do not interact with the four *N*-methyldiethanolammonium groups at the upper rim of the macrocyclic receptor in solution. While it may be expected that the charged groups at the upper rim cause a steric encumbrance that prevent the guest to enter the cavity, the lack of heat recorded upon titration allows one to rule out also other kinds of interactions between the guest and the calixarene polar head groups.

Since it was observed that all guests are not able to enter or interact with the host cavity and with the long alkyl tails at the lower rim when the calixarene is in its monomeric form, it may be concluded that the cooperative effect generated by the assembling in micelles is the boost for the efficient drug entrapment/interaction by both MedeaC4dod and CholineC4dod.

Data obtained by ITC measurements were analyzed using a model that assumes the formation of a 1:1 species between the guest and the micellar aggregate, in line with many research groups that employ the "one site" binding model for the refinement of the thermodynamic parameters of these systems (Maity et al., 2015; Banipal et al., 2017).

Calorimetric data were analyzed by HypCal (Arena et al., 2016), a software designed for the determination of binding affinity and ΔH values for the formation of host–guest or micelle–guest adducts. Multiple titrations were simultaneously refined by the program. A typical HypCal output for the adducts formed by tetracycline with the micellar aggregate based on CholineC4dod is shown in **Supplementary Figure 24**; for each titration, the overlap between observed and calculated values is displayed. The binding constants and the thermodynamic parameters for the micelle–guest complex formation are reported in **Tables 1**, **2** and shown in **Figures 4**, **5**.

Data reported in **Tables 1**, **2** show no relevant difference in the binding parameters for CholineC4dod and MedeaC4dod as the two calixarenes, although bearing a different polar head, have the same C12 aliphatic chains, which are functional to the micelle formation.

The binding affinity values for the adduct formation of the micellar aggregates with chloramphenicol and ofloxacin are similar, but the splitting of ΔG into ΔH and ΔS values enabled the highlighting of factors and forces that are not expressed in the free Gibbs energy value. Indeed, the binding of chloramphenicol to the calixarene-based micelles is enthalpically favored and driven ($|\Delta H| > |T\Delta S|$) but entropically unfavored (Sgarlata et al.,

TABLE 1 | Log*K* values and thermodynamic parameters for the interaction of CholineC4dod-based micelles and model drugs at 25°C in neutral aqueous solution (pH 7.2, MOPS buffer).

Guest	Log*K*	ΔH (kJ mol^{-1})	ΔS (J mol^{1} deg^{-1})
Tetracycline	5.1 (3)	2.41 (4)	107 (6)
Ofloxacin	2.5 (1)	23.5 (1)	127 (2)
Chloramphenicol	2.6 (1)	−21.35 (3)	−21.5 (9)

σ *in parentheses.*

TABLE 2 | Log*K* values and thermodynamic parameters for the interaction of MedeaC4dod-based micelles and model drugs at 25°C in neutral aqueous solution (pH 7.2, MOPS buffer).

Guest	Log*K*	ΔH (kJ mol^{-1})	ΔS (J mol^{-1} deg^{-1})
Tetracycline	5.1 (3)	2.31 (4)	105 (7)
Ofloxacin	2.6 (1)	19.2 (1)	114 (2)
Chloramphenicol	2.6 (1)	−18.55 (3)	−11.7 (9)

σ *in parentheses.*

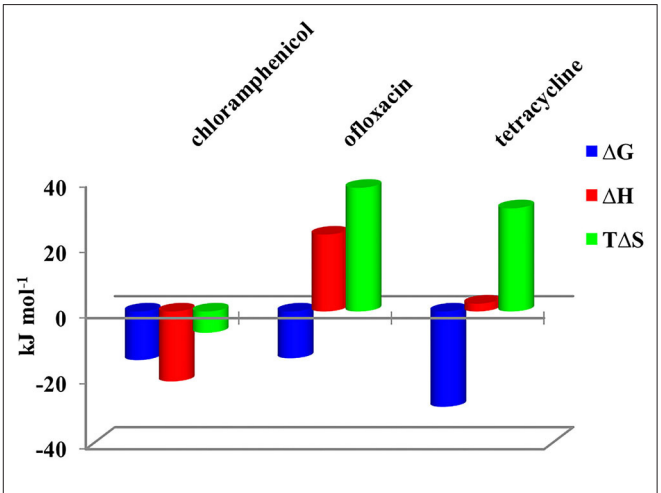

FIGURE 4 | Thermodynamic parameters for the complex formation of CholineC4dod-based micelles with model drugs at 25°C in neutral aqueous solution.

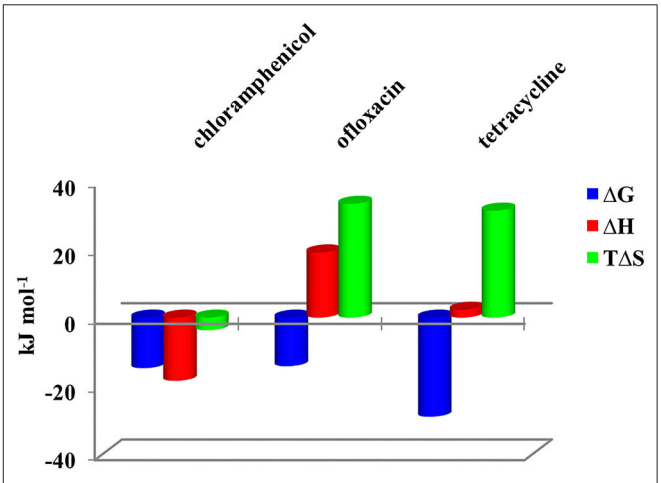

FIGURE 5 | Thermodynamic parameters for the complex formation of MedeaC4dod-based micelles with model drugs at 25°C in neutral aqueous solution.

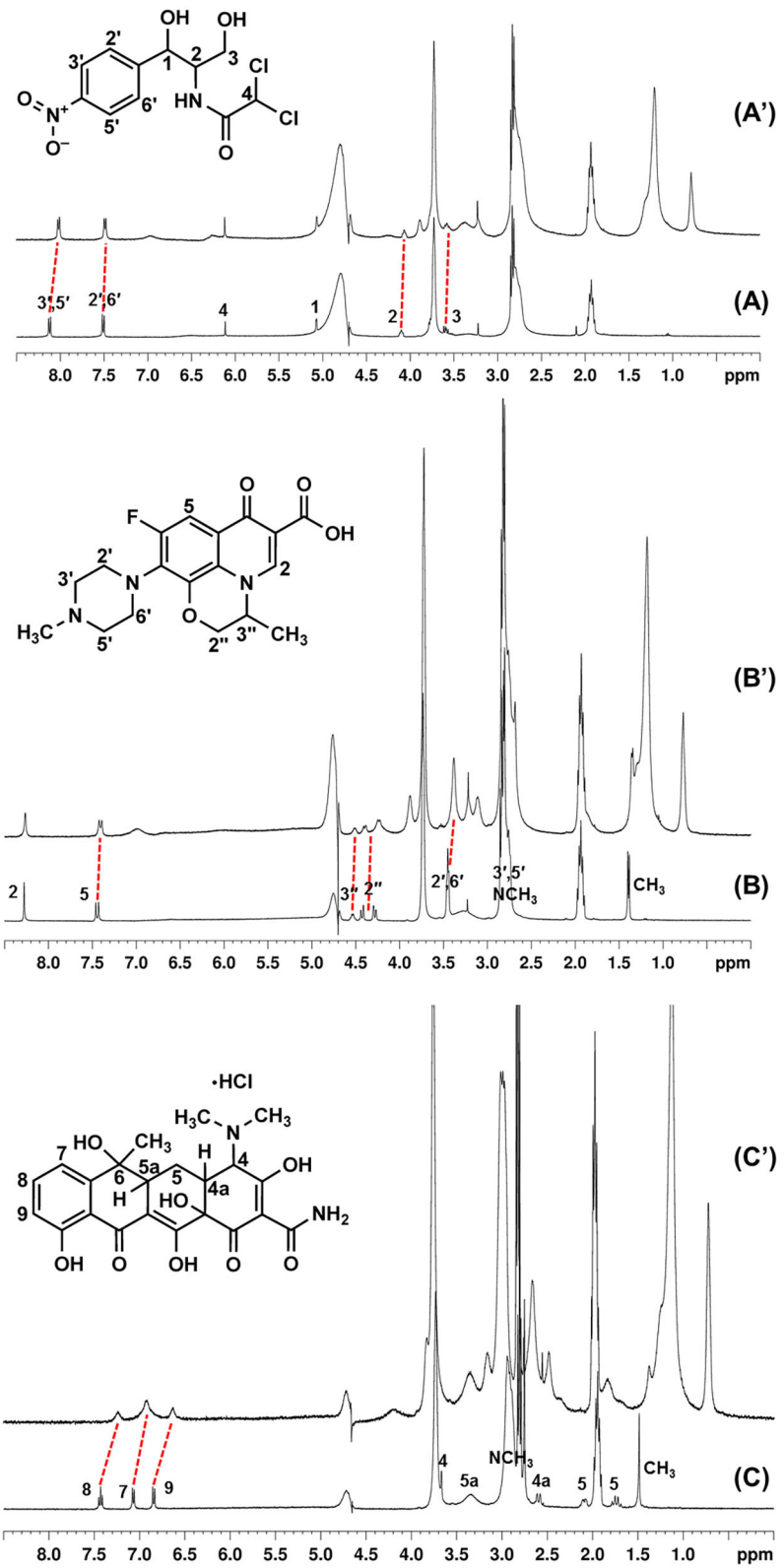

FIGURE 6 | ^{1}H-NMR spectra of chloramphenicol **(A)**, ofloxacin **(B)**, and tetracycline **(C)** alone and in the presence of CholineC4dod (**A'**, **B'** and **C'** respectively), pD 7.4 (MOPS buffer/D_2O), 297 K.

2009b; Bonaccorso et al., 2012, 2017). The favorable enthalpic contribution may be due to the insertion of chloramphenicol within the micelle palisade layer by establishing CH–π, ion–π, and van der Waals interactions between the calixarenes and the aromatic ring and/or the nitro group of chloramphenicol (Choudhary et al., 2015; Mukhija and Kishore, 2017). This favorable enthalpic contribution could also be attributed to "frustrated" water molecules that leave the micelle core and create a new hydrogen bonding network with the bulk water molecules and the micelle surface.

Conversely, the interaction of ofloxacin with both calixarene-based micelles is an entropy-driven and favored ($|\Delta H| < |T\Delta S|$) but enthalpy unfavored process. The entropic contribution is due to the desolvation of the guest as well as of the micelle surface upon guest binding to the micellar aggregate. These results suggest that ofloxacin should not be able to insert into the palisade layer of the micelles while (weakly) interacting with the positively charged exterior surface of the micelles. These interactions with the surface of the aggregates cause the release of water of hydration to the bulk solvent (large and positive entropy values). The enthalpic cost for desolvation (bonds breaking) results in a positive ΔH value.

The interaction of tetracycline with both the calixarene-based micelles is an entropy-driven and favorite ($|\Delta H| < |T\Delta S|$) but enthalpy unfavored process, as already observed for ofloxacin. However, despite the fact that the general trend of the thermodynamic parameters is similar for these two antibiotics, $\Delta H_{\text{tetracycline}} < \Delta H_{\text{ofloxacin}}$ (2.41 vs. 23.50 kJ mol^{-1}), the binding affinity of tetracycline to the micelles is larger ($\log K_{\text{tetracycline}} = 5.1$ vs. $\log K_{\text{ofloxacin}} = 2.5$). The less unfavorable ΔH value observed for tetracycline, which eventually leads to a larger affinity for the micelles in solution, is probably due to cation–π interactions between the calixarene hydrophilic head and the aromatic rings of the tetracycline backbone, which advantageously balance the enthalpic cost for desolvation. As in the case of ofloxacin, the large and favorable entropic contribution is due to the release of water molecules from both the guest and the calixarene micellar aggregates (Choudhary et al., 2015; Mukhija and Kishore, 2017).

NMR Characterization of the Drug–Micelle Systems

NMR is one of the techniques used to gain deeper insight into micelle–drug interactions (Wong, 2006). Due to the accuracy and precision of a NMR spectrometer, a change of 0.01 ppm or greater in the proton resonance is considered a significant change. Thus, to confirm the binding features and interactions of the micellar calixarenes with the antibiotics and support the ITC results, we recorded mono- and bi-dimensional proton spectra of CholineC4dod in combination with chloramphenicol, ofloxacin, or tetracycline in neutral aqueous solution (MOPS/D_2O).

The proton signals of chloramphenicol in the presence of the micellar CholineC4dod (**Figure 6**) showed an upfield shift of 0.106 ppm and 0.024 ppm for ArH (3′,5′and 2′,6′respectively), 0.036 ppm for CH-N (2), and 0.014 ppm for CH_2OH (3). These evidences could be indicative of CH–π, ion–π, and van der Waals interactions between the calixarene and the aromatic ring and/or the nitro group of the chloramphenicol, in agreement with the higher upfield shift of the chloramphenicol ArH (3′,5′) near the nitro group. Nuclear Overhauser effect (NOESY) correlations between the chloramphenicol aromatic protons and the CH_2 protons of the dodecyl chains at the calix[4]arene lower rim (**Supplementary Figure 25**) corroborated the insertion of the guest within the micelle palisade layer suggested by ITC analysis.

The interaction of ofloxacin with the micellar CholineC4dod was supported by the upfield shift of the antibiotic ArH (5, 0.034 ppm), N-CH_2 (2′,6′, 0.065 ppm), N-CH (3′′, 0.02 ppm), O-CH_2 (2′′, 0.026 and 0.044 ppm), and C-CH_3 (0.037 ppm) protons (**Figure 6**). In NOESY experiments, the overlap of the ofloxacin N-CH_2 (3′,5′) and N-CH_3 signals with the resonances of CholineC4dod N-CH_3 and MOPS buffering agent made difficult the exact signal assignment. Nevertheless, if we attribute the observed NOESY signals, which are absent in the spectra recorded with the other antibiotics, to the ofloxacin protons (**Supplementary Figure 26**), the correlations with the calix[4]arene ArH, $ArCH_2Ar$, CH_2N and $CH_2OH/ArOCH_2$ (overlapped) groups suggest that ofloxacin lies in a more external region of the micelle if compared to chloramphenicol. Beside cation–π and CH–π interactions, the electron-rich fluorine atom and the carboxyl group of the ofloxacin could establish ion–dipole and ion–ion interactions with the nitrogen atoms of CholineC4dod.

Overlapping phenomena made also difficult the assignment/detection of some tetracycline signals in the drug–micelle NMR spectra. Nevertheless, the clear-cut upfield shift of the tetracycline aromatic protons (0.19, 0.15, and 0.21 ppm for the protons in positions 8, 7, and 9, respectively) and C-CH_3 protons (0.059 ppm) compared to the free tetracycline (**Figure 6**) suggested the existence of interactions between the calixarene hydrophilic heads and the aromatic rings on the tetracycline backbone in line with ITC evidences. The higher shift of the tetracycline proton in position 9 could also be ascribable to interactions between the OH group of tetracycline and the choline heads in the micelle surface. These data indicate a more superficial positioning of tetracycline in the micelle–drug adduct when compared to the other two antibiotics.

CONCLUSIONS

Calixarene-based micelles are promising DDSs and the assessment of what forces drive the drug recognition processes is a fundamental step to the design and development of increasingly efficient nanocarriers. Since there is a strong demand for antibiotic delivery systems that could be valid allies in the fight against antibiotic-resistant bacteria, which are a serious threat to the health of all living beings, we investigated the interaction of three old-generation antibiotics with polycationic calix[4]arene amphiphiles in neutral aqueous solutions.

At the tested conditions, the antibiotics successfully interacted only with the calix[4]arene derivatives able to

form micellar aggregates evidencing that micelle formation is crucial for the guest recognition process to occur in solution. ITC measurements showed that the formation of the chloramphenicol–micelle adduct is always an enthalpically driven process while the adducts with ofloxacin and tetracycline are always entropically driven and enthalpically unfavored. Combined ITC and NMR analysis suggested a different location of the three antibiotics in the micelle backbone depending on their structure, charge, and functional groups.

DATA AVAILABILITY STATEMENT

The raw data supporting the conclusions of this article will be made available by the authors, without undue reservation.

AUTHOR CONTRIBUTIONS

CS and GC: conceptualization, methodology, supervision, and writing—review and editing. RM, GG, and AR: investigation, methodology, and formal analysis. RM, CS, and GC: writing—original draft preparation. All authors: contributed to the article and approved the submitted version.

FUNDING

The authors thank University of Catania (Piano della Ricerca d'Ateneo 2016-18, linea 2) for financial support.

ACKNOWLEDGMENTS

We thank Mrs. Concetta Rocco (CNR-ICB) for recording NMR spectra.

SUPPLEMENTARY MATERIAL

The Supplementary Material for this article can be found online at: https://www.frontiersin.org/articles/10.3389/fchem.2020.626467/full#supplementary-material

REFERENCES

Arena, G., Gans, P., and Sgarlata, C. (2016). HypCal, a general-purpose computer program for the determination of standard reaction enthalpy and binding constant values by means of calorimetry. *Anal. Bioanal. Chem.* 408, 6413–6422. doi: 10.1007/s00216-016-9759-6

Banipal, T. S., Kaur, H., and Banipal, P. K. (2017). Studies on the binding ability of diclofenac sodium to cationic surfactants micelles in aqueous ethanol solutions. *J. Therm. Anal. Calorim.* 128, 501–511. doi: 10.1007/s10973-016-5889-5

Bonaccorso, C., Ciadamidaro, A., Zito, V., Sgarlata, C., Sciotto, D., and Arena, G. (2012). Molecular recognition of organic anions by a water-soluble calix[4]arene: evidence for enthalpy–entropy compensation. *Thermochim. Acta* 530, 107–115. doi: 10.1016/j.tca.2011.12.014

Bonaccorso, C., Migliore, R., Volkova, M. A., Arena, G., and Sgarlata, C. (2017). Self-assembling of supramolecular adducts by sulfonato-calix[4]arene and pyridinium gemini guests in neutral aqueous solution. *Thermochim. Acta* 656, 47–52. doi: 10.1016/j.tca.2017.08.009

Bouchemal, K. (2008). New challenges for pharmaceutical formulations and drug delivery systems characterization using isothermal titration calorimetry. *Drug Discov. Today* 13, 960–972. doi: 10.1016/j.drudis.2008.06.004

Bundle, D. R., and Sigurskjold, B. W. (1994). Determination of accurate thermodynamics of binding by titration microcalorimetry. *Methods Enzym.* 247, 288–305. doi: 10.1016/S0076-6879(94)47022-7

Chen, C., Malek, A. A., Wargo, M. J., Hogan, D. A., and Beattie, G. A. (2010). The ATP-binding cassette transporter Cbc (choline/betaine/carnitine) recruits multiple substrate-binding proteins with strong specificity for distinct quaternary ammonium compounds. *Mol. Microbiol.* 75, 29–45. doi: 10.1111/j.1365-2958.2009.06962.x

Choudhary, S., Talele, P., and Kishore, N. (2015). Thermodynamic insights into drug–surfactant interactions: Study of the interactions of naproxen, diclofenac sodium, neomycin, and lincomycin with hexadecytrimethylammonium bromide by using isothermal titration calorimetry. *Colloids Surf. B* 132, 313–321. doi: 10.1016/j.colsurfb.2015.05.031

Consoli, G. M. L., Granata, G., and Geraci, C. (2018a). "Calixarene-based micelles: properties and applications," in *Design and Development of New Nanocarriers,* eds Grumezescu A. M., 1st Edn (Norwich, NY: William Andrew), 89–143. doi: 10.1016/B978-0-12-813627-0.00003-X

Consoli, G. M. L., Granata, G., Picciotto, R., Blanco, A. R., Geraci, C., Marino, A., et al. (2018b). Design, synthesis and antibacterial evaluation of a polycationic calix[4]arene derivative alone and in combination with antibiotics. *Med. Chem. Commun.* 9, 160–164. doi: 10.1039/C7MD00527J

De Lisi, R., Milioto, S., and Muratore, N. (2009). Thermodynamics of surfactants, block copolymers and their mixtures in water: the role of the isothermal calorimetry. *Int. J. Mol. Sci.* 10, 2873–2895. doi: 10.3390/ijms10072873

Di Bari, I., Fraix, A., Picciotto, Blanco, A. R., Petralia, S., Conoci, S., Granata, G., et al. (2016a). Supramolecular activation of the photodynamic properties of porphyrinoid photosensitizers by calix[4]arene nanoassemblies. *RSC Adv.* 6, 105573–105577. doi: 10.1039/C6RA23492E

Di Bari, I., Picciotto, R., Granata, G., Blanco, A. R., Consoli, G. M. L., and Sortino, S. (2016b). A bactericidal calix[4]arene-based nanoconstruct with amplified NO photorelease. *Org. Biomol. Chem.* 14, 8047–8052. doi: 10.1039/C6OB01305H

Dinić, J., Efferth, T., García-Sosa, A. T., Grahovac, J., Padrón, J. M., Pajeva, I., et al. (2020). Repurposing old drugs to fight multidrug resistant cancers, *Drug Resist. Updat.* 52:100713. doi: 10.1016/j.drup.2020.100713

Eleraky, N. E., Allam, A., Hassan, S. B., and Omar, M. M. (2020). Nanomedicine fight against antibacterial resistance: an overview of the recent pharmaceutical innovations. *Pharmaceutics* 12:142. doi: 10.3390/pharmaceutics12020142

Filippone, A., Consoli, G. M. L., Granata, G., Casili, G., Lanza, M., Ardizzone, A., et al. (2020). Topical delivery of curcumin by choline-Calix[4]arene-based nanohydrogel improves its therapeutic effect on a psoriasis mouse model. *Int. J. Mol. Sci.*, 21, 5053–5068. doi: 10.3390/ijms21145053

Formosa, C., Grare, M., Jauvert, E., Coutable, A., Regnouf-de-Vains, J. B., Mourer, M., et al. (2012). Nanoscale analysis of the effects of antibiotics and CX1 on a *Pseudomonas aeruginosa* multidrug-resistant strains. *Sci. Rep.* 2:575. doi: 10.1038/srep00575

Giglio, V., Sgarlata, C., and Vecchio, G. (2015). Novel amino-cyclodextrin cross-linked oligomer as efficient carrier for anionic drugs: a spectroscopic and nanocalorimetric investigation. *RSC Adv.* 5, 16664–16671. doi: 10.1039/C4RA16064A

Granata, G., Paterniti, I., Geraci, C., Cunsolo, F., Esposito, E., Cordaro, M., et al. (2017). Potential eye drop based on a calix[4]arene nanoassembly for curcumin delivery: Enhanced drug solubility, stability, and anti-inflammatory effect. *Mol. Pharm.* 14, 1610–1622. doi: 10.1021/acs.molpharmaceut.6b01066

Granata, G., Petralia, S., Forte, G., Conoci, S., and Consoli, G. M. L. (2020). Injectable supramolecular nanohydrogel from a micellar self-assembling calix[4]arene derivative and curcumin for a sustained drug release. *Mater. Sci. Eng. C* 111, 110842. doi: 10.1016/j.msec.2020.110842

Grare, M., Dibama, H. M., Lafosse, S., Regnouf-de-Vains, J.-B., Finance, C., and Duval, R. E. (2010). Cationic compounds with activity against multidrug-resistant bacteria: interest of a new compound compared with two older antiseptics, hexamidine and chlorhexidine. *Clin. Microbiol. Infect.* 16, 432–438. doi: 10.1111/j.1469-0691.2009.02837.x

Grare, M., Mourer, M., Fontanay, S., Regnouf-de-Vains, J. B., Finance, C., and Duval, R. E. (2007). *In vitro* activity of para-guanidinoethylcalix[4]arene against

susceptible and antibiotic-resistant Gram-negative and Gram-positive bacteria. *J. Antimicrob. Chemother.* 60, 575–581. doi: 10.1093/jac/dkm244

Gupta, A., Mumtaz, S., Li, C. H., Hussain, I., and Rotello, V. M. (2019). Combatting antibiotic-resistant bacteria using nanomaterials. *Chem. Soc. Rev.* 48, 415–427. doi: 10.1039/C7CS00748E

Gutsche, C. D. (1989). "Calixarenes," in *Monographs in Supramolecular Chemistry*, ed J. F. Stoddart (Cambridge: The Royal Society of Chemistry), 1.

Hansen, L. D., Fellingham, G. W., and Russell, D. J. (2011). Simultaneous determination of equilibrium constants and enthalpy changes by titration calorimetry: Methods, instruments, and uncertainties. *Anal. Biochem.* 409, 220–229. doi: 10.1016/j.ab.2010.11.002

Huang, Z., Ma, C., Wu, M., Li, X., Lu, C., Zhang, X., et al. (2020). Exploring the drug-lipid interaction of weak-hydrophobic drug loaded solid lipid nanoparticles by isothermal titration calorimetry. *J. Nanopart. Res.* 22, 3. doi: 10.1007/s11051-019-4671-6

Kaur, H., Aggarwal, N., Sood, A. K., and Banipal, T. S. (2020). Analysis of micellar, thermodynamic and structural parameters of gemini surfactants in aqueous solutions of vitamins. *J. Mol. Liq.* 310:113237. doi: 10.1016/j.molliq.2020.113237

Kobayashi, R. K., and Nakazato, G. (2020). Nanotechnology for antimicrobials. *Front. Microbiol.* 11, 1421–1423. doi: 10.3389/fmicb.2020.01421

Lallemand, F., Daull, P., Benita, S., Buggage, R., and Garrigue, J.-S. (2012). Successfully improving ocular drug delivery using the cationic nanoemulsion, Novasorb. *J. Drug Deliv.* 2012:604204. doi: 10.1155/2012/604204

Lee, M., Lee, S. J., and Jiang, L. H. (2004). Stimuli-responsive supramolecular nanocapsules from amphiphilic calixarene assembly. *J. Am. Chem. Soc.* 126, 12724–12725. doi: 10.1021/ja045918v

Lima, R., Del Fiol, F. S., and Balcão, V. M. (2019). Prospects for the use of new technologies in combating multidrug-resistant bacteria. *Front. Pharmacol.* 10:692. doi: 10.3389/fphar.2019.00692

Loh, W., Brinatti, C., and Tam, K. C. (2016). Use of isothermal titration calorimetry to study surfactant aggregation in colloidal systems. *Biochim. Biophys. Acta, Gen. Subj.* 1860, 999–1016. doi: 10.1016/j.bbagen.2015.10.003

Lucchesi, G. I., Pallotti, C., Lisa, A. T., and Domenech, C. E. (1998). Constitutive choline transport in *Pseudomonas aeruginosa*. *FEMS Microbiol. Lett.* 162, 123–126. doi: 10.1111/j.1574-6968.1998.tb12988.x

Maity, B., Chatterjee, A., Ahmed, S. A., and Seth, D. (2015). Interaction of the nonsteroidal anti-inflammatory drug indomethacin with micelles and its release. *J. Phys. Chem. B* 119, 3776–3785. doi: 10.1021/acs.jpcb.5b00467

Malek, A. A., Chen, C., Wargo, M. J., Beattie, G. A., and Hogan, D. A. (2011). Roles of three transporters, CbcXWV, BetT1, and BetT3, in *Pseudomonas aeruginosa* choline uptake for catabolism. *J. Bacteriol.* 193, 3033–3041. doi: 10.1128/JB.00160-11

Moulik, S. P., and Mitra, D. (2009). Amphiphile self-aggregation: An attempt to reconcile the agreement–disagreement between the enthalpies of micellization determined by the van't Hoff and Calorimetry methods. *J. Colloid Interface Sci.* 337, 569–578. doi: 10.1016/j.jcis.2009.05.064

Mourer, M., Dibama, H. M., Fontanay, S., Grare, M., Duval, R. E., Finance, C., et al. (2009). p-Guanidinoethyl calixarene and parent phenol derivatives exhibiting antibacterial activities. Synthesis and biological evaluation. *Bioorg. Med. Chem.* 17, 5496–5509. doi: 10.1016/j.bmc.2009.06.040

Mukhija, A., and Kishore, N. (2017). Partitioning of drugs in micelles and effect on micellization: physicochemical insights with tryptophan and diclofenac sodium. *Colloids Surf. A* 513, 204–214. doi: 10.1016/j.colsurfa.2016.10.044

Patra, J. K., Das, G., Fraceto, L. F., Ramos Campos, E. V., del Pilar Rodriguez-Torres, M., Acosta-Torres, L. S., et al. (2018). Nano based drug delivery systems: recent developments and future prospects. *J. Nanobiotechnol.* 16:71. doi: 10.1186/s12951-018-0392-8

Perger, T. M., and Bešter-Rogač, M. (2007). Thermodynamics of micelle formation of alkyltrimethylammonium chlorides from high performance electric conductivity measurements. *J. Colloid Interface Sci.* 313, 288–295. doi: 10.1016/j.jcis.2007.04.043

Pham, T. N., Loupias, P., Dassonville-Klimpt, A., and Sonnet, P. (2019). Drug delivery systems designed to overcome antimicrobial resistance. *Med. Res. Rev.* 39, 2343–2396. doi: 10.1002/med.21588

Pushpakom, S., Iorio, F., Eyers, P. A., Escott, K. J., Hopper, S., Wells, A., et al. (2019). Drug repurposing: progress, challenges and recommendations. *Nat. Rev. Drug Discov.* 18, 41–58. doi: 10.1038/nrd.2018.168

Rodik, R. V., Anthony, A. S., Kalchenko, V. I., Melya, Y., and Klymchenko, A. S. (2015). Cationic amphiphilic calixarenes to compact DNA into small nanoparticles for gene delivery. *New J. Chem.* 39,1654–1664. doi: 10.1039/C4NJ01395F

Sgarlata, C., Bonaccorso, C., Gulino, F. G., Zito, V., Arena, G., and Sciotto, D. (2009a). Inclusion of aromatic and aliphatic anions into a cationic water-soluble calix[4]arene at different pH values. *Tetrahedron Lett.* 50, 1610–1613. doi: 10.1016/j.tetlet.2009.01.100

Sgarlata, C., Bonaccorso, C., Gulino, F. G., Zito, V., Arena, G., and Sciotto, D. (2009b). Stereochemistry and thermodynamics of the inclusion of aliphatic and aromatic anionic guests in a tetracationic calix[4]arene in acidic and neutral aqueous solutions. *N. J. Chem* 33, 991–997. doi: 10.1039/b901164c

Sgarlata, C., Zito, V., and Arena, G. (2013). Conditions for calibration of an isothermal titration calorimeter using chemical reactions. *Anal. Bioanal. Chem.* 405, 1085–1094. doi: 10.1007/s00216-012-6565-7

Wang, J., Ding, X., and Guo, X. (2019). Assembly behaviors of calixarene-based amphiphile and supra-amphiphile and the applications in drug delivery and protein recognition. *Adv. Colloid Interface Sci.* 269, 187–202. doi: 10.1016/j.cis.2019.04.004

Waters, L. J., Hussain, T., and Parkes, G. M. (2012). Titration calorimetry of surfactant–drug interactions: Micelle formation and saturation studies. *J. Chem. Thermodyn.* 53, 36–41. doi: 10.1016/j.jct.2012.04.021

Wong, T. C. (2006). "Micellar systems: nuclear magnetic resonance spectroscopy," in *Encyclopedia of Surface and Colloid Science*. 2nd edition, ed. P. Somasundaran (New York, NY: Taylor & Francis CRC Press), 3738–3756.

Conflict of Interest: The authors declare that the research was conducted in the absence of any commercial or financial relationships that could be construed as a potential conflict of interest.

The handling editor declared a past co-authorship with one of the author CS.

frontiers in Chemistry

MINI REVIEW
published: 20 January 2021
doi: 10.3389/fchem.2020.625945

Recent Approaches for Chemical Speciation and Analysis by Electrospray Ionization (ESI) Mass Spectrometry

Serena Indelicato, David Bongiorno and Leopoldo Ceraulo*

Dipartimento di Scienze e Tecnologie Biologiche Chimiche e Farmaceutiche (STEBICEF), Università degli studi di Palermo, Palermo, Italy

In recent years, the chemical speciation of several species has been increasingly monitored and investigated, employing electrospray ionization mass spectrometry (ESI-MS). This soft ionization technique gently desolvates weak metal–ligand complexes, taking them in the high vacuum sectors of mass spectrometric instrumentation. It is, thus, possible to collect information on their structure, energetics, and fragmentation pathways. For this reason, this technique is frequently chosen in a synergistic approach to investigate competitive ligand exchange-adsorption otherwise analyzed by cathodic stripping voltammetry (CLE-ACSV). ESI-MS analyses require a careful experimental design as measurement may face instrumental artifacts such as ESI adduct formation, fragmentation, and sometimes reduction reactions. Furthermore, ESI source differences of ionization efficiencies among the detected species can be misleading. In this mini-review are collected and critically reported the most recent approaches adopted to mitigate or eliminate these limitations and to show the potential of this analytical technique.

Keywords: electrospray ionization, metals speciation, metallomics, mass spectrometry, speciation analysis

OPEN ACCESS

Edited by:
Ottavia Giuffrè,
University of Messina, Italy

Reviewed by:
Constantinos M. Athanassopoulos,
University of Patras, Greece
Fabio Mazzotti,
Other, Rende, Italy

****Correspondence:***
David Bongiorno
david.bongiorno@unipa.it

Specialty section:
This article was submitted to Analytical Chemistry, a section of the journal Frontiers in Chemistry

Received: *05 November 2020*
Accepted: *30 November 2020*
Published: *20 January 2021*

Citation:
Indelicato S, Bongiorno D and Ceraulo L (2021) Recent Approaches for Chemical Speciation and Analysis by Electrospray Ionization (ESI) Mass Spectrometry. Front. Chem. 8:625945. doi: 10.3389/fchem.2020.625945

INTRODUCTION

The IUPAC has defined the term "speciation analysis" as the "analytical activities of identifying and/or measuring the quantities of one or more individual chemical species in a sample." It is also defined as "speciation of an element" the "distribution of an element amongst defined chemical species in a system." Taking into account the development of the field and the wave of other -omic sciences, the term "metallomics" has been recently coined, defining "metallome" as the ensemble of metals and metalloids present in cells or tissues taking into consideration their nature, quantity, and localization.

To accomplish the complexity of this new research field, several new analytical methods have been developed, and integrated mass spectrometric tools were found to be fitting for this purpose.

In particular, for metallomics approaches, the combined use of chromatographic (or electrophoresis) separation and inductively coupled plasma-mass spectrometry (ICP-MS) is useful, whereas electrospray ionization-mass spectrometry (ESI-MS) allows the discrimination of species containing the same metal and to obtain structural elucidation.

ELECTROSPRAY IONIZATION

ESI has been developed as a soft ionization technique (Whitehouse et al., 1985) that gently takes into the gas phase metal–ligand complexes and allows gathering a wealth of information on their dissociation energetics, shapes, and fragmentation pathways. ESI-MS analyses require a careful experimental design as instrumental artifacts, such as adduct formation, source fragmentation, and sometimes reduction reactions, can occur.

Attention also must be paid to quantitative determination as differences in ionization efficiencies among the detected species can lead to misleading results. We here report the most recent approaches adopted to mitigate or eliminate these drawbacks. The potential of complementing ESI-MS results with quantum mechanical information and the coupling of the ESI sources with ion mobility (IM), high-resolution mass spectrometry (HR-MS), or tandem mass spectrometry (MS-MS) experiments, are also evidenced to provide unique information on the gas phase complexes.

The coupling of ICP and ESI sources with MS analyzers allows collapsing each ion into a single signal with a specific m/z value and precise intensity. This is immensely helpful to address the complex speciation problem associated with multiple complexation reactions that can take place in a solution. ESI as a "soft" ionization technique provides valuable information concerning the extracting ligands or complex stoichiometry, and ICP-MS analysis can give information only on the presence of the metal and on its abundance. However, one of the most debated arguments concerning ESI-MS spectra is the effective correspondence between the ionic species therein evidenced and the status of the correspondent ions or molecules in the bulk solution (Bongiorno et al., 2011a). Di Marco and Bombi (2006) have evidenced that perturbations of solution composition with respect to equilibrium take place during the ionization process. It is indeed common in the application of ESI-MS to ascertain differences between the relative abundance of the signals recorded in the spectra and the actual relative concentration of the species present in the condensed phase. These quantitative differences are due to differing gas-phase acidities/basicities, cation/anion affinities of the ionizing species, that lead to differing ionization efficiencies of the investigated species (Oss et al., 2010). Besides this, even large qualitative differences between solution phase and gas phase have been observed, self-assembly of alkali salts (Anacleto et al., 1992) or surfactant molecules being some of the most notable ones (Borysik and Robinson, 2012, Bongiorno et al., 2016). For these reasons, ESI requires a careful setup of experimental conditions to obtain reliable results. One of the most important parameters to optimize is the cone voltage that defines the so-called "*soft and hard*" ESI conditions (Bongiorno et al., 2011b). This potential is applied between the orifice and the skimmers. It can be useful, increasing ions' internal energy, to reduce the presence of residual clusters but can also lead to a more effective ion fragmentation and, therefore, to marked differences between abundances in solution and the gas phase (Indelicato et al., 2016). It follows that, despite the soft nature of ESI, fragmentation and/or polymerization phenomena may occur, and the spectra of species, that are sensitive to different instrumental parameters, may have different response factors (Espinosa et al., 2016). For this reason, a careful evaluation of the cone voltage has been crucial to determine polychalcogenids in solutions and to get reliable information for polysulfide ion speciation (Gun et al., 2004; Dorhout et al., 2017). Other authors (Wen et al., 2019) lowered cone voltages and temperatures to preserve the solution state at maximum.

The nature of solvents, cosolvents, and pH must be carefully evaluated as they are strongly related to ESI ionization efficiency. The introduction of methanol as a cosolvent is known to alter the solvent structure of water, leading to changes in both complexation kinetics and thermodynamics (Hawlicka and Swiatla-Wojcik, 2002; Accorsi et al., 2005; Wang et al., 2014). The pH variation directs the formation of protonated species and can have a strong influence on the relative abundance of formed complexes, leaving qualitatively unmodified the observed species (Espinosa et al., 2016). Besides this, the flux can have a small influence on the relative abundances of the aggregates (Bongiorno et al., 2005). Once these experimental factors are carefully defined, ESI-MS provides a reliable tool to extract quantitative information.

COUPLING ESI WITH MASS SPECTROMETRY ANALYZERS

The general approach followed by most of the authors developing ESI-MS methods to identify and characterize metallated species is represented in **Scheme 1**.

ESI sources have been coupled to several types of MS analyzers, and therefore, metal speciation experiments have been conducted in low-resolution MS, tandem MS (MS-MS), or high-resolution MS. However, there are some limitations for low-resolution MS for exploratory speciation analysis as evidenced by Bierla et al. (2018). Most of the drawbacks are due to slow scanning speed during HPLC runs, a blurred isotopic pattern due to background from concomitant species, and low sensitivity in full scan mode. It is possible to overcome these limitations by adopting multiple low-resolution analyzer systems (for MS-MS experiments) or adopting instruments with an increasing resolution power, such as time of flight (TOF), Fourier transform-orbital traps (FT-MS), and Fourier transform-ion cyclotron resonance (FT-ICR) mass spectrometers (de Hoffman and Stroobant, 2007). These different technological approaches lead to differing results in terms of resolution. Modern TOF instruments take advantage of a reflection grid to refocus ions in the space with the same mass, leading to a final resolution power of up to 50,000 full width at half maximum (FWHM). FT-MS traps ions in an orbital trap (generating a spindle-shaped electrostatic field). Ion masses are determined by applying the Fourier transform to the complex waveform of the image current, generated on the surface of the outer electrode by the ions orbiting in the trap. This approach leads to resolution of up to 1,000,000 FWHM. FT-ICR instrumentation takes the resolution a step further, up to and over 5,000,000 FWHM, but requires

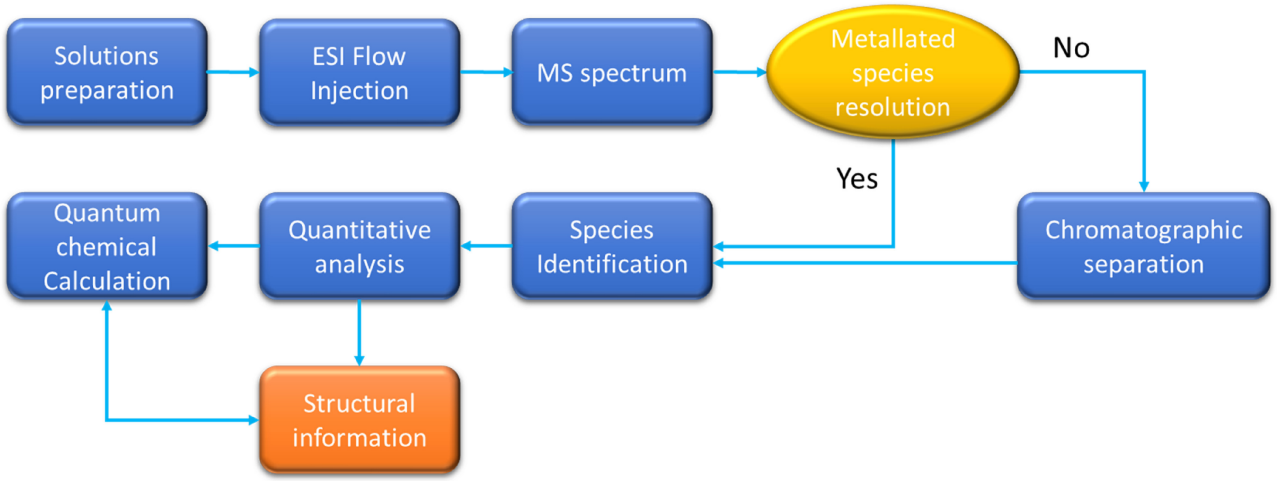

SCHEME 1 | ESI-MS workflow for metal speciation.

superconducting high field magnets to trap ions while Fourier transformation is applied to the waveform generated as image potential by the ions orbiting altogether in the magnetic field, each one with its own natural ion cyclotron resonance frequency.

ESI-MS-MS FOR METAL SPECIATION

In several cases, the MS-MS approach for metal speciation is sufficient, guarantees exceptional sensitivity, and is well-suited for quantitative analysis. At least two independent approaches have been described by Liu et al. (2018) for speciation determination and quantitation of arsenic and its metabolites employing MS-MS.

Tsednee et al. (2016) developed an analytical application for identifying several transition metal (Co, Cu, Fe, Ni, Zn) complexes with deoxymugineic acid or nicotinamide by tandem mass spectrometry (ESI-MS-MS). It monitored, by multireaction monitoring (MRM), the release of free metals from the corresponding metal–ligand complexes. This MS-MS method allowed easily separating metal species whose mass spectra peaks were clustered together.

Tie et al. (2015) shows that HPLC-ESI-MS-MS is a sensitive and accurate method for the identification and quantification of the speciation of selenium. They monitored Se-methyselenocysteine (Se-MeSeCys) and selenomethionine (Se-Met) in soybean proteolytic digests through MRM mode. The evaluation of the fragmentation pattern of precursor ions (m/z 184 for Se-MeSeCys and m/z 198 for Se-Met) led to the selection of fragments due to the neutral loss of ammonia. Therefore, the transitions at m/z values of 184→ 167 for Se-MeSeCys and m/z values of 198→181 for Se-Met were monitored.

Quantitation of the appropriate HPLC peaks shows that inorganic selenium absorbed by the soybean has been biotransformed mainly into Se-MeSeCys. This species represented 66.4% of the selenium in Se-protein and 29.2% of the total selenium in the soybean.

ESI COUPLED TO HIGH-RESOLUTION MASS SPECTROMETRY ANALYZERS

Although exploiting MS-MS sensitivity is still an actual approach, in metal speciation, it is far more common to take advantage of high-resolution sectors, which are capable of well resolving isotopic clusters even in multiply charged adduct peaks.

The most common application of the simplest high-resolution mass spectrometry technology is the development of screening methods. Several authors followed this route. Raymond et al. (2018) developed a screening method for the characterization of beryllium complexes with aminopolycarboxylate and some related ligands. The approach requires only tiny amounts of material in analyte solutions and provides a quick and safe strategy for screening beryllium complexes. With a similar setup, Jo et al. (2019) investigated metal speciation of palladium in Pd-catalyzed pharmaceutical processes to verify the removal of elemental impurities from the reaction product mixture. They used metal speciation data to provide both critical information on the fate of each elemental impurity and a deeper understanding of the catalytic mechanism investigated. Using an ESI-TOF device, Wen et al. (2019) semi-quantitatively detected more than 30 types of aqueous vanadium species with <5% relative error. This led to a straightforward unambiguous molecular formula and ionic composition determination. Indelicato et al. (2014) investigated by ESI-MS, tandem mass spectrometry (ESI-MS-MS), and energy-resolved mass spectrometry (ER-MS) some lanthanide-functionalized surfactants: the ytterbium and erbium salts of bis(2-ethylhexyl)-sulfosuccinate (AOT). Evaluating the cone voltage effect on the metallated surfactant aggregation, they obtained detailed information on the stability and structural features of positively and negatively singly charged metallated species evidencing the formation of very large aggregates containing up to 5 Yb^{3+} or Er^{3+} ions.

Finally, Feng et al. (2015) exploited a similar instrumental setup to identify Al species in a complex mass spectrum.

The authors introduce a novel theoretical calculation method based on the relative intensity of Gaussian-shaped peak clusters found in the spectra. Changes in m/z and molecular formulas of oligomers in five typical poly aluminum chloride (PAC) flocculants were easily deduced.

Exploiting more complex MS experiments and adopting time-resolved ESI-MS, Cao et al. (2016) monitored the "one-pot" method for the synthesis of polyoxometalates (POMs), produced using silicotungstates and vanadium salts. These authors discovered that the reaction conditions, such as concentration, temperature, and reaction time, sensitively changed the speciation.

The latest development of TOF technology, the so-called ion mobility mass spectrometry (IMMS) allows correlating the time of flight (drift time) of the ions within a "high pressure" mobility sector to determine collisional cross-sections of several type of ions ranging from peptides, small and large clusters, up to protein complexes (Lapthorn et al., 2013, Bongiorno et al., 2014).

Davis and Clowers (2018) recently used this cutting-edge approach for the rapid speciation of uranyl complexes. The authors were capable of stabilizing simple uranyl complexes during the ionization process and ion-mobility separation to aid speciation and isotope profile analysis. They measured mobilities of different uranyl species in simple mixtures by promoting stable gas-phase conformations with the addition of sulfoxides [i.e., dimethyl sulfoxide (DMSO), dibutyl sulfoxide (DBSO), and methyl phenyl sulfoxide (MPSO)]. As an outcome, this setup allowed the determination of the reduced mobilities of uranyl salts.

Opposite to the fast sensitivity-oriented approach of quadrupole ESI-MS or ESI-(q)TOF experiments, the adoption of FT-MS high-resolution analyzers allows for the development of more complex gas-phase experiments, opening a wide range of investigations allowed by the trapping of the ions in the analyzer for times that arrive to seconds. Waska et al. (2016) exploited high-resolution FT-ICR to overcome ESI-MS artifact and to characterize the equilibria of the model ligand citrate, EDTA, 1-nitroso-2-naphthol, and salicylaldoxime with iron (Fe^{3+}) and copper (Cu^{2+}). This approach allowed the detection of the whole metal–organic compounds. A cosolvent effect was ascertained, and methanol-containing samples gave higher sensitivities compared to those containing only water. It is important, however, to underline that, in comparing conditional stability constants determined by competitive ligand exchange-adsorptive cathodic stripping voltammetry (CLE-ACSV) with that of FT-ICR-MS determination, a difference was found. Therefore, the FT-ICR-MS-derived conditional stability constants can only be compared between similarly processed sample types.

Mapolelo et al. (2009) exploited the high-resolution capabilities of a custom-built FT-ICR analyzer, coupled with an infrared multiphoton dissociation CO_2 continuous wave laser to gather the most information on the interaction of naphthenic acids with divalent (Ca^{2+}, Fe^{2+}, Mg^{2+}) or monovalent (Na^{+}, K^{+}) ions in produced waters. These authors evidenced calcium naphthenate deposits that consist mainly of a C80 tetraprotic acid known as ARN acid bound to Ca^{2+}. It was also possible to identify low-molecular-weight ARN acids with a C60-77 hydrocarbon skeleton in one calcium naphthenate deposit.

ESI-MS AND QUANTUM MECHANICAL CALCULATIONS

As it is evidenced so far, the coupling of ESI-MS information with data obtained from synergistic techniques, such as ICP-MS, NMR, X-RAY, and CLE-ACSV, is common practice. It is not a surprise to find out that the information obtained from ESI-MS speciation experiments is often compared to results of Ab-Initio or DFT quantum mechanical calculations. ESI-MS detects species in the gas phase, in which weak solvent interactions are absent.

This allows building quantum chemical simple and realistic models that are not impacted by the complex solvation. Theoretical calculations can be more easily compared to experimental results, and the model geometry suggests the structural information that is lacking in an ESI-MS spectrum. Exploiting these synergistic features, Raymond et al. (2019) investigated gas-phase coordination chemistry of Be^{2+} with 1,2- and 1,3-diketone ligands. Their results evidenced the tendency of beryllium to form stable polynuclear species with oxido, hydroxido, or diketonato ligands bridging the metal centers. In ESI-MS spectra were evidenced ions corresponding

TABLE 1 | Research articles summary, based on investigated metallic specie.

Speciated metal	Analytical approach
Ag	ESI-MS (Jaklová Dytrtová et al., 2016)
Al	ESI-TOF (Feng et al., 2015; Raymond et al., 2018)
As	ESI-MS-MS (Liu et al., 2018)
Au	DESI-MS (Kazimi et al., 2019)
Be	ESI-TOF (Raymond et al., 2018)
Ca	ESI-FT-ICR (Mapolelo et al., 2009)
Co	ESI-MS-MS (Tsednee et al., 2016)
Cu	ESI-MS (Jaklová Dytrtová et al., 2016), ESI-MS-MS (Tsednee et al., 2016), ESI-FT-ICR (Waska et al., 2016)
Er	ESI-TOF (Indelicato et al., 2014)
Fe	ESI-MS-MS, (Tsednee et al., 2016), ESI-FT-MS (Waska et al., 2016, Mapolelo et al., 2009)
K	ESI-FT-ICR (Mapolelo et al., 2009)
Mg	ESI-FT-ICR (Mapolelo et al., 2009)
Na	ESI-FT-ICR (Mapolelo et al., 2009)
Ni	ESI-MS-MS (Tsednee et al., 2016)
Pd	ESI-TOF (Jo et al., 2019)
Ru	DESI-MS (Perry et al., 2011)
Se	ESI-MS-MS (Tie et al., 2015)
U	ESI-TOF (Davis and Clowers, 2018)
V	ESI-TOF (Wen et al., 2019), ESI-TOF (time resolved) (Cao et al., 2016)
W	ESI-TOF (time resolved) (Cao et al., 2016)
Yb	ESI-TOF (Indelicato et al., 2013)
Zn	ESI-MS-MS (Tsednee et al., 2016)

to predominant bis-chelated beryllium complexes known to be formed with the monoanionic 1,3-diketonate ligands.

ESI-MS measurements, along with differential functional theory calculations, have been exploited (Kumar et al., 2016) to understand the speciation of various uranyl species with α-hydroxyisobutyric acid. Quantum chemical calculations evidenced that uranyl complexes with 3 ligands (ML3 with M = UO2 and L = α-hydroxyisobutyric acid) are more energetically favorable over the ML2, which, in turn, are more favorable than ML1. The relative abundance of ML1 < ML2 < ML3 species in ESI-MS suggest a qualitative correlation between calculated free energies and observed complex relative stabilities. A similar approach was adopted to investigate the speciation of uranium–mandelic acid complexes (Kumar et al., 2017) determining structures and free energies of the complexes that were in fair agreement with the ESI spectra. Based on the energetics of this latter study, the authors further predicted the formation of T-shaped dimeric uranyl complexes in the complexation process.

DESORPTION ESI AND AMBIENT MASS SPECTROMETRY APPLICATIONS

To enhance ESI capabilities, some authors have developed some ancillary devices to couple with ESI sources. Jaklová Dytrtová et al. (2016) developed an electrochemical device that takes advantage of the high reactivity of electrochemically generated metallic ions *in statu nascendi*. This is suitable for ionization of various organic compounds (e.g., lipids, lipoproteins, pesticides, drugs, metabolites, lipids, lipoproteins) in biological and other matrices. The applicability of the electrochemical device is demonstrated by the electrochemical activation of pesticide cyproconazole (Cyp) in a soil solution matrix via formation and separation of its adducts with Ag and Cu cations without chromatographic support.

Finally, desorption electrospray ionization (DESI), an ESI-related technique that allows ionizing samples in the open environment and introducing them into the mass spectrometer reducing sample manipulation, is gaining momentum. Some authors studied Ru^{+2} complexes (Perry et al., 2011) evidencing that, in the short time scales of DESI, it is possible to detect trace levels (pmol) of short-lived intermediates characterized by lifetimes in the order of milliseconds. In a more recent work, Kazimi et al. (2019) exploited DESI to investigate, in the solid phase, a gold-based drug actually in clinical trials for its anticancer properties: auranofin. Auranofin was reacted with thiol-containing amino acids to evaluate the ligand exchange/scrambling reactions. These latter results evidence how the DESI-MS technique can be a game-changer in monitoring the reactions involving coordination compounds in the solid state.

CONCLUSIONS

In conclusion, ESI-MS accompanied by its most recent variants, such as ambient MS (DESI), is proposing itself as a very informative method on metal complex–generated binding ligands, such as anions, bases, peptides, and proteins (see **Table 1**) The most important drawback of ESI-MS still lies in the possible difference between relative abundances of the species in the gas phase and in solution. This often requires validating the quantitative results with alternative spectroscopic techniques (Feng et al., 2015; Wen et al., 2019).

ESI is especially informative when matrix or ion suppression effects are tolerable or negligible. When the matrix proves to be a serious drawback in the ESI determination of the speciated metals, the complementary information obtained by ICP-MS is still fundamental (Liu 2018). Some authors (Bierla et al., 2018) point out, however, that ESI-MS starts outpacing ICP-MS in terms of detection limits with the further advantage of the possibility to use the multiple reaction monitoring for quantification of adducts even in the case of incomplete separations. This increased sensitivity and the possibility of large-scale data acquisition is opening new opportunities even in tasks demanding high sensitivity, such as metallo-metabolomics and metallo-proteomics of body fluids and tissues of higher organisms (Bierla et al., 2018).

AUTHOR CONTRIBUTIONS

All the authors equally contributed to the bibliographical research of the references cited and to the article redaction.

REFERENCES

Accorsi, A., Morrone, B., Benzo, M., Gandini, C., Raffi, G. B., and Violante, F. S. (2005). Simultaneous determination of unmodified sevoflurane and of its metabolite hexafluoroisopropanol in urine by headspace sorptive extraction-thermal desorption-capillary gas chromatography-mass spectrometry. *J. Chromatogr. A* 1071, 131–134. doi: 10.1016/j.chroma.2004.09.039

Anacleto, J. F., Pleasance, S., and Boyd, R. K. (1992). Calibration of ion spray mass spectra using cluster ions. *Org. Mass Spectrom.* 27, 660–666. doi: 10.1002/oms.1210270603

Bierla, K., Godin, S., Lobinski, R., and Szpunar, J. (2018). Advances in electrospray mass spectrometry for the selenium speciation: focus on Se-rich yeast. *Trends Anal. Chem.* 104, 87–94. doi: 10.1016/j.trac.2017.10.008

Bongiorno, D., Ceraulo, L., Giorgi, G., Indelicato, S., Ferrugia, M., Ruggirello, A., et al. (2011b). Effects of the net charge on abundance and stability of supramolecular surfactant aggregates in gas phase. *J. Mass Spectrom.* 46, 195–201. doi: 10.1002/jms.1872

Bongiorno, D., Ceraulo, L., Giorgi, G., Indelicato, S., and Turco Liveri, V. (2011a). Do electrospray mass spectra of surfactants mirror their aggregation state in solution? *J. Mass Spectrom.* 46, 1262–1267. doi: 10.1002/jms.2013

Bongiorno, D., Ceraulo, L., Indelicato, S., Turco Liveri, V., and Indelicato, S. (2016). Charged supramolecular assemblies of surfactant molecules in gas phase. *Mass Spectrom. Rev.* 35, 170–187. doi: 10.1002/mas.21476

Bongiorno, D., Ceraulo, L., Ruggirello, A., Liveri, V. T., Basso, E., Seraglia, R., et al. (2005). Surfactant self-assembling in gas phase: electrospray ionization- and matrix-assisted laser desorption/ionization-mass spectrometry of singly charged AOT clusters. *J. Mass Spectrom.* 40, 1618–1625. doi: 10.1002/jms.965

Bongiorno, D., Indelicato, S., Giorgi, G., Scarpella, S., Liveri, V. T., and Ceraulo, L. (2014). Electrospray ion mobility mass spectrometry of positively charged sodium bis(2-ethylhexyl)sulfosuccinate aggregates. *Eur. J. Mass Spectrom. (Chichester)* 20, 169–175. doi: 10.1255/ejms.1261

Borysik, A. J., and Robinson, C. V. (2012). Formation and dissociation processes of gas-phase detergent micelles. *Langmuir* 28, 7160–7167. doi: 10.1021/la3002866

Cao, J., Liu, C., and Jia, Q., Di (2016). Complex solution chemistry behind the simple "one-pot" synthesis of vanadium-substituted polyoxometalates unraveled by electrospray ionization mass spectrometry. *Rapid Commun. Mass Spectrom*. 30, 14–19. doi: 10.1002/rcm.7641

Davis, A. L., and Clowers, B. H. (2018). Stabilization of gas-phase uranyl complexes enables rapid speciation using electrospray ionization and ion mobility-mass spectrometry. *Talanta* 176, 140–150. doi: 10.1016/j.talanta.2017.07.090

de Hoffman, E., and Stroobant, V. (2007). *Mass Spectroscopy: Principles and Applications, 3rd Edn*. NewYork, NY: John Wiley & Sons Ltd.

Di Marco, V. B., and Bombi, G. G. (2006). Electrospray mass spectrometry (ESI-MS) in the study of metal–ligand solution equilibria. *Mass Spectrom. Rev*. 25, 347–379. doi: 10.1002/mas.20070

Dorhout, P. K., Ford, N. B., and Raymond, C. C. (2017). Understanding the polychalcogenides as building blocks to solid state materials: speciation of polychalcogenides in solutions. *Coord. Chem. Rev*. 352, 537–550. doi: 10.1016/j.ccr.2017.10.017

Espinosa, M. S., Servant, R., and Babay, P. A. (2016). Study of metal-ligand species by ESI-MS: the case of La, Nd, and Th complexes with EDTA. *Microchem. J*. 129, 151–157. doi: 10.1016/j.microc.2016.06.018

Feng, C., Bi, Z., and Tang, H. (2015). Electrospray ionization time-of-flight mass spectrum analysis method of polyaluminum chloride flocculants. *Environ. Sci. Technol*. 49, 474–480. doi: 10.1021/es503681p

Gun, J., Modestov, A. D., Kamyshny, A., Ryzkov, D., Gitis, V., Goifman, A., et al. (2004). Electrospray ionization mass spectrometric analysis of aqueous polysulfide solutions. *Microchim. Acta* 146, 229–237. doi: 10.1007/s00604-004-0179-5

Hawlicka, E., and Swiatla-Wojcik, D. (2002). MD Simulation studies of selective solvation in methanol–water mixtures: an effect of the charge density of a solute. *J. Phys. Chem. A* 106, 1336–1345. doi: 10.1021/jp012662w

Indelicato, S., Bongiorno, D., Ceraulo, L., Calabrese, V., Piazzese, D., Napoli, A., et al. (2016). Electrospray ion mobility mass spectrometry of positively and negatively charged (1R,2S)-dodecyl(2-hydroxy-1-methyl-2-phenylethyl)dimethylammonium bromide aggregates. *Rapid Commun. Mass Spectrom*. 30, 230–238. doi: 10.1002/rcm.7422

Indelicato, S., Bongiorno, D., Indelicato, S., Drahos, L., Turco Liveri, V., Turiák, L., et al. (2013). Degrees of freedom effect on fragmentation in tandem mass spectrometry of singly charged supramolecular aggregates of sodium sulfonates. *J. Mass Spectrom*. 48, 379–383. doi: 10.1002/jms.3161

Indelicato, S., Bongiorno, D., Liveri, V. T., Mele, A., Panzeri, W., Castiglione, F., et al. (2014). Self-assembly and intra-cluster reactions of erbium and ytterbium bis(2-ethylhexyl)sulfosuccinates in the gas phase. *Rapid Commun. Mass Spectrom*. 28, 2523–2530. doi: 10.1002/rcm.7045

Jaklová Dytrtová, J., Jakl, M., Navrátil, T., Cvačka, J., and Pačes, O. (2016). An electrochemical device generating metal ion adducts of organic compounds for electrospray mass spectrometry. *Electrochim. Acta* 211, 787–793. doi: 10.1016/j.electacta.2016.06.108

Jo, J., Tu, Q., Xiang, R., Li, G., Zou, L., Maloney, K. M., et al. (2019). Metal Speciation in Pharmaceutical Process Development: Case Studies and Process/Analytical Challenges for a Palladium-Catalyzed Cross-Coupling Reaction. *Organometallics* 38, 185–193. doi: 10.1021/acs.organomet.8b00638

Kazimi, S. G. T., Iqbal, M. S., Mulligan, C. C., Frank Shaw, C., Iram, F., Stelmack, A. R., et al. (2019). Ligand exchange/scrambling study of gold(I)-phosphine complexes in the solid phase by DESI-MS analysis. *J. Am. Soc. Mass Spectrom*. 30, 2289–2296. doi: 10.1007/s13361-019-02319-y

Kumar, P., Jaison, P. G., Telmore, V. M., Alamelu, D., Aggarwal, S. K., Sadhu, B., et al. (2016). Gas phase reactions of uranyl with α-hydroxyisobutyric acid using electrospray ionization mass spectrometry and density functional theory. *J. Radioanal. Nucl. Chem*. 308, 303–310. doi: 10.1007/s10967-015-4664-6

Kumar, P., Jaison, P. G., Telmore, V. M., Sadhu, B., and Sundararajan, M. (2017). Speciation of uranium-mandelic acid complexes using electrospray ionization mass spectrometry and density functional theory. *Rapid Commun. Mass Spectrom*. 31, 561–571. doi: 10.1002/rcm.7817

Lapthorn, C., Pullen, F., and Chowdhry, B. Z. (2013). Ion mobility spectrometry-mass spectrometry (IMS-MS) of small molecules: separating and assigning structures to ions. *Mass Spectrom. Rev*. 32, 43–71. doi: 10.1002/mas.21349

Liu, Q., Lu, X., Peng, H., Popowich, A., Tao, J., Uppal, J. S., et al. (2018). Speciation of arsenic—a review of phenylarsenicals and related arsenic metabolites. *Trends Anal. Chem*. 104, 171–182. doi: 10.1016/j.trac.2017.10.006

Mapolelo, M. M., Stanford, L. A., Rodgers, R. P., Yen, A. T., Debord, J. D., Asomaning, S., et al. (2009). Chemical speciation of calcium and sodium naphthenate deposits by electrospray ionization FT-ICR mass spectrometry. *Energy Fuels* 23, 349–355. doi: 10.1021/ef800642b

Oss, M., Kruve, A., Herodes, K., and Leito, I. (2010). Electrospray ionization efficiency scale of organic compounds. *Anal. Chem*. 82, 2865–2872. doi: 10.1021/ac902856t

Perry, R. H., Splendore, M., Chien, A., Davis, N. K., and Zare, R. N. (2011). Detecting reaction intermediates in liquids on the millisecond time scale using desorption electrospray ionization. *Angew. Chem.* 123, 264–268. doi: 10.1002/ange.201004861

Raymond, O., Brothers, P. J., Buchner, M. R., Lane, J. R., Müller, M., Spang, N., et al. (2019). Electrospray ionization mass spectrometric study of the gas-phase coordination chemistry of Be 2+ ions with 1,2- and 1,3-diketone ligands. *Inorg. Chem*. 58, 6388–6398. doi: 10.1021/acs.inorgchem.9b00578

Raymond, O., Henderson, W., Brothers, P. J., and Plieger, P. G. (2018). Electrospray Ionisation Mass Spectrometric (ESI MS) screening and characterisation of beryllium complexes with potentially encapsulating aminopolycarboxylate and related ligands. *Eur. J. Inorg. Chem*. 2018, 1120–1130. doi: 10.1002/ejic.201701435

Tie, M., Li, B., Zhuang, X., Han, J., Liu, L., Hu, Y., et al. (2015). Selenium speciation in soybean by high performance liquid chromatography coupled to electrospray ionization-tandem mass spectrometry (HPLC-ESI-MS/MS). *Microchem. J*. 123, 70–75. doi: 10.1016/j.microc.2015.05.017

Tsednee, M., Huang, Y. C., Chen, Y. R., and Yeh, K. C. (2016). Identification of metal species by ESI-MS/MS through release of free metals from the corresponding metal-ligand complexes. *Sci. Rep*. 6, 1–13. doi: 10.1038/srep26785

Wang, C.-H., Bai, P., Siepmann, J. I., and Clark, A. E. (2014). Deconstructing hydrogen-bond networks in confined nanoporous materials: implications for alcohol–water separation. *J. Phys. Chem. C* 118, 19723–19732. doi: 10.1021/jp502867v

Waska, H., Koschinsky, A., and Dittmar, T. (2016). Fe- and Cu-complex formation with artificial ligands investigated by ultra-high resolution fourier-transform ion cyclotron resonance mass spectrometry (FT-ICR-MS): implications for natural metal-organic complex studies. *Front. Mar. Sci*. 3, 1–19. doi: 10.3389/fmars.2016.00119

Wen, J., Ning, P., Cao, H., Zhao, H., Sun, Z., and Zhang, Y. (2019). Novel method for characterization of aqueous vanadium species: a perspective for the transition metal chemical speciation studies. *J. Hazard. Mater*. 364, 91–99. doi: 10.1016/j.jhazmat.2018.09.069

Whitehouse, C. M., Dreyer, R. N., Yamashita, M., and Fenn, J. B. (1985). Electrospray interface for liquid chromatographs and mass spectrometers. *Anal. Chem*. 57, 675–679. doi: 10.1021/ac00280a023

Conflict of Interest: The authors declare that the research was conducted in the absence of any commercial or financial relationships that could be construed as a potential conflict of interest.

frontiers in Chemistry

ORIGINAL RESEARCH
published: 02 February 2021
doi: 10.3389/fchem.2020.628749

Organic Copper Speciation by Anodic Stripping Voltammetry in Estuarine Waters With High Dissolved Organic Matter

Jasmin Pađan[1], Saša Marcinek[1], Ana-Marija Cindrić[1], Chiara Santinelli[2], Simona Retelletti Brogi[2], Olivier Radakovitch[3,4], Cédric Garnier[5] and Dario Omanović[1]**

[1]*Ruđer Bošković Institute, Center for Marine and Environmental Research, Zagreb, Croatia,* [2]*CNR-Biophysics Institute, Pisa, Italy,* [3]*CNRS, IRD, INRAE, Coll France, CEREGE, Aix-Marseille University, Marseille, France,* [4]*IRSN (Institut de Radioprotection et de Sûreté Nucléaire), PSE-ENV/SRTE/LRTA, Saint-Paul-Les-Durance, France,* [5]*Mediterranean Institute of Oceanology, ECEM, Toulon University, La Garde, France*

The determination of copper (Cu) speciation and its bioavailability in natural waters is an important issue due to its specific role as an essential micronutrient but also a toxic element at elevated concentrations. Here, we report an improved anodic stripping voltammetry (ASV) method for organic Cu speciation, intended to eliminate the important problem of surface-active substances (SAS) interference on the voltammetric signal, hindering measurements in samples with high organic matter concentration. The method relies on the addition of nonionic surfactant Triton-X-100 (T-X-100) at a concentration of 1 mg L^{-1}. T-X-100 competitively inhibits the adsorption of SAS on the Hg electrode, consequently 1) diminishing SAS influence during the deposition step and 2) strongly improving the shape of the stripping Cu peak by eliminating the high background current due to the adsorbed SAS, making the extraction of Cu peak intensities much more convenient. Performed tests revealed that the addition of T-X-100, in the concentration used here, does not have any influence on the determination of Cu complexation parameters and thus is considered "interference-free." The method was tested using fulvic acid as a model of natural organic matter and applied for the determination of Cu speciation in samples collected in the Arno River estuary (Italy) (in spring and summer), characterized by a high dissolved organic carbon (DOC) concentration (up to 5.2 mgC L^{-1}) and anthropogenic Cu input during the tourist season (up to 48 nM of total dissolved Cu). In all the samples, two classes of ligands (denoted as L_1 and L_2) were determined in concentrations ranging from 3.5 ± 2.9 to 63 ± 4 nM eq Cu for L_1 and 17 ± 4 to 104 ± 7 nM eq Cu for L_2, with stability constants $\log K_{Cu,1}$ = 9.6 ± 0.2–10.8 ± 0.6 and $\log K_{Cu,2}$ = 8.2 ± 0.3–9.0 ± 0.3. Different linear relationships between DOC and total ligand concentrations between the two seasons suggest a higher abundance of organic ligands in the DOM pool in spring, which is linked to a higher input of terrestrial humic substances into the estuary. This implies that terrestrial humic substances represent a significant pool of Cu-binding ligands in the Arno River estuary.

Keywords: Arno River estuary, copper, organic ligands concentration, speciation, trace metals, surface active substances, metal complexing capacity

OPEN ACCESS

Edited by:
Carlos Rey-Castro, Universitat de Lleida, Spain

Reviewed by:
Pablo Lodeiro, GEOMAR Helmholtz Center for Ocean Research Kiel, Germany
Sylvia Gertrud Sander, University of Otago, New Zealand

****Correspondence:***
Saša Marcinek
smarcin@irb.hr
Dario Omanović
omanovic@irb.hr

Specialty section:
This article was submitted to Analytical Chemistry, a section of the journal Frontiers in Chemistry

Received: *12 November 2020*
Accepted: *29 December 2020*
Published: *02 February 2021*

Citation:
Pađan J, Marcinek S, Cindrić A-M, Santinelli C, Retelletti Brogi S, Radakovitch O, Garnier C and Omanović D (2021) Organic Copper Speciation by Anodic Stripping Voltammetry in Estuarine Waters With High Dissolved Organic Matter. Front. Chem. 8:628749. doi: 10.3389/fchem.2020.628749

INTRODUCTION

Copper (Cu) is an essential micronutrient in natural waters, required for the proper functioning of metabolic and respiratory processes for many aquatic species (Peers et al., 2005; Peers and Price, 2006; Annett et al., 2008; Glass and Orphan, 2012; Jacquot et al., 2014). It is also known for its toxic effects when exceeding a critical concentration threshold (Karlsson et al., 2010; Ytreberg et al., 2010) and thus is considered a specific pollutant of great ecotoxicological concern (Corcoll et al., 2019; Lopez et al., 2019). It is not the total copper concentration that is directly related to ecotoxicological effects but the fraction available for biological uptake (free and/or labile concentration) (Campbell et al., 2002; Sanchez-Marin et al., 2016; Zitoun et al., 2019). Therefore, for an accurate assessment of its potential impact on biota, the knowledge of Cu speciation, i.e., predicting the concentration of its bioavailable fraction, is of primary concern. The most important factor influencing Cu speciation in seawater is the concentration and quality (chemical structure) of the dissolved organic matter (DOM) (Sanchez-Marin et al., 2016). The range of copper concentrations between its necessity and toxicity is relatively narrow (Amin et al., 2013; Zitoun et al., 2019). However, the formation of strong complexes with organic ligands can reduce the bioavailable Cu fraction and, in most cases, maintains it in the optimal range (Buck et al., 2012; Whitby and van den Berg, 2015; Whitby et al., 2017). The presence of organic ligands is therefore of main significance in assessing the Cu bioavailability, with respect to both toxicity and necessity. Nevertheless, there is evidence that even organically complex copper is acquired by marine phytoplankton and bacteria (Semeniuk et al., 2015). Coastal areas and estuaries are the most relevant areas for Cu speciation studies because of the high potential for anthropogenic Cu contamination (e.g., Helland and Bakke, 2002; Blake et al., 2004; Louis et al., 2009) including secondary contamination by the release from sediment during estuarine mixing (e.g., Cobelo-Garcia and Prego, 2003). These areas are usually characterized by high concentrations of DOM from both allochthonous and autochthonous sources (Fellman et al., 2011; Retelletti Brogi et al., 2020), including biogenic thiol compounds and terrestrially derived humic and fulvic acids, which all form strong Cu complexes (Tang et al., 2000; Kogut and Voelker, 2001; Laglera and van den Berg, 2003; Shank et al., 2004; Whitby et al., 2017; Dulaquais et al., 2020). Besides regulating its bioavailable concentration, binding with these organic ligands in coastal waters is an important factor in Cu transport to the ocean (Helland and Bakke, 2002).

Due to experimental limitations of separation, extraction, and direct measurement of different metal-organic ligand complexes in seawater, an alternative approach based on complexometric titrations using electrochemical techniques (known as the determination of the metal complexing capacity of the sample) is preferentially used (Buck et al., 2012; Pižeta et al., 2015). As the concentration of metals in seawater is very low, various electrochemical techniques with low detection limits are commonly used, mainly stripping techniques: anodic and competitive ligand exchange adsorptive cathodic stripping voltammetry (ASV and CLE-AdCSV, respectively) (Sanchez-Marin et al., 2010; Buck et al., 2012; Omanović et al., 2015; Pižeta et al., 2015; Whitby et al., 2018). Knowledge about sources and chemical identity of detected ligands is scarce (Vraspir and Butler, 2009) and its acquisition is hindered by very complex chemical composition of natural DOM (Repeta, 2015). Useful qualitative information about the DOM pool in the aquatic environment (e.g., average aromaticity degree, molecular weight, and occurrence of humic-like, fulvic-like, and protein-like substances) can be gained indirectly via UV/Vis and fluorescence spectroscopic studies of its optically active fractions (colored and fluorescent dissolved organic matter, CDOM and FDOM) (Yamashita et al., 2011; Osburn et al., 2012; Lee et al., 2018; Galletti et al., 2019; Marcinek et al., 2020). Including this information in speciation studies could improve our understanding of the sources and composition of metal-binding organic ligands (Sanchez-Marin et al., 2010; Slagter et al., 2017; Watanabe et al., 2018; Wong et al., 2019; Whitby et al., 2020). However, these methods cannot characterize the binding sites or give information about nonfluorescent substances in DOM. This is possible by analyses of the molecular composition of DOM isolated from estuarine water (Minor et al., 2001; Minor et al., 2002; Dalzell et al., 2009; Abdulla et al., 2010; Zhang et al., 2018; Daoud and Tremblay, 2019; Thibault et al., 2019), e.g., using Fourier-transform infrared spectroscopy (FTIR) and nuclear magnetic resonance spectroscopy (NMR) (Abdulla et al., 2010; Zhang et al., 2018) or direct temperature-resolved mass spectrometry (DT-MS) complemented with either size-exclusion chromatography (Minor et al., 2002) or wet chemical techniques (Minor et al., 2001), which provide qualitative and quantitative analyses of major functional groups and information about their distribution.

Voltammetric stripping techniques are particularly sensitive to the composition of the sample solution. The well-known interferences in natural samples are due to the adsorption of surface-active substances (SAS) on the surface of the working electrode (usually Hg-drop) (Sander and Henze, 1996; Batley et al., 2004; Hurst and Bruland, 2005). This is obstructing both deposition/adsorption and stripping steps in ASV and CLE-AdCSV, resulting in lower sensitivity and/or deformation of the resultant voltammetric peak (Boussemart et al., 1993; Scarano and Bramanti, 1993; Plavšić et al., 1994; Louis et al., 2008). The extent to which SAS adsorbs on the electrode surface depends on the sample composition and the type of SAS. The final negative effect of the SAS influence is the inaccuracy of speciation parameters (Louis et al., 2008). Given that SAS is a significant fraction of DOM in seawater (Ciglenečki et al., 2020), the analysis of samples with high DOM content is particularly challenging. At potentials < −1.4 V, desorption of SAS from the electrode surface occurs (Sahlin and Jagner, 1996). Therefore, for removing the interferences during measurement, the "desorption step" (DS) was proposed (Louis et al., 2008; Louis et al., 2009; Gibbon-Walsh et al., 2012), i.e., switching to very negative potentials (e.g., −1.5 V) for a short time (e.g., 1–3 s), at the end of the main deposition period. DS reduces the effects of interferences to a large extent and enables a better electrode

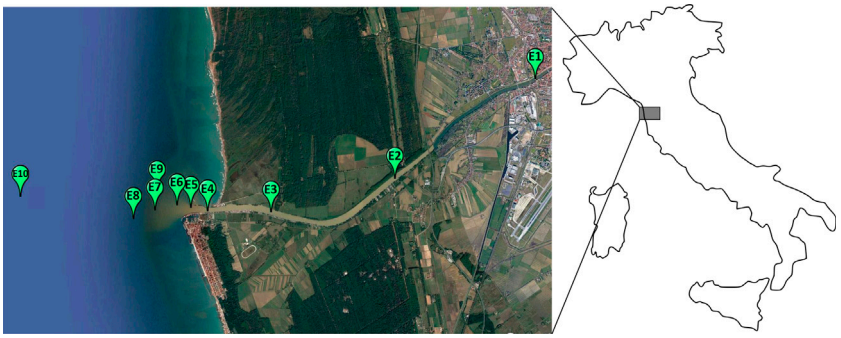

FIGURE 1 | Sampling sites along the Arno River estuary (Pisa, Italy) (image source: Google Earth Pro).

response and the formation of a well-defined peak. However, in samples with high DOM content, adsorption interferences cannot be completely removed, and some effects still exist. Previous studies showed that nonionic surfactant Triton-X-100 (T-X-100) added to the sample has an influence on the redox processes of Cu (Krznarić et al., 1994; Plavšić et al., 1994) and helps in obtaining reliable Cu complexation parameters in model solutions (Omanović et al., 1996). Based on this evidence, we assumed that its adsorption properties could be beneficial also for Cu speciation in natural samples hindered by the adsorbed SAS.

The main objective of this study is to explore the ability of nonionic surfactant T-X-100 to eliminate SAS interferences on the mercury electrode in the presence of high concentrations of DOM, without disturbing the original chemical speciation of Cu in the sample. The method was tested using fulvic acid (obtained from the International Humic Substances Society, IHSS) as a model of natural organic matter. The benefit of the proposed method for copper speciation studies is demonstrated in samples from the Arno River estuary (Italy), characterized by high organic matter content (up to 5.2 mg L^{-1} of dissolved organic carbon, DOC) and significant anthropogenic copper concentration (up to 48 nM of total dissolved copper, DCu). Obtained complexation parameters (i.e., detected Cu-binding ligands) are complemented with UV/Vis and fluorescence measurements (PARAFAC analysis) of DOM present in the estuary.

MATERIALS AND METHODS

Study Area

The Arno River is 242 km long (the 5th largest river in Italy) and its catchment covers an area of 8,228 km^2. The river flows into the Ligurian Sea about 10 km downstream from Pisa. The Arno River is impacted by various anthropogenic sources. Industrial activities like paper-mills, textile, electrochemical plants, and tanneries contribute to high levels of various inorganic and organic contaminants (Dinelli et al., 2005; Cortecci et al., 2009). For example, the Arno River accounts for 7% of the total DOC flux entering the western Mediterranean Sea, highlighting its relevant contribution (Retelletti Brogi et al., 2020).

For this study, the sampling was carried out at the Arno River estuary (**Figure 1**). The estuary region is 12 km long, highly stratified, and characterized by river flow extremes measured from 6 $m^3 s^{-1}$ during summer and up to 2000 $m^3 s^{-1}$ in winter [average discharge of 82.4 $m^3 s^{-1}$ (Retelletti Brogi et al., 2020)].

The lower part of the estuary hosts numerous anchored recreational/sailing boats, whose antifouling paint is a source of copper (Cindrić et al., 2015). This can potentially have unfavorable biological effects on the ecosystem in the estuary and the coastal region. Sampling was carried out in the periods of the year when the most intensive nautical traffic and the highest biological activity was expected (September 27, 2015, and April 5, 2016). Surface samples were collected at 10 sites along the salinity gradient (**Figure 1**).

Samples Collection

Surface samples (depth ~0.5 m) were collected using a van Dorn type 2.2 L horizontal water sampler (Wildco). Bottles for the sampling and sample storage for dissolved Cu measurement and Cu speciation analyses (FEP, fluorinated ethylene propylene, or PFA, perfluoroalkoxy, Nalgene) were previously cleaned with 10% HNO_3 (analytical reagent grade), rinsed several times with ASTM Type I water (labeled hereafter as Milli-Q water, 18.2 MΩ, Millipore, USA), and finally filled with Milli-Q water until use. FEP/PFA bottles were thoroughly rinsed with the sample and 1 L of a sample was then immediately taken for on-board filtration. Samples for dissolved organic carbon (DOC), chromophoric dissolved organic matter (CDOM), and fluorescent dissolved organic matter (FDOM) analyses were collected into 2 L acid-washed polycarbonate bottles (Nalgene) and kept refrigerated and in the dark.

Vertical profiles of the main physicochemical parameters (salinity, temperature, pH, and dissolved oxygen) along the salinity gradient were measured *in situ* at each site using a Hydrolab DS5 multiparameter (CTD) probe. The CTD probe was calibrated before each campaign.

Samples Preparation

For the determination of dissolved Cu concentrations and Cu speciation studies (determination of Cu complexing capacity, CuCC), samples were filtered on-board using precleaned (acid + Milli-Q) 0.22 μm cellulose-acetate syringe filters (Minisart,

Sartorius). For the analysis of total dissolved Cu concentrations, samples were acidified in the Lab with trace metal grade nitric acid (*TraceSelect*, Fluka) to pH < 2 and within the next few days UV-irradiated (150 W medium pressure Hg lamp, Hanau, Germany) directly in the FEP/PFA bottles for at least 24 h in order to decompose natural organic matter (Omanović et al., 2006; Monticelli et al., 2010; Cindrić et al., 2015). Samples for Cu speciation studies were kept at natural pH (pH = 8.2 ± 0.1) and stored in the fridge (+4°C) until analysis which was performed within 2 months.

Samples for DOC, CDOM, and FDOM were filtered in the laboratory (within 4 h of sampling) through a 0.2 µm pore size filter (Whatman Polycap, 6,705–3,602 capsules) and dispensed into 3 × 60 ml acid-washed polycarbonate (Nalgene) bottles, used as analytical replicates. DOC, CDOM, and FDOM were immediately measured after filtration. The filtration system (syringe + both filter types) was selected after several tests with Milli-Q water, since the filtered water showed no contamination with Cu or DOC, CDOM, and FDOM.

Determination of Dissolved Cu

Concentrations of dissolved Cu were determined by differential pulse anodic stripping voltammetry (DPASV). Measurements were carried out on Metrohm-Autolab (EcoChemie) potentiostat (PGSTAT128N) controlled by GPES 4.9 software in a three-electrode cell (663 VA Stand, Metrohm). Ag|AgCl|sat. NaCl electrode was used as the reference electrode, a Pt wire as the auxiliary, and a hanging mercury drop (HMDE) as the working electrode. The DPASV parameters used for the measurement of DCu are presented in **Supplementary Table S1**. Analyses were performed using a fully automated system consisting of the instrument, a home-made autosampler, and five Cavro XL 3000 syringe pumps (Tecan, United States). For the preparation of the project file for the GPES software, as well as for the treatment of the voltammograms and final calculations, the handling software was developed (https://sites.google.com/site/daromasoft/home/voltaa).

Concentrations of trace metals were determined by means of the standard addition method. A certified "Nearshore seawater reference material for trace metals," CASS-5 (NRC CNRC), was used for the validation of the Cu analysis. The obtained value (±standard deviation) was 0.370 ± 0.030 µg L^{-1} (certified value is 0.380 ± 0.028 µg L^{-1}).

Copper Speciation Analysis: Determination of Cu Complexing Capacity (CuCC)

For the determination of CuCC, the DPASV method was used (Louis et al., 2008). The experiments were performed using the same electrochemical system as described in the previous section (excluding the use of the autosampler). The parameters used for the DPASV measurements of electrolabile Cu are presented in **Supplementary Table S1**. In order to avoid the adsorption of Cu into the walls of cell compartments, a quartz cell was used (Cuculić and Branica, 1996). Three automatic burette systems were used to automate Cu titration (XL 3000 syringe pumps).

The titrations of natural samples were performed at a pH of 8.2 buffered with 0.01 M borate/ammonia buffer (the final concentration in the cell). The electrochemical cell was conditioned for ~1/2 h with 15 ml of the sample before a new 10 ml aliquot of the sample was measured. The titrations were performed by measuring the ambient Cu concentration (without Cu addition) and by increasing Cu concentration up to the maximum of 300 nM of total Cu concentration ($[Cu]_T$) (using 10^{-5} M and 10^{-4} M Cu stock solutions prepared by appropriate dilutions of an atomic absorption spectrometry standard solution, TraceCERT, Fluka). Each titration was composed of a total of 15 separate points (measured in triplicate), with the Cu concentrations equally distributed in logarithmic scale, i.e., similar increments in log $[Cu]_T$ (Garnier et al., 2004; Louis et al., 2009). Final points that deviated from the linear part of the titration curve were discarded, and thus some of the final titration curves were composed of less than 15 points (12–14). After each Cu addition, 30 min was estimated as enough time to reach the equilibrium conditions in the titration cell. For each Cu addition, 3 repetitive measurements were performed and peak intensities of all the points were thereafter used for the construction of complexometric curves. Before each titration, a Milli-Q test was performed to check the procedural blank. The concentration of Cu in Milli-Q was always below 0.1 nM. The theoretical background of the complexometric parameter calculation can be found elsewhere (Garnier et al., 2004; Omanović et al., 2015; Pižeta et al., 2015). Obtained complexometric curves were then treated by using the ProMCC software tool (Omanović et al., 2015). The number of ligand classes was estimated based on the shape of the Scatchard plot. For all titrations, the Scatchard plot showed a clear convex shape, indicating the presence of the 2-ligand classes. Complexation parameters were calculated by a nonlinear fitting of the Langmuir-Gerringa isotherm in a "logarithmic mode" (Omanović et al., 2015). The ambient speciation of Cu ($[Cu^{2+}]$ $[CuL_1]$ and $[CuL_2]$) originally present in the water sample was calculated from the concentrations of total dissolved Cu ([DCu]), $[L]_i$, and the conditional stability constants ($\log K_i$) of the Cu-binding organic ligands in the sample.

Model experiments with isolated organic matter (4 mg L^{-1} fulvic acid (FA), IHSS, batch 2S101F) were performed in organic-free, UV-digested seawater (UVSW) at the same pH as samples (pH = 8.2) adjusted with the borate/ammonia buffer. The UVSW was cleaned by MnO_2 slurry following the common procedure (van den Berg, 2006).

Dissolved Organic Carbon (DOC) and Dissolved Organic Matter Optical Properties Measurements

The DOC concentration was determined by high-temperature catalytic oxidation using a Shimadzu TOC-VCSN carbon analyzer (Santinelli et al., 2015). Prior to oxidation, samples were acidified with 2 M high purity HCl and purged for 3 min with pure air to remove inorganic carbon. To achieve satisfying analytical precision (±1%), up to 5 replicate injections were performed. The instrument performance was verified by

comparison of data with the DOC Consensus Reference Material (CRM) (Hansell, 2005) (batch #13/08-13, nominal concentration: 41–44 μM measured concentration: 43.2 ± 1.5 μM, n = 4). A calibration curve was measured with potassium hydrogen phthalate as the organic standard.

UV-Vis absorbance spectra were measured using a Jasco UV-visible spectrophotometer (Mod-7850) equipped with a 10 cm quartz cuvette, following the method reported by (Retelletti Brogi et al., 2015). Scans were performed at excitation wavelengths of between 230 and 700 nm. The spectrum of Milli-Q water, measured in the same conditions, was used as blank and subtracted from each sample. Absorbance spectra were treated by using the ASFit tool (Omanović et al., 2019). Absorbance at 254 nm (A_{254}) was expressed as the absorption coefficient (a_{254}) in m^{-1} (Stedmon and Nelson, 2015). The specific UV absorbance at 254 nm ($SUVA_{254}$) was calculated by dividing the absorption coefficient at 254 nm by the DOC concentration ($m^2\ g^{-1}$ C) and used as an indicator of the percentage of CDOM in the total DOM pool (Marcinek et al., 2020).

Fluorescence excitation-emission matrices (EEMs) were recorded using the Aqualog spectrofluorometer (Horiba-Jobin Ivon) in a 1 × 1 cm quartz cuvette as described in detail by (Retelletti Brogi et al., 2020). Briefly, EEMs were scanned at the excitation wavelength range of 250–450 nm with 5 nm increments and emission wavelengths ranged between 212 and 619 nm with 3 nm increments. Procedural blanks were checked by measuring EEM of Milli-Q water. Fluorescence intensities were normalized to Raman units (R.U.) using daily measured Raman peak of Milli-Q water (λ_{ex} = 350 nm, λ_{em} = 371–428 nm) (Lawaetz and Stedmon, 2009). Parallel factorial analysis (PARAFAC) was applied to identify the different components in the FDOM pool by using the decomposition routines for EEMs drEEM toolbox (version 0.2.0 for MATLAB (R2016a) (Murphy et al., 2013).

RESULTS AND DISCUSSION

Study of SAS Influence on the Voltammetric Signal of Cu

Problem Description

Initial examinations of the samples for the determination of the Cu speciation using the DPASV method with high DOC concentration (>2 mg L^{-1}) revealed that a characteristic Cu oxidation peak at the ambient Cu concentration is not present (even at relatively high Cu concentrations, e.g., 20–50 nM) and that an unusually high background current is obtained. The lack of a Cu oxidation peak was rather expected because the majority of the Cu present in the samples with a high DOM load is predicted to be complexed by strong organic ligands, which are not reducible at the applied deposition potential.

However, the unusually high background current, with one or two wide peaks, obtained in most of the samples, signified a potential problem. This is clearly visible in curve #1 in **Figure 2A**. In this example, the voltammetric procedure consisted specifically of only the deposition step at E_{dep} = −0.5 V, in the sample without any addition, except the borate buffer. The high background current in voltammetric measurements as the result of adsorbed SAS is not unusual, as it was shown for several metals (Scarano and Bramanti, 1993; Louis et al., 2008; Pađan et al., 2019; Pađan et al., 2020). To overcome problems caused by SAS adsorption, a "desorption step" (DS) (the application of a very negative potential, e.g., −1.5 V, for a short period, e.g., 1–3 s), at the end of the deposition period was proposed (Louis et al., 2008). However, in our case, the application of DS did not provide the

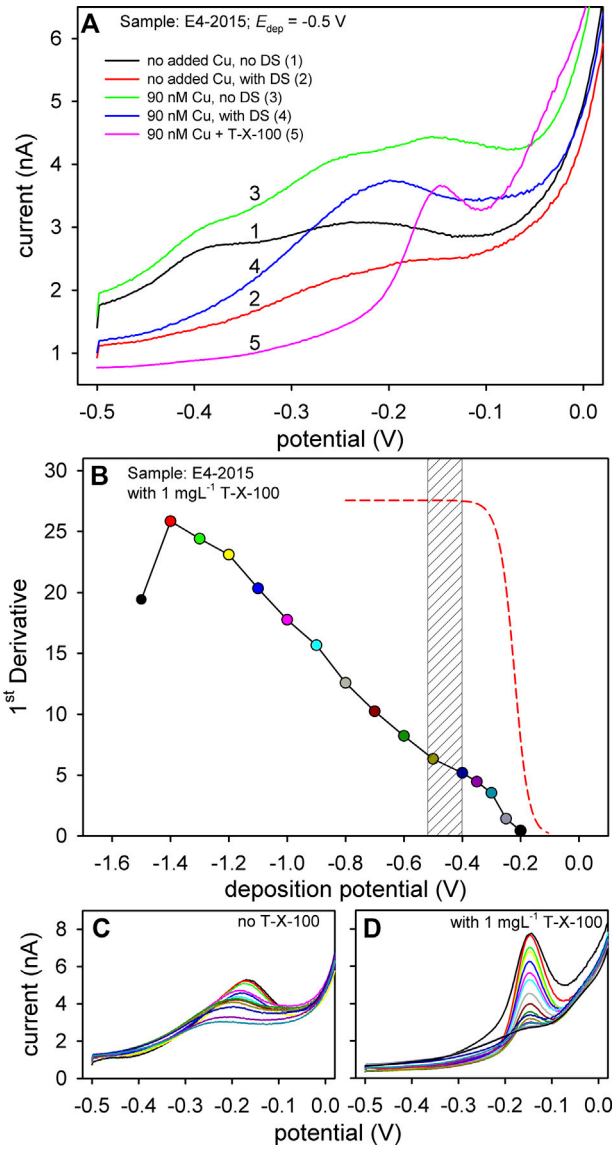

FIGURE 2 | (A) DPASV curves obtained at various scanning conditions, solution compositions, and Cu concentrations as indicated in the figure. **(B)** Pseudopolarogram of Cu obtained in sample taken at the site E4 (2015) with $[Cu]_T$ = 90 nM and with the addition of 1 mg L^{-1} T-X-100. The red dashed line illustrates the Cu pseudopolarogram without organic matter. Bottom plots represent the obtained voltammograms of pseudopolarographic measurements ($[Cu]_T$ = 90 nM) without the addition of T-X-100 but using the desorption step **(C)** and with the addition of 1 mg L^{-1} T-X-100 **(D)**. Different colors represent voltammograms obtained at different deposition potentials.

expected result due to the high content of organic matter, i.e., SAS present in the samples. Although a much better signal was obtained by applying a DS (curve #2, **Figure 2A**), the shape of the voltammogram at the potential range of the anodic Cu peak was still not adequate for the extraction of its intensity. The undefined wide stripping peak at the given potential was present even if the deposition of Cu was performed at potentials more positive than its redox potential; $E_{dep} = > -0.2$ V (either with or without the DS). The problem of the strange background current was even more apparent when the measurements were performed with the addition of Cu. Without the DS, a totally undistinguishable voltammogram was obtained at 90 nM Cu concentration (curve #3, **Figure 2A**). Although considerably better, the scan with the DS still produced a wide and poorly resolved peak (curve #4, **Figure 2A**). Intensities extracted from such voltammograms would be questionable, and consequently, constructed complexation curves and obtained complexation parameters would be entirely unreliable.

To resolve the problem of the adsorbed layer of the SAS on the Cu voltammetric signal, the idea was to introduce a competitive adsorptive process. The used compound should have a competitive effect on SAS adsorption but not on the Cu speciation chemistry in the bulk of the solution. Thus, a nonionic surfactant Triton-X-100 (T-X-100) was chosen for this purpose, since it does not form a complex with Cu (Krznarić et al., 1994; Omanović et al., 1996; Plavšić et al., 2009). The modified procedure employed here consists of adding T-X-100 at a concentration of 1 mg L^{-1} to the sample being analyzed. It has already been shown by several authors that T-X-100 could be beneficial in resolving some of the voltammetric issues. For example, T-X-100 was used for the voltammetric determination of iodine in seawater samples (Luther et al., 1988; Žic et al., 2012), for the separation of poorly resolved redox processes of Cu and Cu-EDTA (Omanović et al., 1996), and for the enhancement of the Cu oxidation by destabilizing formed $CuCl_2^-$ during the anodic scan (Plavšić et al., 1994). The benefit of adding T-X-100 to our samples is illustrated by curve #5 in **Figure 2A**. Compared to all other curves in the graph, a clearly resolved and narrow anodic Cu peak was obtained, from which extraction of Cu peak intensities is much more convenient.

For characterization of the interaction of metals with organic ligands, pseudopolarographic measurements (known also as stripping chronopotentiometry at scanned deposition potential, SSCP, or scanned stripping voltammetry, SSV) are proposed using either Hg (drop or film) or a solid electrode (Lewis et al., 1995; Luther III et al., 2001; Omanović and Branica, 2004; Town and van Leeuwen, 2004; Serrano et al., 2007; Domingos et al., 2008; Gibbon-Walsh et al., 2012; Bi et al., 2013; Town and van Leeuwen, 2019). The methodology has advanced in recent years, enabling the full characterization of the SSCP/pseudopolarographic waves (Serrano et al., 2007; Pinheiro et al., 2020) providing the heterogeneity of labile macromolecular metal-organic complexes. The full characterization of Cu complexes still has to be done using this methodology. As such, it is often used to make a "fingerprint" of the sample (Louis et al., 2008; Nicolau et al., 2008; Domingos et al., 2016). In **Figure 2B**, an example of the Cu pseudopolarogram obtained in an estuarine sample (E4, 2015) is presented, along with the illustrated pseudopolarogram representing the expected shape of labile inorganic Cu in the absence of organic matter (red dashed line). At this point, our goal with pseudopolarographic measurement is only to show the inherent complexity of Cu speciation by using ASV and adequately present the influence of SAS on its voltammetric behavior. The pseudopolarogram presented in **Figure 2B** served as an example of the sample "fingerprint" and to support the estimation of adequate deposition potential for the Cu complexation measurements (shaded region). Based on the basic features of presented waves (the shift of the pseudopolarograms toward negative potentials upon complexation with inorganic/organic ligands or its inclination) (Lewis et al., 1995; Serrano et al., 2007; Bi et al., 2013; Pinheiro et al., 2020), there is clear evidence that the reduction of various Cu-organic complexes occurs along the scanned deposition potentials. The increase of the intensity could be explained by the progressive reduction of various Cu-organic complexes (heterogeneous binding sites). Note that the presented pseudopolarogram was obtained with the addition of T-X-100. The corresponding voltammograms from which the pseudopolarogram was constructed are presented in the right bottom plot, clearly showing the fully resolved Cu peak at the same position. The construction of an analog pseudopolarogram in the sample without T-X-100 was not possible due to inadequate Cu anodic peaks, even with the applied DS step (left bottom plot). A clear difference between voltammograms with and without the added T-X-100 is shown here and is evident during Cu titrations as well (**Supplementary Figure S1**). It is interesting to point out the drop of the peak intensity of the point obtained at $E_{dep} = -1.5$ V. Namely, from this to more negative potentials, the adsorption of T-X-100 strongly decreases (Omanović et al., 1996; Sander and Henze, 1996), and its benefit on the shape of Cu anodic peak weakens (top black voltammogram at right bottom plot).

Although the positive effect of the T-X-100 addition was significant, we kept the desorption step as a procedural parameter because it was found that it does not have a negative effect on the final voltammogram if applied for only 1 s. However, the potential of the DS should not be more negative than −1.5 V and it should be as short as possible to avoid complete desorption of T-X-100.

To verify the proposed method, additional test experiments were performed in "organic-free" seawater (UVSW) with and without added fulvic acid as a model of natural organic matter.

Verification of the Methodology

Organic-Free Seawater

As noted previously, it is very important that added T-X-100 does not have a competitive effect on Cu complexation by natural ligands (especially organic). If that was the case, the effect would be visible on titration curves and pseudopolarograms. According to the basic model experiments, presented in the following sections, this is not the case.

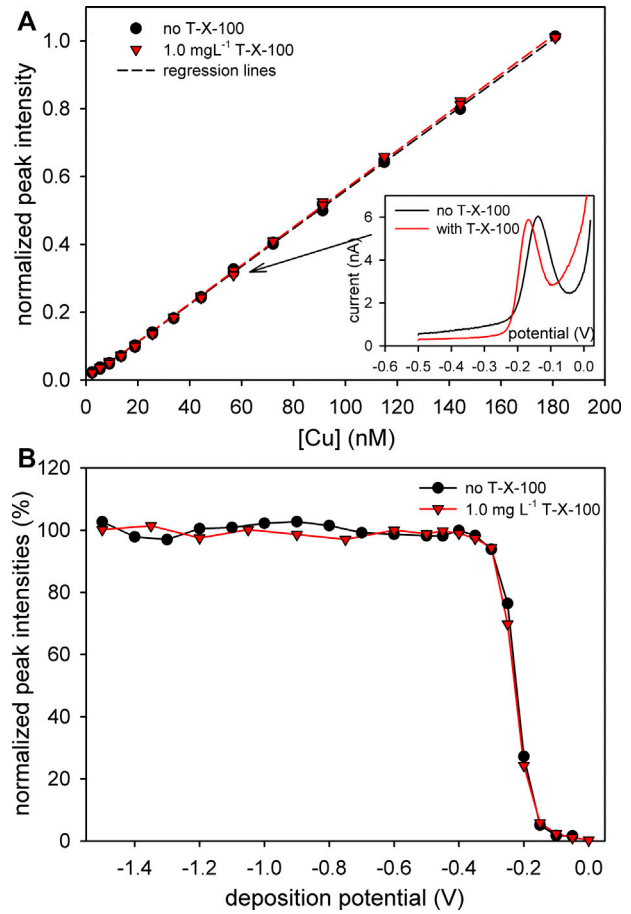

FIGURE 3 | (A) Copper titration curves obtained in UVSW (pH = 8.2) with and without the addition of 1 mg L^{-1} T-X-100 (for better comparison, the peak intensities were normalized on the highest value). Inset: Cu voltammograms with and without T-X-100 corresponding to Cu concentration indicated by the arrow. **(B)** Normalized pseudopolarograms obtained with and without the addition of 1 mg L^{-1} of T-X-100 (intensities normalized to the estimated limiting value).

Titrations with increasing Cu concentrations were first performed in UVSW (i.e., in the absence of organic ligands) with and without added T-X-100. As shown in **Figure 3A**, normalized intensities (with and without added T-X-100) showed the same linear relationship with increasing concentration of Cu. Normalized intensities (the 1st derivative as an analytical signal) were used for better comparison. In both cases, well-resolved Cu anodic voltammograms were obtained (inset in **Figure 3A**) and there is no curvature shape at the foot of the titration curves, characteristic for titration of samples with organic ligands (Pižeta et al., 2015), indicating that there is no complexation of Cu by T-X-100. The small negative shift and a slightly narrower anodic peak obtained with T-X-100 could be explained by the destabilization of formed $CuCl^{2-}$ during the anodic scan (Plavšić et al., 1994).

Furthermore, in cases where Cu forms a complex with T-X-100, a shift and/or a change in the shape of pseudopolarograms at a potential range more negative than the reduction potential of inorganic Cu would be expected (Lewis et al., 1995; Omanović, 2006; Gibbon-Walsh et al., 2012; Pinheiro et al., 2020). However, the pseudopolarograms obtained with and without the addition of T-X-100 showed almost the same shape (**Figure 3B**). This is in slight contrast from the experiment performed by (Sahlin and Jagner, 1996) using striping potentiometry with a mercury film electrode with a fully saturated T-X-100 layer (1,000 mg L^{-1}) in which a slight shift of the pseudopolarographic wave was observed. However, the concentration of T-X-100 used in their experiment was 1,000× higher (1 g L^{-1}) than in our work and as such is not directly comparable. Therefore, based on our experiments presented in **Figure 3**, it can be assumed, with great confidence, that, at the concentration used in our work, T-X-100 did not form a complex with Cu and as such it works as "interference-free" for Cu speciation studies using ASV.

FA as a Model of Natural Organic Matter

Further examination of the proposed methodology using T-X-100 (1 mg L^{-1}) was performed in UVSW with the addition of 4 mg L^{-1} of FA as a model of terrestrial organic matter showing considerable surface activity and 50 nM of added Cu (all experiments performed at pH = 8.2). The selected voltammograms are presented in **Figure 4A** and corresponding pseudopolarograms in **Figure 4B**. For comparison purposes, a voltammogram without FA (but with T-X-100) is presented by curve #1 in **Figure 4A**. In the sample with 4 mg L^{-1} FA and 50 nM of Cu and without the applied DS, a relatively high background current was obtained, with a relatively wide Cu peak (curve #2, **Figure 4A**).

Compared to the poorly shaped Cu signal in the real estuarine sample presented in **Figure 2A**, this peak seems easily resolvable despite the curvature baseline under the peak. However, the voltammogram in the presence of FA without added Cu shows a small peak at a slightly more positive potential (curve #2′, **Figure 4A**), making the manual construction of the curvature baseline more complicated. The above-mentioned problem in the Cu intensity determination is more profound at the low Cu intensities, which correspond to the foot of the titration curve where strong complexing ligands dominate. This in turn may introduce a high uncertainty in the determination of the complexation parameters, making them ultimately unreliable (Omanović et al., 2010). By applying DS, a better resolved and higher Cu peak is obtained (curve #3, **Figure 4A**). It was shown that the main influence of the adsorbed FA occurs during the stripping step, with Cu-FA considered as a labile complex (Town, 1997). Due to the nature of the differential pulse technique, Cu oxidized during the applied pulse is being progressively concentrated in the vicinity of the electrode surface and immediately complexed by the accumulated organic ligands, causing the shift of the oxidation peak to a more negative potential (Town, 1998). This scenario is likely to occur taking into account the fact that the Cu complex with FA is directly reducible (Whitby and van den Berg, 2015). The lability of Cu-FA complexes and problems associated with DPASV measurement of Cu in the case of adsorbable ligands, such as FA, are already documented in the literature (Soares and Vasconcelos, 1994; 1995).

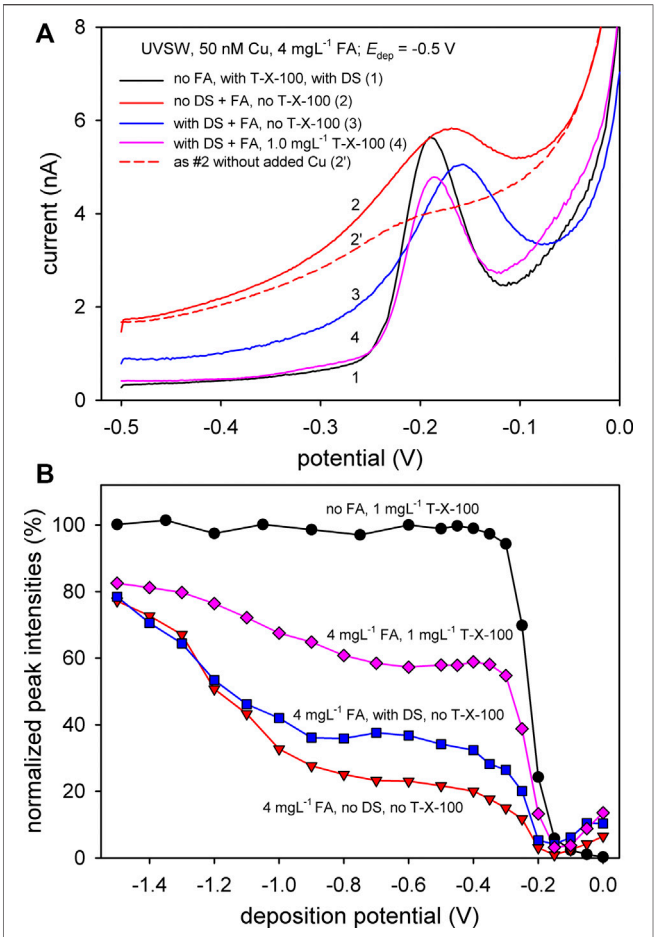

FIGURE 4 | (A) DPASV curves obtained in UVSW at various scanning conditions and solution composition as indicated in figure. **(B)** Pseudopolarogram of Cu obtained in UVSW at various scanning conditions and solution composition as indicated in the figure.

The Cu stripping peak was further improved by the addition of T-X-100 (curve #4, **Figure 4A**). The same shape and the peak potential in presence of FA, after the addition of T-X-100, as the one without added FA (curve #1, **Figure 4A**) indicate that T-X-100 practically eliminated the influence of the SAS adsorbed during the stripping step.

The problems associated with the stripping voltammetry of Cu in the presence of a high concentration of organic matter are reflected in the shape of the pseudopolarograms. As presented in **Figure 4B**, a clear reversible pseudopolarographic wave of Cu was obtained in the absence of FA. Upon the addition of FA, the form of the pseudopolarogram considerably changed. For all pseudopolarograms with added FA, the decrease of the intensity of the initial value without FA was around 20% at a high deposition potential (E_{dep} = −1.5 V). However, in the potential range between −0.8 and −0.4 V, the decrease of the intensity was much higher: ~ 40% in the presence of 1 mg L^{-1} T-X-100 and even ~75% (w/o DS) and ~65% (with DS) in the absence of T-X-100. The decrease of intensities at more positive potentials is already reported in the literature (Town and Filella, 2000; Gibbon-Walsh et al., 2012), indicating the complexation of the Cu with the added FA.

As mentioned earlier, the shift of the pseudopolarographic wave in the case of labile reversible Cu complexes, or those which are irreversibly reduced, could be used to determine the stability constants of formed complexes by using the so-called "chelate scale" (Lewis et al., 1995; Omanović, 2006; Gibbon-Walsh et al., 2012). With this in mind, the steep increase of intensities in pseudopolarograms without T-X-100 at potentials more negative than −0.9 V may indicate the presence of very strong organic complexes with high stability constants which are irreversibly reduced (Lewis et al., 1995; Branica and Lovrić, 1997; Gibbon-Walsh et al., 2012). This increase was not observed in experiments with Cu-FA performed using a gold-vibrating electrode (Gibbon-Walsh et al., 2012), whereas in experiments of (Town and Filella, 2000) or (Chakraborty et al., 2007), this range of deposition potentials was not scanned and could not be compared. If the metal-to-ligand ratio in the bulk of the solution used in the work of (Gibbon-Walsh et al., 2012) is compared to our ratio, the extent of the decrease of intensities at E_{dep} range between −0.8 and −0.4 V in our experiment is larger than expected. This is probably caused by the above-discussed strong influence of accumulated FA on the stripping process, which is much stronger on a Hg electrode than on the vibrating Au-microelectrode. The observed increase of intensities toward more negative potentials could also be partially related to the decreasing FA adsorption. This is supported by the progressive shift of Cu peak potentials (up to ~ Δ20 mV between −1.5 and −0.7 V) in voltammograms used for the construction of pseudopolarograms without DS (data not shown). With the applied DS, the shift was only ~ Δ5 mV, which confirms that DS removes the accumulated FA to a great extent. There was "only" ~ 40% decrease of intensity (of the initial value without FA) at E_{dep} range between −0.8 and −0.4 V after the addition of T-X-100 (with no change in the Cu peak potentials across the scanned range), which is much closer to the values obtained by Gibbon-Walsh et al. (2012). Even after the addition of T-X-100, the small increase of intensities, from E_{dep} = −0.9 V to more negative values, remained. This is also evident in the pseudopolarogram of the natural estuarine sample (**Fig. 2B**). It indicates that 1) there is still a portion of FA adsorbed during the deposition step or 2) a portion of the strong Cu-FA complexes are irreversibly reduced at this range of potentials (Lewis et al., 1995; Gibbon-Walsh et al., 2012). The detailed examination of Cu-FA interactions is beyond the scope of this paper and was not further studied.

Copper Speciation in the Estuarine Samples

Figure 5 presents all the results relevant for the Cu speciation study in samples collected for two different periods, the early spring and the late summer.

Total Dissolved Copper

A strong decrease of dissolved copper (DCu) concentrations with increasing salinity was observed for both campaigns with a slightly different distribution in the salinity gradient (**Figure 5A**). For the late summer campaign (September 2015), which is characterized by a lower river discharge (as evident from

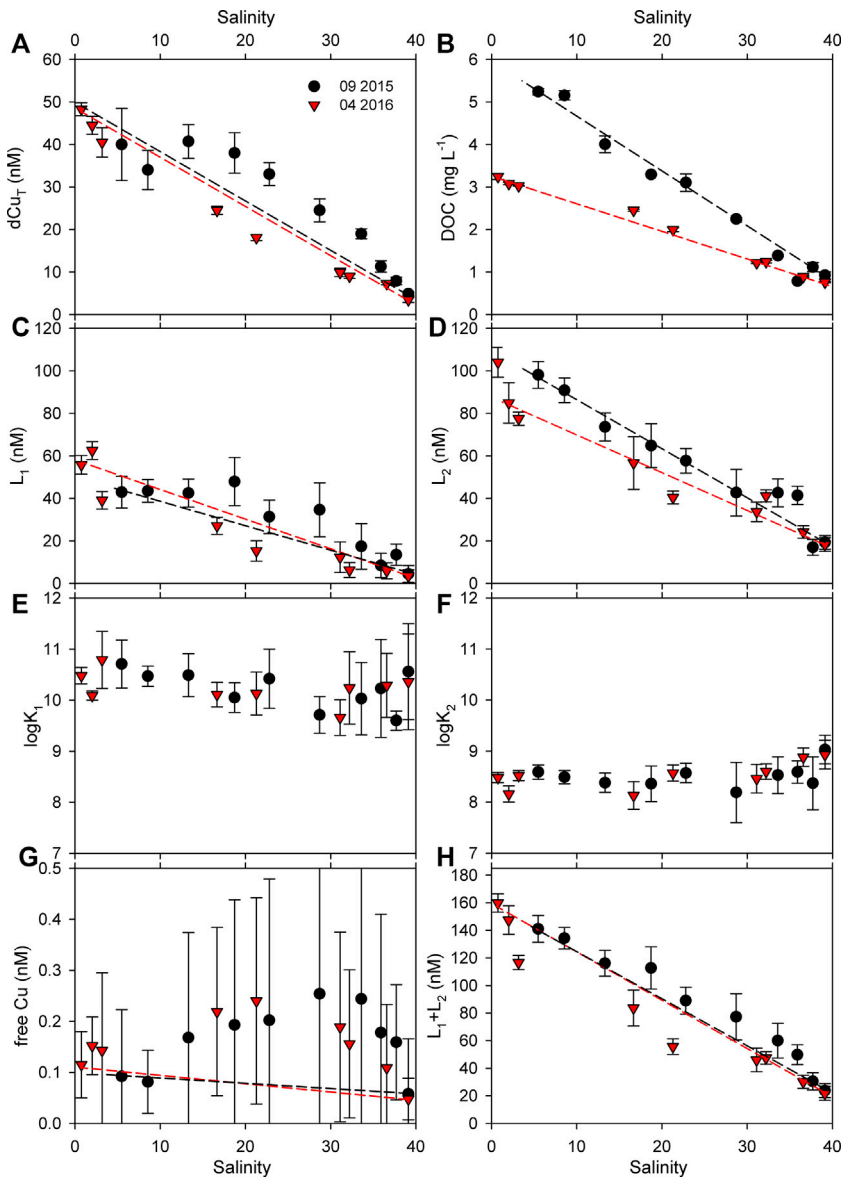

FIGURE 5 | Measured parameters along the estuarine segment for two sampling periods. Uncertainties are expressed as 95% confidence intervals. Dashed lines represent the projected conservative trends.

the salinity at the first site, E1, and the salinity contour plot in **Supplementary Figure S2**) (Retelletti Brogi et al., 2020), there is an increase of Cu concentration at the site E3, most likely caused by an anthropogenic input of Cu. Namely, numerous boat anchorage sites are found in the part of the estuary that begins between sites E2 and E3 (**Supplementary Figure S3**). In the summer period, these locations were fully occupied by boats. Thus, the observed increase of Cu in that region could be ascribed to the leaching of the Cu from the boats' antifouling paints, in which Cu is used as the biocide component (Turner, 2010; Cindrić et al., 2015). In the spring campaign (April 2016), due to the absence of the anchored boats (**Supplementary Figure S3**), Cu input was low. In this period, removal of dissolved Cu along the salinity gradient is implied by its deviation from the conservative line. This is probably the result of the flocculation process, which is common at lower salinities (Sholkovitz, 1976; Waeles et al., 2008). The concentrations of dissolved Cu in the seawater end-member for both periods reached the range characteristic for a clean coastal and open Mediterranean Sea area (Oursel et al., 2013; Migon et al., 2020).

Dissolved Organic Carbon

DOC concentrations show clear conservative behavior along the salinity gradient in both campaigns, with decreasing concentrations toward the sea end-member. Removal and/or production of DOM have a small impact on the DOC

concentration within the estuary, suggesting that the dilution of DOC in riverine water with marine water is the main process affecting DOC dynamics in the estuary. The DOC concentration is almost 2× higher in the late summer than in the spring campaign in the river end-member (5.2 mg L^{-1} in September 2015 in contrast to 3.3 mg L^{-1} in April 2016), whereas the sea end-member shows the same DOC values in both periods (~0.8 mg L^{-1}). In both periods, in the river end-member (at the E1 site), the measured DOC concentrations are in agreement with the DOC seasonal cycle observed in the river (Retelletti Brogi et al., 2020). High concentrations of DOC in the Arno River are the result of the weathering processes, especially during flood events, which primarily bring the terrestrial DOM, as well as the autochthonous production during spring and summer periods (Retelletti Brogi et al., 2020). Anthropogenic input of DOM also plays a role, because of the numerous anthropogenic activities in the upstream riverine region.

Copper-Binding Ligands and Estimation of Copper Bioavailability

Applying the adapted methodology for the determination of Cu speciation, well-shaped complexometric titration curves were obtained (examples are given in **Supplementary Figure S4**). Two classes of ligands were identified in all samples, denoted as L_1 and L_2, corresponding to a stronger and a weaker class of organic ligands, respectively. Concentrations of L_1 ranged from 3.5 ± 2.9 to 63 ± 4 nM eq Cu, whereas L_2 concentrations were higher and ranged from 17 ± 4 to 104 ± 7 nM eq Cu (**Figures 5C,D**). The concentration of both ligand classes decreased with the salinity, as was similarly observed for DCu and DOC. Along the estuary, the concentrations of ligands exceeded the corresponding total dissolved Cu concentrations, which are usually obtained in coastal regions (Bruland et al., 2000; Hurst and Bruland, 2005; Louis et al., 2009; Plavšić et al., 2009; Wong et al., 2018). The apparent stability constants ($\log K_{Cu}$) of the two ligand classes ranged from 9.6 ± 0.2 to 10.8 ± 0.6 for L_1 and from 8.2 ± 0.3 to 9.0 ± 0.3 for L_2, without a noticeable difference between the two sampling periods (**Figures 5E,F**). The ranges of estimated constants are typical for estuarine and coastal regions obtained by the ASV method and reflect the so-called "detection window" (DW) of the method (Apte et al., 1988; Bruland et al., 2000; Pižeta et al., 2015).

One of the purposes of the determination of metal complexing parameters is to estimate the free metal concentration, which is considered to be the most bioavailable/toxic. Having in mind the potential overestimation of free Cu using the ASV method, as will be discussed later, we refer to it as "free" Cu (quoted). In our study, the estimated "free" Cu concentrations ranged from 50 to 250 pM, following the strong positive deviation from the projected conservative line. The obtained trends are the result of the estimated complexation parameters, along with the dissolved Cu concentration. These are fairly high values of "free" Cu, taking into account the fact that the estimated threshold toxicity level is around 10 pM (Sunda et al., 1987; Gledhill et al., 1997), but as already mentioned they are likely overestimated due to the methodological problems.

The measured concentrations of the stronger ligand class (L_1) are similar to dissolved Cu concentrations. Although in some cases L1 was almost saturated with Cu at its ambient concentration, Cu was still mainly controlled by the abundance of strong ligand class (L_1) with high stability constants: between ~55 and 90% of dissolved Cu exists solely in the form of strong complexes.

Optical Properties of DOM

PARAFAC analysis applied to all the samples revealed 5 FDOM components. The components spectra were compared with previous studies by using the Openfluor database (Murphy et al., 2014) and identified as microbial humic-like (C1), terrestrial fulvic-like (C2), protein-like (C3), terrestrial humic-like (C4), and protein + PAH-like (polycyclic aromatic hydrocarbons) (C5). In both periods examined here, the protein-like component dominates the FDOM pool (**Supplementary Table S2**). This is in agreement with the two-year study performed in the Arno River (Retelletti Brogi et al., 2020). The average percentage of microbial humic-like (C1) and protein-like (C3) components is approximately the same in the two seasons (25.1% and 25.1% for C1 and 31.7% and 34.0% for C3 in spring and late summer, respectively), whereas terrestrial components (C2 and C4) represent a higher average percentage of the FDOM pool in spring (21.0% for C2 and 15.8% for C4) than in late summer (14.6% for C2 and 9.6% for C4) (**Supplementary Table S2**), due to the higher river discharge in spring. However, the highest difference is observed for the protein + PAH-like component (C5), whose average percentage in the whole FDOM pool was 6.4% in spring and 16.7% in late summer. This can be the consequence of intense touristic activity in late summer, i.e., extensive automobile and boat traffic in the area, introducing PAH-like DOM from the exhaust. $SUVA_{254}$ supports a change in DOM pool between the two seasons, suggesting a higher percentage of chromophoric DOM in late summer than in spring (**Supplementary Figure S5**).

Linking Copper Organic Ligands with DOM Properties

The stability constants obtained in this study appear to be lower at midsalinity range than at the end-members for both ligand types (**Figures 5E,F**). However, considering the associated uncertainties, there is no clear statistical difference among them. Despite that, the obtained trends could indicate the change in the composition of the organic ligands at different salinities. A change in DOM composition in the salinity gradient is suggested by the decrease of $SUVA_{254}$ and DOC normalized PARAFAC components toward the sea end-member (excluding the C5/DOC in spring) (**Supplementary Figure S5**), signifying the decrease of the chromophoric and fluorescent fraction in the DOM pool (the addition of nonchromophoric DOM and/or removal of chromophoric DOM). While the sum of the ligands (ΣL) correlates with the distribution of DOC, a_{254}, and all PARAFAC components ($r^2 > 0.9$), the obtained trends of stability constants in the salinity gradient do not show a strong link with any of the optical properties of DOM (CDOM/FDOM) (data not shown). Higher stability constants at a high salinity could be a consequence of the addition of organic ligands with

stronger binding constants (Whitby et al., 2017) not visible by UV/Vis and fluorescent measurements. Another possibility is that removal of ASV-labile organic ligands occurs at a high salinity which could lead to a slight increase of conditional stability constants.

A different relationship between the sum of the ligands (ΣL) and the DOC is observed in spring and summer: the estimated slope of their relationship is ~2× higher during spring than during summer (**Figure 6A**). Although the DOC, a_{254}, $SUVA_{254}$ and DOC normalized fluorescence intensities of all PARAFAC components (**Supplementary Figure S5**) are higher in late summer than in spring, the DOM pool in spring is more abundant with Cu-binding ligands. This can be linked to a higher percentage of terrestrial fulvic and humic components (C2 and C4, respectively) in the FDOM pool in spring (**Figures 6C,E**).

This is in agreement with other studies performed in estuarine regions, which suggest that humic and fulvic acids are the major source of organic ligands in these environments (Kogut and Voelker, 2001; Yang and van den Berg, 2009; Whitby and van den Berg, 2015; Wong et al., 2018; Dulaquais et al., 2020). Along with the humic substances, it was found that biogenic thiourea-type thiols are abundant ligands in estuarine environments (Whitby et al., 2017). A strong positive correlation between ΣL and the dissolved Cu concentration is observed in our study, which is on average the same for both periods (**Supplementary Figure S6**), suggesting that Cu-binding ligands could be the driver of DCu estuarine geochemistry. The increase of the organic ligands in the midsalinity range (S = 15–30), in late summer, could be a biological response to Cu release in the boat anchorage area (Zitoun et al., 2019). *In situ* production mainly releases protein-like substances (Osburn et al., 2012) and in this study, the protein component does indeed show an increase in the midsalinity range in late summer, while in the spring this is not the case. However, a similar increase is observed for all other components, showing a positive correlation with ΣL. Even though *in situ* production can also cause the increase of humic-like components (Romera-Castillo et al., 2010; Marcinek et al., 2020), without additional biological information we cannot conclude that the correlation between ΣL and the DCu in late summer is related to any extent to a biological response to Cu-stress.

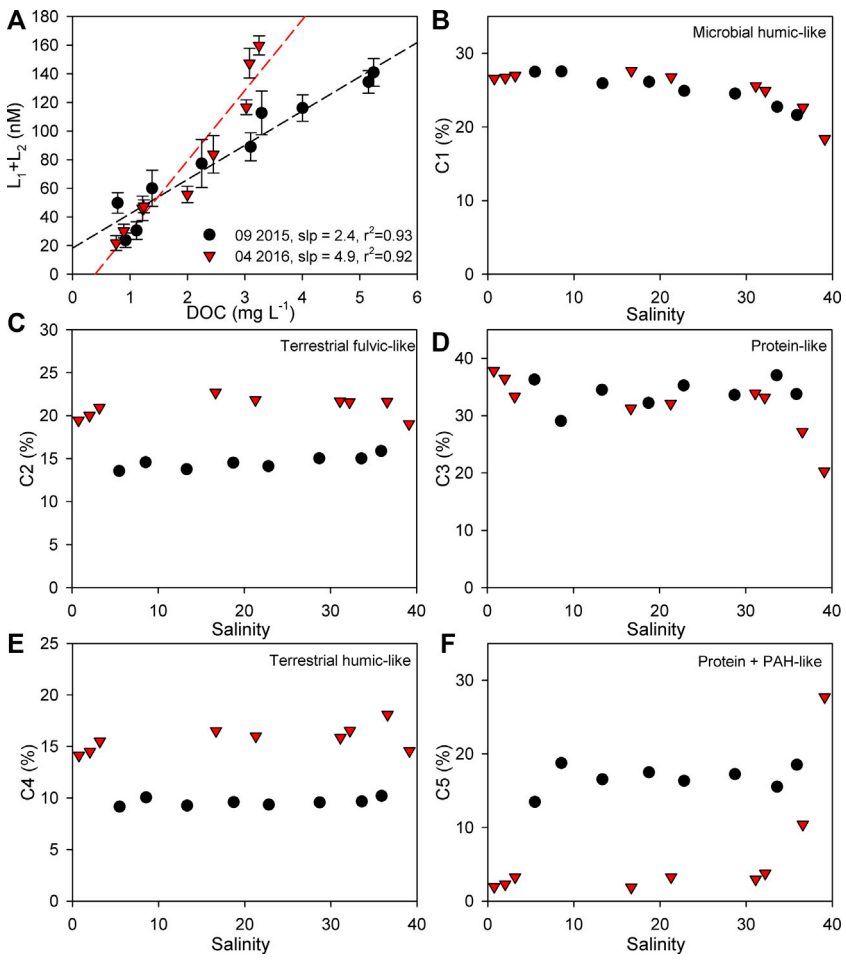

FIGURE 6 | Relationship between the sum of organic ligands (L_1+L_2) and DOC **(A)** and the variation in the percentage of PARAFAC components (C1–C5) along the salinity gradient **(B–F)**. Dashed lines represent the linear regression of the data.

Evaluation of Derived Complexation Parameters and Anodic Stripping Voltammetry Method Limitations

The method of calculation of complexation parameters (free and/or inorganic Cu, ligand concentrations, and conditional stability constants) in natural samples using both ASV and CLE-AdCSV provides results which are "operationally defined" (Bruland et al., 2000). Namely, the derived apparent stability constants depend strongly on the applied DW, which is expressed as the "side reaction coefficient" (α) (Bruland et al., 2000; Buck et al., 2012; Pižeta et al., 2015). For ASV, α is much smaller than it is for the CLE-AdCSV method in which the ligand with known stability constants is used as a competing ligand. In our measurements, the calculated logα is 1.13 (the ratio of the sum of all inorganic Cu species vs. free Cu concentration), whereas for CLE-AdCSV, logα depends on the used competitive ligand type and its concentration, and for Cu, it is usually logα >3 (Bruland et al., 2000; Buck et al., 2012; Whitby et al., 2017; Wong et al., 2018). Thus, if compared to CLE-AdCSV, it might seem like the stronger class of ligands are underestimated (Dulaquais et al., 2020); however, this is the consequence of DW which is not comparable to these two methods. It should also be noted that theoretically the method for calculation of complexation parameters using ASV assumes that the measured signal corresponds purely to the inorganic Cu. However, it is known that, during the deposition time at the appropriate deposition potential, kinetically labile complexes are actually accumulated, which include not only fully labile inorganic Cu species but also a portion of the kinetically labile organic complexes (Town, 1997; Bruland et al., 2000; Town and van Leeuwen, 2004; Chakraborty et al., 2007; Gibbon-Walsh et al., 2012). To prevent the reduction of labile organic complexes as much as possible, the deposition potential should be selected at the most positive value at the range of limiting currents (top of the wave) of the Cu pseudopolarogram without the addition of organic ligands (shaded area in **Figure 2B**). It is generally assumed that stronger complexes are less kinetically labile than the weaker complexes, and as such, it is expected that this problem will more greatly impact the weaker class of ligands.

This problem is partly reflected in the estimated "free/bioavailable" Cu. However, as Cu exists mainly in the form of strong complexes at ambient concentrations, it could be considered that the contribution of kinetically labile complexes to the bioavailable fraction is not high. Despite these potential methodological problems in the estimation of free Cu (which is the basis for the assessment of Cu toxicity), it should be mentioned that some model toxicological experiments showed a very good agreement with the labile Cu estimated by ASV and its bioavailability/toxicity (Tubbing et al., 1994; Lage et al., 1996; Tait et al., 2016; Sánchez-Marín, 2020). Furthermore, the free Cu concentrations obtained by the ASV method in estuarine samples (Jones and Bolam, 2007; Louis et al., 2009) were found to correlate well with those predicted by WHAM VII modeling (Stockdale et al., 2015), highlighting a particular feature of the ASV method.

Overall, it should be noted that each of the currently most-utilized techniques for the estimation of metal speciation (and their bioavailability) in natural waters (diffusive gradients in thin films (DGT), CLE-AdCSV, and ASV) provide results that are essentially "operationally defined"; i.e., they are technique-dependent.

CONCLUSIONS

Here, we present an adapted ASV methodology of copper speciation in estuarine samples with high DOM concentration. The method relies on the addition of the nonionic surfactant T-X-100, which competitively inhibits the adsorption of DOM on the Hg electrode during the deposition and stripping steps. Tests performed with and without the addition of fulvic acid (FA) as a model organic ligand revealed that, at the concentration level used here (1 mg L^{-1}), T-X-100 does not have any detectable influence on the redox process of Cu, labeling it "interference-free" for Cu speciation studies.

The proposed method improvement enabled the Cu speciation analysis in the Arno River estuary (Italy) characterized by high concentrations of both Cu and DOC. Mixing with the clean seawater leads to a decrease in their concentrations, reaching the value characteristic for a clean coastal region. Speciation analyses revealed the existence of the two types of organic ligands responsible for Cu complexation: a strong ligand class (L_1) with a concentration level similar to that of dissolved Cu and a weaker one (L_2) found at higher concentrations. The calculated free Cu concentrations in analyzed samples were above the toxicity threshold level. However, due to the ASV methodological specificities, these values might have been slightly overestimated. The sum of the ligand concentrations (ΣL) had the same linear relationship with dissolved Cu for both sampling periods. By contrast, a different relationship between ΣL and DOC was found in the two sampling periods, implying a change in the contribution of Cu-binding organic ligands to the DOM pool between seasons. The results indicate that the DOM pool comprised a higher percentage of Cu-binding ligands in spring than in summer, due to the higher percentage of terrestrial fulvic and humic components in the FDOM pool. However, as a separate quantification of specific ligand types was not performed, a direct link with detected the Cu-binding ligand classes was not possible to confirm. Assigning the exact type of the organic ligands able to complex Cu in the Arno River estuary demands more detailed studies with additional ligand characterization methods.

DATA AVAILABILITY STATEMENT

The raw data supporting the conclusions of this article will be made available by the authors, without undue reservation.

AUTHOR CONTRIBUTION

JP, CS, SB, OR, CG, and DO performed sampling and sample preparation. JP performed analyses of samples, analyzed the data, and drafted the manuscript. SM conceptualized the manuscript,

organized data processing and interpretation, and wrote the manuscript. A-MC performed analyses and validation of the technique. CS and SB performed analyses of DOM and interpreted the DOM results. OR, CG, CS, and DO organized and conceptualized the study in the Arno River estuary. OR and CG acquired the funding. DO designed the experiments, supervised the method development, and acquired the funding. All authors contributed to results interpretation and manuscript writing/editing.

FUNDING

This study was realized within the framework of the COMECOM project as a part of the "MerMex-WP3-C3A" project (PIs: OR and CG), as well as within the scope of the project "New methodological approach to biogeochemical studies of trace metal speciation in coastal aquatic ecosystems" (MEBTRACE), financially supported by the Croatian Science Foundation under the project number IP-2014-09-7530 (PI DO).

ACKNOWLEDGMENTS

This paper is dedicated to our friend, colleague, and mentor Cédric Garnier (1977–2018). We have lost a great person, an excellent scientist, and a loyal colleague. We will always remember him. The authors would like to thank all colleagues who participated in sampling campaigns and sample preparations.

SUPPLEMENTARY MATERIAL

The Supplementary Material for this article can be found online at: https://www.frontiersin.org/articles/10.3389/fchem.2020.628749/full#supplementary-material.

REFERENCES

Abdulla, H. A. N., Minor, E. C., Dias, R. F., and Hatcher, P. G. (2010). Changes in the compound classes of dissolved organic matter along an estuarine transect: a study using FTIR and C-13 NMR. *Geochem. Cosmochim. Acta* 74 (13), 3815–3838. doi:10.1016/j.gca.2010.04.006

Amin, S. A., Moffett, J. W., Martens-Habbena, W., Jacquot, J. E., Han, Y., Devol, A., et al. (2013). Copper requirements of the ammonia-oxidizing archaeon Nitrosopumilus maritimus SCM1 and implications for nitrification in the marine environment. *Limnol. Oceanogr.* 58 (6), 2037–2045. doi:10.4319/lo.2013.58.6.2037

Annett, A. L., Lapi, S., Ruth, T. J., and Maldonado, M. T. (2008). The effects of Cu and Fe availability on the growth and Cu: C ratios of marine diatoms. *Limnol. Oceanogr.* 53 (6), 2451–2461. doi:10.4319/lo.2008.53.6.2451

Apte, S. C., Gardner, M. J., and Ravenscroft, J. E. (1988). An evaluation of voltammetric titration procedures for the determination of trace-metal complexation in natural-waters by use of computer-simulation. *Anal. Chim. Acta* 212 (1–2), 1–21. doi:10.1016/S0003-2670(00)84124-0

Batley, G. E., Apte, S. C., and Stauber, J. L. (2004). Speciation and bioavailability of trace metals in water: progress since 1982. *Aust. J. Chem.* 57 (10), 903–919. doi:10.1071/CH04095

Bi, Z. S., Salaun, P., and van den Berg, C. M. G. (2013). The speciation of lead in seawater by pseudopolarography using a vibrating silver amalgam microwire electrode. *Mar. Chem.* 151, 1–12. doi:10.1016/j.marchem.2013.02.003

Blake, A. C., Chadwick, D. B., Zirino, A., and Rivera-Duarte, I. (2004). Spatial and temporal variations in copper speciation in San Diego Bay. *Estuaries.* 27 (3), 437–447. doi:10.1007/Bf02803536

Boussemart, M., Menargues, L., and Benaim, J. Y. (1993). Anodic-stripping voltammetry of copper in natural-waters-a qualitative approach to the additional peak(S) occurrence. *Electroanalysis.* 5 (2), 125–133. doi:10.1002/elan.1140050206

Branica, G., and Lovrić, M. (1997). Pseudopolarography of totally irreversible redox reactions. *Electrochim. Acta* 42 (8), 1247–1251. doi:10.1016/S0013-4686(96)00297-6

Bruland, K. W., Rue, E. L., Donat, J. R., Skrabal, S. A., and Moffett, J. W. (2000). Intercomparison of voltammetric techniques to determine the chemical speciation of dissolved copper in a coastal seawater sample. *Anal. Chim. Acta* 405 (1–2), 99–113. doi:10.1016/S0003-2670(99)00675-3

Buck, K. N., Moffett, J., Barbeau, K. A., Bundy, R. M., Kondo, Y., and Wu, J. F. (2012). The organic complexation of iron and copper: an intercomparison of competitive ligand exchange-adsorptive cathodic stripping voltammetry (CLE-ACSV) techniques. *Limnol. Oceanogr. Methods* 10, 496–515. doi:10.4319/lom.2012.10.496

Campbell, P. G., Errécalde, O., Fortin, C., Hiriart-Baer, V. P., and Vigneault, B. (2002). Metal bioavailability to phytoplankton--applicability of the biotic ligand model. *Comp. Biochem. Physiol. C. Toxicol. Pharmacol.* 133 (1–2), 189–206. doi:10.1016/s1532-0456(02)00104-7

Chakraborty, P., Fasfous, I. I., Murimboh, J., and Chakrabarti, C. L. (2007). Simultaneous determination of speciation parameters of Cu, Pb, Cd and Zn in model solutions of Suwannee River fulvic acid by pseudopolarography. *Anal. Bioanal. Chem.* 388 (2), 463–474. doi:10.1007/s00216-007-1185-3

Ciglenečki, I., Vilibić, I., Dautović, J., Vojvodić, V., Ćosović, B., Zemunik, P., et al. (2020). Dissolved organic carbon and surface active substances in the northern Adriatic Sea: long-term trends, variability and drivers. *Sci. Total Environ.* 730. doi:10.1016/j.scitotenv.2020.139104

Cindrić, A. M., Garnier, C., Oursel, B., Pižeta, I., and Omanović, D. (2015). Evidencing the natural and anthropogenic processes controlling trace metals dynamic in a highly stratified estuary: the Krka River estuary (Adriatic, Croatia). *Mar. Pollut. Bull.* 94 (1–2), 199–216. doi:10.1016/j.marpolbul.2015.02.029

Cobelo-García, A., and Prego, R. (2003). Land inputs, behaviour and contamination levels of copper in a Ria Estuary (NW Spain). *Mar. Environ. Res.* 56 (3), 403–422. doi:10.1016/S0141-1136(03)00002-3

Corcoll, N., Yang, J., Backhaus, T., Zhang, X., and Eriksson, K. M. (2018). Copper affects composition and functioning of microbial communities in marine biofilms at environmentally relevant concentrations. *Front. Microbiol.* 9 (3248). doi:10.3389/fmicb.2018.03248

Cortecci, G., Boschetti, T., Dinelli, E., Cidu, R., Podda, F., and Doveri, M. (2009). Geochemistry of trace elements in surface waters of the Arno River Basin, northern Tuscany, Italy. *Appl. Geochem.* 24 (5), 1005–1022. doi:10.1016/j.apgeochem.2009.03.002

Cuculić, V., and Branica, M. (1996). Adsorption of trace metals from sea-water onto solid surfaces: analysis by anodic stripping voltammetry. *Analyst* 121 (8), 1127–1131. doi:10.1039/An9962101127

Dalzell, B. J., Minor, E. C., and Mopper, K. M. (2009). Photodegradation of estuarine dissolved organic matter: a multi-method assessment of DOM transformation. *Org. Geochem.* 40 (2), 243–257. doi:10.1016/j.orggeochem.2008.10.003

Daoud, A. B., and Tremblay, L. (2019). HPLC-SEC-FTIR characterization of the dissolved organic matter produced by the microbial carbon pump. *Mar. Chem.* 215. doi:10.1016/j.marchem.2019.103668

Dinelli, E., Cortecci, G., Lucchini, F., and Zantedeschi, E. (2005). Sources of major and trace elements in the stream sediments of the Arno river catchment (northern Tuscany, Italy). *Geochem. J.* 39 (6), 531–545. doi:10.2343/geochemj.39.531

Domingos, R. F., Carreira, S., Galceran, J., Salaün, P., and Pinheiro, J. P. (2016). AGNES at vibrated gold microwire electrode for the direct quantification of free

copper concentrations. *Anal. Chim. Acta* 920, 29–36. doi:10.1016/j.aca.2016.03.035

Domingos, R. F., Lopez, R., and Pinheiro, J. P. (2008). Trace metal dynamic speciation studied by scanned stripping chronopotentiometry (SSCP). *Environ. Chem.* 5 (1), 24–32. doi:10.1071/EN07088

Dulaquais, G., Waeles, M., Breitenstein, J., Knoery, J., and Riso, R. (2020). Links between size fractionation, chemical speciation of dissolved copper and chemical speciation of dissolved organic matter in the Loire estuary. *Environ. Chem.* 17 (5), 385–399. doi:10.1071/EN19137

Fellman, J. B., Petrone, K. C., and Grierson, P. F. (2011). Source, biogeochemical cycling, and fluorescence characteristics of dissolved organic matter in an agro-urban estuary. *Limnol. Oceanogr.* 56 (1), 243–256. doi:10.4319/lo.2011.56.1.0243

Galletti, Y., Gonnelli, M., Brogi, S. R., Vestri, S., and Santinelli, C. (2019). DOM dynamics in open waters of the Mediterranean Sea: new insights from optical properties. *Deep-Sea Res. Part I Oceanogr. Res. Pap.* 144, 95–114. doi:10.1016/j.dsr.2019.01.007

Garnier, C., Pižeta, I., Mounier, S., Benaïm, J. Y., and Branica, M. (2004). Influence of the type of titration and of data treatment methods on metal complexing parameters determination of single and multi-ligand systems measured by stripping voltammetry. *Anal. Chim. Acta* 505 (2), 263–275. doi:10.1016/j.aca.2003.10.066

Gibbon-Walsh, K., Salaün, P., and van den Berg, C. M. (2012). Pseudopolarography of copper complexes in seawater using a vibrating gold microwire electrode. *J. Phys. Chem.* 116 (25), 6609–6620. doi:10.1021/jp3019155

Glass, J. B., and Orphan, V. J. (2012). Trace metal requirements for microbial enzymes involved in the production and consumption of methane and nitrous oxide. *Front. Microbiol.* 3, 61. doi:10.3389/fmicb.2012.00061

Gledhill, M., Nimmo, M., Hill, S. J., and Brown, M. T. (1997). The toxicity of copper(II) species to marine algae, with particular reference to macroalgae. *J. Phycol.* 33 (1), 2–11. doi:10.1111/j.0022-3646.1997.00002.x

Hansell, D. A. (2005). Dissolved organic carbon reference material program. *Eos. Trans. Am. Geophys. Union.* 86 (35), 318. doi:10.1029/2005eo350003

Helland, A., and Bakke, T. (2002). Transport and sedimentation of Cu in a microtidal estuary, SE Norway. *Mar. Pollut. Bull.* 44 (2), 149–155. doi:10.1016/s0025-326x(01)00195-3

Hurst, M. P., and Bruland, K. W. (2005). The use of nafion-coated thin mercury film electrodes for the determination of the dissolved copper speciation in estuarine water. *Anal. Chim. Acta* 546 (1), 68–78. doi:10.1016/j.aca.2005.05.015

Jacquot, J. E., Horak, R. E. A., Amin, S. A., Devol, A. H., Ingalls, A. E., Armbrust, E. V., et al. (2014). Assessment of the potential for copper limitation of ammonia oxidation by Archaea in a dynamic estuary. *Mar. Chem.* 162, 37–49. doi:10.1016/j.marchem.2014.02.002

Jones, B., and Bolam, T. (2007). Copper speciation survey from UK marinas, harbours and estuaries. *Mar. Pollut. Bull.* 54 (8), 1127–1138. doi:10.1016/j.marpolbul.2007.04.021

Karlsson, J., Ytreberg, E., and Eklund, B. (2010). Toxicity of anti-fouling paints for use on ships and leisure boats to non-target organisms representing three trophic levels. *Environ. Pollut.* 158 (3), 681–687. doi:10.1016/j.envpol.2009.10.024

Kogut, M. B., and Voelker, B. M. (2001). Strong copper-binding behavior of terrestrial humic substances in seawater. *Environ. Sci. Technol.* 35 (6), 1149–1156. doi:10.1021/es0014584

Krznarić, D., Plavšić, M., and Ćosović, B. (1994). Voltametric investigations of the effect of Triton X-100 on copper processes in the presence of oxygen. *Electroanalysis.* 6 (2), 131–137. doi:10.1002/elan.1140060210

Lage, O. M., Soares, H. M. V. M., Vasconcelos, M. T. S. D., Parente, A. M., and Salema, R. (1996). Toxicity effects of copper(II) on the marine dinoflagellate Amphidinium carterae: influence of metal speciation. *Eur. J. Phycol.* 31 (4), 341–348. doi:10.1080/09670269600651571

Laglera, L. M., and van den Berg, C. M. G. (2003). Copper complexation by thiol compounds in estuarine waters. *Mar. Chem.* 82 (1–2), 71–89. doi:10.1016/S0304-4203(03)00053-7

Lawaetz, A. J., and Stedmon, C. A. (2009). Fluorescence intensity calibration using the Raman scatter peak of water. *Appl. Spectrosc.* 63 (8), 936–940. doi:10.1366/000370209788964548

Lee, M. H., Osburn, C. L., Shin, K. H., and Hur, J. (2018). New insight into the applicability of spectroscopic indices for dissolved organic matter (DOM) source discrimination in aquatic systems affected by biogeochemical processes. *Water Res.* 147, 164–176. doi:10.1016/j.watres.2018.09.048

Lewis, B. L., Luther, G. W., Lane, H., and Church, T. M. (1995). Determination of metal-organic complexation in natural-waters by swasv with pseudopolarograms. *Electroanalysis* 7 (2), 166–177. doi:10.1002/elan.1140070213

Lopez, J. S., Lee, L., and Mackey, K. R. M. (2019). The toxicity of copper to crocosphaera watsonii and other marine phytoplankton: a systematic review. *Front. Mar. Sci.* 5 (511). doi:10.3389/fmars.2018.00511

Louis, Y., Cmuk, P., Omanović, D., Garnier, C., Lenoble, V., Mounier, S., et al. (2008). Speciation of trace metals in natural waters: the influence of an adsorbed layer of natural organic matter (NOM) on voltammetric behaviour of copper. *Anal. Chim. Acta* 606 (1), 37–44. doi:10.1016/j.aca.2007.11.011

Louis, Y., Garnier, C., Lenoble, V., Mounier, S., Cukrov, N., Omanović, D., et al. (2009). Kinetic and equilibrium studies of copper-dissolved organic matter complexation in water column of the stratified Krka River estuary (Croatia). *Mar. Chem.* 114 (3–4), 110–119. doi:10.1016/j.marchem.2009.04.006

Luther, G. W., III, Rozan, T. F., Witter, A., and Lewis, B. (2001). Metal-organic complexation in the marine environment. *Geochem. Trans.* 2, 65–74. doi:10.1186/1467-4866-2-65

Luther, G. W., Swartz, C. B., and Ullman, W. J. (1988). Direct determination of iodide in seawater by cathodic stripping square-wave voltammetry. *Anal. Chem.* 60 (17), 1721–1724. doi:10.1021/Ac00168a017

Marcinek, S., Santinelli, C., Cindrić, A. M., Evangelista, V., Gonnelli, M., Layglon, N., et al. (2020). Dissolved organic matter dynamics in the pristine Krka River estuary (Croatia). *Mar. Chem.* 225, 103848. doi:10.1016/j.marchem.2020.103848

Migon, C., Heimburger-Boavida, L. E., Dufour, A., Chiffoleau, J. F., and Cossa, D. (2020). Temporal variability of dissolved trace metals at the DYFAMED time-series station, Northwestern Mediterranean. *Mar. Chem.* 225, 3845. doi:10.1016/j.marchem.2020.103846

Minor, E. C., Boon, J. J., Harvey, H. R., and Mannino, A. (2001). Estuarine organic matter composition as probed by direct temperature-resolved mass spectrometry and traditional geochemical techniques. *Geochem. Cosmochim. Acta* 65 (17), 2819–2834. doi:10.1016/S0016-7037(01)00643-3

Minor, E. C., Simjouw, J. P., Boon, J. J., Kerkhoff, A. E., and van der Horst, J. (2002). Estuarine/marine UDOM as characterized by size-exclusion chromatography and organic mass spectrometry. *Mar. Chem.* 78 (2–3), 75–102. doi:10.1016/S0304-4203(02)00011-7

Monticelli, D., Carugati, G., Castelletti, A., Recchia, S., and Dossi, C. (2010). Design and development of a low cost, high performance UV digester prototype: application to the determination of trace elements by stripping voltammetry. *Microchem. J.* 95 (2), 158–163. doi:10.1016/j.microc.2009.11.002

Murphy, K. R., Stedmon, C. A., Graeber, D., and Bro, R. (2013). Fluorescence spectroscopy and multi-way techniques. PARAFAC. *Anal. Methods* 5 (23), 6557–6566. doi:10.1039/c3ay41160e

Murphy, K. R., Stedmon, C. A., Wenig, P., and Bro, R. (2014). OpenFluor- an online spectral library of auto-fluorescence by organic compounds in the environment. *Anal. Methods* 6 (3), 658–661. doi:10.1039/c3ay41935e

Nicolau, R., Louis, Y., Omanović, D., Garnier, C., Mounier, S., and Pizeta, I. (2008). Study of interactions of concentrated marine dissolved organic matter with copper and zinc by pseudopolarography. *Anal. Chim. Acta* 618 (1), 35–42. doi:10.1016/j.aca.2008.04.038

Omanović, D., Garnier, C., Louis, Y., Lenoble, V., Mounier, S., and Pižeta, I. (2010). Significance of data treatment and experimental setup on the determination of copper complexing parameters by anodic stripping voltammetry. *Anal. Chim. Acta* 664 (2), 136–143. doi:10.1016/j.aca.2010.02.008

Omanović, D., and Branica, M. (2004). Pseudopolarography of trace metals. Part II. The comparison of the reversible, quasireversible and irreversible electrode reactions. *J. Electroanal. Chem.* 565 (1), 37–48. doi:10.1016/j.jelechem.2003.09.026

Omanović, D., Gamier, C., and Pižeta, I. (2015). ProMCC: an all-in-one tool for trace metal complexation studies. *Mar. Chem.* 173, 25–39. doi:10.1016/j.marchem.2014.10.011

Omanović, D., Kwokal, Z., Goodwin, A., Lawrence, A., Banks, C. E., Compton, R. G., et al. (2006). Trace metal detection in Sibenik Bay, Croatia: cadmium, lead

and copper with anodic stripping voltammetry and manganese via sonoelectrochemistry. A case study. *J. Iran. Chem. Soc.* 3 (2), 128–139. doi:10.1007/Bf03245940

Omanović, D., Pižeta, I., Peharec, Z., and Branica, M. (1996). Voltametric determination of the metal complexing capacity in model solutions. *Mar. Chem.* 53 (1–2), 121–129. doi:10.1016/0304-4203(96)00018-7

Omanović, D. (2006). Pseudopolarography of trace metals. Part III. Determination of stability constants of labile metal complexes. *Croat. Chem. Acta* 79 (1), 67–76. doi:10.1021/ja01227a043

Omanović, D., Santinelli, C., Marcinek, S., and Gonnelli, M. (2019). ASFit - an all-inclusive tool for analysis of UV-Vis spectra of colored dissolved organic matter (CDOM). *Comput. Geosci.* 133. doi:10.1016/J.Cageo.2019.104334

Osburn, C. L., Handsel, L. T., Mikan, M. P., Paerl, H. W., and Montgomery, M. T. (2012). Fluorescence tracking of dissolved and particulate organic matter quality in a river-dominated estuary. *Environ. Sci. Technol.* 46 (16), 8628–8636. doi:10.1021/es3007723

Oursel, B., Garnier, C., Durrieu, G., Mounier, S., Omanović, D., and Lucas, Y. (2013). Dynamics and fates of trace metals chronically input in a Mediterranean coastal zone impacted by a large urban area. *Mar. Pollut. Bull.* 69 (1–2), 137–149. doi:10.1016/j.marpolbul.2013.01.023

Pađan, J., Marcinek, S., Cindrić, A. M., Layglon, N., Lenoble, V., Salaün, P., et al. (2019). Improved voltammetric methodology for chromium redox speciation in estuarine waters. *Anal. Chim. Acta* 1089, 40–47. doi:10.1016/j.aca.2019.09.014

Pađan, J., Marcinek, S., Cindrić, A. M., Layglon, N., Garnier, C., Salaun, P., et al. (2020). Determination of sub-picomolar levels of platinum in the pristine Krka River estuary (Croatia) using improved voltammetric methodology. *Environ. Chem.* 17 (2), 77–84. doi:10.1071/EN19157

Peers, G., and Price, N. M. (2006). Copper-containing plastocyanin used for electron transport by an oceanic diatom. *Nature.* 441 (7091), 341–344. doi:10.1038/nature04630

Peers, G., Quesnel, S. A., and Price, N. M. (2005). Copper requirements for iron acquisition and growth of coastal and oceanic diatoms. *Limnol. Oceanogr.* 50 (4), 1149–1158. doi:10.4319/lo.2005.50.4.1149

Pinheiro, J. P., Galceran, J., Rotureau, E., Companys, E., and Puy, J. (2020). Full wave analysis of stripping chronopotentiometry at scanned deposition potential (SSCP): obtaining binding curves in labile heterogeneous macromolecular systems for any metal-to-ligand ratio. *J. Electroanal. Chem.* 873, 114436. doi:10.1016/j.jelechem.2020.114436

Pižeta, I., Sander, S. G., Hudson, R. J. M., Omanović, D., Baars, O., Barbeau, K. A., et al. (2015). Interpretation of complexometric titration data: an intercomparison of methods for estimating models of trace metal complexation by natural organic ligands. *Mar. Chem.* 173, 3–24. doi:10.1016/j.marchem.2015.03.006

Plavšić, M., Krznarić, D., and Ćosović, B. (1994). The electrochemical processes of copper in the presence of Triton X-100. *Electroanalysis* 6 (5–6), 469–474. doi:10.1002/elan.1140060518

Plavšić, M., Kwokal, Z., Strmečki, S., Peharec, Z., Omanović, D., and Branica, M. (2009). Determination of the copper complexing ligands in the krka River estuary. *Fresenius Environ. Bull.* 18 (3), 327–334.

Repeta, D. J. (2015). "*Chemical characterization and cycling of dissolved organic matter.*," in *Biogeochemistry of marine dissolved organic matter.* Editors D. A. Hansell and C. A. Carlson (Cambridge: Academic Press), 21–63.

Retelletti Brogi, S., Gonnelli, M., Vestri, S., and Santinelli, C. (2015). Biophysical processes affecting DOM dynamics at the Arno river mouth (Tyrrhenian Sea). *Biophys. Chem.* 197, 1–9. doi:10.1016/j.bpc.2014.10.004

Retelletti Brogi, S., Balestra, C., Casotti, R., Cossarini, G., Galletti, Y., Gonnelli, M., et al. (2020). Time resolved data unveils the complex DOM dynamics in a Mediterranean river. *Sci. Total Environ.* 733. doi:10.1016/j.scitotenv.2020.139212

Romera-Castillo, C., Sarmento, H., Alvarez-Salgado, X. A., Gasol, J. M., and Marrase, C. (2010). Production of chromophoric dissolved organic matter by marine phytoplankton. *Limnol. Oceanogr.* 55 (1), 446–454. doi:10.4319/lo.2010.55.1.0446

Sahlin, E., and Jagner, D. (1996). Influence of Triton X-100 in stripping potentiometry. *Anal. Chim. Acta* 333 (3), 233–240. doi:10.1016/0003-2670(96)00310-8

Sánchez-Marín, P., Aierbe, E., Lorenzo, J. I., Mubiana, V. K., Beiras, R., and Blust, R. (2016). Dynamic modeling of copper bioaccumulation by *Mytilus edulis* in the presence of humic acid aggregates. *Aquat. Toxicol.* 178, 165–170. doi:10.1016/j.aquatox.2016.07.021

Sánchez-Marín, P., Santos-Echeandía, J., Nieto-Cid, M., Alvarez-Salgado, X. A., and Beiras, R. (2010). Effect of dissolved organic matter (DOM) of contrasting origins on Cu and Pb speciation and toxicity to *Paracentrotus lividus* larvae. *Aquat. Toxicol.* 96 (2), 90–102. doi:10.1016/j.aquatox.2009.10.005

Sánchez-Marín, P. (2020). A review of chemical speciation techniques used for predicting dissolved copper bioavailability in seawater. *Environ. Chem.* 17 (7), 469. doi:10.1071/EN19266

Sander, S., and Henze, G. (1996). Alternating current investigations at the mercury drop electrode on the adsorption potential of metal complexes. *Electroanalysis.* 8 (3), 253–262. doi:10.1002/elan.1140080310

Santinelli, C., Follett, C., Brogi, S. R., Xu, L., and Repeta, D. (2015). Carbon isotope measurements reveal unexpected cycling of dissolved organic matter in the deep Mediterranean Sea. *Mar. Chem.* 177, 267–277. doi:10.1016/j.marchem.2015.06.018

Scarano, G., and Bramanti, E. (1993). Voltametric behavior of marine hydrophobic copper-complexes-effect of adsorption processes at a mercury-electrode. *Anal. Chim. Acta* 277 (1), 137–144. doi:10.1016/0003-2670(93)85098-5

Semeniuk, D. M., Bundy, R. M., Payne, C. D., Barbeau, K. A., and Maldonado, M. T. (2015). Acquisition of organically complexed copper by marine phytoplankton and bacteria in the northeast subarctic Pacific Ocean. *Mar. Chem.* 173, 222–233. doi:10.1016/j.marchem.2015.01.005

Serrano, N., Diaz-Cruz, J. M., Arino, C., Esteban, M., Puy, J., Companys, E., et al. (2007). Full-wave analysis of stripping chronopotentiograms at scanned deposition potential (SSCP) as a tool for heavy metal speciation: theoretical development and application to Cd(II)-phthalate and Cd(II)-iodide systems. *J. Electroanal. Chem.* 600 (2), 275–284. doi:10.1016/j.jelechem.2006.10.007

Shank, G. C., Skrabal, S. A., Whitehead, R. F., and Kieber, R. J. (2004). Strong copper complexation in an organic-rich estuary: the importance of allochthonous dissolved organic matter. *Mar. Chem.* 88 (1–2), 21–39. doi:10.1016/j.marchem.2004.03.001

Sholkovitz, E. R. (1976). Flocculation of dissolved organic and inorganic matter during mixing of river water and seawater. *Geochem. Cosmochim. Acta* 40 (7), 831–845. doi:10.1016/0016-7037(76)90035-1

Slagter, H. A., Reader, H. E., Rijkenberg, M. J. A., van der Loeff, M. R., de Baar, H. J. W., and Gerringa, L. J. A. (2017). Organic Fe speciation in the eurasian basins of the arctic ocean and its relation to terrestrial DOM. *Mar. Chem.* 197, 11–25. doi:10.1016/j.marchem.2017.10.005

Soares, H. M., and Vasconcelos, M. T. (1995). Application of potentiometric stripping analysis for speciation of copper complexes with a non-adsorbable ligand on a mercury electrode. *Talanta* 42 (3), 621–626. doi:10.1016/0003-2670(95)00283-6

Soares, H. M. V. M., and Vasconcelos, M. T. S. D. (1994). Study of the lability of copper(ii)-fulvic acid complexes by ion-selective electrodes and potentiometric stripping analysis. *Anal. Chim. Acta* 293 (3), 261–270. doi:10.1016/0003-2670(94)85031-3

Stedmon, C. A., and Nelson, N. B. (2015). "*Chapter 10 - the optical properties of DOM in the ocean.*," in *Biogeochemistry of marine dissolved organic matter.* 2nd Edn, Editors D. A. Hansell and C. A. Carlson (Boston: Academic Press), 481–508.

Stockdale, A., Tipping, E., and Lofts, S. (2015). Dissolved trace metal speciation in estuarine and coastal waters: comparison of wham/model vii predictions with analytical results. *Environ. Toxicol. Chem.* 34 (1), 53–63. doi:10.1002/etc.2789

Sunda, W. G., Tester, P. A., and Huntsman, S. A. (1987). Effects of cupric and zinc ion activities on the survival and reproduction of marine copepods. *Mar. Biol.* 94 (2), 203–210. doi:10.1007/Bf00392932

Tait, T. N., Rabson, L. M., Diamond, R. L., Cooper, C. A., McGeer, J. C., and Smith, D. S. (2016). Determination of cupric ion concentrations in marine waters: an improved procedure and comparison with other speciation methods. *Environ. Chem.* 13 (1), 140–148. doi:10.1071/EN14190

Tang, D. G., Hung, C. C., Warnken, K. W., and Santschi, P. H. (2000). The distribution of biogenic thiols in surface waters of Galveston Bay. *Limnol. Oceanogr.* 45 (6), 1289–1297. doi:10.4319/lo.2000.45.6.1289

Thibault, A., Derenne, S., Parlanti, E., Anquetil, C., Sourzac, M., Budzinski, H., et al. (2019). Dynamics of organic matter in the Seine Estuary (France): bulk and structural approaches. *Mar. Chem.* 212, 108–119. doi:10.1016/j.marchem.2019.04.007

Town, R. M. (1998). Chronopotentiometric stripping analysis as a probe for copper(II) and lead(II) complexation by fulvic acid: limitations and potentialities. *Anal. Chim. Acta* 363 (1), 31–43. doi:10.1016/S0003-2670(97)00671-5

Town, R. M., and Filella, M. (2000). Determination of metal ion binding parameters for humic substances - Part 2. Utility of ASV pseudo-polarography. *J. Electroanal. Chem.* 488 (1), 1–16. doi:10.1016/S0022-0728(00)00186-8

Town, R. M. (1997). Potentiometric stripping analysis and anodic stripping voltammetry for measurement of copper(II) and lead(II) complexation by fulvic acid: a comparative study. *Electroanalysis* 9 (5), 407–415. doi:10.1002/elan.1140090511

Town, R. M., and van Leeuwen, H. P. (2004). Dynamic speciation analysis of heterogeneous metal complexes with natural ligands by stripping chronopotentiometry at scanned deposition potential (SSCP). *Aust. J. Chem.* 57 (10), 983–992. doi:10.1071/CH04088

Town, R. M., and van Leeuwen, H. P. (2019). Stripping chronopotentiometry at scanned deposition potential (SSCP): an effective methodology for dynamic speciation analysis of nanoparticulate metal complexes. *J. Electroanal. Chem.* 853. doi:10.1016/j.jelechem.2019.113530

Tubbing, D. M. J., Admiraal, W., Cleven, R. F. M. J., Iqbal, M., Vandemeent, D., and Verweij, W. (1994). The contribution of complexed copper to the metabolic inhibition of algae and bacteria in synthetic media and river water. *Water Res.* 28 (1), 37–44. doi:10.1016/0043-1354(94)90117-1

Turner, A. (2010). Marine pollution from antifouling paint particles. *Mar. Pollut. Bull.* 60 (2), 159–171. doi:10.1016/j.marpolbul.2009.12.004

van den Berg, C. M. G. (2006). Chemical speciation of iron in seawater by cathodic stripping voltammetry with dihydroxynaphthalene. *Anal. Chem.* 78 (1), 156–163. doi:10.1021/ac051441

Vraspir, J. M., and Butler, A. (2009). Chemistry of marine ligands and siderophores. *Ann. Rev. Mar. Sci.* 1, 43–63. doi:10.1146/annurev.marine.010908.163712

Waeles, M., Tanguy, V., Lespes, G., and Riso, R. D. (2008). Behaviour of colloidal trace metals (Cu, Pb and Cd) in estuarine waters: an approach using frontal ultrafiltration (UF) and stripping chronopotentiometric methods (SCP). *Estuar. Coast Shelf Sci.* 80 (4), 538–544. doi:10.1016/j.ecss.2008.09.010

Watanabe, K., Fukuzaki, K., Fukushima, K., Aimoto, M., Yoshioka, T., and Yamashita, Y. (2018). Iron and fluorescent dissolved organic matter in an estuarine and coastal system in Japan. *Limnology* 19 (2), 229–240. doi:10.1007/s10201-017-0536-9

Whitby, H., Planquette, H., Cassar, N., Bucciarelli, E., Osburn, C. L., Janssen, D. J., et al. (2020). A call for refining the role of humic-like substances in the oceanic iron cycle. *Sci. Rep.* 10 (1), 6144. doi:10.1038/S41598-020-62266-7

Whitby, H., Hollibaugh, J. T., and van den Berg, C. M. G. (2017). Chemical speciation of copper in a salt marsh estuary and bioavailability to thaumarchaeota. *Front. Mar. Sci.* 4. doi:10.3389/Fmars.2017.00178

Whitby, H., Posacka, A. M., Maldonado, M. T., and van den Berg, C. M. G. (2018). Copper-binding ligands in the NE pacific. *Mar. Chem.* 204, 36–48. doi:10.1016/j.marchem.2018.05.008

Whitby, H., and van den Berg, C. M. G. (2015). Evidence for copper-binding humic substances in seawater. *Mar. Chem.* 173, 282–290. doi:10.1016/j.marchem.2014.09.011

Wong, K. H., Obata, H., Kim, T., Mashio, A. S., Fukuda, H., and Ogawa, H. (2018). Organic complexation of copper in estuarine waters: an assessment of the multi-detection window approach. *Mar. Chem.* 204, 144–151. doi:10.1016/j.marchem.2018.07.001

Wong, K. H., Obata, H., Kim, T., Wakuta, Y., and Takeda, S. (2019). Distribution and speciation of copper and its relationship with FDOM in the East China Sea. *Mar. Chem.* 212, 96–107. doi:10.1016/j.marchem.2019.04.005

Yamashita, Y., Panton, A., Mahaffey, C., and Jaffe, R. (2011). Assessing the spatial and temporal variability of dissolved organic matter in Liverpool Bay using excitation-emission matrix fluorescence and parallel factor analysis. *Ocean Dyn.* 61 (5), 569–579. doi:10.1007/s10236-010-0365-4

Yang, R., and van den Berg, C. M. (2009). Metal complexation by humic substances in seawater. *Environ. Sci. Technol.* 43 (19), 7192–7197. doi:10.1021/es900173w

Ytreberg, E., Karlsson, J., and Eklund, B. (2010). Comparison of toxicity and release rates of Cu and Zn from anti-fouling paints leached in natural and artificial brackish seawater. *Sci. Total Environ.* 408 (12), 2459–2466. doi:10.1016/j.scitotenv.2010.02.036

Zhang, Y. L., Yang, K. L., Du, J. Z., Zhang, F. F., Dong, Y. P., and Li, W. (2018). Chemical characterization of fractions of dissolved humic substances from a marginal sea-a case from the Southern Yellow Sea. *J. Oceanol. Limnol.* 36 (2), 238–248. doi:10.1007/s00343-017-6202-6

Žic, V., Truesdale, V. W., Garnier, C., and Cukrov, N. (2012). The distribution of iodine in the Croatian marine lake, Mir - the missing iodate. *Estuar. Coast Shelf Sci.* 115, 377–387. doi:10.1016/j.ecss.2012.07.026

Zitoun, R., Clearwater, S. J., Hassler, C., Thompson, K. J., Albert, A., and Sander, S. G. (2019). Copper toxicity to blue mussel embryos (*Mytilus galloprovincialis*): the effect of natural dissolved organic matter on copper toxicity in estuarine waters. *Sci. Total Environ.* 653, 300–314. doi:10.1016/j.scitotenv.2018.10.263

Conflict of Interest: The authors declare that the research was conducted in the absence of any commercial or financial relationships that could be construed as a potential conflict of interest.

frontiers in Chemistry

ORIGINAL RESEARCH
published: 24 February 2021
doi: 10.3389/fchem.2021.640219

Ca^{2+} Complexation With Relevant Bioligands in Aqueous Solution: A Speciation Study With Implications for Biological Fluids

*Donatella Aiello[1], Federica Carnamucio[2], Massimiliano Cordaro[2], Claudia Foti[2], Anna Napoli[1] and Ottavia Giuffrè[2]**

[1]*Dipartimento di Chimica e Tecnologie Chimiche, Università Della Calabria, Arcavacata di Rende, Italy,* [2]*Dipartimento di Scienze Chimiche, Biologiche, Farmaceutiche Ed Ambientali, Università di Messina, Messina, Italy*

A speciation study on the interaction between Ca^{2+} and ligands of biological interest in aqueous solution is reported. The ligands under study are L-cysteine (*Cys*), D-penicillamine (*PSH*), reduced glutathione (*GSH*), and oxidized glutathione (*GSSG*). From the elaboration of the potentiometric experimental data the most likely speciation patterns obtained are characterized by only protonated species with a 1:1 metal to ligand ratio. In detail, two species, $CaLH_2$ and CaLH, for systems containing *Cys*, *PSH*, and *GSH*, and five species, $CaLH_5$, $CaLH_4$, $CaLH_3$, $CaLH_2$, and CaLH, for system containing *GSSG*, were observed. The potentiometric titrations were performed at different temperatures ($15 \leq t/°C \leq 37$, at $I = 0.15$ mol L^{-1}). The enthalpy and entropy change values were calculated for all systems, and the dependence of the formation constants of the complex species on the temperature was evaluated. ^1H NMR spectroscopy, MALDI mass spectrometry, and tandem mass spectrometry (MS/MS) investigations on Ca^{2+}-ligand solutions were also employed, confirming the interactions and underlining characteristic complexing behaviors of *Cys*, *PSH*, *GSH*, and *GSSG* toward Ca^{2+}. The results of the analysis of ^1H NMR experimental data are in full agreement with potentiometric ones in terms of speciation models and stability constants of the species. MALDI mass spectrometry and tandem mass spectrometry (MS/MS) analyses confirm the formation of Ca^{2+}-L complex species and elucidate the mechanism of interaction. On the basis of speciation models, simulations of species formation under conditions of some biological fluids were reported. The sequestering ability of *Cys*, *PSH*, *GSH*, and *GSSG* toward Ca^{2+} was evaluated under different conditions of pH and temperature and under physiological condition.

Keywords: Ca^{2+}, biological ligands, speciation in biological fluids, sequestration, potentiometry, ^1H NMR spectroscopy, mass spectrometry, thermodynamic parameters

OPEN ACCESS

Edited by:
Alberto Salomone, University of Turin, Italy

Reviewed by:
Artik Elisa Angkawijaya, National Taiwan University of Science and Technology, Taiwan
Luca Rivoira, School of Nature Sciences, University of Turin, Italy

****Correspondence:***
Ottavia Giuffrè
ogiuffre@unime.it

Specialty section:
This article was submitted to Analytical Chemistry, a section of the journal Frontiers in Chemistry

Received: *10 December 2020*
Accepted: *11 January 2021*
Published: *24 February 2021*

Citation:
Aiello D, Carnamucio F, Cordaro M, Foti C, Napoli A and Giuffrè O (2021) Ca^{2+} Complexation With Relevant Bioligands in Aqueous Solution: A Speciation Study With Implications for Biological Fluids. Front. Chem. 9:640219. doi: 10.3389/fchem.2021.640219

INTRODUCTION

Calcium is the fifth most important element in the human body. It is indispensable for life, for the regulation of metabolism and maintenance of structure (Peterlik and Stoeppler, 2004). It behaves like an intracellular "second messenger" in numerous processes, namely, neurotransmitter release, cellular proliferation and differentiation, and control of exocrine and endocrine secretions (Bringhurst and Potts., 1979; Broaudus, 1993). In human body, about 99% of total calcium

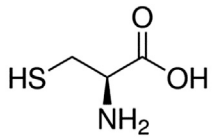

(R)-2-amino-3-sulfhydrylpropanoic acid or L-Cysteine (*Cys*)

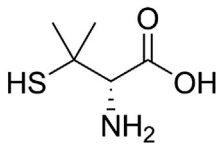

(2S)-2-amino-3-methyl-3- sulfanylbutanoic acid or D-Penicillamine (*PSH*)

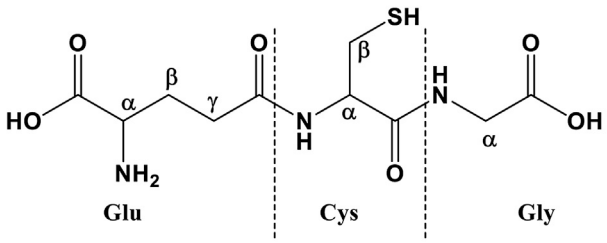

γ- L-glutamyl-L-cysteinyl-glycine or glutathione (*GSH*)

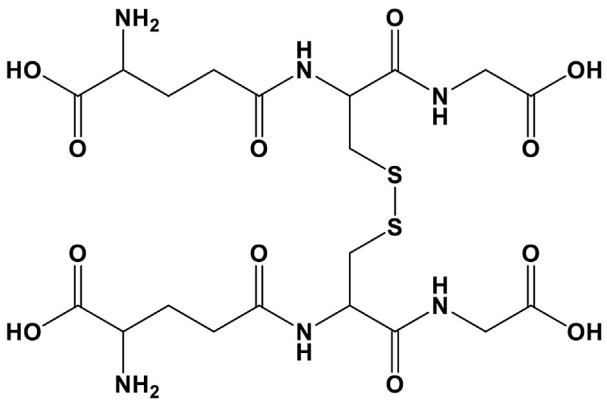

2-amino-4-[(2-{[2-(4-amino-4-carboxybutanamido)-2-[(carboxymethyl)carbamoyl]ethyl]disulfanyl}-1-[(carboxymethyl)carbamoyl]ethyl)carbamoyl]butanoic acid or Oxidized glutathione (*GSSG*)

FIGURE 1 | Ligands under study.

(1.0–1.3 kg in adults) (Hluchan and Pomerantz, 2002) is found in the bones. The remaining part, 1%, is present in intra- and extracellular fluids. Free calcium concentration in the cell ranges between 10^{-6} and 10^{-8} mol kg^{-1}. It is about 10^{-3} mol kg^{-1} in the sarcoplasm (Frausto da Silva and Williams, 2001a). The mean Ca^{2+} concentration in the plasma

is 2.5 mmol L^{-1}, of which about 50% is present as free ion; the remaining part is bound for 40% to plasma proteins and for 10% to citrate and phosphate. The rigid control of free calcium in the plasma is very crucial, as even small concentration changes can cause significant variations in the skeletal site, as well as intracellular free calcium, with harmful consequences for bone health (Peterlik and Stoeppler, 2004; Whedon, 1980). Calcium homeostasis is based on a dynamic equilibrium of its fluxes between three different body compartments, namely, extracellular fluid, intracellular one, and skeletal tissue. As regards the physiological role of calcium, it includes the control of many kinase reactions in metabolism, of dioxygen release in photosynthesis, and of dehydrogenases in oxidative phosphorylation (Frausto da Silva and Williams, 2001b). Ca^{2+} interacts preferably with oxygen donor groups. In the body fluids it can bind polymers, such as proteins, *via* carboxylate and phosphate sidechains. In the proteins, the main donor groups toward Ca^{2+} are represented by carboxylate and carbonyl centers (Frausto da Silva et al., 2001a).

Cys is one of the most important binding agents for metal cations in biological fluids (Laurie et al., 1979). Its concentration in normal human plasma is in the micromolar range (Brigham et al., 1960). The drug penicillamine, which has a very similar structure to *Cys*, was commonly employed in the treatment of Wilson's disease (Walshe, 1956; Jones, 1991). *GSH* is a tripeptide consisting of the amino acids L-glutamic acid (Glu), *Cys*, and glycine (Gly). It exists in two forms: a reduced (*GSH*) and an oxidized one, i.e., dimer glutathione disulfide (*GSSG*) (Labib et al., 2016). *GSH* is ubiquitous antioxidant present in cells as well as in bacteria (Sies, 1999; Pompella et al., 2003; Kretzschmar et al., 2020; Meister and Anderson, 1983). In mammalian cells, concentrations greater than 12 mmol L^{-1} are reported (Dringen, 2000). Both *GSH* and its oxidized form, *GSSG*, are fundamental for the maintenance of the intracellular redox state (Shahid et al., 2020). They are considered biomarkers of oxidative stress in biological fluids as well as for the diagnosis of certain clinical disorders (Labib et al., 2016; Olmos Moya et al., 2017). The mechanism of antioxidant cellular defense *in vivo* is governed by *GSH*, oxidized continuously to disulfide glutathione (*GSSG*) (Davis and Hanumegowda, 2008). In healthy cells, the *GSH* form constitutes over 90% of glutathione (Labib et al., 2016). In addition to protecting cells from oxidative damage, *GSH* is involved in the complexation and transport reactions of metal ions (Olmos Moya et al., 2017). In blood, the normal values of *GSH* and *GSSG* are 3.8–5.5 and 0.2–0.5 μmol L^{-1}, respectively (Labib et al., 2016).

Given all these aspects, reliable assessment of the speciation of biologically relevant ligands with Ca^{2+} is crucial to understand and to model the behavior of these systems. Ligands under study are reported in **Figure 1**. In this study, the experimental measurements were performed by different techniques: potentiometry, ^{1}H NMR spectroscopy, MALDI mass spectrometry, and MS/MS. The potentiometric titrations were carried out at different temperatures, $15 \leq t/°C \leq 37$ and I = 0.15 mol L^{-1} in NaCl. Some simulations of species formation under conditions of biological fluids were reported. The sequestering ability of all ligands understudy toward Ca^{2+} was evaluated under different conditions of pH and temperature.

TABLE 1 | Experimental conditions for potentiometric and ^{1}H NMR titrations at I = 0.15 mol L^{-1} in NaCl.

Technique	t/°C	C_M/mmol L^{-1}	C_L/mmol L^{-1}	M/L	pH range
Potentiometry	15–37	1–5	2–6	0.33–2	2–10
^{1}H NMR	25	5–10	5–10	0.75–1.5	2–10.5
^{1}H NMR	25	–	10[a]	–	2–10.5

[a]*Protonation measurements for GSSG ligand.*

MATERIAL AND METHODS

Materials

The solutions containing calcium metal cation were obtained by weighing and dissolving the corresponding salt, calcium (II) chloride dihydrate (purity >99%, Fluka/Honeywell, Charlotte, North Carolina, US). Afterward calcium solutions were standardized by titration with EDTA (Ethylenediaminetetraacetic acid disodium salt, BioUltra, ≥99%, Sigma-Aldrich/Merck, Darmstadt, Germany) standard solution. Ligand solutions were prepared by weighing and dissolving, without further purification, the following products: L-cysteine (purity ≥99.5%, Fluka/Honeywell, Charlotte, North Carolina, US), D-penicillamine (purity ≥97%, Alfa-Aesar/Thermo Fisher, Kandel, Germany), reduced glutathione (purity ≥98%, Alfa-Aesar, Thermo Fisher, Kandel, Germany), and oxidized glutathione (purity 98%, Sigma-Aldrich/Merck, Darmstadt, Germany). The purity of the ligands was checked by alkalimetric titration. It was found to be greater than 99%. Solutions of hydrochloric acid and sodium hydroxide were obtained by dilution of Fluka (Fluka/Honeywell, Charlotte, North Carolina, US) ampoules and afterward they were standardized with sodium carbonate (≥99.5%, Sigma-Aldrich/Merck, Darmstadt, Germany) and potassium biphthalate (≥99.5%, Sigma-Aldrich/Merck, Darmstadt, Germany), respectively. Both salts were previously dried in an oven at 110 °C. Solutions of sodium hydroxide were reprepared very frequently and were kept in bottles with soda lime traps. Solutions of sodium chloride were obtained by weighing the corresponding salt (puriss., Sigma-Aldrich/Merck, Darmstadt, Germany), previously dried in an oven at 110 °C. Distilled water (conductivity <0.1 μS cm^{-1}) and grade A glassware were employed for the preparation of all the solutions.

Potentiometric Apparatus and Procedure

Two distinct systems were employed for the potentiometric titrations. In detail, the systems consist in an identical configuration consisting in an automatic dispenser Metrohm Dosino 800, a Metrohm model 809 Titrando potentiometer, and a Metrohm LL-Unitrode WOC combined glass electrode. Each potentiometric system was connected to a PC and the experimental titration data were acquired by the Metrohm

TIAMO 2.2 software. It can control several parameters, such as e.m.f. stability, titrant delivery, and data acquisition. Estimated accuracy of this apparatus is ±0.15 mV and ±0.002 ml for e.m.f. and for readings of titrant volume, respectively.

Each titration consists in additions of volumes of NaOH standard to 25 ml of the solution containing Ca^{2+}, ligand, and a supporting electrolyte (NaCl). Experimental details on potentiometric titrations are reported in **Table 1**. Glass jacket thermostated cells were employed for the measurements performed under different conditions of temperature ($15 \leq t/°C \leq 37$), by bubbling pure N_2 in order to avoid CO_2 and O_2 inside the solutions and under magnetic stirring. For each measurement, an independent titration of HCl with standard NaOH was performed to calculate the standard electrode potential E^0 and the pK_w value, under the same experimental ionic strength and temperature conditions.

NMR Apparatus and Procedure

The spectrometer employed for the collection of ^1H NMR spectra is a Varian 500 F T-NMR. 1,4-Dioxane was used as internal reference ($\delta_{CHdioxane}$ = 3.70 ppm); the chemical shifts are referred to tetramethylsilane (TMS). All the measurements were carried out in a 9:1 H_2O/D_2O solution at t = 25 °C. Presaturation technique was employed to suppress the water signal. Experimental details on ^1H NMR titrations are reported in **Table 1**.

Mass Spectrometric Apparatus and Procedure

A water solution of 2 equivalents of each ligand (*Cys*, *PSH*, *GSH*, *GSSG*) was added dropwise to 1 mmol of $CaCl_2$ dissolved in water with magnetic stirring for 2 h at room temperature. MALDI MS and MS/MS analyses were performed using a 5800 MALDI-TOF-TOF Analyzer (AB SCIEX) in reflection positive ion mode with a mass accuracy of 5 ppm. At least 5000 laser shots were typically accumulated with a laser pulse rate of 400 Hz and 1000 Hz in the MS and MS/MS mode, respectively. MS/MS experiments were performed using ambient air as collision gas with a medium pressure of 10^{-6} Torr and a collision energy of 1 kV, with a mass accuracy of 20 ppm. After acquisition, spectra were processed using Data Explorer version 4.0. MALDI MS and MS/MS experimental conditions were optimized using sinapinic acid (SA, 5 mg/ml in H_2O/CH_3CN 40:60, v/v; with 0.1% TFA) as matrix for all ligands. The sample loading was performed by dried droplet method for all ligands, spotting 1 μL of sample/matrix premixed solution (1:5, v/v ratio).

Calculations

Experimental data of potentiometric titrations were processed using BSTAC and STACO programs. They allow for obtaining the best speciation model for each system under study, the formation constant values of the species, and the parameters of a titration (standard potential E^0, analytical concentration of the reagents, and junction potential). The parameters for the dependence of complex formation constants on temperature were obtained by LIANA program. More details on software employed in the refinement of the experimental data are reported in De Stefano et al. (1997). For ^1H-NMR titrations, HypNMR software was employed to obtain protonation and formation constant values, as well as the individual chemical shift of each species, using the observed signals and assuming fast mutual exchange in the NMR time scale (Frassineti et al., 1995). HySS program was used to obtain the speciation diagrams and the formation percentages of the complex species (Alderighi et al., 1999).

TABLE 2 | Formation constants of Ca^{2+}-*Cys*, *PSH*, *GSH*, *GSSG* species at different temperatures at I = 0.15 mol L^{-1} in NaCl.

Ligand	Species	logβ [a]		
		t = 15 °C	t = 25 °C	t = 37 °C
Cys	MLH_2	21.22 ± 0.01[b]	20.76 ± 0.03[b]	20.10 ± 0.06[b]
	MLH	12.62 ± 0.03	12.50 ± 0.04	12.14 ± 0.06
PSH	MLH_2	20.86 ± 0.08	21.30 ± 0.08	21.65 ± 0.08
	MLH	13.00 ± 0.08	13.37 ± 0.09	13.89 ± 0.08
GSH	MLH_2	20.39 ± 0.05	19.97 ± 0.03	20.14 ± 0.01
	MLH	11.53 ± 0.06	11.02 ± 0.07	11.66 ± 0.02
GSSG	MLH_5	29.88 ± 0.09	30.18 ± 0.09	30.45 ± 0.06
	MLH_4	28.28 ± 0.06	28.16 ± 0.09	27.77 ± 0.06
	MLH_3	25.40 ± 0.06	25.12 ± 0.08	24.73 ± 0.06
	MLH_2	21.64 ± 0.04	21.19 ± 0.07	20.66 ± 0.04
	MLH	12.66 ± 0.03	12.15 ± 0.08	11.62 ± 0.05
			log$K$[c]	
Cys	MLH_2	2.45	2.46	2.32
	MLH	2.20	2.34	2.26
PSH	MLH_2	2.07	2.89	3.66
	MLH	2.25	2.83	3.58
GSH	MLH_2	1.77	1.89	2.41
	MLH	1.81	1.57	2.41
GSSG	MLH_5	1.90	2.71	3.56
	MLH_4	2.48	2.84	2.99
	MLH_3	2.71	2.91	3.05
	MLH_2	2.72	2.75	2.75
	MLH	2.80	2.53	2.27

[a]*Overall formation constants.*
[b]*≥95% of confidence interval.*
[c]*Stepwise formation constants.*

RESULTS AND DISCUSSION

In the calculations, protonation constants of ligands understudy (Cardiano et al., 2008; Crea et al., 2008; Cardiano et al., 2013) and hydrolytic constant of Ca^{2+} were taken into account. They are reported in **Supplementary Tables S1** and **S2**.

Potentiometric measurements were carried out under different conditions of temperature and metal-ligand ratios, to choose the most appropriate speciation model and to be able to refine the formation constants of the species in solution. The formation constants of Ca^{2+}(M)-ligand(L) species are expressed as overall formation constants (β) and stepwise formation constants (K). The reactions are the following (charges are omitted for simplicity):

$$M + L + rH = MLH \quad \beta^{MLHr}, \tag{1}$$

$$M + LH_r = MLH_r \quad K^{MLHr}. \tag{2}$$

Within the speciation studies, the most reliable model for a metal-ligand system is chosen by taking into account several factors,

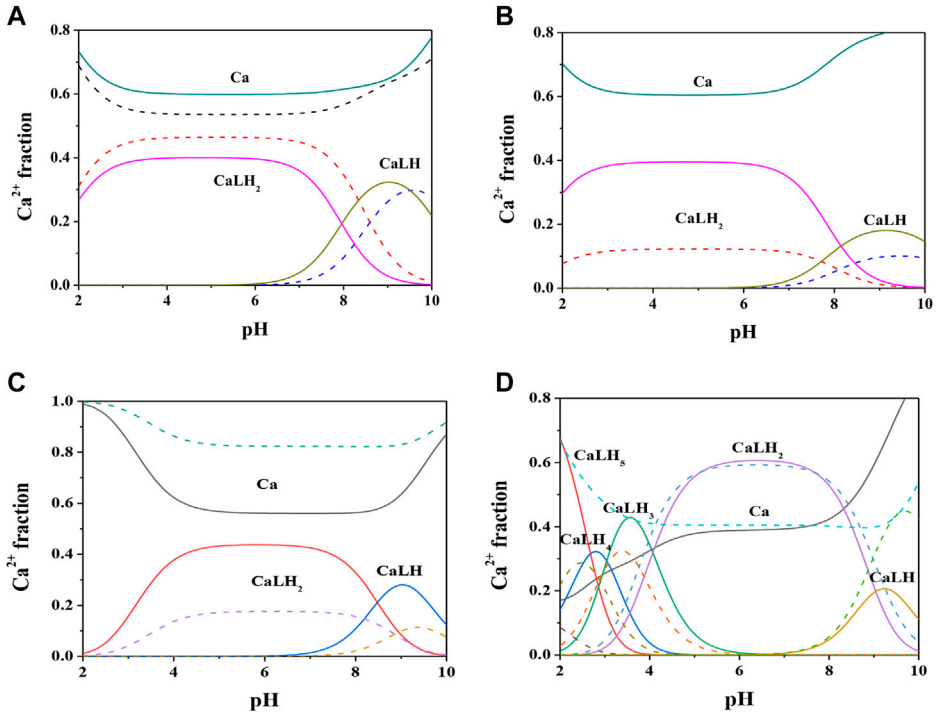

FIGURE 2 | Speciation diagrams of Ca^{2+}-ligand (L) systems at t = 15 °C (dotted lines) and t = 37 °C (solid lines), C_M = 2 mmol L^{-1}, C_L = 4 mmol L^{-1}, I = 0.15 mol L^{-1} in NaCl **(A)** L = *Cys* **(B)** L = *PSH* **(C)** L = *GSH* **(D)** L = *GSSG*.

such as the simplicity of the model itself, the statistical parameters (standard and mean deviation on the fit), the variance ratio between the chosen model and others, and the formation percentages of the formed species (Filella, 2005).

Speciation Profiles and Aqueous Behavior

Formation constant values of Ca^{2+}-*Cys*, *PSH*, *GSH*, *GSSG* species obtained *via* potentiometric measurements at different temperatures and I = 0.15 mol L^{-1} were reported in **Table 2**. The speciation pattern for all the systems includes only 1:1 M:L species. *Cys*, *PSH*, and *GSH* show a very similar behavior with the same speciation model including only two significant species, namely, MLH_2 and MLH. For all three systems, the stability of complex species in terms of stepwise formation constants is between a minimum of 1.57 (MLH species for Ca^{2+}-*GSH* system, t = 25 °C) and a maximum of 3.66 (MLH_2 species for Ca^{2+}-*PSH* system, t = 37 °C). In **Figure 2A** the speciation diagram of Ca^{2+}-*Cys* species is depicted at I = 0.15 mol L^{-1} and t = 15, 37 °C. Under physiological conditions (t = 37 °C, I = 0.15 mol L^{-1}), MLH_2 species is formed in the range 2 ≤ pH ≤ 9 and reaches a metal fraction of 0.4 in the range 3 ≤ pH ≤ 7. The main complex species in the range 8 ≤ pH ≤ 10 is MLH with a maximum metal fraction corresponding to 0.3 at pH = 9.5.

Formation constants of Ca^{2+}-*PSH* species are quite higher with respect to Ca^{2+}-*Cys* ones. For example, stepwise formation constant values at t = 37 °C resulted between 3.58 and 3.66. The differences between stepwise formation constants of species formed by *PSH* and *Cys* with Ca^{2+}, under physiological conditions, are $\Delta\log K$ = 1.3 for both MLH_2 and MLH. The speciation diagram, represented in **Figure 2B**, refers to Ca^{2+}-*PSH* system, under physiological conditions. MLH_2 species is formed in the wide interval 2 ≤ pH ≤ 8, reaching a maximum metal fraction of 0.4; MLH species is present in the range 8 ≤ pH ≤ 10 with a lower metal fraction (0.2).

For Ca^{2+}-*GSH* system, stepwise formation constant values at t = 37 °C are equal to 2.41 for both species. The differences between formation constants of Ca^{2+}-*PSH* and -*GSH* species, under physiological conditions are $\Delta\log K$ = 1.2 for both. The speciation diagram, depicted in **Figure 2C**, refers to Ca^{2+}-*GSH* system, under physiological conditions. It shows that MLH_2 is the main complex species in the wide interval 2 ≤ pH ≤ 9, with a maximum metal fraction of 0.4, and MLH predominates in the range 8.5 ≤ pH ≤ 10, with a metal fraction of 0.3.

A separate discussion must be made for the system containing *GSSG*. As expected from the presence of the numerous protonable groups on molecule, the speciation model is very rich in complex species, namely, MLH_5, MLH_4, MLH_3, MLH_2, and MLH. Their stability is comparable to the values found for the other ligands already discussed. As an example, at t = 37 °C and I = 0.15 mol L^{-1}, log$K$ values, referring to stepwise formation constants, range between 2.27 and 3.56 for the five species. Speciation profile for Ca^{2+}-*GSSG* system is represented in **Figure 2D**. Under physiological conditions, the less significant species is MLH one, while the most significant species is MLH_2, which predominates in the pH range between 4.5 and 9 reaching metal fraction of 0.6. The most protonated species, MLH_5, MLH_4,

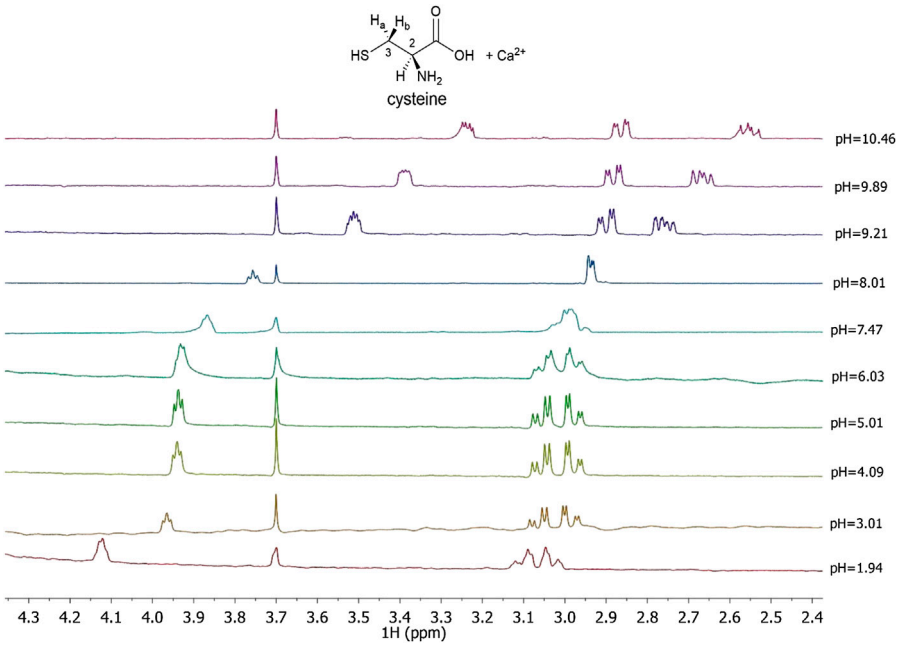

FIGURE 3 | ^{1}H NMR spectra on solutions containing Ca^{2+} (M) and *Cys*(L) at C_M = 7.5 mmol L^{-1}, C_L = 10 mmol L^{-1}, t = 25 °C, I = 0.15 mol L^{-1} in NaCl, 1.94 ≤ pH ≤ 10.46.

and MLH_3, predominant at pH < 4.5, reach maximum metal fractions equal to 0.65, 0.3, and 0.45, respectively. MLH species is significant only at pH > 9, with a metal fraction of 0.2.

^{1}H NMR Spectroscopy

The interaction of ligands of biological interest with metal cations in aqueous solution had been already studied by our research group with several spectroscopic techniques, such as ^{1}H NMR (Cardiano et al., 2008; Cardiano et al., 2011; Cardiano et al., 2013; Cardiano et al., 2016), UV-Vis (Falcone et al., 2011; De Stefano et al., 2014), Mössbauer (Cardiano et al., 2006), and Raman (Cassone et al., 2019). In the literature, there are some recent papers that report ^{1}H NMR investigations on *GSSH* and *PSH* with metal cations other than Ca^{2+} (Sisombath et al., 2014; Kretzschmar et al., 2020). More in detail, Sisombath *et al.* report a complexation study on Pb^{2+} with *PSH* by ^{1}H NMR analysis, in D_2O solutions at pH = 9.6, at various M:L molar ratios. The data here reported are comparable with that reference and specifically it is possible to underline the same trend relative to the significant chemical shift of CH-2 (Δδ = 0.6 ppm) and of only one of the two -CH_3.

In this paper ^{1}H NMR spectra of Ca^{2+}-*Cys* species, reported in **Figure 3** at different pH values and t = 25 °C, show a chemical shift of the signals related to the proton in 2 and to the two protons in 3, indicated as H-2, H_a-3, and H_b-3, respectively for *Cys*. At pH < 8 there is a triplet for H-2 and a double doublet (*dd*) for H_a-3 and H_b-3. At pH > 8, the complexity of the signals increases wherein a multiplet for H-2, a *dd* for H_a-3, and a *dd* for H_b-3 are shown. The chemical shift of the H-2 proton to the increase of pH is approximately 0.8 ppm upfield due to the increase in the negative charge for the deprotonation of the carboxyl group and subsequently of the thiol group. A similar trend is evident for protons in 3; in this case the chemical shift is about 0.3 ppm. Much more interesting is the splitting of the signals into two different *dd*, which can be interpreted with greater rigidity of the ligand for the presence of a dianion or for the interaction with the metal cation as well. This AMX system is therefore due to the different magnetic properties of the

TABLE 3 | Comparison between the experimental formation constants of Ca^{2+}–ligand species and protonation constants of *GSSG* obtained *via* ^{1}H NMR and potentiometry at t = 25 °C and I = 0.15 mol L^{-1}.

Ligand	Species		logβ[a]
		^{1}H NMR	Potentiometry
Cys	MLH_2	20.4 (2)[b]	20.76
	MLH	12.4 (1)	12.50
PSH	MLH_2	21.0 (2)[b]	20.60
	MLH	12.15	12.15
GSH	MLH_2	20.49 (8)[b]	19.97
	MLH	10.9 (3)	11.02
GSSG	LH	9.3 (2)[b]	9.618
	LH_2	18.35 (9)	18.442
	LH_3	22.22 (4)	22.212
	LH_4	25.43 (6)	25.319
	LH_5	27.467	27.467
	LH_6	28.987	28.987
	MLH_5	30.18	30.18
	MLH_4	28.16	28.16
	MLH_3	25.12	25.12
	MLH_2	21.21 (6)[b]	21.19
	MLH	12.04 (7)	12.15

[a]*Overall formation constants.*
[b]*≥95% of confidence interval.*

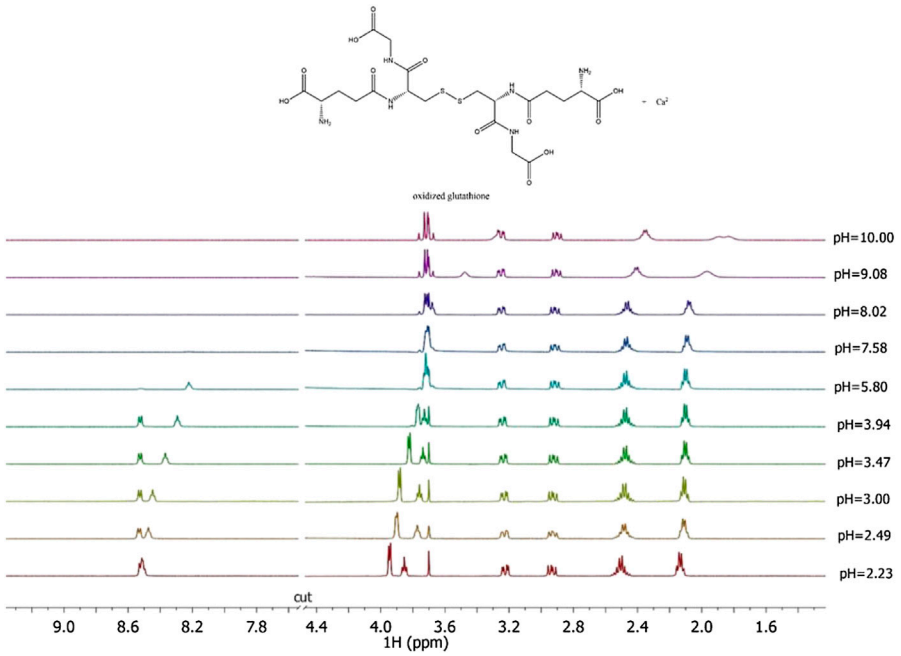

FIGURE 4 | ^{1}H NMR spectra on solutions containing Ca^{2+} (M) and *GSSG*(L) at C_M = 8 mmol L^{-1}, C_L = 6 mmol L^{-1}, t = 25 °C, I = 0.15 mol L^{-1} in NaCl, 2.23 ≤ pH ≤ 10.00.

two protons in 3 and consequent more complex coupling between the three protons H-2, H_a-3, and H_b-3. The interaction with Ca^{2+} is evident from the comparison with the corresponding chemical shift values of *Cys* alone, under the same experimental conditions.

^{1}H NMR spectra of Ca^{2+}-*PSH*, Ca^{2+}-*GSH* solutions were reported in **Supplementary Figures S2-S3**. Both ligands evidenced a similar behavior to *Cys*, as their spectra NMR showed a significant shift in signals at the change of pH. The interaction of each ligand with Ca^{2+} is highlighted by the comparison with the corresponding chemical shift values of the ligand in the absence of the metal cation under the same experimental conditions. The comparison of the formation constant values obtained *via* potentiometric and ^{1}H NMR measurements (see **Table 3**) shows satisfactory correspondence.

Here the NMR analysis of the free *GSSG* ligand at different pH values is reported. ^{1}H NMR spectra of *GSSG* in 10% D_2O/H_2O solution show only six signals due to the symmetry to the S-S bond. **Table 3** shows the comparison between the protonation constant values obtained by potentiometric and ^{1}H NMR measurements. It was possible to obtain the values relating to the first four protonation constants (LH, LH_2, LH_3, and LH_4), while those relating to the LH_5 and LH_6 species were kept constant using the values obtained by potentiometry. The agreement among the results obtained by the two different techniques was excellent. ^{1}H NMR spectra registered on Ca^{2+}-*GSSG* solutions at t = 25 °C and I = 0.15 mol L^{-1}, represented in **Figure 4**, show substantially the same signal pattern observed in the spectra relating to the solutions containing *GSSG* ligand (**Supplementary Figure S4**). In detail, at pH = 2.2 are present amide protons 4 and 13 at δ = 8.5 ppm (2 singlets), proton in 3 at 3.95 ppm (quartet), proton in 11 at δ = 3.85 ppm (multiplet), proton in 14 at δ = 3.22 ppm (multiplet), proton in 2 at δ = 2.93 ppm (dd), proton in 9 at δ = 2.50 ppm (multiplet), and proton in 10 at δ = 2.13 ppm (multiplet).

The chemical shift values of the individual species were calculated on the basis of formation percentages of each species in solution. These chemical shifts, reported in **Supplementary Table S3**, were used to determine the values of the formation constants of the complex species. In **Table 3** these formation constant values obtained by ^{1}H NMR titrations were reported, together with potentiometric ones. It is possible to notice a good agreement among the values determined by the two different techniques. For Ca^{2+}-*GSSG* species only the values referring to MLH_2 and MLH species were refined, keeping constant ones obtained by potentiometry related to MLH_5, MLH_4, and MLH_3 species. The speciation model considered for all the systems is also confirmed by the complete overlap of the experimental and calculated chemical shift values shown in **Figure 5**. It should be noted that, at pH > 8, ^{1}H NMR spectra on the solutions containing ligands in the presence of Ca^{2+} show significant differences with respect to the corresponding free ligands. At pH > 8, differences of Δδ between 0.05 and 0.10 ppm were calculated on average for all ligands, except for *GSSG*. From this experimental evidence, it can be assumed that *Cys*, *PSH*, *GSH*, and *GSSG* could behave as divalent ligands, binding Ca^{2+} and giving rise to cyclic complexes.

MALDI MS and MS/MS

Mass spectrometry combined with soft ionization methods as electrospray ionization (ESI) and matrix assisted laser desorption

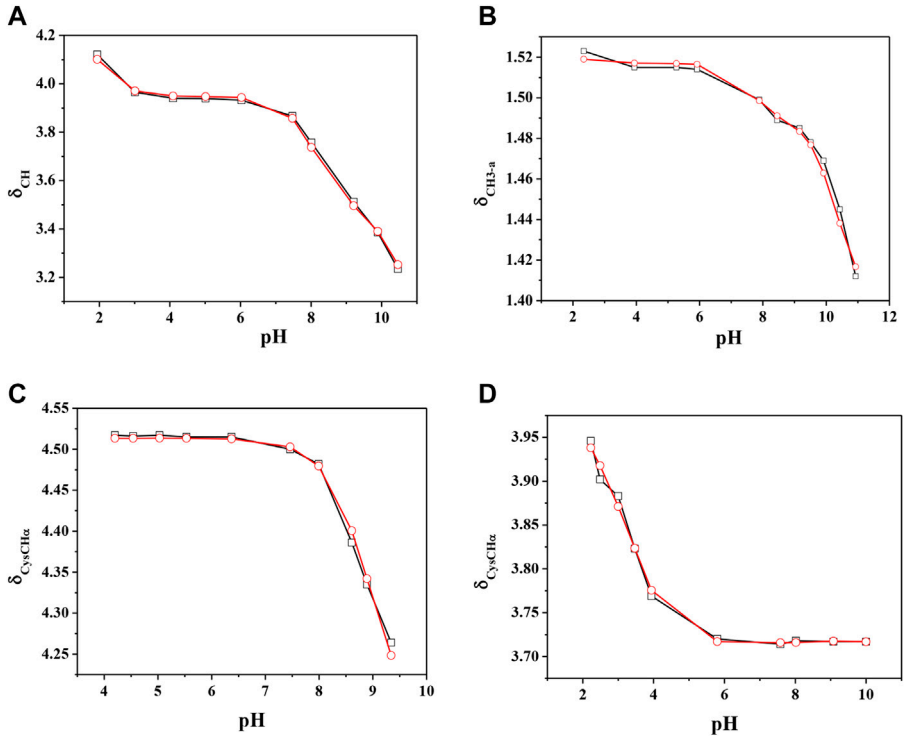

FIGURE 5 | Experimental (□) and calculated (○) chemical shift values (in ppm) *vs*. pH of **(A)** CH on Ca^{2+}(M)-*Cys*(L) solutions, **(B)** $CH_{3\text{-}a}$ on Ca^{2+}(M)-*PSH*(L) solutions, **(C)** CysCHα on Ca^{2+}(M)-*GSH*(L) solutions, **(C)** CysCHα on Ca^{2+}(M)-*GSSG*(L) solutions.

ionization (MALDI) is currently becoming a strategic approach to clarify structures and coordination sites in compounds where metals are chelated by biological ligands (Cardiano et al., 2009; Furia et al., 2014; Aiello et al., 2017; Aiello et al., 2018a; Chillè et al., 2020). MALDI-TOF/TOF-MS platforms can be used for the highly sensitive analysis of low molecular weight compounds (Aiello et al., 2020a) in complex matrices (Aiello et al., 2018b; Aiello et al., 2020b; Imbrogno et al., 2019; Salvatore et al., 2020). In order to investigate whether calcium binding by *Cys*, *PSH*, *GSH*, and *GSSG* induces formation of complexes, a water solution of 2 equivalents of each ligand was added dropwise to 1 equivalent of $CaCl_2$ and complex association was analyzed by MALDI MS using sinapinic acid as matrix. Signals corresponding to complex ML with 1:1 stoichiometry are the most intense signals in the spectrum for all investigated systems. The molecular masses derived from these measurements are in good agreement with the calculated mass (within 5 ppm, **Table 4**). The simplest systems, represented by Ca^{2+}-*Cys* and Ca^{2+}-*PSH*, will briefly be discussed. Both ligands hold multiple donor sites that are capable of intramolecular stabilization of the metal-ligand species. The carboxylic acids, bearing donor groups in their α or β positions, generally act as bidentate ligands giving rise to cyclic structures (Aiello et al., 2018a; Falcone et al., 2013). Accordingly, the formation of $[MLH]^+$ species suggests that *Cys* and *PSH* act as bidentate ligands giving rise to six-membered cycles (**Figure 6**). The simplicity of the MS/MS spectra suggests that only few fragmentation pathways are allowed for the decomposition of complexes. MALDI MS/MS spectrum of the system Ca^{2+}-*Cys* (**Figure 6A**) reveals that the main fragmentation pathways of the precursor $[MLH]^+$ (m/z 159.97, $[CaC_3H_6NSO_2]^+$) consist in the loss of low molecular species such as NH_2 (m/z 144.96 $[CaC_3H_5SO_2]^+$) and CH_2NH (m/z 130.95 ($[CaC_2H_3SO_2]^+$). However, some characteristic fragment ions can be found and correlate with the proposed structure. In particular, the formation of the ions of m/z 130.95 ($[CaC_2H_3SO_2]^+$), m/z 118.95 ($[CaC_2H_7SO]^+$), and m/z 90.95 ($[CaH_3SO]^+$) arises from across ring fragmentation of a six-membered structure. Analogously, *PSH* leads to a cyclic structure ($[MLH]^+$ of m/z 188.01 ($[CaC_5H_{10}NO_2S]^+$). Several distinguishing ion products were detected in the MS/MS spectra; all the peak assignments are described in **Table 4** and **Figure 6B**. In agreement with the NMR data, it can be reasonably stated that *Cys* and *PSH* act as divalent ligands and that they bind the Ca^{2+} ion through O and S giving rise to six-membered cyclic complexes, as already observed for other ligands containing carboxylic and thiol groups (Cardiano et al., 2009).

GSH is a tripeptide bearing two free -COOH groups, a $-NH_2$ group, and a -SH group; it provides a hydrophilic interface and a handle for further reactivity with other functional molecules as well as metal ions. The metal coordination ability of *GSH* is well documented, highlighting its multichelating nature. The speciation of both reduced and oxidized forms of *GSH* in MS/MS condition was considered. Information about molecular mass of the Ca^{2+}-*GSH* as well as Ca^{2+}-*GSSG* complex is easily obtained using 1:1 Ca^{2+}-*GSH* molar ratios. The peak at m/z 346.04 corresponds to the ion $[MLH]^+$ in which *GSH* is deprotonated

TABLE 4 | Mass spectrometry data of Ca^{2+}-L species, reported as m/z values, formula assignments, and MS/MS values for fragment ions.

	Formula	m/z	Δppm
[(M-*Cys*)H]$^+$	$[CaC_3H_6NSO_2]^+$	159.97	5.0
	$[CaC_3H_5SO_2]^+$	144.96	4.5
	$[CaC_2H_3SO_2]^+$	130.95	6.0
	$[CaCH_3SO_2]^+$	118.95	5.3
	$[CaH_3SO]$+	90.95	4.8
	$[CaOH]^+$	56.97	4.0
[(M-*PSH*)H]$^+$	$[CaC_5H_{10}NO_2S]^+$	188.01	6.0
	$[CaC_4H_5O_2S]^+$	156.96	4.5
	$[CaC_4H_9O_2S]^+$	161.00	5.5
	$[C_5H_7O]^+$	83.05	5.3
	$[CaOH]^+$	56.97	4.8
[(M-*GSH*)H]$^+$	$[CaC_{10}H_{16}N_3SO_6]^+$	346.04	5.0
	$[CaC_{10}H_{16}N_3SO_5]^+$	330.04	4.5
	$[CaC_{10}H_{14}N_3O_6]^+$	312.05	5.5
	$[CaC_9H_{16}N_3SO_4]^+$	302.05	5.1
	$[CaC_8H_{11}N_2SO_4]^+$	271.01	4.8
	$[CaC_8H_{13}N_2SO_3]^+$	219.05	4.7
	$[C_6H_{11}N_2O_3S]^+$	191.04	4.1
	$[C_3H_4NO_2]^+$	125.98	3.9
	$[CaOH]^+$	56.97	5.3
[(M-*GSSG*)H]$^+$	$[CaC_{20}H_{31}N_6O_{12}S_2]$+	651.10	4.0
	$[CaC_{20}H_{31}N_6S_2O_{11}]^+$	635.60	4.2
	$[CaC_{20}H_{31}N_6S_2O_{10}]^+$	619.76	4.8
	$[CaC_{18}H_{25}N_5S_2O_{10}]^+$	576.07	5.2
	$[CaC_{15}H_{24}N_5S_2O_5]^+$	522.06	4.1
	$[CaC_{12}H_{19}N_4S_2O_6]^+$	379.07	4.7
	$[CaC_{10}H_{12}N_3SO_6]^+$	346.04	5.3
	$[CaC_{10}H_{14}N_3O_6]^+$	312.05	5.5
	$[CaC_8H_{11}N_2SO_4]^+$	271.01	4.8
	$[C_3H_4NO_2]^+$	125.98	3.9

(i.e., GSH^{2-}) and therefore presumably bound to Ca^{2+} *via* -COOH and -NH amino groups. The calcium complex of *GSH* (m/z 346.04 $[CaC_{10}H_{16}N_3SO_6]^+$) decomposes to give, besides major H_2O and CO_2 and H_2S losses, small abundances of w_{3b}*, a_3*, b_2*, c_2*, b_1*, and d_{2a}* calcium containing and z_1 non-calcium product ions (**Figure 7A**). Product ions, which contain the C terminus, are formed by losses of residues comprised of only one amino acid, suggesting that the primary binding site for the Ca^{2+} is the N terminus of the peptide. The formation of the ion of m/z 125.98 ($[C_3H_4CaNO_2]^+$) and its counterpart m/z 219.05 $[C_8H_{13}N_2O_3S]^+$ indicates that *Glu* is calcium-binding amino acid. The Ca^{2+}-*GSSG* (m/z 651.10 $[C_{20}H_{31}CaN_6O_{12}S_2]^+$) complex decomposes giving a remarkably simple spectrum; it breaks down releasing *Glu* (m/z 522.06 $[CaC_{15}H_{24}N_5S_2O_5]^+$), *Gly* (m/z 576.07 $[CaC_{18}H_{26}N_5S_2O_{10}]^+$), and OH (m/z 635.60 $[CaC_{20}H_{31}N_6S_2O_{11}]^+$) as neutrals. The further formation of the most informative calcium containing products of m/z 619.76, m/z 346.04, and m/z 379.07 (**Figure 7B**) is also observed. The breakage of CH_2-S and S-S bonds leads to the formation of the ions of m/z 379 and 346, respectively. Thereafter, both calcium containing species decompose giving rise to low intensity ion series. Appearance of small mass calcium containing ions, in MS/MS spectrum of Ca-*GSSG* peptide complex, is additional evidence that calcium binding is *via* N terminus of the peptide. Therefore, *GSSG* involves calcium in an "open" type complex, in which the metal ion is not coordinated from both glutamic acids, assuming a behavior like a simple amino acid. Finally, the simplicity of MS/MS spectra indicates that the binding of Ca^{2+} ions to *GSH* and *GSSG* is to the deprotonated glutamyl carboxylic residue and to the NH amino function. Ca^{2+}-peptide complexes undergo fragmentations that are determined by the location of the Ca binding site.

Speciation in Biological Fluids

In order to evaluate the relevance of the systems under study under real conditions, two biological fluids were considered. The first application consists in the evaluation of formation percentages of Ca^{2+} complex species, by considering plasma concentration, temperature, and ionic strength conditions (t = 37 °C, I = 0.15 mol L^{-1}, C_{Ca} = 2.5 mmol L^{-1}, C_{Cys} = 0.01 mmol L^{-1}; C_{GSH} = 5.5 μmol L^{-1}, C_{GSSG} = 0.5 μmol L^{-1}, C_{Cl} = 0.1037 mol L^{-1}, C_{SO4} = 0.49 mmol L^{-1}, C_{CO3} = 24.9 mmol L^{-1}, C_{PO4} = 1.6 mmol L^{-1}) (Lentner, 1983). In these conditions, at pH = 7.4 the main species is $CaPO_4$, with a percentage of 60.9%. The most important species among ones under study are Ca*Cys*H_2 and Ca*Cys*H, although their sum just reaches 10.3%, as shown in **Figure 8A**.

The second application is based on lens aqueous solution. In the human eye the aqueous humor is located between the lens and the cornea. It is a gelatinous fluid where antioxidants, such as *GSH* and *Cys*, were investigated widely, since they serve as markers for eye diseases and infections. In the lens, the antioxidant *GSH* and ascorbic acid have unusually high concentration (Pescosolido et al., 2016). The functions performed by *GSH* with ascorbic acid in the lens are manifold. Among them, very important is the protection of protein thiol groups against oxidation agents and the detoxification of hydrophobic species in reactions catalyzed by glutathione S-transferase enzymes. In cataractous lens as well as in the aging lens, calcium concentration increases, and destruction of ascorbic acid and reduction of *GSH* content also occur (Chandorkar et al., 1980; Pescosolido et al., 2016). Accordingly, two different simulations were performed considering the composition of electrolyte and biological ligands in normal and in cataractous lens water. The obtained results are very different. **Figure 8B** represents the pie plot of Ca^{2+} complex species at pH = 7.2, by considering normal lens water concentrations (C_{Ca} = 0.01 mmol L^{-1}, C_{Cys} = 0.0143 mmol L^{-1}; C_{GSH} = 3.28 mmol L^{-1}, C_{GSSG} = 0.095 mmol L^{-1}, C_{Cl} = 0.79 mmol L^{-1}, $C_{Ascorbic\ Acid}$ = 1 mmol L^{-1}) (Chandorkar et al., 1980; Königsberger et al., 2015). In this case, among species formed by Ca^{2+}-ligands under study, those containing *GSH* form with higher percentages with a sum of 44.4%. The results significantly change by considering concentrations in cataractous lens water. Several studies reported that the level of reduced *GSH* in the lens decreases with the development of cataract (Kisic et al., 2012; Pescosolido et al., 2016). In this way over the years, *GSH* content reduces up to 73%, and *GSSG* content levels increase up to 18% (Pescosolido et al., 2016). Accordingly, the pie plot at pH = 7.2, under cataractous lens water conditions, was depicted in **Figure 8C** (C_{Ca} = 0.12 mmol L^{-1}, C_{Cys} = 0.0143 mmol L^{-1}; C_{GSH} = 0.9 mmol L^{-1}, C_{GSSG} = 0.11 mmol L^{-1}, C_{Cl} = 0.43 mmol L^{-1})

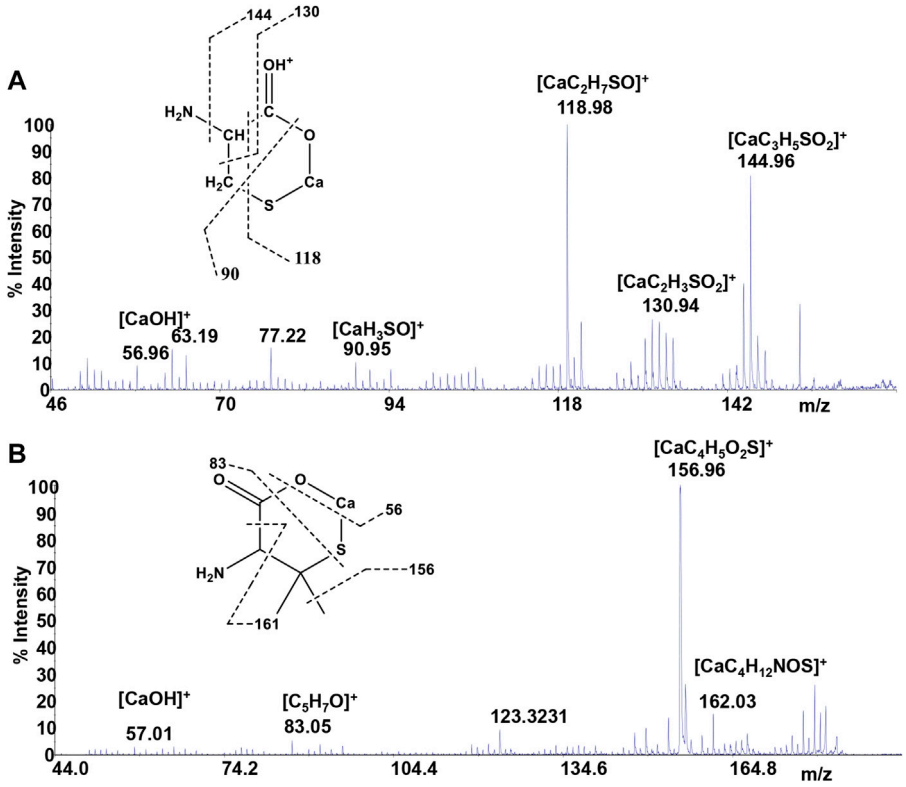

FIGURE 6 | MS/MS spectrum of **(A)** *Cys* and **(B)** *PSH* in the presence of Ca^{2+}.

(Chandorkar et al., 1980; Kisic et al., 2012; Königsberger et al., 2015; Pescosolido et al., 2016). In this case, percentage of Ca*GSH*H_2 species drastically decreases while remaining significant (from 41.9 to 18%); Ca*GSSG*H_2 increases slightly while resulting in an irrelevant species. These simulations confirm the need of knowledge of reliable formation constants at different conditions to predict the relevance of the species in real systems.

Dependence of Formation Constants on the Temperature

Formation constant values of the complex species reported in **Table 2**, obtained by potentiometric measurements at t = 15, 25, 37 °C, were analyzed for the determination of the formation enthalpy changes of the species, *via* the van't Hoff equation, already employed for several other systems (Cardiano et al., 2019; Cordaro et al., 2019; Foti and Giuffre, 2020; Giuffrè et al., 2019; Giuffrè et al., 2020):

$$\log\beta_T = \log\beta_\theta + \Delta H^0 (1/\theta - 1/T) R \ln 10, \quad (3)$$

where $\log\beta_T$ is the formation constant at a specific ionic strength and temperature (expressed in Kelvin), $\log\beta_\theta$ is the formation constant at T = 298.15 K, and ΔH^0 is the formation enthalpy change at T = 298.15 K in kJ mol^{-1}, R = 8.314,472 J K^{-1} mol^{-1}.

The values of formation enthalpy changes of all the species of Ca^{2+}-*Cys*, -*PSH*, -*GSH*, and -*GSSG* systems are collected in **Table 5**, together with entropy and free energy values. They are also shown as bar plot in **Figure 9**, to better highlight the contribution to the formation free energy of the enthalpy and entropy thermodynamic parameters. Since the interactions between Ca^{2+} and the ligands understudy are mainly of electrostatic nature, it is expected that the entropic term gives the highest contribution to the free energy change, due to the orientation disorder given by the solvation water molecules. This was found for most species (except for MLH one formed by the interaction with *Cys* ligand, MLH_2, and MLH ones containing *GSSG* ligand).

Sequestering Ability

The sequestering capacity represents the tendency, in solution, of a ligand to complex metal cation forming metal-ligand species, which allow for reducing the concentration of the free metal cation in solution. The stability of the complex species formed in solution influences the concentration of the free metal ion. The higher the stability of the formed species, the lower the concentration of the free cation. Considering the whole pH range, different metal-ligand species are formed in solution; each of them contributes to the sequestration of the metal cation. In order to describe the sequestering capacity of a given ligand with respect to a metal cation, it is not enough to know the formation constant values and the formation percentages of the different metal-ligand species. It is necessary to consider that different metal-ligand systems, having formation constants different from each other, can

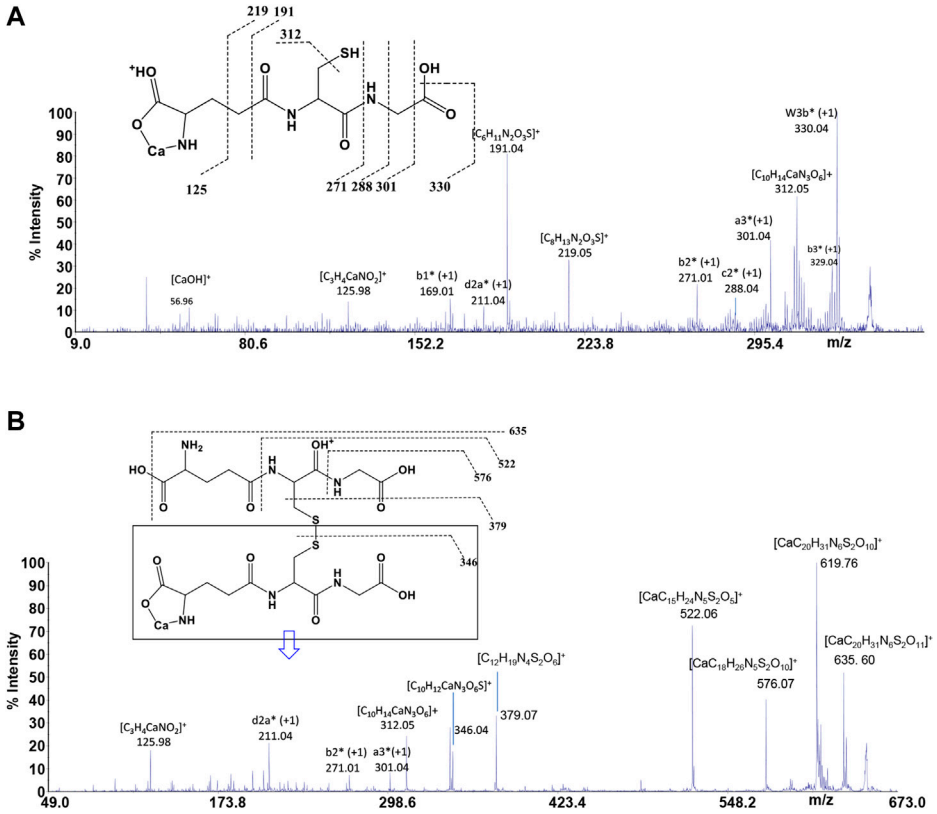

FIGURE 7 | MS/MS spectrum of **(A)** *GSH* and **(B)** *GSSG* in the presence of Ca^{2+}.

show the same formation percentages at a given pH and vice versa. Furthermore, all the equilibria in which the ligand and the metal ion under study take part must be considered, namely, ligand protonation, metal ion hydrolysis reactions, and weak interactions with the background salt. For these reasons, an empirical parameter, $pL_{0.5}$, was proposed, which represents the cologarithm of the ligand concentration necessary to sequester 50% of the metal cation present in traces. The traces are precisely the concentration conditions with which many metal cations are present in natural fluids. To evaluate for quantitative purposes the sequestering capacity of a ligand with respect to a metal cation, the following Boltzmann-type equation with asymptotes 0 for $pL \rightarrow 0$ and 1 for $pL \rightarrow \infty$ was used (Gianguzza et al., 2012; Falcone et al., 2013; De Stefano et al., 2016):

$$\chi = \frac{1}{1 + 10^{(pL - pL_{0.5})}}, \quad (4)$$

where χ is the sum of the molar fractions of the metal-ligand species and pL is the cologarithm of the total ligand concentration. This parameter depends on system conditions, such as temperature, pH, and ionic strength.

In order to evaluate the sequestering capacity of *Cys*, *PSH*, *GSH*, and *GSSG* ligands toward Ca^{2+}, $pL_{0.5}$ values at different pH and temperatures were calculated. The results obtained are reported in **Supplementary Table S5**. **Figure 10** illustrates the sequestering capacity of *Cys*, *PSH*, *GSH*, and *GSSG* ligands toward Ca^{2+} under physiological conditions (pH = 7.4, t = 37 °C, I = 0.15 mol L^{-1}). As can be seen, the sequestering capacities of the ligands toward Ca^{2+} under physiological conditions follow the order:

$$pL_{0.5}(GSSG) > pL_{0.5}(GSH) > pL_{0.5}(Cys) > pL_{0.5}(PSH)$$

By comparing these data with those relating to the stepwise formation constants of Ca^{2+}-ligand species, obtained by potentiometric measurements under physiological conditions, it is possible to find a different order of stability for the MLH_2 species:

$$\log K(PSH) > \log K(GSSG) > \log K(GSH) > \log K(Cys)$$

and a further different order for the MLH species:

$$\log K(PSH) > \log K(GSH) > \log K(GSSG) \approx \log K(Cys)$$

This underlines the importance of calculating the sequestering ability that, taking into account all the interactions, can be different with respect to the order of stability assessed for a single species and reveal the "real" trend of the ligands.

Literature Comparisons

In literature databases there are few thermodynamic data on interactions of ligands under study with Ca^{2+} (Martell et al., 2004;

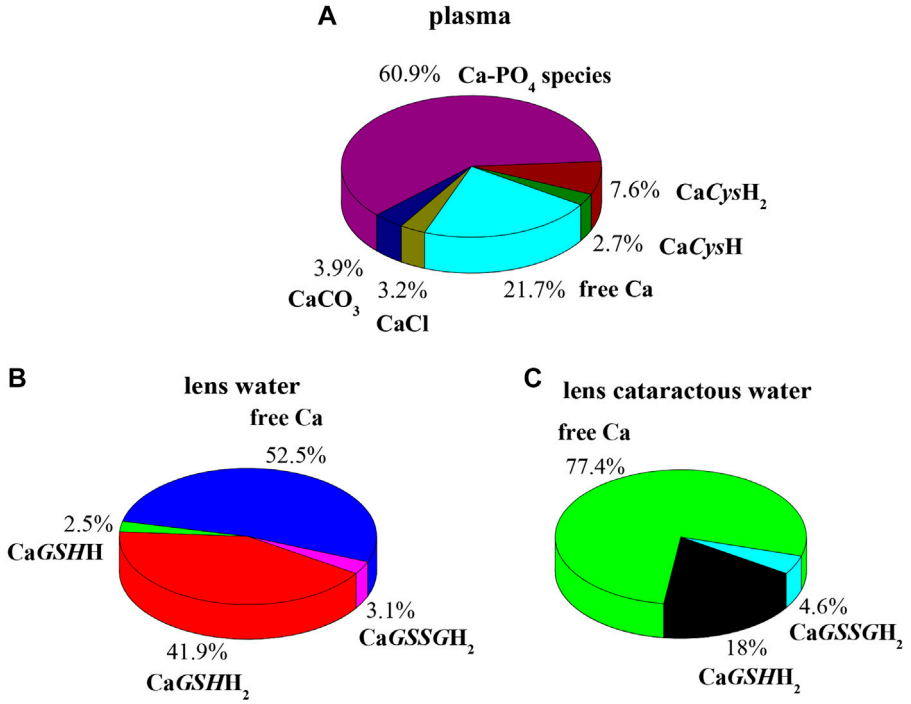

FIGURE 8 | Ca-*Cys*, *GSH*, *GSSG* species in biological fluids at $t = 37$ °C, $I = 0.15$ mol L^{-1}. **(A)** Plasma conditions (pH = 7.4); **(B)** lens water conditions (pH = 7.2); **(C)** lens cataractous water conditions (pH = 7.2).

TABLE 5 | Thermodynamic formation parameters of Ca^{2+}-*Cys*, -*PSH*, -*GSH*, -*GSSG* species at $t = 25$ °C, $I = 0.15$ mol L^{-1} in NaCl.

Ligand	Species	$-\Delta G$ [ab]	ΔH [ab]	$T\Delta S$ [ab]
Cys	MLH_2	118.5	−87 (2) [c]	31
	MLH	71.3	−36 (3)	35
PSH	MLH_2	117.6	−5 (8)	113
	MLH	68.2	−8 (8)	60
GSH	MLH_2	114.0	−18 (12)	96
	MLH	62.9	8 (18)	71
GSSG	MLH_5	172.3	45 (12)	217
	MLH_4	160.7	−36 (16)	125
	MLH_3	143.4	−51 (12)	92
	MLH_2	121.0	−76 (10)	45
	MLH	69.4	−82 (9)	−13

[a]*Referring to overall formation constants.*
[b]*Expressed in kJ mol^{-1}.*
[c]*≥95% of confidence interval.*

May and Murray, 2001; Pettit and Powell, 2001). As regards Ca^{2+}-*Cys* system, a paper reports at $t = 25$ °C and $I = 0.1$ mol L^{-1} logβ = 1.92 for ML species and several ternary species with other ligands (Ramamoorthy and Manning, 1975). This only value cannot be compared with the results with this paper, since the speciation model is totally different. In the case of Ca^{2+}-*GSH* system, a speciation model at $t = 37$ °C and $I = 0.15$ mol L^{-1} with four species, namely, MLH_2, MLH, ML, and MLOH, with logβ = 20.68, 12.89, 3.84, -6.46, respectively, is reported (Touche and Williams, 1976). These values can be compared with ours, as regards the common species, *i.e.*, MLH_2 and MLH, in the same experimental conditions (logβ = 20.14, 11.66, respectively). The significant differences probably can be attributed to the different speciation model considered. In a paper of Singh, where formation constant values of *GSH* with several metal cations, namely, Ca^{2+}, Mg^{2+}, Cu^{2+}, Pb^{2+}, Ni^{2+}, Zn^{2+}, Co^{2+}, Cd^{2+}, and Mn^{2+}, are reported, only one formation constant value referred to ML species was obtained for each system, including one containing Ca^{2+} (Singh et al., 2001). For this reason, this formation constant value cannot be compared with results here reported.

In a more recent paper, a fairly similar speciation model with three species was found, namely, MLH_2, MLH, and ML, where logβ = 19.27, 11.08, 1.60, respectively ($t = 25$ °C, $I = 0.15$ mol L^{-1}) (Cigala et al., 2012). In this paper, the values obtained under the same conditions for MLH_2 and ML species are logβ = 20.39, 11.53, respectively. The agreement in this case, mainly for MLH species, is quite satisfactory.

CONCLUSION

The main purpose of this study was obtaining consistent speciation models and reliable thermodynamic data referring to Ca^{2+}-bioligands systems, based on the results gained *via* different analytical techniques. Speciation models and stability formation constants obtained by potentiometry were confirmed by ^1H NMR spectroscopy. Indeed, the comparative analysis of the chemical shift values of the studied bioligands allows for reasonably affirming that all of them act as chelating agents of Ca^{2+}. MALDI MS confirmed the formation of complexes and

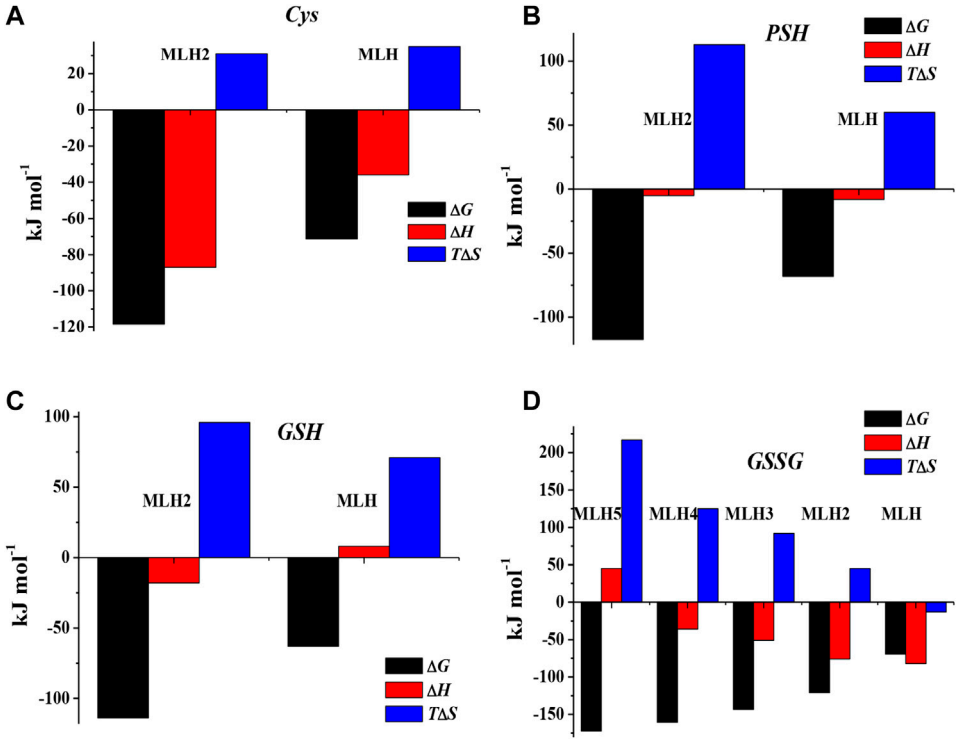

FIGURE 9 | Bar plot of ΔG, ΔH, and $T\Delta S$ referring to Ca^{2+}-*Cys* **(A)**, Ca^{2+}-*PSH* **(B)**, Ca^{2+}-*GSH* **(C)**, and Ca^{2+}-*GSSG* **(D)** species at $t = 25$ °C, $I = 0.15$ mol L^{-1} in NaCl, according to overall formation reaction.

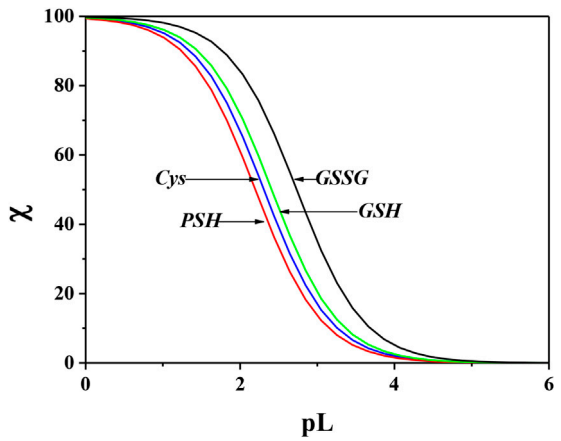

FIGURE 10 | Comparison of sequestering ability of *Cys*, *PSH*, *GSH*, and *GSSG* toward Ca^{2+} under physiological conditions (pH = 7.4, t = 37 °C, I = 0.15 mol L^{-1}).

MS/MS experiments and, moreover, indicated different complexing behaviors of the ligands toward Ca^{2+}. The results suggest that *Cys* and *PSH* act as bidentate ligands giving rise to six-membered cycles *via* O and S; *GSH* and *GSSG* bind to Ca^{2+} ion *via* O and N. By potentiometry, formation constant values under different temperatures were evaluated. In this way were also obtained $T\Delta S$ and ΔH values, necessary to calculate formation constants at different temperatures. The sequestering ability of *Cys*, *PSH*, *GSH*, and *GSSG* toward Ca^{2+} was evaluated under different pH and temperature conditions, with particular attention to those simulating biological fluids, evidencing an interesting trend.

Finally, obtained stability data were crucial to gain simulations under biological fluid conditions, as blood and lens water, and pointed out the importance of reliable thermodynamic data for simulations useful for applications to real systems, characterized by variable composition and pH.

DATA AVAILABILITY STATEMENT

The original contributions presented in the study are included in the article/**Supplementary Material**; further inquiries can be directed to the corresponding author.

AUTHOR CONTRIBUTIONS

OG planned the experiments, supervised and organized the analysis, performed speciation calculations and simulations, and wrote the manuscript. CF contributed to conception, design of the study, analysis of the results, and manuscript revision. FC performed the potentiometric measurements, prepared the solutions for ^{1}H

NMR experiments, and contributed to spectra acquisition. MC performed the ^{1}H NMR experiments and the qualitative analysis of the spectra and contributed to ^{1}H NMR section. DA contributed to experimental design of the study. DA and AN performed MALDI MS and MS/MS experiments and wrote mass spectrometry discussion. All authors contributed to manuscript revision, read, and approved the submitted version.

FUNDING

Publication fees will be covered by the University of Messina FFABR 2020 funds, University of Calabria funds and by Frontiers discount (Discount Code: DSC-11002218503PRD).

ACKNOWLEDGMENTS

The authors OG and CF thank University of Messina for Research & Mobility 2017 funds (ARCADIA project) and for FFABR 2020 funds. The authors DA and AN thank University of Calabria for funds. All the authors thank Frontiers Fee Support Team for the discount granted.

SUPPLEMENTARY MATERIAL

The Supplementary Material for this article can be found online at: https://www.frontiersin.org/articles/10.3389/fchem.2021.640219/full#supplementary-material.

REFERENCES

Aiello, D., Giambona, A., Leto, F., Passarello, C., Damiani, G., Maggio, A., et al. (2018b). Human coelomic fluid investigation: a MS-based analytical approach to prenatal screening. *Sci. Rep.* 8, 10973. doi:10.1038/s41598-018-29384-9

Aiello, D., Siciliano, C., Mazzotti, F., Di Donna, L., Athanassopoulos, C. M., and Napoli, A. (2020a). A rapid MALDI MS/MS based method for assessing saffron (Crocus sativus L.) adulteration. *Food Chem* 307, 125527. doi:10.1016/j.foodchem.2019.125527

Aiello, D., Cardiano, P., Cigala, R. M., Gans, P., Giacobello, F., Giuffrè, O., et al. (2017). Sequestering ability of oligophosphate ligands toward Al^{3+} in aqueous solution. *J. Chem. Eng. Data* 62, 3981–3990. doi:10.1021/acs.jced.7b00685

Aiello, D., Furia, E., Siciliano, C., Bongiorno, D., and Napoli, A. (2018a). Study of the coordination of ortho-tyrosine and trans-4-hydroxyproline with aluminum(III) and iron(III). *J. Mol. Liq* 269, 387–397. doi:10.1016/j.molliq.2018.08.074

Aiello, D., Siciliano, C., Mazzotti, F., Di Donna, L., Risoluti, R., and Napoli, A. (2020b). Protein extraction, enrichment and MALDI MS and MS/MS analysis from bitter orange leaves (citrus aurantium). *Molecules* 25, 1485. doi:10.3390/molecules25071485

Alderighi, L., Gans, P., Ienco, A., Peters, D., Sabatini, A., and Vacca, A. (1999). Hyperquad simulation and speciation (HySS): a utility program for the investigation of equilibria involving soluble and partially soluble species. *Coord. Chem. Rev* 184, 311–318.

Brigham, M. P., Stein, W. H., and Moore, S. (1960). The concentrations of cysteine and cystine in human blood plasma. *J. Clin. Invest* 39, 1633–1638. doi:10.1172/JCI104186

Bringhurst, F. R., and Potts, J. T. (1979). "Calcium and phosphate," in *Endocrinology*. Editor L. J. e. a. De Groot (New York: Grune & Stratton).

Broaudus, A. E. (1993). "Physiological functions of calcium, magnesium and phosphorous and mineral ion balance," in *Primer on the metabolic bone diseases and disorders of mineral metabolism*. Editor M. J. Favus (New York: Raven Press).

Cardiano, P., De Stefano, C., Giuffrè, O., and Sammartano, S. (2008). Thermodynamic and spectroscopic study for the interaction of dimethyltin(IV) with L-cysteine in aqueous solution. *Biophys. Chem* 133, 19–27. doi:10.1016/j.bpc.2007.11.005

Cardiano, P., Falcone, G., Foti, C., Giuffrè, O., and Napoli, A. (2013). Binding ability of glutathione towards alkyltin(IV) compounds in aqueous solution. *J. Inorg. Biochem* 129, 84–93. doi:10.1016/j.jinorgbio.2013.09.004

Cardiano, P., Cordaro, M., Chillè, D., Foti, C., and Giuffrè, O. (2019). Interactions of inosine 5′-monophosphate with Ca^{2+} and Mg^{2+}: a thermodynamic and spectroscopic study in aqueous solution. *J. Chem. Eng. Data* 64, 2859–2866. doi:10.1021/acs.jced.9b00231

Cardiano, P., Cucinotta, D., Foti, C., Giuffrè, O., and Sammartano, S. (2011). Potentiometric, calorimetric and ^{1}H-NMR investigation on Hg^{2+}-mercaptocarboxylate interaction in aqueous solution. *J. Chem. Eng. Data* 56, 1995–2004. doi:10.1021/je101007n

Cardiano, P., Giacobello, F., Giuffrè, O., and Sammartano, S. (2016). Thermodynamics of Al^{3+}-thiocarboxylate interaction in aqueous solution. *J. Mol. Liq* 222, 614–621. doi:10.1016/j.molliq.2016.07.077

Cardiano, P., Giuffrè, O., Napoli, A., and Sammartano, S. (2009). Potentiometric, 1H-NMR, ESI-MS investigation on dimethyltin(IV) cation-mercaptocarboxylate interaction in aqueous solution. *New J. Chem* 33, 2286–2295. doi:10.1039/b908114c

Cardiano, P., Giuffrè, O., Pellerito, L., Pettignano, A., Sammartano, S., and Scopelliti, M. (2006). Thermodynamic and spectroscopic study of the binding of dimethyltin(IV) by citrate at 25°C. *Appl. Organomet. Chem* 20, 425–435. doi:10.1002/aoc.1076

Cassone, G., Chillè, D., Giacobello, F., Giuffrè, O., Mollica Nardo, V., Ponterio, R. C., et al. (2019). Interaction between As(III) and simple thioacids in water: an experimental and ab initio molecular dynamics investigation. *J. Phys. Chem. B* 123, 6090–6098. doi:10.1021/acs.jpcb.9b04901

Chandorkar, A. G., Bulakh, P. M., and Albal, M. V. (1980). Electrolyte composition in normal and cataractous lenses. *Indian J. Ophthalmol* 28, 135–138.

Chillè, D., Aiello, D., Grasso, G. I., Giuffrè, O., Napoli, A., Sgarlata, C., et al. (2020). Complexation of As(III) by phosphonate ligands in aqueous fluids: thermodynamic behavior, chemical binding forms and sequestering abilities. *J. Environ. Sci. (China)* 94, 100–110. doi:10.1016/j.jes.2020.03.056

Cigala, R. M., Crea, F., De Stefano, C., Lando, G., Milea, D., and Sammartano, S. (2012). Modeling the acid-base properties of glutathione in different ionic media, with particular reference to natural waters and biological fluids. *Amino Acids* 43, 629–648. doi:10.1007/s00726-011-1110-0

Cordaro, M., Foti, C., Giacobello, F., Giuffrè, O., and Sammartano, S. (2019). Phosphonic derivatives of nitrilotriacetic acid as sequestering agents for Ca^{2+} in aqueous solution: a speciation study for application in natural waters. *ACS Earth Space Chem* 3, 1942–1954. doi:10.1021/acsearthspacechem.9b00183

Crea, P., De Stefano, C., Kambarami, M., Millero, F. J., and Sharma, V. K. (2008). Effect of ionic strength and temperature on the protonation of oxidized glutathione. *J. Solut. Chem* 37, 1245–1259. doi:10.1007/s10953-008-9310-2

Davis, C. D., and Hanumegowda, U. M. (2008). *Drug metabolism handbook*. Hoboken, NJ: John Wiley & Sons.

De Stefano, C., Foti, C., Giuffrè, O., and Milea, D. (2016). Complexation of Hg^{2+}, CH_3Hg^{+}, Sn^{2+}, and $(CH_3)_2Sn^{2+}$ with phosphonic NTA derivatives. *New J. Chem* 40, 1443–1453. doi:10.1039/C5NJ02531A

De Stefano, C., Foti, C., Giuffrè, O., and Sammartano, S. (2014). Acid-base and UV behaviour of 3-(3,4-dihydroxyphenyl)-propenoic acid (caffeic acid) and complexing ability towards different divalent metal cations in aqueous solution. *J. Mol. Liquids* 195, 9–16. doi:10.1016/j.molliq.2014.01.027

De Stefano, C., Sammartano, S., Mineo, P., and Rigano, C. (1997). "Computer tools for the speciation of natural fluids," in *Marine chemistry - an environmental analytical chemistry approach*. Editors A. Gianguzza, E. Pelizzetti, and S. Sammartano (Amsterdam: Kluwer Academic Publishers), 71–83.

Dringen, R. (2000). Metabolism and functions of glutathione in brain. *Prog. Neurobiol* 62, 649–671. doi:10.1016/s0301-0082(99)00060-x

Falcone, G., Foti, C., Gianguzza, A., Giuffrè, O., Napoli, A., Pettignano, A., et al. (2013). Sequestering ability of some chelating agents towards methylmercury(II). *Anal. Bioanal. Chem* 405, 881–893. doi:10.1007/s00216-012-6336-5

Falcone, G., Giuffrè, O., and Sammartano, S. (2011). Acid-base and UV properties of some aminophenol ligands and their complexing ability towards Zn^{2+} in aqueous solution. *J. Mol. Liquids* 159, 146–151. doi:10.1016/j.molliq.2011.01.003

Filella, M., and May, P.M. (2005). Reflections on the calculation and publication of potentiometrically-determined formation constants. *Talanta* 65, 1221–1225.

Foti, C., and Giuffrè, O. (2020). Interaction of ampicillin and amoxicillin with Mn^{2+}: a speciation study in aqueous solution. *Molecules* 25, 3110. doi:10.3390/molecules25143110

Frassineti, C., Ghelli, S., Gans, P., Sabatini, A., Moruzzi, M. S., and Vacca, A. (1995). Nuclear magnetic resonance as a tool for determining protonation constants of natural polyprotic bases in solution. *Anal. Biochem* 231, 374–382. doi:10.1006/abio.1995.9984

Frausto da Silva, J. J. R., and Williams, R. J. P. (2001a). "Calcium: controls and triggers," in *The biological chemistry of the elements: the inorganic chemistry of life*. Oxford University Press, 278–314.

Frausto da Silva, J. J. R., and Williams, R. J. P. (2001b). "The principles of the uptake and chemical speciation of the elements in biology," in *The biological chemistry of the elements: the inorganic chemistry of life*. Oxford University Press.

Furia, E., Aiello, D., Di Donna, L., Mazzotti, F., Tagarelli, A., Thangavel, H., et al. (2014). Mass spectrometry and potentiometry studies of Pb(II)-, Cd(II)- and Zn(II)-cystine complexes. *Dalton Trans* 43, 1055–1062. doi:10.1039/c3dt52255e

Gianguzza, A., Giuffrè, O., Piazzese, D., and Sammartano, S. (2012). Aqueous solution chemistry of alkyltin(IV) compounds for speciation studies in biological fluids and natural waters. *Coord. Chem. Rev* 256, 222–239. doi:10.1016/j.ccr.2011.06.027

Giuffrè, O., Aiello, D., Chillè, D., Napoli, A., and Foti, C. (2020). Binding ability of arsenate towards Cu^{2+} and Zn^{2+}: thermodynamic behavior and simulation under natural water conditions. *Environ. Sci. Process. Impacts* 22, 1731–1742. doi:10.1039/d0em00136h

Giuffrè, O., Angowska, S., Foti, C., and Sammartano, S. (2019). Thermodynamic study on the interaction of ampicillin and amoxicillin with Ca^{2+} in aqueous solution at different ionic strengths and temperatures. *J. Chem. Eng. Data* 64, 800–809. doi:10.1021/acs.jced.8b01081

Hluchan, S. E., and Pomerantz, K. (2002). "Calcium and calcium alloys," in *Ullmann's Encyclopedia of industrial chemistry*. Weinheim, Germany: Wiley-VCH Verlag GmbH&Co KGaA, 41–44.

Imbrogno, S., Aiello, D., Filice, M., Leo, S., Mazza, R., Cerra, M. C., et al. (2019). MS-based proteomic analysis of cardiac response to hypoxia in the goldfish (*Carassius auratus*). *Sci. Rep* 9, 18953. doi:10.1038/s41598-019-55497-w

Jones, M. M. (1991). New developments in therapeutic chelating agents as antidotes for metal poisoning. *Crit. Rev. Toxicol* 21, 209–233. doi:10.3109/10408449109089880

Kisic, B., Miric, D., Zoric, L., Ilic, A., and Dragojevic, I. (2012). Antioxidant capacity of lenses with age-related cataract. *Oxid. Med. Cell. Longev*, 2012, 467130. doi:10.1155/2012/467130

Königsberger, L.-C., Königsberger, E., Hefter, G., and May, P. M. (2015). Formation constants of copper(I) complexes with cysteine, penicillamine and glutathione: implications for copper speciation in the human eye. *Dalton Trans* 44, 20413–20425. doi:10.1039/C5DT02129D

Kretzschmar, J., Strobel, A., Haubitz, T., Drobot, B., Steudtner, R., Barkleit, A., et al. (2020). Uranium(VI) complexes of glutathione disulfide forming in aqueous solution. *Inorg. Chem* 59, 4244–4254. doi:10.1021/acs.inorgchem.9b02921

Labib, M., Sargent, E. H., and Kelley, S. O. (2016). Electrochemical methods for the analysis of clinically relevant biomolecules. *Chem. Rev* 116, 9001–9090. doi:10.1021/acs.chemrev.6b00220

Laurie, S. H., Prime, D. H., and Sarkar, B. (1979). Analytical potentiometric and spectroscopic study of the equilibria in the aqueous nickel(II)-triethylenetetramine and nickel(II)–D-penicillamine systems. *Can. J. Chem* 57, 1411–1417. doi:10.1139/v79-230

Lentner, C. (1983). *Geigy scientific Tables*. Basilea, Switzerland: CIBA-Geigy.

Martell, A. E., Smith, R. M., and Motekaitis, R. J. (2004). *Critically selected stability constants of metal complexes*. Garthersburg, MD: National Institute of Standard Technology.

May, P. M., and Murray, K. (2001). Database of chemical reactions designed to achieve thermodynamic consistency automatically. *J. Chem. Eng. Data* 46, 1035–1040. doi:10.1021/je000246j

Meister, A., and Anderson, M. E. (1983). Glutathione. *Annu. Rev. Biochem* 52, 711–760. doi:10.1146/annurev.bi.52.070183.003431

Olmos Moya, P. M., Martínez Alfaro, M., Kazemi, R., Alpuche-Avilés, M. A., Griveau, S., Bedioui, F., et al. (2017). Simultaneous electrochemical speciation of oxidized and reduced glutathione. Redox profiling of oxidative stress in biological fluids with a modified carbon electrode. *Anal. Chem* 89, 10726–10733. doi:10.1021/acs.analchem.7b01690

Pescosolido, N., Barbato, A., Giannotti, R., Komaiha, C., and Lenarduzzi, F. (2016). Age-related changes in the kinetics of human lenses: prevention of the cataract. *Int. J. Ophthalmol* 9, 1506–1517. doi:10.18240/ijo.2016.10.23

Peterlik, M., and Stoeppler, M. (2004). "Calcium," in *Elements and their compounds in the environment*. Editors E. Merian, M. Anke, M. Ihnat, and M. Stoeppler (Weinheim: Wiley VCH), 599–618.

Pettit, L. D., and Powell, K. J. (2001). *IUPAC stability constants database*. IUPAC: Academic Software.

Pompella, A., Visvikis, A., Paolicchi, A., De Tata, V., and Casini, A. F. (2003). The changing faces of glutathione, a cellular protagonist. *Biochem. Pharmacol* 66, 1499–1503. doi:10.1016/s0006-2952(03)00504-5

Ramamoorthy, S., and Manning, P. G. (1975). Equilibrium studies of solutions containing Al^{3+}, Ca^{2+} or Cd^{2+} and cysteine, orthophosphate and a carboxylic acid. *J. Inorg. Nucl. Chem* 37, 363–367. doi:10.1016/0022-1902(75)80206-5

Salvatore, L., Gallo, N., Aiello, D., Lunetti, P., Barca, A., Blasi, L., et al. (2020). An insight on type I collagen from horse tendon for the manufacture of implantable devices. *Int. J. Biol. Macromol* 154, 291–306. doi:10.1016/j.ijbiomac.2020.03.082

Shahid, N. M., Khalid, S., Bibi, I., Bundschuh, J., Khan Niazi, N., and Dumat, C. (2020). A critical review of mercury speciation, bioavailability, toxicity and detoxification in soil-plant environment: ecotoxicology and health risk assessment. *Sci. Total Environ* 711, 134749. doi:10.1016/j.scitotenv.2019.134749

Sies, H. (1999). Glutathione and its role in cellular functions. *Free Radic. Biol. Med* 27, 916–921. doi:10.1016/s0891-5849(99)00177-x

Singh, P. K., Garg, B. S., Kumar, D. N., and Singh, B. K. (2001). Complexation equilibria and evaluation of thermodynamic parameters of bivalent metal complexes of glutathione. *Indian J. Chem* 40A, 1339–1343.

Sisombath, N. S., Jalilehvand, F., Schell, A. C., and Wu, Q. (2014). Lead(II) binding to the chelating agent D-Penicillamine in aqueous solution. *Inorg. Chem* 53, 12459–12468. doi:10.1021/ic5018714

Touche, M. L. D., and Williams, D. R. (1976). Thermodynamic considerations in Co-ordination. Part XXI formation of ternary complexes containing two dissimilar metal ions and the implication for metal-metal stimulation phenomena *in vivo*. *J. Chem. Soc. Dalton Trans*, 1355–1359. doi:10.1039/DT9750001757

Walshe, J. M. (1956). Penicillamine, a new oral therapy for Wilson's disease. *Am. J. Med* 21, 487–495. doi:10.1016/0002-9343(56)90066-3

Whedon, G. D. (1980). "Recent advances in management of osteoporosis," in *Phosphate and mineral in health and disease. Advances in experimental medicine and biology*. Editors S. G. Massry, E. Ritz, and H. Jahn (Boston: Springer), 600–613.

Conflict of Interest: The authors declare that the research was conducted in the absence of any commercial or financial relationships that could be construed as a potential conflict of interest.

frontiers in Chemistry

ORIGINAL RESEARCH
published: 04 March 2021
doi: 10.3389/fchem.2021.626630

Microfluidic Flow Injection Immunoassay System for Algal Toxins Determination: A Case of Study

Lorenzo Celio[1†‡], *Matteo Ottaviani*[2†‡], *Rocco Cancelliere*[1†‡], *Alessio Di Tinno*[1,3†], *Peter Panjan*[4,5‡], *Adama Marie Sesay*[4,6]* *and Laura Micheli*[1]*

[1]Departement of Chemical Sciences and Technologies, University of Rome Tor Vergata, Rome, Italy, [2]Department of Analytical Chemistry, University of Turin, Turin, Italy, [3]Department of Electrical and Information Engineering, University of Cassino and Southern Lazio, Cassino (FR), Italy, [4]Measurement Technology Research Unit, Oulu University, Kajaani, Finland, [5]Essi Tech d.o.o., Ljubljana, Slovenia, [6]Wyss Institute of Bioinspired Engineering, Harvard University, Boston, MA, United States

A novel flow injection microfluidic immunoassay system for continuous monitoring of saxitoxin, a lethal biotoxin, in seawater samples is presented in this article. The system consists of a preimmobilized G protein immunoaffinity column connected in line with a lab-on-chip setup. The detection of saxitoxin in seawater was carried out in two steps: an offline incubation step (competition reaction) performed between the analyte of interest (saxitoxin or Ag, as standard or seawater sample) and a tracer (an enzyme-conjugated antigen or Ag*) toward a specific polyclonal antibody. Then, the mixture was injected through a "loop" of a few μL using a six-way injection valve into a bioreactor, in line with the valve. The bioreactor consisted of a small glass column, manually filled with resin upon which G protein has been immobilized. When the mixture flowed through the bioreactor, all the antibody-antigen complex, formed during the competition step, is retained by the G protein. The tracer molecules that do not interact with the capture antibody and protein G are eluted out of the column, collected, and mixed with an enzymatic substrate directly within the microfluidic chip, via the use of two peristaltic pumps. When Ag* was present, a color change (absorbance variation, ΔAbs) of the solution is detected at a fixed wavelength (655 nm) by an optical chip docking system and registered by a computer. The amount of saxitoxin, present in the sample (or standard), that generates the variation of the intensity of the color, will be directly proportional to the concentration of the analyte in the analyzed solution. Indeed, the absorbance response increased proportionally to the enzymatic product and to the concentration of saxitoxin in the range of 3.5×10^{-7}–2×10^{-5} ng ml^{-1} with a detection limit of 1×10^{-7} ng ml^{-1} (RSD% 15, S N^{-1} equal to 3). The immunoanalytical system has been characterized, optimized, and tested with seawater samples. This analytical approach, combined with the transportable and small-sized instrumentation, allows for easy *in situ* monitoring of marine water contaminations.

Keywords: FI-IA, algal toxins, saxitoxin, immunoanalytical system, microchip flow-chamber system

OPEN ACCESS

Edited by:
Anna Napoli,
University of Calabria, Italy

Reviewed by:
Camelia Bala,
University of Bucharest, Romania
Ilaria Palchetti,
University of Florence, Italy

***Correspondence:**
Adama Marie Sesay
Adama.Sesay@wyss.harvard.edu
Laura Micheli
laura.micheli@uniroma2.it

[†]These authors have contributed equally to this work
[‡]ORCID:
Lorenzo Celio
https://orcid.org/0000-0001-6953-6733
Matteo Ottaviani
https://orcid.org/0000-0003-2985-8871
Rocco Cancelliere
https://orcid.org/0000-0002.3278-0414
Peter Panjan
https://orcid.org/0000-0001-9685-207X

Specialty section:
This article was submitted to Analytical Chemistry, a section of the journal Frontiers in Chemistry

Received: *06 November 2020*
Accepted: *04 January 2021*
Published: *04 March 2021*

Citation:
Celio L, Ottaviani M, Cancelliere R, Di Tinno A, Panjan P, Sesay AM and Micheli L (2021) Microfluidic Flow Injection Immunoassay System for Algal Toxins Determination: A Case of Study. Front. Chem. 9:626630. doi: 10.3389/fchem.2021.626630

INTRODUCTION

The development of rapid and sensitive analytical methods for the determination of trace analytes in liquid samples is an important goal to be achieved in analytical chemistry. In the last decade, the demand for continuous monitoring systems has increased in clinical, pharmaceutical, and environmental chemistry, thus favoring an ever-greater development of high throughput in flow systems (Fintschenko and Wilson, 1998; Ishimatsu et al., 2020). Flow analysis methods have been widespread in the field of chemical analysis since the middle of the last century when Růžička and Hansen first introduced the term "Flow Injection Analysis (FIA)" (1975) (Růžička and Hansen, 1975). This is considered the cornerstone of a new paradigm in analytical chemistry (McKelvie, 2008). These publications gave rise to FIA and with it to an entire field of research that, over the following 3 decades, has involved thousands of researchers, which to date has resulted in more than 16,000 publications in the scientific literature (McKelvie, 2008; Rocha and Zagatto, 2020). This technique is generally based on straightforward and cost-effective manifolds with the possibility of being adapted to distinct analytical requests (Passos et al., 2015). Flow injection immunoassays (FI-IA), combining FIA technique with immunoassay (IA), provide specific detection and allow rapid and reliable determination. Immunological methods, which are based on the specific interaction between the antibody and antigen, exhibit some significant advantages over classical flow injection techniques such as simple layout, inexpensiveness, and, most importantly, sensitivity and specificity. The merits of the two methods are exploited simultaneously. The aforementioned system fits well with applications in the determination of different analytes in real samples. Pesticides (Krämer and Schmid, 1991), food (Waseem et al., 2013), tumor markers determination (Wu et al., 2006; Zhang et al., 2013), control of microbial growth (Wang et al., 2012), monitoring of chemicals in wastewater (Shi et al., 2018), and evaluation of harmful algal blooms in seawater samples (Shitanda et al., 2009) are among the most important and worthy of these applications. Algal toxins are harmful organic molecules released by naturally decaying or degrading unicellular algae (algal toxins are primarily produced in detrimental concentrations during harmful algal bloom) (Vilariño et al., 2013). This overcrowding can give rise to a phenomenon of accumulation in seawater animals (mollusks, shellfish, and fishes), causing intoxication along the entire food chain that involves cetaceans, birds, other mammals, and finally humans. Over the past few years, many different analytical approaches have been explored in the area of algal toxin detection from environmental samples, including liquid chromatography coupled with mass-spectroscopy (LC-MS) (Vilariño et al., 2013), high-performance liquid chromatography (HPLC) (Van Egmond et al., 1994), enzyme-linked immunosorbent assay (ELISA) (Micheli et al., 2002; Yu et al., 2002; Petropoulos et al., 2019), and electrochemical biosensors (Zhang et al., 2018). Most of the research has been focused on the saxitoxin (STX) and STX-related compounds, as they are found to be more common in neurotoxic paralytic shellfish toxins (PSTs) (Deeds et al., 2008). These PSTs represent a group of naturally occurring neurotoxic alkaloids. STX is the most researched PST to date, and since its discovery in 1957, 57 analogues have been described. Intoxication with PSTs may result in a serious and occasionally fatal illness known as paralytic shellfish poisoning (PSP) (Anderson et al., 1996; Falconer, 1993; García et al., 2004): this illness manifests itself when PSTs reversibly bind voltage-gated Na^+ channels in an equimolar ratio. This is mediated by the interaction among different functional groups: the positively charged guanidinium groups of STX interact with negatively charged carboxyl groups of the Na^+ channel, thereby blocking the pore. The threat of PSP is not only a major cause of concern for public health but also deleterious to the economy. Outbreaks of PSTs often result in the death of marine life and livestock and the closure of contaminated fisheries. Moreover, the frequent disbursement required for running monitoring programs, together with the aforementioned critical issues, presents a major economic burden around the world (Guy and Griffin, 2009; Ferrão-Filho Ada and Kozlowsky-Suzuki, 2011). The officially prescribed and validated methods for STX detection in the European Union were the mouse bioassay (MBA), based on the injection of 1 ml test solution in live mouse and observing the time from injection to death (with a limit of detection ca. 40 mg STX eq/100 g shellfish) (Cusick and Sayler, 2013), and the Association of Official Analytical Chemists (AOAC) official method 2005.06 (Lawrence method) with a precolumn derivatization and fluorescence detection (LC-FLD) (He et al., 2005). The liquid chromatography postcolumn oxidation (PCOX) method was acknowledged by AOAC in 2011 as the official method. The Interstate Shellfish Sanitation Conference (ISSC, United States) certified two commercially available immunological methods-based products, namely, Abraxis ELISAs and Scotia LFAs as "Approved Limited Use Method for Marine Biotoxin" (Li and Persson, 2021). For drinking water, the American EPA listed Enzyme-Linked Immunosorbent Assays (ELISA) together with LC-MS for PST detection [United States Environmental Protection Agency (EPA), 2019]. In parallel, four immunological categories (immunoassay, immunosensor, lateral flow immunoassay, and radioimmunoassay) were developed for the detection of algal toxins in shellfish and water. These methods for PSTs are suitable for field testing because the extraction and detection are simple. They are also quick to perform and of relatively low cost per sample, need minimal equipment, and are relatively simple and sensitive. They are used widely in the food industry in a variety of countries, with rapid results enabling real-time decisions on the fate of harvested shellfish products (Anfossi et al., 2018; European Food Safety Authority (EFSA), 2009; Micheli et al., 2002). Recently, several interesting overviews about analytical methods developed for the detection of algal toxins are published with a comparison of the advantages and the limits. The conclusions of these overviews are important for developing fast screening methods that should be combined with highly sensitive and accurate analytical methods such as liquid chromatography/liquid chromatograph-mass spectrometry (LC/LC-MS) for confirming the results. LC/LC-MS is able to separate and detect all major PSTs in ranges between 14.95 and

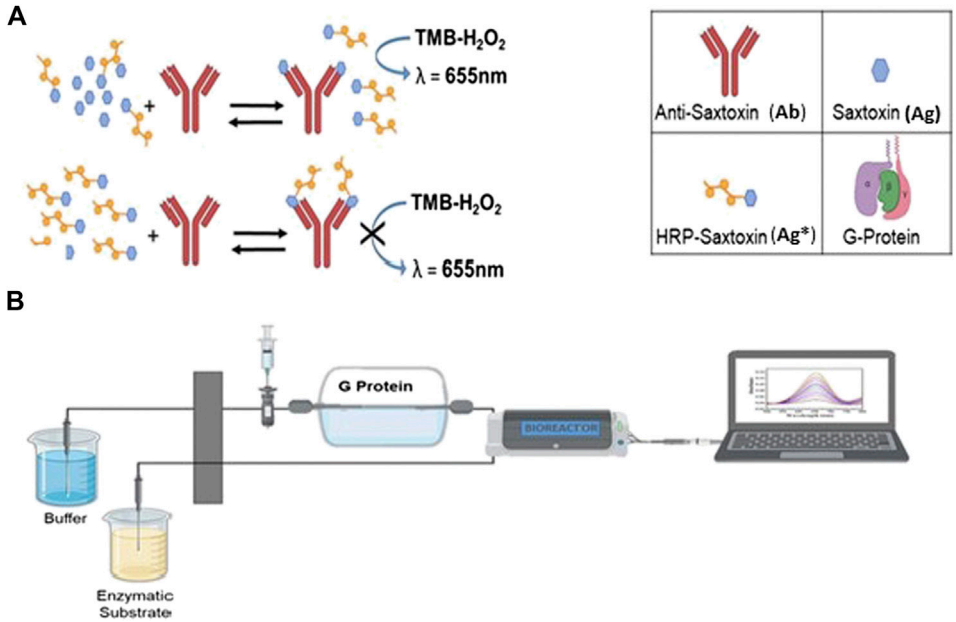

FIGURE 1 | Scheme of FI-IA approach where the bioreactor is in line with the lab-on-chip cartridge and connected to a laptop. In particluar, 1b: **(A)** offline incubation between STX, HRP-STX, and PAb; **(B)** injection of the mixture in the FI-IA system.

299 and 1.5–8.97 ng L^{-1} (Dell'Aversano et al., 2005; Botana et al., 2013). Further developments of this technique have enabled detection limits in concentration ranges of 1.5–14.95 and 7.48–59.80 ng L^{-1}, with excellent linearity; however, this technique was not applicable out of the laboratory (Halme et al., 2012; Cusick and Sayler, 2013). Tian et al. (2020) reported an overall vision about the recent progress of optical and electrochemical biosensors developed for the detection of shellfish toxins in food and drinking water, showing the advantages of the strategy, analyte, sensing unit, method, and property for their future application in field fast screening (Tian et al., 2020). For a prompt response to potential pollution of seawater, limited poor information is present about continuous monitoring of the health of seawater in terms of the presence of PSTs, in particular STX (Pöhlmann and Elßner, 2020). Innovative methods in aquatic toxins detection are mainly focused on the production of rapid, easy-to-use, and highly sensitive multianalyte detection for on-site detection of the dangerous agent (Campbell et al., 2011; Stroka, 2011). An easy-to-perform, high-throughput assay would be a highly valuable tool considering the increase in the number of samples to be processed by routine testing laboratories. In this article, we aim at demonstrating the applicability of the FI-IA technique connected to a microfluidic system to the determination of STX in seawater samples. This kind of microfluidic systems avoids using high volumes of samples and reagents. This allows decreasing the cost of chemical analysis and reducing wastes. Moreover, injecting the analyte directly in an enclosed environment averts interaction between analyte and external interferents, giving more reliable results and decreasing analytes loss. Lastly, the sample travels throughout the system in a short time range, thus giving high performance and reproducibility. The proposed FI-IA system consists of a bioreactor in line with a lab-on-chip (LOC) microfluidic system for reagents mixing and colorimetric detection (**Figure 1** and **Supplementary Figure S1**).

This monitoring tool allows a detection limit (LOD) for STX as low as 1×10^{-4} ng L^{-1}, with a working range equal to 3.5×10^{-4}–2×10^{-2} ng L^{-1} in seawater samples with a column shelf life of 38 sequential measurements directly *in situ*. The main feature of this system, as well as its greatest advantage, is the application of a small volume sample (25 µL loop), allowing for small consumption of reagents and reducing waste. The preliminary study, presented here, illustrates its potential of being used as a field-deployable portable analytical device able to work *in situ* and with continuous water samples without any treatment of the sample compared with the chromatographic and immunological methods reported previously. The high sensitivity, low detection limit, and short time of analysis make the proposed system suitable for field assays in which the speed of analysis is one of the most important parameters.

MATERIALS AND METHODS

Chemicals and Bioreagents

Saxitoxin (STX) 100 g L^{-1}, horseradish peroxidase (HRP) 150 U mg^{-1}, 3,3′,5,5′-tetramethylbenzidine (TMB, enzymatic substrate ready to use), and G protein immobilized on 4% agarose were purchased from Sigma-Aldrich (United States). Polyclonal antibodies anti-STX (PAb) AS111663 was purchased from Agrisera Antibodies (LiStarFish, IT). Sodium

azide (NaN_3), sodium phosphate (NaH_2PO_4), sodium carbonate (Na_2CO_3), sodium acetate ($C_2H_3NaO_2$), and Patent Blue V (E131) were purchased from Sigma-Aldrich, United States. Buffer solutions used are 20 mM phosphate buffer solution, pH 7.4; 200 mM sodium carbonate buffer solution, pH 9.6; 1 mM acetate buffer solution, pH 4.4. All reagents are of analytical grade unless otherwise stated.

Lab-on-Chip Components

The microfluidic chip (PMMA) was fabricated at the Measurement Technology Unit, CEMIS-Oulu (University of Oulu, Finland) using the Arduino Nano Board (Arduino, IT) and spectrophotometric detector compatible with Arduino Board (Arduino, IT). The PMMA microfluidic chip was fabricated using a CO_2 laser to carve PMMA (black and transparent) and bonded together by double-sided medical grade adhesive tape, 100 um thick. The channels were cut out of the adhesive tape and therefore had a defined depth; that is, they were 100 um deep. Herringbone structure was carved for an additional 100 um into the PMMA, yielding a maximum depth of 200 um.

Flow Injection Immunoassays System's Components

The FI-IA system (**Supplementary Figure S1**) consists of a 25 µL loop (made in-house) and Rheodyne® Model 7125 syringe loading injector (United States), Glass Omnifit® column (length: 2.5 cm; seating capacity: 0.35 ml), and PTFE Frits (pores' diameter: 25 µm) purchased from Omnifit® (Rockville Center, NY, United States). Gilson Minipuls® 3 pumps (model M312, Gilson, United States), four-way peristaltic pumps and their tubes (PVC pipes compatible with Gilson Minipuls®3), PVC pipes compatible with Gilson Minipuls® 3 (model: F117934, ø = 0.51 mm), PVC pipes compatible with Gilson Minipuls® 3 (model: F117936, ø = 0.76 mm), and PVC pipes compatible with Gilson Minipuls®3 (model: F117938, ø = 1.02 mm) were purchased from Gilson® (France). The column is packed with G protein immobilized on agarose beads (Sigma-Aldrich, United States).

Principle of Methods

The proposed FI-IA method (**Figure 1**) for STX quantification consists of an offline incubation of the sample containing STX (Ag) with fixed amounts of anti-STX antibody (Ab) and STX labeled with peroxidase (Ag*); in this mixture, a competition between Ag and Ag* for the binding sites of Ab occurs. After this step, the mixture is injected into a flow system where the separation of free Ag* and the antibody-bound tracer (Ab-Ag*) is performed in a column with the coated G protein. The competition mixture is injected through a six-way injection valve, the same type as those used in chromatography, equipped with a fixed volume loop (25 µL). The column is placed in line with the injection system. The microfluidic system is equipped with two inlet channels, the first one for the solution leaving the bioreactor and the second one for the enzymatic substrate, and a single outlet channel for the enzymatic product. In the proposed system, two microfluidic mixers are present where the solution, eluted by the bioreactor and containing the Ag*, mixes with the enzymatic substrate TMB. After the mixing zone, there is a serpentine incubation channel where TMB is oxidized by the enzymatic reaction. The formed enzymatic product is continuously read through the microchip optically clear channel, by a fixed wavelength filter (655 nm), present in the housing of the microfluidic system, to which a laptop is connected for online absorbance acquisition.

Proposed System

The complete microfluidic system consists of two peristaltic pumps, a 25 µL loop circuit, which includes a six-way injection valve, a bioreactor, an Arduino Nano Board, and a spectrophotometric detector compatible with the latter, and a microfluidic chip. Each inlet and outlet is linked using PVC tubes and the detector system is connected to a notebook. The microfluidic chip (**Figure 2A**) consists of four polymethacrylate (PMMA) surfaces (**Figures 2A,a,b**): the external plates are transparent and 0.25 cm thick, whereas the internal ones are black, opaque, and 0.5 cm thick (1.5 cm full-thickness). The microfluidic path (**Figures 2A,c**) is engraved by laser: it consists of a Y channel that connects the two inlets (one for the TMB-enzymatic substrate and the other for the analytes eluted from the bioreactor) and mixes the two entering flows by diffusion; a herringbone mixer that mixes the running solution further by mechanically imposing a "turbulent" flow regime; a coil path (which restores the laminar flow regime); the 1 cm long optical detection chamber (**Figures 2A,c**). The latter is then linked directly to the outlet. The microfluidic path has a depth of 100 µm, except for the herringbone mixer that has 100 µm depth and alternate 200 µm drops. Chip, detector, and valve are located in a 3D printed Acrylonitrile Butadiene Styrene (ABS) housing (**Figure 2B**).

Procedures for the Preparation for the Conjugation of STX With HRP

STX was conjugated to horseradish peroxidase (HRP) via the periodate reaction (Micheli et al., 2002). The STX-HRP concentration was evaluated using the Pierce Bicinchoninic Acid Assay, where bovine serum albumin (BSA) was used as a reference protein. The assay was performed on flat-bottom 96-well plate MaxiSorp (NUNC, Roskilde, Denmark) by adding 5 µL of BSA dilutions to 150 µL of BCA reagents to the well plate; following this step, 5 µL of sample was added to 150 µL BCA reagents, and then the whole plate was incubated for 30 min at 37°C and read spectrophotometrically at 570 nm in triplicate. The assay showed a conjugated STX-HRP concentration of 80 µg ml^{-1} of protein. The residual activity was defined by following the ABTS [2,2′-azino-bis(3-ethylbenzothiazoline-6-sulphonic acid) Sigma-Aldrich, United States] protocol adding 1 mM H_2O_2 and 14.6 mM ABTS on phosphate buffer 50 mM; the subsequent spectrophotometric measure at 403 nm showed a residual activity of 1.73 U mL^{-1} against 5.02 U mL^{-1} of native protein.

Bioreactor Column

The bioreactor consists of a borosilicate glass chromatography column (25 mm length, 0.35 ml bed volume) filled with G protein (immobilized onto 4% agarose bead, with a dynamic binding capacity of 20 mg human IgG mL^{-1}), housing made.

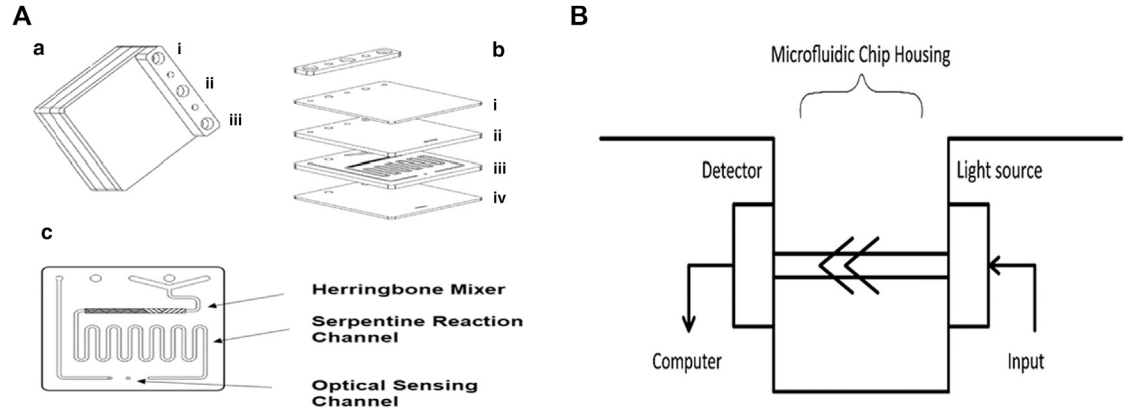

FIGURE 2 | Schematization of the microfluidic lab-on-chip system: **(A)** microfluidic bioreactor and components; **(B)** microfluidic chip detector housing (LED 655 nm and photodiode). In particular, in **(A)**: (a) i) outlet; ii) substrate inlet; iii) sample inlet; (b) lab-on-chip components: i) top plate, ii) black PMMA herringbone etched plate, iii) microfluidic channels, and iv) clear bottom plate; (c) microfluidic mixing chamber, reaction channel, and optical paths.

Preparation of the Bioreactor and Its Storage

Column Packing

Omnifit® chromatographic column (see *FI-IA System's Components*), applied in the FI-IA system, is packed by means of 40 mg of agarose particles activated by G protein and solubilized in 20 mM phosphate buffer, pH 7.4. The buffer solution is kept flowing for 1 h to make sure the column packing is as homogeneous as possible and stored at 4°C after the addition of 30 mM NaN_3 prepared in phosphate buffer. Before using the bioreactor, it was washed with phosphate buffer for 15 min in order to remove all NaN_3 present.

Column Preservation

When the analysis was over, packed chromatographic column is cleaned up with a solution of 30 mM of NaN_3 in 10 ml of 20 mM phosphate buffer, pH 7.4, and then preserved at 4°C. This is done in order to avoid mold development or bacterial attacks.

Preparation of the FI-IA Microfluidic Tool

The system is assembled by connecting with its components (two peristaltic pumps, the "housing" part containing the detector and the injection valve, the bioreactor, and the microfluidic system). After the full system is assembled, the carrier buffer solution is left to flow for 60 min before starting the measurements. This is necessary to fill the whole system and eliminate any air bubbles trapped inside.

Sample Injection

A 200 µL of the solution, containing the sample and the immunoreagent (Ab and Ag*), is injected into the system using a microsyringe; in this way, the loop (25 µL) is being loaded with the sample solution. Then, 20 mM phosphate buffer solution, pH 7.4, as a carrier, is fluxed at 0.1 ml min^{-1}, using the peristaltic pump, dragging the mixture through the column. As soon as the whole sample is injected, the loop is opened and kept that way for 4 min, thus beginning the analysis. The peristaltic pump, set to maximum flow speed, carries the immunocomplex and the other bioreagents through the bioreactor. Thus, all the volume flows through the column and gets to the microfluidic system, in which it gets mixed with the enzymatic substrate (TMB) and gets detected with the detector set at 655 nm. After 20 min from the previous injection and only when the system is cleaned (done directly while performing the analysis, after 10 min from the injection), it is then possible to proceed with the next injection.

FI-IA Procedure for Saxitoxin Determination

FI-IA procedure consists of two fundamental steps: offline incubation of the sample (or the standard) for the competitive assay and its injection in the "flow system." The first step consists in the addition of solution containing the sample into a vial (or the standard, Ag) with a fixed amount (1:75,000 v v^{-1}) of primary anti-STX polyclonal antibody (PAb) and STX-HRP (Ag*) (1:600 v v^{-1}). The solution is then incubated for 2 h. In this condition, a competition reaction is carried out between Ag and Ag* toward the binding sites of the specific antibody (Ab). After the incubation step time, this mixture is injected through the flow system for the analysis (second step). Once the mixture passes through the bioreactor, all the antibodies are withheld by G protein and bioreagents that have not been caught by the antibody (large excess Ag*) are eluted from the column. These molecules proceed until they enter one of the two inlets of the microfluidic system, whereas in the other inlet, enzymatic substrate is flowing through. Later, both the solutions enter in the first microfluidic mixer, the T sensor, where they undergo a first mixing by diffusion. If the conjugated Ag* is present, a colorimetric variation, due to the development of enzymatic product (oxidized TMB, blue), will happen. Conversely, if the desired analyte (Ag) is absent within the sample, all the conjugated Ag* will remain bound to the antibody and will be retained inside the column, giving no colorimetric change. By increasing Ag concentration, competition will occur between Ag and Ag* for the binding of the antibody sites. The free Ag*, not retained in the bioreactor, will be eluted and will react with the enzymatic substrate (TMB), giving a colored enzymatic product

proportional to the concentration of the sample (or the standard). After the first mixer, which links both the inlets into one microfluidic channel, a second mixer is present, the herringbone mixer, which further mechanically mixes analytes and reagents by changing flow's nature from laminar to turbulent. After this last mixing procedure, a long microfluidic channel allows the flow to laminar flow once again, giving a further and definitive homogenization of the enzymatic product. Eventually, the fluids get to the detector chamber, in which absorbance is measured periodically at 1 s intervals.

Analytical Parameters Calculation

Measuring occurs by connecting the system to a notebook in line with the LOC. The notebook itself powers the Arduino Nano Board and the linked optical detector. Through a firmware implemented on the same board, the light source emits a light ray at fixed wavelength (655 nm) every second. With the same time range, the detector (placed in front of the source and on the same axis of the light ray) measures the intensity of the radiation. The enzymatic reaction which occurs between the enzymatic substrate (TMB) and the labeled antigen (Ag*), eluted from the column, produces a signal output. The intensity of the latter is directly proportional to the concentration of the eluted Ag* and directly proportional to the concentration of injected analyte sample. The unknown analyte concentration is determined by using a calibration curve previously built, analyzing standard samples of known concentration of the analyte itself.

FIA Peaks Analysis

Once collected from continuous analysis, data are plotted to give a peak-like shape of which height (H), width (W), and area (A) contain the analytical information of interest. Moreover, the detector gives a linear and instantaneous answer because once the microfluidic channel has been fully covered, analytes are homogeneously mixed thanks to diffusion and turbulent flow (which is then restored to laminar before entering the detector). Thus, there is no limitation in choosing one of the three parameters. In our experiment, height (H) at peak maximum is the desired parameter, and it coincides with absorbance maximum because it is easily measurable and strictly related to the detector's reading, particularly with absorbance measuring. The response of this latter, achieved by detecting the amount of colored enzymatic product in the detection chamber, has a bell function-like shape. In fact, it is a usual procedure in FIA to treat these data by making a fit with a three-parameter Gaussian distribution (Růžička and Hansen, 1988). Thus, a no-linear fitting is made from collected and plotted data by using the following equation (**Eq. 1**):

$$y = a \cdot e^{\left[-5\ \left(\frac{x-x_0}{b}\right)^2\right]}, \tag{1}$$

where **a** is the normalizing constant equal to $1/\sigma\cdot\sqrt{2\pi}$; b as doubled variance is equal to $\sqrt{\frac{1}{n}\sum_{i=1}^{n}(x_i - \overline{x})^2}$, where x_i is the *i*th measure, $\overline{x}$ is the measures' average, and $\mathbf{x_0}$ is desired value, which corresponds to the x-coordinate of the absorbance maximum of a determined peak. Thus, the desired parameter is x_0, which enables us to determine the peak's height and the absorbance maximum. Moreover, x_0 is directly proportional to the concentration of the enzyme-antigen complex eluted from the column and proportional to the concentration of the injected analyte. Reproducibility measures have been conducted by subsequent injections of the same analyte. From the collected data, the relative standard deviation (RSD%) has been calculated and expressed in percentage terms.

FIA Peaks Analysis Applied to the Determination of STX

Absorbance response depends on concentration and gives a sigmoidal trend. This latter can be defined with a 3-parameter logistic function (**Eq. 2**), which is characteristic of immune-enzymatic assays.

$$y = \frac{a}{1 + \left(\frac{x}{x_0}\right)^b}, \tag{2}$$

with a, b, and x_0 values are equal to **Eq. 1**. Moreover, to allow a comparison between different calibration curves, obtained absorbance values have been converted as percentages by applying the following equation (**Eq. 3**):

$$\%\frac{A}{A_{sat}} = 100x\frac{A - A_0}{A_{sat} - A_0}, \tag{3}$$

where A is equal to the detected absorbance when the analyte is present; A_{sat} and A_0 are, respectively, absorbance values at the zero competition and at saturating concentration of the analyte.

The limit of detection (LOD) is estimated from the analysis of ten different samples in which the requested analyte is not present (blank); thus, with the obtained current values, the standard deviation (SD) is estimated. Thus, the results found were included in the formula (detection limit: LOD = $A_{NC} - 3\sigma$) in which SD_{nc} and A_{NC} are the standard deviation and absorbance of the no competition point (no Ag), respectively.

Seawater Sampling

The calibration curve was achieved through a matrix matching method with surface seawater sampled from Santa Severa Bay (RM, IT) and Acquafredda bay (PZ, IT). The surface seawaters were sampled with 500 ml PET Water Sampling Bottles (Sterilin, Thermo Fisher Scientific, United States) about 50 m off the coast. The samples were filtered on Millex-GV (hydrophilic PVDF 0.22 μm membrane, Sigma-Aldrich, United States) and stored at 4°C until analysis. Seawater pH and conductivity were measured with a pH meter (Xs Instruments, Modena, IT). Santa Severa seawater showed a 7.85 pH and 57.00 mS conductivity, and Acquafredda seawater a 7.51 pH and 59.10 mS conductivity.

RESULTS AND DISCUSSION

Study of the of Operational Parameters

The aim of this study is to combine the selectivity and sensibility of the Fl-IA method with the repeatability and the continuous online analysis in microfluidic systems ready to use in the field.

TABLE 1 | Flow rate optimization parameters.

Internal tube diameter, (ø) (mm)	RPM	Average time, <t> (s)	Flow rate, v_φ (ml min^{-1})	RSD (%)
0.51	1.00	3.33 + 0.09	0.03	3
	1.18	2.50 + 0.06	0.04	2
	3.33	1.02 + 0.02	0.10	2
0.76	1.50	1.067 + 0.006	0.09	0.6
	1.75	0.913 + 0.006	0.11	0.7
	2.38	0.667 + 0.006	0.15	0.9
1.02	1.00	1.133 + 0.006	0.09	0.5
	1.10	1 + 0	0.10	0
	1.20	0.96 + 0.2	0.10	21
	1.40	0.873 + 0.005	0.11	0.6

Before connecting the bioreactor to the chip, several parameters have been studied. Flow rate is one of the fundamental parameters needed to correctly operate this microfluidic system. Due to the structural features of the chip itself, the flow rate cannot be higher than 0.15 ml min^{-1}, while the bioreactor is able to work at higher flow rates. The first set of tests has been carried out to determine the revolutions per minute (RPM) at which each peristaltic pump can operate with the most efficiency (**Table 1**) with different PVC tubes' diameters.

Tubes of 0.51 mm diameter with an RSD% equal to 2%, were used for the inlet flow, whereas for the outlet flow, larger pipes of 1.02 mm internal diameter were chosen to drop counter pressure interference. The best detector response (in variation of absorbance), reported in **Figure 3A**, has been obtained by studying three different flow rates according to mechanical limits (0.05, 0.075, and 0.10 ml $min^{-1,}$ respectively). The repeatability of the measurement, calculated on subsequent injections of the same dye dilution at 0.1 ml min^{-1} (good agreement between reproducibility and analysis time) is around 4%. The second set of tests has been conducted to evaluate the response of the microfluidic detector. Multiple injections of a blue food coloring (Patent Blue V E131) at different dilutions (1:100, 1:50, and 1:5 v v^{-1}) have been used for the microfluidic detector evaluation since this latter is set at 655 nm. As can be seen in **Figure 3B**, dilution of 1:100 v v^{-1} gives a signal too weak to be acceptable. That is due to the low concentration of the analyte (the noise given by the moving flow is prevailing over the signal).

HRP Concentration Optimization

The response of microfluidic system has been evaluated, by a simulation of the immune-enzymatic assay, by measuring of enzymatic substrate flowing in channels I and II of **Figure 3B**, several concentrations of antigen labeled with HRP (Ag*) and TMB substrate, respectively. As reported in **Figure 3B**, the enzyme was mixed with its substrate in the herringbone mixer giving the enzymatic product, TMBox, colored in blue and measured in the optical sensing channel. The LOD of TMBox of this system has been calculated measuring multiple sequential injections of different HRP concentrations (0.0001, 0.001, and 0.1 μg ml^{-1}), in 20 mM phosphate buffer, pH 7.4, and mixed with a fixed amount of TMB substrate (enzymatic substrate ready to use, Sigma-Aldrich, United States). The results (**Figure 4**) showed that 1 ng ml^{-1} is the concentration limit for the sensitivity of the detector.

Up to 1 μg ml^{-1}, the concentration of TMB is unstable (TMS is photosensitive) changing the color from blue to orange. A calibration curve of TMBox (from 0 to 1 μg ml^{-1}) was realized using different concentrations of HRP and fixed amount of TMB substrate as such (**Table 2**). Each measure has been made in triplicate to evaluate the working range and the repeatability without stopping the flow (**Figure 5**).

FI-IA OPTIMIZATION USING BIOREACTOR

In order to develop the FI-IA system before its connection with the fluidic microchip, several analytical parameters (flow rate, antibody concentration, and interaction time in the

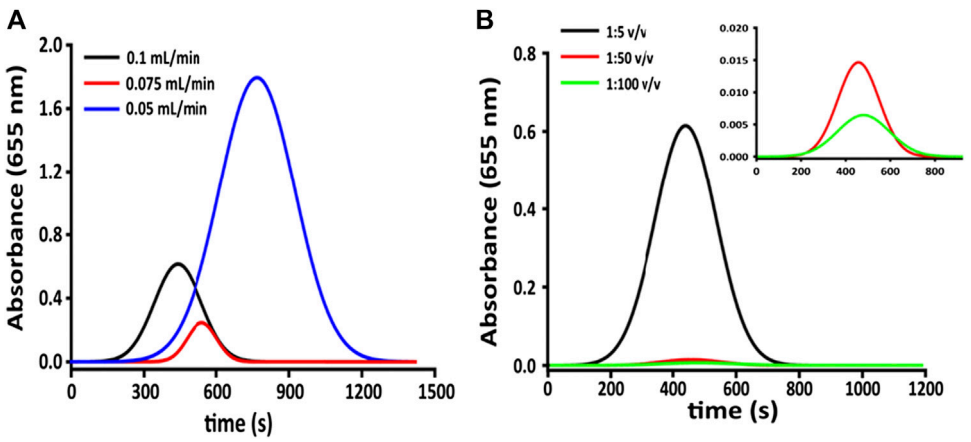

FIGURE 3 | (A) Detector response (variation of absorbance) at fixed dilution of the colored substrate and different flow rates; **(B)** detector response (in variation of absorbance) at different dilutions and fixed flow rate (0.1 ml min^{-1}).

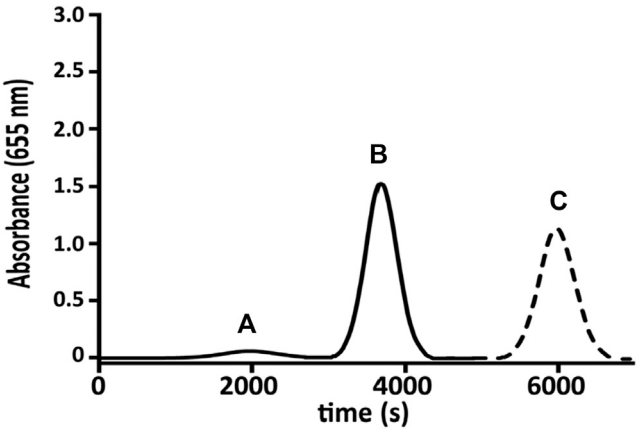

FIGURE 4 | Gaussian regression of several responses [0.0001 **(A)**, 0.001 **(B)**, and 0.1 μg ml^{-1} **(C)**], sequentially injected in the full system at 0.1 ml·min^{-1}.

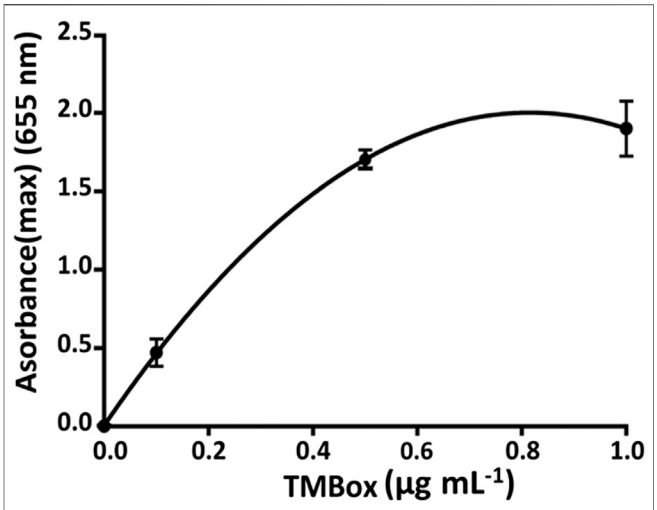

FIGURE 5 | Calibration curve of HRP in the microfluidic system using 0.1 ml min^{-1} flow rate.

bioreactor) were studied, collecting the solution eluted of the bioreactor up to a maximum volume of 200 μL. The solution was collected in tubes and read on the spectrophotometer at 655 nm (only TMBox) and 450 nm (after blocking with 100 μL of H_2SO_4).

Binding Curve and Competition Time Using Bioreactor

The concentration of PAb to be used in the competition step is one of the very important parameters to be able to obtain an assay sensitive to low concentrations of STX. For the binding study (**Figure 6**), several dilutions of anti-STX PAb (1: 500,000, 1:100,000, 1:75,000, 1:50,000, 1:20,000, 1:10,000, 1: 5,000 v v^{-1}, and no PAb, corresponding to the maximum of absorbance) and fixed amount of STX-HRP (1:600 v v^{-1}) were incubated in different vials at room temperature. After 2 h (data not shown), the mixture was injected into the flow system with an increase of flow rate (0.15 ml min^{-1} flow rate instead 0.1 ml min^{-1}, optimized for the only microchip) using a loop of 25 μL. A slight increase in the flow rate was necessary to create the right pressure for eluting the solution from the bioreactor and for transporting it inside to the microchip (due to the differences in the diameter of the tubes and channels, respectively).

TABLE 2 | Calibration curve parameters for TMBox in the function of the concentration of HRP using microfluidic system.

Concentration (μg ml^{-1})	<Absorbance>	RSD (%)
0	0.05 ± 0.04	2
0.1	0.47 ± 0.08	17
0.5	1.70 ± 0.04	2
1	1.90 ± 0.18	10

After 3 min, a volume of 200 μL is eluted and collected in a vial in presence of 100 μL of TMB, the enzymatic substrate of HRP. After 1 min, the enzymatic reaction was blocked adding 100 μL of 1 mM H_2SO_4 causing the color turning from blue (TMox, 655 nm absorbance) to yellow (450 nm absorbance) and read spectrophotometrically.

In **Figure 6**, the absorbance is shown proportional to eluted STX-HRP from the bioreactor, not reacting with PAb (linked to G protein in the bioreactor) and inversely proportional to PAb. For the competition step, the selected dilution of PAb was equal to 1:75,000 v v^{-1}, the 70% of the binding curve.

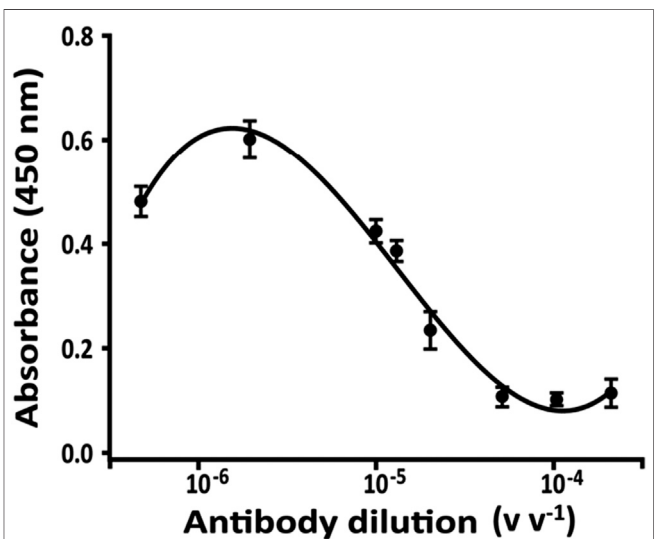

FIGURE 6 | Binding curve for anti-STX PAb obtained with a fixed amount of STX-HRP (600 v v^{-1}) in 20 mM phosphate buffer pH 7.4, after 2 h of incubation; flow rate, 0.15 ml min^{-1}. The analysis was carried out using only bioreactor of the FI-IA system and the solution was collected.

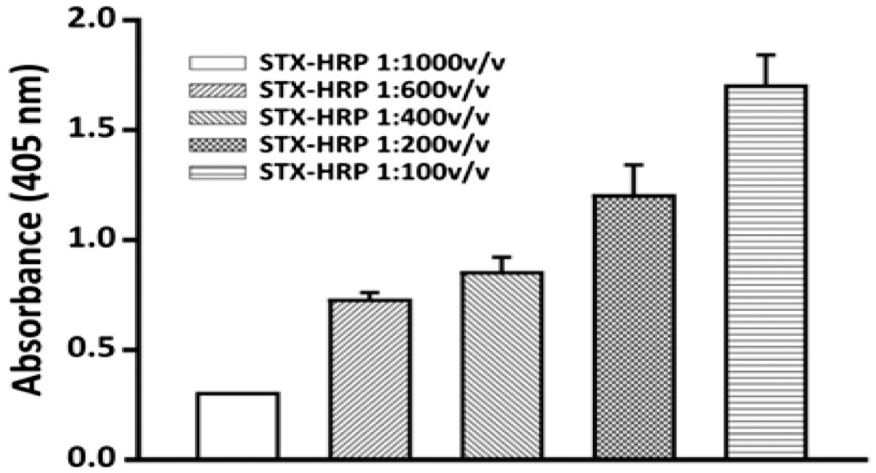

FIGURE 7 | Selection of the STX-HRP dilution to use for the competition assay: 1:75,000 v v^{-1} dilutions of anti-STX PAb in 20 mM phosphate buffer pH 7.4, for 2 h at room temperature; flow rate, 0.15 ml min^{-1}. The analysis was carried out using only the bioreactor of the FI-IA system.

Concentration of STX-HRP Using Bioreactor

To establish the dilution of STX-HRP to use for the competition step, several amounts of STX-HRP were added to fixed dilution of PAb (1:75,000 v v^{-1}), extrapolated for the binding study (*Binding Curve and Competition Time Using Bioreactor*).

The experiment was carried out using the same incubation times and procedures previously studied. **Figure 7** reports the results obtained for several STX-HRP dilutions, where 1:600 v v^{-1} is selected (the absorbance respects the Lambert–Beer law with lower RSD% equal to 5%).

Flow Optimization Using Bioreactor

The flow rate parameter has a significant influence on the retention of antigen-antibody complex by the G protein present in the bioreactor. Using the dilution selected in the previous study, 1:75,000 v v^{-1} of PAb and 1:600 v v^{-1} of STX-HRP, several flow rates are tested. Several flow rates were studied (**Supplementary Figure S2**), showing better results in terms of absorbance and reproducibility at 0.15 ml min^{-1}.

Calibration Curve Using the Bioreactor

Calibration curve for STX determination in buffer (**Figure 8**) was obtained using the optimized parameters in the previous paragraph: 1:75,000 v v^{-1} of anti-PAB dilution, 1:600 v v^{-1} of STX-HRP, flow rate equal to 0.15 ml min^{-1}, and competition time of 2 h at room temperature (data not shown). For this study, several concentrations of STX in buffer were prepared between 0 and 10^{-1} ng L^{-1}. Every sample was prepared 15 min from each other in order to gain the best reproducibility due to the elution time of each solution and the washing time of the FI-IA system. A volume of 0.2 ml of samples was injected in the FI-IA system starting from the less concentrated solutions. After 3 min of elution time, the STX-HRP solution was collected in a vial with 100 µL of substrate TMB and left to react one more minute; the enzymatic reaction was blocked with H_2SO_4 lastly measured spectrophotometrically at 450 nm. Between measures, the system was washing in flow with 20 mM phosphate buffer NaH_2PO_4/Na_2HPO_4, pH 7.4, for 15 min, while the loop and the column were washed with approximately 0.4 ml of buffer every 5 min. The results indicate a "Hook Effect" (**Supplementary Figure S3**) for the higher concentrations of STX, a phenomenon due, probably, to the crowding near the antibody recognition sites and the difficulty of the toxin to be recognized for the formation of the immune complex. In fact, the signal response may decrease at extremely high concentrations as shown as a

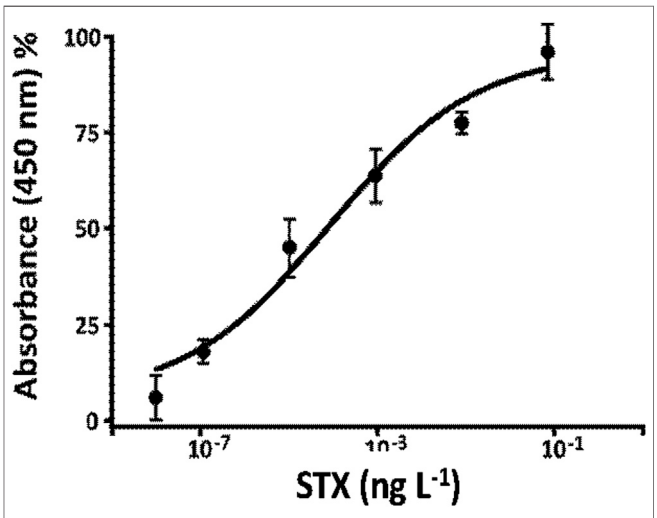

FIGURE 8 | Calibration curve, using only bioreactor, for STX determination STX-HRP (1:600 v v^{-1}) for the Anti-STX (1:75,000 v v^{-1}) in 20 mM phosphate buffer pH 7.4, flow rate 0.15 ml min^{-1}.

TABLE 3 | Summary of results obtained with FI-IA system in diluted seawater samples.

	Bioreactor	Full system
LOD (ng ml^{-1})	5×10^{-8}	1×10^{-7}
WR (ng ml^{-1})	8×10^{-7}–7×10^{-5}	3.5×10^{-7}–2×10^{-5}
RSD%	12%	15%
Parameters	a = 0,9392; b = –0,2293; $x_0 = 2{,}523 \times 10^{-9}$	b0 = 0.0357; b1 = 2.0635; b2 = –0.7858; $r^2 = 0.98$

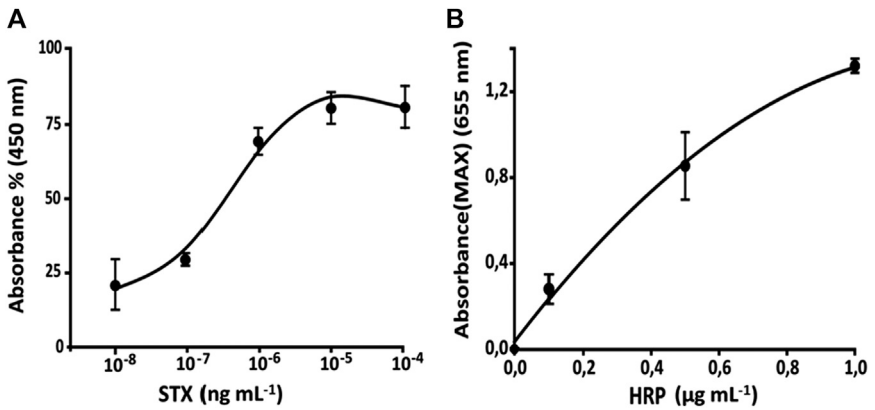

FIGURE 9 | (A) Calibration curve for STX determination STX-HRP (1:600 v v^{-1}) for the anti-STX (1:75,000 v v$^{-1)}$ in diluted seawater (1:3 v v^{-1} with double distilled water) using bioreactor. (**B)** Calibration curve for STX obtained using microfluidic FI-IA system.

dip in the calibration curve range (Reverberi and Reverberi, 2007; Vashist and Luong, 2018). The results are demonstrated with a three-parameter logistic function trend, and the parameters are shown in **Table 3** (calculated as reported in *FIA Peaks Analysis Applied to the Determination of STX*).

Seawater Matrix Effect Using Bioreactor

The system reliability was tested in a matrix matching method. The incubation protocol between STX and PAb in *Calibration Curve Using the Bioreactor* was performed in diluted seawater (1:3 v v^{-1} with double distilled water) and tested with different free STX concentrations. As a matter of fact, the matrix effect can influence the antigen-antibody interaction while performing analysis of STX concentration of 10^{-7}, 10^{-6}, 10^{-5}, and 10^{-4} ng L^{-1} on seawater samples. Moreover, when concentrations values are higher than 10^{-4} ng L^{-1}, a decrement of the signal ("Hook effect") (Reverberi and Reverberi, 2007) may occur (**Figure 9A**) due to the crowding fo antigen vs. the antibodies immobilized on a small surface. The analytical parameters, extrapolated by the assay carried out in seawater, are reported in **Table 3**.

CALIBRATION CURVE FOR THE FULL SYSTEM (BIOREACTOR AND MICROFLUIDIC CHIP)

Regarding the results (**Tables 3, 4**) of the last set (which correspond with the fully operational microfluidic system linked with the bioreactor), linearity is acceptable in relation to the used HRP concentrations (**Figure 9B**). Keeping in mind absorbance's values for each HRP concentration, it is possible to observe (**Figure 9**) a lesser dispersion of the enzyme inside the bioreactor, thus causing a decrease of concentration in the mixing chamber between the first and last measure. This is probably due to lower enzyme mobility given by the column's packing. This kind of system shows a LOD of 1×10^{-7}, 3.5×10^{-7}–2×10^{-5} ng mL^{-1} as working range, and an overall 15 RSD% (**Table 3**). Moreover, microfluidic chip's structural features bind the working flow rate.

TABLE 4 | Calibration curve parameters for the determination of STX using full system (bioreactor and microfluidic chip).

Concentration (µg ml^{-1})	<Absorbance>	RSD (%)
0	0.010 ± 0.003	30
0.1	0.28 ± 0.07	25
0.5	0.85 ± 0.16	19
1	1.319 ± 0.002	0.152

CONCLUSION

This article outlines for the first time a novel FI-IA bioreactor connected with a microfluidic chip for the determination of STX, an important and harmful biotoxin present in seawater. The proposed system gives the possibility of analyzing in

several continuous samples, reading in an automated way the results. The resin bead–based bioreactor sample capacity allows analysis of up to 38 sequential samples to be performed before it needs to be changed. The preliminary study, presented here, illustrates its potential to being used as a field-deployable portable analytical device able to work *in situ* and with continuous water samples without any pretreatment for monitoring the health and safety status of marine environments tool to warn and protect against the consumption of contaminated marine produce.

DATA AVAILABILITY STATEMENT

The original contributions presented in the study are included in the article/**Supplementary Material**; further inquiries can be directed to the corresponding authors.

AUTHOR CONTRIBUTIONS

LC and MO wrote sections of the manuscript and planned the experiments. LC performed the architecture and analysis using a microfluidic system. MO performed the experiment with bioreactor and the immunoassay offline. RC and AT organized and wrote the first draft of the manuscript. AS and PP contributed to conception and design of the study. LM supervised and organized the analysis. All authors contributed to manuscript revision, read, and approved the submitted version.

SUPPLEMENTARY MATERIAL

The Supplementary Material for this article can be found online at: https://www.frontiersin.org/articles/10.3389/fchem.2021.626630/full#supplementary-material.

REFERENCES

Anderson, D. M., Kulis, D. M., Qi, Y. Z., Zheng, L., Lu, S., and Lin, Y. T. (1996). Paralytic shellfish poisoning in Southern China. *Toxicon* 34, 579–590. doi:10.1016/0041-0101(95)00158-1

Anfossi, L., Di Nardo, F., Cavalera, S., Giovannoli, C., and Baggiani, C. (2018). Multiplex lateral flow immunoassay: an overview of strategies towards high-throughput point-of-need testing. *Biosensors* 9 (1), 2. doi:10.3390/bios9010002

Botana, A. M., Otero, P., Rodríguez, P., Alfonso, A., and Botana, L. M. (2013). Current situation on analysis of marine toxins. *Rev. Anal. Chem.* 32 (1), 15–34. doi:10.1515/revac-2012-0020

Campbell, K., Rawn, D. F., Niedzwiadek, B., and Elliott, C. T. (2011). Paralytic shellfish poisoning (PSP) toxin binders for optical biosensor technology: problems and possibilities for the future: a review. *Food Addit. Contam. Part A Chem. Anal. Control Expo. Risk Assess.* 28, 711–725. doi:10.1080/19440049.2010.531198

Cusick, K., and Sayler, G. S. (2013). An overview on the marine neurotoxin, saxitoxin: genetics, molecular targets, methods of detection and ecological functions. *Mar. Drugs* 11, 991–1018. doi:10.3390/md11040991

Deeds, J., Landsberg, J., Etheridge, S., Pitcher, G., and Longan, S. W. (2008). Non-traditional vectors for paralytic shellfish poisoning. *Mar. Drugs* 6, 308–348. doi:10.3390/md20080015

Dell'Aversano, C., Hess, P., and Quilliam, M. A. (2005). Hydrophilic interaction liquid chromatography–mass spectrometry for the analysis of paralytic shellfish poisoning (PSP) toxins. *J. Chromatogr. A* 1081, 190–201. doi:10.1016/j.chroma.2005.05.056

European Food Safety Authority (EFSA) (2009). Marine biotoxins in shellfish-saxiton group. *Eur. Food Saf. Authority* 1019, 1–76.

Ferrão-Filho, A. d. S., and Kozlowsky-Suzuki, B. (2011). Cyanotoxins: bioaccumulation and effects on aquatic animals. *Mar. Drugs* 9, 2729–2772. doi:10.3390/md9122729

Fintschenko, Y., and Wilson, G. S. (1998). Flow injection immunoassays: a review. *Mikrochim. Acta* 129, 7–18. doi:10.1007/bf01246843

García, C., del Carmen Bravo, M., Lagos, M., and Lagos, N. (2004). Paralytic shellfish poisoning: post-mortem analysis of tissue and body fluid samples from human victims in the Patagonia fjords. *Toxicon* 43, 149–158. doi:10.1016/j.toxicon.2003.11.018

Guy, A. L., and Griffin, G. (2009). Adopting alternatives for the regulatory monitoring of shellfish for paralytic shellfish poisoning in Canada: interface between federal regulators, science and ethics. *Regul. Toxicol. Pharmacol.* 54, 256–263. doi:10.1016/j.yrtph.2009.05.002

Halme, M., Rapinoja, M. L., Karjalainen, M., and Vanninen, P. (2012). Verification and quantification of saxitoxin from algal samples using fast and validated hydrophilic interaction liquid chromatography-tandem mass spectrometry method. *J. Chromatogr. B Analyt. Technol. Biomed. Life Sci.* 880, 50–57. doi:10.1016/j.jchromb.2011.11.015

He, H. Z., Li, H. B., Jiang, Y., and Chen, F. (2005). Determination of paralytic shellfish poisoning toxins in cultured microalgae by high-performance liquid chromatography with fluorescence detection. *Anal. Bioanal. Chem.* 383, 1014–1017. doi:10.1007/s00216-005-0092-8

I. R. Falconer (Editor) (1993). *Algal toxins in seafood and drinking water*. London, United Kingdom: Academic Press.

Ishimatsu, R., Shimizu, S., Hongsibsong, S., Nakano, K., Malasuk, C., Oki, Y., et al. (2020). Enzyme-linked immunosorbent assay based on light absorption of enzymatically generated aniline oligomer: flow injection analysis for 3-phenoxybenzoic acid with anti-3-phenoxybenzoic acid monoclonal antibody. *Talanta* 218, 121102. doi:10.1016/j.talanta.2020.121102

Krämer, P., and Schmid, R. (1991). Flow injection immunoanalysis (FIIA)–a new immunoassay format for the determination of pesticides in water. *Biosens. Bioelectron.* 6, 239–243. doi:10.1016/0956-5663(91)80009-m

Li, J., and Persson, K. M. (2021). Quick detection method for paralytic shellfish toxins (PSTs) monitoring in freshwater–a review. *Chemosphere* 265, 128591. doi:10.1016/j.chemosphere.2020.128591

McKelvie, I. D. (2008). "Principles of flow injection analysis," in *Comprehensive analytical chemistry*. Editors S. D. Kolev and I. D. Mckelvie (Amsterdam, Netherlands: Elsevier), Vol. 54, 81–109. doi:10.1016/S0166-526X(08)00604-1

Micheli, L., Di Stefano, S., Moscone, D., Palleschi, G., Marini, S., Coletta, M., et al. 2002). Production of antibodies and development of highly sensitive formats of enzyme immunoassay for saxitoxin analysis. *Anal. Bioanal. Chem.* 373, 678–684. doi:10.1007/s00216-002-1399-3

Passos, M. L., Pinto, P. C., Santos, J. L., Saraiva, M. L., and Araujo, A. R. (2015). Nanoparticle-based assays in automated flow systems: a review. *Anal. Chim. Acta* 889, 22–34. doi:10.1016/j.aca.2015.05.052

Petropoulos, K., Bodini, S. F., Fabiani, L., Micheli, L., Porchetta, A., Piermarini, S., et al. (2019). Re-modeling ELISA kits embedded in an automated system suitable for on-line detection of algal toxins in seawater. *Sens. Actuators B* 283, 865–872. doi:10.1016/j.snb.2018.12.083

Pöhlmann, C., and Elßner, T. (2020). Multiplex immunoassay techniques for on-site detection of security sensitive toxins. *Toxins* 12 (11), 727. doi:10.3390/toxins12110727

Reverberi, R., and Reverberi, L. (2007). Factors affecting the antigen-antibody reaction. *Blood Transfus.* 5, 227–240. doi:10.2450/2007.0047-07

Rocha, F. R. P., and Zagatto, E. A. G. (2020). Flow analysis during the 60 years of Talanta. *Talanta* 206, 120185. doi:10.1016/j.talanta.2019.120185

Růžička, J., and Hansen, E. H. (1988). "Flow injection analysis," in *Chemical analysis*. 2nd Edn. New York, NY: John Wiley & Sons.

Růžička, J., and Hansen, E. H. (1975). Flow injection analyses. *Anal. Chim. Acta* 78, 145–157. doi:10.1016/S0003-2670(01)84761-9

Shi, J., Xu, M., Tang, Q., Zhao, K., Deng, A., and Li, J. (2018). Highly sensitive determination of diclofenac based on resin beads and a novel polyclonal

antibody by using flow injection chemiluminescence competitive immunoassay. *Spectrochim. Acta Mol. Biomol. Spectrosc.* 191, 1–7. doi:10.1016/j.saa.2017.09.068

Shitanda, I., Takamatsu, S., Watanabe, K., and Itagaki, M. (2009). Amperometric screen-printed algal biosensor with flow injection analysis system for detection of environmental toxic compounds. *Electrochim. Acta* 54, 4933–4936. doi:10.1016/j.electacta.2009.04.005

S. K. Vashist and J. Luong (Editors) (2018). *Handbook of immunoassay technologies: approaches, performances, and applications*. London, United Kingdom: Elsevier/AP, Academic Press, an imprint of Elsevier.

Stroka, J. (2011). Food additives and contaminants: Part A: chemistry, analysis, control, exposure & risk assessment. Foreword. *Food Addit. Contam. Part A Chem. Anal. Control Expo. Risk Assess.* 28, 259. doi:10.1080/19440049.2011.561599

Tian, Y., Du, L., Zhu, P., Chen, Y., Chen, W., Wu, C., et al. (2020). Recent progress in micro/nano biosensors for shellfish toxin detection. *Biosens. Bioelectron.* 176, 112899. doi:10.1016/j.bios.2020.112899

United States Environmental Protection Agency (EPA) (2019). Cyanobacteria and cyanotoxins: information for drinking water systems. Available at: https://www.epa.gov/sites/production/files/2019-07/documents/cyanobacteria_and_cyanotoxins_fact_sheet_for_pws_final_06282019.pdf.pdf.

Van Egmond, H. P., van den Top, H. J., Paulsch, W. E., Goenaga, X., and Vieytes, M. R. (1994). Paralytic Shellfish Poison reference materials: an intercomparison of methods for the determination of saxitoxin. *Food Addit. Contam.* 11, 39–56. doi:10.1080/02652039409374201

Vilariño, N., Louzao, M. C., Fraga, M., Rodríguez, L. P., and Botana, L. M. (2013). Innovative detection methods for aquatic algal toxins and their presence in the food chain. *Anal. Bioanal. Chem.* 405, 7719–7732. doi:10.1007/s00216-013-7108-6

Wang, C., Wu, J., Zong, C., Xu, J., and Ju, H.-X. (2012). Chemiluminescent immunoassay and its applications. *Chin. J. Anal. Chem.* 40, 3–10. doi:10.1016/s1872-2040(11)60518-5

Waseem, A., Yaqoob, M., and Nabi, A. (2013). Analytical applications of flow injection chemiluminescence for the determination of pharmaceuticals–a review. *Current Pharm. Anal.* 9, 363–395. doi:10.2174/15734129113099990002

Wu, J., Tang, J., Dai, Z., Yan, F., Ju, H., and El Murr, N. (2006). A disposable electrochemical immunosensor for flow injection immunoassay of carcinoembryonic antigen. *Biosens. Bioelectron.* 22, 102–108. doi:10.1016/j.bios.2005.12.008

Yu, F. Y., Liu, B. H., Chou, H. N., and Chu, F. S. (2002). Development of a sensitive ELISA for the determination of microcystins in algae. *J. Agric. Food Chem.* 50, 4176–4182. doi:10.1021/jf0202483

Zhang, W., Dixon, M. B., Saint, C., Teng, K. S., and Furumai, H. (2018). Electrochemical biosensing of algal toxins in water: the current state-of-the-art. *ACS Sens.* 3, 1233–1245. doi:10.1021/acssensors.8b00359

Zhang, Y., Liu, W., Ge, S., Yan, M., Wang, S., Yu, J., et al. (2013). Multiplexed sandwich immunoassays using flow-injection electrochemiluminescence with designed substrate spatial-resolved technique for detection of tumor markers. *Biosens. Bioelectron.* 41, 684–690. doi:10.1016/j.bios.2012.09.044

Conflict of Interest: The authors declare that the research was conducted in the absence of any commercial or financial relationships that could be construed as a potential conflict of interest.

frontiers in Chemistry

ORIGINAL RESEARCH
published: 15 March 2021
doi: 10.3389/fchem.2021.613083

Aptamer Turn-On SERS/RRS/Fluorescence Tri-mode Platform for Ultra-trace Urea Determination Using Fe/N-Doped Carbon Dots

Chongning Li[1,2,3], *Jiao Li*[1,2,3], *Aihui Liang*[1,2,3], *Guiqing Wen*[1,2,3]* *and Zhiliang Jiang*[1,2,3]*

[1]State Key Laboratory for Chemistry and Molecular Engineering of Medicinal Resources, School of Chemistry and Pharmaceutical Science, Guangxi Normal University, Guilin, China, [2]Key Laboratory of Ecology of Rare and Endangered Species and Environmental Protection (Guangxi Normal University), Ministry of Education, Guilin, China, [3]Guangxi Key Laboratory of Environmental Pollution Control Theory and Technology for Science and Education Combined with Science and Technology Innovation Base, Guilin, China

Sensitive and selective methods for the determination of urea in samples such as dairy products are important for quality control and health applications. Using ammonium ferric citrate as a precursor, Fe/N-codoped carbon dots (CD_{FeN}) were prepared by a hydrothermal procedure and characterized in detail. CD_{FeN} strongly catalyzes the oxidation of 3,3′,5,5′-tetramethylbenzidine (TMB) by H_2O_2 to turn on an indicator molecular reaction, forming an oxidized tetramethylbenzidine (TMB_{ox}) probe with surface-enhanced Raman scattering, resonance Rayleigh scattering, and fluorescence (SERS, RRS, and FL) signals at 1,598 cm^{-1}, 370 nm, and 405 nm, respectively. The urea aptamer (Apt) can turn off the indicator reaction to reduce the tri-signals, and the addition of urea turns on the indicator reaction to linearly enhance the SERS/RRS/FL intensity. Thus, a novel Apt turn-on tri-mode method was developed for the assay determination of ultra-trace urea with high sensitivity, good selectivity, and accuracy. Trace adenosine triphosphate and estradiol can also be determined by the Apt-CD_{FeN} catalytic analytical platform.

Keywords: Fe/N-doped carbon dots, catalysis amplification, aptamer, surface-enhanced Raman scattering, resonance Rayleigh scattering, fluorescence

OPEN ACCESS

Edited by:
Ottavia Giuffrè,
University of Messina, Italy

Reviewed by:
Alessandro Paolini,
Bambino Gesù Children Hospital (IRCCS), Italy
Nisha Agarwal,
Ontario Tech University, Canada

***Correspondence:**
Guiqing Wen
gqwen@gxnu.edu.cn
Zhiliang Jiang
zljiang@mailbox.gxnu.edu.cn

Specialty section:
This article was submitted to Analytical Chemistry, a section of the journal Frontiers in Chemistry

Received: *01 October 2020*
Accepted: *18 January 2021*
Published: *15 March 2021*

Citation:
Li C, Li J, Liang A, Wen G and Jiang Z (2021) Aptamer Turn-On SERS/RRS/Fluorescence Tri-mode Platform for Ultra-trace Urea Determination Using Fe/N-Doped Carbon Dots. Front. Chem. 9:613083. doi: 10.3389/fchem.2021.613083

INTRODUCTION

Urea is a naturally occurring metabolite of nitrogen-containing compounds (Dervisevic et al., 2018). It has many applications and can be found in both fertilizer and dermatological cream. Because it can in some cases cause adverse effects, urea detection methods are common in clinical chemistry, agriculture, and biology. Currently, urea detection methods include surface-enhanced Raman scattering (SERS), colorimetric, electrochemical, and fluorescence (FL) approaches, (Safitri et al., 2017; Migliorini et al., 2018), most of which operate in a single mode with low sensitivity. The development of urea detection methods with enhanced sensitivity, such as highly sensitive SERS, FL, and resonance Rayleigh scattering (RRS) tri-mode reactions, has therefore attracted significant attention.

CDs are carbon-based nanomaterials with good water solubility and surfaces that can be easily functionalized with various organic polymers, inorganic moieties, or biological species (Karthikeyan

et al., 2019). They have been widely used in chemistry, environmental science, food science, and biotechnology (Rong et al., 2018; Zheng et al., 2018). CDs can be doped with inorganic metal ions, which is an effective method for improving their optical and electrical properties. For example, Fe is an abundant element that is compatible with carbon-based materials. Fe-doped CDs (CD_{Fe}) are suitable for various prospective applications and can be made to fluoresce. Fluorescent CD_{Fe} have been prepared using a one-step hydrothermal carbonization method, with methylthymol blue sodium salt and $FeCl_3{\cdot}6H_2O$ as precursors (Zhu et al., 2019). These CD_{Fe} were employed in a glucose/CD_{Fe} ratio FL sensing system to quantify H_2O_2 and glucose presence in the concentration ranges of 0–133 and 0–300 μM with limits of detection (LODs) of 0.47 and 2.5 μM, respectively. N and Fe-containing CDs (CD_{FeN}) have been used to measure dopamine content by colorimetry and fluorometry (Wang et al., 2016). Furthermore, L-tartaric acid, urea, and $FeCl_3{\cdot}6H_2O$ have been used as precursors in a solvothermal procedure to synthesize CD_{FeN} for the immunosorbent spectrophotometric detection of carcinoembryonic antigens at levels as low as 0.1 pg/ml (Yang et al., 2017). Ethylenediamine tetraacetate and iron nitrate have been used as carbon and iron sources, respectively, to obtain CD_{Fe} through a one-step hydrothermal carbonization, which provided a favorable electron acceptor near the CD_{Fe} and produced high quenching efficiency (Zhuo et al., 2019). This FL response can quantify dopamine in the range of 0.01–50 μM with an LOD of 5 nM. However, to the best of our knowledge, there have been no reports on the use of a single precursor to prepare CD_{FeN} or the catalytic amplification of tri-signals and their utilization to detect trace urea using an aptamer (Apt).

Apts are ideal for detecting target molecules, such as urea, as they bind to a chosen molecule. Moreover, they are easy to synthesize and modify, chemically stable, and can be stored for long periods. They have already been used to specifically capture metal ions and small organic molecules in recent trace substance analyses (Zhou and Rossi, 2017). For example, the use of a single-labeled multifunctional probe comprising a Cd(II)-specific Apt for measuring Cd(II) by FL with an LOD of 2.15 nM has been demonstrated (Zhu et al., 2017). A label-free fluorescent Apt sensor for tetracycline junction Apts and thiazole orange for the selective and sensitive FL detection of 0.05–100 μg/ml tetracycline has also been established (Sun et al., 2018). Furthermore, a label-free and off-FL method for the quantitative detection of 0.7–10 nmol/L kanamycin based on functional molecular beacons was recently developed (Zhu et al., 2018). The interaction between silver nanoparticles (AgNPs) and CdTe quantum dots to detect 0.1–30 nM adenosine has also been successfully demonstrated (Song et al., 2018). In conjunction with SERS, Apts can contribute significantly to the detection of trace urea.

SERS is a molecular spectroscopy technique based on Raman scattering and local surface plasmon resonance of nanoparticles. It has been used in numerous fields, including nanomaterial research, bioanalysis, and food testing (Chen et al., 2017b; Deng et al., 2017; Li et al., 2018b). Graphene oxide nanoribbons with a strong catalytic effect on the reduction of $HAuCl_4$ by H_2O_2, forming gold nanoparticles with SERS activity, were developed (Li et al., 2018a). Coupling with an Apt reaction allowed for the quantitative analysis of 2–75 nmol/L Pb(II) with the molecular probe Victoria Blue B. The thickness of Fe_2O_3 coatings on Fe_2O_3 at graphene nanostructures was adjusted by changing the number of Fe_2O_3 atomic layer deposition cycles (Zhang et al., 2017). Fe_2O_3 was deposited on a graphene surface, and combination with an Apt yielded a simple, fast, and sensitive electrochemical Apt sensor for the detection of 1.0×10^{-11}–4.0×10^{-9} M thrombin with an LOD of 1.0×10^{-12} M.

Dual-mode molecular probes (e.g., FL/colorimetry (Li et al., 2017), FL/light scattering (Liu et al., 2017), and FL/SERS (You et al., 2017)) also play a pivotal role in this experiment. They have attracted widespread attention owing to their simplicity while displaying higher sensitivity than traditional optical sensors. A SERS/FL dual-mode nanosensor with a signal transduction mechanism based on the conformational transformation of human telomeric G-quadruplex was developed (Liu et al., 2015). The nanosensor exhibited an excellent SERS/FL response to the complementary strand of the G-quadruplex. Based on T-Hg^{2+}-T coordination chemistry, the sensor can be used to detect Hg^{2+} at an LOD as low as 1 ppt. Zou et al. (Zou et al., 2015) used graphene quantum dot tags to design a new dual-mode immunoassay method based on SERS and FL to detect tuberculosis through a newly developed linear comparison sensing platform for the antigen CFP-10. The sandwich-type immunoassay uses a dual-mode nanoprobe to recognize SERS signals and FL images in a highly sensitive and selective manner with an LOD of 0.0511 pg/ml. However, there have been few reports on tri-mode methods with the nanocatalytic amplification of signals. For example, Li et al. (Li et al., 2018b) reported the colorimetric/FL/SERS tri-mode sensing of nitrite based on a Griess-reaction-modulated gold nanorod–Azo–nanogold assembly. Colorimetric and FL detection were carried out in solution, whereas SERS was performed on a solid substrate, achieving LODs of 0.05, 0.01, and 0.0008 μM by their respective methods.

The gold nanoparticle-TMB-H_2O_2 (TMB = 3,3′,5,5′-tetramethylbenzidine) system can be used as an ultrasensitive colorimetric pH indicator, with the gold nanoparticles acting as a catalyst to mimic the function of horseradish peroxidase (Deng et al., 2016). In this catalytic reaction, the absorbance of the yellow product at 450 nm remained linear in the pH range of 6.40–6.60, and the LOD of urea was 5 μM. A nanoparticle-based urea FL sensing scheme has also been reported (Shao et al., 2015). Graphene quantum dots displayed pH-sensitive green FL upon photoexcitation at 460 nm, and urease-catalyzed urea hydrolysis led to a local increase in pH and gradual FL quenching. This approach can be used to quantify urea in the concentration range of 0.1–100 mM with an LOD of 0.01 mM. SnO_2 quantum dot/reduced graphene oxide composites were used to prepare enzyme-free ultrasensitive urea sensors (Dutta et al., 2014). These SnO_2 quantum dots can be modified on the reduced graphene oxide layer, and urea can be detected by evaluating the sensor characteristics. The electrode prepared with the composite was sensitive to urea in a concentration range of 1.6×10^{-14}–3.9×10^{-12} M with an LOD of 11.7 mM. SERS

technology is a highly sensitive detection technology, and its signal enhancement mainly depends on the probe molecule and substrates. The structure and small scattering cross-section of urea molecules cannot directly produce SERS signals on gold or silver substrates. Therefore, urea molecules are ineffective as probe molecules. In this study, we developed an indirect method to detect ultra-trace urea. We found that CD_{FeN} catalyzes the oxidation of TMB to form TMB_{ox}, an effective SERS probe. Furthermore, urea Apt can inhibit the catalysis of CD_{FeN} and simultaneously reduce its FL. The prepared CD_{FeN} was used to catalyze the formation of TMB_{ox} from H_2O_2-TMB, from which a novel, highly sensitive, and selective Apt reaction turn-on SERS/RRS/FL tri-mode analytical platform was developed for the detection of ultra-trace small organic molecules, as demonstrated herein with urea.

MATERIALS AND METHODS

Instruments and Reagents

Instruments

A Hitachi F-7000 FL spectrophotometer (Hitachi High-tech), TU-1901 dual-beam ultraviolet-visible spectrophotometer (Beijing General Analysis General Instruments), and DXR smart Raman spectrometer (Thermo, United States) with an excitation wavelength of 633 nm, laser power of 3.5 mW, slit width of 50 μm, and acquisition time of 5 s were used to measure the CD system signals. The following were used to synthesize and characterize the CD systems: a desktop centrifuge (Zhuhai Heima Medical Instrument); ultrasonic cleaner (Shanghai Kedao Ultrasonic Instrument); SYZ-550 quartz sub-boiling distilled water device (Jiangsu Crystal Glass Instrument Factory); 79-1 magnetic heating stirrer (Jiangsu Zhongda Instrument Factory); HH-S2 electric heating thermostatic water bath (Jintan Dadi Automation Instrument Factory); KP-216 air energy light wave furnace (Zhongshan Qiaokang Electric Manufacturing, rated power 1200 W); pH meter (Mettler-Toledo Instruments Shanghai); Nano-2s nanometer particle size and zeta potential analyzer (Malvern, United Kingdom); and an S-4800 field emission scanning electron microscope (SEM; Hitachi Hi-tech).

Reagents

Urea ssDNA Apt (Apt_{urea}) with the sequence 5′-3′ CAC AAG CAC AGA CAG CTG TTC CAC AT was acquired from Shanghai Biotech Biological, Shanghai, China. Ammonium ferric citrate (Sinopharm Group Chemical Reagent, Shanghai, China), 30% H_2O_2 (10^5 times dilution, Shanghai Chemical Reagent, Shanghai, China), 0.1 mol/L HCl, 0.1 mol/L Tris solution, 5.05 mmol/L pH 4.4 Tris-HCl (concentration based on the amount of HCl: 500 μL of 0.1 mol/L Tris and 505 μL of 0.1 mol/L HCl were prepared in 10 ml of ultra-pure water), and 0.5 mmol/L TMB (storage: 2–8°C, T818493-5 g, CAS: 54827-17-7, Shanghai McLean Biochemical Technology, Shanghai, China) were employed for synthesis and analyses. TMB (0.012 g) was weighed and dissolved in 100 ml of an ethanol solution (ethanol: water = 1:1) to obtain the stock solution. Water (44 ml) was added to an Erlenmeyer flask and combined with 2 ml of 10 mmol/L $AgNO_3$, 2.0 ml of 100 mm/L trisodium citrate, 600 μL of 30% H_2O_2, and 600 μL of 0.1 mol/L $NaBH_4$ added sequentially under stirring until the color turned blue. AgNPs were added to the analysis system as an SERS enhancement substrate. Without the addition of AgNPs, the system could generate very weak Raman signals. The prepared blue AgNP gel was then immediately transferred into a light-wave oven and heated at 250°C for 10 min to obtain an orange-red transparent AgNP gel. After cooling naturally, water was added to the product to obtain a total volume of 50 ml at a concentration of 4.0×10^{-4} mol/L AgNPs. All reagents were analytical grade, and all experiments employed secondary distilled water.

Preparation of CD_{Fe} and CD_{FeN}

Ferric citrate or ammonium ferric citrate powder (0.02 g) was accurately weighed and dissolved in 30 ml of ultra-pure water. The dark yellow solution was then transferred to a polytetrafluoroethylene-based autoclave. After sealing, a hydrothermal reaction was performed in a muffle furnace at the optimal temperature of 180°C for 3 h. After the reaction was complete, ice water was used to cool the product to room temperature to obtain a brown solution. The brown-yellow solution was centrifuged at 10000 rpm for 10 min to remove the precipitate, and the supernatant was dialyzed against a dialysis bag with a molecular weight cutoff of 3,500 Da for 12 h to obtain 0.67 mg/ml CD_{Fe} or CD_{FeN}, which was diluted for further use.

Optimization and Characterization of CDs

CD synthesis was optimized based on the product FL intensity. As shown in **Supplementary Figure S1**, FL was the strongest when the reaction was performed at 180°C for 30 min. The amount of precursor was selected according to the strength of the catalytic effect of the CDs. Generally, the amount corresponding to the maximum CD concentration and the maximum slope of the FL intensity curve of the TMB oxidation product were selected. The experimental results indicated that 0.02 g of ammonium ferric citrate yielded CDs with the best catalytic effect. Compared with reported procedures for the preparation of CD_{Fe} (**Supplementary Table S1**) (Faraji et al., 2018; Yue et al., 2019; Zhang et al., 2019; Yadav et al., 2020), our procedure is simpler and requires a shorter hydrothermal reaction time. In addition, only one reagent, ammonium ferric citrate, was used to prepare CD_{FeN}.

Five molecular techniques were used to characterize the CDs. The FL intensity of different CD_{Fe} concentrations in a Tris-HCl buffer solution was measured. Under the conditions of voltage = 500 V, excitation slit = emission slit = 10 nm, and λ_{ex} = 305 nm, the system generated a FL peak at 420 nm. With increasing CD_{Fe} concentration, the FL intensity gradually increased (**Supplementary Figure S2A**). The FL intensity of the CD_{FeN}-Tris-HCl system at different concentrations was measured. The system generated an FL peak at 420 nm, which increased gradually in intensity with increasing CD_{FeN} concentration (**Supplementary Figure S2B**). The CD_{FeN} FL was stronger than that of CD_{Fe} due to the doped N element. The RRS intensity of the CD_{Fe}/CD_{FeN}-Tris-HCl system with different concentrations was measured. Under the conditions of voltage = 350 V and excitation slit = emission slit = 5 nm, the system produced a strong RRS peak at 375 nm, the intensity of which

gradually increased with CD_{Fe}/CD_{FeN} concentration (**Supplementary Figures S2C,D**). The CD_{FeN} RRS was stronger than that of CD_{Fe} due to the resonance between the large π-bond electrons and doped Fe electrons of the CDs. The UV-vis absorbance intensity of the CD_{FeN}/CD_{Fe}-Tris-HCl system was measured. As the concentration of CD_{FeN}/CD_{Fe} increased, an absorption peak appeared at 320 nm (**Supplementary Figures S2E,F**). The absorbance of both CDs was similar due to the low sensitivity of the spectrophotometric method.

A 0.025 g/ml CD_{Fe} solution (10 ml) was placed in a material tray, pre-frozen in a vacuum drying freezer cold trap for 5 h, and dried at 0.1 Pa for 24 h. The obtained solid sample and the precursor materials (ferrocene powder A, ferric ammonium citrate powder, and potassium bromide) were mixed in equal amounts and ground uniformly in an agate mortar to prepare powder tablets for infrared spectral analysis. The infrared spectra of ammonium ferric citrate (**Supplementary Figures S2G**) contained strong peaks at 3,189 cm^{-1} (O-H stretching); 1,616 cm^{-1} (C=C conjugate stretching); 1,394 cm^{-1} (CO_2^- symmetric stretching); 1,250 and 1,066 cm^{-1} (C-O stretching); and 909, 851, and 642 cm^{-1} (C=C-H bending). The infrared spectra of CD_{FeN} (**Supplementary Figure S2H**) contained strong peaks at 3,411 cm^{-1} (O-H telescopic vibration); 1,617 cm^{-1} (C=C conjugate telescopic vibration), 1,384 cm^{-1} (CO_2^- symmetric telescopic vibration), 1,049 cm^{-1} (C-O telescopic vibration), 560 cm^{-1} (C-H out-of-plane bending), and 470 cm^{-1} (C=C-H bending). The infrared spectra of the CDs and the corresponding precursors were significantly different. The infrared peak at 3,411 cm^{-1} (O-H stretching vibration) indicated the presence of hydroxyl groups in the CDs, confirming that the precursor material was successfully modified and had good water dispersion. Raman spectra of both the CD_{FeN} and CD_{Fe} solutions were examined, and no Raman peaks were observed. Using AgNPs in solution as a SERS substrate, weak SERS peaks were recorded (as shown in **Supplementary Figures 2SI,J**) at 1,160 and 1,620 cm^{-1} for CD_{FeN} and 1,620 cm^{-1} for CD_{Fe}.

Experimental Procedures

In a 5 ml stoppered graduated test tube, 200 μL of a 0.67 μg/ml $CD_{Fe/N}$ solution, 100 μL of a 0.1 mmol/L H_2O_2 solution, 100 μL of a 0.5 mmol/L TMB solution, 250 μL of a 5.05 mmol/L pH 4.07 Tris-HCl solution, 200 μL of a 0.1 μmol/L Apt solution, and an appropriate amount of a urea solution were added sequentially. Water was then added to obtain a final volume of 1.5 ml. The reaction was performed at 50°C in a water bath for 30 min and then terminated by placing it in an ice water bath. Subsequently, 400 μL of a 0.4 mmol/L AgNP solution and then water was added to reach a total volume of 2 ml. Finally, the SERS and FL/RRS spectra were acquired using a Raman spectrometer and FL spectrophotometer, respectively.

RESULTS AND DISCUSSION

Methodology

In the Tris-HCl buffer solution, the H_2O_2-TMB reaction was slow because the transfer of redox electrons is difficult between H_2O_2 and TMB. CD_{FeN} is rich in π-electrons and Fe metal electrons, which can enhance the redox electron transfer to effectively catalyze the formation of large π-bond TMB_{ox} in the H_2O_2-TMB system and generate a strong FL signal to turn on the FL indicator reaction. Apt_{urea} and the CDs form a complex morphology that suppresses the catalytic performance of the CDs, which thus reduces the system FL signal to turn off the indicator reaction. Based on the three-dimensional structure of Apt_{urea} and its flexibility, the spatial structure formed by the extension of the nucleic acid chain in solution affords a large contact area with urea, causing the CDs to change to a free state. This restores the catalytic activity to turn on the reaction, leading to an increase in the FL signal of the system. Within 3.33–20 nmol/L, the change in FL intensity displayed a linear relationship with urea concentration and TMB_{ox} exhibited good SERS activity on the AgNP substrates; the SERS signal of the system linearly increased within this concentration range. Thus, two FL and SERS analysis methods for urea were developed based on this CD_{FeN} catalytic amplification reaction. Because the formed TMB_{ox} results in AgNP aggregation, the RRS intensity also increased linearly with urea concentration. As a result, a simple, sensitive, Apt-mediated CD_{FeN} catalytic reaction with SERS, FL, and RRS tri-mode signals was established for the determination of urea (**Figure 1**).

SERS Analysis of CD-H_2O_2-TMB-Apt-Urea Nanocatalytic Systems

The SERS signal mainly arose from the TMB_{ox} molecule when AgNPs were added to the analysis system as a substrate. AgNPs were added as a uniformly dispersed colloidal system, and probe molecules could be homogeneously adsorbed on the surface of bare AgNPs to produce SERS. No SERS signal was observed when only AgNPs were employed. Although changes in the chemical environment may cause a shift in the position of the SERS peak (e.g., the presence of urea), the observed SERS peak in this study is that of TMB_{ox}. In a pH 4.07 Tris-HCl buffer solution at 50°C in a water bath, CD catalyzed the oxidation of TMB by H_2O_2, and the TMB_{ox} exhibited SERS activity. The addition of Apt_{urea} can wrap around the CDs, which inhibits their catalytic ability and reduces the formation of TMB_{ox} and the corresponding SERS intensity. When the target molecule urea was added, it specifically bound to the corresponding Apt_{urea} and released the CDs, restoring their catalytic activity. The Raman spectrum was obtained with a light source power of 2.5 mW and slit of 25.0 μm. The SERS intensity at 1,598 cm^{-1}, $I_{1598cm^{-1}}$, was measured, the blank value $(I_{1598cm^{-1}})_0$ without the urea solution was recorded, and $\Delta I_{1598cm^{-1}} = I_{1598cm^{-1}} - (I_{1598cm^{-1}})_0$ was calculated. When AgNPs were added, stronger Raman peaks at 1,284, 1,356, and 1,598 cm^{-1} appeared. The CD systems showed strong Raman peaks at 1,183, 1,328, and 1,598 cm^{-1}, and the SERS signal of the system increased linearly (**Figures 2A,B**).

FL Spectra of Nanocatalytic and Apt System

CDs are fluorescent nanomaterials, and in this study, the FL peak height at 405 nm was monitored instead of the peak area to approximate the FL intensity. This method is not very precise, but

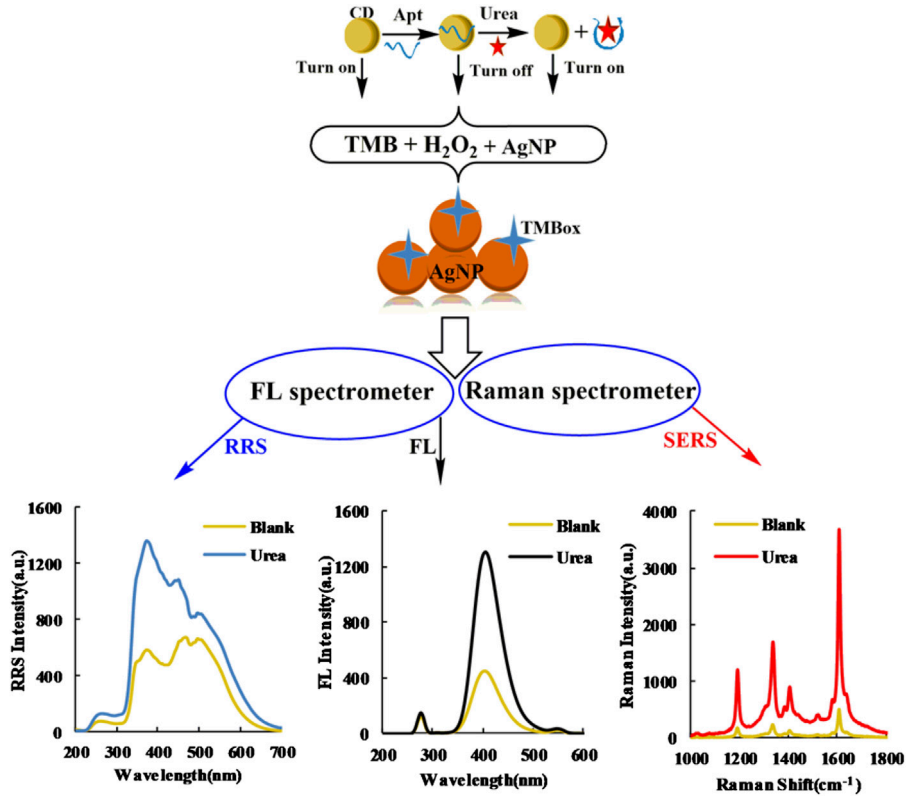

FIGURE 1 | Schematic of SERS/RRS/FL tri-mode method to detect ultra-trace urea coupling Apt_{urea} with CD_{FeN} catalysis.

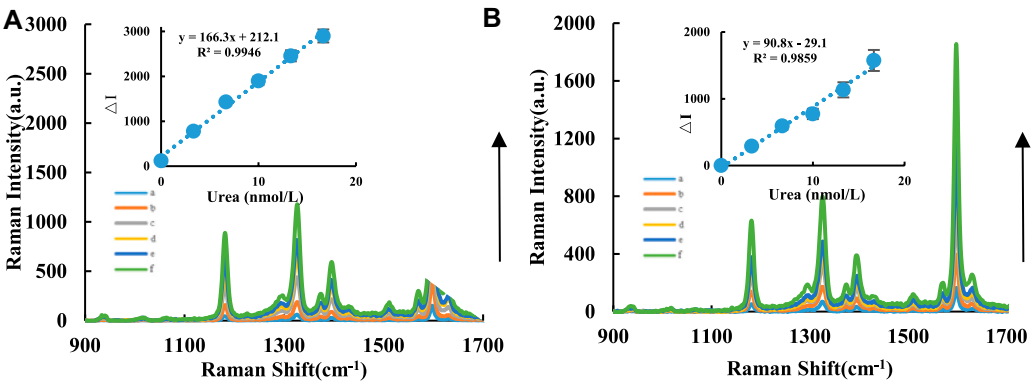

FIGURE 2 | SERS spectra of CD-H_2O_2-TMB-Apt-AgNP analysis system. A/B compared the catalytic effects between CD_{Fe} and CD_{FeN} in the urea analysis system. **(A)**: CD_{Fe}-H_2O_2-TMB-Tris-HCl-Apt-Urea-AgNPs system, a: 0.04 μg/ml CD_{Fe}+5.0 μmol/L H_2O_2+ 0.03 mmol/L TMB+0.51 mmol/L PH = 4.07 Tris-HCl+10 nmol/L Apt+ Urea+0.08 mmol/L AgNPs; b: a+3.33 nmol/L Urea; c: a+6.66 nmol/L Urea; d: a+9.99 nmol/L Urea; e: a+13.32 nmol/L Urea; f: a+16.65 nmol/L Urea. **(B)**: CD_{FeN}-H_2O_2-TMB-Tris-HCl-Apt-Urea-AgNPs system, a: 0.04 μg/ml CD_{FeN}+ 5.0 μmol/L H_2O_2+ 0.03 mmol/L TMB+ 0.51 mmol/L PH = 4.07 Tris-HCl+10 nmol/L Apt+ Urea+0.08 mmol/L AgNPs; b: a+3.33 nmol/L Urea; c: a+6.66 nmol/L Urea; d: a+9.99 nmol/L Urea; e: a+13.32 nmol/L Urea; f: a+16.65 nmol/L Urea.

the calculations are easy; this caused the problem related to the change in the slope of adjacent points at both ends of the linear range. For the CD-H_2O_2-TMB nanocatalytic system, within a 0.02 – 0.14 μg/ml CD concentration range, the FL intensity increased from CDs more strongly catalyzing the oxidation of TMB by H_2O_2 (**Supplementary Figures S3A,B**). For the Apt inhibition system CD-HCl-H_2O_2-TMB-Apt, the CDs are wrapped when Apt_{urea} is added, which inhibits the ability of the CDs to catalyze H_2O_2-TMB, reduces TMB_{ox} formation, and thus decreases the FL intensity. FL spectra of the CD-H_2O_2-TMB-Apt system were measured with voltage = 350 V and excitation slit = emission slit = 10 nm. With increasing Apt_{urea}

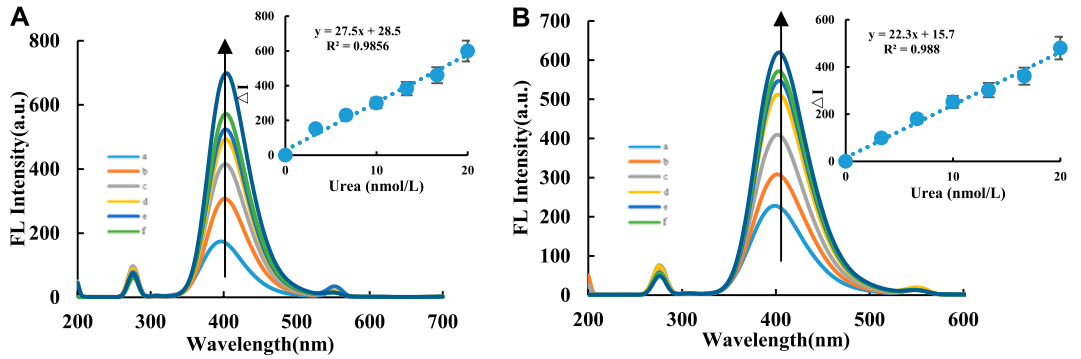

FIGURE 3 | FL spectra of CD-H_2O_2-TMB analysis system. Without H_2O_2-TMB probe, A/B compared the fluorescence between CD_{Fe} and CD_{FeN} in the urea analysis system. **(A)**: CD_{Fe}-H_2O_2-TMB-Tris-HCl-Apt-Urea system. a: 0.04 μg/ml CD_{Fe}+ 6.7 μmol/L H_2O_2+ 0.03 mmol/L TMB+ 0.84 mmol/L PH = 4.4 Tris-HCl+16.65 nmol/L Apt; b: a+3.33 nmol/L Urea; c: a+6.66 nmol/L Urea; d: a+9.99 nmol/L Urea; e: a+13.32 nmol/L Urea; f: a+16.65 nmol/L Urea; g: a+20 nmol/L Urea; **(B)**: CD_{FeN}-H_2O_2-TMB-Tris-HCl-Apt-Urea system, a: 0.04 μg/ml CD_{FeN}+6.7 μmol/L H_2O_2+0.03 mmol/L TMB+ 0.84 mmol/L PH = 4.4 Tris-HCl+16.65 nmol/L Apt; b: a+3.33 nmol/L Urea; c: a+6.66 nmol/L Urea; d: a+9.99 nmol/L Urea; e: a+13.32 nmol/L Urea; f: a+16.65 nmol/L Urea; g: a+20 nmol/L Urea.

concentration, the FL intensity of the system gradually and linearly weakened (**Supplementary Figures S3C,D**). For the FL intensity of the CD_{Fe}-Apt system, the conditions of voltage = 500 V, excitation slit = emission slit = 10 nm, and λ_{ex} = 305 nm generated a FL peak at 395 nm. With increasing Apt_{urea} concentration, the FL intensity of the system gradually decreased. For the CD_{FeN}-Apt system, the conditions of voltage = 500 V, excitation slit = emission slit = 10 nm, and λ_{ex} = 310 nm generated a FL peak at 405 nm. With increasing Apt_{urea} concentration, the FL intensity of the system gradually decreased (**Supplementary Figures S3E,F**). Based on these results, Apt_{urea} can effectively wrap the CDs to linearly decrease the FL intensity of the system with increasing Apt_{urea} concentration, demonstrating the interaction between the CDs and Apt_{urea}, and the applicability of the CDs as FL probes to identify the interaction. For the CD-H_2O_2-TMB-Apt-Urea system, when the target molecule urea was added, urea and Apt_{urea} formed a stable conjugate and released the CDs, thus restoring their catalytic activity. As a result, the FL intensity of the system gradually increased. Under the conditions of voltage = 350 V, excitation slit = emission slit = 10 nm, and λ_{ex} = 275 nm, the system generated a FL peak at 405 nm. Within 3.33 – 20 nmol/L, the FL intensity displayed a linear relationship with the urea concentration (**Figures 3A,B**).

RRS Analysis of Nanocatalyst and Apt System

RRS is a synchronous FL scanning technology where the excitation light wavelength is equal to the emission light wavelength ($\Delta\lambda = \lambda_{em} - \lambda_{ex} = 0$). The signal intensity mainly originates from the scattering of excitation light by nanoparticles. The degree of aggregation of particles in the system and changes in particle size cause signal changes. For the CD_{Fe}/CD_{FeN}-Apt system, under the conditions of voltage = 400 V and excitation slit = emission slit = 5 nm, RRS peaks appeared at 370, 380 and 385 nm. The RRS intensity of the system gradually decreased with increasing Apt_{urea} concentration (**Supplementary Figures S4A,B**). Therefore, Apt_{urea} can effectively wrap the CDs to linearly decrease the RRS intensity of the system with increasing Apt concentration. In the absence of AgNPs, the CD-H_2O_2-TMB catalytic reaction of the system occurs, but the nanocatalyst CD concentration was low and the TMB concentration was very low (0.03 mmol/L). Thus, the TMB_{ox} molecules produced were low with a very weak RRS signal, resulting in weak overall RRS spectral intensities of the system. However, the CD-H_2O_2-TMB-AgNP system generated a strong RRS peak at 380 nm since the produced TMB_{ox} resulted in AgNP aggregation (Yao et al., 2019). As the CD concentration increased, the RRS intensity of the system gradually increased (**Supplementary Figures S4C,D**). For the CD-H_2O_2-TMB-Apt-Urea system, when the target molecule urea was added, urea and Apt_{urea} formed a stable conjugate and released the CDs. This restored the CD catalytic activity, causing the RRS intensity of the system to gradually increase. Under the conditions of voltage = 350 V and excitation slit = emission slit = 5 nm, the CD-H_2O_2-TMB-Apt-Urea system produced a scattering peak at 370 nm. Within 2.5–12.5 nmol/L, the RRS intensity had a linear relationship with urea concentration (**Figures 4A,B**).

SEM and Laser Scattering of the System

SEM samples were prepared by dropping a small aliquot of each sample on the surface of a dried silicon wafer and allowing it to dry naturally. The average particle size of CD_{Fe} was approximately 50 nm (**Figure 5A**), and that of CD_{FeN} was approximately 30 nm (**Figure 5B**). CD_{Fe} and CD_{FeN} exhibited spectral peaks at 0.2, 5.2, and 5.5 keV corresponding to elemental Fe (**Figure 5C, 5D**); CD_{FeN} also showed a weak peak at 0.45 keV corresponding to N. Due to the presence of N, the CDs exhibited excellent catalytic activity. When no urea was added, the Apt_{urea} in the system wrapped the CD_{FeN}, thereby inhibiting CD_{FeN} from catalyzing the oxidation of TMB by H_2O_2. As a result, fewer TMB_{ox} fluorescent probes were formed, and the extent of aggregation was low after adding AgNPs (aggregate size of 50 nm, **Figure 5E**). Upon addition of urea, CD_{FeN} encapsulation decreased, and the catalytic effect of the system

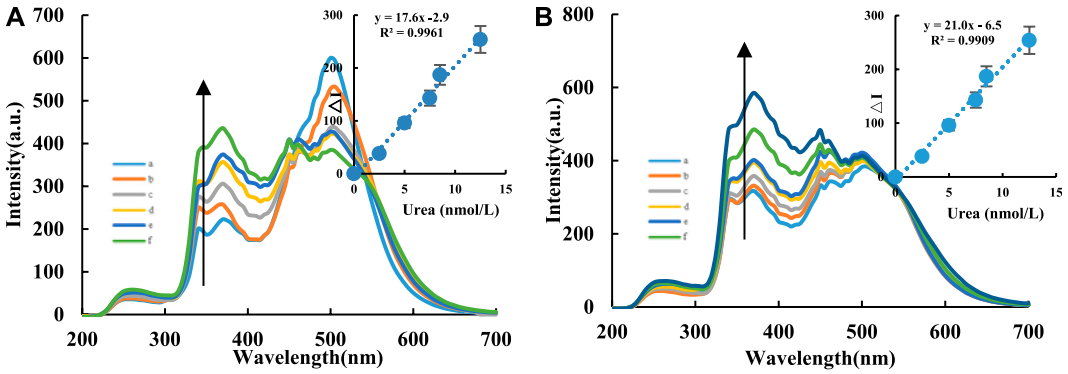

FIGURE 4 | RRS spectra of CD-Tris-HCl-Apt analysis system. A/B compared the RRS analysis system of urea using CD_{Fe} and CD_{FeN}, respectively. **(A)**: CD_{Fe}-H_2O_2-TMB-Tris-HCl-Apt-Urea-AgNPs system, a: 0.04 μg/ml CD_{Fe} + 6.7 μmol/L H_2O_2+ 0.03 mmol/L TMB+ 0.84 mmol/L PH = 4.4 Tris-HCl+16.65 nmol/L Apt+0.08 mmol/L AgNPs; b: a+2.5 nmol/L Urea; c: a+5 nmol/L Urea; d: a+7.5 nmol/L Urea; e: a+8.5 nmol/L Urea; f: a+12.5 nmol/L Urea. **(B)**: CD_{FeN}-H_2O_2-TMB-Tris-HCl-Apt-Urea-AgNPs system, a:0.04 μg/ml CD_{FeN} + 6.7 μmol/L H_2O_2+ 0.03 mmol/L TMB+ 0.84 mmol/L PH = 4.4 Tris-HCl+16.65 nmol/L Apt+0.08 mmol/L AgNPs; b: a+2.5 nmol/L Urea; c: a+5 nmol/L Urea; d: a+6 nmol/L Urea; e: a+7.5 nmol/L Urea; f: a+10 nmol/L Urea; g: a+12.5 nmol/L Urea.

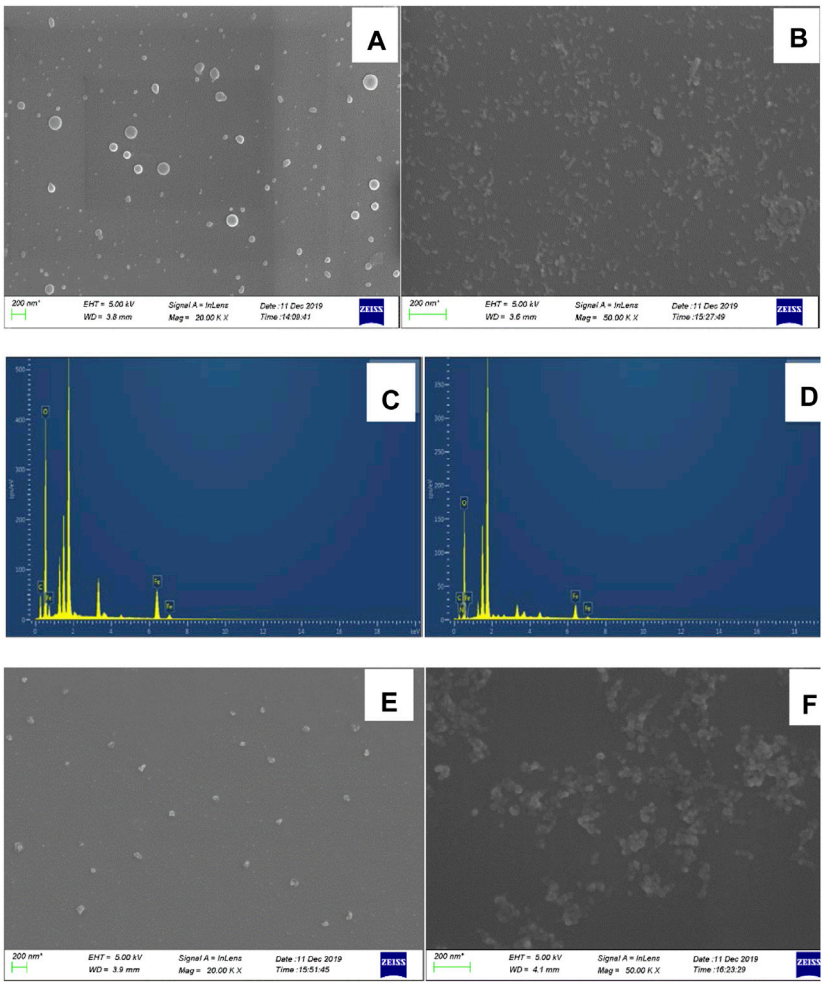

FIGURE 5 | SEM and energy spectra images of analysis system. **(A)**: SEM of CD_{Fe}; **(B)**: SEM of CD_{FeN}; **(C)**: energy spectrum of CD_{Fe}; **(D)**: energy spectrum of CD_{FeN}; **(E)**: Analysis system without urea, 0.08 μg/ml CD_{FeN}+ 5.0 μmol/L H_2O_2+ 0.03 mmol/L TMB+ 0.51 mmol/L pH 4.07 Tris-HCl+10 nmol/L Apt+0.08 mmol/L AgNPs; **(F)**: Analysis system with urea. E+12.5 nmol/L Urea.

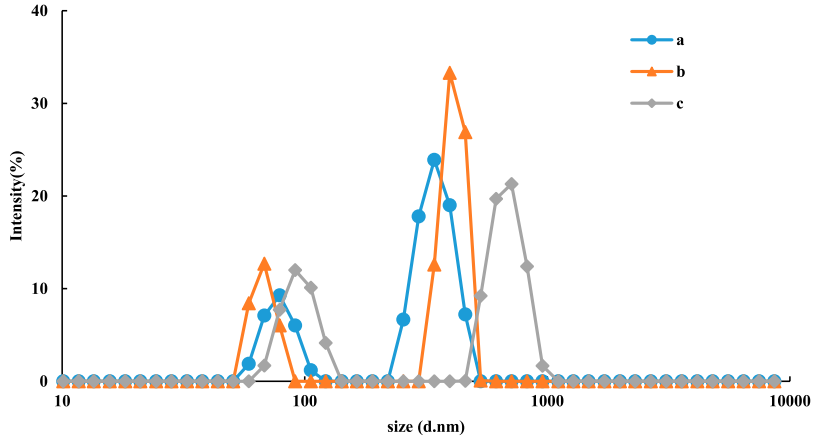

FIGURE 6 | Particle size distribution of CD_{FeN}-H_2O_2-TMB-Tris-HCl-Apt-Urea-AgNPs system. a: 0.08 μg/ml CDFeN+ 5.0 μmol/L H_2O_2+ 0.03 mmol/L TMB+ 0.51 mmol/L Tris-HCl (PH = 4.07)+10 nmol/L Apt+ Urea+0.08 mmol/LAgNPs; b: a+5.0 nmol/L Urea; c: a+12.5 nmol/L Urea.

TABLE 1 | The tri-mode analytical platform for assay of urea.

System	Methods	LR (nmol/L)	Regression equation	Coefficient	DL (nmol/L)
CD_{Fe}-Urea	FL	3.33–20	$\Delta F_{405\ nm}$ = 27.5C + 28.5	0.9856	1.4
	SERS	3.33–16.65	$\Delta I_{1598\ cm^{-1}}$ = 166.3C + 221.1	0.9946	1.3
	RRS	2.5–12.5	$\Delta I_{370\ nm}$ = 17.6C–2.9	0.9939	1.6
CD_{FeN}-Urea	FL	3.33–20	$\Delta F_{405\ nm}$ = 22.3C + 15.7	0.9880	1.0
	SERS	1.1–16.65	$\Delta I_{1598\ cm^{-1}}$ = 90.8C + 29.1	0.9895	0.06
	RRS	2.5–12.5	$\Delta I_{370\ nm}$ = 21.0C–6.5	0.9909	1.71

was restored. As a result, the number of TMB_{ox} fluorescent probes formed gradually increased, and the extent of AgNPs-TMB_{ox} aggregation increased in the system to reach a size of 70 nm (**Figure 5F**), resulting in a linear increase in RRS intensity.

Particle size analysis was used to determine the particle size distribution of the nanoparticles in the system. With increasing urea concentration, the target molecule urea and Apt_{urea} formed a stable conjugate and released the CDs, which restored their catalytic activity. Therefore, the product TMB_{ox} gradually increased along with TMB_{ox}-AgNP aggregation. The particle sizes of the reaction product of the CD_{FeN}-H_2O_2-TMB-Apt-Urea-AgNP system were 98, 110, and 130 nm, respectively (**Figure 6**), due to aggregation in the system.

Optimization of Analysis Conditions

The effect of the experimental parameters on the SERS and FL signal intensities was systematically examined. As shown in **Supplementary Figure S5** and in accordance with the experiments described in Section *Optimization and Characterization of CDs* containing 0.1 nmol/L urea, the use of a 0.51 mmol/L pH 4.07 Tris-HCl solution and 0.03 mmol/L TMB resulted in the strongest SERS signal. For the FL intensity, the optimized parameters were 5.0 μmol/L H_2O_2, 10 nmol/L Apt_{urea}, 0.07 μg/ml CDs, 0.08 mmol/L AgNPs, a water bath temperature of 50°C, and a reaction time of 35 min.

Working Curve

In this study, the FL, SERS, and RRS spectra of the CD-H_2O_2-TMB-Apt-Urea system were measured (**Table 1**). For the H_2O_2-TMB reaction, the catalytic effects of the two CDs (CD_{Fe} and CD_{FeN}) were studied. The slope of the working curve corresponds to the catalytic ability of the CDs. The slope *K* of the working curve of the CD_{FeN}-H_2O_2-TMB-Apt-Urea system was larger than that of the CD_{Fe} system, indicating that the former can be used for the FL detection of urea with a linear range of 3.33– 20 nmol/L and LOD of 1.0 nmol/L. Similar to FL, the SERS and RRS methods using the CD_{FeN} system were more sensitive than CD_{Fe} according to the evaluated slopes. Of the three modes, FL is simplest, as it does not require the addition of AgNPs, whereas SERS is the most sensitive. Compared with other reported urea analysis methods (**Table 2**) (Liu et al., 2010; Kumar et al., 2015; Chen et al., 2017a; Momenzadeh and Azadbakht, 2017; Mansouri and Azadbakht, 2019; Yarahmadi et al., 2019), this SERS method is more accurate and precise.

Effects of Interfering Ions

The interference of coexisting ions on 10 nmol/L urea in the system was studied by RRS. The results indicated that 10 μmol/L K^+, Cr^{6+}, NH_4^+, Zn^{2+}, SiO_3^{2-}, Mg^{2+}, CO_3^{2-}, I^-, Ca^{2+}, and SO_4^{2-}; 5 μmol/L Al^{3+}, Mn^{2+}, Ba^{2+}, Hg^{2+}, Cu^{2+}, and HSA; and 2 μmol/L Co^{2+}, Fe^{2+}, NO_2^-, Fe^{3+}, Br^-, Cr^{3+}, and BSA did not interfere with the measurement. The interference of coexisting ions on 10 nmol/

TABLE 2 | Comparison of reported Urea analysis methods.

Method	Analysis principle	Linear range	Detection limit	Analysis characteristics	RSD (%)	Ref.
FL	The urea-specific DNA aptamer was isolated by an exponential enrichment method. In terms of inherent fluorescence differences and color changes, the aptamer sensor used unmodified gold nanoparticles (AuNP) to transduce the signal of aptamer-urea binding, thereby showed high selectivity to urea.	20–150 mM	20 mM	Simple operation and low sensitivity	—	36
Electrochemical	A mixture of carbon nanotubes and platinum nanoparticle-reduced graphene oxide (rGO) was used to surface modify the glassy carbon electrode (GCE). The urea aptamer was then immobilized on the nanocomposite by covalent bonding. Thus, aptamers with high affinity and selectivity for urea were used to quantify urea.	0.0–0.1 nM, 1.0–150 nM	1.9 pM	Complex operation and expensive equipment	7.9%	37
Electrochemical	Molecularly imprinted polymers (MIPs) also contained DNA aptamers on gold nanoparticles containing carbon nanotube networks (AuNP/CNT). The material was placed on a glass-carbon electrode (GCE), and GCE showed double recognition ability after removing urea from the MIP cavity. After the modified electrode was exposed to urea, the interface charge transfer of the redox probe hexacyanoferrate was measured under certain conditions. The change of the charge transfer resistance depended on the urea concentration, so the urea can be detected with high specificity.	0.005–0.1 nM, 1–500 nM	900 fM	Complex operation and high sensitivity	5.5%	38
Electrochemical	The primary amine was functionalized GO by a one-pot solvothermal method using ethylene glycol as the solvent and ammonia as the nitrogen precursor. Based on the signal amplification of carbon nanotubes/amine-functionalized GO as a sensing platform, and Apt as a probe, the label-free electrochemical analysis of urea was performed.	1–30 nM, 100–2000 nM	370 pM	Complex operation and high sensitivity	6.7–11.5%	39
SERS	The substrate made from Au/Cu hybrid nanostructure arrays was used to detect urea. Adjusting the gap size between adjacent nanorods to a sub-10 nm range produced high-density hot spots, which enables the substrate to detect urea signals at low concentrations.	—	1 mM	Simple operation and low sensitivity	9.5%	34
SERS-FL	Apt mediated the CD_{FeN} catalyzed H_2O_2 oxidation of TMB to form trifunctional probes of TMBox. The FL/SERS/Abs signals had a linear relationship with the concentration of Urea.	Flu:3.33–13.32 nmol/L; SERS:3.33–16.65 nnmol/L	1.12 nmol/L,1 nmol/L	Simple operation and high sensitivity	1.45–5.32%	This method

L urea in the system was then investigated by the SERS method. Similarly, the results showed that 10 μmol/L Ba^{2+}, K^{+}, Cr^{6+}, NH_4^{+}, Zn^{2+}, SiO_3^{2-}, Mg^{2+}, Hg^{2+}, CO_3^{2-}, I^{-}, and Ca^{2+}; 5 μg/L Al^{3+}, Co^{2+}, Mn^{2+}, Cu^{2+}, HSA, and SO_4^{2-}; and 2 μmol/L Fe^{2+}, NO_2^{-}, Fe^{3+}, Br^{-}, Cr^{3+}, and BSA did not interfere with the measurement. The interference of coexisting ions on 10 nmol/L urea in the system was studied by FL. The results indicated that 10 μmol/L K^{+}, NH_4^{+}, Zn^{2+}, SiO_3^{2-}, SO_4^{2-}, Mg^{2+}, CO_3^{2-}, and Ca^{2+}; 5 μmol/L Al^{3+}, Mn^{2+}, Fe^{2+}, Ba^{2+}, Hg^{2+}, Cu^{2+} and NO_2^{-}; and 2 μmol/L Co^{2+}, Br^{-}, I^{-}, Cr^{3+}, HSA, and BSA did not interfere with the measurement. Therefore, our method has good selectivity.

Real Sample Determination

Urea content determination plays an important role in the dairy industry, as its content in milk and dairy products should be less than 0.70 mg/g (Kumar et al., 2015). If the urea content in milk powder exceeds the normal range, consumption can lead to certain health problems. Thus, we detected the urea content in milk samples using our new method. Five milk samples were purchased from a supermarket and treated to obtain sample solutions according to an established method (Liang et al., 2019). The samples were then analyzed by the proposed method (the results are shown in **Supplementary Table S2**). The recovery rates were in the range of 96.4–106%, and the results of the

proposed method for the determination of urea from milk samples were in agreement with the spectrophotometric method.

CONCLUSION

In this study, a single reagent was used as a precursor to synthesize stable Fe/N-doped CDs (CD_{FeN}) by a hydrothermal procedure. The molecular and spectral characteristics of the CD_{FeN} and their catalytic effect on the reaction of H_2O_2 and TMB were studied in detail using SERS, RRS, FL, and UV-vis absorption spectra. Apt_{urea} can adsorb onto the surface of the CD_{FeN} to turn off the nanocatalytic tri-mode indicator reaction. When the target molecule urea is added, Apt_{urea} releases the CD_{FeN} due to its specific binding, thereby restoring the CD_{FeN} catalytic activity to turn on the indicator reaction. With increasing urea concentration, the change in SERS/RRS/FL signals were linear, which establishes our method as a highly sensitive Apt-mediated, doped-CD, catalytic amplification, tri-spectroscopic platform.

DATA AVAILABILITY STATEMENT

The original contributions presented in the study are included in the article/**Supplementary Material**, further inquiries can be directed to the corresponding authors.

AUTHOR CONTRIBUTIONS

The manuscript was written through contributions by all authors. JL and CL contributed equally to this article.

FUNDING

This work was supported by the National Natural Science Foundation of China (No. 21767004).

SUPPLEMENTARY MATERIAL

The Supplementary Material for this article can be found online at: https://www.frontiersin.org/articles/10.3389/fchem.2021.613083/full#supplementary-material.

REFERENCES

Chen, K., Zhang, X., and MacFarlane, D. R. (2017a). Ultrasensitive surface-enhanced Raman scattering detection of urea by highly ordered Au/Cu hybrid nanostructure arrays. *Chem. Commun.* 53, 7949–7952. doi:10.1039/C7CC03523C

Chen, Y., Li, X., Yang, M., Yang, L., Han, X., Jiang, X., et al. (2017b). High sensitive detection of penicillin G residues in milk by surface-enhanced Raman scattering. *Talanta* 167, 236–241. doi:10.1016/j.talanta.2017.02.022

Deng, H., Hong, G., Lin, F., Liu, A., Xia, X., and Chen, W. (2016). Colorimetric detection of urea, urease, and urease inhibitor based on the peroxidase-like activity of gold nanoparticles. *Analytica Chim. Acta* 915, 74–80. doi:10.1016/j.aca.2016.02.008

Deng, R., Qu, H., Liang, L., Zhang, J., Zhang, B., Huang, D., et al. (2017). Tracing the therapeutic process of targeted aptamer/drug conjugate on cancer cells by surface-enhanced Raman scattering spectroscopy. *Anal. Chem.* 89, 2844–2851. doi:10.1021/acs.analchem.6b03971

Dervisevic, M., Dervisevic, E., and Şenel, M. (2018). Design of amperometric urea biosensor based on self-assembled monolayer of cystamine/PAMAM-grafted MWCNT/Urease. *Sensors Actuators B: Chem.* 254, 93–101. doi:10.1016/j.snb.2017.06.161

Dutta, D., Chandra, S., Swain, A. K., and Bahadur, D. (2014). SnO2 quantum dots-reduced graphene oxide composite for enzyme-free ultrasensitive electrochemical detection of urea. *Anal. Chem.* 86, 5914–5921. doi:10.1021/ac5007365

Faraji, M., Derakhshi, P., Tahvildari, K., and Yousefian, Z. (2018). High performance Fe and N-codoped graphene quantum dot supported Pd3Co catalyst with synergistically improved oxygen reduction activity and great methanol tolerance. *Solid State Sci.* 83, 152–160. doi:10.1016/j.solidstatesciences.2018.07.012

Karthikeyan, R., Nelson, D. J., and John, S. A. (2019). Non-enzymatic determination of purine nucleotides using a carbon dot modified glassy carbon electrode. *Anal. Methods* 11, 3866–3873. doi:10.1039/C9AY00718K

Kumar, P., Ramulu Lambadi, P., and Kumar Navani, N. (2015). Non-enzymatic detection of urea using unmodified gold nanoparticles based aptasensor. *Biosens. Bioelectron.* 72, 340–347. doi:10.1016/j.bios.2015.05.029

Li, C., Fan, P., Liang, A., Liu, Q., and Jiang, Z. (2018a). Aptamer based determination of Pb(II) by SERS and by exploiting the reduction of HAuCl4 by H2O2 as catalyzed by graphene oxide nanoribbons. *Microchim. Acta* 185, 177. doi:10.1007/s00604-018-2714-9

Li, D., Ma, Y., Duan, H., Deng, W., and Li, D. (2018b). Griess reaction-based paper strip for colorimetric/fluorescent/SERS triple sensing of nitrite. *Biosens. Bioelectron.* 99, 389–398. doi:10.1016/j.bios.2017.08.008

Li, Z., Liu, R., Xing, G., Wang, T., and Liu, S. (2017). A novel fluorometric and colorimetric sensor for iodide determination using DNA-templated gold/silver nanoclusters. *Biosens. Bioelectron.* 96, 44–48. doi:10.1016/j.bios.2017.01.005

Liang, A., Wang, H., Yao, D., and Jiang, Z. (2019). A simple and sensitive SERS quantitative analysis method for urea using the dimethylglyoxime product as molecular probes in nanosilver sol substrate. *Food Chem.* 271, 39–46. doi:10.1016/j.foodchem.2018.07.149

Liu, D.-Z., Chen, K., Ge, K., Me, L.-H., and Yao, S.-Z. (2010). Surface acoustic wave sensor system applied to the kinetic study of urease in plant seeds. *Chin. J. Chem.* 13, 231–240. doi:10.1002/cjoc.19950130307

Liu, G., Xuan, C., Feng, D., Hua, D., Liu, T., Qi, G., et al. (2017). Dual-modal fluorescence and light-scattering sensor based on water-soluble carbon dots for silver ions detection. *Anal. Methods* 9, 5611–5617. doi:10.1039/C7AY01873H

Liu, M., Wang, Z., Pan, L., Cui, Y., and Liu, Y. (2015). A SERS/fluorescence dual-mode nanosensor based on the human telomeric G-quadruplex DNA: application to mercury (II) detection. *Biosens. Bioelectron.* 69, 142–147. doi:10.1016/j.bios.2015.02.009

Mansouri, R., and Azadbakht, A. (2019). Aptamer-based approach as potential tools for construction the electrochemical aptasensor. *J. Inorg. Organomet. Polym.* 29, 517–527. doi:10.1007/s10904-018-1024-3

Migliorini, F. L., Sanfelice, R. C., Mercante, L. A., Andre, R. S., Mattoso, L. H. C., and Correa, D. S. (2018). Urea impedimetric biosensing using electrospun nanofibers modified with zinc oxide nanoparticles. *Appl. Surf. Sci.* 443, 18–23. doi:10.1016/j.apsusc.2018.02.168

Momenzadeh, H., and Azadbakht, A. (2017). A glassy carbon electrode modified with carbon nanotubes and reduced graphene oxide decorated with platinum-gold nanoparticles for voltammetric aptasensing of urea. *Microchim. Acta* 184, 4685–4694. doi:10.1007/s00604-017-2494-7

Rong, M., Liang, Y., Zhao, D., Chen, B., Pan, C., Deng, X., et al. (2018). A ratiometric fluorescence visual test paper for an anthrax biomarker based on

functionalized manganese-doped carbon dots. *Sensors Actuators B: Chem.* 265, 498–505. doi:10.1016/j.snb.2018.03.094

Safitri, E., Heng, L., Ahmad, M., and Ling, T. (2017). Fluorescence bioanalytical method for urea determination based on water soluble ZnS quantum dots. *Sensors Actuators B: Chem.* 240, 763–769. doi:10.1016/j.snb.2016.08.129

Shao, T., Zhang, P., Tang, L., Zhuo, S., and Zhu, C. (2015). Highly sensitive enzymatic determination of urea based on the pH-dependence of the fluorescence of graphene quantum dots. *Microchim. Acta* 182, 1431–1437. doi:10.1007/s00604-015-1469-9

Song, Y., Xu, G., Wei, F., Cen, Y., Sohail, M., Shi, M., et al. (2018). Aptamer-based fluorescent platform for ultrasensitive adenosine detection utilizing Fe3O4 magnetic nanoparticles and silver nanoparticles. *Microchim. Acta* 185, 139. doi:10.1007/s00604-018-2681-1

Sun, C., Su, R., Bie, J., Sun, H., Qiao, S., Ma, X., et al. (2018). Label-free fluorescent sensor based on aptamer and thiazole orange for the detection of tetracycline. *Dyes Pigm.* 149, 867–875. doi:10.1016/j.dyepig.2017.11.031

Wang, B., Chen, Y., Wu, Y., Weng, B., Liu, Y., and Li, C. M. (2016). Synthesis of nitrogen- and iron-containing carbon dots, and their application to colorimetric and fluorometric determination of dopamine. *Microchim. Acta* 183, 2491–2500. doi:10.1007/s00604-016-1885-5

Yadav, A. N., Bindra, J. K., Jakhar, N., and Singh, K. (2020). Switching-on superparamagnetism in diluted magnetic Fe(III) doped CdSe quantum dots. *CrystEngComm* 22, 1738–1745. doi:10.1039/C9CE01391A

Yang, W., Huang, T., Zhao, M., Luo, F., Weng, W., Wei, Q., et al. (2017). High peroxidase-like activity of iron and nitrogen co-doped carbon dots and its application in immunosorbent assay. *Talanta* 164, 1–6. doi:10.1016/j.talanta.2016.10.099

Yao, D., Li, C., Liang, A., and Jiang, Z. (2019). A facile SERS strategy for quantitative analysis of trace glucose coupling glucose oxidase and nanosilver catalytic oxidation of tetramethylbenzidine. *Spectrochimica Acta A: Mol. Biomol. Spectrosc.* 216, 146–153. doi:10.1016/j.saa.2019.03.026

Yarahmadi, S., Azadbakht, A., and Derikvand, R. M. (2019). Hybrid synthetic receptor composed of molecularly imprinted polydopamine and aptamers for impedimetric biosensing of urea. *Microchim. Acta* 186, 71. doi:10.1007/s00604-018-3180-0

You, L., Li, R., Dong, X., Wang, F., Guo, J., and Wang, C. (2017). Micron-sized surface enhanced Raman scattering reporter/fluorescence probe encoded colloidal microspheres for sensitive DNA detection. *J. Colloid. Interf. Sci.* 488, 109–117. doi:10.1016/j.jcis.2016.10.086

Yue, G., Li, S., Liu, W., Ding, F., Zou, P., Wang, X., et al. (2019). Ratiometric fluorescence based on silver clusters and N, Fe doped carbon dots for determination of H2O2 and UA: N, Fe doped carbon dots as mimetic peroxidase. *Sensors Actuators B: Chem.* 287, 408–415. doi:10.1016/j.snb.2019.02.060

Zhang, H., Zhang, B., Chen, A., and Qin, Y. (2017). Controllable n-Fe2O3@ graphene nanomaterials by ALD applied in an aptasensor with enhanced electrochemical performance for thrombin detection. *Dalton Trans.* 46, 7434–7440. doi:10.1039/C7DT01184A

Zhang, L., Liang, P., Man, X., Wang, D., Huang, J., Shu, H., et al. (2019). Fe, N co-doped graphene as a multi-functional anchor material for lithium-sulfur battery. *J. Phys. Chem. Sol.* 126, 280–286. doi:10.1016/j.jpcs.2018.11.027

Zheng, M., Wang, C., Wang, Y., Wei, W., Ma, S., Sun, X., et al. (2018). Green synthesis of carbon dots functionalized silver nanoparticles for the colorimetric detection of phoxim. *Talanta* 185, 309–315. doi:10.1016/j.talanta.2018.03.066

Zhou, J., and Rossi, J. (2017). Aptamers as targeted therapeutics: current potential and challenges. *Nat. Rev. Drug Discov.* 16, 181–202. doi:10.1038/nrd.2016.199

Zhu, D., Zhuo, S., Zhu, C., Zhang, P., and Shen, W. (2019). Synthesis of catalytically active peroxidase-like Fe-doped carbon dots and application in ratiometric fluorescence detection of hydrogen peroxide and glucose. *Anal. Methods* 11, 2663–2668. doi:10.1039/C9AY00342H

Zhu, Y., Li, W., Tan, S., and Chen, T. (2018). A label-free and functional fluorescent oligonucleotide probe based on a G-quadruplex molecular beacon for the detection of kanamycin. *Chem. Res. Chin. Univ.* 34, 541–545. doi:10.1007/s40242-018-7366-0

Zhu, Y., Wang, Y., Zhou, B., Yu, J., Peng, L.-L., Huang, Y., et al. (2017). A multifunctional fluorescent aptamer probe for highly sensitive and selective detection of cadmium(II). *Anal. Bioanal. Chem.* 409, 4951–4958. doi:10.1007/s00216-017-0436-1

Zhuo, S., Guan, Y., Li, H., Fang, J., Zhang, P., Du, J., et al. (2019). Facile fabrication of fluorescent Fe-doped carbon quantum dots for dopamine sensing and bioimaging application. *Analyst* 144, 656–662. doi:10.1039/C8AN01741G

Zou, F., Zhou, H., Tan, T. V., Kim, J., Koh, K., and Lee, J. (2015). Dual-mode SERS-fluorescence immunoassay using graphene quantum dot labeling on one-dimensional aligned magnetoplasmonic nanoparticles. *ACS Appl. Mater. Inter.* 7, 12168–12175. doi:10.1021/acsami.5b02523

Conflict of Interest: The authors declare that the research was conducted in the absence of any commercial or financial relationships that could be construed as a potential conflict of interest.

frontiers in Chemistry

REVIEW
published: 06 April 2021
doi: 10.3389/fchem.2021.624511

Speciation of Inorganic Compounds in Aquatic Systems Using Diffusive Gradients in Thin-Films: A Review

Josep Galceran[1], Yue Gao[2], Jaume Puy[1], Martine Leermakers[2], Carlos Rey-Castro[1], Chunyang Zhou[2] and Willy Baeyens[2]*

[1] Departament de Química, Universitat de Lleida and AGROTECNIO-CERCA, Lleida, Spain, [2] Analytical, Environmental and Geo-Chemistry Department, Vrije Universiteit Brussel, Brussels, Belgium

The speciation of trace metals in an aquatic system involves the determination of free ions, complexes (labile and non-labile), colloids, and the total dissolved concentration. In this paper, we review the integrated assessment of free ions and labile metal complexes using Diffusive Gradients in Thin-films (DGT), a dynamic speciation technique. The device consists of a diffusive hydrogel layer made of polyacrylamide, backed by a layer of resin (usually Chelex-100) for all trace metals except for Hg. The best results for Hg speciation are obtained with agarose as hydrogel and a thiol-based resin. The diffusive domain controls the diffusion flux of the metal ions and complexes to the resin, which strongly binds all free ions. By using DGT devices with different thicknesses of the diffusive or resin gels and exploiting expressions derived from kinetic models, one can determine the labile concentrations, mobilities, and labilities of different species of an element in an aquatic system. This procedure has been applied to the determination of the organic pool of trace metals in freshwaters or to the characterization of organic and inorganic complexes in sea waters. The concentrations that are obtained represent time-weighted averages (TWA) over the deployment period.

Keywords: trace metal speciation, DGT, diffusive domain, kinetic model, mobility, lability

OPEN ACCESS

Edited by:
Óscar Nieto Palmeiro, University of Vigo, Spain

Reviewed by:
Francesco Crea, University of Messina, Italy
Pawel Pohl, Wrocław University of Science and Technology, Poland

***Correspondence:**
Yue Gao
yue.gao@vub.be

Specialty section:
This article was submitted to Analytical Chemistry, a section of the journal Frontiers in Chemistry

Received: *31 October 2020*
Accepted: *02 March 2021*
Published: *06 April 2021*

Citation:
Galceran J, Gao Y, Puy J, Leermakers M, Rey-Castro C, Zhou C and Baeyens W (2021) Speciation of Inorganic Compounds in Aquatic Systems Using Diffusive Gradients in Thin-Films: A Review. Front. Chem. 9:624511. doi: 10.3389/fchem.2021.624511

INTRODUCTION

Trace elements occur in a variety of chemical forms in natural aquatic systems. The dynamics of these natural systems induce transfers from one chemical form into another one, so that the relative importance of each of these chemical forms changes with time. In the water column, phytoplankton blooms can produce high amounts of organic compounds that can bind to trace elements forming very strong complexes, but, in the sediments, diagenetic processes influence the distribution of the trace element species much more. The mineralization of organic matter and the corresponding reduction of a suite of electron acceptors control the exchange between the dissolved and solid phases.

The chemical forms which are most interesting to be studied in solution are the free ion, the kinetically labile (usually weakly bound) complexes, the non-labile (usually strongly bound) complexes, and the colloidal fraction. Several studies demonstrated that the free ion and some labile complexes are the most easily assimilated by organisms and, hence, they constitute the bioavailable fraction (Schintu et al., 2010; Sondergaard et al., 2014; Kim et al., 2016; Vannuci-Silva et al., 2017). In natural aquatic systems, the bioavailable fraction is also the toxic fraction, when the element is considered as toxic, or the micronutrient fraction, if the element is an essential element. We must

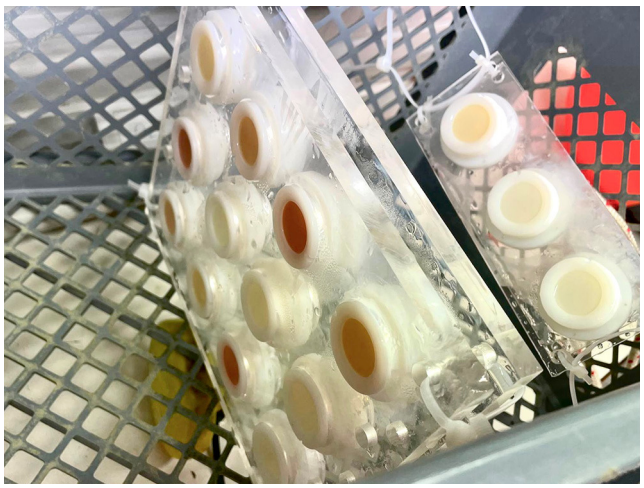

Graphical Abstract |

notice that some elements, such as Cu or Cd, may change from micronutrient at low concentration to a toxicant at higher concentrations.

It is, thus, clear that the total dissolved element concentration cannot be used to inform us about the bioavailable amount and, thus, neither about its risk for the ecosystem, if it is a toxic element, nor about the limitation of phytoplankton growth, if it is an essential element. Speciation techniques to distinguish between the various chemical forms of an element are, thus, definitely required. There exists no analytical technique that can measure all chemical forms of an element in solution, hence it is necessary to combine several methods to obtain a general picture. The free ion concentration is, for some elements, especially in open ocean water, extremely low. There are some techniques designed to specifically measure free concentrations like ISE, AGNES, and DMT although there are some restrictions related to the cations that can be analyzed, to the salinity range, or to the limit of detection (Bakker et al., 2000; Temminghoff et al., 2000; Galceran et al., 2004; Pesavento et al., 2009; Weng et al., 2011; Chito et al., 2012; Companys et al., 2017). Concentrations of labile complexes can be assessed using another set of techniques. Some of them, like ASV or SSCP (van Leeuwen and Town, 2003; Town and van Leeuwen, 2019; Cindric et al., 2020), are of voltammetric nature, but there is an increasing use of techniques based on membranes. These techniques involve the dissociation of the labile complexes followed by the non-reversible trapping of the released ions in a solid substrate such as a resin. The amount bound to the resin is afterwards measured with a specific element analyzer such as ICP-MS. An example of a technique that can pre-concentrate labile metal or metalloid complexes is the Diffusive Gradients in Thin-films (DGT) technique (Zhang and Davison, 1995). The labile fraction depends on the particular instrumental characteristics (van Leeuwen et al., 2005), since each technique defines an operational time window for the dissociation. Complexes that fit into this window are labile in this technique, but could be less labile in another one defining a shorter time scale. The direct determination of non-labile or strongly bound element complexes and colloids is more difficult. Since colloids have a size between 1 nm and 1 μm (compounds with a molecular weight of 300–500,000 Dalton), by using ultrafiltration membranes of appropriate pore sizes, one can distinguish between colloids of various dimensions (Waeles et al., 2008), nevertheless, such measurements are mostly very laborious. The concentrations of the colloidal fraction(s) can, then, be measured with a specific element analyzer, after mineralization of the colloidal particles.

Strongly bound element complexes, which are mainly complexes involving organic ligands, can be destroyed by intense UV-light in acidic conditions.

In freshwater, the total dissolved concentration can be directly measured with minor or no sample treatment, if a technique such as ICP-MS is used, but this is not possible when marine samples are involved. For marine samples, often a SeaFast pre-concentration technique (Wuttig et al., 2019) is applied to eliminate the salt matrix and to increase the low concentrations often encountered in seawater samples.

The direct measurement of natural, uncontaminated water samples is often not feasible for trace metals, which are typically present in very low concentrations close to the femtomolar (fmol L^{-1}, pg L^{-1}) range. An alternative is to use *ex-situ* pre-concentration techniques like Solid Phase Extraction (SPE) with ion-exchange resins (Pohl, 2006), which can even be coupled to fractionation schemes such as (ultra)filtration, in order to obtain information about different speciation pools. However, the use of *in-situ* pre-concentrating passive samplers like DGT represents an advantage in terms of minimization of contamination and perturbation of speciation due to sample transport and management in the lab.

In this paper, we will mainly focus on the bioavailable fraction of Cd, Co, Cu, Fe, Hg, Mn, Ni, Pb, and Zn in the water column of aquatic systems. This means that the concentration of the free ion plus that of the labile complexes will be addressed. A tool that responds to that requirement is the DGT technique, which consists of a hydrogel diffusive layer backed by a resin layer. The composition of the hydrogel and the resin will be adapted to the kind of chemical compound to be determined. The sampling of labile complexes (and sometimes free ions) of the different metals with DGT will be discussed in detail. In addition, different models that can provide information (about the meaning of c_{DGT} and about the lability and dissociation constants of element complexes) are presented.

DIFFUSIVE GRADIENT IN THIN-FILMS TECHNIQUE

The DGT is a passive sampling technique and is preferred to other passive sampling techniques because its result is, in many instances, independent from the flow conditions in the aquatic system, in particular the turbulence. Indeed, the diffusive gel and filter in front of the binding layer define a region where diffusion is the only transport phenomenon. For more accurate determinations, a relatively small Diffusive Boundary

Layer (DBL) in the sampled environment has to be added to the thicknesses of the diffusive gel and filter. A schematic drawing of the DGT is shown in **Figure 1**. The classic DGT device is composed of a cylindrical plastic molding (a cap and a piston base), holding together three successive layers, which are: a membrane filter, a diffusive hydrogel (polyacrylamide or APA hydrogel−0.8 mm thick), and a resin gel (binding Chelex®-100 binding resin−0.4 mm thick). The most common filters are 0.45 μm pore size cellulose acetate/HVLP Durapore−0.125 mm thick, but any filter membrane that is suitable for the element to be determined can be used. Hydrogels are used to guarantee a diffusive domain with a certain thickness where not only the analyte transport is diffusion controlled, but where also the dissociation of the labile complexes occurs. Hydrogels with several thicknesses can be used (0.2, 0.4, 0.8, 1.2 mm) and the thicker the diffusive domain, the longer the time that a complex has to dissociate. The characteristic time for an element M traveling through the diffusive domain equals:

$$t = \frac{\left(\Delta g + \delta^{\mathrm{dbl}}\right)^2}{2D_{\mathrm{M}}} \tag{1}$$

where Δg is the aggregate thickness of diffusive gel plus filter (i.e., the thickness of the material diffusion layer), δ^{dbl} indicates the thickness of DBL, and D_{M} is the diffusion coefficient of the element (e.g., a metal) when assumed to be the same in solution as in the gel and filter. For well-mixed media, the DBL is small compared to the thickness of the diffusive gel and it can often be neglected.

For diffusive domain thicknesses of 0.5, 1.0, and 1.5 mm, a residence time in that domain of, respectively, 8, 33, and 75 min can be roughly estimated. Thus, the thicker the diffusive domain, the larger the labile fraction of metal species will be assessed. Hydrogels have distinct properties such as a high water content and controllable swelling behavior and are generally limited to two types for use in DGTs: polyacrylamide or agarose. They are synthesized via a polymerization process and, depending on the amount and type of cross-linker that is added, they will have smaller or larger pore-sizes (Zhang and Davison, 2000; Scally et al., 2006; Baeyens et al., 2011; Shiva et al., 2015; Turull et al., 2019). Polyacrylamide is the most commonly used gel, but for some elements that show interactions with this gel, it is replaced by agarose. A suite of resins can be used to bind the analytes (dos Anjos et al., 2017; Menegario et al., 2017).

A DGT device allows trace elements to diffuse through the diffusive gel and bind to the resin gel. Therefore, based on total amounts of accumulated elements on the resin gel during deployment, a labile solute concentration can be calculated using Fick's law, Equation (2), assuming a perfect sink condition (i.e., all ions arriving at the interface between the diffusive hydrogel and the resin gel are completely bound to the resin gel) and steady-state regime:

$$c_{\mathrm{DGT}} = \frac{M\left(\Delta g + \delta^{\mathrm{dbl}}\right)}{D_{\mathrm{M}} A t} \tag{2}$$

where c_{DGT} is the DGT-labile metal concentration in the water, M is the mass of trace element accumulated on the resin gel, A is the exposure area of the DGT device, and t is the DGT deployment time.

Notice that Equation (2) is based on the first Fick's law assuming a fixed effective concentration in the solution. Thus, when only free metal is present in the solution, c_{DGT} stands for the total labile metal concentration in the solution and Equation (2) indicates that DGT allows this measurement with the knowledge of only one specific parameter of the analyte: the diffusion coefficient. When different metal species are present in the solution that can contribute to the transport and accumulation of the metal by dissociation, c_{DGT} stands for the apparent or effective free metal concentration in a solution that would give rise to the same accumulation than the sample (Galceran and Puy, 2015; Puy et al., 2016).

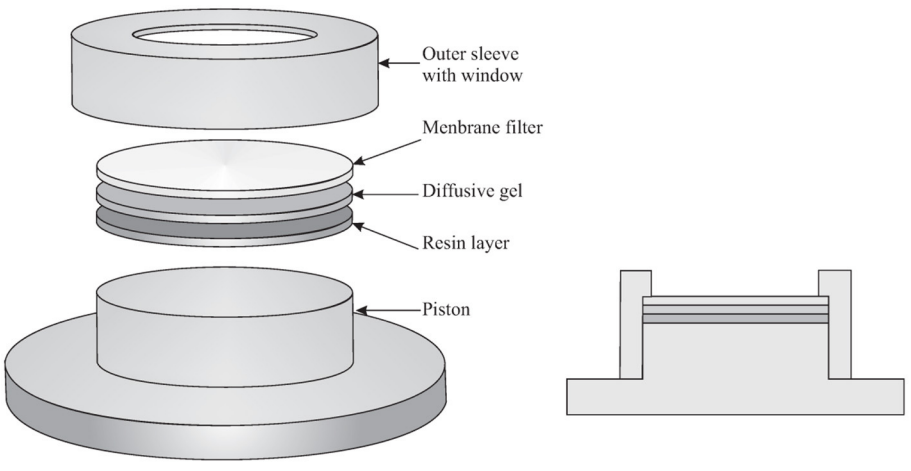

FIGURE 1 | Schematic drawing of the DGT device (Adapted from Averós et al., 2020).

c_{DGT} can also be interpreted in terms of the real species present in the sample, as indicated in Equation (3) below. The lability degree, ξ_j, quantifies the contribution of a given complex M^jL to the actual flux received by the DGT in comparison with the maximum possible flux of this complex if it was fully labile (local equilibrium fulfilled all throughout the diffusion domain or, equivalently, infinitely large dissociation rate constant; Galceran et al., 2001; Puy and Galceran, 2017). ξ ranges between 0, for inert complexes, to 1, for fully labile complexes. If there are h parallel complexes (Galceran and Puy, 2015; Puy et al., 2016; Zhao et al., 2020).

$$c_{DGT} = c_M + \sum_{j=1}^{h} \xi_j \varepsilon_j c_{M^jL} \tag{3}$$

where the normalized diffusion coefficients are

$$\varepsilon_j = \frac{D_{M^jL}}{D_M} \tag{4}$$

By just taking all lability degrees at their maximum values ($\xi_j = 1$), Equation (3) reverts to the useful and widely-used concept of "maximum dynamic concentration" (Unsworth et al., 2006; Balistrieri and Blank, 2008; Bradac et al., 2009; Warnken et al., 2009; Davison and Zhang, 2012; Han et al., 2014; Zhang and Davison, 2015; Zhu and Gueguen, 2016; Macoustra et al., 2019; Cindric et al., 2020),

$$c_{dyn}^{max} = c_M + \sum_{j=1}^{h} \varepsilon_j c_{M^jL} \geq c_{DGT} \tag{5}$$

We turn now our attention toward the assessment and implications of the DBL. The velocity of a liquid flow becomes zero at the interface with a solid phase. This suggests to approximate the transport of the species in the vicinity of the solid surface as if there was just diffusion of the species in a stagnant region (DBL) extending from the solid surface up to a distance (δ^{dbl}) where bulk concentrations are assumed to be restored by the flow and/or turbulences. With increasing rate of solution flow, the DBL layer becomes thinner, but it still exists even when the deployment solution for DGT devices is vigorously stirred. Therefore, to ensure optimal accuracy, DBL should be considered when calculating the concentration measured by DGT (Garmo et al., 2006; Warnken et al., 2006). It has been suggested that the thickness of the DBL can be assessed by using DGT devices with diffusive gels of different thickness. If DGT pistons equipped with different thickness of the diffusive gels, for example 0.40, 0.80, and 1.20 mm, are deployed in natural water systems, Equation (2) can be rewritten as:

$$\frac{1}{M} = \frac{\Delta g}{c_{DGTe} D_M^g A t} + \frac{\delta^{dbl}}{c_{DGTe} D_M^w A t} \tag{6}$$

where the superscripts g and w refer to the diffusive gel (and filter) and water solution, respectively. The added subscript "e" stands for the extended definition of DGT given by Equation (6) [instead of Equation (2) where $D_M^g = D_M^w$ was assumed; Davison and Zhang, 2016]. Equation (6) suggests that plotting $1/M$ *vs.* Δg enables the estimation of both c_{DGTe} and δ^{dbl}, if the diffusion coefficients are known. If the behavior of $1/M$ *vs.* Δg is actually linear, the slope (s) and the intercept (b) are given by:

$$s = \frac{1}{c_{DGTe} D_M^g A t} \tag{7}$$

$$b = \frac{\delta^{dbl}}{c_{DGTe} D_M^w A t} \tag{8}$$

However, a straight line assumes that c_{DGTe} is constant *vs.* Δg, and this is not the case if the solution contains partially labile ML complexes, which dissociate more with increasing Δg. Fortunately, the DBL is a physical quantity that depends on the flow pattern in the vicinity of the solid surface, but it is essentially independent of the nature and quantity of the analyte used in Equation (6). Therefore, in field conditions the DBL could be assessed with an analyte that forms no complexes, for example an organic compound such as E2 (17 beta-estradiol) (Guo et al., 2019) or a metal that forms only very labile complexes in the studied aquatic system (Warnken et al., 2007). This DBL is, thus, also valid for all other analytes that are assessed in the same aquatic system.

For a turbulent system, when the DBL is only about 10% of the diffusive layer thickness (Δg is typically around 1 mm), the DBL can be considered negligible. In this case, Equation (2) can be simplified to:

$$c_{DGT} = \frac{M \Delta g}{D_M A t} \tag{9}$$

TRANSITION METALS

The elements most studied with the DGT technique are, without any doubt, transition metals such as Cd, Co, Cu, Fe, Mn, Ni, Pb, Zn, because they all have a good to strong affinity for the Chelex resin and polyacrylamide can be used as a suitable hydrogel (Zhang and Davison, 1995; Garmo et al., 2003; Scally et al., 2006; Gao et al., 2019). In some studies, mercury was also determined with Chelex resin and polyacrylamide but, in other studies, resins with thiol groups and agarose as the hydrogel were recommended (see the section Mercury Speciation). Therefore, mercury speciation will be separately discussed from the other transition metals. According to Bio-Rad Laboratories, the affinity order of the various metals for Chelex is $Hg^{+2} > Cu^{+2} >> Pb^{+2} > Fe^{+3} > Ni^{+2} > Zn^{+2} > Co^{+2} > Cd^{+2} > Fe^{+2} > Mn^{+2}$, and the capacity of the resin is around 0.5 mmol/mL which means 15 μmol for a 0.4 mm thick standard resin gel. If the concentration of the trace metal in solution is 1 μmol/L, then after 1 day of DGT exposure with typical parameter values ($D = 5 \times 10^{-6}$ cm^2/s; $A = 3.14$ cm^2; diffusion domain thickness = 0.1 cm), the mass in the resin is 0.014 μmol. This means that just about 0.1% of the resin capacity is reached and

TABLE 1 | Trace metal diffusion coefficients (in 10^{-6} cm^2 s^{-1}) in polyacrylamide gel (www.dgtresearch.com).

T (°C)	Cd	Co	Cu	Fe	Mn	Ni	Pb	Zn
5	3.29	3.21	3.36	3.3	3.16	3.12	4.34	3.28
15	4.57	4.46	4.67	4.58	4.39	4.33	6.03	4.56
25	6.09	5.94	6.23	6.11	5.85	5.77	8.03	6.08

that, assuming only this analyte present, it would take 1,000 days before capacity was reached.

$$\mathrm{Log}D_T = 1.37023(T-25) + 8.36\times10^{-4}(T-25)^2/(109+T) + \log(D_{25}(273+T)/298) \quad (10)$$

There are three important factors that have an influence on the effective diffusion coefficients presented in **Table 1**, besides the temperature effect, which is expressed by Equation (10): the ionic strength of the solution, the pore size of the gel, and the size of the chemical compounds.

In addition to diffusion, at low ionic strengths (e.g., <1 mmol/L), some electrostatic effects can modify the transport of the analytes. At these conditions, the gel could have a small positive charge (leading to Donnan partitioning of cations at the gel surface) which depresses the metal concentration at the gel surface (Warnken et al., 2005). This lower surface concentration has the effect of lowering the net diffusion coefficient measured from solution to the resin, while the diffusion coefficient in the gel itself is actually unchanged. Since only a small percentage of world's freshwater systems have an ionic strength <1 mmol/L, measurements of trace metals—in poorly complexing media—by DGT should be rather straightforward to interpret. Besides the commented (occasional) electrostatic effects of the gel, the resin, especially in the case of Chelex, exhibits a high negative charge which induces a Donnan partitioning at the resin/diffusive gel interface (Puy et al., 2014). This partitioning will have an important effect on the accumulation of elements which have non-negligible concentrations of partially labile charged complexes, which will be pre-accumulated or excluded (depending on the sign of the electrical charge) from the resin domain (where complexes can penetrate, Mongin et al., 2011; Uribe et al., 2011). The electrostatic effects of the resin charge are also very relevant when perfect sink is not fulfilled for the target ion (Altier et al., 2016). When the metal concentration drops to zero at the resin/diffusive gel interface and complexes are labile, this effect can be neglected. This can be checked by using DGT devices with a stack of resin disks which are eluted separately.

Hydrogels with different pore sizes can be prepared by varying the concentrations and type of crosslinker. Scally et al. (2006) and Shiva et al. (2015) studied the diffusion coefficients of transition metal ions in classic open pore gel (0.12% cross-linker; pore size >5 nm) and restricted pore gel (0.8% cross-linker; pore size <1 nm). They found for the open pore gel D^g/D^w ratios of about 85%, while for the restricted pore gel this ratio decreased to 60%. Thus, in restricted pore gel, the ion diffusion coefficient is about 70% of that in open pore gel. Since the radius of trace metal ions is smaller (<0.3 nm) than the restricted gel pore size (≈1 nm), the mechanism of retardation is likely due to the greater diffusional path length (tortuosity) within the restricted gel compared with the open pore gel (≈5 nm pore size).

Metal complexes are larger in size than metal ions, which can have an influence on their diffusion coefficients. Diffusion coefficient of Pb complexes decreased with increasing size of the ligand, in the order of diglycolic acid (DGA), nitrilotriacetic acid (NTA), fulvic acid (FA), and humic acid (HA) (Scally et al., 2006).

Diffusion coefficients of PbNTA and PbDGA showed a decrease of 20–30% in the open pore gel compared to that of the free metal, while this decrease is about 90% for PbHA. In freshwaters, fulvic species are generally more common and, for some metals, they may dominate the solution species. Provided they are sufficiently labile to dissociate while they traverse the diffusion layer and penetrate into the resin layer, which is usually the case, they will contribute to the mass of metal measured by open pore DGT with about 20% of the sensitivity of uncomplexed metal (Scally et al., 2006).

Several parameters have an influence on the Limits of Detection (LODs), such as the pre-conditioning/cleaning of all materials including filter, resin, and hydrogel, the quality of the chemical reagents (including the purity of water used for dilutions), the air quality in the laboratory and the measuring conditions (type of analysis instrument, stability of the instrument, background signal). Moreover, DGT-LODs are only indicative, because the longer the DGT is deployed in the aquatic system, the lower the LOD becomes. Nevertheless, it is useful to have an idea about the concentration levels of labile trace metals that can be measured for a fixed time period of deployment. In **Table 2** we compare the blank value results of unexposed Chelex resin observed by Garmo et al. (2003) with those determined by Zhou and co-workers (Gaulier et al., 2021). The blank values are similar in both studies, except for Mn, Pb, and Ni while the STDs and LODs are similar, except for Co, Pb, and Fe. The largest variation, which is more than one order of magnitude, is observed for the LODs of Co and results from the large difference in standard deviation measured in the two cases.

Numerous surveys of labile trace metals have been successfully carried out in fresh- and sea-water environments, but we will present here one case study of trace metal speciation in each of those aquatic systems.

TABLE 2 | DGT blanks (with standard deviation STD) and Limits of Detection (LOD) for 24 h exposure time.

	Reference 1			References 2 and 3		
	Mean blanks ng	STD ng	LOD DGT ng/ml	Mean blanks ng	STD ng	LOD DGT ng/ml
Cd	0.053	0.015	0.0032	0.059	0.017	0.0029
Co	0.100	0.19	0.037	0.036	0.0057	0.001
Cu	0.970	0.26	0.047	0.55	0.12	0.02
Mn	0.360	0.11	0.021	1.54	0.091	0.016
Ni	4.10	0.48	0.087	0.68	0.32	0.057
Pb	1.000	0.16	0.019	0.086	0.0076	0.001
Zn	6.30	2.2	0.58	8.55	1.58	0.27
Fe	17.5	5.6	2.6	5.51	0.72	0.12

Reference 1 (Garmo et al., 2003); references 2 and 3 (Zhou, pers. Comm.) and (Gaulier et al., 2021). LOD DGT $= \frac{3\sigma_{blank}\Delta g}{D_M^g At}$ *where σ is the STD of the blank; t = 24 h; A = 3.14 cm²; Δg = 0.08 cm, and* D_M^g *the diffusion coefficient.*

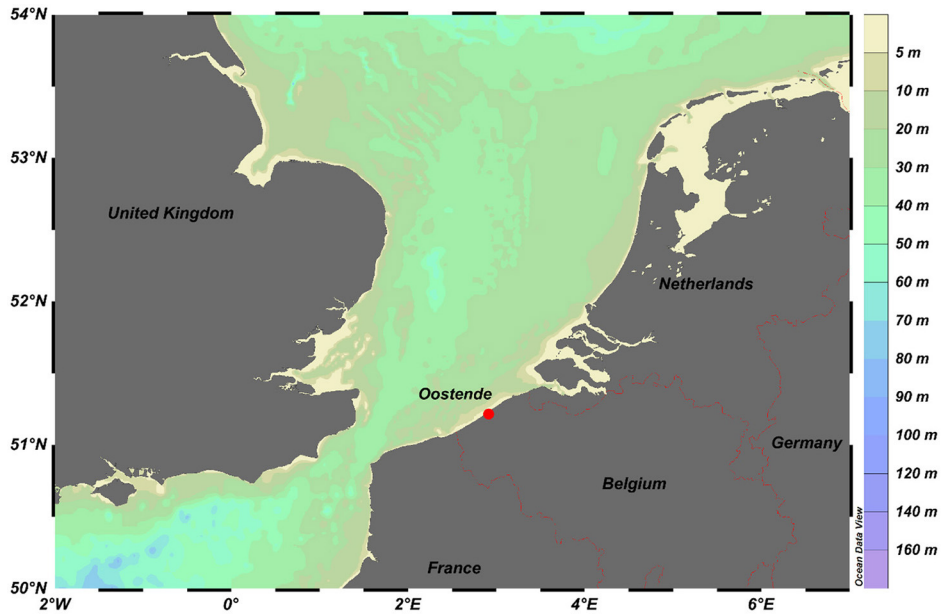

FIGURE 2 | Sampling station Oostende at the Belgium coast (Schlitzer, Reiner; Ocean Data View, https://odv.awi.de, 2020).

Speciation Results in Marine Water Ecosystems

In coastal areas, not only metal levels are generally higher than in offshore areas, but also other abiotic and biotic parameters are different, which can have an influence on the metal speciation. Therefore, the Oostende sampling site (see **Figure 2**), which is a coastal station at the Belgium coast that is heavily influenced by anthropogenic inputs, was selected for assessing the metal fraction that is labile (and, hence, also more bioavailable) and for comparing these labile metal fractions to those found in an offshore area in the Mediterranean Sea (Gao et al., 2019). Diffusive Gradients in Thin-films devices with different thicknesses of the diffusion domain allow one to provide information on the labile metal fractions at the coastal station and in the offshore area. The ratios of the field to blank concentrations in the Belgian Coastal Zone (BCZ) (Gaulier et al., 2021) are higher than in the Mediterranean Sea except for Cd (Baeyens et al., 2018). All ratios are higher than 8, except for Cd in the BCZ and Fe in the Mediterranean Sea, which are high enough to calculate accurate concentrations. The DGT concentrations of Cd and Fe in seawater can be very low, while, on the other hand, the blank values of the commercial Chelex resin in DGT can be high, resulting in those low ratios. However, when an acid pre-treatment of the resin is performed, all blank concentrations decreased and, for example, the field-to-blank ratio of Fe in the Mediterranean Sea became also higher than 10. During the same Mediterranean Sea cruise, the reproducibility of the DGT samplers was also investigated. For the classic ($n = 5$; hydrogel layer thickness is 0.8 mm) as well as the fast DGT ($n = 2$; no hydrogel layer) the relative

$$\xi = 1 - \frac{\left(1+\varepsilon K'\right)}{\varepsilon K' + \frac{\Delta g+\delta^{\mathrm{dbl}}}{\sqrt{\frac{D_{\mathrm{ML}}}{k_{\mathrm{d}}(1+\varepsilon K')}}} \coth\left(\frac{\Delta g+\delta^{\mathrm{dbl}}}{\sqrt{\frac{D_{\mathrm{ML}}}{k_{\mathrm{d}}(1+\varepsilon K')}}}\right) + \frac{\Delta g+\delta^{\mathrm{dbl}}}{\sqrt{\frac{D_{\mathrm{ML}}}{k_{\mathrm{d}}}}} (1+\varepsilon K') \tanh\left(\frac{\delta^{\mathrm{r}}}{\sqrt{\frac{D_{\mathrm{ML}}}{k_{\mathrm{d}}}}}\right)} \tag{16}$$

standard deviations (RSD) for Cd, and Cu were below 20%. For Fe, that only could be determined with the fast DGT, the RSD was 33%.

The DBL was taken as 0.2 mm (Guo et al., 2019). Total dissolved (TD) and labile metal (classic DGT, with a $\Delta g = 0.8 + 0.125$ mm) concentrations at the coastal station of Oostende are shown in **Figure 3**. As expected, labile concentrations are lower than TD concentrations. The labile concentrations (relative to the TD) are low for Pb and Cu, and high for Mn, as expected.

Two metal-complex pools are considered: one, labeled inorganic ML_{in}, for smaller molecules and another one, labeled organic ML_{org}. The normalized diffusion coefficients of these pools, are ε_{in} and ε_{org}. The total dissolved amount can be considered as the summation of the free metal pool c_M, the inorganic pool $c_{ML,in}$, and the organic pool $c_{ML,org}$.

$$c_{T,M} = c_M + c_{ML,in} + c_{ML,org} \tag{11}$$

Total dissolved metal concentrations ($c_{T,M}$) and percentages of free metal, inorganic complexes and organic complexes were taken from the literature (see **Table 3**). Conditional stability constants (in excess of ligand) can be used, e.g., for the inorganic pool

$$K'_{in} = \frac{c_{ML,in}}{c_M} \tag{12}$$

Equation (3) can be invoked for this particular case, i.e., c_{DGT} is split as a summation of the labile fractions, each weighted by its normalized diffusion coefficient ε_j. For the different configurations used in these experiments (no hydrogel, 0.4 and 0.8 mm thick diffusive hydrogel layer) DGTs, Equation (3) becomes:

$$c^{g0}_{DGT} = c_M + \varepsilon_{in}\xi^{g0}_{in} c_{ML,in} + \varepsilon_{org}\xi^{g0}_{org} c_{ML,org} \tag{13}$$

$$c^{g4}_{DGT} = c_M + \varepsilon_{in}\xi^{g4}_{in} c_{ML,in} + \varepsilon_{org}\xi^{g4}_{org} c_{ML,org} \tag{14}$$

$$c^{g8}_{DGT} = c_M + \varepsilon_{in}\xi^{g8}_{in} c_{ML,in} + \varepsilon_{org}\xi^{g8}_{org} c_{ML,org} \tag{15}$$

where ξ_j is the lability degree for each metal complex pool (j = in or org) for the different DGT configurations (superscripts g8, g4, or g0, see **Table 3**). Neglecting mixture effects (Altier et al., 2018), one can approximate the true ξ in a mixture of ligands (or pools, in this case) with the ξ computed for the case where there is only one ligand (i.e., one pool). Assuming excess of ligand and perfect-sink conditions, the lability degree can be written as a function of the dissociation rate constant (k_d), the normalized diffusion coefficient of the complex and the thicknesses of the just-diffusion (gel disc and filter, $\Delta g + \delta^{\mathrm{dbl}}$), and of the reaction-diffusion (resin disc, $\delta^r = 0.4$ mm) domains as derived in Uribe et al. (2011),

where k_d indicates the corresponding dissociation constant of the considered complex pool.

The thicknesses of the diffusion domain ($\Delta g + \delta^{\mathrm{dbl}}$) were computed with the filter thickness (0.125 mm), the DBL thickness (0.2 mm) and the corresponding diffusive gel thickness.

It is worth noticing that the lability degree is not entirely an intrinsic parameter of a complex. Even though ξ_j is a function of the dissociation rate constant and diffusion coefficient (which are, indeed, specific of the complex), it also depends on the geometric characteristics of the sensor (Δg) and the composition of the media (e.g., ligand concentrations). Nevertheless, the presence of concomitant complexes of the same element has usually a low influence on the total accumulation, since the impact of a complex on another one is mutually opposite (ca. 10% or lower), particularly under ligand excess conditions (see Altier et al., 2018).

Using Equations (2) and (13) to (16) with literature data on concentrations (see Gao et al., 2019 for details), the lability degrees and dissociation rates of the metal complex pools in the BCZ were derived. A value of $\varepsilon_{in} = 1$ was taken as well as a literature value of $D_{ML,org}$ (Balch and Gueguen, 2015) for the organic pool.

Table 3 shows results for BCZ. As expected, labilities increase when increasing the thickness of the diffusive gel, when other factors are fixed. For a given metal and DGT configuration, the inorganic pool is always more labile than the organic one, as expected. **Table 3** allows to suggest that the lability of the metal complexes might in general be higher in open sea (Baeyens et al., 2018) than in the BCZ. This could be related to the presence of strong ligands released from industrial activities in the harbor at the BCZ. The lability degrees of inorganic Cd, Ni, Co, and Cu complexes in the Mediterranean Sea are high (around 90%) for the classic DGT. Something alike happens with inorganic Zn complexes in the BCZ, while inorganic Cu and Pb lability degrees (in the classic DGT) drop to 68 and 51%, respectively. Labilities of organic Cu complexes are equal in the BCZ and in the Mediterranean Sea. Lability degrees of organic Fe complexes are higher in the BCZ than in the Mediterranean Sea.

In high ionic strength solutions, some drawbacks may occur. Perfect sink conditions are not always met, such as for example the DGT accumulation of Mn in seawater or in other solutions with high Ca or Mg concentrations (Altier et al., 2016). In that case, Mn concentration calculations should be carried out with a modified version of Equation (2), taking into account the competition of Mn with Ca and Mg ions for the resin sites, or via specific calibration curves of Mn (same solution composition and same exposure time as for field samples) accumulated on the DGT resin *vs*. the Mn concentration in seawater.

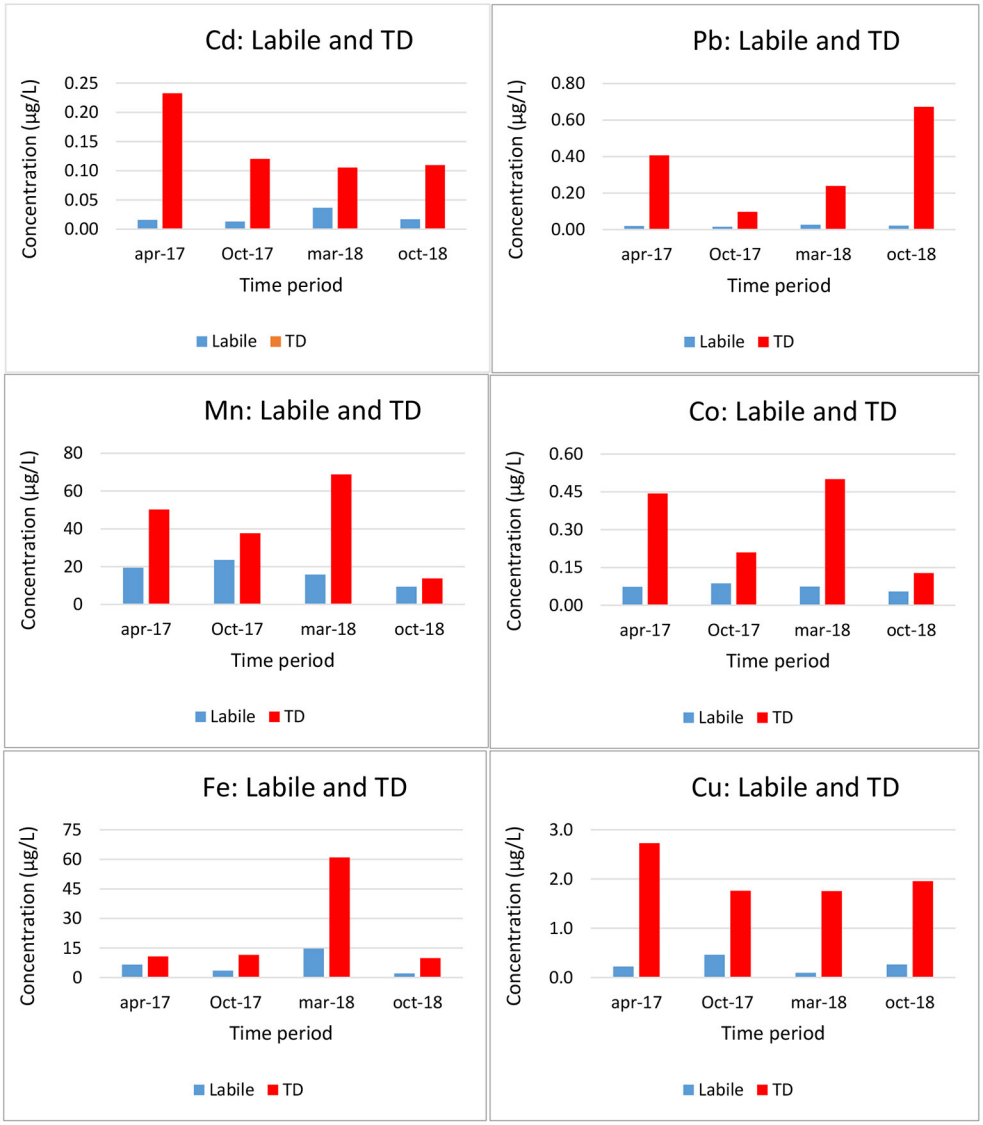

FIGURE 3 | Total dissolved (TD) and labile (DGT) trace metal concentrations at station Oostende in the Belgian Coastal Zone (Gao et al., 2019).

Speciation Results in Freshwater Ecosystems

Diffusive Gradients in Thin-films was used *in-situ* in the river Wyre (UK, see **Figure 4**), a pristine freshwater ecosystem with a high DOC level (15 mg/L), to study: (1) the equilibrium distribution of metal ions amongst three pools: simple inorganic complexes (free cation plus complexes with inorganic ligands), organic complexes with fulvic acid (FA), and non-dynamic (inert) metal species (particles, colloids); and (2) the rates of dissociation of the organic complexes. Diffusive Gradients in Thin-films devices were deployed with different diffusion layer thicknesses (0.3, 0.54, 1.34, and 2.14 mm) and with gels of different pore size (either polyacrylamide of normal pore size or restricted gel of small pore size) (Warnken et al., 2008). All samples, including dissolved trace metal samples and DGT eluant samples, were analyzed using a Thermo X7 series. Accuracy and precision were verified by analyzing the National Research Council Canada (NRCC) river water reference material, SLRS-4; the obtained values were within the 95% confidence intervals reported.

The seven spot samples collected during the DGT deployments and used to calculate the mean total dissolved metal concentrations had a RSD between 10% (Fe) and 43% (Mn). However, this is not a precision error, as replicate analyses were within 5%. Rather, it reflects the changes in concentration that are already taken into account in the integrating DGT measurements. The RSD (%) on the DGT measurements (n = 10) are between 11% (Ni and Pb) and 17% (Co and Cu). No

TABLE 3 | Lability degrees (ξ) of metal complexes obtained in the Mediterranean Sea and in the Belgian coastal Zone (BCZ) (Gao et al., 2019).

Element	$c_{T,M}$	Free metal	DGT no gel (g0)	DGT thin gel (g4)	DGT-classic (g8)	ξ_{in}^{g0}	ξ_{org}^{g0}	ξ_{in}^{g4}	ξ_{org}^{g4}	ξ_{in}^{g8}	ξ_{org}^{g8}
	nmol L^{-1}	nmol L^{-1}	nmol L^{-1}	nmol L^{-1}	nmol L^{-1}						
MEDITERRANEAN SEA											
Cd	0.066	0.0029	0.049		0.062	0.694	–			0.89	–
Fe	5.54	5.3×10^{-13}	0.47		–	–	0.152			–	–
Ni	4.9	0.49	2.95		3.18	0.88	–			0.96	–
Co	0.12	0.019	0.058		0.064	0.81	–			0.94	–
Cu	4.53	0.0044	0.41		0.98	0.70	0.14			0.89	0.36
BELGIAN COSTAL ZONE											
Pb	0.473	0.0047	0.0458	0.0644	0.073	0.22	3.8×10^{-10}	0.40	1.1×10^{-9}	0.51	2.0×10^{-9}
Fe	205	1.6×10^{-9}	37.3	66.6	72.9	–	0.34	–	0.53	–	0.64
Ni	39.5	5.53	5.65	8.17	9.91	0.04	0.04	0.11	0.10	0.18	0.17
Cu	27.7	0.070	3.62	7.61	8.09	0.38	0.14	0.58	0.27	0.68	0.37
Zn	180	10.8	33.6	45.0	50.2	0.96	0.07	0.98	0.16	0.99	0.25

$c_{T,M}$ is the total dissolved metal concentration; values for Co from Dulaquais et al. (2017) and for the other metals from Ebling and Landing (2015) in the case of the Mediterranean Sea and our data in the case of BCZ. Percentages of each pool (free, inorganic, and organic) are from Stockdale et al. (2011, 2015, 2016). "in" stands for inorganic and "org" for organic. Superscripts: g0 indicates no hydrogel layer, g4 0.4 mm and g8 0.8 mm hydrogel layer.

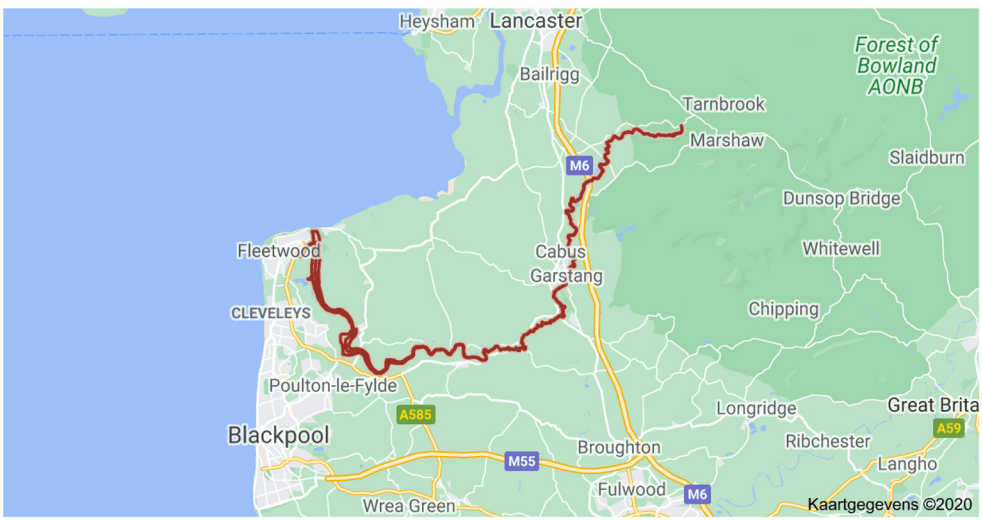

FIGURE 4 | Sampling station at Garstang in River Wyre, Lancaster, UK (Google maps).

RSD-values on the classic DGTs were reported, but we found during a cruise in the Southern Ocean (Baeyens et al., 2011) that they are generally lower (maximum of 21%), than the RSD-values on the restricted DGTs (maximum of 57%).

Labile metal concentrations of Mn, Fe, Co, Ni, Cu, Cd, and Pb were calculated assuming inorganic complexes to be fully labile and sharing the same diffusion coefficient as the free metal, while inert complexes did not contribute to the DGT accumulations. These calculations provided the inorganic and organic concentrations and the dissociation rate constant of the organic complexes.

To account for the reduced accumulation found with partially labile complexes, the authors used the approach of an extra diffusion length specific for each element and associated to the kinetic limitation. This length can be written in terms of the dissociation rate constant k_d and concentrations of real species, as discussed in Warnken et al. (2007, 2008), Mongin et al. (2011), Uribe et al. (2011), Levy et al. (2012), and Puy et al. (2016). This approach can be seen as parallel to the treatment applied in section Speciation Results in Marine Water Ecosystems. Although either ξ or the extra kinetic limitation length depend on the thickness of the diffusive gel used in the DGT device, the number of unknowns is reduced to only k_d and diffusion coefficients or concentrations because of these theoretical expressions. However, we have to notice that in Warnken et al. (2008), the expression for the extra kinetic limitation length in terms of the dissociation rate constant corresponds to a situation where the complex was not allowed

TABLE 4 | Percentage distribution of lumped inorganic species, ($c_M + c_{ML,in}$) organic Complexes, $c_{ML,org}$, and Non-dynamic Species, c_{nd} in the Wyre river (Warnken et al., 2008) when taking $D_{ML,org}$ as twice of those for isolated fulvic acid complexes.

	Mn	Fe	Co	Ni	Cu	Cd	Pb
% ($c_M + c_{ML,in}$) /TD	92.2	15.7	30.7	11.3	5.51	27.4	2.01
% $c_{ML,org}$/TD	9.80	14.7	23.3	65.6	21.8	11.4	0.69
% c_{nd} / TD	−1.90	69.6	46.0	23.1	72.6	61.2	97.3

to penetrate into the resin domain, which could be considered a limitation of this treatment. **Table 4** shows the percentage distribution of (lumped) inorganic species, $c_M + c_{ML,in}$ (i.e., aggregating the free metal ion concentration with that of the inorganic complexes assumed fully labile and mobile), organic complexes, $c_{ML,org}$, and non-dynamic species, c_{nd} (calculated as the difference between the total dissolved concentration minus those of the inorganic and organic complexes) in the Wyre river.

Taking diffusion coefficients of FA-complexes from diffusion cell experiments led to negative non-dynamic concentrations of Mn and Ni. The authors suggested that the mean diffusion coefficients obtained for the isolated FA in the diffusion cell might underestimate the mean diffusion coefficients of complexes that are binding the metals in the river water. So, they performed the final mathematical treatment applying a factor of 2 to all FA-complexes diffusion coefficients (**Table 4**). The non-dynamic fraction resulted generally in a higher amount than the colloidal fraction measured via ultrafiltration. This may indicate a non-negligible inert metal fraction. More than half of the total filtered Cd was not measured by DGT, consistent with a large colloidal or inert fraction. The authors concluded that Cd is less strongly bound to natural organic material than to extracted fulvic acid. Ni speciation was dominated by DGT-labile organic complexes, in contrast to model predictions made by WHAM6 suggesting that between 40 and 60% of the Ni would be present as inorganic species (Unsworth et al., 2006). Pb behaved quite different than Ni, with a dominant fraction of colloidal species (∼97% of total dissolved Pb). The small remaining fraction (∼3%) consisted mainly of free Pb and its inorganic complexes. Cu also showed a large inert colloidal fraction (∼73%), with a non-negligible fraction bound to humic complexes. The authors could not completely compare with literature data for Fe, Co, and Mn. Fe species were found to be polydispersed (Horowitz et al., 1992) and strongly complexed (Gimpel et al., 2003). The predominant inorganic complexation of Mn agreed with previous results (Gimpel et al., 2003), and the abundances of organically complexed and colloidal Co reported in **Table 4** were also consistent with previous work.

These two above-commented cases demonstrated that, in principle, it is possible to use a dynamic technique like DGT to obtain simultaneously information on the distribution of species and their rates of exchange. However, several difficulties such as the uncertainty in the diffusion coefficients of metal complexes, the nature of the organic ligands in the natural aquatic system, the stability constants of the metal–organic ligand complexes, etc., render it difficult to reach straightforward conclusions.

MERCURY SPECIATION

Mercury, as one of the most toxic elements in the environment, has lately attracted great attention due to its high toxicity and widespread occurrence (Morel et al., 1998). The most important chemical forms are elemental Hg, inorganic Hg, monomethylmercury (MeHg), and dimethylmercury (DMHg), which are all toxic, making mercury probably one of the most hazardous pollutants to aquatic biota (Akagi and Nishimura, 1991; Mason, 1995; Baeyens et al., 2003). It enters the environment from natural and anthropogenic sources, with coal-fired power plants, waste incinerators, and chlor-alkali plants as the most important ones (Turull et al., 2017b). Although mercury is essentially discharged in the inorganic form, it can be converted by sulfate reducing bacteria into methylmercury (MeHg), the most toxic mercury compound in the environment, bio-accumulated in plankton and biomagnified through the aquatic food chain (Mason, 1995; Storelli et al., 2002; Baeyens et al., 2003). The main exposure route of Hg to humans is through the consumption of marine fishery products (Oken et al., 2005). Fish and fish products account for most of the organic mercury in food. It is important to note that fish species can contain a broad range of mercury levels, even in the same aquatic environment.

Bioavailability depends on the chemical lability, but also on passive, active or facilitated cellular interaction with both Hg^{2+} and MeHg, a mechanism which is not yet completely understood (Schaefer and Morel, 2009; Faganeli et al., 2014). Due to the fact that Hg bioavailable species cause ultimately damage to human and ecosystems health, clearly more research into Hg bioavailability is needed (Bradley et al., 2017). Size-fractionating filtration to determine dissolved Hg is often employed to describe the labile fraction that interacts with biota (Faganeli et al., 2003). Similarly, the easily reducible (labile) fraction of Hg^{2+} (referred to as reactive Hg) is used as proxy for photo- and bioreduction, and biomethylation (Horvat et al., 1999). Likewise, experiments of methylation and demethylation potential are based on the assumption that the added non-complexed Hg species is bioavailable (Hines et al., 2006). Moreover, the ratio between MeHg and total mercury (THg) in various aquatic systems is sometimes used to compare the methylation potential, and thus, by extent, the bioavailability of the precursor, although methylation may occur also extracellularly and abiotically (Hines et al., 2006).

Diffusive Gradients in Thin-films has been increasingly used to evaluate lability and, by approximation, bioavailability of and potential exposure to Hg species (Amirbahman et al., 2013; Fernández-Gómez et al., 2015). Hg^{2+} and MeHg in

natural waters are often present in femtomolar (fmol L^{-1}, pg L^{-1}) concentrations, which require ultra clean passive sampling methods and very sensitive, precise analytical procedures. Diffusive Gradients in Thin-films technique is capable of long-term passive accumulation of labile Hg species onto a binding resin, effectively pre-concentrating inorganic Hg and MeHg at such ultralow concentrations in aquatic environments, thus avoiding issues associated with trace metal sampling (Docekalova and Divis, 2005; Clarisse and Hintelmann, 2006; Gao et al., 2014).

The combination of the polyacrylamide diffusive gel and Chelex-100 resin gel, which is commonly used in DGT for the assessment of most trace metals as seen in section Transition Metals, has also been applied for the determination of labile Hg concentrations (mainly inorganic Hg) in the aquatic environment (Cattani et al., 2008), but several drawbacks appeared. The polyacrylamide gel showed a high affinity for mercury and was therefore replaced by an agarose gel (Docekalova and Divis, 2005). Moreover, the adsorption efficiency of the Chelex-100 resin for Hg is also controversial. Docekalova and Divis (2005) compared the Hg pre-concentration by a DGT containing a Chelex-100 resin with one containing a Spheron-Thiol resin (Slovák et al., 1979). They concluded that they were able to assess ionic mercury and labile mercury complexes with both resins, but the Chelex-100 resin had a lower accumulation rate than the Spheron-Thiol one (Gao et al., 2014). Moreover, Cattani et al. (2008) reported that using Chelex-100 as the resin gel in the DGT, only 50–58% of the Hg could be recovered from their solution, while this was 83–97% with the Spheron-Thiol resin. Other thiol-based resins such as mercaptopropyl (Howard and Khdary, 2004; Merritt and Amirbahman, 2007; Clarisse et al., 2009) or dithiocarbamate-based resins (Lansens et al., 1990; Goubert-Renaudin et al., 2007) have been investigated, all with good success, for the pre-concentration of inorganic and organic mercury species at ng L^{-1} level. However, many of them are not or no longer commercially available due to interrupted production; only 3-mercaptopropylsilica (3-MFS) and Purolite S924 are still commercially available (Gao et al., 2011; Bratkic et al., 2019; Reichstädter et al., 2020). However, individual research groups have synthesized new home-made resins for assessment of Hg and other trace metal in aquatic systems (Gao et al., 2011; Turull et al., 2017a; Elias et al., 2020; Reichstädter et al., 2021). Due to the very strong binding between the functional groups of the resin and Hg, the elution procedures for Hg are also different from those for other trace metals (elution procedures can be found in **Table 5**). It is clearly shown that aqua regia digestion of resin gels produced the most uniform and efficient elution results. Employment of higher HCl concentrations also improve the elution of Hg.

Diffusive Gradients in Thin-films determination of mercury is, compared to DGT determination of other trace metals, still under development. Therefore, the validation of the whole methodology is strongly recommended. Considering the instruments used for Hg analysis, it varies from one laboratory to another due to available facilities. Cold Vapor coupled with Atomic Absorption Spectrometry (CV-AAS), ICP-AES, and ICP-MS are commonly used devices in several studies (see **Table 5**).

Due to the higher toxicity of organic mercury species, especially methylmercury (MeHg), it is important to detail speciation of the Hg compounds in environmental samples. However, in aquatic systems, MeHg occurs at ultra-low concentration levels, which makes the DGT a promising technique for its assessment. Only a few studies have been published on MeHg determination using DGT samplers, which contained polyacrylamide diffusive and Spheron-Thiol resin gel (Liu et al., 2012; Tafurt-Cardona et al., 2015). In their studies, high uncertainties were obtained for water concentration estimates. Diffusion coefficients in the gel appeared to be variable and this might be linked to the employment of polyacrylamide, since it was reported that this gel binds inorganic mercury and MeHg (Docekalova and Divis, 2005; Gao et al., 2014). Moreover, the utilization of thiourea to elute the Hg species from the gel can strongly interfere the ethylation reaction of MeHg (see **Table 6**), which is a key step for the measurement of MeHg using Cold Vapor-AAS or Headspace-Gas Chromatography-Atomic Fluorescence Spectrometry. Alternatively, agarose was employed as a diffusive gel in the DGT, while detection was carried out with IC-ICP-MS to avoid an ethylation reaction after the thiourea elution. Moreover, a SPE step was used to extract MeHg from thiol-based resin gels (**Table 6**).

Mercury speciation using the DGT has been applied in diverse environments including freshwater (Gao et al., 2011, 2014; Hong et al., 2011; Fernández-Gómez et al., 2014; Tafurt-Cardona et al., 2015; Bretier et al., 2020), seawater (Hong et al., 2011), sediments (Amirbahman et al., 2013; Noh et al., 2016; Bratkic et al., 2019), and paddy soil (Liu et al., 2012). Care must be taken for the selection of the diffusion gel and the accurate determination of diffusion coefficients to obtain meaningful results. Due to different selection of diffusive gels, either polyacrylamide or agarose, the diffusion coefficients for different mercury species vary from one study to another. The diffusion coefficient in water and the hydrogels should theoretically decrease as: water > agarose diffusive gel > polyacrylamide diffusive gel > bisacrylamide-crosslinked polyacrylamide (restrictive) diffusive gel, and this due to the decrease of the gel pore size (Davison and Zhang, 2016). The pore size of the polyacrylamide gel is around 10 nm, with a range of 5–20 nm (Zhang and Davison, 1995; Scally et al., 2006) and the one of the agarose is around 40 nm, with a range of 35–47 nm (Zhang and Davison, 1999; Fatin-Rouge et al., 2004). Therefore, it is logic that the diffusion coefficients of mercury species in agarose gel are larger than those obtained in polyacrylamide diffusive gel. Although speciation of bioavailable mercury is technically feasible, careful selection of hydrogel and binding resin for the DGT and appropriate lab processing and analysis should be warranted. Also, biofilm formation with agarose gel is still problematic for long deployment times, which are sometimes necessary due to the very low *in-situ* concentrations of MeHg.

SATURATION/COMPETITION EFFECTS

Diffusive Gradients in Thin-films devices were initially designed to obtain linear accumulations of metals in natural unpolluted waters using deployment times of the order of days. However, too long deployments or deployments in highly contaminated

TABLE 5 | Extraction procedures for dissolved labile mercury.

Eluent	f_e	T (°C)	Time	Analyser	References
10% NaOH	60–75%	N/A	N/A	CV-AAS	Minagawa et al., 1980
30% NaOH	60–75%	N/A	N/A	CV-AAS	Minagawa et al., 1980
2% thiourea in 0.1 M HCl	54%	N/A	24 h	CV-AFS	Ren et al., 2018
1.3 mM thiourea in 0.1 M HCl	25%	N/A	24 h	CV-AFS	Ren et al., 2018
5% thiourea in 0.5% HCl	100%	N/A	N/A	CV-AAS	Minagawa et al., 1980
10% thiourea in 0.1 M HCl	21%	N/A	24 h	CV-AFS	Ren et al., 2018
1 M thiourea	<30%	N/A	N/A	ICP-AES	Pohl and Prusisz, 2004
2 M thiourea in 0.5 M HCl	<30%	N/A	N/A	ICP-AES	Pohl and Prusisz, 2004
1 M HNO_3	68%	25°C	24 h	ICP-MS	Reichstädter et al., 2020
2 M HNO_3	16%	N/A	24 h	CV-AFS	Ren et al., 2018
2 M HNO_3	91%	N/A	24 h	CV-AFS	Colaco et al., 2014
2 M HNO_3	16%	N/A	24 h	CV-AFS	Ren et al., 2018
3 M HNO_3	8%	N/A	N/A	ICP-AES	Sook-Young et al., 2001
1 M HCl	5–20%	N/A	24 h	CV-AFS	Noh et al., 2019
2 M HCl	0.5–5.2%	N/A	N/A	ICP-AES	Pohl and Prusisz, 2004
2 M HCl	5–20%	N/A	24 h	CV-AFS	Noh et al., 2019
2 M HCl	17%	N/A	24 h	CV-AFS	Ren et al., 2018
3 M HCl	19%	N/A	24 h	CV-AFS	Ren et al., 2018
5 M HCl + microwave	95%	55°C	15 min	LC-CV-AFS	Pelcová et al., 2015
6 M HCl	100%	N/A	24 h	CV-AFS	Noh et al., 2019
12 M HCl	54%	110°C	5 h	CV-AFS	Fernández-Gómez et al., 2011
7:3 HNO_3:H_2SO_4	92%	110°C	5 h	CV-AFS	Fernández-Gómez et al., 2011
7:3 HNO_3:H_2SO_4	74%	N/A	24 h	CV-AFS	Noh et al., 2016
H_2SO_4, conc. w/ 30% H_2O_2	92–101%	N/A	N/A	ICP-AES	Pohl and Prusisz, 2004
Aqua regia	96%	N/A	overnight	ICP-MS	Bratkic et al., 2019
Aqua regia	97%	110°C	5 h	CV-AFS	Fernández-Gómez et al., 2011
Aqua regia	88%	N/A	24 h	CV-AFS	Ren et al., 2018
Aqua regia	98%	70°C	24 h	ICP-MS	Reichstädter et al., 2020
Aqua regia	84%	N/A	24 h	CV-AFS	Noh et al., 2016
10% sodium sulfide	60–75%	N/A	N/A	CV-AAS	Minagawa et al., 1980
5% disodium-EDTA	20–30%	N/A	N/A	CV-AAS	Minagawa et al., 1980
5% pentasodium-DTPA	20–30%	N/A	N/A	CV-AAS	Minagawa et al., 1980
10% BrCl	101%	N/A	24 h	CV-AFS	Amirbahman et al., 2013
0.3 M BrCl	90%	N/A	24 h	CV-AFS	Noh et al., 2016

The extraction efficiency (f_e), temperature (T), time of extraction, and the analyzing method are detailed.

waters can cause saturation effects. These are clearly evidenced by recording the time dependence of the accumulation. Saturation effects lead to downwards deviations of the accumulation indicating that the flux is decreasing with time and the accumulation proceeds out of steady state.

The arising of saturation effects is, then, a phenomenon that depends on the deployment time, the concentrations of the target analyte in the sample, the effective capacity of the resin disc and the affinity of the analyte for the resin sites.

As for the effective capacity, it depends not only on the amount of resin used in the disc, but also on the presence of competing cations. Indeed, natural samples usually consist of mixtures of multiple analytes and ligands. Protons and other concurrent metal cations compete with each other and with the probe metal ion(s) for the binding to the resin sites. The subsequent decrease in the concentration of available (free) resin sites leads to a drop in the effective rate of association between the analyte and the resin (Jimenez-Piedrahita et al., 2017) and to a decline in the rate of metal accumulation in the DGT device. At longer times, the accumulation approaches the effective equilibrium value between the resin and the bulk solution concentration:

$$\frac{c_{\mathrm{MR}}^{\mathrm{eq}}}{c_{\mathrm{T,R}}} = \frac{K_{\mathrm{MR}} c_{\mathrm{M}}}{1 + K_{\mathrm{MR}} c_{\mathrm{M}}} \tag{17}$$

where $c_{\mathrm{T,R}}$, $c_{\mathrm{MR}}^{\mathrm{eq}}$, and K_{MR} are the total concentration of resin sites, the concentration of sites occupied by M at equilibrium, and the metal-resin binding constant, respectively. The previous

TABLE 6 | Extraction procedures for dissolved methylmercury.

Eluent	f_e	T (°C)	Time	Analyser	References
2 M HNO_3	37%	N/A	24 h	CV-AFS	Ren et al., 2018
1 M HCl	97%	N/A	24 h	CV-AFS	Tafurt-Cardona et al., 2015
2 M HCl	40%	N/A	24 h	CV-AFS	Ren et al., 2018
3 M HCl	43%	N/A	24 h	CV-AFS	Ren et al., 2018
18% KBr, 5% H_2SO_4, 1 M $CuSO_4$, CH_2Cl_2	N/A	N/A	1 h	HS-GC-CV-AFS	Bratkic et al., 2019
18% KBr, 5% H_2SO_4, 1 M $CuSO_4$, CH_2Cl_2	100%	N/A	2.5 h	HS-GC-CV-AFS	Gao et al., 2014
Acidic thiourea	N/A	N/A	24 h	IC-ICP-MS/HPLC-ICP-MS	Hong et al., 2011
0.001 mM thiourea, 0.1 M HCl	32%	N/A	24 h	GC-CV-AFS	Noh et al., 2016
0.01 mM thiourea, 0.1 M HCl	33%	N/A	24 h	GC-CV-AFS	Noh et al., 2016
0.1 mM thiourea, 0.1 M HCl	34%	N/A	24 h	GC-CV-AFS	Noh et al., 2016
1 mM thiourea, 0.1 M HCl	88%	N/A	24 h	GC-CV-AFS	Noh et al., 2016
1.3 mM thiourea in 0.1 M HCl	85%	N/A	24 h	CV-AFS	Amirbahman et al., 2013
1.31 mM thiourea, 0.1 M HCl	N/A	N/A	24 h	CV-AFS	Liu et al., 2012
1.31 mM thiourea, 0.1 M HCl	N/A	N/A	24 h	HS-SPME-Py-AFS	Fernández-Gómez et al., 2014
1.31 mM thiourea	91%	N/A	N/A	GC-ICP-MS	Clarisse and Hintelmann, 2006
1.3 mM thiourea, 0.1 M HCl	68%	N/A	24 h	CV-AFS	Ren et al., 2018
1.3 mM thiourea, 0.1 M HCl	N/A	N/A	12 h	ID-GC-ICP-MS	Bretier et al., 2020
10 mM thiourea, 0.1 M HCl	83%	N/A	24 h	GC-CV-AFS	Noh et al., 2016
0.5–50 mM thiourea	< LOD	N/A	24 h	HS-GC-CV-AFS	Gao et al., 2014
100 mM thiourea, 0.1 M HCl	69%	N/A	24 h	GC-CV-AFS	Noh et al., 2016
1000 mM thiourea, 0.1 M HCl	31%	N/A	24 h	GC-CV-AFS	Noh et al., 2016
2% thiourea, 0.1 M HCl	100%	N/A	24 h	CV-AFS	Ren et al., 2018
10% thiourea, 0.1 M HCl	50%	N/A	24 h	CV-AFS	Ren et al., 2018

The extraction efficiency (f_e), temperature (T), time of extraction, and the analyzing method are mentioned.

equation strictly holds when only the species M is bound to the resin. In a general situation, it should be substituted by a suitable competitive isotherm. In the particular case of competition between M and protons with a stoichiometric exchange ratio of 1:1, the intrinsic value of K_{MR} may be replaced with a conditional (effective) value that depends on pH and incorporates the decrease in the number of available sites due to protonation. The competitive effect is, then, interpreted as a lowering of this effective binding constant as pH decreases, which leads to a lower value of c_{MR}^{eq} and, consequently, to a more significant curvature of the accumulation plot at low deployment times. Equation (17) is included here as an example of how the effective binding capacity of the resin may be significantly lower than the absolute (intrinsic) binding capacity (i.e., $\frac{c_{MR}^{eq}}{c_{T,R}} < 1$) depending on the environmental conditions of the sample.

Moreover, a significant concentration of dissolved ligands with an affinity high enough to compete with resin sites for the binding of the probe ion(s) (Mongin et al., 2013) might also lower the effective strength of the resin, leading again to a curvature of the mass accumulation *vs. t* plot as it approaches the equilibrium value:

$$c_{MR}^{eq} = \frac{K_{MR} c_{ML} c_R}{K'_{ML}} \quad (18)$$

where c_R is the concentration of free resin sites and K'_{ML} is the effective binding constant of the complex with the high-affinity ligand. The larger the value of K'_{ML}, the sooner the accumulation deviates from linearity.

Any of the previous two phenomena leads to a departure from the linear accumulation regime (at shorter times than expected for a significant saturation of the resin) and to an underestimation of the actual species concentration in solution. Mongin et al. (2013) reported some guiding contour plots to help define the range of experimental conditions (pH, K'_{ML}) where the linear accumulation regime prevails. As an example, the relative error in the calculation of c_{DGT} with the steady-state, perfect-sink (linear) Equation (2) remains below 5% (as compared with an "exact" value computed from numerical simulation results) after 10 h of deployment at pH 7 or higher in solutions containing a strong (but fully labile) complex with $K'_{ML} > 3$. For partially labile systems, the range of deployment times where the linear behavior is valid becomes multiplied by $1/\xi_{ML}$.

C_{DGT} AS A TIME-WEIGHTED AVERAGE CONCENTRATION

Another issue of practical interest is the elucidation of the relationship between the measured value of c_{DGT} and the value of the bulk concentrations averaged over the deployment time. Temporal variations in the concentration of pollutants are frequent in natural waters as a result of the dynamics of natural and anthropogenic cycles. The integrative nature of

DGT passive samplers suggests that they can provide time-weighted average (TWA) concentrations of the analytes over the deployment time, in contrast with conventional grab sampling (which yields a snapshot of the sampling site at one particular moment; Allan et al., 2007; Dunn et al., 2007; Huang et al., 2016, 2017). The response of DGT devices to changes in concentration during the deployment time has been studied both theoretically and experimentally through DGT deployments in solutions of different concentrations during controlled time periods (Altier et al., 2019). The results indicate that, if the duration of a pulsed fluctuation is much longer than the characteristic time to reach steady state (*ca.* 10 min in the standard DGT configuration), the transient effects can be neglected. Divergences between c_{DGT} and the metal concentration increase as the duration of successive concentration jumps decreases, although the errors may cancel out in the case of regular, periodical fluctuations.

When transient effects are negligible and the deployment takes place under perfect-sink conditions (linear accumulation regime), it can be seen that c_{DGT} corresponds to the time-weighted average of the labile concentration in the sample (Altier et al., 2019). This general result, together with the expression of c_{DGT} in terms of the concentration of real species, Equation (3), leads to a general equation for the interpretation of c_{DGT} in fluctuating systems. For a sample containing a mixture of h different ligands:

$$c_{DGT} = \langle c_M \rangle + \sum_{j=1}^{h} \frac{D_{M^jL}}{D_M} \left\langle \xi_j c_{M^jL} \right\rangle \approx \langle c_M \rangle + \sum_{j=1}^{h} \frac{D_{M^jL}}{D_M} \xi_j \left\langle c_{M^jL} \right\rangle \tag{19}$$

where angle brackets are used to denote averages over time. This equation can be seen as applying averages to Equation (3). The approximation in the last r.h.s. of this equation was carried out under the assumption that the dependence of the lability degrees with concentration is negligible (which is reasonable in excess of ligand conditions). In the particular case of only one strong ligand, where the free metal concentration can be neglected, the previous equation simplifies to:

$$c_{DGT} \approx \frac{D_{ML}}{D_M} \xi_{ML} \langle c_{ML} \rangle \tag{20}$$

Equation (20) allows to correct c_{DGT} in order to obtain a better estimation of the metal concentration in the sample when the diffusion coefficient and the lability degree of the complex are known, as has been shown for the case of Ni in solutions with nitrilotriacetic acid (Altier et al., 2019).

CONCLUSIONS

Diffusive Gradients in Thin-films has evolved, since the pioneering work of Davison and Zhang (1994), to become a mature technique for *in-situ* measurement of the availability of metal cations, anions and, more recently, organic compounds in natural waters, soils, and sediments. In addition to the simplicity of this technique, an attractive characteristic is its ability to determine labile concentrations from the knowledge of the diffusion coefficient of the target analytes and the thickness of the diffusive domain (DBL+filter+hydrogel layer). The diffusive domain regulates the metal flux arriving to the resin gel, so that the association rate constants between the target analyte and the resin sites do not influence the accumulation.

Deployment of DGTs in freshwater and seawater allowed the characterization of inorganic and organic trace metal complexes. Labile fractions varied for each element according to the conditions in the aquatic environment (load and nature of organic ligands, redox and pH conditions, ionic strength, etc.). Using DGT devices with different thicknesses (together with complementary techniques) opens the way to an even more detailed characterization of the trace metal availability in natural media. Mercury speciation has benefited from new binding agents and improved elution and detection of the accumulated amount, although more work is still needed.

Amongst further developments to improve the speciation of inorganic species in the aquatic environment, we can highlight: (1) lowering the detection limits for open ocean, by lowering the blanks or by increasing the amount accumulated on the resin e.g., by using ultra-thin diffusive domains; (2) better knowledge of major groups of organic ligands with performant organic analytical instruments; (3) more efficient binding materials for the different analytes; and (4) combination of complementary techniques to build up an integrated description of equilibrium and dynamic speciation.

AUTHOR CONTRIBUTIONS

JG contributed to modeling, validation, investigation, and writing. YG contributed to supervision, writing, data analysis, reviewing, and editing. JP contributed to supervision and writing. ML contributed to analysis, data analysis, and editing. CR-C contributed to modeling, software, and editing. CZ contributed to data analysis and visualization. WB contributed to supervision, writing, and experimental design. All authors contributed to the article and approved the submitted version.

FUNDING

JG, JP, and CR-C gratefully acknowledge support for this research from the Spanish Ministry of Science and Innovation (Project PID2019-107033GB-C21). YG and ML acknowledge FWO LEAD project (FWO AL911) and VUB SRP II. CZ is supported by Chinese Scholarship Council (PhD fellowship 201606190219).

REFERENCES

Akagi, H., and Nishimura, H. (1991). "Speciation of mercury in the environment," in Advances in Mercury Toxicology, eds T. Suzuki, N. Imura, and T. W. Clarkson (Boston, MA: Springer), 53–76. doi: 10.1007/978-1-4757-9071-9_3

Allan, I. J., Knutsson, J., Guigues, N., Mills, G. A., Fouillac, A. M., and Greenwood, R. (2007). Evaluation of the Chemcatcher and DGT passive samplers for monitoring metals with highly fluctuating water concentrations. *J. Environ. Monit.* 9, 672–681. doi: 10.1039/b701616f

Altier, A., Jimenez-Piedrahita, M., Rey-Castro, C., Cecilia, J., Galceran, J., and Puy, J. (2016). Accumulation of Mg to Diffusive Gradients in Thin Films (DGT) devices: kinetic and thermodynamic effects of the ionic strength. *Anal. Chem.* 88, 10245–10251. doi: 10.1021/acs.analchem.6b02961

Altier, A., Jimenez-Piedrahita, M., Uribe, R., Rey-Castro, C., Cecilia, J., Galceran, J., et al. (2018). Effects of a mixture of ligands on metal accumulation in diffusive gradients in thin films (DGT). *Environ. Chem.* 15, 183–193. doi: 10.1071/EN17232

Altier, A., Jimenez-Piedrahita, M., Uribe, R., Rey-Castro, C., Galceran, J., and Puy, J. (2019). Time weighted average concentrations measured with Diffusive Gradients in Thin films (DGT). *Anal. Chim. Acta* 1060, 114–124. doi: 10.1016/j.aca.2019.01.056

Amirbahman, A., Massey, D. I., Lotufo, G., Steenhaut, N., Brown, L. E., Biedenbach, J. M., et al. (2013). Assessment of mercury bioavailability to benthic macroinvertebrates using diffusive gradients in thin films (DGT). *Environ. Sci. Process Impacts* 15, 2104–2114. doi: 10.1039/c3em00355h

Averós, J. C., Llorens, J. P., and Uribe-Kaffure, R. (2020). Numerical simulation of non-linear models of reaction-diffusion for a DGT sensor. *Algorithms* 13:98. doi: 10.3390/a13040098

Baeyens, W., Bowie, A. R., Buesseler, K., Elskens, M., Gao, Y., Lamborg, C., et al. (2011). Size-fractionated labile trace elements in the Northwest Pacific and Southern Oceans. *Mar. Chem.* 126, 108–113. doi: 10.1016/j.marchem.2011.04.004

Baeyens, W., Gao, Y., Davison, W., Galceran, J., Leermakers, M., Puy, J., et al. (2018). *In situ* measurements of micronutrient dynamics in open seawater show that complex dissociation rates may limit diatom growth. *Sci. Rep.* 8:16125. doi: 10.1038/s41598-018-34465-w

Baeyens, W., Leermakers, M., Papina, T., Saprykin, A., Brion, N., Noyen, J., et al. (2003). Bioconcentration and biomagnification of mercury and methylmercury in North Sea and Scheldt estuary fish. *Arch. Environ. Contam. Toxicol.* 45, 498–508. doi: 10.1007/s00244-003-2136-4

Bakker, E., Pretsch, E., and Buhlmann, P. (2000). Selectivity of potentiometric ion sensors. *Anal. Chem.* 72, 1127–1133. doi: 10.1021/ac991146n

Balch, J., and Gueguen, C. (2015). Effects of molecular weight on the diffusion coefficient of aquatic dissolved organic matter and humic substances. *Chemosphere* 119, 498–503. doi: 10.1016/j.chemosphere.2014.07.013

Balistrieri, L. S., and Blank, R. G. (2008). Dissolved and labile concentrations of Cd, Cu, Pb, and Zn in the South Fork Coeur d'Alene River, Idaho: comparisons among chemical equilibrium models and implications for biotic ligand models. *Appl. Geochem.* 23, 3355–3371. doi: 10.1016/j.apgeochem.2008.06.031

Bradac, P., Behra, R., and Sigg, L. (2009). Accumulation of cadmium in periphyton under various freshwater speciation conditions. *Environ. Sci. Technol.* 43, 7291–7296. doi: 10.1021/es9013536

Bradley, M. A., Barst, B. D., and Basu, N. (2017). A review of mercury bioavailability in humans and fish. *Int. J. Environ. Res. Public Health* 14:169. doi: 10.3390/ijerph14020169

Bratkic, A., Klun, K., and Gao, Y. (2019). Mercury speciation in various aquatic systems using passive sampling technique of diffusive gradients in thin-film. *Sci. Total Environ.* 663, 297–306. doi: 10.1016/j.scitotenv.2019.01.241

Bretier, M., Dabrin, A., Billon, G., Mathon, B., Miège, C., and Coquery, M. (2020). To what extent can the biogeochemical cycling of mercury modulate the measurement of dissolved mercury in surface freshwaters by passive sampling? *Chemosphere* 248:126006. doi: 10.1016/j.chemosphere.2020.126006

Cattani, I., Spalla, S., Beone, G. M., Del Re, A. A. M., Boccelli, R., and Trevisan, M. (2008). Characterization of mercury species in soils by HPLC–ICP-MS and measurement of fraction removed by diffusive gradient in thin films. *Talanta* 74, 1520–1526. doi: 10.1016/j.talanta.2007.09.029

Chito, D., Weng, L., Galceran, J., Companys, E., Puy, J., van Riemsdijk, W. H., et al. (2012). Determination of free Zn^{2+} concentration in synthetic and natural samples with AGNES (Absence of Gradients and Nernstian Equilibrium Stripping) and DMT (Donnan Membrane Technique). *Sci. Total Environ.* 421–422, 238–244. doi: 10.1016/j.scitotenv.2012.01.052

Cindric, A. M., Marcinek, S., Garnier, C., Salaun, P., Cukrov, N., Oursel, B., et al. (2020). Evaluation of diffusive gradients in thin films (DGT) technique for speciation of trace metals in estuarine waters - a multimethodological approach. *Sci. Total Environ.* 721:137784. doi: 10.1016/j.scitotenv.2020.137784

Clarisse, O., Foucher, D., and Hintelmann, H. (2009). Methylmercury speciation in the dissolved phase of a stratified lake using the diffusive gradient in thin film technique. *Environ. Pollut.* 157, 987–993. doi: 10.1016/j.envpol.2008.10.012

Clarisse, O., and Hintelmann, H. (2006). Measurements of dissolved methylmercury in natural waters using diffusive gradients in thin film (DGT). *J. Environ. Monit.* 8, 1242–1247. doi: 10.1039/b614560d

Colaco, C. D., Yabuki, L. N. M., Rolisola, A. M., Menegario, A. A., de Almeida, E., Suarez, C. A., et al. (2014). Determination of mercury in river water by diffusive gradients in thin films using P81 membrane as binding layer. *Talanta* 129, 417–421. doi: 10.1016/j.talanta.2014.05.025

Companys, E., Galceran, J., Pinheiro, J. P., Puy, J., and Salaün, P. (2017). A review on electrochemical methods for trace metal speciation in environmental media. *Curr. Opin. Electrochem.* 3, 144–162. doi: 10.1016/j.coelec.2017.09.007

Davison, W., and Zhang, H. (1994). In situ speciation measurements of trace components in natural waters using thin-film gels. *Nature* 367, 546–548. doi: 10.1038/367546a0

Davison, W., and Zhang, H. (2012). Progress in understanding the use of diffusive gradients in thin films (DGT) – back to basics. *Environ. Chem.* 9, 1–13. doi: 10.1071/EN11084

Davison, W., and Zhang, H. (2016). "Principles of measurements in simple solutions," in Diffusive Gradients in Thin-Films for Environmental Measurements, ed W. Davison (Cambridge: Cambridge University Press), 24–27. doi: 10.1017/CBO9781316442654.003

Docekalova, H., and Divis, P. (2005). Application of diffusive gradient in thin films technique (DGT) to measurement of mercury in aquatic systems. *Talanta* 65, 1174–1178. doi: 10.1016/j.talanta.2004.08.054

dos Anjos, V. E., Abate, G., and Grassi, M. T. (2017). Determination of labile species of As(V), Ba, Cd, Co, Cr(III), Cu, Mn, Ni, Pb, Sr, V(V), and Zn in natural waters using diffusive gradients in thin-film (DGT) devices modified with montmorillonite. *Anal. Bioanal. Chem.* 409, 1963–1972. doi: 10.1007/s00216-016-0144-2

Dulaquais, G., Planquette, H., L'Helguen, S., Rijkenberg, M. J. A., and Boye, M. (2017). The biogeochemistry of cobalt in the Mediterranean Sea. *Global Biogeochem. Cycles* 31, 377–399. doi: 10.1002/2016GB005478

Dunn, R. J. K., Teasdale, P. R., Warnken, J., and Arthur, J. M. (2007). Evaluation of the *in situ*, time-integrated DGT technique by monitoring changes in heavy metal concentrations in estuarine waters. *Environ. Pollut.* 148, 213–220. doi: 10.1016/j.envpol.2006.10.027

Ebling, A. M., and Landing, W. M. (2015). Sampling and analysis of the sea surface microlayer for dissolved and particulate trace elements. *Mar. Chem.* 177, 134–142. doi: 10.1016/j.marchem.2015.03.012

Elias, G., Diez, S., Zhang, H., and Fontas, C. (2020). Development of a new binding phase for the diffusive gradients in thin films technique based on an ionic liquid for mercury determination. *Chemosphere* 245:125671. doi: 10.1016/j.chemosphere.2019.125671

Faganeli, J., Hines, M. E., Horvat, M., Falnoga, I., and Covelli, S. (2014). Methylmercury in the gulf of trieste (northern adriatic sea): from microbial sources to seafood consumers. *Food Technol. Biotechnol.* 52, 188–197.

Faganeli, J., Horvat, M., Covelli, S., Fajon, V., Logar, M., Lipej, L., et al. (2003). Mercury and methylmercury in the Gulf of Trieste (northern Adriatic Sea). *Sci. Total Environ.* 304, 315–326. doi: 10.1016/S0048-9697(02)00578-8

Fatin-Rouge, N., Starchev, K., and Buffle, J. (2004). Size effects on diffusion processes within agarose gels. *Biophys. J.* 86, 2710–2719. doi: 10.1016/S0006-3495(04)74325-8

Fernández-Gómez, C., Bayona, J. M., and Díez, S. (2014). Comparison of different types of diffusive gradient in thin film samplers for measurement of dissolved methylmercury in freshwaters. *Talanta* 129, 486–490. doi: 10.1016/j.talanta.2014.06.025

Fernández-Gómez, C., Bayona, J. M., and Díez, S. (2015). Diffusive gradients in thin films for predicting methylmercury bioavailability in freshwaters after photodegradation. *Chemosphere* 131, 184–191. doi: 10.1016/j.chemosphere.2015.02.060

Fernández-Gómez, C., Dimock, B., Hintelmann, H., and Díez, S. (2011). Development of the DGT technique for Hg measurement in water: comparison of three different types of samplers in laboratory assays. *Chemosphere* 85, 1452–1457. doi: 10.1016/j.chemosphere.2011.07.080

Galceran, J., Companys, E., Puy, J., Cecília, J., and Garcés, J. L. (2004). AGNES: a new electroanalytical technique for measuring free metal ion concentration. *J. Electroanal. Chem.* 566, 95–109. doi: 10.1016/j.jelechem.2003.11.017

Galceran, J., and Puy, J. (2015). Interpretation of diffusion gradients in thin films (DGT) measurements: a systematic approach. *Environ. Chem.* 12, 112–122. doi: 10.1071/EN14068

Galceran, J., Puy, J., Salvador, J., Cecília, J., and van Leeuwen, H. P. (2001). Voltammetric lability of metal complexes at spherical microelectrodes with various radii. *J. Electroanal. Chem.* 505, 85–94. doi: 10.1016/S0022-0728(01)00475-2

Gao, Y., De Canck, E., Leermakers, M., Baeyens, W., and Van Der Voort, P. (2011). Synthesized mercaptopropyl nanoporous resins in DGT probes for determining dissolved mercury concentrations. *Talanta* 87, 262–267. doi: 10.1016/j.talanta.2011.10.012

Gao, Y., De Craemer, S., and Baeyens, W. (2014). A novel method for the determination of dissolved methylmercury concentrations using diffusive gradients in thin films technique. *Talanta* 120, 470–474. doi: 10.1016/j.talanta.2013.12.023

Gao, Y., Zhou, C. Y., Gaulier, C., Bratkic, A., Galceran, J., Puy, J., et al. (2019). Labile trace metal concentration measurements in marine environments: from coastal to open ocean areas. *Trac. Trends Anal. Chem.* 116, 92–101. doi: 10.1016/j.trac.2019.04.027

Garmo, O. A., Naqvi, K. R., Royset, O., and Steinnes, E. (2006). Estimation of diffusive boundary layer thickness in studies involving diffusive gradients in thin films (DGT). *Anal. Bioanal. Chem.* 386, 2233–2237. doi: 10.1007/s00216-006-0885-4

Garmo, O. A., Royset, O., Steinnes, E., and Flaten, T. P. (2003). Performance study of diffusive gradients in thin films for 55 elements. *Anal. Chem.* 75, 3573–3580. doi: 10.1021/ac026374n

Gaulier, C., Zhou, C. Y., Gao, Y., Guo, W., Reichstadter, M., Ma, T. H., et al. (2021). Investigation on trace metal speciation and distribution in the Scheldt estuary. *Sci. Total Environ.* 757:143827 doi: 10.1016/j.scitotenv.2020.143827

Gimpel, J., Zhang, H., Davison, W., and Edwards, A. C. (2003). *In situ* trace metal speciation in lake surface waters using DGT, dialysis, and filtration. *Environ. Sci. Technol.* 37, 138–146. doi: 10.1021/es0200995

Goubert-Renaudin, S., Schneider, R., and Walcarius, A. (2007). Synthesis of new dithiocarbamate-based organosilanes for grafting on silica. *Tetrahedron Lett.* 48, 2113–2116. doi: 10.1016/j.tetlet.2007.01.119

Guo, W., Van Langenhove, K., Vandermarken, T., Denison, M. S., Elskens, M., Baeyens, W., et al. (2019). *In situ* measurement of estrogenic activity in various aquatic systems using organic diffusive gradients in thin-film coupled with ERE-CALUX bioassay. *Environ. Int.* 127, 13–20. doi: 10.1016/j.envint.2019.03.027

Han, S. P., Zhang, Y., Masunaga, S., Zhou, S. Y., and Naito, W. (2014). Relating metal bioavailability to risk assessment for aquatic species: Daliao River watershed, China. *Environ. Pollut.* 189, 215–222. doi: 10.1016/j.envpol.2014.02.023

Hines, M. E., Faganeli, J., Adatto, I., and Horvat, M. (2006). Microbial mercury transformations in marine, estuarine and freshwater sediment downstream of the Idrija Mercury Mine, Slovenia. *Appl. Geochem.* 21, 1924–1939. doi: 10.1016/j.apgeochem.2006.08.008

Hong, Y. S., Rifkin, E., and Bouwer, E. J. (2011). Combination of diffusive gradient in a thin film probe and IC-ICP-MS for the Simultaneous Determination of CH_3Hg^+ and Hg^{2+} in oxic water. *Environ. Sci. Technol.* 45, 6429–6436. doi: 10.1021/es200398d

Horowitz, A. J., Elrick, K. A., and Colberg, M. R. (1992). The effect of membrane filtration artifacts on dissolved trace-element concentrations. *Water Res.* 26, 753–763. doi: 10.1016/0043-1354(92)90006-P

Horvat, M., Covelli, S., Faganeli, J., Logar, M., Mandić, V., Rajar, R., et al. (1999). Mercury in contaminated coastal environments; a case study: the Gulf of Trieste. *Sci. Total Environ.* 237–238, 43–56. doi: 10.1016/S0048-9697(99)00123-0

Howard, A. G., and Khdary, N. H. (2004). Spectrofluorimetric determination of surface-bound thiol groups and its application to the analysis of thiol-modified silicas. *Analyst* 129, 860–863. doi: 10.1039/b407566h

Huang, J., Bennett, W. W., Teasdale, P. R., Kankanamge, N. R., and Welsh, D. T. (2017). A modified DGT technique for the simultaneous measurement of dissolved inorganic nitrogen and phosphorus in freshwaters. *Anal. Chim. Acta* 988, 17–26. doi: 10.1016/j.aca.2017.08.024

Huang, J. Y., Bennett, W. W., Welsh, D. T., and Teasdale, P. R. (2016). Determining time-weighted average concentrations of nitrate and ammonium in freshwaters using DGT with ion exchange membrane-based binding layers. *Environ. Sci. Process Impacts* 18, 1530–1539. doi: 10.1039/C6EM00260A

Jimenez-Piedrahita, M., Altier, A., Cecilia, J., Puy, J., Galceran, J., Rey-Castro, C., et al. (2017). Extending the use of Diffusive Gradients in Thin Films (DGT) to solutions where competition, saturation, and kinetic effects are not negligible. *Anal. Chem.* 89, 6567–6574. doi: 10.1021/acs.analchem.7b00704

Kim, M. S., Choi, M. S., and Kim, C. K. (2016). Monitoring trace metals in seawater using a diffusive gradient in thin film probe in Ulsan Bay, East Sea, Korea: comparison with transplanted mussels. *Ocean Sci. J.* 51, 169–182. doi: 10.1007/s12601-016-0015-y

Lansens, P., Meuleman, C., Leermakers, M., and Baeyens, W. (1990). Determination of methylmercury in natural waters by headspace gas chromatography with microwave-induced plasma detection after preconcentration on a resin containing dithiocarbamate groups. *Anal. Chim. Acta.* 234, 417–424. doi: 10.1016/S0003-2670(00)83585-0

Levy, J. L., Zhang, H., Davison, W., Galceran, J., and Puy, J. (2012). Kinetic signatures of metals in the presence of suwannee river fulvic acid. *Environ. Sci. Technol.* 46, 3335–3342. doi: 10.1021/es2043068

Liu, J., Feng, X., Qiu, G., Anderson, C. W. N., and Yao, H. (2012). Prediction of methyl mercury uptake by rice plants (*Oryza sativa* L.) using the diffusive gradient in thin films technique. *Environ. Sci. Technol.* 46, 11013–11020. doi: 10.1021/es302187t

Macoustra, G., Holland, A., Stauber, J., and Jolley, D. F. (2019). Effect of various natural dissolved organic carbon on copper lability and toxicity to the tropical freshwater microalga Chlorella sp. *Environ. Sci. Technol.* 53, 2768–2777. doi: 10.1021/acs.est.8b04737

Mason, R. P. (1995). "The bioaccumulation of mercury, methylmercury and other toxic elements into pelagic and benthic organisms," in *Coastal and Estuarine Risk Assessment*, eds N. C. Newman, M. H. Roberts, and R. C. Hale (Boca Raton, FL: Lewis Publishers), 127–149.

Menegario, A. A., Yabuki, L. N. M., Luko, K. S., Williams, P. N., and Blackburn, D. M. (2017). Use of diffusive gradient in thin films for *in situ* measurements: a review on the progress in chemical fractionation, speciation and bioavailability of metals in waters. *Anal. Chim. Acta* 983, 54–66. doi: 10.1016/j.aca.2017.06.041

Merritt, K. A., and Amirbahman, A. (2007). Mercury mobilization in estuarine sediment porewaters: a diffusive gel time-series study. *Environ. Sci. Technol.* 41, 717–722. doi: 10.1021/es061659t

Minagawa, K., Takizawa, Y., and Kifune, I. (1980). Determination of very low levels of inorganic and organic mercury in natural waters by cold-vapor atomic absorption spectrometry after preconcentration on a chelating resin. *Anal. Chim. Acta* 115, 103–110. doi: 10.1016/S0003-2670(01)93147-2

Mongin, S., Uribe, R., Puy, J., Cecilia, J., Galceran, J., Zhang, H., et al. (2011). Key role of the resin layer thickness in the lability of complexes measured by DGT. *Environ. Sci. Technol.* 45, 4869–4875. doi: 10.1021/es200609v

Mongin, S., Uribe, R., Rey-Castro, C., Cecilia, J., Galceran, J., and Puy, J. (2013). Limits of the linear accumulation regime of DGT sensors. *Environ. Sci. Technol.* 47, 10438–10445. doi: 10.1021/es400609y

Morel, F. M. M., Kraepiel, A. M. L., and Amyot, M. (1998). The chemical cycle and bioaccumulation of mercury. *Annu. Rev. Ecol. Syst.* 29, 543–566. doi: 10.1146/annurev.ecolsys.29.1.543

Noh, S., Hong, Y. S., and Han, S. (2016). Application of diffusive gradients in thin films and core centrifugation methods to determine inorganic mercury and monomethylmercury profiles in sediment porewater. *Environ. Toxicol. Chem.* 35, 348–356. doi: 10.1002/etc.3193

Noh, S. Kim, Y.-h., Kim, H., Seok, K.-s., Park, M., Bailon, M. X., et al. (2019). The performance of diffusive gradient in thin film probes for the long-term monitoring of trace level total mercury in water. *Environ. Monit. Assess.* 192. doi: 10.1007/s10661-019-7966-2

Oken, E., Wright, R. O., Kleinman, K. P., Bellinger, D., Amarasiriwardena, C. J., Hu, H., et al. (2005). Maternal fish consumption, hair mercury, and infant cognition in a U.S. *Cohort. Environ. Health Perspect.* 113, 1376–1380. doi: 10.1289/ehp.8041

Pelcová, P., Dočekalová, H., and Kleckerová, A. (2015). Determination of mercury species by the diffusive gradient in thin film technique and liquid chromatography – atomic fluorescence spectrometry after microwave extraction. *Anal. Chim. Acta* 866, 21–26. doi: 10.1016/j.aca.2015.01.043

Pesavento, M., Alberti, G., and Biesuz, R. (2009). Analytical methods for determination of free metal ion concentration, labile species fraction and metal complexation capacity of environmental waters: a review. *Anal. Chim. Acta* 631, 129–141. doi: 10.1016/j.aca.2008.10.046

Pohl, P. (2006). Application of ion-exchange resins to the fractionation of metals in water. *Trac. Trends Anal. Chem.* 25, 31–43. doi: 10.1016/j.trac.2005.04.020

Pohl, P., and Prusisz, B. (2004). Preconcentration of mercury using duolite GT-73 in the analysis of water samples by inductively coupled plasma atomic emission spectrometry. *Anal. Sci.* 20, 1367–1370. doi: 10.2116/analsci.20.1367

Puy, J., and Galceran, J. (2017). Theoretical aspects of dynamic metal speciation with electrochemical techniques. *Curr. Opin. Electrochem.* 1, 80–87. doi: 10.1016/j.coelec.2017.01.001

Puy, J., Galceran, J., Cruz-Gonzalez, S., David, C. A., Uribe, R., Lin, C., et al. (2014). Metal accumulation in DGT: impact of ionic strength and kinetics of dissociation of complexes in the resin domain. *Anal. Chem.* 86, 7740–7748. doi: 10.1021/ac501679m

Puy, J., Galceran, J., and Rey-Castro, C. (2016). "Interpreting the DGT measurement: speciation and dynamics," in Diffusive Gradients in Thin-Films for *Environmental Measurements*, W. Davison (Cambridge: Cambridge University Press), 93–122. doi: 10.1017/CBO9781316442654.006

Reichstädter, M., Divis, P., Abdulbur-Alfakhoury, E., and Gao, Y. (2020). Simultaneous determination of mercury, cadmium and lead in fish sauce using Diffusive Gradients in Thin-films technique. *Talanta* 217:121059. doi: 10.1016/j.talanta.2020.121059

Reichstädter, M., Gao, Y., Diviš, P., Ma, T., Gaulier, C., and Leermakers, M. (2021). Cysteine-modified silica resin in DGT samplers for mercury and trace metals assessment. *Chemosphere* 263:128320. doi: 10.1016/j.chemosphere.2020.128320

Ren, M., Wang, Y., Ding, S., Yang, L., Sun, Q., and Zhang, L. (2018). Development of a new diffusive gradient in the thin film (DGT) method for the simultaneous measurement of CH_3Hg^+ and Hg_2^+. *New J. Chem.* 42, 7976–7983. doi: 10.1039/C8NJ00211H

Scally, S., Davison, W., and Zhang, H. (2006). Diffusion coefficients of metals and metal complexes in hydrogels used in diffusive gradients in thin films. *Anal. Chim. Acta* 558, 222–229. doi: 10.1016/j.aca.2005.11.020

Schaefer, J. K., and Morel, F. M. M. (2009). High methylation rates of mercury bound to cysteine by Geobacter sulfurreducens. *Nat. Geosci.* 2, 123–126. doi: 10.1038/ngeo412

Schintu, M., Marras, B., Durante, L., Meloni, P., and Contu, A. (2010). Macroalgae and DGT as indicators of available trace metals in marine coastal waters near a lead-zinc smelter. *Environ. Monit. Assess.* 167, 653–661. doi: 10.1007/s10661-009-1081-8

Shiva, A. H., Teasdale, P. R., Bennett, W. W., and Welsh, D. T. (2015). A systematic determination of diffusion coefficients of trace elements in open and restricted diffusive layers used by the diffusive gradients in a thin film technique. *Anal. Chim. Acta* 888, 146–154. doi: 10.1016/j.aca.2015.07.027

Slovák, Z. M., SmrŽ, Dočekal, B., and Slováková, S. (1979). Analytical behaviour of hydrophilic glycolmethacrylate gels with bound thiol groups. *Anal. Chim. Acta* 111, 243–249. doi: 10.1016/S0003-2670(01)93267-2

Sondergaard, J., Bach, L., and Gustavson, K. (2014). Measuring bioavailable metals using diffusive gradients in thin films (DGT) and transplanted seaweed (*Fucus vesiculosus*), blue mussels (*Mytilus edulis*) and sea snails (*Littorina saxatilis*) suspended from monitoring buoys near a former lead-zinc mine in West Greenland. *Mar. Pollut. Bull.* 78, 102–109. doi: 10.1016/j.marpolbul.2013.10.054

Sook-Young, K., Jae-Suk, L., Young-Man, K., and Beom-Suk, C. (2001). A study on the desorption behaviors of some heavy metals on duolite GT-73 chelating resin. *Anal. Sci. Technol.* 14, 530–534.

Stockdale, A., Tipping, E., Hamilton-Taylor, J., and Lofts, S. (2011). Trace metals in the open oceans: speciation modelling based on humic-type ligands. *Environ. Chem.* 8, 304–319. doi: 10.1071/EN11004

Stockdale, A., Tipping, E., and Lofts, S. (2015). Dissolved trace metal speciation in estuarine and coastal waters: comparison of WHAM/model VII predictions with analytical results. *Environ. Toxicol. Chem.* 34, 53–63. doi: 10.1002/etc.2789

Stockdale, A., Tipping, E., Lofts, S., and Mortimer, R. J. G. (2016). Effect of ocean acidification on organic and inorganic speciation of trace metals. *Environ. Sci. Technol.* 50, 1906–1913. doi: 10.1021/acs.est.5b05624

Storelli, M. M., Stuffler, R. G., and Marcotrigiano, G. O. (2002). Total and methylmercury residues in tuna-fish from the Mediterranean sea. *Food Addit. Contam. A Chem.* 19, 715–720. doi: 10.1080/02652030210153569

Tafurt-Cardona, M., Eismann, C. E., Suarez, C. A., Menegario, A. A., Luko, K. S., and Sargentini, E. (2015). *In situ* selective determination of methylmercury in river water by diffusive gradient in thin films technique (DGT) using baker's yeast (*Saccharomyces cerevisiae*) immobilized in agarose gel as binding phase. *Anal. Chim. Acta* 887, 38–44. doi: 10.1016/j.aca.2015.07.035

Temminghoff, E. J. M., Plette, A. C. C., van Eck, R., and van Riemsdijk, W. H. (2000). Determination of the chemical speciation of trace metals in aqueous systems by the Wageningen Donnan Membrane Technique. *Anal. Chim. Acta* 417, 149–157. doi: 10.1016/S0003-2670(00)00935-1

Town, R. M., and van Leeuwen, H. P. (2019). Stripping chronopotentiometry at scanned deposition potential (SSCP): an effective methodology for dynamic speciation analysis of nanoparticulate metal complexes. *J. Electroanal. Chem.* 853:113530. doi: 10.1016/j.jelechem.2019.113530

Turull, M., Elias, G., Fontas, C., and Diez, S. (2017a). Exploring new DGT samplers containing a polymer inclusion membrane for mercury monitoring. *Environ. Sci. Pollut. Res.* 24, 10919–10928. doi: 10.1007/s11356-016-6813-z

Turull, M., Fontas, C., and Diez, S. (2019). Diffusive gradient in thin films with open and restricted gels for predicting mercury uptake by plants. *Environ. Chem. Lett.* 17, 1353–1358. doi: 10.1007/s10311-019-00864-2

Turull, M., Grmanova, G., Dago, A., Arino, C., Diez, S., Diaz-Cruz, J. M., et al. (2017b). Phytochelatin synthesis in response to Hg uptake in, aquatic plants near a chlor-alkali factory. *Chemosphere* 176, 74–80. doi: 10.1016/j.chemosphere.2017.02.092

Unsworth, E. R., Warnken, K. W., Zhang, H., Davison, W., Black, F., Buffle, J., et al. (2006). Model predictions of metal speciation in freshwaters compared to measurements by *in situ* techniques. *Environ. Sci. Technol.* 40, 1942–1949. doi: 10.1021/es051246c

Uribe, R., Mongin, S., Puy, J., Cecilia, J., Galceran, J., Zhang, H., et al. (2011). Contribution of partially labile complexes to the DGT metal flux. *Environ. Sci. Technol.* 45, 5317–5322. doi: 10.1021/es200610n

van Leeuwen, H. P., and Town, R. M. (2003). Stripping chronopotentiometry at scanned deposition potential (SSCP) Part 3. Irreversible electrode reactions. *J. Electroanal. Chem.* 556, 93–102. doi: 10.1016/S0022-0728(03)00334-6

van Leeuwen, H. P., Town, R. M., Buffle, J., Cleven, R., Davison, W., Puy, J., et al. (2005). Dynamic speciation analysis and bioavailability of metals in aquatic systems. *Environ. Sci. Technol.* 39, 8545–8585. doi: 10.1021/es050404x

Vannuci-Silva, M., de Souza, J. M., de Oliveira, F. F., de Araujo, M. A. G., Francioni, E., Eismann, C. E., et al. (2017). Bioavailability of

metals at a Southeastern Brazilian coastal area of high environmental concern under anthropic influence: evaluation using transplanted bivalves (*Nodipecten nodosus*) and the DGT technique. *Water Air Soil. Pollut.* 228:222. doi: 10.1007/s11270-017-3387-4

Waeles, M., Tanguy, V., Lespes, G., and Riso, R. D. (2008). Behaviour of colloidal trace metals (Cu, Pb and Cd) in estuarine waters: an approach using frontal ultrafiltration (UF) and stripping chronopotentiometric methods (SCP). *Estuar. Coast Shelf Sci.* 80, 538–544. doi: 10.1016/j.ecss.2008.09.010

Warnken, K. W., Davison, W., and Zhang, H. (2008). Interpretation of *in situ* speciation measurements of inorganic and organically complexed trace metals in freshwater by DGT. *Environ. Sci. Technol.* 42, 6903–6909. doi: 10.1021/es800359n

Warnken, K. W., Davison, W., Zhang, H., Galceran, J., and Puy, J. (2007). *In situ* measurements of metal complex exchange kinetics in freshwater. *Environ. Sci. Technol.* 41, 3179–3185. doi: 10.1021/es062474p

Warnken, K. W., Lawlor, A. J., Lofts, S., Tipping, E., Davison, W., and Zhang, H. (2009). *In situ* speciation measurements of trace metals in headwater streams. *Environ. Sci. Technol.* 43, 7230–7236. doi: 10.1021/es900112w

Warnken, K. W., Zhang, H., and Davison, W. (2005). Trace metal measurements in low ionic strength synthetic solutions by diffusive gradients in thin films. *Anal. Chem.* 77, 5440–5446. doi: 10.1021/ac050045o

Warnken, K. W., Zhang, H., and Davison, W. (2006). Accuracy of the diffusive gradients in thin-films technique: diffusive boundary layer and effective sampling area considerations. *Anal. Chem.* 78, 3780–3787. doi: 10.1021/ac060139d

Weng, L. P., Vega, F. A., and van Riemsdijk, W. H. (2011). Strategies in the application of the Donnan membrane technique. *Environ. Chem.* 8, 466–474. doi: 10.1071/EN11021

Wuttig, K., Townsend, A. T. P., van der Merwe, Gault-Ringold, M., Holmes, T., Schallenberg, C., Latour, P., et al. (2019). Critical evaluation of a seaFAST system for the analysis of trace metals in marine samples. *Talanta* 197, 653–668. doi: 10.1016/j.talanta.2019.01.047

Zhang, H., and Davison, W. (1995). Performance characteristics of diffusion gradients in thin films for the *in situ* measurement of trace metals in aqueous solution. *Anal. Chem.* 67, 3391–3400. doi: 10.1021/ac00115a005

Zhang, H., and Davison, W. (1999). Diffusional characteristics of hydrogels used in DGT and DET techniques. *Anal. Chim. Acta* 398, 329–340. doi: 10.1016/S0003-2670(99)00458-4

Zhang, H., and Davison, W. (2000). Direct *in situ* measurements of labile inorganic and organically bound metal species in synthetic solutions and natural waters using diffusive gradients in thin films. *Anal. Chem.* 72, 4447–4457. doi: 10.1021/ac0004097

Zhang, H., and Davison, W. (2015). Use of diffusive gradients in thin-films for studies of chemical speciation and bioavailability. *Environ. Chem.* 12, 85–101. doi: 10.1071/EN14105

Zhao, J. J., Cornett, R. J., and Chakrabarti, C. L. (2020). Assessing the uranium DGT-available fraction in model solutions. *J. Hazard. Mater.* 384. doi: 10.1016/j.jhazmat.2019.121134

Zhu, Y., and Gueguen, C. (2016). Evaluation of free/labile concentrations of trace metals in Athabasca oil sands region streams (Alberta, Canada) using diffusive gradient in thin films and a thermodynamic equilibrium model. *Environ. Pollut.* 219, 1140–1147. doi: 10.1016/j.envpol.2016.09.018

Conflict of Interest: The authors declare that the research was conducted in the absence of any commercial or financial relationships that could be construed as a potential conflict of interest.

Advantages of publishing in Frontiers

OPEN ACCESS
Articles are free to read for greatest visibility and readership

FAST PUBLICATION
Around 90 days from submission to decision

HIGH QUALITY PEER-REVIEW
Rigorous, collaborative, and constructive peer-review

TRANSPARENT PEER-REVIEW
Editors and reviewers acknowledged by name on published articles

Frontiers
Avenue du Tribunal-Fédéral 34
1005 Lausanne | Switzerland

Visit us: www.frontiersin.org
Contact us: frontiersin.org/about/contact

REPRODUCIBILITY OF RESEARCH
Support open data and methods to enhance research reproducibility

DIGITAL PUBLISHING
Articles designed for optimal readership across devices

FOLLOW US
@frontiersin

IMPACT METRICS
Advanced article metrics track visibility across digital media

EXTENSIVE PROMOTION
Marketing and promotion of impactful research

LOOP RESEARCH NETWORK
Our network increases your article's readership